NATO Science for Peace and Security Series - B:
Physics and Biophysics

Boron Rich Solids

Sensors, Ultra High Temperature Ceramics, Thermoelectrics, Armor

Edited by
Nina Orlovskaya
Mykola Lugovy

Springer

NATO OTAN

This publication is supported by:

The NATO Science for Peace and Security Programme

Boron Rich Solids

NATO Science for Peace and Security Series

This Series presents the results of scientific meetings supported under the NATO Programme: Science for Peace and Security (SPS).

The NATO SPS Programme supports meetings in the following Key Priority areas: (1) Defence Against Terrorism; (2) Countering other Threats to Security and (3) NATO, Partner and Mediterranean Dialogue Country Priorities. The types of meeting supported are generally "Advanced Study Institutes" and "Advanced Research Workshops". The NATO SPS Series collects together the results of these meetings. The meetings are co-organized by scientists from NATO countries and scientists from NATO's "Partner" or "Mediterranean Dialogue" countries. The observations and recommendations made at the meetings, as well as the contents of the volumes in the Series, reflect those of participants and contributors only; they should not necessarily be regarded as reflecting NATO views or policy.

Advanced Study Institutes (ASI) are high-level tutorial courses intended to convey the latest developments in a subject to an advanced-level audience

Advanced Research Workshops (ARW) are expert meetings where an intense but informal exchange of views at the frontiers of a subject aims at identifying directions for future action

Following a transformation of the programme in 2006 the Series has been re-named and re-organised. Recent volumes on topics not related to security, which result from meetings supported under the programme earlier, may be found in the NATO Science Series.

The Series is published by IOS Press, Amsterdam, and Springer, Dordrecht, in conjunction with the NATO Public Diplomacy Division.

Sub-Series

A.	Chemistry and Biology	Springer
B.	Physics and Biophysics	Springer
C.	Environmental Security	Springer
D.	Information and Communication Security	IOS Press
E.	Human and Societal Dynamics	IOS Press

http://www.nato.int/science
http://www.springer.com
http://www.iospress.nl

Series B: Physics and Biophysics

Boron Rich Solids

Sensors, Ultra High Temperature Ceramics, Thermoelectrics, Armor

edited by

Nina Orlovskaya
Department of Mechanical, Materials,
and Aerospace Engineering
University of Central Florida
Orlando, U.S.A.

and

Mykola Lugovy
Institute for Problems of Materials Science
Kyiv, Ukraine

Springer

Published in cooperation with NATO Public Diplomacy Division

Proceedings of the NATO Advanced Research Workshop on
Boron Rich Solids: Sensors for Biological and Chemical Detection,
Ultra High Temperature Ceramics, Thermoelectrics, Armor
Orlando, Florida, USA
14-18 December 2009

Library of Congress Control Number: 2010936469

ISBN 978-90-481-9823-8 (PB)
ISBN 978-90-481-9817-7 (HB)
ISBN 978-90-481-9818-4 (e-book)

Published by Springer,
P.O. Box 17, 3300 AA Dordrecht, The Netherlands.

www.springer.com

Printed on acid-free paper

CONTENTS

LIST OF CONTRIBUTORS

A. Bales
Fraunhofer-Institut für Keramische Technologien und Systeme,
IKTS, Winterbergstrasse 28, D-01277 Dresden, Germany

L.B. Begrambekov
National Research Nuclear University - MEPhI, 31 Kashirskoye shosse,
115409 Moscow, Russia

A. Bellosi
Institute of Science and Technology for Ceramics, Via Granarolo 64,
I-48018 Faenza, Italy

M. Belogolovskii
Donetsk Institute for Physics and Engineering, 83114 Donetsk,
Ukraine

R.G. Blair
University of Central Florida, 4000 Central Florida Blvd, Orlando,
FL 32816, USA

O.I. Buzhinsky
SRC RF TRINITI, Pushkovyh Str., Building 2, 142190 Troitsk,
Russia

C. Carpenter
University of Central Florida, 4000 Central Florida Blvd, Orlando,
FL 32816, USA

M. Donohue
University of Central Florida, 4000 Central Florida Blvd, Orlando,
FL 32816, USA

D.D. Fabbriche
Institute of Science and Technology for Ceramics, Via Granarolo 64,
I-48018 Faenza, Italy

I. Felner
The Racah Institute of Physics, The Hebrew University of Jerusalem,
91904 Jerusalem, Israel

V.A. Gasparov
Institute of Solid State Physics, 2 Institutskaya Str., 142432 Chernogolovka, Russia

R. Gautier
University of Rennes 1, Avenue du General Leclerc, 35042 Rennes Cedex, France

D. Ghosh
University of Florida, 231 MAE-A, P.O. Box 116250, Gainesville, FL 32611, USA

J. Gou
University of Central Florida, 4000 Central Florida Blvd, Orlando, FL 32816, USA

T. Graule
Empa, Ueberlandstrasse 129, 8600 Duebendorf, Switzerland

S. Guicciardi
Institute of Science and Technology for Ceramics, Via Granarolo 64, I-48018 Faenza, Italy

J.-F. Halet
University of Rennes 1, Avenue du General Leclerc, 35042 Rennes Cedex, France

M. Hebbache
University of Paris 7, 4, rue Elsa Morante, 75205 Paris Cedex 13, France

M. Herrmann
Fraunhofer-Institut für Keramische Technologien und Systeme, IKTS, Winterbergstrasse 28, D-01277 Dresden, Germany

J. Kuebler
Empa, Ueberlandstrasse 129, 8600 Duebendorf, Switzerland

S. Lassoued
University of Rennes 1, Avenue du General Leclerc, 35042 Rennes Cedex, France

F. Liang
University of Central Florida, 4000 Central Florida Blvd, Orlando,
FL 32816, USA

J. E. Lowther
University of the Witwatersrand, 1 Jan Smuts Avenue, Braamfontein 2000,
Johannesburg, South Africa

M. Lugovy
Institute for Problems of Materials Science, 3 Krzhizhanivskii Str.,
03142 Kyiv, Ukraine

V. Medri
Institute of Science and Technology for Ceramics, Via Granarolo 64,
I-48018 Faenza, Italy

C. Melandri
Institute of Science and Technology for Ceramics, Via Granarolo 64,
I-48018 Faenza, Italy

F. Monteverde
Institute of Science and Technology for Ceramics, Via Granarolo 64,
I-48018 Faenza, Italy

T. Mori
National Institute for Material Science (NIMS), 1-1 Namiki, Tsukuba-shi,
Ibaraki 305-0044, Japan

Yu. Moriya
Department of Nano Science and Engineering, Waseda University,
3-4-1 Okubo, Shinjuku-ku, Tokyo 169-8555, Japan

A. R. Oganov
Department of Geosciences, Department of Physics and Astronomy,
and New York Center for Computational Sciences, Stony Brook University,
Stony Brook, New York 11794-2100, USA

N. Orlovskaya
University of Central Florida, 4000 Central Florida Blvd, Orlando,
FL 32816, USA

C. Oshima
Department of Nano Science and Engineering, Waseda University,
3-4-1 Okubo, Shinjuku-ku, Tokyo 169-8555, Japan

S. Otani
National Institute for Material Science, 1-1 Namiki, Tsukuba-shi,
Ibaraki 305-0044, Japan

V.G. Otroshchenko
SRC RF TRINITI, Pushkovyh Str., Building 2, 142190 Troitsk,
Russia

J. Raethel
Fraunhofer-Institut für Keramische Technologien und Systeme,
IKTS, Winterbergstrasse 28, D-01277 Dresden, Germany

L. Sartinska
Institute for Problems of Materials Science, 3 Krzhizhanivskii Str.,
03142 Kyiv, Ukraine

K. Sempf
Fraunhofer-Institut für Keramische Technologien und Systeme,
IKTS, Winterbergstrasse 28, D-01277 Dresden, Germany

D. Sciti
Institute of Science and Technology for Ceramics, Via Granarolo 64,
I-48018 Faenza, Italy

V. Shaternik
Institute of Metal Physics, 36 Vernadskogo Blvd, 03142 Kyiv,
Ukraine

I. Sigalas
University of the Witwatersrand, 1 Jan Smuts Avenue, Braamfontein 2000,
Johannesburg, South Africa

L. Silvestroni
Institute of Science and Technology for Ceramics, Via Granarolo 64,
I-48018 Faenza, Italy

V. Slyunyayev
Institute for Problems of Materials Science, 3 Krzhizhanivskii Str.,
03142 Kyiv, Ukraine

V. Subbotin
Institute for Problems of Materials Science, 3 Krzhizhanivskii Str., 03142 Kyiv, Ukraine

G. Subhash
University of Florida, 231 MAE-A, P.O. Box 116250, Gainesville, FL 32611, USA

M. Thiele
Fraunhofer-Institut für Keramische Technologien und Systeme, IKTS, Winterbergstrasse 28, D-01277 Dresden, Germany

A. Tillekaratne
Department of Chemistry, University of Illinois at Chicago, 845 W. Taylor St., Chicago, IL 60607, USA

M. Trenary
Department of Chemistry, University of Illinois at Chicago, 845 W. Taylor St., Chicago, IL 60607, USA

H. Werheit
University of Duisburg-Essen, Lotharstr. 1, D-47048 Duisburg, Germany

T. Yorisaki
Department of Chemistry, University of Illinois at Chicago, 845 W. Taylor St., Chicago, IL 60607, USA

A. Zakharov
SRC RF TRINITI, Pushkovyh Str., Building 2, 142190 Troitsk, Russia

D. Živković
Technical Faculty in Bor, University of Belgrad, 12 Vojske Jugoslavije, 19210 Bor, Serbia

PREFACE

The objective of this book is to discuss the current status of research and development of boron-rich solids as sensors, ultra high temperature ceramics, thermoelectric, and armor. Novel biological and chemical sensors made of stiff and light weight boron-rich solids are very exciting and efficient for application in medical diagnoses, environmental surveillance and pathogen and biological/chemical terrorism agent detection. Ultra high temperature ceramic composites exhibit excellent oxidation and corrosion resistance for hypersonic vehicles' application. Boron-rich solids are also promising candidates for high temperature thermoelectric conversion. Armor is another very important application of boron-rich solids since most of them exhibit very high hardness, which makes them perfect candidates with high resistance to ballistic impact.
The following topic areas are presented:

- boron rich solids: science and technology;
- synthesis and sintering strategies of boron rich solids;
- microcantilever sensors;
- screening of the possible boron based thermoelectric conversion materials;
- ultra high temperature ZrB_2 and HfB_2 based composites
- magnetic, transport and high-pressure properties of boron rich solids;
- restrictions of the sensor's dimensions for chemical detection;
- armor

The members of the International Program Committee of NATO ARW "Boron Rich Solids: Sensors for Biological and Chemical Detectio, Ultra-High Temperature Composites, Thermoelectrics, Armor" were Nina Orlovskaya (UCF, USA), Mykola Lugovy (IPMS, Ukraine), Lynnette Madsen (NSF, USA), Jay Kapat (UCF, USA), Masa Ishigami (UCF, USA), Richard Blair (UCF, USA), Marcel Ilie (UCF, USA), Seetha Raghavan (UCF, USA), Ghatu Subhash (UF, USA), and Jean-Francois Halet (University of Rennes, France).

Nina Orlovskaya, Mykola Lugovy
Co-Directors, NATO ARW
"Boron Rich Solids: Sensors for Biological and Chemical Detection,
Ultra-High Temperature Composites, Thermoelectrics, Armor"

ACKNOWLEDGMENT

We would like to thank NATO for the financial support that made this ARW possible. In particular, we would like to thank Dr. F. Pedrazzini, Programme Director, Physical and Engineering Science and Technology for considering our application in his programme as well as his advice, understanding, and support during the organization of the meeting.

We would like to thank Dr. Lynnette D. Madsen, The Program Director of Ceramics at the Division of Materials Research, at the National Science Foundation, for her support for research in boron rich solids, where one of the Co-Directors of the Workshop (N.O.) was supported by the project 0748364 "CAREER: Hard and Tough Boron Rich Ceramic Laminates Designed to Contain Thermal Residual Stresses". We would also like to thank the Department of Mechanical, Materials, and Aerospace Engineering at the University of Central Florida, which provided major resources to have this workshop succeed.

Our thanks and appreciation is extended to the Interim Chairs of the Department, Professor D. Nicholson and Professor L. Chaw whose contribution to the workshop was very important. We are also very grateful for the contributions from Professor J. Kapat, Professor S. Raghavan, Professor R. Blair, Professor M. Ishigami, and Professor M. Ilie, for their organization and participation in the workshop.

A special thank you goes to Mrs. S. Gavarrete, Mechanical, Materials, and Aerospace Engineering Department, who was the one who definitely made this workshop happen. Her professionalism, knowledge, and organizational skills help to make this workshop a huge success.

We also would like to express our gratitude to Mrs. Patricia Colyer, Mr. William Scaggs, Brian James Wirth, Andrew Stagner, and Anay Lopez, from the Mechanical, Materials and Aerospace Engineering Department at the University of Central Florida for their help with hotels and transportation reservations, and for their abilities and willingness to create an atmosphere conductive for the success of the meeting.

Our thanks and appreciations are also extended to Mr. Luis Miguel Ayalde, Mechanical, Materials, and Aerospace Engineering, for his significant help with all the editorial work on the ARW proceedings, to Mrs. Laurianne Torres, Office of Research, University of Central Florida, for doing and excellent job in handling the budget.

Last but not least we would like to thank all the speakers, session chairs, and participants of the workshop for their excellent contributions that made this meeting a success.

Nina Orlovskaya, Mykola Lugovy
Co-Directors, NATO ARW
“Boron Rich Solids: Sensors for Biological and Chemical Detection,
Ultra-High Temperature Composites, Thermoelectrics, Armor”

BORON CARBIDE/BORON CARBIDE-CARBON NANOFIBERS LAMINATES WITH WEAK INTERFACES

NINA ORLOVSKAYA*[1], MYKOLA LUGOVY[2], VIKTOR SLYUNYAYEV[2], VLADIMIR SUBBOTIN[2], FEI LIANG[1], JIHUA GOU[1], JAKOB KUEBLER[3], THOMAS GRAULE[3]

[1] *University of Central Florida, Orlando, USA*

[2] *Institute for Problems of Materials Science, Kyiv, Ukraine*

[3] *Empa, Duebendorf, Switzerland*

Abstract Three layered B_4C/B_4C-$C_{nanofibers}$ laminates have been produced using a hot pressing technique. The laminates were designed with thick (~2.6 mm) outer layers of B_4C and a thin (~90 μm) center layer of B_4C-70 wt% $C_{nanofibers}$. It was found that low tensile thermal residual stress develops in the thick B_4C outer layers. The compressive thermal residual stresses exist in the thin central layer. The magnitude of the tensile residual stress was estimated as 11.3 ± 2.5 MPa. The effect of weak interfaces on failure mechanism of the laminate was studied.

Keywords: laminate, ceramic, fracture toughness, residual stress, delamination

1. Introduction

Ceramic matrix composites have a broad range of industrial applications. They have been extensively used as structural components in order to improve the mechanical, thermal, and chemical performance of engineering devices. However, despite a high hardness, an excellent oxidation resistance, and high temperature stability, ceramics are inherently brittle. One of the strategies to decrease brittleness and improve composite performance is through the design of ceramic laminates [1]. One of the ways to enhance mechanical performance of a layered structure is the development of laminates with weak interfaces for crack deflection [2].

The mismatch of thermal expansion coefficients between different layers inevitably generates thermal residual stresses during subsequent cooling of layered ceramics [1]. The relative thickness of different layers determines

* Nina Orlovskaya, University of Central Florida, Orlando, USA, e-mail: norlovsk@mail.ucf.edu

N. Orlovskaya and M. Lugovy (eds.), *Boron Rich Solids: Sensors, Ultra High Temperature Ceramics, Thermoelectrics, Armor*, DOI 10.1007/978-90-481-9818-4_1,

the relative magnitudes of compressive and tensile stress, while the strain mismatch between the layers dictates the absolute values of the residual stresses.

Although fracture toughness of layered composites can be measured experimentally, it is an apparent value because of the superposition of different effects like stress shielding and intrinsic properties of the structure, such as grain size, composition, interfaces, etc. In fracture mechanics, both residual and applied stresses are usually included in the crack driving force. However, it can be useful to consider residual stresses as part of the crack resistance. It was shown that in order to obtain the higher resistance to failure, the tensile layer should be made as stiff as possible (i.e. a high elastic modulus), whereas the compressive layers should be as compliant as feasible (i.e. a low elastic modulus) [3].

The concept of improving the resistance to crack growth of an inherently brittle material by having a series of layers, separated by weak interfaces capable of deflecting cracks, is well established [2]. The basic requirement is that, as a crack propagates through the base material, is should be deflected at weak interfaces oriented transversely to the main crack propagation direction. It is expected that the toughness of the material will be optimized when the interfaces are just weak enough to ensure that crack deflection consistently occurs.

Typically, the energy criteria determine an advance of an interfacial crack. An incremental advance of the crack during stable crack growth, or a macroscopic advance during unstable crack growth, occurs to a degree determined by the elastic strain energy released [2]. If this is sufficient to drive the crack to the end of the beam, then any excess energy is dissipated and is not available to drive any subsequent through-thickness or interfacial cracking.

There is a physical mechanism which produces a driving force for interfacial crack growth before the primary crack reaches the interface [4]. It is confirmed by the observed crack deflection process. When defects exist in the interface, the condition for the occurrence of crack deflection is determined by whether the observed interfacial defect can grow, rather than whether a primary crack can change its path upon reaching a weak defect-free interface.

A large macroscopic advance of an interfacial crack means a delamination of the material along interface between layers. Through-thickness crack propagation after delamination is typically assumed to occur when the load on the intact portion of the beam gives rise to a stress equal to the failure stress of an un-notched bar of the same dimensions, i.e. it is assumed that the beam is completely notch insensitive.

There are many ways to create a weak interface in a laminate. However, they are not investigated enough. Typically, residual stresses arise in laminates with layers of different materials. These stresses make own contribution to the failure of layered material with weak interfaces. This contribution requires an additional investigation.

The possibility of a weak interface creation using a thin layer of B_4C-70 wt% $C_{nanofibers}$ is investigated. The effect of the residual stress on the apparent fracture toughness and crack growth in B_4C-based layered composites with weak interfaces is also analyzed in this study. Special attention is paid to study the effect of weak interfaces on failure mechanism of the laminate.

2. Experimental

Three layered laminates with thick outer layers of pure boron carbide and a thin inner layer of carbon nanofiber paper, as well as bulk boron carbide specimens, were fabricated. The main manufacturing steps for the laminates included grinding of raw powders, stacking boron carbide powders and carbon nanofiber paper together to form three layered structure, and hot pressing of laminates. Only grinding of raw powders and hot pressing for bulk boron carbide specimens was done. The hot pressing conditions were as follows: a heating rate of 100°C/min, a hot pressing temperature of 2150°C, a pressure of 30 MPa, and a dwell time of 1 h. As a result, dense laminate samples (98–99% relative density) and bulk boron carbide specimens were obtained and further machined into 3 × 5 × 45 mm bars for four point bending and fracture toughness experiments.

Carbon nanofiber paper sheets were produced from PR-25-Carbon Nanofibers. The individual nanofiber diameter and length were ~80 nm and ~30-100 μm, respectively. PR-25 is fiber with a high electrical conductivity which features a highly ordered graphitic surface, with low surface energy, low iron content, and smaller diameter. The processing of carbon nanofiber paper included three steps. First, the carbon nanofibers were pre-mixed in water and the B_4C particles were mixed in water through boiling process. Second, the nanofiber suspension was sonicated and mixed with B_4C solution. Third, the nanofiber and B_4C suspension were filtrated. Carbon nanofiber paper sheet has good strength and flexibility to allow for handling like traditional fiber material.

The Young's modulus was measured at room temperature using the impulse excitation method and a Grindo – Sonic MK 5 (Lemmens, Germany). A four point bending strength was measured in the setup with 20 mm loading and 40 mm supporting span. The tests were carried out with a cross-head displacement speed of 1 mm/min at room temperature using a Universal Testing Machine (UPM-Zwick 1478, Germany) in accordance to EN 843-1 [5].

Fracture toughness was measured using the single edge V notch beam (SEVNB) method [6]. The notches of different length were inserted using a notching machine and the final notching was made using 1 μm diamond paste and a steel razor blade [6]. The cross-head displacement speed of 0.3 mm/min was used for measurements at room temperature (USM, Zwick Z005, Germany). Outer and inner support spans of the four-point bending fixture for SEVNB samples were 40 and 20 mm, respectively. Specimens with different notches (0.2, 0.4, 0.6, 0.8, 1, 1.2, 1.4, and 2 mm) were tested. Fractographic analysis by Scanning Electron Microscopy (SEM) was carried out on selected specimens using a Hitachi S-4700 Field Emission Scanning Electron Microscope.

3. Results and Discussion

The layered specimens have thick outer layers of B_4C with a thickness of 2625 ± 110 μm and a thin central layer of B_4C + carbon nanofibers with thickness of 90 ± 10 μm. The fracture surface of the central layer is shown in Fig. 1. The elastic modulus of boron carbide was 455 ± 8 GPa. Poisson's ratio and thermal expansion coefficient were 0.17 and $5.6 \cdot 10^{-6}$ K^{-1} respectively. The fracture toughness of bulk B_4C was measured as 3.53 $MPa/m^{1/2}$

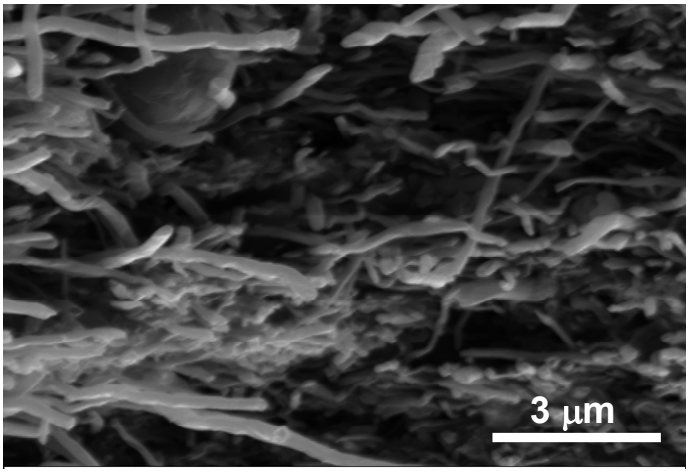

Figure 1. Fracture surface of central layer.

A weight function analysis has been used to estimate the apparent fracture toughness in laminates with residual stresses [1, 7–10]. The choice of coordinate system is of great importance to the apparent fracture toughness calculations because of a significant simplification of the procedure. The

most appropriate coordinate origin is on the tensile surface of the sample under bending. The geometry of the multilayered material analyzed here is such that the problem can be reduced to one dimension and that analytically tractable solutions can be used [1, 10].

An experimental value of the apparent fracture toughness can be found using the expression [11]:

$$K_{app} = Y(\alpha)\sigma_m a^{1/2}, \tag{1}$$

where

$$Y(\alpha) = \frac{1.99 - \alpha(1-\alpha)(2.15 - 3.93\alpha + 2.7\alpha^2)}{(1+2\alpha)(1-\alpha)^{3/2}}, \tag{2}$$

$$\sigma_m = \frac{1.5P(s_1 - s_2)}{bw^2} \text{ and } \alpha = a/w, \tag{3}$$

where P is the critical load (the applied bending load corresponding to specimen failure) and s_1 and s_2 are outer and inner support spans of the four-point bending fixture for SEVNB samples.

The apparent fracture toughness of the layered composite can be calculated analytically by [1, 10]:

$$K_{app} = \frac{6Y(\alpha)a^{1/2}(I_{L1}^2 - I_{L0}I_{L2})(K_{1c}^{(i)} - K_r)}{w^2\left\{E'_{n+1}\int_{x_n}^{a} h(\frac{x}{a},\alpha)\left[I_{L0}x - I_{L1}\right]dx + \sum_{i=1}^{n} E'_i \int_{x_{i-1}}^{x_i} h(\frac{x}{a},\alpha)\left[I_{L0}x - I_{L1}\right]dx\right\}} \tag{4}$$

where $K_{1c}^{(i)}$ is the intrinsic fracture toughness of the *i*-th layer material, K_r is the stress intensity due to the residual stresses $\sigma_r^{(i)}(x)$:

$$K_r = \int_{x_n}^{a} h\left(\frac{x}{a},\alpha\right)\sigma_r^{(n+1)}(x)dx + \sum_{i=1}^{n}\int_{x_{i-1}}^{x_i} h\left(\frac{x}{a},\alpha\right)\sigma_r^{(i)}(x)dx, \tag{5}$$

$$\sigma_r^{(i)}(x) = \frac{E'_i}{I_{L1}^2 - I_{L0}I_{L2}}\left[I_{L1}J_{L1} - I_{L2}J_{L0} + (I_{L1}J_{L0} - I_{L0}J_{L1})x - \tilde{\varepsilon}_i(I_{L1}^2 - I_{L0}I_{L2})\right], \tag{6}$$

$h(x/a,\alpha)$ is the weight function for an edgecracked sample [8–10], x_i is the coordinate of interface between *i*-th and (*i*+1)-th layers, $E_i' = E_i/(1-\nu_i)$, and E_i and ν_i are the elastic modulus and Poisson ratio of the *i*th layer, respectively. The expressions for I_{Lj} (j = 0, 1, 2) and J_{Lj} (j = 0, 1) were obtained in [10] as follows:

$$I_{Lj} = \frac{1}{j+1}\sum_{i=1}^{N} E_i'(x_i^{j+1} - x_{i-1}^{j+1}), \tag{7}$$

$$I_{Lj} = \frac{1}{j+1}\sum_{i=1}^{N} \widetilde{\varepsilon}_i E_i'(x_i^{j+1} - x_{i-1}^{j+1}), \tag{8}$$

where $\widetilde{\varepsilon}_i$ is the strain in the *i*-th layer, which is associated with thermal expansion:

$$\widetilde{\varepsilon}_i = \int_{T_0}^{T_j} \beta_i(T)dT, \tag{9}$$

where $\beta_i(T)$ is the thermal expansion coefficient of the *i*-th layer at the temperature *T*. T_0 and T_j are the actual and ‘‘joining’’ temperatures, respectively. Below a certain temperature, called the ‘‘joining’’ temperature, the different components become bonded together and residual stresses appear. In our case the ‘‘joining’’ temperature is equal to the hot pressing temperature 2150°C. If $\beta_i(T)$ is a linear function, $\widetilde{\varepsilon}_i = \langle\beta_i\rangle\Delta T$, where $\Delta T = T_j - T_0$, $\langle\beta_i\rangle = \dfrac{\beta_i(T_0)+\beta_i(T_j)}{2}$ is the average value of the thermal expansion coefficient in the temperature range from T_0 to T_j.

The apparent fracture toughness K_{app} in layered specimens can be analyzed as a function of the crack length parameter $\widetilde{a}$, where $\widetilde{a} = Y(\alpha)a^{1/2}$ [1]. The crack length parameter $\widetilde{a}$ is the most appropriate to demonstrate critical conditions of a crack growth. One of the advantages of this parameter is that the stress intensity factor of an edge crack for a fixed value of the applied stress σ_m is a straight line from the coordinate origin in the coordinate system $K_{app} - \widetilde{a}$. Since $K_1 = \sigma_m\widetilde{a}$, the slope of the straight line is the applied stress σ_m. The conditions for unstable crack

growth in the internal stress field are as follows [12]: $K_1(\sigma_m, a) = K_{app}(a)$; $dK_1(\sigma_m, a)/da \geq dK_{app}(a)/da$. Using parameter $\tilde{a}$, these conditions become $\sigma_m \tilde{a} = K_{app}(\tilde{a})$ and $\sigma_m \geq dK_{app}(\tilde{a})/d\tilde{a}$, which can be reduced to: $K_{app}(\tilde{a})/\tilde{a} \geq dK_{app}(\tilde{a})/d\tilde{a}$. In this case the applied stress intensity factor becomes higher than the fracture resistance of the material.

The dependence of apparent fracture toughness on crack length parameter in three layered structure is shown in Fig. 2. The solid line corresponds to calculated values. The solid circles are experimental data. The calculated values were obtained by adjusting residual stress magnitude to provide the best fit of experimental data using the above calculation procedure. In our case the magnitude of the residual stress was estimated as 11.3 ± 2.5 MPa. One can see that the apparent fracture toughness decreased when V-notch length increased in the first layer. At the same time, there is sharp increase of apparent fracture toughness in the second layer. It was shown earlier that an such increase has resulted in crack arrest in the Si_3N_4-based laminates [1, 10]. The maximum value of apparent fracture toughness was found to be about 11 MPa/m$^{1/2}$. The apparent fracture toughness decreases again when crack length parameter increases in the third layer.

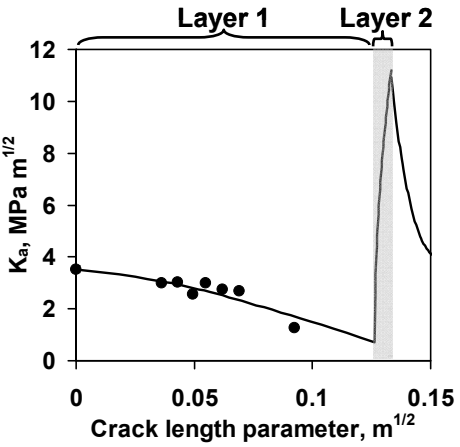

Figure 2. Dependence of apparent fracture toughness on crack length parameter in three layered structure.

The SEM pictures of the sample tested for fracture toughness determination are shown in Fig. 3a, b. Schematic of crack development in three layered structure with weak interfaces is presented in Fig. 3c. The primary crack propagates in the straightforward manner from the V-notch tip to the interface between the first and second layer. The direction of its propagation is perpendicular to the interface. Note that the primary crack changes its direction at the interface between the first and second layer. There is a small deflection of crack along the interface. After this, the crack passes the second layer. The large area of delamination is formed along the interface between the second and third layers. Finally, the secondary crack propagates in the straightforward manner from the interface between the second and third layers.

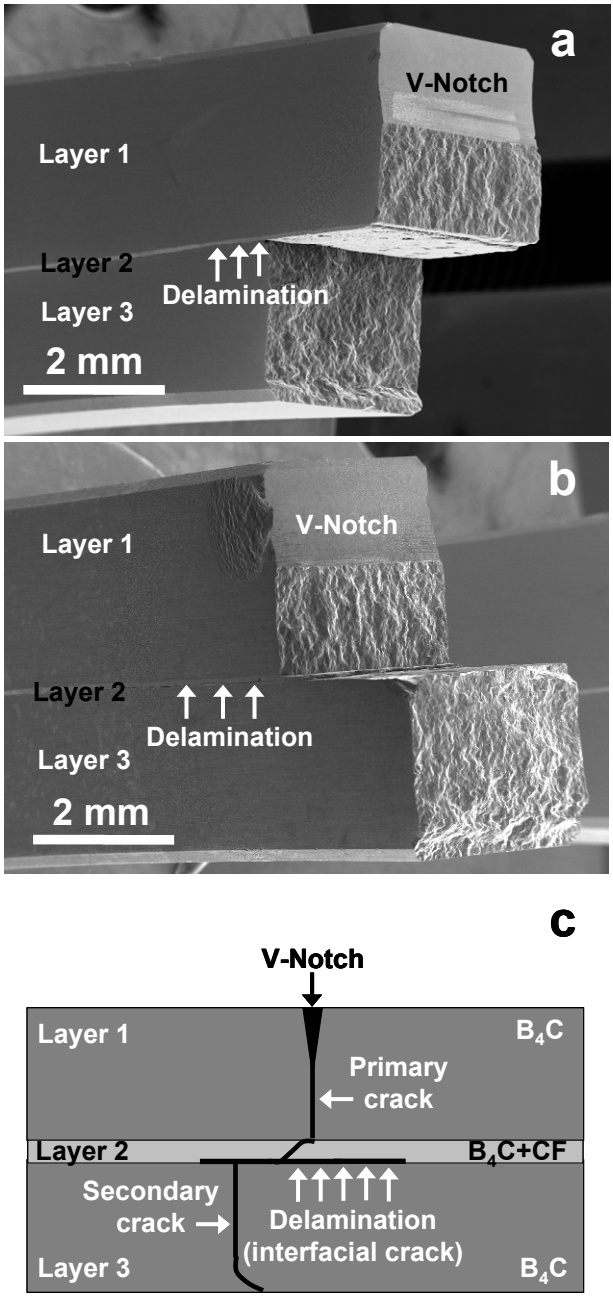

Figure 3. Failure of the laminate: (**a**) left part of the sample tested for fracture toughness determination; (**b**) right part of the sample tested for fracture toughness determination; (**c**) schematic presentation of crack development in three layered structure with weak interfaces.

When the stress intensity factor reaches the apparent fracture toughness level for V-notch tip the unstable growth of primary crack starts [1]. One can assume that the primary crack passes the interface between the first and second layer with high velocity after some acceleration in the thick first layer. Due to a high velocity of propagation the crack has only a small deflection along the interface between the first and second layer. Then the crack slows up to a complete stop in the second layer due to essential increasing apparent fracture toughness. The unstable growth changes to stable propagation. The small intact ligament remains between the crack tip and the interface between the second and third layer. The primary crack promotes the development of an interfacial crack along the interface between the second and third layer in this configuration. In this case the interface between the first and second layer locates behind of the primary crack tip and don't participate in the fracture process already. Then the ligament of the second layer breaks after large delamination along the interface between the second and third layer [4]. After this the third layer fails as a separate bending unnotched specimen. Typically this failure appears at a higher load than the primary crack start. In fact the stress of the secondary crack start does not depend on the V-notch length and is determined by the strength of third layer.

The typical force-time diagram for fracture toughness test of the layered specimen is shown in Fig. 4. One can see the linear dependence of the force on time corresponding to elastic behavior of specimen up to the first maximum. The maximum corresponds to the primary crack start. This is followed by some force drop due to the decrease of the specimen stiffness resulting from the primary crack propagation. The almost linear dependence of applied force on time is observed after the force drop. The second maximum corresponds to the secondary crack start. This is followed by the total failure of specimen.

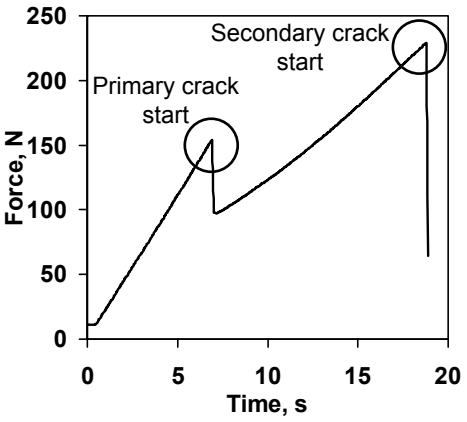

Figure 4. Typical force-time diagram for fracture toughness test of layered specimen.

4. Conclusions

It was shown that a thin layer of boron carbide mixed with carbon nanofibers can be used to create a weak interface in laminate for crack deflection. Tensile residual stress in the first layer has an effect on apparent fracture toughness of the laminate. The magnitude of the stress was estimated as 11.3 ± 2.5 MPa. When the crack length increased, apparent fracture toughness decreased in the first layer and grew in the second layer. Primary crack originated from V-notch propagates across the first thick layer of B_4C. Then the delamination process appears along the interface between the second and third layer when the crack approaches the interface. After this an intact ligament in the central layer between the primary crack and interfacial crack breaks. A secondary crack starts from the free surface created as a result of delamination. In fact, the stress of the secondary crack start is independent on the V-notch length and is determined by the strength of the third layer.

Acknowledgement

This work was supported by NSF project 0748364 “CAREER: Hard and tough boron rich ceramic laminates designed to contain thermal residual stresses” and NATO ARW Grant “Boron Rich solids: Sensors for Biological and Chemical Detection, Ultra-high Temperature Composites, Thermo-electrics, Armor”.

References

1. M. Lugovy, V. Slyunyayev, N. Orlovskaya, G. Blugan, J. Kuebler, and M. Lewis, Apparent Fracture Toughness of Si_3N_4-based Laminates with Residual Compressive or Tensile Stresses in Surface Layers, Acta Materialia, vol. 53, pp. 289–296, 2005.
2. A.J. Phillipps, W.J. Clegg, and T.W. Clyne, Fracture Behaviour of Ceramic Laminates in Bending–I. Modelling of Crack Propagation, Acta Materialia, vol. 41, pp. 805–817, 1993.
3. K. Hbaieb and R.M. McMeeking, Threshold Strength Predictions for Laminar Ceramics with Cracks That Grow Straight, Mechanics of Materials, vol. 34, pp. 755–772, 2002.
4. W. Lee, S.J. Howard, and W.J. Clegg, Growth of Interface Defects and Its Effect on Crack Deflection and Toughening Criteria, Acta Materialia, vol. 44, pp. 3905–3922, 1996.
5. European Standard, EN 843-1, Advanced Technical Ceramics–Monolithic Ceramics–General and Textural Properties, Part 1. Determination of flexural strength, 2006.
6. J. Kuebler, Fracture Toughness of Ceramics using the SEVNB Method: From a Preliminary Study to a Test Method, in: J.A. Salem, G.D. Quinn, M.G. Jenkins (Eds.), ASTM STP 1409, ASTM 2002, pp. 93–106.

7. R. Lakshminarayanan, D.K. Shetty, and R.A.N. Cutler, Toughening of Layered Ceramic Composites with Residual Surface Compression, Journal of the American Ceramic Society, vol. 79, pp. 79–87, 1996.
8. R.J. Moon, M. Hoffman, J. Hilden, K. Bowman, K. Trumble, and J. Roedel, Weight Function Analysis on the R-Curve Behavior of Multilayered Alumina-Zirconia Composites, Journal of the American Ceramic Society, vol. 85, pp. 1505–1511, 2002.
9. T. Fett, and D. Munz, Influence of Crack-Surface Interactions on Stress Intensity Factor in Ceramics, Journal of Materials Science Letters, vol. 9, pp. 1403–1406, 1990.
10. M. Lugovy, V. Slyunyayev, V. Subbotin, N. Orlovskaya, and G. Gogotsi, Crack Arrest in Si_3N_4-based Layered Composites with Residual Stress, Composites Science and Technology, vol. 64, pp. 1947–1957, 2004.
11. J.E. Srawley, Wide Range Stress Intensity Factor Expressions for ASTM E 399 Standard Fracture Toughness Specimens, International Journal of Fracture, vol. 12, pp. 475–476, 1976.
12. V.M. Sglavo, L. Larentis, and D.J. Green, Flaw-Insensitive Ion-Exchanged Glass: I, Theoretical Aspects, vol. 84, pp. 1827–1831, 2001.

ALL CERAMIC CANTILEVER SENSORS WITH BORON CARBIDE LAYER: ADVANTAGES AND DIMENSIONAL LIMITATIONS

MYKOLA LUGOVY*
Institute for Problems of Materials Science, Kyiv, Ukraine
E-mail: nil2903@gmail.com

Abstract A model that predicts minimal length and thickness of all ceramic two layer cantilever sensors for chemical and biological detection is proposed. The model allows the estimation of minimal length and thickness where the conditions for the safe cantilever operation are satisfied. Two materials have been chosen for the consideration of the piezoelectric and non-piezoelectric layers in the layered cantilever. A piezoelectric material is lead zirconate titanate and a non-piezoelectric material is boron carbide. Different conditions, such as von Mises criterion and Mohr's strength theory are considered to find a safe stress level in the clamped cross-section of the cantilever.

Keywords: cantilever; ceramic; sensor; sensitivity; piezoelectric

1. Introduction

Biological and chemical sensors have a wide-range of applications in medical diagnoses, environmental surveillance, and pathogen and biological/chemical agent detection [1–4]. One type of the sensors available for temperature, surface stress, and mass detection is a piezoelectric microcantilever sensor, which transduces the recognition event from its surface into electrical signals further analyzed for the detection.

The piezoelectric microcantilever sensor consists of a piezoelectric layer bonded to a non-piezoelectric layer [5]. The adsorption of a target agent onto the piezoelectric material causes a change in the cantilever's mass, which in turn causes a shift in the resonance frequency [6, 7]. The sensitivity of piezoelectric microcantilever sensors is determined by the resonance frequency shift Δf per mass change Δm which depends on the effective

* Mykola Lugovy, Institute for Problems of Materials Science, Kyiv, Ukraine, e-mail: nil2903@gmail.com

N. Orlovskaya and M. Lugovy (eds.), *Boron Rich Solids: Sensors, Ultra High Temperature Ceramics, Thermoelectrics, Armor*, DOI 10.1007/978-90-481-9818-4_2,

elastic modulus, effective density of the cantilever and cantilever dimensions (length l, width w). $\Delta f / \Delta m$ will increase with decreasing cantilever dimensions and density, and with increasing elastic modulus [5].

Lead zirconate titanate (PZT) is a material's choice for the piezoelectric layer of microcantilever (E = 61 GPa, ρ = 7.5 g/cm^3 [5]). For the non-piezoelectric layer, a stainless steel (E = 200 – 250 GPa, ρ = 7.7 – 8 g/cm^3) is frequently used [4]. However, if the non-piezoelectric ceramic layer in the microcantilever layered structure could be replaced with a material of higher elastic modulus and lower density, the sensitivity of the sensor could significantly be increased. One of such stiff and light-weight materials is boron carbide (E = 483 GPa, ρ = 2.52 g/cm^3 [8, 9]).

Generally all ceramic cantilevers are more sensitive than steel based cantilevers (Fig. 1). For example, boron carbide-based cantilever has the sensitivity about 7 times higher than steel based one. All ceramic cantilevers have also other advantages compared with traditional steel-based cantilevers. They have a higher resistance to cyclic loading and a higher stability in aggressive media.

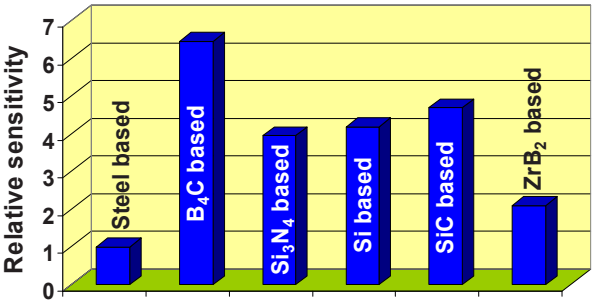

Figure 1. Relative sensitivity of the cantilevers with the same dimensions.

The sensitivity of the microcantilever sensor will increase when its dimensions decrease. As the dimensions of a cantilever are reduced by a factor of α, the sensitivity is enhanced by a factor of α^{-4} [5]. However, when such a decrease of dimensions happens, another factor comes into play which needs to be considered. When the piezoelectric layer becomes thinner, at a given applied voltage, the strain mismatch between piezo- and non-piezoelectric layer becomes larger and larger, which could lead to a rise in the residual stresses. When the residual stresses reach a certain critical value, a deterioration of the service properties, due to appearance of the irreversible strain in the piezoelectric layer, or even a complete failure of the sensor will occur. Therefore, the lower dimensional limits for the safe cantilever operation are important to be determined. Static analysis for multi-layered piezoelectric cantilevers were developed in [10]. However, the lower limit of the cantilever size has not been considered.

The goal of this work is to evaluate the lower dimensional limit of a two layer microcantilever sensor, where a piezoelectric layer is made of lead

zirconate titanate ceramic, and a non-piezoelectric layer is made of boron carbide, which is capable to exhibit high sensitivity and good service properties. The evaluation is made by a simplified analytical model based on von Mises criterion and Mohr's strength theory.

2. Model Development

2.1. MODEL ASSUMPTIONS

A schematic presentation of a micro-cantilever sensor with defined dimensions of the piezoelectric and non-piezoelectric layers is shown in Fig. 2a. The maximum deflection state of the microcantilever is schematically shown in Fig. 2b, which will be used for the analysis with no intermediate deflections between zero and maximum deformation being considered. Figure 2c presents an orientation of the cantilever with a defined horizon line. These parameters presented in Fig. 2a–c are used for the estimation of the lower limit of the sensor dimensions which are still feasible for the reliable sensor operation. The main assumptions of the model are summarized as follows:

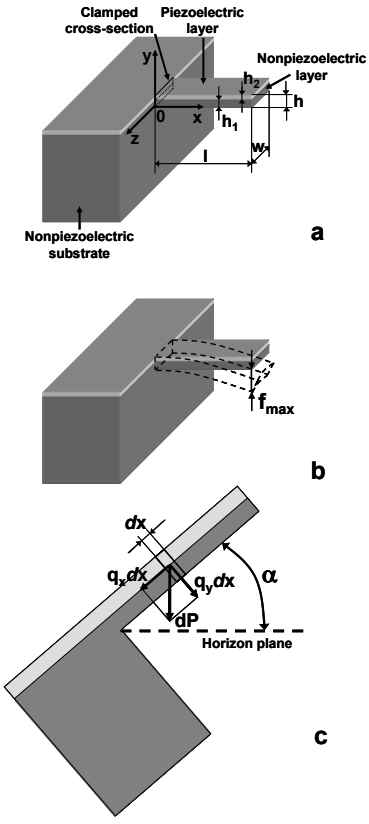

Figure 2. Schematic presentations of cantilever: (**a**) geometric parameters; (**b**) state of maximum deflection; (**c**) orientation of cantilever.

1. Only stress distribution in the clamped cross-section of a cantilever is considered, as it is the most critical one.
2. A cantilever is allowed to expand and compress without any constraints along a *y*-direction perpendicular to the layers (Fig. 2a) which results in the stress component in this direction to be equal to zero.
3. The clamped cross-section of the cantilever is assumed to be a plane and it has a rectangular shape for all deformations (Fig. 2a). Therefore, the stress components along a *z*-direction perpendicular to the longitudinal axis of the cantilever and parallel to the layers do not change.

4. Only a cantilever with a maximum deflection $f_{\max}$ will be evaluated. We name it "a static problem" (Fig. 2b).
5. Only the upper estimate of deflection $f_{\max}$ of the cantilever free end is considered.
6. The cantilever is analyzed only for the case where the *z*-axis is parallel to the horizon plane (Fig. 2c).
7. The mismatch of the coefficients of thermal expansion between the two layers of the cantilever at room temperature is not considered.
8. Shear stresses in a clamped cross-section of the cantilever are neglected since they are substantially smaller than normal stresses analyzed.
9. The interface between two layers is suggested to be indestructible and two layers are bonded rigidly (without sliding).

A simple model which would take into account different parameters of the successful sensor operation is developed which allows the estimation of the minimal dimensions without reaching the critical stress level in the sensor's layers. The model applicability is determined by the deflection criterion:

$$f_{\max} / h < a\,, \tag{1}$$

where

$f_{\max}$ is the maximum deflection of the cantilever free end (Fig. 2b),

h is the total thickness of cantilever (Fig. 2a), and

a is a prescribed value less than one (0.1 in this work).

The ultimate state of the cantilever can be achieved when at least one of two criteria are fulfilled. The first criterion is applicable to a failure of the non-piezoelectric layer and a second criterion is applicable to the appearance of irreversible strain in the piezoelectric layer. The challenge is to determine the conditions to avoid the ultimate state of the cantilever.

The failure of the non-piezoelectric layer will not occur, according to Mohr's strength theory [11], when the following condition is met:

$$\sigma_M < \sigma_+\,, \tag{2}$$

where the effective stress σ_M is

$$\sigma_M = \max(\sigma_{x1}, \sigma_{y1}, \sigma_{z1}) - \frac{\sigma_+}{\sigma_-} \min(\sigma_{x1}, \sigma_{y1}, \sigma_{z1})\,, \tag{3}$$

and

σ_+ is the tensile strength of the non-piezoelectric material. σ_+ can be also evaluated as its bending strength.

σ_- is the strength of non-piezoelectric material under compression,

σ_{x1}, σ_{y1}, σ_{z1} are normal stress components in directions *x*, *y*, *z*, respectively, acting in the non-piezoelectric layer.

The cantilever will also reach its ultimate state when the irreversible strain in the piezoelectric layer appears. The irreversible strain is a result of the ferroelastic domain switching under loading of the piezoelectric material at certain stress levels [12]. The safe stress level which will not result in the appearance of the irreversible deformation can be evaluated using von Mises criterion [13]:

$$\sigma_i < \sigma_0, \tag{4}$$

where

$$\sigma_i = \frac{1}{\sqrt{2}} \sqrt{(\sigma_{x2} - \sigma_{y2})^2 + (\sigma_{y2} - \sigma_{z2})^2 + (\sigma_{z2} - \sigma_{x2})^2} \tag{5}$$

is the stress intensity, where shear stresses are neglected in our consideration,

σ_0 is the stress at the appearance of the irreversible strain in the piezoelectric material,

σ_{x2}, σ_{y2}, σ_{z2} are normal stress components in directions *x*, *y*, *z*, respectively, acting in the piezoelectric layer.

2.2. MODEL EQUATIONS

To determine the model applicability using deflection criterion Eq. (1) the maximum deflection $f_{\max}$ of the free end of cantilever should be estimated. The upper estimate of bending deflection of the free end can be made from the assumption that maximum curvature of the cantilever (at clamped end) remains constant along the whole length of the cantilever:

$$f_{\max} = \frac{2}{k_x} \sin^2\left(\frac{lk_x}{2}\right). \tag{6}$$

where

k_x is the cantilever curvature at a clamped end in the *x*-*y* plane. Expression (6) overestimates the deflection but results in the most reliable evaluation of the model's applicability.

To find the conditions to avoid the ultimate state of the cantilever, the stress distribution in the clamped cross-section of the cantilever should be determined. The stress component σ_{xi} directed along *x* axis (perpendicular to the cross-section plane) in the *i*-th layer, obtained from a hypothesis of plane sections [14] is as follows

$$\sigma_{xi}(y) = E_i'(\varepsilon_x(0) + k_x y - \Delta\varepsilon_{xi} - \nu_i \Delta\varepsilon_{zi}), \tag{7}$$

where $E_i' = \dfrac{E_i}{1-\nu_i^2}$ (i = 1, 2),

E_1, ν_1 and E_2, ν_2 are elastic modulus and Poisson's ratio of non-piezoelectric and piezoelectric layers respectively,

$\varepsilon_x(0)$ is the total strain component oriented along the *x* axis in the clamped cross-section at $y = 0$,

$\Delta\varepsilon_{xi}$ and $\Delta\varepsilon_{zi}$ (i = 1, 2) are the components of strain which are not connected with stress. $\Delta\varepsilon_{x1} = \Delta\varepsilon_{z1} = 0$ in the non-piezoelectric layer (thermal strains are neglected in our consideration). $\Delta\varepsilon_{x2}$ and $\Delta\varepsilon_{z2}$ are piezoelectric strains in piezoelectric layer. Most PZT films exhibit piezoelectric coefficients d_{31} = −58 pm/V and d_{33} = 190–250 pm/V [15]. Components of piezoelectric strain oriented along *x* and *y* axes are

$$\Delta\varepsilon_{x2} = \Delta\varepsilon_{z2} = \frac{d_{31}U}{h_2}, \tag{8}$$

$$\Delta\varepsilon_{y2} = \frac{d_{33}U}{h_2}, \tag{9}$$

respectively, where

U is the electric voltage applied to the piezoelectric layer, and

h_2 is the thickness of the piezoelectric layer.

The cantilever is allowed to expand and compress without any constraints along the *y* axis which results in $\sigma_{yi} = 0$. A stress component directed along the *z* axis in a clamped cross-section in the *i*-th layer can be determined from the condition $\varepsilon_z = 0$, where ε_z is the total strain oriented along the *z* axis and a hypothesis of plane sections as follows:

$$\sigma_{zi}(y) = E_i'[\nu_i(\varepsilon_x(0) + k_x y - \Delta\varepsilon_{xi}) - \Delta\varepsilon_{zi}]. \quad (10)$$

The curvature k_x and the strain $\varepsilon_x(0)$ can be found from equilibrium conditions for the cantilever, since only the static problem is analyzed. We have two equilibrium conditions. The first condition is a force balance and the second condition is a moment balance, and both are equal to zero in the clamped cross-section. These two conditions are determined by the system of two linear equations:

$$\begin{cases} w\sum_{i=1}^{2}\int_{y_{i-1}}^{y_i}\sigma_{xi}(y)dy + F_x(0) = 0, \\ w\sum_{i=1}^{2}\int_{y_{i-1}}^{y_i}\sigma_{xi}(y)(y - y_c)dy + M(0) = 0, \end{cases} \quad (11)$$

where

$\sigma_{xi}(y)$ is determined by Eq. (7),

w is the cantilever width (Fig. 2a),

$y_0 = 0$,

$y_1 = h_1$,

$y_2 = h_1 + h_2 = h$,

h_1, h_2 are the thicknesses of non-piezoelectric and piezoelectric layers, respectively (Fig. 2a).

$y_c = \dfrac{E_1'h_1^2 + E_2'(h^2 - h_1^2)}{2(E_1'h_1 + E_2'h_2)}$ is the coordinate of the neutral axis in the clamped cross-section of the cantilever derived from a balance of static moments of the cross-section,

$F_x(0) = -q_x l$ is the longitudinal force in the cantilever clamped end,

$M(0) = \dfrac{q_y l^2}{2}$ is the bending moment in the clamped cross-section,

l is the cantilever length (Fig. 2a).

$q_x = gw\rho_{eff}h\sin\alpha$ (which can be obtained from the expression for a gravitational force $dP = gdm = gw\rho_{eff}hdx$ acting on an elementary volume $whdx$ taking into account the angle α) (Fig. 2c),

$q_y = gw\rho_{eff}h\cos\alpha$,

$\rho_{eff} = \dfrac{\rho_1 h_1 + \rho_2 h_2}{h}$ is the effective density of the cantilever,

ρ_1 and ρ_2 are densities of the non-piezoelectric and piezoelectric layers, respectively,
g is the gravitational acceleration,
α is the angle between x axis and the horizon plane (Fig. 2c).

The solution of system of the two linear equations (11) is

$$\varepsilon_x(0) = \frac{B_1 A_{22} - B_2 A_{12}}{A_{11} A_{22} - A_{12}^2}, \tag{12}$$

$$k_x = \frac{B_2 A_{11} - B_1 A_{12}}{A_{11} A_{22} - A_{12}^2}, \tag{13}$$

where

$$A_{11} = E_1' h_1 + E_2' (h - h_1),$$

$$A_{12} = \frac{1}{2}\left[E_1' h_1^2 + E_2' (h^2 - h_1^2)\right],$$

$$A_{22} = \frac{1}{3}\left[E_1' h_1^3 + E_2' (h^3 - h_1^3)\right],$$

$$B_1 = E_1' h_1 \Delta\varepsilon_1 + E_2' (h - h_1)\Delta\varepsilon_2 + \frac{q_x l}{w},$$

$$B_2 = \frac{1}{2}\left[E_1' h_1^2 \Delta\varepsilon_1 + E_2' (h^2 - h_1^2)\Delta\varepsilon_2 + \frac{l}{w}(2 y_c q_x - l q_y)\right].$$

Knowing the curvature k_x and the strain $\varepsilon_x(0)$ we can evaluate the applicability of the model and determine a stress distribution in the clamped cross-section of the cantilever in order to find the safe conditions of the cantilever operation.

3. Results and Discussion

The effective stress and stress intensity in the clamped end of the cantilever have been calculated using Eqs. (7)–(10), (12), and (13). The maximum bending deflection of the cantilever free end has been estimated using Eq. (6). The following geometric considerations have been taken into account for the calculations: $l/w = 2.6$, $h_1/h = 0.5$, and $\alpha = 0$ (Fig. 2). The constant ratio $l/h = 16.25$ was used for the calculation of critical parameters as a function of the cantilever's length. The cantilever length was taken as 65 μm when

the effect of l/h and h_1/h on critical parameters was estimated. While the effective stress and stress intensity in the cantilever's clamped end and the maximum bending deflection of the cantilever free end do not depend on the *l*/*w* ratio, this ratio is used to determine the sensitivity of the cantilever $\Delta f_n / \Delta m$ (the resonance frequency shift per unit loaded mass) [5]:

$$\frac{\Delta f_n}{\Delta m} = \frac{\nu_n^2}{4\pi} \frac{1}{l^4} \frac{l}{w} \left(\frac{1}{0.236\sqrt{12}\rho_{eff}} \sqrt{\frac{\widetilde{E}}{\rho_{eff}}} \right), \tag{14}$$

where

ν_n^2 is the dimensionless *n*th-mode eigenvalue,

$$\widetilde{E} = \frac{E_1^2 r_1^4 + E_2^2 r_2^4 + 2E_1 E_2 r_1 r_2 (2r_1^2 + 2r_2^2 + 3r_1 r_2)}{E_1 r_1 + E_2 r_2}$$

is the effective elastic modulus, and $r_1 = h_1/h$ and $r_2 = h_2/h$.

The properties of the materials used for the calculation of the effective stress, stress intensity, and maximum bending deflection are presented in Table 1.

TABLE 1. Parameters of layers used in the calculation.

	Elastic modulus E_i, GPa	Poisson ratio ν_i	Density ρ_i, g/cm^3	Strength σ_+, MPa	Yield point σ_0, MPa
B_4C layer	483	0.16	2.52	300	-
PZT layer	61	0.25	7.5	300	10

The dependence of the dimensionless parameters σ_M/σ_+, σ_i/σ_0 and f_{max}/ah as a function of the cantilever's length in the clamped cross-section of the cantilever, with an applied voltage of 5 V on the piezoelectric layer are shown in Fig. 3. The ultimate state of the cantilever is shown by the dashed line. The ultimate state will be achieved when one of two characteristic parameters σ_M and σ_i approaches its own limit, i.e. $\sigma_M = \sigma_+$ and $\sigma_i = \sigma_0$. The f_{max}/ah parameter determines the applicability of the model used in the current work. The f_{max}/ah is approaching its limit at much smaller cantilever lengths than that of σ_i (Fig. 3), which means that the model is indeed applicable in the area where σ_i reaches its critical value σ_0, and the cantilever reaches its ultimate state.

As one can see from Fig. 3, there is a similar trend for all three parameters (σ_M/σ_+, σ_i/σ_0, and f_{max}/ah). For example, all three parameters plotted as a function of the cantilever length exhibit a minimum. Such dependencies are determined by two major factors affecting the stresses in the clamped end of the cantilever. The first factor is a piezoelectric strain. If l/h and h_1/h ratios are constant, the contribution of the piezoelectric strain becomes more and more significant when the length of the cantilever decreases because of the decrease of the piezoelectric layer thickness. The second factor affecting the stresses in the clamped end of the cantilever is its own weight, which is proportional to its length.

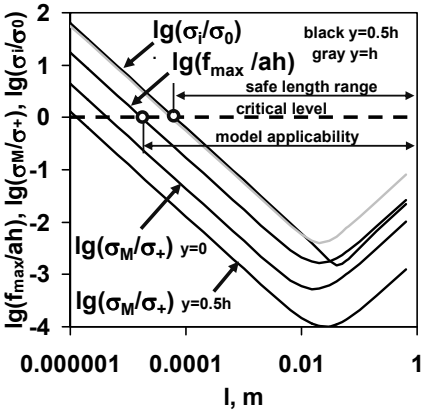

Figure 3. Dependence of cantilever parameters on its length at 5 V.

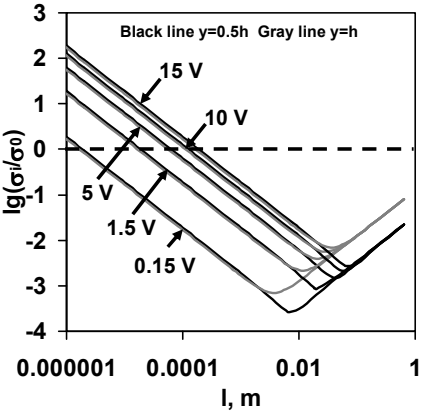

Figure 4. Dependence of stress intensity parameter on cantilever length.

Thus, the smallest geometric dimensions of the cantilever which are safe for reliable operation are those with the level of the stresses in the clamped end of the cantilever lower than the corresponding ultimate stress. It is important to notice that the first criterion, which is fulfilled as the length of the cantilever decreases, is $\sigma_i = \sigma_0$ in the piezoelectric layer. It is also clear that the most dangerous points in the clamped cross-section are those which are located at the interface between layers. Thus, the intersection point between $\sigma_i/\sigma_0|_{y = 0.5h} = f(l)$ curve and the dashed line is to the right of the intersection of the dashed line with $\sigma_i/\sigma_0|_{y = h} = f(l)$. The failure of the non-piezoelectric layer (criterion $\sigma_M = \sigma_+$) can be achieved at a much smaller length of the cantilever. Therefore, the most detrimental parameter of the safe operation of the cantilever is σ_i/σ_0 in the clamped cross-section of the piezoelectric layer at the interface between layers.

The effect of the applied voltage to the piezoelectric layer on the stress intensity in the clamped cross-section of the piezoelectric layer in two points, where $y = h$ and $y = 0.5h$ is shown in Fig. 4. The critical stress intensity with decreasing length is always achieved first at the interface between layers, e.g. when $y = 0.5h$ for all voltages used in the calculations. The increase of the applied voltage U significantly influences the stress intensity causing an increase in the critical length of the cantilever, where the condition of the safe stress intensity is still maintained. Thus, the increase of the applied voltage by an order of two, from 0.15 to 15 V, leads to the increase of the critical length of the cantilever by two orders of magnitude, from ~1.9 to 190 μm.

Dependences of dimensionless parameters σ_M/σ_+, σ_i/σ_0 and f_{max}/ah on the l/h ratio in the cantilever's clamped cross-section with an applied voltage of 5 V on the piezoelectric layer are shown in Fig. 5, which are presented as straight lines in the bilogarithmic scale. All three parameters approach and exceed the critical level equal to zero as the l/h ratio increases, e.g. if the cantilever's thickness decreases but the length remains constant. The most important parameter is again σ_i/σ_0 since it reaches the critical value before any other parameter, when l/h ratio is the smallest.

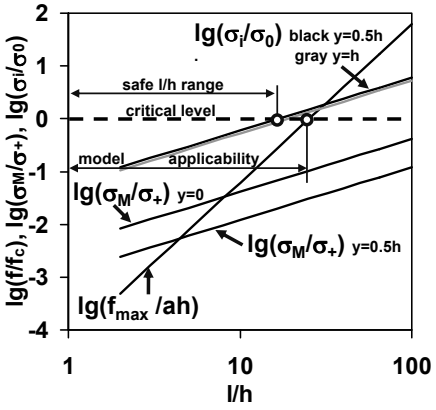

Figure 5. Dependence of cantilever parameters on the ratio l/*h* at 5 V.

The effect of the applied voltage to the piezoelectric layer and the l/h ratio on the dimensionless stress intensity in the clamped cross-section of the piezoelectric layer is presented in Fig. 6. The higher voltage results in larger values of σ_i/σ_0 parameter, meaning that the appearance of the ireversible strain is facilitated by the increase in applied voltage. At the given voltage the stress intensity is always higher at the interface between piezoelectric and non-piezoelectric layers than that at the free surface of the piezoelectric layer. Therefore, for a given voltage and cantilever's length the ultimate cantilever's thickness exists below which the cantilever's operation becomes unsafe and non-reliable. For example, the ultimate thickness is equal to 3.87 μm at the applied voltage of 5 V and 65 μm of the cantilever's length.

Dependences of dimensionless parameters on relative thickness of the non-piezoelectric layer (its thickness divided by total thickness of the cantilever) in the cantilever's clamped cross-section for voltage of 5 V are shown in Fig. 7. Only stress intensity riches values higher than critical level. Lower voltage results in higher critical relative thickness of the non-piezoelectric layer and, in such a way, lower relative thickness of the piezoelectric layer (Fig. 8).

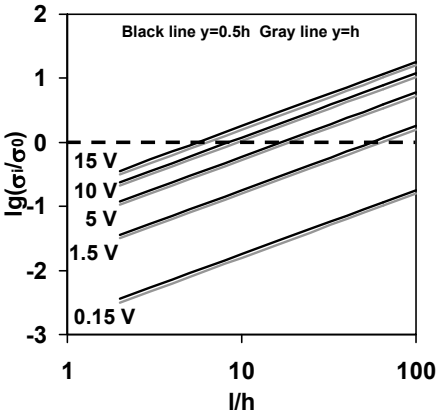

Figure 6. Dependence of stress intensity parameter on the ratio *l*/*h*.

One can show that increasing the stress level σ_0, when the irreversible deformation will show up in a piezoelectric material (for example, by pre-polarization [15]), decreases the ultimate cantilever size. For example, increasing σ_0 by a factor of 3 results in an ultimate length of 0.65 μm. This corresponds to a cantilever sensitivity of about $5 \cdot 10^{24}$ Hz/kg according to Eq. (14). If a detectable frequency shift is 10 Hz, the minimum detectable mass in this case is about $18 \cdot 10^{-24}$ kg, which is approximately the mass of 6 atoms of mercury. The calculations of cantilever sensitivity using (14) have also shown that, if the sensitivity of the steel-based microcantilever is taken as 1, the replacement of steel with B_4C ceramics will increase the sensitivity by a factor of about seven.

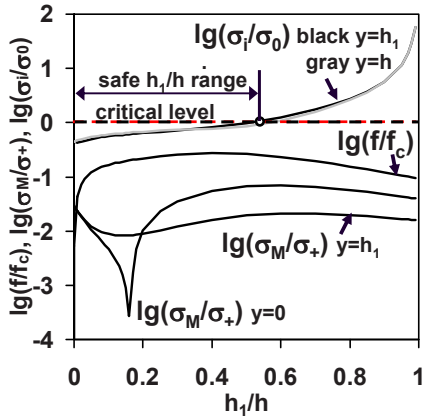

Figure 7. Dependence of cantilever parameters on the ratio h_1/h at 5 V.

4. Conclusions

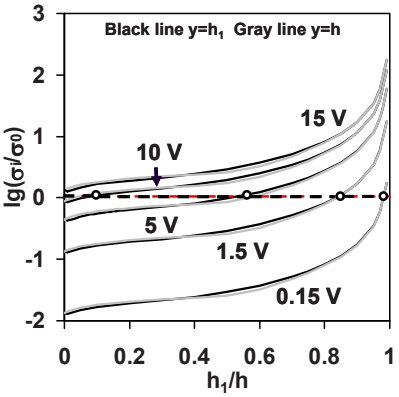

Figure 8. Dependence of stress intensity parameter on the ratio h_1/h.

As a result of our study, a model has been developed which allows an estimation of the dimensional limits of the two layer microcantilever sensors. The model applicability for all considered cantilever lengths has been verified using the maximum deflection criterion proposed in this work.

It was shown for cantilever parameters used for the calculation that von Mises criterion places more serious restrictions on the cantilever length compared to the Mohr's theory of strength, therefore it should be satisfied first. In the proposed model, a stress distribution in the clamped cross-section of cantilever does not depend on the cantilever's width.

It was shown that the stress intensity in the clamped cross-section has different trends as a function of the cantilever length. Thus, for small length range, the stress intensity is increasing as length is decreasing, but for the larger lengths, the stress intensity is increasing as the length is increasing. The stress intensity has a minimum at some intermediate value of the length. The dependence of stress intensity on the cantilever length can be conditionally split into three different ranges, which can be found in the plots obtained for all applied voltage values. The first range is for the small cantilever lengths, where the effect of the self weight is negligibly small. In the opposite range, where the lengths are large, the piezoelectric strain will have minor effects on the stress intensity in comparison with the self weight of the cantilever. In the length's interval between these two ranges, where there is a minimum of the stress intensity, the piezoelectric strain and the effect of the self weight are comparable.

The critical minimal cantilever length could be found when other conditions, such as applied voltage, material parameters, and the thickness ratio of the two layers, are held constant. When the length of the cantilever decreases, the irreversible strain in the piezoelectric layer at a given voltage increases. Thus, at a certain critical cantilever length, the appearance of irreversible strain will result in unsafe cantilever operation. For a given applied voltage and cantilever's length the ultimate cantilever's thickness exists below which the cantilever's operation becomes unsafe and non-reliable as well. The higher voltage results in increased values of the ultimate thickness. At a given voltage, the stress intensity is always higher at

the interface between layers than at the free surface of the piezoelectric layer.

Acknowledgement

This work was supported by NATO Collaborative Linkage Grant “Layered ceramic sensors for biological and chemical detection” and NATO ARW Grant “Boron Rich solids: Sensors for Biological and Chemical Detection, Ultra-high Temperature Composites, Thermoelectrics, Armor”.

References

1. H.-J. Butt, P. Siedle, K. Seifert, T. Seeger, K. Fendler, E. Bamberg, K. Goldie, and A. Engel, Scan Speed Limit in Atomic Force Microscopy, Journal of Microscopy, vol. 169, pp. 75–84, 1993.
2. P.I. Oden, Gravimetric Sensing of Metallic Deposits Using an End-Loaded Microfabricated Beam Structure, Sensors and Actuators B, vol. 53, pp. 191–196, 1998.
3. W.Y. Shih, X. Li, H. Gu, W.H. Shih, and I.A. Aksay, Simultaneous Liquid Viscosity and Density Determination with Piezoelectric Unimorph Cantilevers, Journal of Applied Physics, vol. 89, pp. 1497–1505, 2001.
4. J.W. Yi, W.Y. Shih, R. Mutharasan, and W.-H. Shih, In Situ Cell Detection Using Piezoelectric Lead Zirconate Titanate – Stainless Steel Cantilevers, Journal of Applied Physics, vol. 93, pp. 619–625, 2003.
5. J.W. Yi, W.Y. Shih, and W.-H. Shih, Effect of Length, Width, and Mode on the Mass Detection Sensitivity of Piezoelectric Unimorph Cantilevers, Journal of Applied Physics, vol. 91, pp. 1680–1686, 2002.
6. B. Ilic, D. Czaplewsli, H.G. Craighead, P. Neuzil, C. Campagnolo, and C. Batt, Mechanical Resonant Immunospecific Biological Detector, Applied Physics Letters, vol. 77, pp. 450–452, 2000.
7. T. Thundat, E.A. Wachter, S.L. Sharp, and R.J. Warmack, Detection of Mercury Vapor Using Resonating Microcantilevers, Applied Physics Letters, vol. 66, pp. 1695–1697, 1995.
8. N. Orlovskaya, M. Lugovy, V. Subbotin, O. Radchenko, J. Adams, M. Chheda, J. Shih, J. Sankar, and S. Yarmolenko, Robust Design and Manufacturing of Ceramic Laminates with Controlled Thermal Residual Stresses for Enhanced Toughness, Journal of Materials Science, vol. 40, pp. 5483–5490, 2005.
9. G. de With, High Temperature Fracture of Boron Carbide: Experiments and Simple Theoretical Models, Journal of Materials Science, vol. 19, pp. 457–466, 1984.
10. H.J. Xiang, and Z.F. Shi, Static Analysis for Multi-Layered Piezoelectric Cantilevers, International Journal of Solids and Structures, vol. 45, pp. 113–128, 2008.
11. S. Timoshenko, Strength of Materials, 3rd ed, Krieger Publishing Company, 1976.
12. S.C. Hwang, and R.M. McMeeking, A Finite Element Model of Ferroelastic Polycrystals, International Journal of Solids and Structures, vol. 36, pp. 1541–1556, 1999.

13. A. Nadai, Theory of Flow and Fracture of Solids, Vol. 1, McGraw-Hill, New York, 1950.
14. S.P. Timoshenko, and J.N. Goodier, Theory of Elasticity, McGraw-Hill, New York, 1970.
15. Z. Shen, W.Y. Shih, and W.-H. Shih, Self-Exciting, Self-Sensing $PbZr_{0.53}Ti_{0.47}O_3/SiO_2$ Piezoelectric Microcantilevers with Femtogram/Hertz Sensitivity, Applied Physics Letters, vol. 89, 023506, 2006.

RAMAN EFFECT IN BORON AND BORON-RICH COMPOUNDS

HELMUT WERHEIT[1]* AND VOLODIMIR FILIPOV[2]
[1]*Institute of Physics, University Duisburg-Essen, Campus Duisburg D-47048 Duisburg, Germany*
[2]*REE refractory compounds laboratory, Institute for Problems of Materials Science; National Academy of Sciences of Ukraine, 3, Krzhyzhanovsky st., 03680 Kiev-142, Ukraine*

Abstract High-resolution Raman spectra of different allotropes of elemental boron and of some selected representatives of boron-rich solids are presented and discussed. Often, the number of modes exceeds that, which is group theoretically predicted for idealized structures. The reason is intrinsic defects, which are typical for most of these structures. Specific Raman modes in the spectra of different groups of icosahedral structures are attributed to inter-icosahedral and intra-icosahedral B–B vibrations respectively and allow assessing the bonding forces related. Badger's rule is satisfactorily fulfilled across all icosahedral structure groups. – Depending on the penetration depth of the exciting radiation, Raman spectra can be significantly different as shown for boron carbide and lanthanum hexaboride.

Keywords: boron, boron-rich compounds, Raman

1. Introduction

Raman spectroscopy is a sensitive tool for determining the phonon spectra of crystalline solids, their modification by changing chemical compositions, and even for detecting structural imperfections. Exemplary, in icosahedral boron-rich solids the following structural imperfections occur; even in the case that high purity boron is used for preparation.

- Natural boron consists of 18.83% ^{10}B and 81.17% ^{11}B; the mass difference of isotopes 8.7% is considerable. Instead of the statistical

* Helmut Werheit Institute of Physics, University Duisburg-Essen, Campus Duisburg D-47048 Duisburg, Germany, e-mail: helmut.werheit@koeln.de; helmut.werheit@uni-due.de.

N. Orlovskaya and M. Lugovy (eds.), *Boron Rich Solids: Sensors, Ultra High Temperature Ceramics, Thermoelectrics, Armor*, DOI 10.1007/978-90-481-9818-4_3,

distribution usually supposed, a preferred occupation of specific sites cannot be excluded.
- The B_{12} icosahedra are slightly distorted in consequence of the Jahn-Teller effect.
- Most structures exhibit intrinsic defects of completely unoccupied or only partly occupied regular atomic sites.
- Carbon has a very high affinity to boron. Therefore carbon impurities in boron structures often occur, sometimes in specific sites.

Structural distortions are important for the electronic properties of icosahedral boron-rich solids; they determine their semiconducting properties in contrast to the metallic behavior predicted by theoretical calculations on idealized structures (see [1, 2]).

Deviations from ideal crystal structures lift the symmetry selection rules, and Raman inactive lattice vibrations become detectable. If such Raman lines can be attributed to the movement of specific atoms or atomic arrangements, they may allow conclusions on specific structural defects.

At the surface, the periodicity of crystals is abruptly terminated, which consequently modifies the bulk properties within a distorted layer of rearranged atoms. Its thickness typically corresponds to some lattice constants, i.e. about 5 nm. For investigating bulk phonons, it must be ensured that Raman scattering within this layer does not essentially contribute to the measured spectra. Beilby or adsorbed layers on the surface can aggravate this problem; however, they can be avoided using freshly cleaved surfaces.

As shown below, Raman spectra of boron carbide and of metal hexaborides are accordingly affected, indeed for different reasons. In boron carbide the fundamental absorption is very high, thus preventing the high energy laser radiation of the Ar ion laser to reach the undistorted bulk, while the Nd:YAG laser in FT-Raman spectroscopy essentially excites bulk phonons. In metallic hexaborides the free carrier absorption increasing towards low frequencies is responsible for the small penetration depth of the Nd:YAG laser; thus mainly the distorted surface range of the sample is excited, while the Ar ion laser preferably excites phonons in the undistorted bulk.

2. Raman Spectra

2.1. ICOSAHEDRAL BORON-RICH SOLIDS

The basic element of the icosahedral boron-rich structures is the B_{12} icosahedron. The simplest structure is α-rhombohedral boron with one icosahedron on the vertex of the rhombohedral unit cell; the most complex structures presently

known are YB_{66} type with more than 1,584 B atoms per cubic unit cell (see [8]). In between there are numerous further complex structures, including the high-temperature allotrope of crystalline boron, β-rhombohedral boron, with ~106.5 atoms per unit cell. Moreover, amorphous boron consists of statistically arranged icosahedra; therefore, it is immediately related to the crystalline icosahedral structures (see [3]).

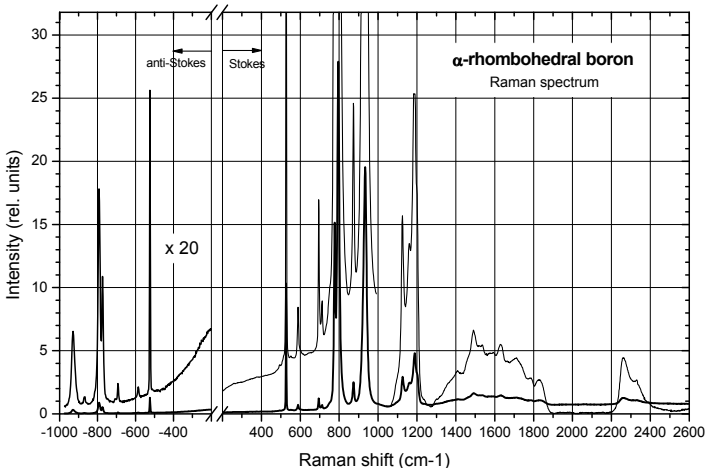

Figure 1. α-rhombohedral boron, Raman spectrum. Thin lines, spectra obtained with longer data accumulation [6].

2.1.1. *α-rhombohedral boron*

α-rhombohedral boron is the simplest icosahedral boron-rich structure. Its unit cell contains one B_{12} icosahedron at each vertex only. According to group theory, for α-rhombohedral boron with D_{3d} point symmetry ten Raman active modes (four A_{1g} singlets, six E_g doublets) are expected [4, 5]. The complete Raman spectrum of α-rhombohedral boron is displayed in Fig. 1, containing the Stokes and the anti-Stokes range as well [6]. The occurrence of modes in both ranges irrefutably proves Raman activity. Unfortunately, for higher Raman shifts this check is difficult because the scattering intensity decreases as λ^4. Moreover, the second order Raman spectrum is shown in Fig. 1. Such modes occur, when two phonons are involved in light scattering. The probability of such processes is much lower than for first-order processes.

The number of Raman lines (Table 1) exceeds that theoretically predicted. Reason is the structural imperfections listed in the introduction. In one case (1187/1201 cm^{-1}) the split of modes is attributed to the isotopes. For a detailed interpretation the allocation between Raman modes and specific vibrations of the lattice is required.

Based on theoretical calculations, Beckel et al. [5] attributed most of the Raman peaks to specific movements of atoms. In this paper, we restrict ourselves to two significant peaks. The range between 1,100 and 1,200 cm^{-1} is essentially related to the radial movement of triangle atoms meaning double stretch and double compression of the strongest bonds, the inter-icosahedral two-centred B–B bonds. The 934 cm^{-1} mode involves distortions of the polar triangles as well as of the equatorial hexagon, where two of the six bonds are stretched, hence preferably representing the intra-icosahedral B–B bonds.

TABLE 1. First order Raman lines of α-rhombohedral boron (according to Fig. 1). Modes #13–16 are attributed to inter-, mode # 9 to intra-icosahedral B–B vibrations

	Experimental (Fig. 1)			Vast et al. [7]:			
	cm^{-1}	Half-width	Remark		Theory	Exp.	Half-width
1	494		Very weak				
2	527	2,9		Eg	529	525	0.8
3	552		Very weak				
4	589	6,5		Eg	608	586	
5	694	4,8		A1g	708	692	5
6	713	5,9		Eg	729	708	
7	750						
8	778	7,1		Eg	790	774	7
9	795	10,8		A1g	815	793	11
10	873	7,7		Eg	890	870	8
11	934	18,8		A1g	947	925	22
12	1,094		Very weak				
13	1,125	11,0		Eg	1,138	1,122	15
14	1,160						
15	1,187		^{11}B	A1g	1,192	1,186	24
16	1,201		^{10}B				
17	1,238		Very weak				

As will be shown below, these peaks can be rather clearly identified in the Raman spectra of other icosahedral boron structures as well.

2.1.2. *Boron carbide*

Boron carbide is the best-investigated representative of the α-rhombohedral boron structure group (see [2, 8, 9] and references therein). Additionally to the icosahedra at the vertex, the rhombohedral cell contains linear arrangements of two or three atoms on the main cell-diagonal, which is parallel to the crystallographic c-axis. However, there is no unit cell representing the

whole structure, containing elementary cells statistically composed of different structure elements. These are B_{12} or $B_{11}C$ icosahedra, C–B–C and C–B–B chains, and B□B arrangements (□, vacancy).

The homogeneity range of boron carbide extends from $B_{4.3}C$ at the carbon-rich to about $B_{\sim 11}C$ at the boron-rich limit (see [9]). The general structure formula is $(B_{12})_n(B_{11}C)_{1-n}(CBC)_p(CBB)_q(B\square B)_{1-p-q}$ for the whole homogeneity range.

For idealized boron carbide structures (B_{12}) X–Y–X and (B_{12}) X–X both, 11 Raman active modes (5 A_{1g} singlets, 6 E_g doublets) are expected. In the real structure the different structure types occur side by side, moreover modified by different actual compositions of icosahedra (B_{12} or $B_{11}C$) and chains. Therefore a higher number of modes are expected to occur, irrespective of other structural distortions.

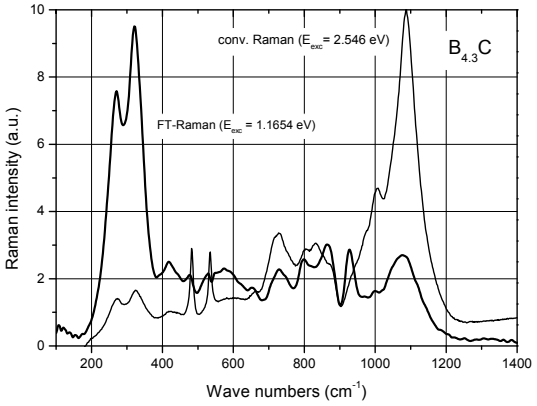

Figure 2. $B_{4.3}C$, Raman spectra [6]. Bold line, bulk spectrum, excitation, Nd:YAG laser (1.56 eV); thin line, surface spectrum, excitation Ar ion laser (2.55 eV).

Raman spectra of boron carbide were controversially discussed because they are significantly different when obtained with different excitation energies. This is illustrated in Fig. 2. The reason for this difference is the extremely high absorption coefficient of boron carbide in the range of fundamental absorption (ΔE = 2.09 eV). If excitation in this range is applied (e.g. with the Ar ion laser at 2.55 eV excitation energy), excitation preferably takes place within the very small penetration depth of about 1.7 μm thickness [11]. Certainly, it is rather improbable that such a big region beneath the surface is distorted; probably the concerning range is limited to several lattice constants, i.e. about 5 nm.

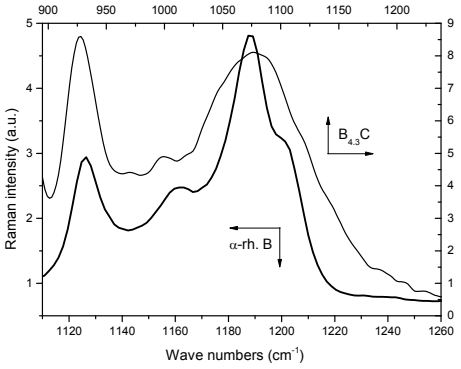

Figure 3. Raman active inter-icosahedral B–B vibrations in α-rhombohedral boron and $B_{4.3}C$ [6]. Bold line, α-rhombohedral boron; thin line, $B_{4.3}C$.

The electron density distributions in the icosahedra of α-rhombohedral boron and $B_{4.3}C$ are very similar [10]. Therefore a close similarity of the concerning parts of their phonon spectra is expected. This is confirmed in Fig. 3 for the Raman-active inter-icosahedral B–B vibrations.

For a more detailed discussion of the surface spectrum of boron carbide, the reader is referred to [11].

2.1.3. *β-rhombohedral boron*

The idealized structure of β-rhombohedral boron has the space group $R\bar{3}m$, structure formula $(B_{12})_4$ $(B_{28})_2$ B. Its unit cell contains 105 atoms with 82 Raman active vibrational modes (31 A_{1g}, 51 E_g) expected.

In the real structure the occupation of site B(13) is 74.5(6)% only; otherwise, there are the additional sites B(16)–B(20) with low occupancies of about 27–4% adding to about 106.5 atoms per unit cell [12]. Accordingly, a higher phonon number is expected.

In Fig. 4, some Raman spectra of β-rhombohedral boron are displayed [11]. Those obtained with different excitation energy, below and above the band gap, largely agree. Therefore a significant influence of the surface range like in boron carbide is not registered. Indeed, the intrinsic absorption in β-rhombohedral boron is much lower than in boron carbide, and the penetration depth of the exciting light is correspondingly larger, and therefore the influence of a surface layer could be masked.

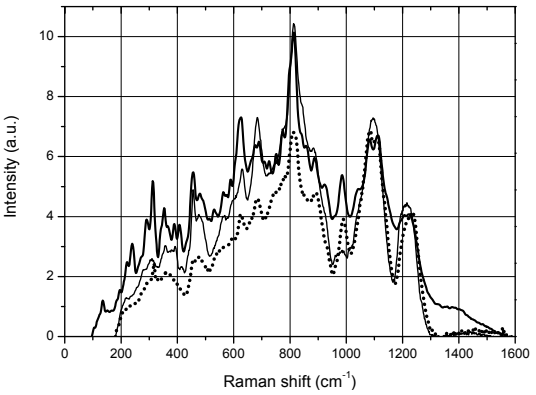

Figure 4. β-rhombohedral boron, Raman spectra [6]. Bold line, FT-R (1.56 eV excitation energy), thin line, Ar-ion laser, 2.55 eV; dotted line, C doped (1.1 at.%).

There is a small but remarkable difference between both spectra; the FTIR spectrum exhibits some more details, in spite of the nominally lower resolution of the equipment, of 2 instead of 1.5 cm^{-1}. Reason could be a small influence of a distorted surface range or a phase transition induced by the power of the Nd:YAG laser.

The influence of carbon doping on the Raman spectrum is small; only the modes seem to be somewhat smearing out. C atoms are preferably accommodated in the polar sites of the icosahedra and slightly displaced towards the center of the icosahedron.

The analysis of the bulk Raman spectrum yields about 35 modes only. However, the dense sequence of numerous modes must be taken into account; and therefore accidental degenerations cannot be excluded.

2.1.4. *Amorphous boron*

Basic structural element of amorphous boron is the B_{12} icosahedron. According to neutron diffraction studies, the icosahedral units are essentially intact with disorder occurring in the linking between the icosahedra. A medium-range order similar to crystalline β-rhombohedral boron was shown to exist, suggesting that the icosahedra are more or less statistically arranged with their external bonds largely covalently saturated [13].

In Fig. 5 the FT-.Raman spectrum of amorphous boron (H.C. Starck, Goslar) is displayed [14]. The spectrum shows two significant features, the strong peak at 1160 cm^{-1} and the shoulder at about 800 cm^{-1}, which can be attributed to the inter- and intra-icosahedral B–B vibrations respectively, and agree with theoretical calculations [15]. According to structural investigations, they are closely related to the according vibrations in the β-rhombohedral boron structure.

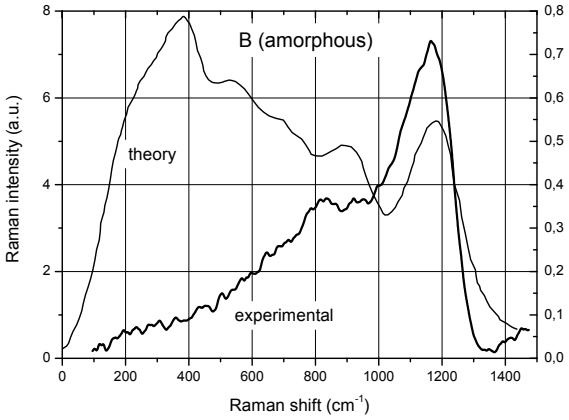

Figure 5. Amorphous boron. Bold line, FT-Raman spectrum [14]; thin line, theory [15].

The spectral position of both B–B modes agrees quite well with theoretical calculations; however, the intensity of the modes at lower frequencies is considerably overestimated by theory [15].

2.1.5. *YB_{66} type structures*

The YB_{66} structure group is the most complex one of the icosahedral boron-rich solids. Its boron framework is composed of $(B_{12})_{13}$ giant icosahedra consisting of a central and 12 surrounding B_{12} icosahedra and B_{80} clusters, whose 80 sites are statistically occupied by 42 B atoms only (Fig. 6). In total, this model contains 1,584 B atoms per unit cell. The Y sites enclose the B_{80} clusters in octahedral arrangements; hence there are eight of such octahedral arrangements per unit cell. However the Y sites are not completely occupied as well; the actual composition is determined by the occupancy of the Y sites, for example 0.5 in the case of YB_{66} [6, 16].

However, the experimentally determined B content in the unit cell is higher than the 1,584 B atoms (see [11]).

Figure 6 shows that spectra of different compounds belonging to this structure group are essentially the same, thus confirming that the spectra are preferably determined by vibrations of the boron framework, and not by the heavy metal atoms, whose contribution is expected at rather low frequencies. We attribute the predominant peak at 1,070 cm^{-1} to the inter-icosahedral and the next strong peak towards lower frequencies at 830 cm^{-1}, to the intra-icosahedral B–B vibrations.

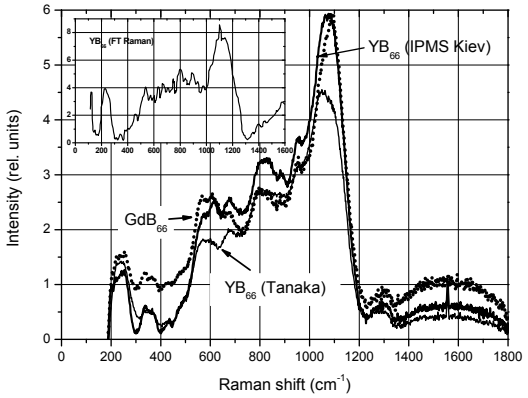

Figure 6. YB_{66} type structures, Raman spectra, Ar ion laser [6]. Bold line, YB_{66} (IPMS Kiev); thin line, YB_{66} (Tanaka); dotted line, GdB_{66} (Tanaka). Insert, FT Raman spectrum of YB_{66} (Tanaka) for comparison [11].

The spectra show that in this complex structure the phonon modes are not well defined, but smeared, hence leading to few, rather broad peaks. In the range of inter-icosahedral and intra-icosahedral vibrations, the similarity of the spectra with that of the amorphous boron is obvious.

2.1.6. *Bonding forces*

As shown above, the Raman modes # 13–16 and mode #9 of α-rhombohedral boron (see Table 1) and corresponding ones in other icosahedral structures [6] can be attributed to essentially the same type of inter-icosahedral and intra-icosahedral B–B vibrations. Accordingly, they are the basis for estimating the force constants related. We presume that the nature of vibrating configurations of atoms is largely independent of the individual structure, which is certainly the better complied the closer the structures are related.

Based on $\omega = \sqrt{k/\mu}$ with $\mu = m_A m_B/(m_A + m_B)$, the relative force constants k of the inter- and intra-icosahedral vibrations relative to α-rhombohedral boron is determined, thus avoiding the problem of unknown masses. The results are displayed in Fig. 7a, b respectively.

After Badger [17] the force constant k in equation $\omega = \sqrt{k/\mu}$ is quite accurately related to the inter-nuclear distance d_0 of the vibrating atoms as $k^{-1/3} = a_{ij}\left(d_0 - b_{ij}\right)$ with the parameters a_{ij} and b_{ij} depending on the nature of the vibrating atoms. Badger initially proved the validity of this relation for two-atomic molecules with equal parameters for all atoms belonging to

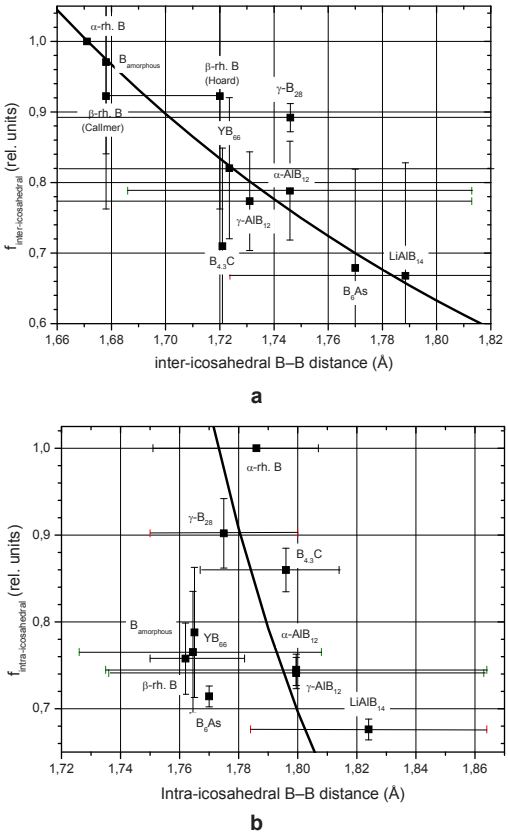

Figure 7. Relative force constants of the inter-icosahedral B–B vibrations in icosahedral boron-rich structures vs. (**a**) inter-atomic distances; (**b**) Intra-atomic distances [6]. Symbols correspond to the average of experimental data; error margins show their extreme limits. Full line, Badger's rule.

the same row of the periodic system of elements. Meanwhile, it has been verified that this relation is applicable for corresponding vibrations in solids as well (see [18]). In Fig. 7a, this is confirmed for the relative force constant of the inter-icosahedral 2-center bond. Badger's rule satisfactorily fits the experimental data.

2.2. HEXABORIDES

Metallic and semiconducting hexaborides MB_6 crystallize in cubic structures with unit cells containing one formula weight each. The boron atoms form regular octahedra at the vertices of the unit cell, whose center is occupied by the metal atom (see [6, 83]).

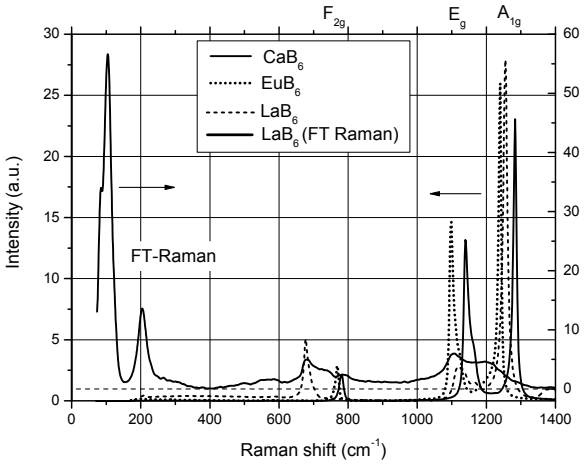

Figure 8. Raman spectra of some MB_6 compounds [19,20].

Group theory predicts three Raman active phonon modes: A_{1g}, E_g, and F_{2g}, belonging to the boron framework of the structure only. They are clearly identified in the spectra obtained with conventional Raman spectroscopy (Fig. 8) [19]. At least in some cases, FT-Raman spectra [20] are significantly different (for LaB_6 see Fig. 8). The Raman-active modes are weak and considerably broadened, and at low wavenumbers strong modes additionally appear, which in the conventionally measured spectra are hardly discernable.

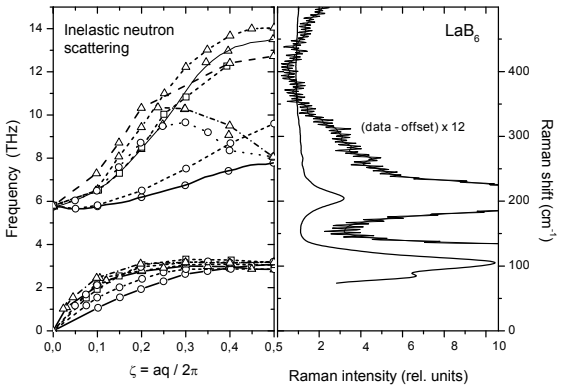

Figure 9. LaB_6. Comparison of FT-Raman spectrum [20] with inelastic neutron scattering [21].

As shown in Fig. 9, inelastic neutron scattering [21] confirms according Raman-inactive phonon modes in further agreement with theoretical calculations [22]. Obviously, the selection rules of these modes are lifted. Taking the considerable broadening of the Raman-active modes into account, we assume that the Nd:YAG laser radiation is essentially absorbed within a distorted surface range because of the high free-carrier absorption.

Magnetic phase transitions and anomalous transport properties in Ca doped EuB_6 at low temperatures were reported by Rhyee et al. [23]. Based on $\omega = \sqrt{k/\mu}$ we determined the modification of the force constants of the Raman-active phonons in $Eu_{1-x}Ca_xB_6$ (x = 0, …, 1), and moreover in C doped EuB_6 from Raman spectra obtained at ambient temperatures (Fig. 10).

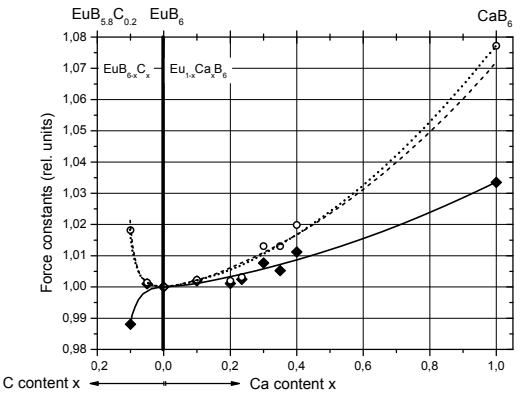

Figure 10. Force constant of the Raman-active modes in $Eu_{1-x}Ca_xB_6$ (x = 0, …, 1) and $EuB_{6-x}C_x$ (x = 0–0.1).[19].

The results indicate the force constants in $Eu_{1-x}Ca_xB_6$ monotonously changing without significant anomalies, at least in the range of the compounds investigated. The lattice parameters (CaB_6, 4.1520 Å; EuB_6, 4.1849 Å) differ by less than 1%, with is essentially due to the slightly different atomic radii of the metal atoms (Ca, 180 pm; Eu 185 pm).

In carbon-doped EuB_6 it is striking that the force constant of the F_{2g} mode varies opposite to those of the E_g and A_{1g} modes, which largely agree among each other. The influence of C doping on the force constants in EuB_6 is considerably strong compared with that occurring, when Eu atoms are exchanged by Ca atoms. C atoms contribute one additional electron to the octahedron, which may be responsible for the considerable change of force constants.

2.3. DODECABORIDES

The crystal structure of the UB_{12} type dodecaborides can be described in terms of a modified fcc unit cell with the metal atoms in the center of regular B_{24} truncated octahedra and B atoms at each of their 24 vertices. This idealized atomic pattern has five Raman active phonon modes (one A_{1g}, two E_g, two F_{2g}) attributed to the boron framework [24].

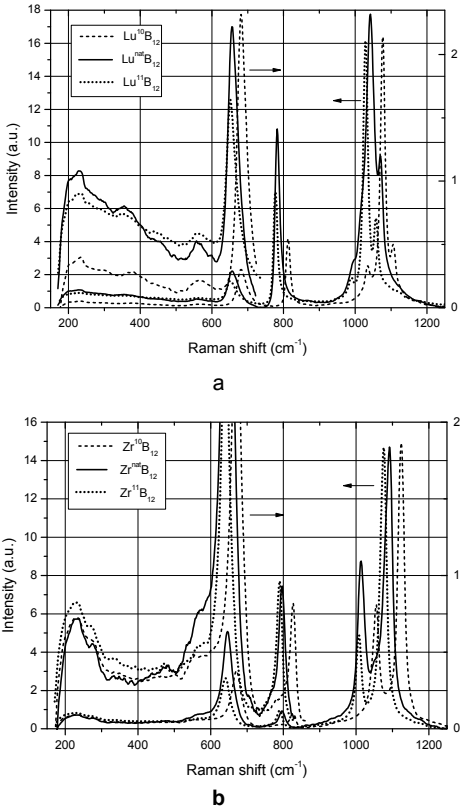

Figure 11. Raman spectra. (**a**) LuB_{12}; (**b**) ZrB_{12} [19].

In Fig. 11 the Raman spectra of LuB_{12} and ZrB_{12} are displayed with ^{10}B, ^{nat}B and ^{11}B, each. The frequency shift of modes evoked by the different isotopes is clearly seen. Nevertheless, besides the frequency shift of the main modes, the spectra of both compounds differ in some details. While for LuB_{12} the resonances near 1,100 cm^{-1} are split into three, ZrB_{12} exhibits only two. In the spectral rang <600 cm^{-1} Raman-inactive modes appear. They are probably evoked by structural defects, which are distinctly different for both compounds. For a preliminary discussion of defects in these structures, see [25].

3. Conclusion

Showing the specific Raman-active modes, Raman spectra are fingerprints of the different crystal structures. Moreover, they sensitively indicate structural defects, even if the quantum mechanical selection rules are slightly lifted only.

Particular care is required for avoiding influences of the surface range on bulk Raman spectra by choosing suitable lasers with sufficiently high penetration depths for excitation. Otherwise, excitations in small penetration depths yield valuable information on structural distortion in the surface range.

In cases, when specific Raman-active vibrations are identified, the structure-dependent variation of force constants can easily be derived from the shift of Raman modes. For icosahedral boron-rich structures Badger's rule is satisfactorily obeyed.

References

1. Schmechel R, Werheit H, 1999, Correlation between Structural Defects and Electronic Properties of Icosahedral Boron-Rich Solids. *J. Phys: Condens. Matter* **11**, 6803
2. Werheit H, 2007, Are there bipolarons in icosahedral boron-rich solids? *J. Phys.: Condens. Matter* **19**, 186–207
3. Werheit H, Schmechel R, 1998, Boron, in *Landolt-Börnstein, Numerical Data and functional relationships in Science and Technology* Group III, Vol. **41C**, O. Madelung ed., Springer, Berlin, p. 3–148
4. Binnenbruck H, Werheit H, 1979, IR-active phonons of boron and boron carbide, *Z. Naturforsch.* **34a**, 787
5. Beckel CL, Yousaf M, Fuka MZ,. Raja SY, Lu N, 1991, Lattice vibrations of the icosahedral solid α- boron, *Phys Rev. B* **44**, 25–35
6. Werheit H, Filipov V, Kuhlmann U, Schwarz U, Armbrüster M, Leithe-Jasper A, Tanaka T, Higashi I, Lundström T, Gurin VN, Korsukova MM, 2010, Raman Effect in Icosahedral Boron-Rich Solids, *Sci. Technol. Adv. Mat.* **11**, 023001
7. Vast N, Baroni S, Zerah G, Besson J. M, Polian A, Grimsditch M, Chervin JC, 1997, Lattice Dynamics of Icosahedral α-Boron under Pressure, *Phys. Rev. Lett.* **78**, 693
8. Werheit H, 2009, Experimentally Founded Charge Transport Models for Icosahedral Boron-Rich Solids, *this volume*
9. Werheit H, Boron Compounds, 2000*, Landolt-Börnstein, Numerical Data and functional relationships in Science and Technology* Group III, Vol. **41D**, Springer, Berlin, p. 1–491
10. Hosoi S, Kim H, Nagata T, Kirihara K, Soga K, Kimura K, Kato K, Takata M, 2007, Electron density distributions in derivative crystals of α-rhombohedral boron, J. Phys. Soc. Japan **76**, 044602
11. Werheit H, Filipov V, Schwarz U, Armbrüster M, Leithe-Jasper A, Tanaka T, Shalamberidze SO, 2010, On surface Raman scattering and luminescence radiation in boron carbide, *J. Phys: Condens. Matter* **22**, 045401

12. Garbauskas MF, Kasper JS, Slack GA, 1986, The incorporation of vanadium in β-rhombohedral boron as determined by single-crystal diffractometry, *J Solid State Chem*. **63** 424
13. Delaplane R.G., Dahlberg U., Graneli B., Fischer P. and Lundstrom T., 1988, A Neutron Diffraction Study of amorphous Boron, *J. Non-Cryst. Sol.* **104**, 249
14. Kuhlmann U, Werheit H, Lundström T, Robers W, 1994, Optical Properties of Amorphous Boron *J. Phys. Chem. Solids* **55**, 579
15. Shirai K, Thorpe MF, Vibrations of Icosahedron-Based Networks: Application to Amorphous Boron 1997*, Phys. Rev. B* **55**, 12244
16. Higashi I, Kobayashi K, Tanaka T, Ishizawa Y, 1997, Structure refinement of YB_{62} and YB_{56} of the YB_{66}-type structure, *J. Solid State Chem.* **133**, 16
17. Badger RM, 1934, A relation between internuclear distances and bond force constants*, J. Chem Phys*. **2** 128
18. Pauling L 1960, The nature of chemical bond and the structure of molecules and crystals, Cornell University Press
19. Werheit H, Filipov V, Schwarz U, Armbrüster, 2009 (in preparation)
20. Schmechel R, Werheit H, and Paderno Yu B, 1997, FT Raman spectroscopy of some metal hexaborides; *Journal of Solid State Chemistry* **133**, 264
21. Smith HG, Dolling G, Kunii S, Kasaya M, Liu B, Takegahara K, Kasuya T, Goto T, 1985, Experimental study of lattice dynamics in LaB_6 AND YbB_6; *Solid State Comm.* **53**, 15
22. Hasegawa T, Ogita N, Udagawa M, 2009, Valence dependence of interatomic interactions in RB_6, *J Phys: Conf. Series* **176**, 012031
23. Rhyee JS, Oh BH, Cho BK, 2004, Magnetic Phase Transitions and Anomalous Transport Properties in Ca-Doped Eu Hexaborides. *J. Korean Phys. Soc.,* **44**, 1509
24. Fujita Y, Ogita N, Shimizu N, Iga F, Takabatake T, Udagawa M, 1999, *J. Phys. Soc. Japan*, **68** 4051
25. Werheit H, Paderno Yu, Filippov V, Paderno V, Pietraszko A, Armbrüster M, Schwarz U, 2006, Peculiarities in the Raman spectra of ZrB_{12} and LuB_{12} single crystals, *J Solid State Chem* **179** 2761

EXPERIMENTALLY FOUNDED CHARGE TRANSPORT MODEL FOR ICOSAHEDRAL BORON-RICH SOLIDS

HELMUT WERHEIT*
Institute of Physics, University Duisburg-Essen, Lotharstr. 1, Campus Duisburg D-47048 Duisburg, Germany

Abstract Charge transport in icosahedral boron-rich solids, in particular in boron carbide, has been controversially discussed. Theoretical band structure calculations, based on idealized instead of real structures, yield qualitatively wrong results; metallic instead of semiconducting behavior in consequence of neglecting intrinsic structural defects. The theoretical bipolaron hypothesis is not compatible with numerous experimental results. In contrast, the actual energy band schemes of β-rhombohedral boron and boron carbide mainly derived from optical investigations allows the consistent description of most of the experimental results. Electronic transport is a superposition of hopping-type and band-type transport, whose share depends on the actual conditions and the antecedent.

Keywords: boron, boron carbide, boron-rich compounds, electronic transport

1. Introduction

Beginnings of the semiconductor investigation on icosahedral boron-rich solids in the sixties of the last century were characterized by expecting to develop β-rhombohedral boron as a competitor of silicon. The odds seemed promising, because the band gap is similar, the mechanical, chemical, and thermal properties are promising, and the melting point is considerably higher.

The unsatisfying transport properties were initially ascribed to impurities, and Wacker Chemistry, in Munich, Germany, purified β-rhombohedral boron to 99.9999%. After this had failed, they prepared high-quality single crystals to exclude the influence of structural defects on the electronic transport. After this turned out to be a failure as well, Wacker terminated its engagement in boron. Nevertheless, β-rhombohedral boron has become one of the best-investigated icosahedral boron-rich solids.

* Helmut Werheit, Institute of Physics, University Duisburg-Essen, Lotharstr. 1, Campus Duisburg D-47048 Duisburg, Germany, e-mail: helmut.werheit@koeln.de; helmut.werheit@uni-due.de

N. Orlovskaya and M. Lugovy (eds.), *Boron Rich Solids: Sensors, Ultra High Temperature Ceramics, Thermoelectrics, Armor*, DOI 10.1007/978-90-481-9818-4_4,

The preparation of macroscopic single crystals of the low-temperature allotrope α-rhombohedral boron with a much simpler crystal structure has proved extremely difficult, and therefore boron carbide, belonging to the same structure group, became the privileged object of investigation. Its industrial manufacturing had already been developed for usage as abrasive and light-weight armor, and the composition B_4C was attributed to the simple structure formula $B_{12}C_3$ with one B_{12} icosahedron and one C–C–C chain per unit cell. Meanwhile, it is known that neither the chemical composition B_4C, nor the simple structure model is correct. In the large homogeneity range extending from $B_{4.3}C$ at the carbon-rich to $B_{\sim 11}C$ at the boron-rich limit, there is no unit cell representing the whole structure, but a statistical arrangement of differently composed elementary cells.

Meanwhile, numerous further icosahedral boron-rich compounds have been developed (see [1]). The most complex one is the YB_{66} type borides with 1,584 B atoms per unit cell. Experimental investigation of their semiconductor properties is limited, and theoretical calculations are missing altogether.

The object of the following discussion of electronic transport properties in icosahedral boron-rich solids will be β-rhombohedral boron and boron carbide, on which substantial theoretical and experimental results are available; as side objects, α-rhombohedral boron and YB_{66} will be considered.

2. Some Details of Structures

2.1. α-RHOMBOHEDRAL BORON STRUCTURE GROUP

In Fig. 1 the structures of α-rhombohedral boron (Fig. 1a) and other members of this structure group (Fig. 1b, c) are shown. The rhombohedral unit cell contains one B_{12} icosahedron. Additionally there occur two- or three-atomic arrangements on the main diagonal of the rhombohedron. In boron carbide both types (C–B–C, C–B–B, and B□B arrangements (□, vacancy) exist side by side; they are statistically distributed in the whole structure. Within the homogeneity range, their concentration depends on the actual chemical composition, and their general structure formula is $(B_{12})_{1-x}(B_{11}C)_x(CBC)_{1-m-n}(CBB)_m(B\square B)_n$ (for details see [1, 2]).

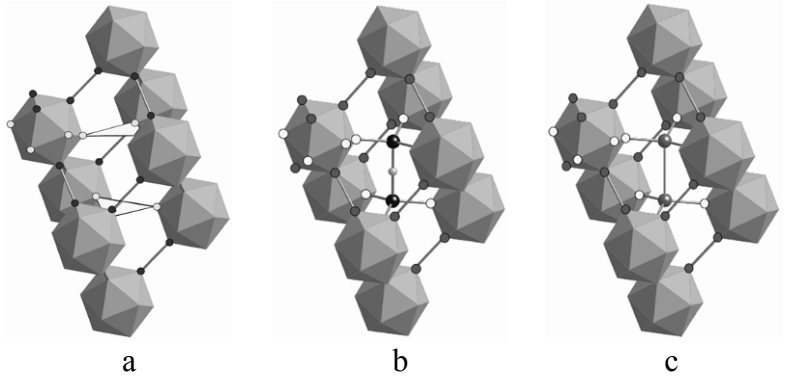

Figure 1. α-rhombohedral boron structure group (**a**) α-rhombohedral boron; (**b**) with three-atomic chain; (**c**) with two-atomic arrangement (with or without bonding in between).

2.2. β-RHOMBOHEDRAL BORON STRUCTURE GROUP

The idealized structure of β-rhombohedral boron (105 atoms per unit cell) is displayed in Fig. 2a. In the real structure the occupation of site B(13) is 74.5(6)% only; additional sites B(16)–B(20) (Fig. 2b) with low occupancies (~27% – ~4%) leading to about 106.5 atoms per unit cell in total. Doping is possible by accommodating foreign atoms in specific interstitial sites (Fig. 2c). As these sites partly coincide with, or are very close to the sites B(16)–B(20); a concurrent occupation is improbable (for details see [3, 4]).

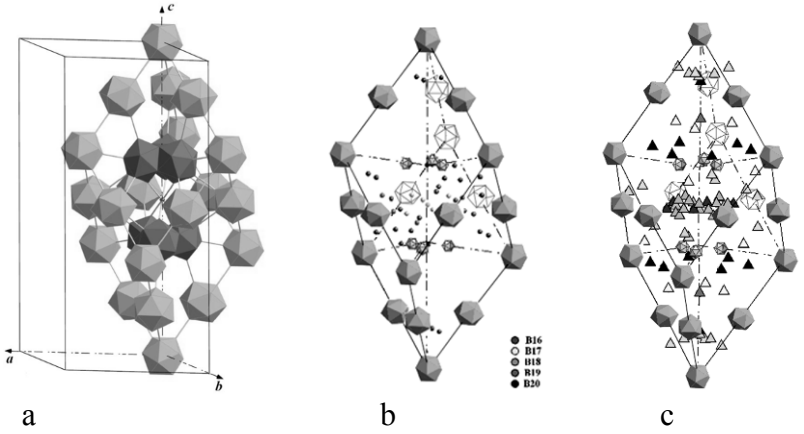

Figure 2. β-rhombohedral boron structure group (**a**), idealized structure; (**b**), partly occupied B sites; (**c**), sites for interstitial doping [7].

C atoms preferably substitute for B atoms in the polar sites of the icosahedra [5]. Compared with B, the C atom is displaced towards the center of the icosahedron by about 5% [6].

2.3. YB_{66} TYPE STRUCTURES

The YB_{66} type structures (Fig. 3) $Y_{24}((B_{12})_{13})_8{\cdot}(B_{80})_8$ are composed of giant icosahedra consisting of a central and 12 surrounding B_{12} icosahedra and B_{80} clusters, whose sites are statistically occupied by 42 B atoms only. In total, there are 1,584 B atoms per unit cell. The Y sites in octahedral Y arrangements are incompletely occupied as well, for example 50% in the case of YB_{66} [7, 8].

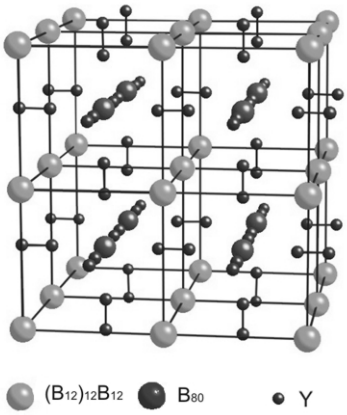

Figure 3. YB_{66} type structures [7].

3. Discrepancies Between Theoretical Band Structure Calculations and Experiments

3.1. BAND STRUCTURES

Theoretical band structure calculations are available for α-rhombohedral boron [9–10], boron carbide (B_{12}(CBC), $B_{11}C$(CBC)) [11–12], and β-rhombohedral boron [13] (see also [1, 2]). For boron carbide and β-rhombohedral boron the calculations suggest metallic character, while according to the experimental results semiconducting behavior is evident. Reason for this discrepancy is that the concentration of intrinsic point defects in these structures is too high by far for being neglected. A painstaking comparison between defect concentration and calculated electron deficiencies makes it clear that they are quantitatively correlated (Table 1) [14, 15].

Point defects in semiconductors generate localized states by shifting the associated valence states into the band gap. Accordingly, this way the before unoccupied valence states of idealized structures are removed. Hence the valence bands of the real structures are completely filled, and the solids are semiconductors in conformance with experiment (see [1, 2]).

TABLE 1. Icosahedral boron-rich structures: Comparison between theoretical electronic properties, experimental characterization and intrinsic point defects experimentally determined

Idealized structure						Real structure		
structure	Valence states (unit cell)$^{-1}$	Ref.	Valence electrons (unit cell)$^{-1}$	Electron deficiency (unit cell)$^{-1}$	Electronic character (theory)	Electronic character (exp.)	Intrinsic point defects (unit cell)$^{-1}$	Ref.
α-rhombohedral boron								
B_{12}	36	[9]	36	0	semicond.	Semicond.	0	[16]
β-rhombohedral boron								
$(B_{12})_4(B_{28})_2B$	320	[15]	315	5	Metal	Semicond.	4.92(20)	[1–3]
boron carbide $B_{13}C_2$								
B_{12}(CBC)	48	[10]	47	1	Metal	Semicond.	0.97(5)	[17–18]
boron carbide $B_{4.3}C$								
$B_{11}C$(CBC)	48	[10]	47,83	0.17	Metal	Semicond.	0.19(1)	[19, 20]
boron carbide B_4C (hypothetical)								
$B_{11}C$(CBC)	48	[10]	48	0	Semicond.	—	—	—
YB_{66}								
$((B_{12})_{13})_8(B_{80})_8$	—		—	—	Metal	Semicond.	304[a]	[21]

[a] ~42 sites of the B_{80} units are occupied implying a defect concentration of 16.1% concerning the idealized structure $((B_{12})_{13})_8(B_{80})_8$ with 1,584 of 1,888 sites occupied.

Boron carbide is shown in Fig. 4; how the compensation of the theoretically determined electron deficiency by intrinsic point defects takes place in the whole homogeneity range [14, 15]. As point defects in boron carbide, the structural deviations from the energetically most favorable structure B_{12} CBC are defined. C atoms replacing B in the icosahedra are donors, a B atom replacing C in the C–B–C chain is an acceptor, and a B□B arrangement replacing a C–B–C chain contributes four acceptors.

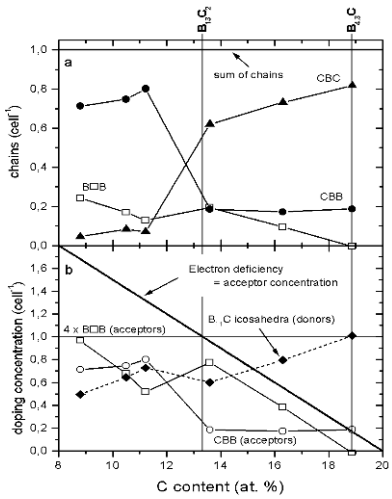

Figure 4. Boron carbide; (**a**) distribution of structural elements in the boron carbide structure; (**b**) valence electron deficiency and its compensation by point defects.

3.2. TRANSPORT THEORY

Such high concentrations of gap states affect the electronic charge transport considerably. Since they are mainly related to valence states, they are particularly responsible for the p-type character and the very low electrical conductivity of the icosahedral boron-rich solids.

A theoretical attempt to solve the problem of electronic transport in the icosahedral boron-rich solids, in particular in boron carbides, was the bipolaron hypothesis designed by Emin et al. [22–23].

The bipolaron model is essentially based on the discrepancy between a hypothetically assumed high concentration of carriers (~10^{21} cm^{-3}), obtained from band structure calculations, and numerous experimental results of different authors (e.g. ESR, transport) consistently proving carrier concentrations of ~10^{19} cm^{-3}. Those free holes are assumed to generate polarons by polarizing their atomic vicinity in $B_{11}C$ icosahedra. However, as shown above, the hypothetical high carrier concentration is the consequence of incorrect assumptions on the microstructure and does not exist in reality. Accordingly, this basic assumption for the (bi)polaron model dissolves.

This and the following results make evident that the (bi)polaron hypothesis is not applicable to boron carbide (for details, see [24]:

- According to Raman spectroscopy, the polarizability in boron carbide is very small. Hence formation of polarons is improbable.
- $B_{11}C$ icosahedra can be excluded from generating polarons because their concentration varies oppositely to such electronic transport properties, whose quantity depends on carrier concentration (dc and dynamical conductivity, reciprocal Seebeck coefficient).
- The effective mass is a central problem in polaron physics (see Devreese [25]). Lugging their polarized surrounding with them, polarons exhibit masses exceeding that of free carriers by several orders of magnitude. In boron carbide the mass of mobile carriers and the band mass concord.
- At high temperatures, the electrical conductivity of boron carbide is thermally activated. This is incompatible with the polaron hypothesis.
- The temperature dependence of the Drude-like optical absorption in boron carbide is opposite to that expected for polarons.

4. Experimentally Determined Band Schemes

As shown, the hitherto available theoretical calculations on energy band structures and electronic transport are not satisfactory. Therefore at present, we rely on band schemes and electronic transport models, which are primarily based on the consistent description of experimental results.

Best investigated icosahedral boron-rich solids are β-rhombohedral boron and boron carbide. Below, their actual band schemes and some basic experimental results are shown to elucidate their electronic transport properties.

4.1. β-RHOMBOHEDRAL BORON

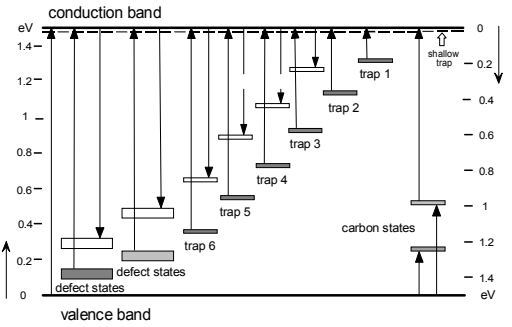

Figure 5. β-rhombohedral boron; actual band scheme. *Full arrows*, experimentally determined transitions; *broken lines*, indirectly concluded transitions.

The actual band scheme of β-rhombohedral boron is displayed in Fig. 5. One essential basis is the optical properties. The absorption edge (Fig. 6) [26] is the superposition of optically excited transitions from occupied into unoccupied electronic states. They can be identified by decomposing the absorption edge considering the different energy dependences of the absorption coefficient α in the case of different transition processes.

For interband transitions Smith [27] determined the following relations between absorption coefficient α and photon energy $\hbar\omega$:

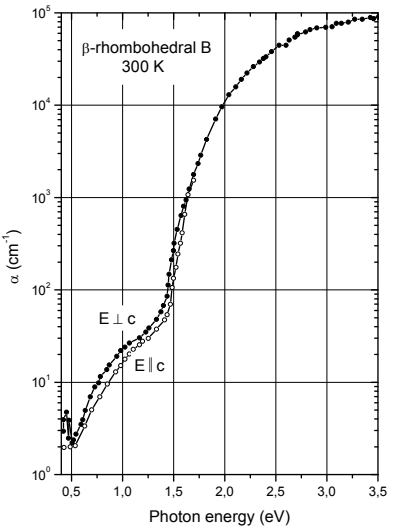

Figure 6. β-rhombohedral boron. Absorption edge [26].

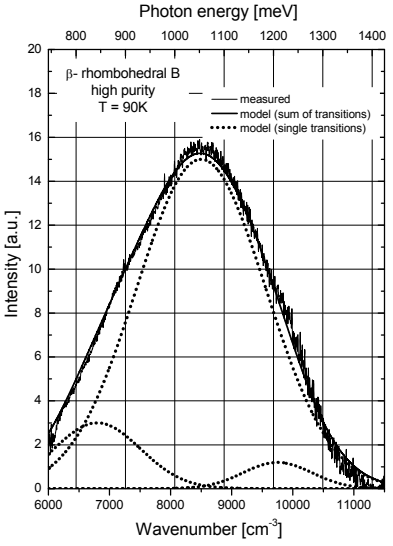

Figure 7. β-rhombohedral boron. Luminescence spectrum [35].

- Direct allowed interband transitions, $\alpha(\hbar\omega) \propto (\hbar\omega - \Delta E)^{1/2}$
- Indirect allowed interband transitions with phonon emission $\alpha(\hbar\omega, T) \propto 1/\hbar\omega \cdot (\hbar\omega - \hbar\Omega_{phonon} - \Delta E(T))^2 / 1 - \exp(-\hbar\Omega_{phonon}/kT)$
- Indirect allowed interband transitions with phonon absorption, $\alpha(\omega) \propto 1/\omega \cdot (\hbar\omega + \hbar\Omega_{phonon} - \Delta E(T))^2 / (\exp(-\hbar\Omega_{phonon}/kT) - 1)$
- Non-direct transitions between localized and band states; Adachi [28] determined $\alpha(\hbar\omega) \propto (\hbar\omega - \Delta E)^2 / \hbar\omega$
- After Lucovsky [29], transitions from a deep level with ionization energy δE and a delta-function-like distribution of states into a parabolic band meet $\alpha(\hbar\omega) \propto \left[\delta E^{1/2} (\hbar\omega - \delta E)^{3/2}\right] / (\hbar\omega)^3$.

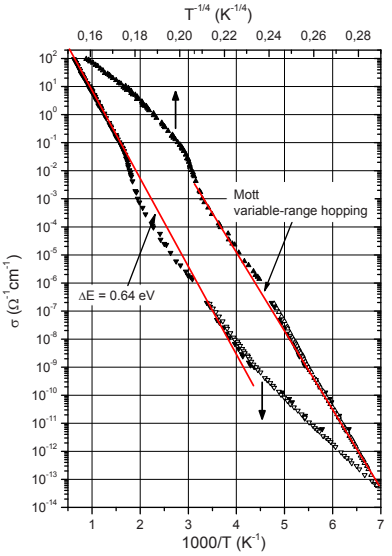

Figure 8. β-rhombohedral boron. Electrical conductivity [30, 31].

Optical emission evoked by the recombination of before optically excited electrons yields the luminescence spectrum displayed in Fig. 7 [35]. For interpretation, it must be considered that the energies of occupied and unoccupied states are different (see Fig. 5).

Electrical conductivity is a basic transport property. Its temperature dependence [30, 31] is essentially determined by the actual transport mechanism. For β-rhombohedral boron (Fig. 8) at high temperatures,

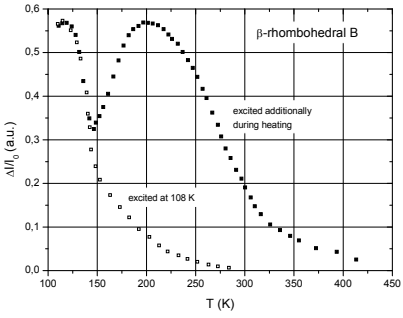

Figure 9. β-rhombohedral boron. T dependence of photoabsorption [32].

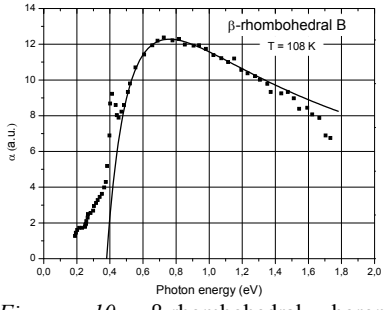

Figure 10. β-rhombohedral boron. Spectrum of photoabsorption at 108 K. *Full line*, theoretical fit [32].

it increases as $\sigma \propto \exp(\Delta E / 2kT)$, thus yielding the gap energy ΔE. At lower T, its varies in accordance to Mott's law of variable-range hopping $\sigma \propto \exp(T / T_0)^{-1/4}$.

Properties of the traps can be investigated by photo-effects. Photo-absorption was measured after optical pre-excitation at low temperatures. In Fig. 9 the temperature dependence is shown without and with additional optical excitation during the heating process [32]. This demonstrates the complex conditions for occupying the traps. The trap excitation spectrum displayed in Fig. 10 was fitted by Eagle's theory [33].

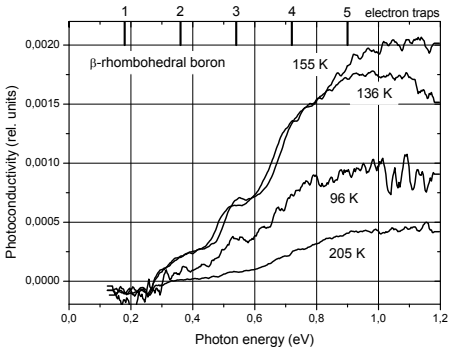

Figure 11. β-rhombohedral boron. Photo-conductivity spectra at different temperatures [34]. Trap positions, marked at the upper margin.

Photoconductivity at low temperatures after optical pre-excitation yields step-like spectra (Fig. 11) evoked by the excitation of electrons from traps in different distances from the conduction band. The steps can easily be attributed to specific electron traps [34]. Thermal emptying reduces the significance of steps at increasing temperatures.

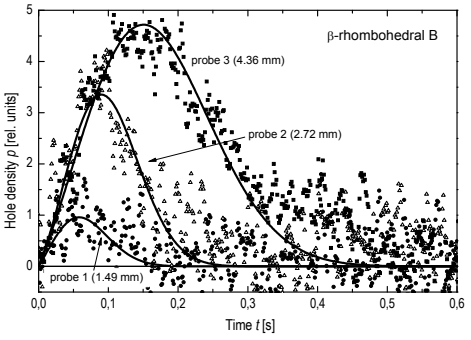

Figure 12. β-rhombohedral boron. Soliton-like drift of optically excited electron–hole pairs [36].

Thermal recombination of optically excited electrons takes place by a cascade-like transfer via the different electron traps shown in Fig. 5. Electrons captured in the uppermost trap are thermally excited into the level of the unoccupied second trap. Subsequently, this relaxes to its energy level of occupancy. Then the thermally generated transition to the next trap takes place, and so on, until the electron reaches the valence band range. The activation energy between the occupied nth trap and the unoccupied (n + 1)th trap is ~0.12 eV in general [35].

Drift experiments of optically excited electron–hole pairs give immediate insight into the movement of free carriers. Electron–hole pairs were optically excited at the front face of a prismatic sample. Determined by the sign of the drift field, holes propagate into the sample. Probe pairs in different distances from the illuminated surface allowed measuring the time-dependent conductivity. Figure 12 shows the separated front range of drift in 1.49, 2.72 and 4.36 mm distance from the illuminated surface [36]. Thermal diffusion is responsible for the peak width increasing with distance. The traps are continuously filled. Therefore, the drift velocity of later carriers increases compared with the preceding ones. The result is a soliton-type motion with a front steepened with distance increasing from the place of generation. The trap-determined mobilities are $\mu_e = 0.11$ and $\mu_h = 0.076$ $cm^2V^{-1}s^{-1}$.

Nevertheless, there is a very low but non-zero probability that a small portion of carriers reach the probes without being trapped. Using a high-sensitive bridge arrangement, which is detuned by the carriers arriving at the probes, we got the flight time of untrapped electron–hole pairs (Fig. 13), and estimated the average ambipolar mobility in β-rhombohedral boron to $\mu_{ambipolar} = 565$ (120) $cm^2V^{-1}s^{-1}$ [37]. This value is comparable to many classical semiconductors.

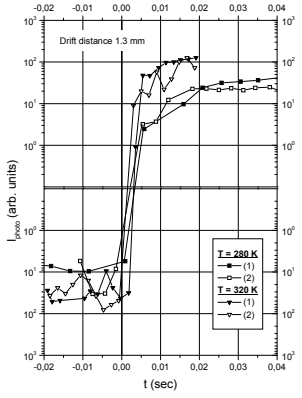

Figure 13. Drift of untrapped electron–hole pairs [37].

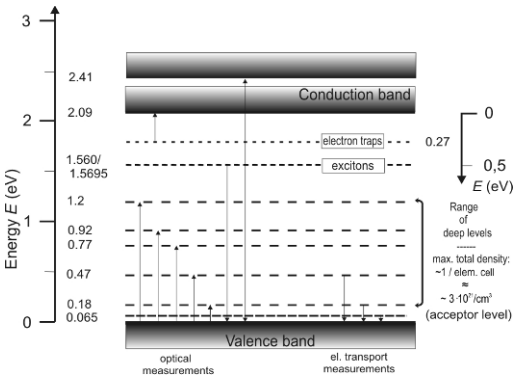

Figure 14. Boron carbide. Actual band scheme. Arrows, experimentally determined transitions [46].

4.2. BORON CARBIDE

The actual band scheme of boron carbide is displayed in Fig. 14 [46]. Evoked by the high concentration of point defects in the structure, there are numerous levels in the band gap.

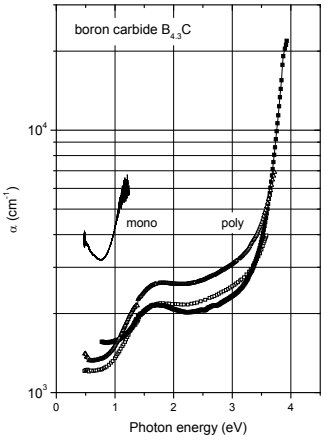

Figure 15. Boron carbide. Absorption edge [43,.45].

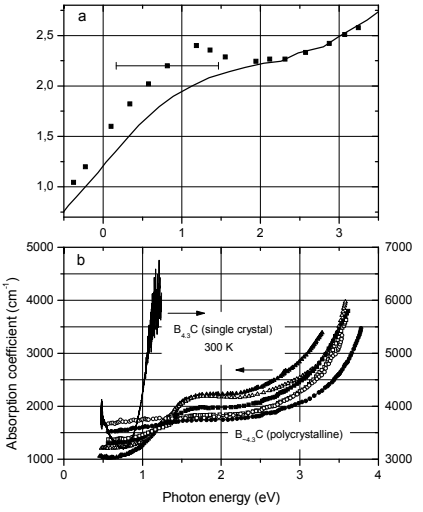

Figure 16. Boron carbide. (a) XRS spectrum [38]; (b) absorption coefficient α; ▲, 80 K; △, 300 K; ■, 300 K; □, 360 K; ●, 540 K; ○, 590 K (polycrystalline); full line, single crystal [40].

As shown above, optical investigations are suitable tools for determining energetical positions of levels and kinds of transitions between them. The absorption edge of boron carbide is shown in Fig. 15 [52, 43]. Some transitions in Fig. 14 were derived by decomposing the absorption edge taking the different energy dependences of transitions into account (see Section 4.1). The strong absorption below the steep edge is significantly higher in single than in polycrystals; obviously the intensity decreases with structural distortions increasing. This conclusion is supported by the temperature dependence of the absorption displayed in Fig. 16b.

In combination with site-specific ab initio calculations, the corresponding near-edge peak in the X-ray Raman scattering (XRS) spectrum, displayed in Fig. 16a, was identified as a p-type exciton due to dominant boron occupation in the centre of the

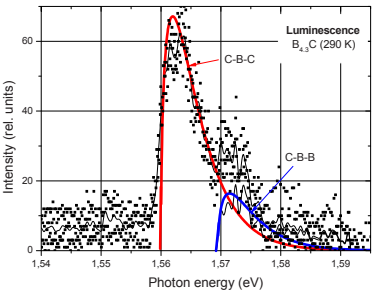

Figure 17. $B_{4.3}C$ boron carbide. Photoluminescence spectrum at 290 K [40].

elementary cell [38]. This was confirmed by refitting the photoluminescence spectrum (Fig. 17) [39] taking into account that a certain difference for the exciton bond energy in C–B–C and in C–B–B chains may occur [40]. Indeed, the fit yields two peaks. The ratio of their areas, 4.1, corresponds quite well to the relation of chain concentrations CBC/CBB = 4.26 (see Fig. 4) at the carbon-rich limit of the homogeneity range.

The electrical conductivity is compatible with the optical results and the band scheme in Fig. 14 respectively. Corresponding to the high concentration of gap states, hopping processes are prevailing in a large temperature range (Fig. 18). At high temperatures above ~500 K, the conductivity is thermally activated (Fig. 19) [2, 41]. The activation energies correspond to the levels optically determined.

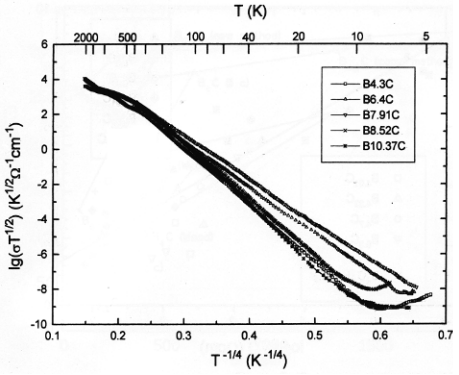

Figure 18. Boron carbide. Electrical conductivity plotted vs. $T^{-1/4}$ (Mott, variable-range hopping (see [2])).

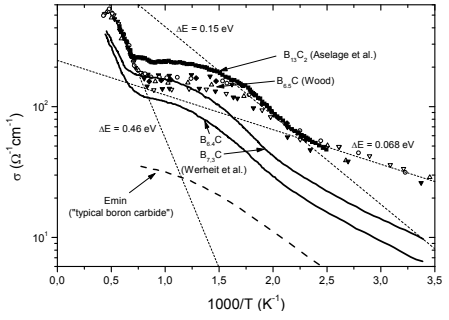

Figure 19. Boron carbide. Electrical conductivity at high T, plotted vs.T^{-1} (see [41] and refs. therein).

For the temperature range, where hopping conductivity takes place, the density of the relevant states was derived within the whole homogeneity range from experimental dc conductivity, dynamical conductivity and Seebeck coefficient using the concerning transport theories (see [41, 42]).

As shown in Fig. 20 the tendency of variation is the same in all cases, but opposite to the concentration of $B_{11}C$ icosahedra, which were assumed to be centers for the formation of bipolarons (see above). As already mentioned, this is one of the experimental evidences disproving bipolarons in the case of boron carbide. In contrast, obviously the B_{12} icosahedra play a significant role for the electronic transport in boron carbide.

Excitations from the valence band into higher conduction bands like that at about 2.4 eV shown in Fig. 13 are of less importance for

electronic transport. Experimental methods for their determination are cited in [46]. Results of experimentally determined electron transitions in boron carbide are listed in Table 2.

Important parameter for electronic transport properties are the effective masses of free carriers. Precise methods for their determination like cyclotron resonance have not been applied to boron carbide so far. Therefore, estimations from less sophisticated experimental methods are available only (Table 3). Compared with classical semiconductors with simple periodic atomic arrangements, the effective masses of carriers are rather high. This is in accordance with the small bending of rather flat energy bands generally obtained in theoretical band structure calculations of icosahedral structures. Nevertheless, the theories approved in classical semiconductors with small effective masses of carriers, are obviously largely applicable to boron carbide as well.

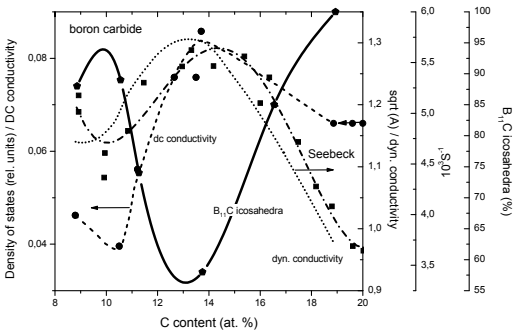

Figure 20. Boron carbide. Density of hopping sites, concentration of $B_{11}C$ icosahedra within the homogeneity range [41, 42].

TABLE 2. Electron transition energies of boron carbide

Optical [43] polycryst.	Optical [44] polycryst.	Optical [45] monocryst.	Optical Div. see [46]	Optical [47] polycryst.	Photoabsorption [44]	El. cond [48]	Hall effect (see[49])	Type of transition
				0.65(5)		0.068(5)	0.061(7)	Valence band – acceptor
0.18(1)						0.15(3)		Deep level to band
					0.27(1)			El.-trap to CB
0.47(1)	0.48(3)					0.46(3)		Nondirect
0.77(1)		0.76(1)						Nondirect
0.92(1)		0.93(1)						Nondirect
1.20(1)								Nondirect
2.09(1)								Indirect interband
			2.4					Interband

TABLE 3. Estimations of hole masses in boron carbide

Band mass of free holes			Effective mass of mobile carriers		
	Method	Ref.		Method	Ref.
~10 m_0	curvature of valence band	[50]	>3 m_0	DC conductivity and ESR	[51]
~10 m_0	luminescence	[39, 40]	3…5 m_0	IR spectra	[52, 53]
			1…10 m_0	Dynamical conductivity	[54, 55]

5. Conclusion and Outlook

Electronic transport in the complex crystal structures of icosahedral boron-rich solids, here represented by β-rhombohedral boron and boron carbide, are essentially determined by high concentration of intrinsic structural defects. The electronic states related are shifted from the valence band into the gap, thus forming partly occupied localized levels with rather high density of states. The preferably acceptor-like character of these states is responsible for the p-type character of these solids.

Variable-range hopping between those states and normal band-type transport occur side by side; their relative share depends on the actual conditions like temperature, optical excitation and antecedents.

Compensation of the intrinsic p-type character requires high donor concentrations, which are sometimes not compatible with the stability of the structure. N-type β-rhombohedral boron has been realized by interstitial accommodation of some metals [3, 56–57]; in the case of boron carbide according attempts failed so far.

This is a considerable barrier for the technical application of the very promising thermoelectric properties of boron carbide exhibiting rather high thermoelectric power up to 2,000 K or probably even more. Reason is that the Fermi level is pinned in the gap states of high concentration, and accordingly intrinsic conductivity is prevented, where the equalising contributions of electrons and holes largely compensate each other. Instead in boron carbide, p-type conduction is maintained up to high temperatures. N-type counterparts with otherwise comparable properties are required. Some other icosahedral structures and hexaborides are promising candidates. For more details, see [58].

After the discovery of superconductivity in MgB_2 at 39 K in 2001 by Akimitsu et al. [59], the possibility of superconductivity in icosahedral boron structures was targeted. The possibility of high T_C superconductivity is suggested for lithium- and magnesium-doped icosahedral boron crystals, alpha- and beta-rhombohedral boron [60]. The influence of high pressure and doping was recently discussed in some detail by Shirai et al. [61].

References

1. Werheit H, Schmechel R, Boron, 1998, in Landolt-Börnstein, Numerical Data and functional relationships in Science and Technology Group III, Vol. 41C, Springer, Berlin, p 3.
2. Werheit H, Boron Compounds, 2000*, Landolt-Börnstein, Numerical Data and functional relationships in Science and Technology* Group III, Vol. 41D, Springer, Berlin, p. 1–491.
3. Werheit H, Schmechel R, Boron, 1998, in Landolt-Börnstein, Numerical Data and functional relationships in Science and Technology Group III, Vol. 41C, Springer, Berlin, p 3.
4. Werheit H, Boron Compounds, 2000*, Landolt-Börnstein, Numerical Data and functional relationships in Science and Technology* Group III, Vol. 41D, Springer, Berlin, p. 1–491.
5. Werheit H, Kuhlmann U, Lundström T 1994, On the insertion of carbon atoms in B_{12} icosahedra and the structural anisotropy of β-rhombohedral boron and boron carbide, *J. Alloys Comp* 204, 197.
6. Bohn RK, Bohn MD, 1971, The Molecular Structures of 1,2-, 1,7-, and 1,12-Dicarba-closo-dodecaborane(12), $B_{10}C_2H_{12}$, *Inorg. Chem.* 10 350.
7. Werheit H, Filipov V, Kuhlmann U, Schwarz U, Armbrüster M, Leithe-Jasper A, Tanaka T, Higashi I, Lundström T, Gurin VN, Korsukova MM, 2010 Raman Effect in Icosahedral Boron-Rich Solids, *Sci. Technol. Adv. Mat.* **11**, 023001
8. Higashi I, Kobayashi K, Tanaka T, Ishizawa Y, 1997, Structure refinement of YB_{62} and YB_{56} of the YB_{66}-type structure, *J. Solid State Chem.* 133, 16.
9. Perrot F 1981 First approach to the band structure of α-rhombohedral boron *Phys. Rev.* B 23 2004
10. Armstrong DR, 1987, The electronic structure of some α-boron compounds and metal borides, Proc 9th. Int. Symp. Boron, Borides, and Rel. Comp., University Duisburg, Germany, 125.
11. Armstrong DR, Bolland J, Perkins PG, Will G and Kirfel A 1983, The nature of the chemical bonding in boron carbide. IV. Electronic band structure of boron carbide, $B_{13}C_2$, and three models of the structure $B_{12}C_3$ *Acta Crystallogr. B* **39** 324.
12. Bylander DM, Kleinman L. 1991, *Phys. Rev. B* **43**, 1487.
13. Bullett D W 1982 Structure and bonding in crystalline boron and $B_{12}C_3$ *J. Phys. C: Solid State Phys* **15** 415.
14. Schmechel R, Werheit H 1999, Correlation between structural defects and electronic properties of icosahedral boron-rich solids *J. Phys.: Condens. Matter* **11** 6803
15. Schmechel R, Werheit H 1997 Structural defects of some icosahedral boron-rich solids and their correlation with the electronic properties, *J. Solid State Chem.* **133** 335
16. Morosin B, Mullendore A W, Emin D and Slack G A 1986 Rhombohedral crystal structure of compounds containing boron-rich icosahedra *Boron-Rich Solids, AIP Conf. Proc. **14**,* 70
17. Slack GA, Hejna CI, Garbauskas MF, Kasper JS 1987, *Proc. 9th Int. Symp. Boron, borides and Rel. Comp.,* ed. H Werheit, University of Duisburg, Germany p 132
18. Slack G A, Hejna C I, Garbauskas M F, Kasper J S 1988 *J Solid State Chem* **76** p 64
19. Kuhlmann U, Werheit H 1992, On the microstructure of boron carbide, *Solid State Comm.* **83** 849
20. Kuhlmann U, Werheit H, Schwetz K A 1992, Distribution of carbon atoms on the boron carbide structure elements, *J. Alloys Comp.* **189** 249

21. Higashi I, Kobayashi K, Tanaka T, Ishizawa Y 1997, Structure refinement of YB_{62} and YB_{56} of the YB_{66}-type structure; *J. Solid State Chem* **133** p 16
22. Emin D 1986 Electronic transport in boron carbides *AIP Conf. Proc.* **140**, p 189
23. Emin D 2006 Unusual properties of icosahedral boron-rich solids *J. Solid State Chem.* **179** pp 2791–2798
24. H. Werheit, 2007, Are there bipolarons in icosahedral boron-rich solids? *J. Phys.: Condens. Matter* **19** 186–207
25. Devreese JT, Polaron 2005, Encyclopedia of Physics, ed R.G. Lerner and G.L. Trigg (Weinheim: Wiley-VCH), Vol. 2, pp 2004–27
26. Werheit H, Hausen A, Binnenbruck H 1972, Optical anisotropy of β-rhombohedral boronfrom 0.4 to 16 μm*, phys. stat. sol. (b)* **51**, 115
27. Smith, R.A., Wave Mechanics in Crystalline Solids, Chapman & Hall, London, 1961
28. Adachi S., Calculation model for the optical constants of amorphous semiconductors, *J. Appl. Phys.* **70**, 2304 (1991)
29. Lucovsky, G., On the Photoionisation of Deep Impurity Centers in Semiconductors, *Solid State Commun*. **3**, 299 (1965)
30. Werheit H, Leis HG, 1970, On the conductivity mechanism of β-rhombohedral boron, *phys. Stat. sol.* **41**, 247
31. Szadkowski A, 1979, Thermally activated hopping in β-rhombohedral boron, *J Less-Common Met.*, **67**, 551
32. Werheit H, 1970, Optical and photoelectric properties of β-rhombohedral boron, *phys. stat. sol.* **39**, 109
33. Eagles DM, 1960, *J. Phys. Chem. Solids* **16**, 76
34. Werheit H, Schmidt M, Schmechel R Lundström T, 2000, Modulated photoconductivity of high-purity and carbon-doped β-rhombohedral boron *J. Solid State Chem* **154**, 93
35. Schmechel R, Werheit H, 2000, Photoluminescence and steady-state interband photoconductivity of hig-purity β-rhombohedral boron, *J. Solid State Chem*. **154**, 68
36. Werheit H, Kummer F, 1995, Soliton propagation and diffusion of optically excited carriers in β-rhombohedral boron, *J. Phys.: Condens. Matter* **7**, 7851
37. Werheit H, Moldenhauer A, 2006, On the diffusion of free carriers in β-rhombohedral boron, *J. Solid State Chem.* **179** 2775
38. Feng Y, Seidler G T, Cross J O, Macrander AT and Rehr JJ 2004, Role of inversion symmetry and multipole effects in nonresonant x-ray Raman scattering from icosahedral B_4C, *Phys. Rev. B* **69** 125402
39. Schmechel R, Werheit H, Kampen T U and Mönch W 2004, Photoluminescence in boron carbide, *J. Solid State Chem.* **177** 566–8
40. Werheit H, 2006, On excitons and other gap states in boron carbide, *J. Phys.: Condens. Matter* **18** 10655.
41. Werheit H 2007, Are there bipolarons in icosahedral boron-rich solids?, *J. Phys.: Condens. Matter* **19**, 186–207.
42. Werheit H, 2009, Present knowledge of electronic properties and charge transport of icosahedral boron-rich solids, *J. Phys.: Conf. Series* 176, 012019
43. Werheit, H., Laux, M., Kuhlmann, U., Telle, R., Optical interband transitions of boron carbide, *Phys. Stat. Sol. (b)* **172** (1992) K 81
44. Werheit, H., Binnenbruck, H., Hausen, A., 1971, Optical properties of boron carbide and comparison with β-rhombohedral boron, *phys.stat. sol. (b)* **47** 153
45. Werheit, H., Leithe-Jasper, A., Tanaka, T., Rotter, H.W., Schwetz, K.A., 2004, Some properties of single-crystal boron carbide, *J. Solid State Chem.* **177** 575

46. Werheit H, Filipov V, Schwarz U, Armbrüster M, Leithe-Jasper A, Tanaka T, Shalamberidze SO, 2010, On surface Raman scattering and luminescence radiation in boron carbide, *J. Phys.: Condens. Matter* **22**, 045401
47. Schmechel, R., Werheit, 1998, H., Dynamical transport in icosahedral boron-rich solids, *J. Mat. Process. Manufact. Sci.* **6** 329
48. Wood, C, 1986, Transport properties of boron carbide, *AIP Conf. Proc.* **140**, 206
49. Schmechel, R., Thesis, Gerhard Mercator University Duisburg, Germany, 1998
50. Armstrong R, Bolland J, Perkins PG, Will G, Kirfel A, 1983, The nature of the chemical bonding in boron carbide IV. Electronic band structure of boron carbide, $B_{13}C_2$, and three models of the structure $B_{12}C_3$, *Acta Crystallogr. B* **39** 324
51. Geist D, Meyer J, Peussner H, 1970, Electrical conductivity and movable carrier electron paramagnetic resonance (EPR), Boron Vol. 3, ed T Niemyski (Warszawa: PWN-Polish Scientific Publishers) p 207
52. Werheit H, Binnenbruck H, Hausen A 1971 Optical properties of boron carbide and comparison with β-rhombohedral boron, *phys. stat. sol. (b)* **47** 153
53. Binnenbruck H, Werheit H 1979, IR-active phonons of boron and boron carbide, *Z. Naturforsch.* **34a** 787
54. Schmechel R, Werheit H 1997 Evidence of the superposition of Drude type and hopping type transport in boron-rich solids, *J. Solid State Chem*. **133** 335
55. Schmechel R, Werheit H 1998 Dynamical transport in icosahedral boron-rich solids *J. Mat. Process. Manufact. Sci.* **6** 329
56. Soga K, Oguri A, Araake S, Terauchi M, Fujiwara A, Kimura K, 2004, Li-and Mg-doping into icosahedral boron crystals, α-and β-rhombohedral boron, targeting high-temperature superconductivity: structure and electronic states, *J. Solid State Chem.* **177**, 498
57. Hyodo H, Araake S, Hosoi S, Soga K, Sato Y, Terauchi M, Kimura K, 2008, Structure and electronic properties of Mg-doped β-rhombohedral boron constructed from icosahedral clusters, *Phys Rev B* **77** 024515.
58. H. Werheit, 2006, Thermoelectric properties of boron-rich solids and their possibilities of technical application, Proc. 25th Int. Conf. on Thermoelectrics (Vienna, Austria, Aug. 2006) ed. P. Rogl (Piscataway, NJ: IEEE, Catalog Nr. 06TH8931) pp. 159–163
59. J. Nagamatsu, N. Nakagawa, T. Muranaka, Y. Zenitani, and J. Akimitsu, 2001, Superconductivity at 39 K in MgB_2, *Nature* **410**, 63.
60. Soga K, Oguri A, Araake S, Terauchi M, Fujiwara A and Kimura K, 2004, Li-and Mg-doping into icosahedral boron crystals, α-and β-rhombohedral boron, targeting high-temperature superconductivity: structure and electronic states, *J Solid State Chem.* **177** 498
61. Shirai K, Dekura H, Masago A, 2009, Superconductivity research on boron solids and an efficient doping method, *J. Phys.: Conf. Series* **176**, 012001

MAGNETIC AND THERMOELECTRIC PROPERTIES OF BORON-RICH SOLIDS

TAKAO MORI*
National Institute for Materials Science (NIMS), Japan

Abstract Boron forms various compounds with metal atoms occupying voids in the boron framework. As a synthesis method it has been found that the addition of small amounts of third elements like carbon, nitrogen, and silicon can result in the formation of novel and varied rare earth boron cluster structures. A wide variation of 1D, 2D, and 3D magnetic behavior with unexpectedly strong magnetic interactions has been discovered in rare earth boron icosahedra compounds which are magnetically dilute, f-electron insulators. As an intriguing phenomenon, the B_{12} icosahedra cluster, which is a building block of the structure, has been indicated to function as a novel mediator of magnetic interaction. These phenomena are presented in this paper together with a review on ferromagnetic (FM) boron-rich borides. Attractive high temperature thermoelectric properties are also emerging in this group of compounds, which is striking due to the great potential of utilizing waste heat. Recent developments on the long awaited n-type counterpart to boron carbide, the homologous series of RE-B-C(N) compounds, $REB_{17}CN$, $REB_{22}C_2N$, and $REB_{28.5}C_4$, will be reviewed together with those of p-type $REB_{44}Si_2$. General new ways to improve the thermoelectric properties are also discussed. For example, seeding with highly electrically conductive metallic borides like REB_4 and REB_6 is found to be a way to significantly increase the thermoelectric figure of merit. Electric resistivity significantly decreases while Seebeck coefficients and thermal conductivity are not sizably affected.

Keywords: boron, magnetic, thermoelectric, ferromagnetic, spintronics, antiferromagnetic, magnetic interaction, dimer, spin glass, superexchange, high temperature, Seebeck, thermal conductivity, icosahedra, cluster, crystal growth, crystallinity, p-type, n-type, boron carbide

* Takao Mori, National Institute for Materials Science (NIMS), Japan, e-mail: MORI.Takao@nims.go.jp

N. Orlovskaya and M. Lugovy (eds.), *Boron Rich Solids: Sensors, Ultra High Temperature Ceramics, Thermoelectrics, Armor*, DOI 10.1007/978-90-481-9818-4_5,

1. Introduction

Boron is an interesting element, tending to form 2D atomic nets and clusters in compounds, similar to carbon, its neighbor in the periodic table. Carbon has been much more extensively studied for such materials as fullerenes, nanotubes, graphite related materials, aromatics, etc. A rich vein of materials science potential remains to be tapped in boron and this is illustrated quite well by the recent discoveries of striking phenomena in compounds containing boron, like the strong magnetic coupling in magnetically dilute insulators [1] and superconductivity in MgB_2 [2], and new elemental form of boron [3], for example.

Boron has one less electron than carbon and therefore it is electron deficient when forming atomic networks compared to carbon constructs such as graphite and fullerenes. However, this causes boron to have a good affinity with the rare earth elements, which are localized and can occupy voids in the boron network while supplying electrons to stabilize novel structures [1]. Furthermore, the shell of f electrons will supply interesting properties like magnetism and also provide possible tuning of the electronic properties.

In terms of functional materials, the strong covalent boron cluster framework supplies a light protective armor which is acid and corrosion resistant and can withstand high temperatures. Attractive electronic, magnetic, and thermal properties can be developed from inside the network through the metal atom constituents [1].

In this paper I will focus on magnetic and thermoelectric properties as promising functionalities for boron compounds. As an emerging novel phenomenon, it has been found that a structural building block; the B_{12} icosahedra cluster, is a novel mediator of magnetic interaction. I will review the wide variety of magnetic behaviour (1D, 2D, 3D) which manifests, together with analysis of the mechanism of interaction. Ferromagnetic borides are also reviewed. In the thermoelectric field, the first intrinsic n-type series of boron icosahedral compounds were recently discovered and they may be the long awaited counterparts to p-type boron carbide. I will present advancements in research for their application as high temperature thermoelectric conversion materials, together with developments for a p-type borosilicide with excellent thermoelectric properties at high temperatures. Possible wide ranging methods to improve properties of compounds in general, will also be given.

2. Magnetic Properties

2.1. FERROMAGNETISM IN BORON-RICH BORIDES

2.1.1. *High temperature ferromagnetism reported in CaB_6 and related systems*

Due to the increasing interest in Spintronics as a new frontier for semiconductor technology, the reports in *Nature* and other scientific journals that the boron semiconductor CaB_6 exhibits high temperature ferromagnetism when substitutionally doped with La (electrons) had attracted great attention worldwide [4].

We have been successful in giving the first clear proof that this phenomenon is actually not intrinsic and originates from iron impurities [5].

As can be seen in Fig. 1, ferromagnetism was observed for $Ca_{1-x}La_xB_6$ crystals. However, it was discovered that by washing the crystals with hydrochloric acid, the ferromagnetism disappears, despite the La doping not being affected.

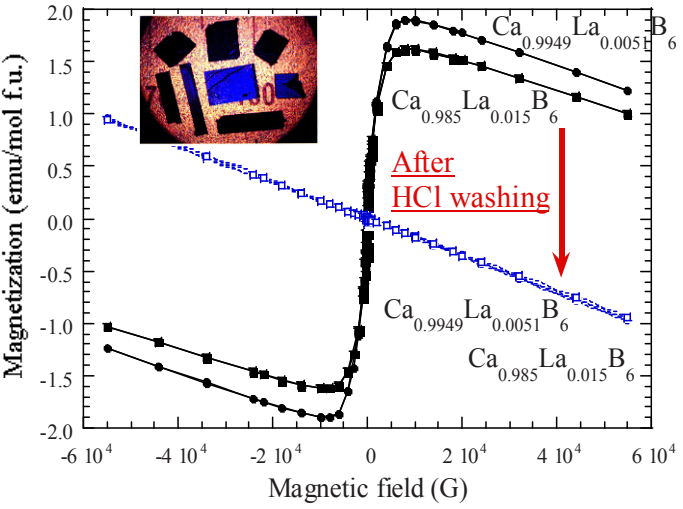

Figure 1. Magnetization of "ferromagnetic" La doped CaB_6.

And lacking in the initial reports, we performed a strict chemical analysis on all the samples which revealed an iron impurity content of typically 0.010 wt% for example, for lanthanum doped crystals before the washing. After the HCl washing, with the disappearance of ferromagnetism, the iron content was also shown to disappear below 0.001 wt%, which is the limit of detection.

Although now it has become standard procedure to check for iron impurity content in work dealing with dilute magnetic semiconductors, at the time of our report, it was not yet a wide practice.

Regarding the origin of the iron impurities in the $Ca_{1-x}La_xB_6$ crystals we proposed that Fe impurities are electrochemically plated onto the surface of the crystals during the flux removal procedure [5]. There are many sources for the iron since raw boron powder material typically has an iron impurity of content of ~600 ppm and crucibles made from alumina, etc. also tend to have traces of iron due to their production processes. And of course, for more "dirty" samples (such as sintered samples) iron impurities can be expected to exist normally.

The electrochemical plating idea for the flux grown crystals gives a reasonable non-intrinsic explanation of why only doped CaB_6 crystals (with lower resistivity) tend to exhibit ferromagnetism since the electrochemical plating reaction becomes more robust in that case [5].

And we have also shown that this non-intrinsic magnetism originating from iron exhibits a shift from the transition temperature of bulk iron (Fig. 2). This can be thought to come from the environment of the iron atoms on the surface (cluster, film-form) and it is demonstrated in this way that the shift itself is not a proof of the intrinsic nature as suggested in the *Nature* paper. Measurements on the surface of CaB_6 crystals yielded the direct observation of the existence of iron there [6].

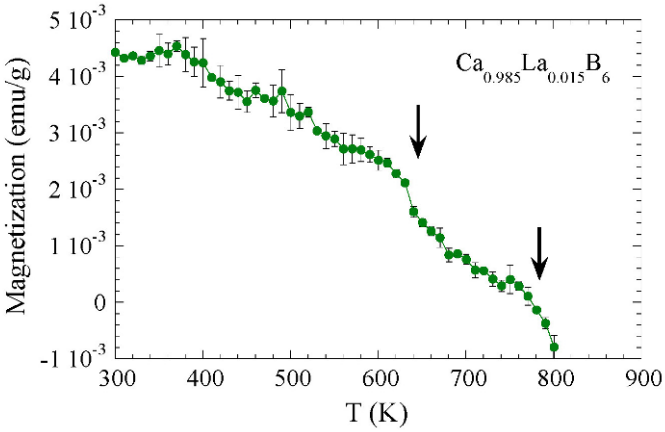

Figure 2. High temperature dependence of the spurious magnetism of La doped CaB_6.

In addition to the high temperature ferromagnetism reported to occur in lanthanum doped CaB_6, it was reported in *Science* that the borocarbide CaB_2C_2 also exhibits high temperature ferromagnetism [7]. The similarity of both compounds having particular molecular orbitals near E_F and difference,

i.e. absence of threefold degeneracy in the energy bands of CaB_2C_2, was also pointed out.

To investigate this, high quality CaB_2C_2 crystalline powder was synthesized from pure elements using a "closed environment" technique we have developed. We discovered that contrary to the previous report, high quality CaB_2C_2 is diamagnetic at room temperature as shown in Fig. 3 [8]. Therefore, it was strongly indicated that iron impurities had been playing a role in the reported ferromagnetism and it was nonintrinsic.

We stress again that magnetic impurities always need to be strongly considered when discussing phenomena having high T_C ferromagnetism and rather small magnetic moments.

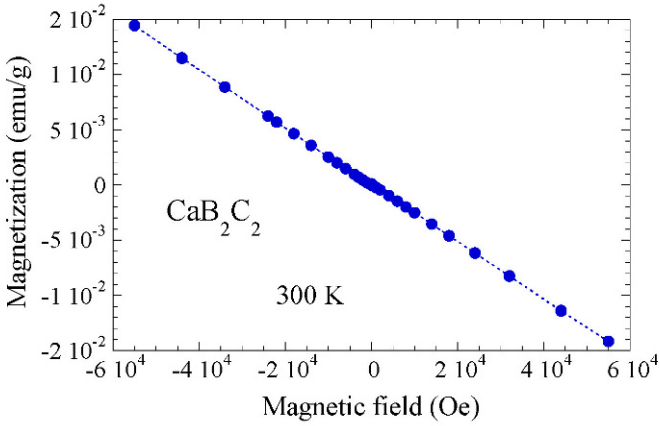

Figure 3. Magnetization of CaB_2C_2.

In the next subsections I will review boron-rich borides which have been found to be intrinsically ferromagnetic. MB_2 diborides are one of the few compound groups of borides which mainly exhibit ferromagnetism [9]. The magnetism of the MB_x ($x \geqq 4$) borides is predominantly antiferromagnetic [10, 11]. Considering compounds overall which contain boron, a rich variety of compounds show interesting and sometimes useful ferromagnetism. Namely, compounds such as $Nd_2Fe_{14}B$, $CeCo_{12}B_6$, and $R_5B_2C_5$, and many others. However, in this review we focus on the boron-rich borides.

2.1.2. *MB_2 (M = rare earth, transition metal)*

REB_2 takes the AlB_2-type crystal structure (P_6/mmm). Possibly because it is harder to grow crystals compared to REB_4 and REB_6 there have been fewer reports on REB_2, despite the fact that many of them exhibit ferromagnetism [9, 10]. As shown in Table 1, TbB_2, DyB_2, HoB_2, ErB_2 exhibit ferromagnetism, while YbB_2 exhibits an antiferromagnetic (AFM)

transition [12]. The magnetism of TmB_2, which lies between the two cases, was not known until recently. TmB_2 was revealed to exhibit a ferromagnetic (FM) transition, with the specific heat exhibiting a sharp λ-type peak indicating long-range ordering at T_C = 7.2 K [13]. The easy-axis direction is indicated to be within the (0 0 1) plane with the spins lying in-plane in the ordered state. As interesting features, a deviation from the Curie-Weiss law in χ and a broad hump in the specific heat were observed below 30 K as shown in Fig. 4. These behaviors were concluded to be due to crystal field effects (CEF). The presence of 6 states of the 13-fold degenerate $^3H_6$ multiplet of Tm^{3+} within this temperature scale was indicated. Band structure calculations also revealed that for TmB_2 the FM ordered state is more stable than AFM ordering by 4.5 K, which agrees well with the experimental results.

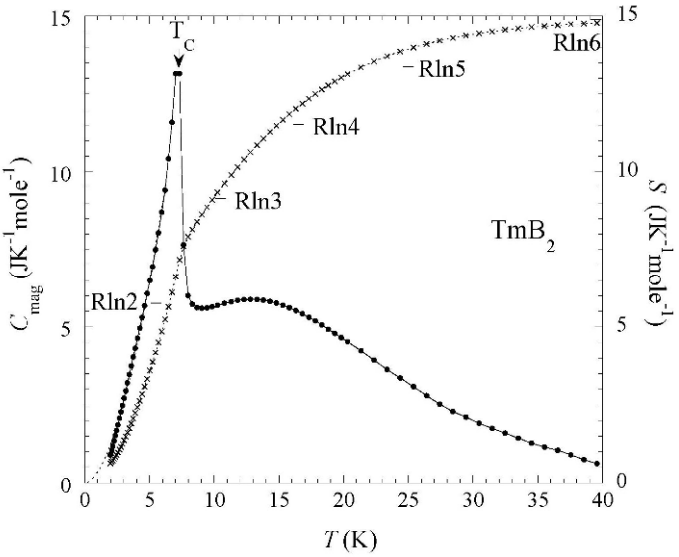

Figure 4. Temperature dependence of specific heat and entropy of TmB_2.

In regard to the transition metal diborides, MnB_2 was initially reported to have FM transitions at 157 and 143 K, however, Kasaya *et al*. elucidated through NMR measurements that there is an AFM transition at 760 K with the spins aligning in the a–b plane which are slightly tilted in the c-axis direction because of *s–d* coupling, leading to a weak FM transition at low temperatures [14]. CrB_2 has an AFM transition at T_N = 86 K and is indicated to be an itinerant system [15].

TABLE 1. Magnetic properties of MB_2

	μ_{eff} (μ_B/R atom)	θ (K)	T_{mag} (K)	Ref.
TbB_2	9.96	151	151	10
DyB_2	10.7	33	55	10
HoB_2	10.2	25	15	10
ErB_2	9.47	9	16	10
TmB_2	7.44	5.3	7.2	13
YbB_2	4.3	−49	5.6[a]	12
MnB_2	2.3	–	760[a], 157[b]	14
CrB_2	2.1	−700	88[a]	15

[a] Antiferromagnetic transition.
[b] Weak ferromagnetic transition.
All others are ferromagnetic transitions.

2.1.3. *PrB_4 and EuB_6*

Among the REB_4 tetraborides, PrB_4 has been reported to be the only FM system with T_C = 24 K [11]. Recently it has also been reported that the magnetism is actually an AFM transition at T_N = 19.5 K with a further FM transition at T_C = 15.9 K [16]. However, since the temperature range in this report is lower than the initial report of ferromagnetism, it is indicated that there may be significant sample dependence in the magnetism of PrB_4.

Geballe first discovered the ferromagnetism in EuB_6 [17]. Despite being discovered around 40 years ago, the detailed magnetic behavior of EuB_6 was only elucidated recently, because of large sample dependence and for example, even disappearance of the FM state with the existence of a small amount of impurities [18].

Two FM transition occur at T_{C1} = 15.3 K and T_{C2} = 12.5 K. From the closeness of the transition temperatures it is indicated that there are two kinds of ferromagnetic ordering with similar energies. The low temperature FM state has [1 1 1] as the magnetic easy axis, which changes to [1 0 0] at $T_{C2} < T < T_{C1}$. Eu^{2+} is an *s* ion and the crystal field symmetry in EuB_6 is cubic so the magnetic anisotropy is weak. However, it is indicated that the anisotropy is playing a role for the two energetically similar FM state to manifest.

The most interesting feature of the magnetism in EuB_6 is that at high temperatures it is a semiconductor with small number of carriers, but upon approaching the FM transition temperature, the number of carriers sharply increases and it turns into a metal. The effective mass and scattering probability also shows a steep drop at this temperature. It has been indicated that above Tc there is a rapid development of magnetic polarons which drive the magnetic transition. The magnetism of EuB_6 has yet to be fully elucidated and investigations continue regarding its interesting behavior such as observation of a crossover in colossal magnetoresistance anisotropy [19].

2.2. A NEW MEDIATOR OF MAGNETIC INTERACTION: THE B_{12} BORON ICOSAHEDRAL CLUSTER

2.2.1. *Introduction*

Up to a decade ago, research on magnetism in borides had been mainly carried out on metallic systems (such as REB_4, REB_6, and REB_{12}) with interesting results being obtained on various magnetic behavior [9–11]. In these systems, the main driving force of the magnetism is the RKKY interaction [20], with additional and sometimes competitive effects from quadrupolar (and octupolar) interactions, magnetic frustration, and dipole–dipole interaction, for example.

In 1999 it was discovered that the TbB_{50} compound, an insulating, relatively magnetic dilute, localized f-electron system, exhibits an antiferromagnetic transition at an unexpectedly high transition temperature (i.e. with strong coupling) [21]. The shortness of the B_{12} icosahedral lattice constant in REB_{50} was indicated to be a critical factor. The hypothesis was made that the B_{12} icosahedron functions as a novel mediator of magnetic interaction [21].

Following this discovery, a rich variety of magnetism (1D, 2D, 3D, etc.) was found to manifest in insulating borides containing the B_{12} icosahedra. There are three notable magnetic systems which will be reviewed briefly in the following subsections.

2.2.2. *REB_{50} and $REB_{44}Si_2$*

REB_{50} starts to decompose above 2,100 K into phases like REB_6 and REB_{66} without melting. It was found that it is possible to grow rare earth borosilicide $REB_{44}Si_2$ crystals isostructural to REB_{50} by adding a small amount of silicon [22, 23]. Incidentally, the addition of silicon has another interesting function in that it expands the lattice constants [24]. This enabled the realization of a GdB_{50}-type compound. Due to the large radius of the gadolinium atom, GdB_{50} will not form. In an example of material design, the GdB_{50}-type compound, $GdB_{44}Si_2$, was obtained by expanding the lattice constants with the addition of silicon to accommodate the gadolinium atoms in the rare earth sites [25]. In general, the silicon addition was found not to have an effect on the magnetic properties of $REB_{44}Si_2$ asides from effects from increased lattice constants, and with crystals, detailed investigation on the physical properties were carried out.

A striking effect was observed upon magnetic dilution of $TbB_{44}Si_2$. Non-magnetic Lu was substitutionally doped (x = 0.05 to 0.50) for Tb. Strikingly, the critical magnetic field of the AFM transition, H_C, was observed to show no variation for any of the Lu substituted samples, even for $Tb_{0.5}Lu_{0.5}B_{44}Si_2$. A correlation was also observed between the number of

free Tb spins and degree of doping, *x*. H_C is proportional to T_N and is a measure of the strength of the magnetic coupling. These results indicate that the AFM transition in $TbB_{44}Si_2$ is of dimer-like nature [26].

ESR further revealed details of the magnetic behavior [27]. Measurements were carried out on $GdB_{44}Si_2$ which is a $^8S_{7/2}$ system. The ESR absorption intensity was found to exhibit a sharp drop at T_N = 7 K clearly indicating the magnetic transition. The *g* factor also exhibited temperature dependence, decreasing rapidly below 30 K, indicating the growth of short range correlation. As shown in Fig. 5, temperature dependence of the ESR linewidth was found to be significantly different from that of a 3D antiferromagnetic system, being indicative of the exchange narrowing of a 1D classical spin system [28]. These results indicate that the Gd ions magnetically form pairs along the bond alternating ladder which is the direction of the second nearest metal–metal spacing.

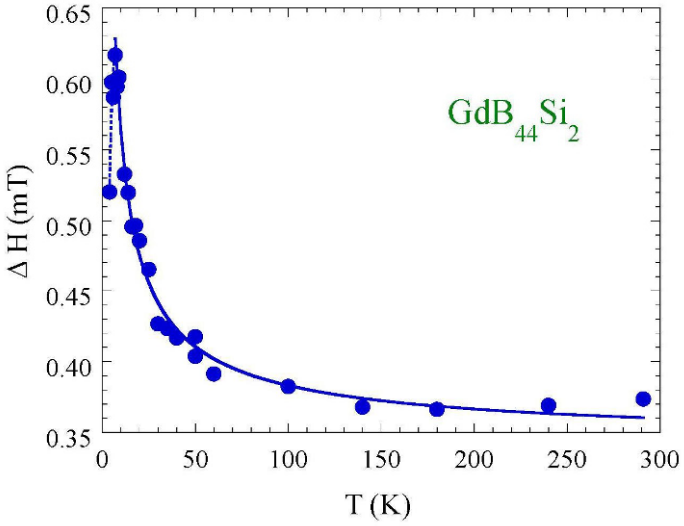

Figure 5. Temperature dependence of ESR linewidth of $GdB_{44}Si_2$.

The magnetic dilution and ESR experimental results pointed to one-dimensionality of magnetism of the $REB_{44}Si_2$ system, indicating the magnetic ions form pairs along the c-axis in a 1D arrangement. This result is consistent with our picture/hypothesis of the B_{12} icosahedra functioning as a novel mediator of the magnetic interaction since they form a chain along the c-axis adjacent to the magnetic ion pairs.

2.2.3. *$REB_{22}CN$ and related compounds*

$REB_{22}C_2N$ yielded the first observation of spin glass behavior in a non-doped boride [29]. As characteristic physical properties, the relaxation of isothermal remanent magnetization was observed, together with existence of wait time effects [30, 31]. The spin glass behavior is indicated to originate from a combination of disorder from partial occupancy of the rare earth atomic sites and also frustration of magnetic interactions. $REB_{17}CN$ and $REB_{28.5}C_4$ compounds which are related to $REB_{22}C_2N$ (i.e. they comprise a homologous series) were also synthesized and investigated [32]. As a result, analogous spin glass behavior was observed (Fig. 6) and it was indicated that the magnetism is governed in the 2D planes.

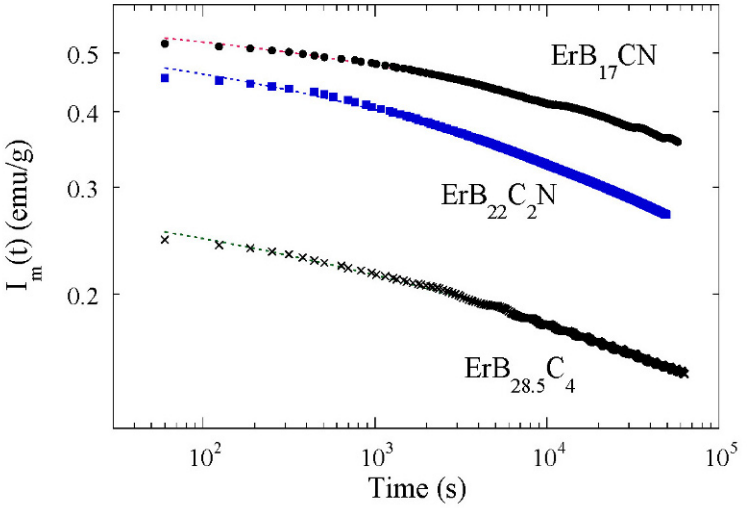

Figure 6. Isothermal remanent magnetization of $ErB_{17}CN$, $ErB_{22}C_2N$, and $ErB_{28.5}C_4$.

A detailed study of the dynamical properties further reveal the physics of the system to be 2D [33]. Ac susceptibility of $HoB_{22}C_2N$, as a compound representative of the homologous spin glass series, was investigated (Fig. 7). Strong frequency dependence was observed which could not be analyzed satisfactorily by the dynamical scaling theory of a 3D spin glass. From analysis of the Argand diagrams, the distribution function of relaxation times g(t) at each temperature could be determined. As temperature is lowered, the distribution of relaxation times g(t) shows a temperature dependence becoming very broad, while the behavior of the median relaxation time τ_C follows a generalized Arrhenius law behavior; $\ln(\tau_C/\tau_0) \propto T^{-(1+\phi\nu)}$ ($\tau_0 = 5.3 \times 10^{-6}$ s, $1 + \phi\nu = 2.5$). Therefore, it is indicated that $HoB_{22}C_2N$ is not a superparamagnetic system (which also exhibits large frequency dependence),

while the value of the exponent, $1 + \phi\nu = 2.5$, demonstrates that $HoB_{22}C_2N$ is a 2D spin glass system.

$REB_{22}CN$ and related compounds, $REB_{17}CN$ and $REB_{28.5}C_4$, can be considered to represent a model case of an f-electron dilute triangular lattice magnetic system.

2.2.4. *$GdB_{18}Si_5$*

The magnetic properties of single crystals of the B_{12} icosahedral compound $GdB_{18}Si_5$ were previously investigated [34]. $GdB_{18}Si_5$ is rhombohedral (space group *R-3m*) a = b = 10.07 Å, c = 16.45 Å. An antiferromagnetic transition was observed (T_N = 3.2 K) and it was indicated that the spins are ordered in the a–b plane. A λ-type peak is observed in the magnetic specific heat and supports a long range order antiferromagnetic transition occurring in this system. Interestingly, this is the first "normal" magnetism, that is, 3D long range order discovered in the higher borides. This is despite the relatively low partial occupancies of the gadolinium atoms, and studies to investigate the detailed magnetic ordering are underway.

2.2.5. *Summary of the magnetism of B_{12} icosahedral compounds*

An important result obtained recently is the discovery of magnetic transitions at moderate temperatures in rare earth B_{12} icosahedral cluster compounds, despite their being insulating, magnetically dilute f-electron systems. A wide range of behavior such as 1D and dimer-like magnetic behavior in REB_{50}-type compounds or 2D spin glass behavior in a series of homologous compounds $REB_{17}CN$, $REB_{22}C_2N$, $REB_{28.5}C_4$ and 3D long range order in $GdB_{18}Si_5$ has been discovered. Importantly it has been indicated that the B_{12} icosahedral clusters play an important role in mediating the magnetic interaction. In other words, it has been demonstrated that the boron icosahedral cluster is supplying a new function to the compound, i.e. magnetism.

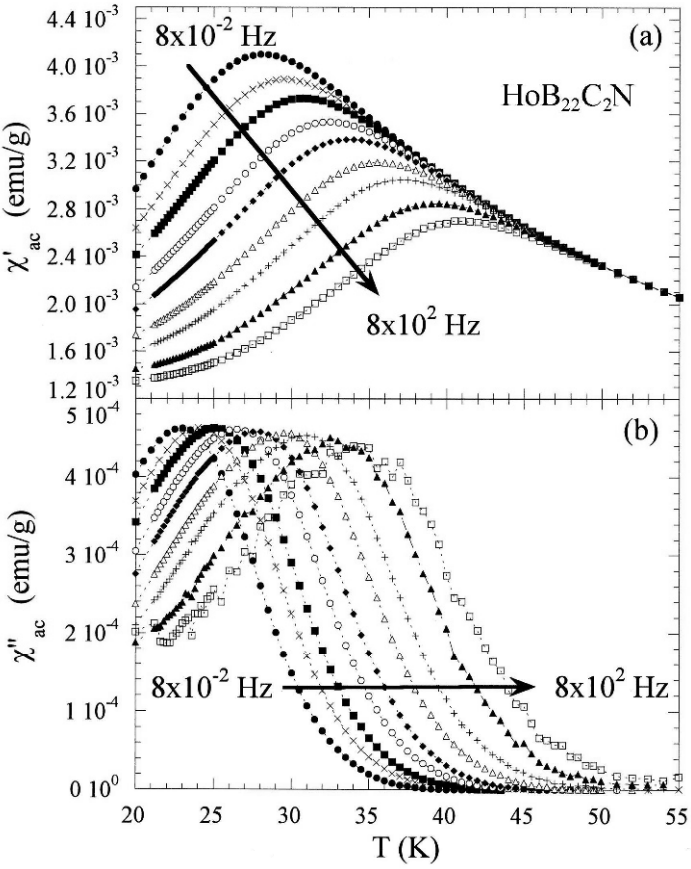

Figure 7. Ac susceptibility of $HoB_{22}C_2N$; (a) real and (b) imaginary components.

Regarding future topics of study, as noted above, moderate magnetic interactions has been discovered in an insulating, magnetically dilute f-electron system. Therefore, naturally there is an interest to evaluate whether these materials could somehow be modified for spintronics application. Work is going on to make clear any interaction of carrier with the magnetism. And as an interesting open question the explicit mechanism of the magnetic interaction (in which the B_{12} icosahedra has been shown to play an important role) still remains to be solved.

3. Thermoelectric Properties

3.1. INTRODUCTION

Research into thermoelectric materials is intensely being carried out throughout the world because of the huge merits of utilizing waste heat [35]. There is obviously a need to develop materials which have good thermoelectric properties at high temperatures to utilize waste heat in power plants, incinerators, and cars, for example.

Boron-rich cluster compounds are attractive as materials because of their excellent stability under high temperature and acidic conditions. And as an attractive feature for thermoelectric application, the thermal conductivity of icosahedral systems has generally been found to be low [36–38]. Previously, boron-rich compounds such as boron carbide [39] and doped β-boron [40] have been investigated as thermoelectric materials for high temperatures. We are particularly interested in the possibilities of our new rare earth boride compounds because the magnitude of the thermal conductivity of boron icosahedral compounds which contain rare earth elements appear to be even lower than the aforementioned compounds. This can be considered to be a good starting point for developing viable thermoelectric materials.

3.2. BOROSILICIDES

The thermoelectric properties of the novel $REB_{44}Si_2$ (RE = Tb, Er, Tm, Yb) compounds were previously investigated at high temperatures [41]. Seebeck coefficients exceeding 200 μV/K were observed at 1,000 K. Thermal conductivity was found to take low values of ~0.02 W/cm/K at high temperatures which is similar to what has been determined previously for REB_{66} [38]. $REB_{44}Si_2$ shows much higher power factors than REB_{66}, and it can be said that the new $REB_{44}Si_2$ compound sustains the low thermal conductivity of the boron cluster network with significant improvement in the electrical quality.

Furthermore, as an attractive temperature dependence the thermoelectric figure of merit,

$$ZT = \alpha^2 \cdot \sigma \cdot \kappa^{-1} \cdot T \qquad (1)$$

(where α = Seebeck coefficient, σ = electrical conductivity and κ = thermal conductivity), increases steeply as temperature increases. For “as-is” samples without doping or composition control, a value of ZT ~ 0.2 can be extrapolated at high temperatures.

Therefore, $REB_{44}Si_2$ shows an excellent p-type thermoelectric quality; and with lower melting points compared to boron carbide, possess a synthetic advantage, wherein they may have potential to replace boron carbide in the future.

3.3. BOROCARBONITRIDES

The magnetism of the homologous rare earth borocarbonitrides, $REB_{17}CN$, $REB_{22}C_2N$, and $REB_{28.5}C_4$, were dealt with in section 2.2.3, and as a striking new development were found to intrinsically exhibit n-type properties for the first time as boron icosahedral compounds [42]. The rare earth borocarbonitrides have a layered structure along the c-axis with B_{12} icosahedra and C–B–C chain layers residing between the B_6 octahedral and the rare earth atomic layers (Fig. 8). The number of interlayer B_{12} icosahedra and C–B–C chain layers increases successively along the series of $REB_{17}CN$, $REB_{22}C_2N$, and $REB_{28.5}C_4$ and in the infinite limit (i.e. with no rare earth-containing layers), the compound is analogous to boron carbide [43].Therefore, the discovery of n-type behavior is exciting because p-type boron carbide is one of the few materials to have been commercially developed, and these rare earth borocarbonitrides can embody the long awaited n-type counterpart of boron carbide [42].

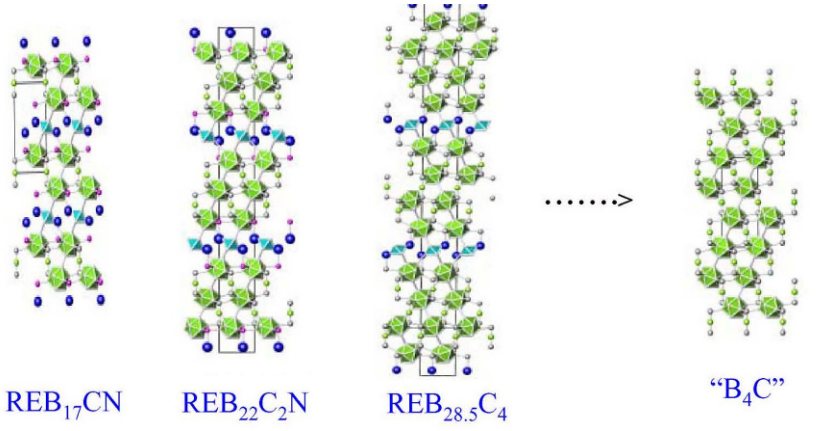

Figure 8. Crystal structure of the rare earth borocarbonitrides.

The largest challenge facing these materials for application is that densification processes have not been fully developed yet. Normal hot pressing of rare earth borocarbonitrides only yields a density about 50% of the theoretical density, while SPS (spark plasma sintering) yielded initial results of about 70% [44].

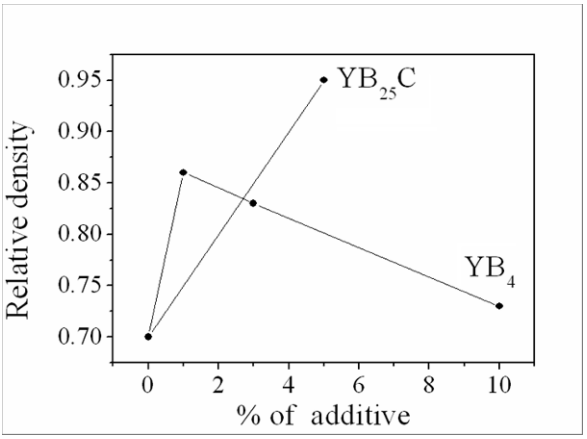

Figure 9. Effect of additives on the densification of $YB_{22}C_2N$.

We have investigated and found that certain sintering additives (or dopants) in the SPS synthesis can be quite effective for densification [45]. Depending on the amount and the nature of the additive/dopant we can decrease the starting temperature of shrinkage, and the decrease of this temperature increases density of the resulting samples. As shown in Fig. 9, YB_4 has been found to have some effect, yielding samples with higher densities of ~85%. And furthermore, it has previously been discovered that the addition/doping of small amounts of metal borides improves the thermoelectric properties as will be described in Section 3.4.2.

Interestingly, the addition of $YB_{25}C$ resulted in a high densification of 93%. However, one detrimental feature of the $YB_{25}C$ addition is that it appears to promote growth of boron carbide impurities in the sample which can be detrimental to the n-type characteristics. Further work on the densification processes of the rare earth borocarbonitrides should be carried out.

3.4. DISCOVERY OF POSSIBLE WIDE RANGING METHODS FOR IMPROVEMENT OF THERMOELECTRIC PROPERTIES

3.4.1. *Zinc doping*

The study of the series of transition metal doping into $YB_{44}Si_2$ yielded discovery of an interesting effect [46]. As a striking result, doping of zinc was discovered to significantly improve the crystal quality even although it does not remain in the final product.

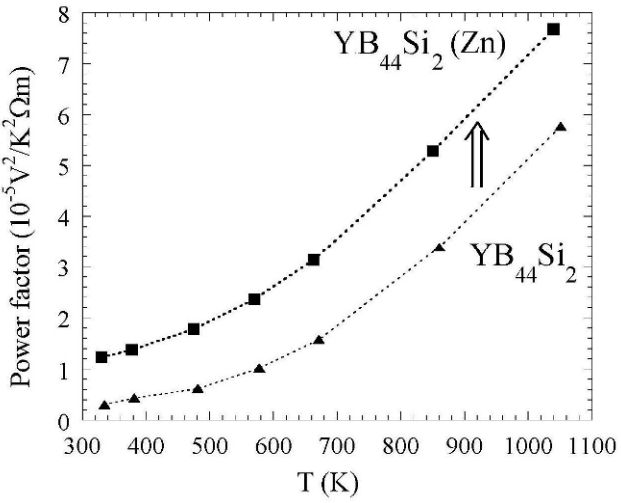

Figure 10. Effect of zinc additive to the synthesis process (it does not remain in the final product) on the thermoelectric power factor of $YB_{44}Si_2$.

As a result of the improved crystallinity, the thermoelectric power factor of $YB_{44}Si_2$ increased by more than 30% (Fig. 10). This discovery of the zinc doping effect may lead to a way to improve the crystal quality of a wide variety of compounds synthesized at high temperatures, not just limited to borosilicides, silicides, and borides.

Therefore, this effect can have a large impact not limited to thermoelectrics. In terms of thermoelectrics, improvement of crystal structure is beneficial when the system possesses intrinsic low thermal conductivity like the boron cluster compounds. In many conventional thermoelectric compounds, much effort has been spent on reduction of the thermal conductivity through introduction of grains, etc. [47]. The intrinsic low thermal conductivity is one of the "built-in" advantages of boron cluster compounds as thermoelectric materials.

3.4.2. *Doping with highly electrically conductive materials (metallic borides)*

Doping with metallic borides like REB_4 and REB_6 is another way in which the thermoelectric properties have been discovered to be improved. With doping, $REB_{17}CN$ and $REB_{22}C_2N$ compounds exhibited a significant decrease up to 2 orders in the electrical resistivity. The Seebeck coefficient and thermal conductivities do not show a large change, so this doping method is revealed to be a highly effective way to increase the figure of merit [44].

The explicit mechanism of improvement of figure of merit is not clear yet. Since metallic borides like REB_4 and REB_6 are highly electrically

conductive materials, it is reasonable to consider that these dopants are functioning as some kind of electrical channel and significantly reducing the electrical resistivity. However, since the percent of doping is small, it seems unlikely that a normal percolation effect is at play here. The doping can have some effect on the morphology which may also be a factor. This phenomenon should be further investigated, especially since it can yield a route of improving the thermoelectric properties of a wide range of compounds not limited to borides.

4. Conclusions

This review has focused on interesting new trends in research on developing functionalities in boron based network compounds (mainly cluster compounds) while utilizing the particular characteristics of the boron network lattice. Two main functionalities described here are magnetic properties and thermoelectric properties. One striking result is the discovery of a wide range of magnetic behavior (1D dimer-like transition, 2D spin glass behavior, and 3D long range order) at moderate temperatures in compounds in which such magnitude of interactions would not be expected, being insulating, magnetically dilute localized f-electron systems. Importantly it has been indicated that the B_{12} icosahedral clusters play an important role in mediating the magnetic interaction. Elucidation of the mystery of the high temperature ferromagnetism reported in some boride compounds, which had generated great interest throughout the world, was also described together with a review on ferromagnetic boron-rich borides.

Another important development is the emerging possibility of developing novel higher borides such as, $REB_{44}Si_2$, $REB_{17}CN$, $REB_{22}C_2N$, and $REB_{28.5}C_4$, as p- and n-type high temperature thermoelectric materials. Two methods with possible wide impact not just limited to borides, enabling improvement of thermoelectric and other properties were also discussed. Zinc doping has been found to be a method to improve the crystallinity, while doping with highly electrically conductive metallic borides improved the thermoelectric properties, namely, significantly decreasing the electrical resistivity while not having a detrimental effect on the Seebeck coefficient.

References

1. T. Mori, “Higher Borides”, in: Handbook on the Physics and Chemistry of Rare Earths, Vol. 38, ed. K. A. Gschneidner Jr., J. -C. Bunzli, and V. Pecharsky (North-Holland, Amsterdam, 2008) p. 105–173.
2. J. Nagamatsu, N. Nakagawa, T. Muranaka, Y. Zenitani, and J. Akimitsu, Nature 410, 63 (2001).

3. A. R. Oganov, J. Chen, C. Gatti, Y. Ma, Y. Ma, C. W. Glass, Z. Liu, T. Yu, O. O. Kurakevych, and V. L.. Solozhenko, Nature 457, 863 (2009).
4. D. P. Young, D. Hall, M. E. Torelli, Z. Fisk, J. L. Sarrao, J. D. Thompson, H. R. Ott, S. B. Oseroff, R. G. Goodrich, and R. Zysler, Nature 397, 412 (1999).
5. T. Mori and S. Otani, Solid State Comm, 123, 287 (2002).
6. C. Meegoda, M. Trenary, T. Mori, and S. Otani, Phys. Rev. B 67, 172410 (2003).
7. J. Akimitsu, K. Takenawa, K. Suzuki, H. Harima, and Y. Kuramoto, Science 293, 1125 (2001).
8. T. Mori and S. Otani, J. Phys. Soc. Jpn, 71, 1789 (2002).
9. K. H. J. Buschow, in: Boron and Refractory Borides, (Heidelberg, Berin, 1977) p. 494.
10. D. Gignoux et al., in: Handbook of Magnetic Materials Vol. 10, (North-Holland, Amsterdam, 1997) p. 239.
11. Yu. B. Paderno and S. Pokrzywnicki, Phys. Stat. Sol. 24, K11 (1967).
12. M. A. Avila, S. L. Bud'ko, C. Petrovic, R. A. Ribeiro, P. C. Canfield, A. V. Tsvyashchenko, and L. N. Fomicheva, J. Alloys Comp. 358, 56 (2003).
13. T. Mori, T. Takimoto, A. Leithe-Jasper, R. Cardoso-Gil, W. Schnelle, G. Auffermann, H. Rosner, and Yu. Grin, Phys. Rev. B 79, 104418 (2009).
14. M. Kasaya and T. Hihara, J. Phys. Soc. Jpn. 29, 336 (1970).
15. S. H. Liu, L. Kopp, W. B. England, and H. W. Myron, Phys. Rev. B 11, 3463 (1975).
16. G.A. Wigger, E. Felder, R. Monnier, H.R. Ott, L. Pham, and Z. Fisk, Phys. Rev. B 72, 14419 (2005).
17. T. H. Geballe, B. T. Matthias, K. Andres, J. P. Maita, A. S. Cooper, and E. Corenzwit, Science, 160, 1443 (1968).
18. S. Sullow, I. Prasad, M.C. Aronson, J.L. Sarrao, Z. Fisk, D. Hristova, A.H. Lacerda, M.F. Hundley, A. Vigliante, D. Gibbs, Phys. Rev. B, 57, 5860 (1998).
19. V Glushkov, M Anisimov, A Bogach, S Demishev, V Ivanov, N Samarin, A Dukhnenko, N Shitsevalova, K Flachbart and N Sluchanko, J. Phys.: Conf. Ser. 150, 022014 (2009).
20. M. A. Ruderman and C. Kittel, Phys. Rev. 96, 99 (1954); T. Kasuya, Prog. Theor. Phys. 16, 45 (1956); K. Yoshida, Phys. Rev. 106, 893 (1957).
21. T. Mori and T. Tanaka, J. Phys. Soc. Jpn, 68, 2033 (1999).
22. T. Tanaka, S. Okada, Y. Ishizawa, J. Solid State Chem. 133, 55 (1997).
23. T. Mori and T. Tanaka, J. Phys. Soc. Jpn, 69, 579 (2000).
24. T. Mori and T. Tanaka , J. Alloys. Comp, 288, 32 (1999).
25. T. Mori and T. Tanaka, Mat. Res. Bull, 36, 2463 (2001).
26. T. Mori, J. Appl. Phys., 95, 7204 (2004).
27. T. Mori, J. Appl. Phys., 99, 08J309 (2006).
28. T. T. P. Cheung, Z. G. Soos, R. E. Dietz, and F. R. Merritt, Phys. Rev. B, 17, 1266 (1978).
29. T. Mori and A. Leithe-Jasper, Phys. Rev. B 66, 214419 (2002).
30. K. Binder and A. P. Young, Rev. Mod. Phys. 58, 801 (1986).
31. J. A. Mydosh, Spin Glasses (Taylor and Francis, London, 1993).
32. T. Mori, F. Zhang, and A. Leithe-Jasper, J. Solid State Chem., 177, 444 (2004).
33. T. Mori and H. Mamiya, Phys. Rev. B 68 214422 (2003).
34. T. Mori and F. Zhang, J. Phys.: Condens. Matter, 14, 11831 (2002).
35. G. S. Nolas, J. Sharp, and H. J. Goldsmid, Thermoelectrics: Basic Principles and New Materials Development (Springer, New York, 2001).
36. G. A. Slack, D. W. Oliver, and F. H. Horn, Phys. Rev. B 4, 1714 (1971).
37. D. G. Cahill, H. E. Fischer, S. K. Watson, R. O. Pohl, and G. A. Slack, Phys. Rev. B 40, 3254 (1989).
38. T. Mori, Physica B 383, 120 (2006).
39. C. Wood and D. Emin, Phys. Rev. B 29, 4582 (1984).

40. H. Werheit, R. Schmechel, V. Kueffel and T. Lundström, J. Alloys Comp.262–263, 372 (1997).
41. T. Mori, J. Appl. Phys, 97, 093703 (2005).
42. T. Mori and T. Nishimura, J. Solid State Chem., 179, 2908 (2006).
43. E. L. Belokoneva and T. Mori, Cryst. Res. Tech., 44, 19 (2009).
44. T. Mori, T. Nishimura, K. Yamaura, E. Takayama-Muromachi, J. Appl. Phys., 101, 093714 (2007).
45. D. Berthebaud, T. Nishimura, and T. Mori, Thermoelectric properties and spark plasma sintering of doped $YB_{22}C_2N$, J. Mat. Res., Vol. 25, No. 4, pp. 665–669, 2010.
46. T. Mori, D. Berthebaud, T. Nishimura, A. Nomura, T. Shishido, and K. Nakajima, Dalton Trans., 39, 1027 (2010).
47. B. Poudel, Q. Hao, Y. Ma, Y. C. Lan, A. Minnich, B. Yu, X. Yan, D. Z. Wang, A. Muto, D. Vashaee, X. Chen, J. M. Liu, M.S. Dresselhaus, G. Chen, and Z. F. Ren, Science 320, 634 (2008).

SCRATCH STUDIES IN BORON-RICH LIGHTWEIGHT AND ULTRAHIGH TEMPERATURE CERAMIC

DIPANKAR GHOSH, GHATU SUBHASH*
Department of Mechanical and Aerospace Engineering, University of Florida, Gainesville, FL 32611, USA

Abstract A ZrB_2-5wt%SiC composite was processed using a non-conventional plasma pressure compaction technique. Due to the potential application as external heat shields in supersonic vehicles, scratch studies were conducted on virgin and oxidized surfaces of the composite. Scratches on virgin surfaces revealed slip-line patterns representing ductile behavior and transgranular microcracks oriented orthogonal to the scratch direction representing brittle behavior. These inelastic deformation features have been rationalized based on the classical stress field solutions under combined normal and tangential loads. Existence of dislocations within ZrB_2 phase has been confirmed from TEM investigations. The readily detectable slip-lines are argued to reflect the metallicity in the bonding present in ZrB_2 crystal structure. An analytical framework for measurement of scratch induced-residual stress within SiC particles has been discussed. Preliminary scratch studies on the oxidized surface of the composite revealed that while the oxide layers are necessary for improved oxidation resistance, they can essentially reduce the mechanical integrity of a structure.

Keywords: ZrB_2, processing, scratch, slip-lines, dislocations, residual stress, oxidation

1. Introduction

Advanced light weight and high strength ceramics and their composites are central to the development of structural components for military and aerospace applications. Among these, ultrahigh temperature ceramics (UHTCs) for thermal protection systems in future hypersonic vehicles have received considerable attention in recent years [1]. Boron-rich UHTCs such as zirconium diboride (ZrB_2), hafnium diboride (HfB_2), and their composites have recently emerged as promising materials for the aforementioned

* Ghatu Subhash Department of Mechanical and Aerospace Engineering, University of Florida, Gainesville, FL 32611, USA, e-mail: subhash@ufl.edu

N. Orlovskaya and M. Lugovy (eds.), *Boron Rich Solids: Sensors, Ultra High Temperature Ceramics, Thermoelectrics, Armor*, DOI 10.1007/978-90-481-9818-4_6,

aerospace applications [1]. For such applications, requirement of materials with controlled and defect free microstructure is paramount. However, a major concern for these UHTCs has been their poor sinterability due to high melting temperature and strong covalent bonding [1]. Moreover, the traditional powder processing/sintering methods do not lend themselves to rapid processing due to long processing times and elevated temperature requirements [2, 3]. Therefore, in recent years, non-conventional processing techniques have been adopted to successfully sinter such boron-rich solids [4, 5]. Towards this end, a new processing method called "plasma pressure compaction" ($P^2C^{®}$) [6, 7] has been used to process high-temperature ceramics.

In the family of UHTCs, zirconium diboride-silicon carbide (ZrB_2–SiC) composites [1] have drawn a special attention owing to their unique properties such as high melting point (>3,000^{o}C), superior oxidation resistance above 1,500^{o}C, excellent thermal shock resistance, low density (6.09 gm/cm^3), and good mechanical and chemical stability at elevated temperatures. Most of the recent investigations in these materials, however, are mainly focused on processing and oxidation behavior [1, 8–10]. While in service (e.g., during takeoff, landing, or reentry in to atmosphere), the structural components in aerospace vehicles are prone to impact by meteorites and atmospheric debris particles at very high velocities. Under such abrasion-dominated scenarios, sharp particles impacting on the exposed surfaces can result in inelastic deformation and material removal. Evolution of damage and fundamental inelastic deformation mechanisms at room-temperature should be fully understood for their successful usage. However, in several recent studies, it has been shown that the surface morphology of the ZrB_2–SiC composite continuously degrades due to oxidation of both the ZrB_2 and SiC phases at elevated temperatures [1, 8–10]. Also, the thickness of the oxidized layers can vary with oxidation time at a given temperature. Presence of oxide layers of different compositions and thicknesses can drastically affect the overall mechanical response of the structure. Therefore, it is also important to investigate the influence of oxide layer on the wear properties. In the current manuscript, first the results of room-temperature scratch studies and associated inelastic deformation mechanisms in ZrB_2–SiC composite will be discussed. Residual stresses induced due to these scratches in SiC particles are then summarized. Finally, some preliminary results of scratch studies on oxidized surfaces of the ZrB_2–SiC composite will be briefly described.

2. Experimental

2.1. PROCESSING OF ZrB_2–SiC COMPOSITE

Unlike the traditional sintering techniques that involve high sintering temperatures and long consolidation times, $P^2C^{®}$ process has been used to successfully sinter metals, alloys and ceramics to near theoretical density in less than 10 min [4–7]. Sintering via this technique involves localized resistive heating (i.e. Joule heating) of a powder compact through the application of a low voltage (~5 V) direct current (DC). In the current work, a ZrB_2-5wt%SiC composite was produced from commercially available ZrB_2 (Grade HS, H.C. Starck, Germany, particles of sizes between 3 and 7 μm) and polycarbosilane ($–(SiHMe–CH_2)_n–$) powders [5]. The mixture was heated above 1,000°C in argon atmosphere where the PCS decomposes to cubic-SiC (3*C*-SiC) and amorphous carbon. Then ZrB_2 and heat-treated PCS mixture was consolidated using the $P^2C^{®}$ technique at a temperature of 1,750°C and a pressure of 43 MPa over a short consolidation period of only 5 min [5]. The sintered compact was produced in the form of a slab of dimensions 75 mm × 52 mm × 8 mm (see Fig. 1). Density of the sintered

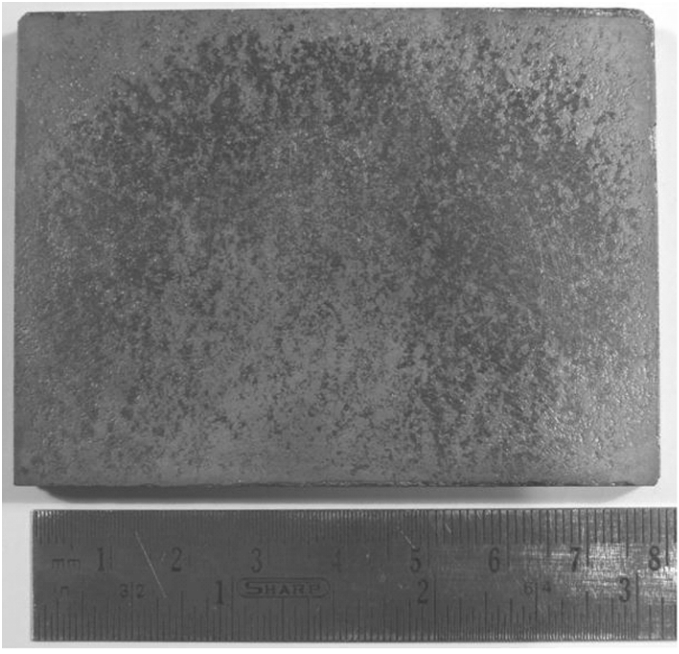

Figure 1. A sintered ZrB_2-5wt%SiC compact processed via $P^2C^{®}$ technique.

compact was measured using Archimedes method. X-ray diffraction (XRD) analysis was carried out on small specimens to investigate the phase content within the consolidated compact. Average grain sizes of the matrix and particulate phases were approximated from the fracture surfaces.

2.2. SCRATCH STUDIES IN VIRGIN AND OXIDIZED ZrB_2–SiC

For scratch experiments, rectangular specimens of dimensions 6 mm × 3 mm × 4 mm were prepared from the sintered compact using a high-speed diamond saw. Scratch studies were conducted on metallographically polished surfaces of the composite using a MTS nanoindenter® XPS system at constant loads (in the load range of 50–250 mN) employing a Berkovich nanoindenter [5]. The resulting inelastic deformation features around the scratches were investigated using optical and scanning electron microscopes. The deformed regions were also analyzed using TEM by extracting specimens from the scratch grooves using a focused ion beam (FIB) technique. To study the scratch response of the oxidized surface of ZrB_2–SiC composite, rectangular specimens of the composite with polished surfaces were first oxidized in air at 1,000°C for 1–15 h. Scratches were then conducted on the oxidized surfaces.

3. Results and Discussion

3.1. MICROSTRUCTURE

XRD pattern collected from the sintered composite revealed the presence of only two crystalline phases; hexagonal (*H*) ZrB_2 and cubic (3*C*) SiC [5]. Density measurements indicated a composite density 96% of theoretical value (5.84 g/cm^3). The theoretical density of the composite was calculated using the rule of mixture. Figure 2 shows low and high magnification SEM micrographs of fractured surfaces of the ZrB_2–SiC composite, which revealed a well-consolidated composite and thus supported the high value of measured density. No porosity was detected within the ZrB_2 matrix or at the ZrB_2–SiC interfaces. However, some agglomerated regions (containing 3*C*-SiC and amorphous carbon) were observed in the sintered compact which probably resulted the measured 4% porosity. SEM micrographs revealed that the SiC phase (dark phase) was uniformly distributed within the ZrB_2 matrix (gray phase). The average grain size of the ZrB_2 phase was estimated to be around 5 μm whereas the SiC particles were around 1 μm in size.

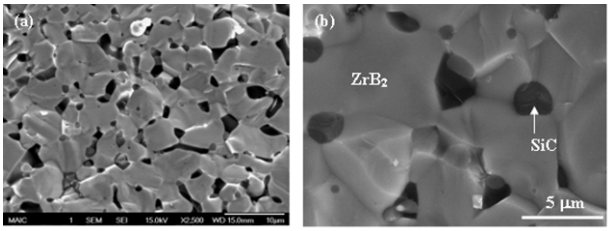

Figure 2. SEM micrographs of the fragmented surface of ZrB_2–SiC composite at (**a**) lower and (**b**) higher magnifications revealing absence of any porosity within ZrB_2 matrix as well as at the ZrB_2–SiC interface areas.

3.2. SCRATCH STUDIES IN UNOXIDIZED ZrB_2–SiC COMPOSITE

Figure 3 shows constant load scratch patterns conducted at three different loads, 50, 150 and 250 mN, on the polished surfaces of the ZrB_2-5wt%SiC composite. At low load range, smooth plastically deformed scratch grooves without any significant macroscopic damage were created. However, at higher loads damages were visible within the scratch grooves. High resolution microscopy revealed two distinct inelastic deformation features that developed within the scratch grooves: (i) multiple sets of parallel and intersecting deformation features in the form of slip-lines limited only within the ZrB_2 matrix, and (ii) transgranular microcracks orthogonal to the scratch direction. Figure 4a shows a residual scratch path at a constant load of 250 mN and magnified views of various damage features induced within the scratch groove have been shown in Fig. 4b–e. Figure 4b reveals slip-lines within the scratch groove where as orthogonal transgranular microcracks within and outside of slip band regions can be seen in Fig. 4b and c, respectively. The slip-lines, indicative of plastic deformation during the scratch process, were also observed within the scratch grooves at other load levels. However, microcracks oriented almost normal to the scratch direction, were mainly observed at scratch loads greater than 100 mN. In addition to these inelastic deformation features at this load level, limited lateral cracking and material removal from the grooves occurred through transgranular fracture as evidenced by the micrographs in Fig. 4d and e.

It was interesting to note that the slip-line spacing remained unaltered across any microcrack. However, the cracks seem to slightly disturb the continuity of the slip-line patterns. Therefore, it is inferred that the slip-lines must have formed before the microcracking during the scratch process. Recently, the authors have developed a mechanistic rationale to describe the evolution sequence of slip-lines and microcracks based on the elastic stress

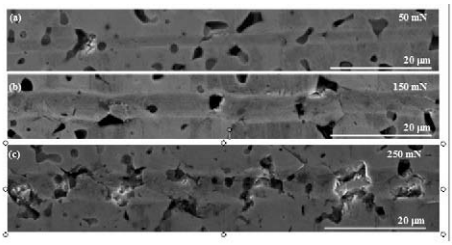

Figure 3. SEM micrographs of residual scratch grooves at (**a**) 50 mN, (**b**) 150 mN and (**c**) 250 mN loads. Scratch grooves were smooth without any macroscopic damage at lower load levels (up to 150 mN). However, as the load increased, brittle fracture and material removal started to occur along the grove as can be seen from scratch at 250 mN.

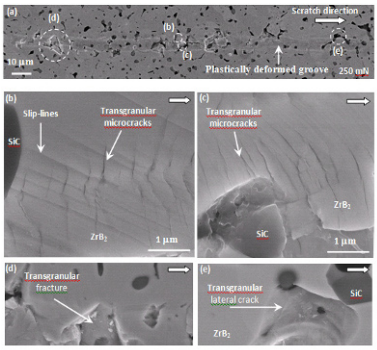

Figure 4. (**a**) A constant load scratch path at 250 mN with higher magnification images of microscopic deformation and damage features along the groove: transgranular microcracks (**a**) within slip-lines and (**b**) in the absence of slip-lines; (**c**) transgranular fracture within the groove and (**d**) transgranular lateral crack. The thick arrows indicate the scratch direction.

field solutions of scratch process [5]. It has been shown that during the scratch process, maximum shear stress ahead of the scratch tool results in the formation of slip-lines and maximum principal tensile stress in the wake of the tool is oriented along the scratch direction, and therefore, causes the microcracks to open orthogonal to the scratch direction. Thus, it is concluded that slip-lines form first followed by microcracks. This mechanistic rationale was in agreement with the experimental observations [5].

The residual stresses developed due to scratch process within 3*C*-SiC particles present in the composite were also investigated using micro-Raman spectroscopy. Towards this end, the authors have calculated the residual elastic stresses induced due to the scratch process, which have been related to the peak shift in Raman spectra [11]. The relationship between the *z*-component of residual stress (σ_Z^R) and change in transverse optical (TO) Raman peak position in 3*C*-SiC as a result of scratch process is given by [11]

$$\sigma_Z^R = -251.66\Delta w_{\mathrm{TO}}.$$

A plot of σ_Z^R and Δw_{TO} ($\Delta w_{TO} - w_{TO} - w_{TO}^0$, where w_{TO}^0 is the TO-peak position in stress-free 3*C*-SiC and w_{TO} is the TO-peak position where residual stress has been developed as a result of scratch process) for various scratch loads have been shown in Fig. 5. It can be clearly seen from Fig. 5 that at lower scratch load, σ_Z^R is compressive, however, as the load increases, it becomes highly tensile.

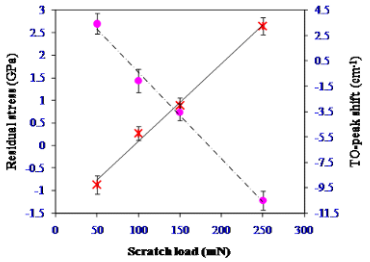

Figure 5. Evolution of residual stress and TO-peak shift in Raman spectra in SiC particles in the ZrB_2–SiC composite as a function of scratch load.

The slip-line patterns observed from the scratch studies in the ZrB_2–SiC composite were also observed in indentation experiments in the composite as well as in monolithic ZrB_2 ceramics [12]. Figure 6 reveals optical micrographs (in Nomarski illumination) of intense slip-line or surface-step formation in the vicinity of indented regions in a polycrystalline ZrB_2 ceramic. Such macroscopic slip-steps are clear evidence of dislocation-induced plasticity and dislocation mobility at room-temperature in ZrB_2 ceramics. However, owing to the extremely high melting temperature and strong covalent bonding, such plastic behavior at room-temperature is unexpected in ZrB_2 ceramics [13].

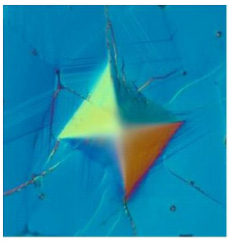

Figure 6. Optical micrograph (in Nomarski illumination) from a polycrystalline ZrB_2 ceramic revealing intense slip-lines in the vicinity of an indentation.

TEM investigations of specimens obtained from the slip-line regions of ZrB_2 revealed that dislocations were indeed generated within the deformed ZrB_2 grains in the regions directly beneath the scratch groove [12]. Figure 7 shows a bright field TEM image revealing dislocations within the ZrB_2

phase. TEM investigations, reported in recent literature by the authors, [12] also showed the presence of multiple dislocations in different orientations, similar to the slip-lines observed from the SEM micrographs. From an in-depth $\vec{g}.\vec{b}$ analysis, $\{10\bar{1}0\}\langle 11\bar{2}0\rangle$ prismatic slip system was identified as the active slip mechanism in ZrB_2 ceramic [12].

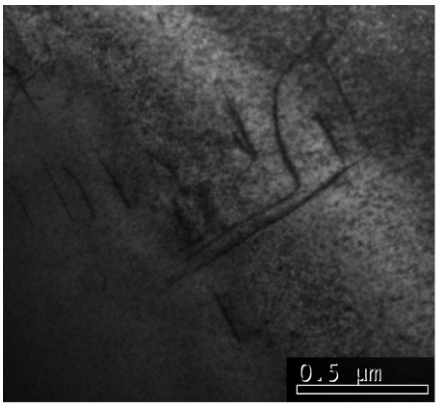

Figure 7. A bright-field TEM micrograph revealing dislocations within the ZrB_2 phase.

The room-temperature dislocation activity and mobility in ZrB_2 ceramics can be interpreted based on the properties, crystal structure and chemical bonding. ZrB_2 has a unique combination of properties that are characteristic of both metals and ceramics [1]. For example, it has high melting temperature (>3,000°C), high elastic modulus (>400 GPa) and superior thermo-chemical stability, typical of ceramics. In addition, ZrB_2 ceramic possesses surprisingly high electrical conductivity ($>10^6$ S/m) comparable to those of the metals, which is completely in contrast to the electrical property in any typical structural ceramic [12].

Recently, Vajeeston et al. [14] and Zhang et al. [15] have studied the electronic structure and chemical bonding in ZrB_2 ceramic and have shown three types of chemical bonds in this crystal structure: (i) B–B, (ii) Zr–B and (iii) Zr–Zr [14, 15]. While the B–B bonds are purely covalent, the Zr–B bonds are a mixture of covalent and ionic characters. Due to a small difference in electronegativity values between Zr and B atoms (1.33 and 2.04 for Zr and B, respectively), its ionicity is less than 8%. In contrast, the Zr–Zr bonds are predominantly metallic in nature due to nearly free-electron non-bonding *d*-orbital state, which contributes significant metallicity in this ceramic.[226,227] Although, the exact mechanism of high electrical conductivity in ZrB_2 is not known, Zhang et al., [15] have correlated this unusually high conductive nature to the presence of Zr–Zr metallic bonding. Recently, the authors have suggested that such bonding characteristics can

contribute to room-temperature plastic deformation and dislocation mobility in ZrB_2 [12], in addition to electrical conductivity. Therefore, it has been argued that such metallic character of chemical bonding in ZrB_2 ceramic is well reflected in their *metal-like* mechanical deformation behavior observed (i.e., slip-line formation) in indentation and scratch studies at room-temperature [5, 12, 16, 17]

3.3. SCRATCH STUDIES IN OXIDIZED ZrB_2–SiC COMPOSITE

Surface morphology of ZrB_2–SiC composite changes with temperature due to oxidation [1, 8–10]. Figure 8a–c show the cross-sectional areas of the ZrB_2-5wt%SiC specimens oxidized at 1,000°C in ambient conditions for 1, 5 and 15 h, respectively. It can be seen from Fig. 8 that upon oxidation different layers were formed from the top. As the oxidation time increased total thickness of the oxidized layers also increased. In the temperature range of 800–1,200°C, oxidation rate of ZrB_2 is higher than that of SiC. ZrB_2 produces molten B_2O_3 (melting point ~450°C) and crystalline ZrO_2 at 1,000°C [1, 8–10]. This process results in a porous layer of crystalline ZrO_2 and SiC above the unoxidized (virgin) ZrB_2–SiC composite. Thus, beyond 1,000°C, the oxidized surface of the ZrB_2–SiC composite consists of a porous ZrO_2+SiC layer covered by a thin B_2O_3 amorphous layer. At this temperature range, further oxidation of unreacted ZrB_2, present below the porous ZrO_2+SiC layer, is controlled by the diffusion of oxygen (O_2) through the thin glassy layer of B_2O_3.

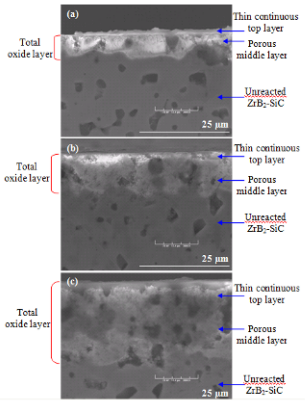

Figure 8. Cross-sections of ZrB_2–SiC specimens oxidized for (**a**) 1 (**b**) 5 and (**c**) 15 h at 1,000°C.

Figure 9a and b present the scratch depth vs. scratch distance profiles at four different constant loads (50, 100, 200 and 300 mN) for the unoxidized and oxidized surfaces, respectively. These studies were conducted on ZrB_2–SiC specimens oxidized for 5 h. Several interesting features can be seen from these depth profiles. While the average depth increased with load for both oxidized and unoxidized surfaces, the scratch depths were significantly higher (almost double) for the oxidized surface at 200 and 300 mN loads compared to virgin surface. This large increase in scratch depth at a given load is a direct result of the presence of porous and weak oxide layer. In addition, it was also noticed that the depth of the scratch on oxidized surface decreased with increase in length of the scratches, especially at 50 and 100 mN loads. This result may be due to uneven surface that was formed due to oxidation at high temperature. However, exact reason or this mechanism was not investigated. These preliminary studies indicate that although the oxide layer is beneficial for the underlying unoxidized ZrB_2–SiC surface from further oxidation, mechanical integrity of the oxidized surface is much weaker compared to that of unoxidized surface. Therefore, during service, impact by atmospheric debris particles can cause more damage to the oxidized surface of components made out of ZrB_2–SiC composite compared to that of virgin surface. As a result of this, the abrasion process may also expose the fresh ZrB_2–SiC surface to the oxidizing atmosphere by removing the weak oxide layer.

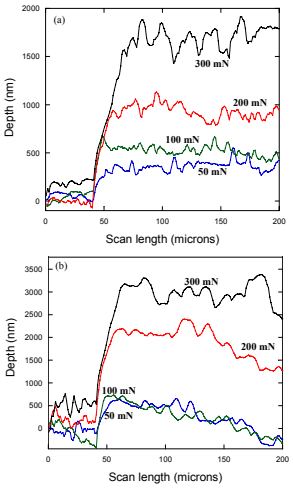

Figure 9. Scratch depth vs. length profiles at different loads for (**a**) unoxidized and (**b**) oxidized ZrB_2–SiC composite, respectively.

4. Conclusions

Plasma pressure compaction technique was successfully employed to produce a dense ZrB_2-5wt%SiC composite at relatively lower processing conditions compared to conventional sintering techniques. Scratch studies in the unoxidized composite revealed two fundamental inelastic deformation mechanisms (i) slip-line patterns and (ii) transgranular microcracks. The formation sequence of these features has been rationalized based on the elastic stress field solutions for normal and tangential point loads. During the scratch process, large shear stress ahead of the indenter results in slip-line formation where as tensile stress, oriented along scratch direction, in the wake of the indenter opens up microcracks orthogonal to the scratch direction. The observed slip-line patterns were limited to the ZrB_2 matrix phase and TEM studies confirmed that such plastic deformation patterns resulted due to the room-temperature dislocation activity and mobility. Scratch studies on the oxidized specimens showed that at a given load, scratch depth is significantly higher for oxidized surface compared to virgin surface of the composite.

References

1. Fahrenholtz WG, Hilmas GE, Talmy IG, Zaykoski JA (2007), Refractory diborides of zirconium and hafnium, J Am Ceram Soc 90:1347
2. Kingery WD, Bowen HK, Uhlmann DR (2003), Introduction to Ceramics, Wiley, New York
3. Rahaman MN (2003), Ceramic Processing and Sintering, M. Dekker, New York
4. Ghosh D, Subhash G, Sudarshan TS, Radhakrishnan R, Gao X-L (2007), Dynamic indentation response of fine-grained boron carbide, J. Am. Ceram. Soc 90:1850
5. Ghosh D, Subhash G, Radhakrishnan R, Sudarshan TS (2008), Scratch-induced microplasticity and microcracking in zirconium diboride-silicon carbide composite, Acta Mater 56:3011
6. Harvey DP II, Kalyanaraman R, Sudarshan (2002), TS Consolidation and mechanical behaviour of nanocrystalline iron powder, Mater Sci Tech 18:959
7. Srivatsan TS, Woods R, Petraroli M, Sudarshan TS (2002), An investigation of the influence of powder particle size on microstructure and hardness of bulk samples of tungsten carbide, Powder Tech 122:54
8. Han J, Hu P, Zhang X, Meng S (2007), Oxidation behavior of zirconium diboride-silicon carbide at 1800^{o}C, Scripta Mater 57:825
9. Rezaie A, Fahrenholtz WG, Hilmas GE (2007), Evolution of structure during the oxidation of zirconium diboride-silicon carbide in air up to 1500^{o}C, J Eur Ceram Soc 27:2495
10. Fahrenholtz WG (2007), Thermodynamic analysis of ZrB_2-SiC oxidation: formation of a SiC-depleted region, J Am Ceram Soc 90:143

11. Ghosh D, Subhash G, Orlovskaya N (2008), Measurement of scratch-induced residual stress within SiC grains in ZrB_2-SiC composite using micro-Raman spectroscopy, Acta Mater 56:5345
12. Ghosh D, Subhash G, Bourne GR (2009), Room-temperature dislocation activity during mechanical deformation of polycrystalline ultra-high-temperature ceramics, Scripta Mater 61:1075
13. Grabco D, Pushcash B, Dyntu M, Shikimaka O (2002), Thermal evolution of deformation zones around microindentations in different types of crystal, Phil Mag A 82:2207
14. Vajeeston P, Ravindran P, Ravi C, Asokamani R (2001), Electronic structure, bonding, and ground-state properties of AlB_2-type transition-metal diborides, Phy Rev B 63:045115-1
15. Zhang X, Luo X, Han J, Li J, Han W (2008), Electronic Structure, elasticity and hardness of diborides of zirconium and hafnium: first principles calculations, Comp Mater Sci 44:411
16. Ghosh D, Subhash G, Bourne GR (2009), Inelastic deformation under indentation and scratch loads in a ZrB_2–SiC composite, J Eur Ceram Soc 29:3053
17. Subhash G, Maiti S, Geubelle PH, Ghosh D (2008), Recent advances in dynamic indentation fracture, impact damage and fragmentation of ceramics, J Am Ceram Soc 91:2777

THE ELECTRONIC PROPERTIES OF METAL BORIDES AND BOROCARBIDES: DIFFERENCES AND SIMILARITIES

SOUHEILA LASSOUED,[1, 2] RÉGIS GAUTIER,[2]
JEAN-FRANÇOIS HALET[2,*]
[1] *Laboratoire de Chimie Appliquée, Université Mohamed Khider, 07000 Biskra, Algeria*
[2] *Sciences Chimiques de Rennes, UMR 6226 CNRS-Ecole Nationale Supérieure de Chimie de Rennes-Université de Rennes 1, F-35042, Rennes cedex, France*

Abstract The bonding and structural arrangement in a few representative ring- or chain-containing solid-state metal borides and boride carbides are analyzed with respect to the electron count of the non-metal entities. Similarities and differences between them are emphasized. More specifically, the bonding in some layered ternary borides of $RETB_4$ formula (*RE* = rare-earth metal and *T* = transition metal) is first analyzed and compared to that of the metal boride carbide ScB_2C_2, which contains a similar non-metal arrangement. Oxidation states are proposed for the boron or boron–carbon networks encountered in these compounds. It seems that they are electron-richer than graphite-like boron networks. In a second part, the bonding in linear boron and boron–carbon chains encapsulated in channels of LiB or $RE_xB_yC_z$ is discussed and compared. Cumulenic bond character is favored in these chains.

Keywords: borides, boride carbides, solid-state compounds, electron counting, theoretical calculations

1. Introduction

Boron is often considered as unique. Indeed it is, think of all the different arrangements it can adopt by itself – it has several allotropic modifications [1] – or combined with many elements of the periodic table. It shows many similarities (but also dissimilarities as we will see later) to its neighbor,

* Jean-François Halet, Sciences Chimiques de Rennes, UMR 6226 CNRS-Ecole Nationale Supérieure de Chimie de Rennes-Université de Rennes 1, F-35042, Rennes cedex, France, e-mail: halet@univ-rennes1.fr (J.-F. H.).

N. Orlovskaya and M. Lugovy (eds.), *Boron Rich Solids: Sensors, Ultra High Temperature Ceramics, Thermoelectrics, Armor*, DOI 10.1007/978-90-481-9818-4_7,

carbon – it is where its name comes from, bor(*ax* + *carb*)on – and its diagonal relative, silicon. Thus, like carbon and silicon, it shows a propensity to form covalent molecular and extended compounds, but it also differs sharply from them in having one less valence electron than the number of valence orbitals. This "electron deficiency" governs its rich chemistry, reflecting the variety of ways in which it seeks to solve the problem of having fewer electrons (three) than atomic orbitals (four) available for bonding. One way for elemental boron would be to adopt metallic bonding with many boron–boron contacts, as do its Group 13 congeners, but its small size and its high ionization energies result in covalent rather than metallic bonding. Multiple bonds are also rather scarce and clustering, which allows three-center-two-electron bonding, is often preferred. The structural units which dominate in boron, are polyhedra as in several metal-poor boride structures where are found B_{12} icosahedra [1]. The linkage of these polyhedra leads to three-dimensional boron arrays in solid-state compounds. This strongly differs from the chemistry of carbon or silicon. But as the boron/non-boron ratio decreases, the dimensionality of the boron network diminishes, and structural connections with carbon and silicon chemistry can be made.

C. Longuet-Higgins and W. N. Lipscomb in the 1950s and early 1960s laid the foundations for the understanding of the bonding in molecular boron chemistry, introducing the concept of three-center-two-electron bonds [2]. This did not come easily due to the complexity of the structures generally adopted by boron compounds compared to that of carbon cousins. Using C. Longuet-Higgins and W. N. Lipscomb's conclusions, K. Wade elegantly established a set of electron-counting rules in the early 1970s, supported since, by a vast amount of theoretical calculations, not only to rationalize known structures, but also to suggest the arrangements of new molecular boron species [2].

Less works have been devoted to extended solids. Despite some real differences, there are strong similarities between the bonding in molecular boron-containing compounds and that in extended boron-containing systems. Interestingly, a bridge can be established since both systems deal with the fundamental questions: Where are the electrons? Where are the bonds? Indeed, there is a popular solid-state idea that in metal-non-metal compounds, the metals transfer their valence electrons to the non-metals, which use them to form bonds in order to obey the octet rule. This very simple concept, often referred as the Zintl-Klemm concept is important not only

because it explains much solid state chemistry, but also because it forges a useful link with molecular main group chemistry [3]. Take the C_2 dumb-bell encountered in the metal dicarbide CaC_2 (see Fig. 1, *left*) Considering $Ca^{2+}(C_2)^{2-}$, the C_2 dianionic unit is isoelectronic to the 10-electron molecule C_2H_2 and can be viewed as a deprotonated ethyne with a triple bond. Indeed the C–C distance of 1.19 Å is comparable to that measured for acetylene. The electron count matters and governs the structural arrangement of main-group rings or chains contained in solid-state compounds! LaC_2 can be synthesized for instance, not NaC_2! The reason is that $(C_2)^{3-}$ anions in octahedral cavities formed from the La^{3+} cations are "viable" [4]. The additional electron populates an antibonding π^* orbital thereby reducing the bond order and increasing the C–C distance to 1.30 Å [5]. On the other hand, with partial depopulation of a σ-bonding orbital, $(C_2)^-$ anions are prone to "instabilities" and the compound $Na^+(C_2)^-$ cannot be made.

Let's consider another example taken out from metal borides: CaB_6. This compound exhibits a three-dimensional (3D) lattice of B_6 octahedral clusters linked to each other through inter-cluster B–B bonds in three directions (see Fig. 1, *right*). The analogy with the molecular borane $(B_6H_6)^{2-}$ is straightforward. The Wade rules generally used to rationalize boranes can also be used for the solid [2]. We can go from $(B_6H_6)^{2-}$ to $(B_6)^{2-}$ in CaB_6 changing the localized B–H bonds into inter-cluster B–B bonds and the two chemical units are then isoelectronic. Such a picture with $(B_6)^{2-}$ and thus Ca^{2+} is supported by the computed DOS which shows a semi-conducting solid with a sequence of low-lying occupied cluster bonding bands separated from empty antibonding cluster bands and Ca bands [2].

This structure is also found with lanthanides such as LaB_6. Thus, given the preferred oxidation state of +3 rather than +2 for La, we should go from $(B_6)^{2-}$ to $(B_6)^{3-}$ octahedra. The molecular borane $(B_6H_6)^{2-}$ has not been successfully reduced! Identically, it is difficult to add extra electrons in B–B antibonding bands without destabilizing the CaB_6 structure. It is like for LaC_2 discussed above, the extra electron of La with respect to Ca need not be transferred to the B network. It can occupy the bottom of the La-based bands in the DOS, which will lie between the low-lying occupied B–B bonding bands and the vacant high-lying B–B antibonding bands. This is a difference with molecules. The metal electrons in a solid-state compound can serve as a reservoir, which can be fully or partially used to supply the electron requirements of the main-group partner. Too many electrons for the main-group partner are fine because some electrons can be retained

by the metals. On the other hand, not enough electrons, generally is not favorable for observing a similar arrangement. Removing electrons in the B–B bonding bands is not favorable. NaB_6 does not exist but NaB_5C does! A bit of carbon is needed, that is some additional electrons, to observe the same arrangement as that of CaB_6 with sodium [1b, 6]. Similarly, the arrangement of GdB_4 largely encountered with lanthanide elements is not observed with Ca, unless some carbon is present in the structure [7].

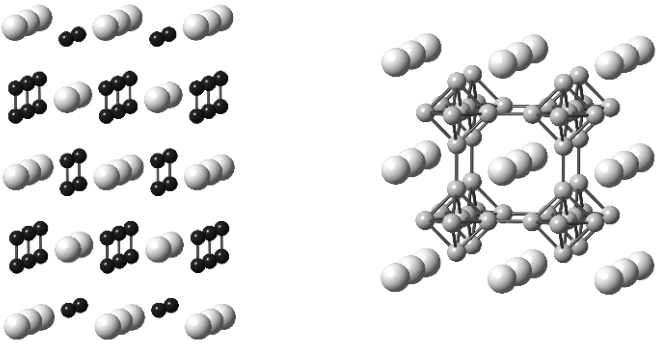

Figure 1. Structural arrangement of CaC_2 (*left*) and CaB_6 (*right*). Large light grey, small dark grey and small black spheres represent Ca, B, and C atoms, respectively.

Of course, this simple notion of ionic model somewhat fails when the electronegativities of the metal and non-metal are not very different, but it is tremendously useful in understanding a great variety of metal borides for instance as we will see. A collection of portraits burrowed from the ternary metal boride or metal boride carbide solid-state chemistry will serve the purpose of this survey, which is to discuss the bonding and some physical properties in some boron extended systems in a certain way that permits some connection with that encountered in some discrete molecule and/or other solid-state architectures containing carbon in addition to boron.

2. Metal Borides

2.1. STRUCTURAL ASPECTS

Boron is an important industrial material, although as pure element it is little used except in fission-reactor control rods to capture neutrons, or to make metal borides, or to be added to metals to improve their conductivity (aluminium), or to make them easier to refine (nickel), or to make them flow better (iron). Some borides conduct electricity many times better than the metal itself and they have very high melting points. Metal borides are

used for making turbine blades, rocket nozzles, high-temperature reaction vessels and inert electrodes for instances [8].

Binary metal borides comprise a group of over 200 binary compounds, which show an amazing diversity of stoichiometries and exhibit an astonishing variety of stable architectures (many more than for the carbide cousins) [9]. These architectures can be systematized by several arrangements of the boron sub-structures, which illustrate the increasing tendency of boron atoms to catenate as their concentration in the boride compound increases (see Fig. 2). Isolated B atoms, that is, B atoms surrounded entirely by metal atoms as nearest neighbors, isolated pairs of B atoms, infinite one-dimensional (1D) linear chains, zigzag chains, branched zigzag chains, double chains encapsulated in metal holes dominate with low boron content. As the boron content increases, two-dimensional (2D) planar (or puckered) sheets, and diverse three-dimensional (3D) networks are encountered in which the metal atoms occupy specific voids or otherwise vacant sites. Interestingly, in classes, which involve appreciable bonding between boron atoms, the B–B distances remain in the same range, ca. 1.8 Å, despite the extensive variation in size and in number of the metal atoms. Some structures with high boron content such as YB_{66} are close to those of boron itself and can be exceedingly complicated, preventing a simple analysis of their bonding. Even with today's powerful computers, no complete theoretical study of the electronic structure of elemental boron has been done. Let us tackle instead the bonding in simpler examples, namely ternary metal borides containing 2D boron sub-lattices.

2.2. EXAMPLES OF RINGS IN TERNARY METAL BORIDES

Boron rings abound in solid-state chemistry. If graphite-like hexagonal rings dominate in 2D binary metal borides, other rings of different sort can be encountered in many ternary solid-state boron-containing compounds [9]. This is the case for instance in some layered ternary borides adopting the $YCrB_4$ [10], $ThMoB_4$ [11] and Y_2ReB_6 [12] structure-types, in which the boron atoms form 2D layers which alternate with metallic sheets made of rare-earth metals (*RE*) and transition metals (*T*) or eventually main group metals [13] (see Fig. 3). All these structures are based on different rings, which merge to each other to form 2D networks of boron atoms. Indeed, these networks differ by the way the boron atoms arrange themselves.

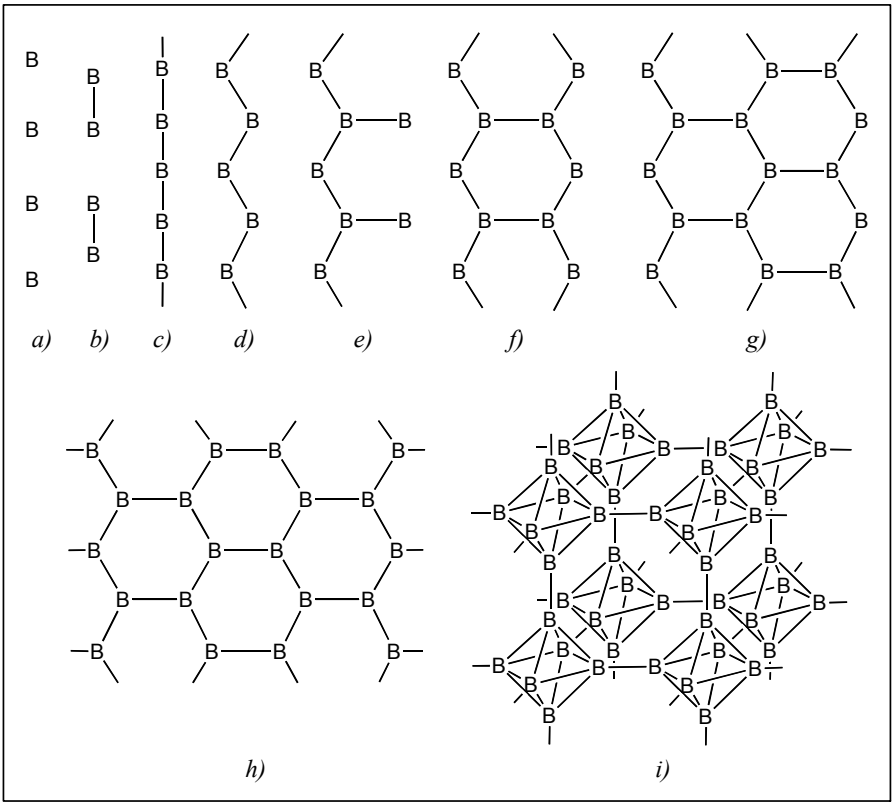

Figure 2. Structural arrangements of boron atoms in the borides: (**a**) isolated atoms (Mn_4B), (**b**) pairs (V_3B_2), (**c**) linear chains (LiB_x), (**d**) zigzag chains (FeB), (**e**) branched zigzag chains ($Ru_{11}B_8$), (**f**) simple ribbons (Ta_3B_4), (**g**) double ribbons (V_2B_3), (**h**) two-dimensional networks (MgB_2), and (**i**) three-dimensional networks (CaB_6).

In both $YCrB_4$ and $ThMoB_4$ structure-types, the boron atoms form pentagonal and heptagonal rings. The pentagons fuse two by two and are surrounded by heptagons. Having the same stoichiometry $RETB_4$, these two arrangements are polymorphic in some ways since they differ by the way the fused pentagons are positioned to each other. In some cases, these two arrangements are characterized with the same metals [14]. The *RE* atoms sit above and below the heptagons and the *T* atoms above and below the pentagons. Somewhat related also, is the structure of stoichiometry RE_2TB_6 exemplified with Y_2ReB_6 [12] where, in addition to pentagons and heptagons, there are hexagons forming the boron layers.

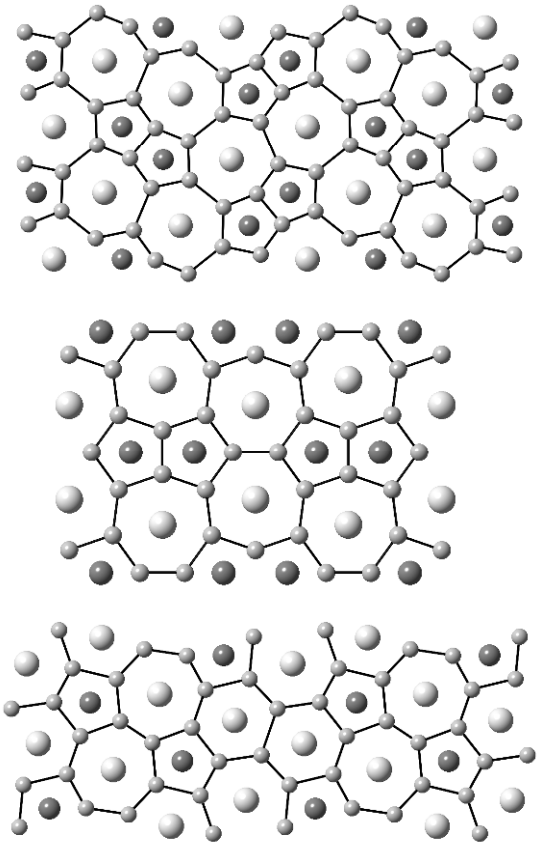

Figure 3. Top views of the $YCrB_4$ (*top*), $ThMoB_4$ (*middle*), and Y_2ReB_6 (*bottom*) structure-types. Large, medium and small spheres represent rare-earth (*RE*) metal, transition (*T*) metal and boron atoms, respectively.

Solid-state chemists and physicists are interested in these compounds because some of them develop interesting physical, especially magnetic properties [15]. We have, on our side, revisited the bonding of this type of compounds with the aid of quantum chemical calculations of the extended-Hückel tight-binding (EH-TB) and periodic density functional theory (DFT) types [16].

The reader may wonder why are we interested in these compounds? Indeed, these compounds consist of layers of boron atoms, as does MgB_2 (see Fig. 4), which was discovered to superconducting at 39 K a few years ago [17]. The metal/non-metal ratio is the same, i.e., 1:2, although the rings themselves differ in shape with benzene-like rings in MgB_2 (isoelectronic to graphite) and, as said previously, pentagons plus heptagons in *RET*B_4. Therefore, we may ask ourselves whether there is a relationship between the

electronic structure of MgB_2 and that of these *RET*B_4 and RE_2TB_6 compounds [18]?

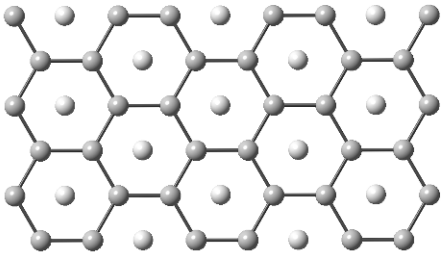

Figure 4. Top view of the MgB_2 structural arrangement. Light grey and dark grey spheres represent Mg and B atoms, respectively.

It is noteworthy that the boron arrangement observed in $YCrB_4$ is strongly related to the 2D B_2C_2 arrangement encountered in the ternary rare-earth metal boron carbide ScB_2C_2 where pentagons and heptagons are also observed [19] (see Fig. 5). We may wonder if there is a relationship between these two compounds?

Looking at these structures, a molecular organic chemist will think about particular carbon rings he can play with. Two fused pentagons make a pentalene-like motif. One pentagon fused to one heptagon corresponds to an azulene-like unit. Fusion of a pentagon, a heptagon and a hexagon leads to a benzazulene-like motif. We may wonder whether there is some interest to compare theses motifs with organic molecules such as pentalene C_8H_6, azulene $C_{10}H_8$ (an isomer of naphthalene) or benzazulene anion $(C_{13}H_9)^-$ (see Fig. 6). With metal above and below the rings, we think of multidecker-like "molecules" in solids. These organic rings can also be complexed with organometallic fragments [20].

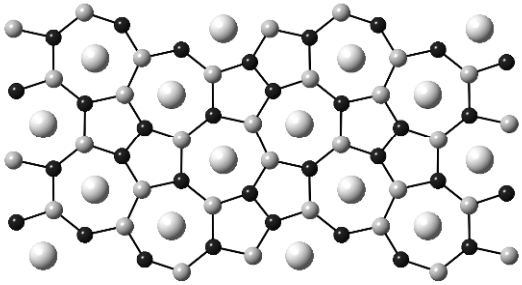

Figure 5. Top view of the ScB_2C_2 structural arrangement. Large light grey, small dark grey, and small black spheres represent Sc, B, and C atoms, respectively.

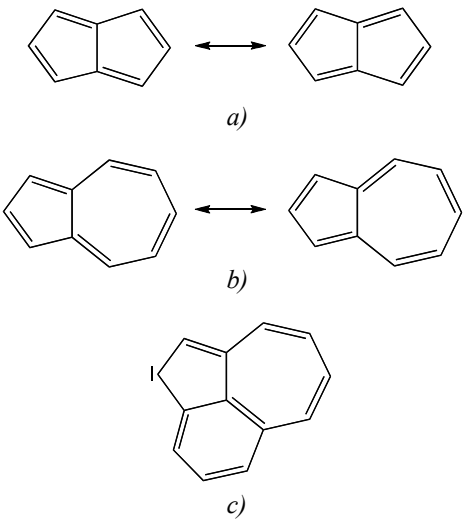

Figure 6. Pentalene C_8H_6 (**a**), azulene $C_{10}H_8$ (**b**), and benzazulene anion $(C_{13}H_9)^-$ (**c**).

TABLE 1. Some ternary compounds which crystallize in the $YCrB_4$ and $ThMoB_4$ structure-types

Structure-type	Compounds			
$YCrB_4$	$YCrB_4$	$GdCoB_4$	$DyCoB_4$	$ErRuB_4$
	$YReB_4$	$TbVB_4$	$DyReB_4$	$ErCoB_4$
	$YFeB_4$	$TbCrB_4$	$HoVB_4$	$TmCrB_4$
	$YRuB_4$	$TbMoB_4$	$HoCrB_4$	$TmAlB_4$
	$YCoB_4$	$TbWB_4$	$HoMoB_4$	$TmReB_4$
	$CeCrB_4$	$TbMnB_4$	$HoWB_4$	$TmFeB_4$
	$CeMnB_4$	$TbReB_4$	$HoMnB_4$	$TmRuB_4$
	$CeFeB_4$	$TbFeB_4$	$HoReB_4$	$TmOsB_4$
	$PrCrB_4$	$TbRuB_4$	$HoFeB_4$	$TmCoB_4$
	$NdCrB_4$	$TbOsB_4$	$HoRuB_4$	α-$YbAlB_4$
	$SmCrB_4$	$TbCoB_4$	$HoOsB_4$	$LuCoB_4$
	$GdVB_4$	$DyVB_4$	$HoCoB_4$	α-$LuAlB_4$
	$GdCrB_4$	$DyCrB_4$	$ErVB_4$	UVB_4
	$GdMoB_4$	$DyMoB_4$	$ErCrB_4$	$UCrB_4$
	$GdWB_4$	$DyWB_4$	$ErMoB_4$	$UMnB_4$
	$GdMnB_4$	$DyMnB_4$	$ErWB_4$	$UFeB_4$
	$GdReB_4$	$DyFeB_4$	$ErMnB_4$	$UCoB_4$
	$GdFeB_4$	$DyRuB_4$	$ErReB_4$	
	$GdRuB_4$	$DyOsB_4$	$ErFeB_4$	
$ThMoB_4$	$ThMoB_4$	$ThReB_4$	UWB_4	β-$YbAlB_4$
	$ThVB_4$	$ThWB_4$	$UReB_4$	β-$LuAlB_4$
	$UMoB_4$			

As said earlier, the electron count governs the shape of molecules and solids [2, 3]. The first question, which arises then is: What is the right electron count for these compounds to exist? Is the ionic model, briefly discussed earlier a useful starting point to work with? It supposes in general a rather large electronegativity difference between the constituting elements. This may be not the case in ternary compounds discussed here. Nevertheless, let us start with such an ionic model. We know it is a crude approximation, but often very useful to understand the electronic properties of the non-metal part in a solid [3]. In other words, what could be the formal oxidation state of the boron network in the *RET*B_4 compounds?

A look at the full list of compounds, which adopt the $YCrB_4$ or $ThMoB_4$ structure types (see Table 1), does not seem to be very helpful. If it is possible to propose an oxidation state for the rare-earth metals (often 3+ or eventually 4+ for Ce or Th), it is less obvious for the transition metals. Indeed, these structure-types are adopted with nearly all the transition metals. A glance at the boron–boron distances experimentally measured in these compounds is neither useful. They range from 1.60 to over 2.00 Å for $YCrB_4$ – the X-ray structure is not very accurate [10] – and from 1.80 to 1.85 Å in $ThMoB_4$ [11] for instance. This indicates formal single B–B bonds, but we know how "flexible" can be boron–boron bonds separations [1, 2, 13].

Obviously, several oxidation states might theoretically be possible for the boron network in the *RET*B_4 compounds. EH-TB calculations were first made on one boron layer with different formal negative charges (from $(B_4)^{4-}$ to $(B_4)^{7-}$). The density of states (DOS) for one boron layer taken out from $YCrB_4$ and $ThMoB_4$ is given on the top and the bottom of Fig. 7, respectively. The shape of the DOS seems to be sensitive to the B–B distances. For the boron layer encountered in $YCrB_4$, holes in DOS at the Fermi level occurs for the charges of 5− and for 6−, whereas a hole at the Fermi level is just observed for the charge of 6− for the boron layer observed in $ThMoB_4$. Indeed, we think that in compounds where the connectivity between the atoms is low, a situation where there is a hole at the Fermi level (closed-shell electron configuration) for the main-group atom sub-lattice is generally preferred over that with a high DOS (that is an open-shell electron configuration). This is often seen as a criterion of "stability". Interestingly enough, in both cases, for the charges of 4−, which would render these layers isoelectronic to graphite and the graphitic-like boron layers of MgB_2, the Fermi level cuts some DOS. This probably means that such boron arrangements made of merged pentagons and heptagons need slightly more electrons with respect to graphite-like arrangements to exist. This leads us to propose that the formal oxidation state for the boron networks in these compounds is $(B_4)^{6-}$ which implies the

metals to adjust: 3+ or 4+ for the *RE* metal and 3+ or 2+ for the *T* metal. The reader may argue that that there is also a hole at the Fermi level for 5− in the case of the boron layer taken out from $YCrB_4$, and consequently, 3+ or 4+ for the *RE* metal and 2+ or + for the *T* metal should also be envisaged. This is true and calculations are in progress to better understand why this is the case for $YCrB_4$ but not for $ThMoB_4$ [16].

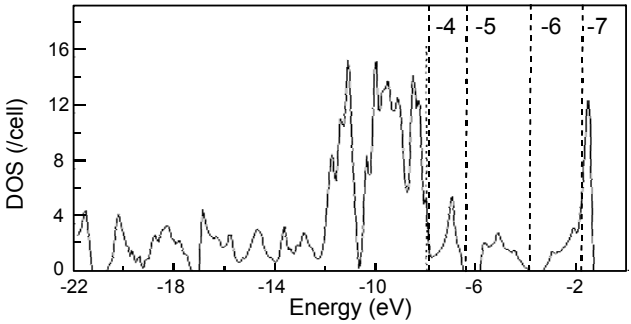

a)

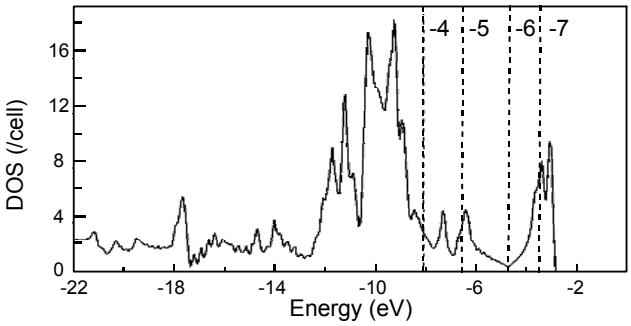

b)

Figure 7. Total EH-TB DOS of one boron $(B_4)^{n-}$ layer encountered in $YCrB_4$ (**a**) and $ThMoB_4$ (**b**). Fermi levels are indicated for $n = 4–7$.

What happens for the 3D compounds? Covalent interactions between the metal and boron atoms in $YCrB_4$ and $ThMoB_4$ modify somewhat the DOS of the boron network, but the main conclusions remain the same. Projected DOS obtained from periodic DFT calculations of LMTO type and shown in Fig. 8 indicate that there is hardly any participation of boron at the Fermi level but rather from the transition metals, Cr or Mo. The contribution of Th is not important and the f band looks empty. The contribution of Y is even weaker. The DOS of the two compounds differ since the Fermi level lies in a narrow hole of DOS in $YCrB_4$ and cut some

DOS in $ThMoB_4$ (see Fig. 8). It turns out then that the conducting properties are essentially governed by the nature of the transition metal into play. $YCrB_4$ is computed to be semi-conducting and $ThMoB_4$ should be metallic in character according to their total DOS. We are not aware of any resistivity measurements on these compounds to confirm or not our conclusions.

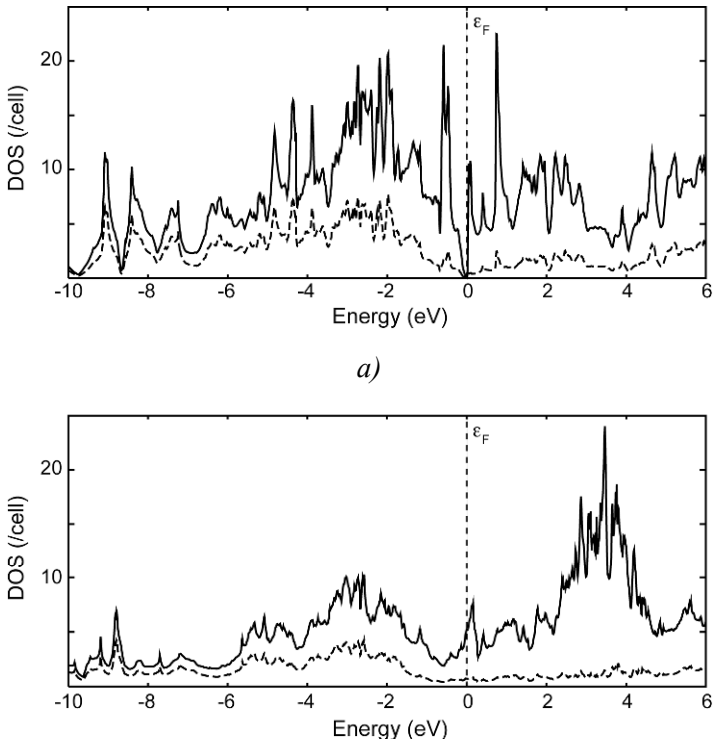

Figure 8. Total (*solid*) and B projected (*dotted*) LMTO DOS of $YCrB_4$ (**a**) and $ThMoB_4$ (**b**).

An interesting question concerns the "stability" of the boron arrangement observed in the $YCrB_4$ structure-type with respect to that encountered in $ThMoB_4$ (see above). Most of these ternary boride compounds crystallise in the $YCrB_4$ structure-type rather than the $ThMoB_4$ structure-type (see Table 1). Is it for thermodynamical reasons, or electronic reasons? Interestingly, both arrangements (called α and β) are adopted for $YbAlB_4$ and $LuAlB_4$, which were published recently [14]. For both compounds, the two forms exhibit slightly different physical properties [14]. In the case of $TmAlB_4$, Mori et al. have even shown that crystals measured are basically of the $YCrB_4$ crystal structure type but with anomalies which could arise from intrinsic

building defects due to the presence of fragments of the closely related $ThMoB_4$ type structure [15]. Indeed, we do not expect much difference in energy between these two "polymorphic" forms since the local arrangement of the boron atoms is fairly similar in both arrangements. They simply differ by the way the fused pentagons are positioned to each other, in a zigzag fashion in $YCrB_4$ and in a linear fashion in $ThMoB_4$ (see Fig. 3).

Full-geometry optimizations carried out at the DFT level of theory for various *RE* and *T* metals with the two arrangements $YCrB_4$ and $ThMoB_4$ indicate that, regardless of the metals, the $YCrB_4$ arrangement is computed to be the most stable by 39 and 21 meV for the $YCrB_4$ and $ThMoB_4$ formulae, respectively. This is in agreement with the experiment for $YCrB_4$. On the other hand, our computed result on $ThMoB_4$ disagrees with the experiment. We conclude that the $YCrB_4$ arrangement is the thermodynamically stable phase whereas the $ThMoB_4$ arrangement is the kinetically stable phase. This seems definitely to be the case for $YbAlB_4$ and $LuAlB_4$ since the authors claimed that "the presence of two polymorphs at the synthesis temperature is that if the temperature was quickly ramped up to 1873 K, more of the α phase crystals [$YCrB_4$ type] would be synthesized, in comparison with the heat treatment at 1673 K. This suggests that the α phase [$YCrB_4$ type] would be the high-temperature phase. Given that these phases are grown in flux, transformation from one polymorph to the other is also possible during cooling." [14]. In agreement with this statement, the computed energy difference between the two arrangements for $LuAlB_4$ is less important than that calculated for $YCrB_4$ and $ThMoB_4$, only 18 meV per motif, but still substantial. Interestingly enough, the Fermi level lies in a hole of density of states in both polymorphs.

2.3. RELATED RINGS IN TERNARY METAL BORIDE CARBIDES

As said earlier, $YCrB_4$ and the boride carbide ScB_2C_2 [19] contain the same topological non-metal layers with pentagons and heptagons (see Fig. 5). Of course replacement of half of the boron atoms by more electron-rich carbon atoms require less electrons from the surrounding metals explaining why there are no metals above and below the pentagons in the latter. Surprisingly enough, preliminary EH-TB calculations on one B_2C_2 layer extracted from ScB_2C_2 show a hole at the Fermi level for $(B_2C_2)^{2-}$, i.e., a system isoelectronic to graphene rather than the $(B_4)^{6-}$ boron network of $YCrB_4$. Sophisticated periodic and molecular calculations are in progress to try to interpret such a result.

With two kinds of atoms, boron and carbon into play we are faced to the question of their distribution. This is termed the *coloring problem*: The same topology, here pentagons and heptagons, but different ways to order

the atoms [21]. Indeed, six "simple" different ways can be envisaged for the B_2C_2 network of ScB_2C_2 [22]. They are shown in Fig. 9.

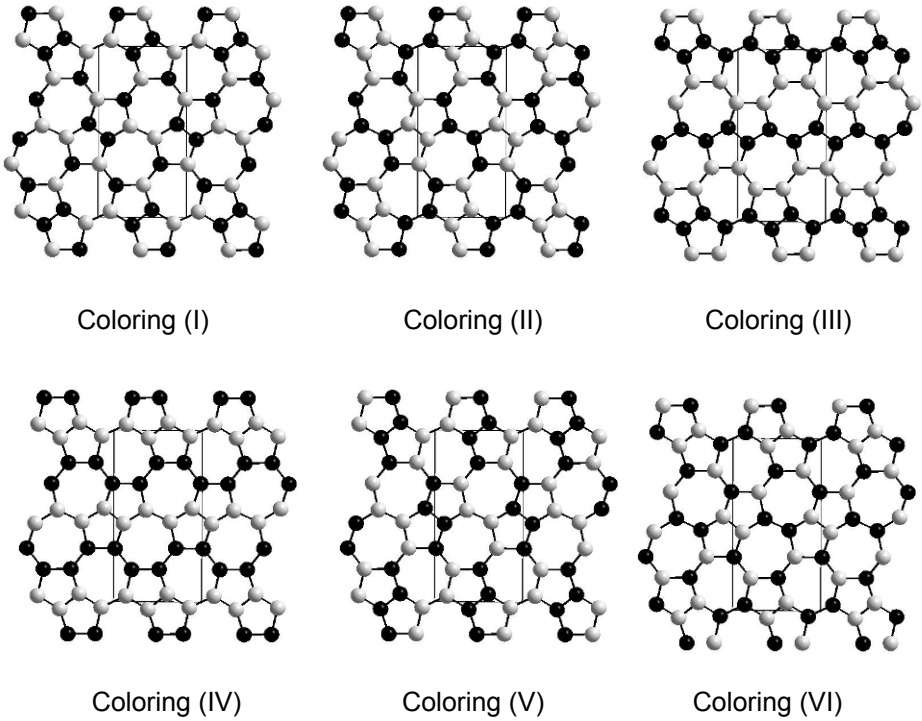

Figure 9. Different possible colorings for the B_2C_2 network of ScB_2C_2. Grey and black spheres represent B and C atoms, respectively.

With carbon–carbon and boron–boron pairs colorings I (experimentally observed) and VI are related to each other. Both colorings III and IV display either zigzag or U-chains of one atom kind. Finally boron and carbon tetramers are present in colorings II and V. This is like isomerism in molecules. Often an isomeric form may be energetically preferred over another one. Similarly in solids, one coloring may be energetically preferred over another one.

We and others tackled this problem some years ago for other layered MB_2C_2 (M = rare-earth or alkaline earth metal) phases [23, 24]. In these compounds, the boron–carbon layers are made of fused rhombuses and octagons (see Fig. 10). The metals are located above and below the octagons. Two distributions inside the layers were experimentally proposed: Either B and C atoms alternate within the diamonds with B–B and C–C contacts between the diamonds, this is coloring I (Fig. 10, left), experimentally proposed with La and Y [23]. Alternatively, B and C atoms alternate within

the diamonds and between the diamonds, this is coloring II (Fig. 10, right), experimentally observed for Ce, but also for Ca [1b, 23]. On the basis of DFT calculations, we were able to claim that regardless of the metal, coloring II was more stable than coloring I. Indeed, it was shown that in these compounds the metals essentially must act as two-electron donors with respect to the boron–carbon network adopting coloring II, the other electrons remaining in the relatively narrow d or f bands of the metals [23]. The same study will be carried out for ScB_2C_2. Preliminary EH-TB calculations indicate that the colorings, which minimize the number of B–B and C–C contacts seem to be energetically preferred. In other words, colorings I and VI are rather close in energy and strongly more stable than the others. Interestingly, band gaps are found in the DOS for $(B_2C_2)^{2-}$ with coloring I (as said earlier) but for $(B_2C_2)^{3-}$ with coloring VI.

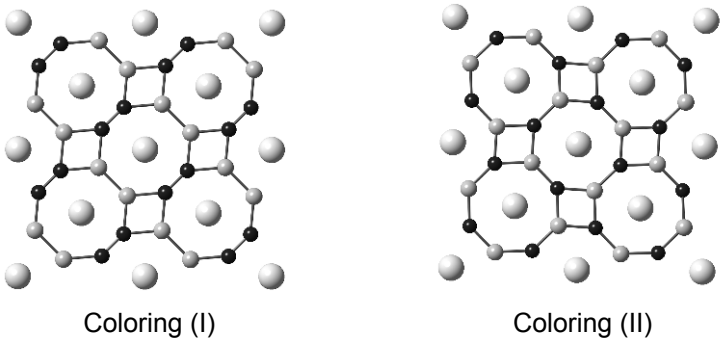

Figure 10. Alternative colorings for the B_2C_2 network in MB_2C_2 (M = rare-earth or alkaline earth metal). Large light grey, small dark grey and small black spheres represent M, B, and C atoms, respectively.

2.4. CHAINS IN METAL BORIDES AND BORIDE CARBIDES

Infinite boron zigzag chains with B–B distances of 1.65–1.90 Å and bond angles of ca. 115° are found in the structure types of CrB, MoB, and FeB [9a]. In all of them, the metal atoms form trigonal prisms which condense along one direction through square faces, making infinite channels in which are inserted the boron atoms (see Fig. 2). There is a large number of binary and ternary representatives of these and other related structure types. For instance, single chains are encountered in Ta_3B_4 [9a] whereas double chains occur in V_5B_6 [9a] (see Fig. 2). On the other hand, infinite linear boron chain is very scarce. Indeed, there is only one example with LiB_x ($0.82 < x \leq 1.0$), which contains infinite boron rods running in channels made by the Li atoms [25] (see Fig. 11). In the Zintl-Klemm paradigm, stoichiometric LiB can be formulated Li^+B^-. B^- being isoelectronic with C, the infinite

boron chain is comparable to the hypothetical metastable allotropic 1D phase of carbon called carbyne (karbin) or chaoite [26]. The preparation and characterization of the latter although claimed by some, remains a challenge. We know that if it were characterized, such an infinite 1D linear carbon chain would be subject to a Peierls distorsion and therefore would be made up of alternating triple and single bonds rather than double bonds [27], analogously to the carbon chains encountered in organic or organometallic wires such as $[Si(C_2H_5)_3]_2(\mu\text{-}C_{32})$ [28] or $[trans\text{-}(p\text{-tol})\{P(p\text{-tol}_3)\}_2Pt]_2$ $(\mu\text{-}C_{28})$ [29]. The bonding situation of the boron rod should be very similar, namely –B≡B–B≡ rather than =B=B=B=. Experimentally, it turns that in LiB_x ($0.82 < x \leq 1.0$) the boron chains are incommensurate with the Li substructure and that the boron atoms seem to be equidistant, suggesting a cumulated double bond system [25, 30].

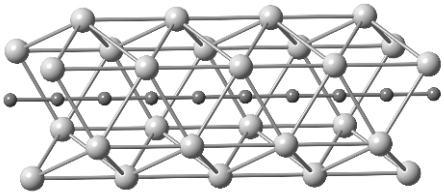

Figure 11. Side view of the structural arrangement of LiB_x. Large light grey and small dark grey spheres represent lithium and boron atoms, respectively.

Insertion of carbon in the boron rod will lead to truncated B_mC_n chains. Indeed, a variety of oligomers from BC_2 up to B_5C_8 up to now, coming from the area of rare-earth metal boron–carbon compounds are known [16, 31]. This is exemplified by LaBC, characterized a while ago during a new investigation of the La–B–C system [32]. In this compound, the metal atoms form distorted square and corrugated metallic layers. They stack in such a way that they form holes in which are encapsulated finite B_5C_5 chains (C–B–C–B–C–B–B–C–B–C, see Fig. 12). These worm-like entities buried in the solid are fairly linear and the measured B–B, B–C and C–C separations, ca. 1.5 Å, correspond approximately to coordinated double bonds. As the reader might guess, proper location of B and C atoms simply on the basis of X-ray measurements is not obvious. This is then often made on the basis of the chemical environment (carbon likes to be in octahedrally surrounded), the electronegativity (carbon will prefer to be at the termination of the chain) as well as theoretical calculations. The latter help also to understand the bonding in these rods and the electrical properties of the compounds [31].

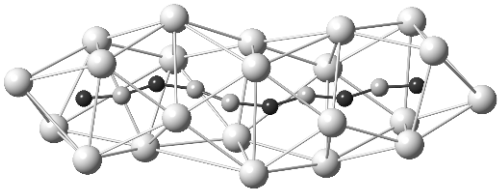

Figure 12. B_5C_5 chain encountered in LaBC. Large light grey, small dark grey and small black spheres represent La, B, and C atoms, respectively.

With formal double bonds between boron and carbon atoms, these B_mC_n oligomers are analogs of cumulenic carbons chains C_n^{4-}, i.e., chains with only C=C double bonds. To obey the octet rule for each atom, a formal charge of 9− is required for the B_5C_5 unit with two lone pairs on the terminal carbon atoms and one negative charge for each boron atom [32]. Indeed theoretical calculations on an isolated $[B_5C_5]^{9-}$ "molecule" indicate a small energy gap separating the highest occupied MO from the lowest unoccupied MO, both of π type [32]. With such a formal anionic charge on the B_5C_5, unit, the La atoms need not be fully oxidized (LaBC ≡ $[La^{1.8+}]_5[B_5C_5]^{9-}$). Consequently, metal electrons must remain in the metallic band and the compound is expected to be an electrical conductor as confirmed by DFT calculations on the 3D LaBC compound [32]. Of course, there are some covalent interactions between the sub-lattices of the B–C chains and the La atoms, but the Zintl-Klemm idea and the electron counting provide a good estimate of the qualitative electronic structure of the compound.

B_5C_5 encountered in LaBC is not the longest boron–carbon chain observed in this kind of compound. As said earlier, the longest chain, up to now, is B_5C_8, found in $La_{10}B_9C_{12}$ [16, 31]. As B_5C_5, B_5C_8 can be considered as a cumulenic-like oligomer with a formal charge of 9−. In principle, there is no reason to stop at this length. It should be possible to adjust the stoichiometry, the size and the electron count to synthesize a solid-state compound containing infinite =B=C=B=C= rods with a cumulenic form, that is, with double bonds between B and C atom. This would constitute another inorganic analog for the hypothetical carbyne discussed earlier, but with equi-spaced atoms since the necessity for a Peierls distortion in the infinite carbyne C_∞ chain or $[B^-]_\infty$ chains is removed in an isoelectronic chain with alternating heteroatoms.

3. Conclusion

The major point of this paper was to show that, as generally observed for molecules, the electron count matters and govern the structural arrangement of main-group sub-lattices contained in metal boride or metal boride carbide solid-state compounds. Similarities and differences between them can emerge depending upon their electron count.

4. Computational Details

Extended Hückel Tight-Binding (EH-TB) calculations [33] were carried out on isolated boron or boron–carbon layers or chains extracted from X-ray crystallographic structures using the program CAESAR [34]. The exponents (ξ) and valence shell ionization potentials (H_{ii} in eV) were, respectively, as follows: 1.3, −15.2 for B 2*s*; 1.3, −8.5 for B 2*p*, and 1.625, −21.4 for C 2*s*; 1.625, −11.4 for C 2*p*. Density functional theory (DFT) band structure calculations of different *RET*B_4 were performed with the scalar relativistic tight-binding linear muffin-tin orbital method in the atomic spheres approximation including the combined correction (LMTO) [35] using the program TB-LMTO-ASA 4.7 [36]. These calculations were carried out using the experimental X-ray crystal structures. Exchange and correlation were treated in the local density approximation using the von Barth-Hedin local exchange correlation potential [37]. The *k*-space integration was performed using the tetrahedron method [38]. Charge self-consistency and average properties were obtained from 135 and 1,710 irreducible *k* points for the calculations of $YCrB_4$ and $ThMoB_4$ structure-types, respectively. The DOS curves were shifted so that the Fermi level lies at 0 eV. Geometry optimizations were performed with the CASTEP 4.3 code [39] with Projector Augmented-Wave potentials [40] using the PBE functional [41]. Both structure-types were considered for the two compounds. A cut-off energy of 500 eV was used for all compounds. The Brillouin zone was sampled with 30 irreducible *k* points calculated using a Monkhorst-Pack scheme.

References

1. See for examples: (a) A. R. Oganov, J. Chen, C. Gatti, Y. Ma, Y.Ma, C. W. Glass, Z. Liu, T. Yu, O. O. Kurakevych, V. L. Solozhenko, Nature 457 (2009) 863. (b) B. Albert, H. Hillebrecht, Angew. Chem. Int. Ed., 48 (2009) 8640.
2. See for example: T. P. Fehlner, J.-F. Halet, J.-Y. Saillard, Molecular Clusters. A Bridge to Solid State Chemistry, Cambridge University Press, Cambridge, UK, 2007.

3. R. Hoffmann, Solids and Surfaces, A Chemist's View of Bonding in Extended Structures, VCH, New York, USA, 1988.
4. R. Hoffmann, P. von Ragué Schleyer, H. F. Schaefer III, Angew. Chem. Int. Ed. 47 (2008) 7164.
5. J. R. Long, J.-F. Halet, J.-Y. Saillard, R. Hoffmann, H.-J. Meyer, New J. Chem. 16 (1992) 839.
6. B. Albert, K. Schmitt, Chem. Mater. 11 (1999) 3406.
7. M. Ben Yahia, O. Reckeweg, R. Gautier, J. Bauer, T. Schleid, J.-F. Halet, J.-Y. Saillard, Inorg. Chem. 47 (2008) 6137.
8. (a) N. N. Greenwood, A. Earnshaw, Chemistry of the Elements, Pergamon Press, Oxford, UK, 1984. (b) J. Emsley, Nature's Building Blocks: An A-Z Guide to the Elements, Oxford University Press, Oxford, UK, 2001.
9. (a) T. Lundström, "Borides: Solid-state Chemistry" in Encyclopedia of Inorganic Chemistry, R. B. King (Ed.), 2nd ed., John Wiley & Sons, Ltd., Chichester, UK, 2005. (b) T. Mori, "Higher Borides" in Handbook on the Physics and Chemistry of Rare Earths, K. A. Gschneidner Jr., J.-C. Bunzli, V. Pecharsky (Eds.), North-Holland, Amsterdam, 2008, p. 105.
10. Yu. B. Kuz'ma, Sov. Phys. Crystallogr., 15 (1970) 312.
11. P. Rogl, H. Nowotny, Monatsh. Chem., 105 (1974) 1082.
12. Yu. B. Kuz'ma, S. I. Svarichevskaya, Kristallografiya, 17 (1972) 658.
13. (a) Yu.B. Kuzma, Crystal Chemistry of Borides, Vyscha Shkola, Lviv, 1983. (b) Yu.B. Kuzma, N.F. Chaban, Binary and Ternary Systems containing Boron, Metallurgia, Moscow, 1990. (c) E. Villars L. D. Calvert, Pearson's Handbook of Crystallographic Data for lntermetallic Phases, ASM International, Materials Park, OH, 2nd. edn., vol. 2, 1991.
14. R. T. Makaluso, S. Nakatsukuji, K. Kuga, E. L. Thomas, Y. Machida, Y. Maeno, Z. Fisk, J. Y. Chan, Chem. Mater. 19 (2007) 1918.
15. (a) T. Mori, H. Borrmann, S. Okada, K. Kudou, A. Leithe-Jasper, U. Burkhardt, Yu. Grin, Phys. Rev. B **76**, (2007) 064404. (b) I. Veremchuk, T. Mori, Yu. Prots, W. Schnelle, A. Leithe-Jasper, M. Kohout, Yu. Grin, J. Solid State Chem. 181 (2008) 1983.
16. S. Lassoued, R. Gautier, A. Boutarfaia, J.-F. Halet, J. Organomet. Chem. 695 (2010) 983.
17. J. Nagamatsu, N. Nakagawa, T. Muranaka, Y. Zenitanl, J. Akimitsu, Nature, 410 (2001) 63.
18. N. I. Medvedeva, Yu. E. Medvedeva, A. L. Ivanovskii, Dokl. Phys. Chem., 383, (2002) 75.
19. G. S. Smith, Q. Johnson, P. C. Nordine, Acta Crystallogr. 19 (1965) 668.
20. See for example: (a) F. Edelmann, S. Töfke, U. Behrens, J. Organomet. Chem. 308 (1986) 27. (b) J. J. Schneider, U. Denninger, Z. Anorg. Allg. Chem. 630 (2004)1908. (c) S. Balduzzi, H. Müller-Bunz, M. J. McGlinchey, Chem. Eur. J. 10 (2004) 5398. (d) S. Bendjaballah, S. Kahlal, K. Costuas, E. Bévillon, J.-Y. Saillard, Chem. Eur. J. 12 (2006) 2048. (e) J. Zhang, S. Petoud, Chem. Eur. J. 14 (2008) 1264.
21. J. K. Burdett, S. Lee, T. J. McLarnan, J. Am. Chem. Soc. 107 (1985) 3063.
22. J. K. Burdett, J. Phys. Chem. 87 (1983) 4368.
23. X. Rocquefelte, S. E. Boulfelfel, M. Ben Yahia, J. Bauer, J.-Y. Saillard, J.-F. Halet, Angew. Chem. Int. Ed. 44 (2005) 7542.
24. (a) J. K. Burdett, E. Canadell, T. Hughbanks, J. Am. Chem. Soc. 108 (1986) 3971. (b) J. M. Olivia, M. Llunell, P. Alemany, E. Canadell, J. Solid State Chem. 176 (2003) 375.
25. M. Wörle, R. Nesper, Angew. Chem., Int. Ed. 39 (2000) 2349.
26. (a) F. Diederich, Nature, 369 (1994) 199. (b) S. Szafert, J. A. Gladysz, Chem. Rev. 103 (2003) 4175, ibid.106 (2006) PR1.
27. R. Hoffmann, C. Janiak, C. Kollmar, Macromolecules 24 (1991) 3725.
28. (a) R. Eastmond, T. R. Johnson, D. R. M. Walton, Tetrahedron 28 (1972) 4601. (b) S. Kim, Angew. Chem. Int. Ed. 48 (2009) 7740. (c) W. A. Chalifoux, R. McDonald, M. J. Ferguson, R. R. Tykwinski, Angew. Chem. Int. Ed. 48 (2009) 7910.

29. Q. Zheng, J. C. Bohling, T. B. Peters, A. C. Frisch, F. Hampel, J. A. Gladysz, Chem. Eur. J. 12 (2006) 6486.
30. (a) H. Rosner, W. E. Pickett, Phys. Rev. B 67 (2003) 054104. (b) M. Wörle, R. Nesper, T. K. Chatterji, Z. Anorg. Allg. Chem. 632 (2006) 1737.
31. (a) J. Bauer, J.-F. Halet, J.-Y. Saillard, Coord. Chem. Rev. 178-180 (1998) 723. (b) M. Ben Yahia, J. Roger, X. Rocquefelte, R. Gautier, J. Bauer, R. Guérin, J.-Y. Saillard, J.-F. Halet, J. Solid State Chem. 179 (2006) 2779.
32. (a) V. Babizhetskyy, Hj. Mattausch, A. Simon, R. Gautier, J. Bauer, J.-F. Halet, Z. Anorg. Allg. Chem., 631 (2005) 1041. (b) V. Babizhetskyy, K. Hiebl, Hj. Mattausch, A. Simon, Solid State Sci. 11 (2009) 501.
33. 33. (a) R. Hoffmann, J. Chem. Phys. 39 (1963) 1397. (b) M.-H. Whangbo, R. Hoffmann, R. B. Woodward, Proc. R. Soc. Lond. A 366 (1979) 23. (c) M.-H. Whangbo, R. Hoffmann, J. Am. Chem. Soc. 100 (1978) 6093.
34. J. Ren, W. Liang, M.-H. Whangbo, Crystal and Electronic Structure Analysis Using CAESAR, 1998, http://www.primec.com.
35. (a) O. K. Andersen, Phys. Rev. B 12 (1975) 3060. (b) O. K. Andersen, Europhys. News. 12 (1981) 4. (c) O. K. Andersen, in The Electronic Structure of Complex Systems, P. Phariseau, W. M. Temmerman (Eds.), Plenum Publishing Corporation, New York, 1984. (d) O. K. Andersen, O. Jepsen, Phys. Rev. Lett. 53 (1984) 2571. (e) H. L. Skriver, The LMTO Method, Springer-Verlag, Berlin, 1984. (f) O. K. Andersen, O. Jepsen, M. Sob, in Electronic Band Structure and Its Application, M. Yussouf (Ed.), Springer-Verlag, Berlin, 1986.
36. G. Krier, O. Jepsen, A. Burkhardt, O.K. Andersen, The TB-LMTO-ASA program, version 4.7, Max-Planck-Institut für Festkörperforschung, Stuttgart, Germany.
37. U. von Barth, L. Hedin, J. Phys. C 5 (1972) 1629.
38. P. E. Blöchl, O. Jepsen, O. K. Andersen, Phys. Rev. B 49 (1994) 16223.
39. M. D. Seagall, P. J. D. Lindan, M. J. Probert, C. J.Pickard, P. J. Hasnip, S. J. Clark, M. C. Payne, Condens. Matter. 14 (2002) 2717.
40. P. E. Blöchl, Phys. Rev. B 50 (1994) 17953.
41. J. P. Perdew, S. Burke, M. Ernzerhof, Phys. Rev. Lett. 77 (1996) 3865.

INVESTIGATION OF HARD BORON RICH SOLIDS: OSMIUM DIBORIDE AND β-RHOMBOHEDRAL BORON

M. HEBBACHE[1*], D. ŽIVKOVIĆ[2]
[1]*Laboratoire Matériaux et Phénomènes Quantiques (UMR 7162), Université Denis Diderot - Paris 7, 10 rue Alice Domon et Lonie Duquet, 75205 Paris Cedex 13, France*
[2]*Department of Metallurgy, University of Belgrade, VJ12, 19210 Bor, Serbia*

Abstract Recently, we succeeded in synthesizing three osmium borides, i.e., $OsB_{1.1}$, Os_2B_3 and OsB_2. Up to date, almost nothing is known about the physical properties of these materials. Microhardness measurements show that OsB_2 is extremely hard. Ab initio calculations show that it is due to formation of covalent bonds between boron atoms. OsB_2 is also a low compressibility material. It can be used for hard coatings. The β-rhombohedral polymorph of boron is the second hardest elemental crystal ($H \approx 33$ GPa). It is also very light and a p-type semiconductor. In early 1970s, it has been shown that the doping of boron with 3d transition elements enhances its hardness by about 25%. We predict that, in general, heavily doped samples MB_x, with $x \leq 31$ or equivalently a dopant concentration larger than 3.2 at.%, should be ultrahard, i.e., $H > 43$ GPa. The relevant dopants M are Al, Cu, Sc, Mn, Mg and Li. In addition to these properties, boron-rich materials have a very low volatility, a high chemical inertness and high melting point. They are suitable for applications under extreme conditions and thermoelectric equipment.

Keywords: boron, osmium diborides, hard materials, lightweight materials, ab initio calculations

1. Introduction

The search for superhard materials has become a real challenge for the materials science community because they have numerous industrial applications. They are used in mechanical, electronic, nuclear and biomedical

* M. Hebbache Laboratoire Matériaux et Phénomènes Quantiques (UMR 7162), Université Denis Diderot - Paris 7, 10 rue Alice Domon et Lonie Duquet, 75205 Paris Cedex 13, France, e-mail: mhe@univ-paris-diderot.fr

N. Orlovskaya and M. Lugovy (eds.), *Boron Rich Solids: Sensors, Ultra High Temperature Ceramics, Thermoelectrics, Armor*, DOI 10.1007/978-90-481-9818-4_8,

industries. Some recent applications are also in oil drilling and body armor. The hardness is measured by loading a diamond indenter on a flat surface of the material or roughly estimated by a scratch test. It is defined as the material resistance to elastic and plastic deformations. The latter is due to the movement of dislocations under shear stress. Diamond which is a polymorph of carbon, is the hardest material (Hv ≈ 90 GPa) and cubic boron nitride (c)BN the second (Hv ≈ 65 GPa). Diamond and (c)BN are difficult to synthesize. Although there are several exceptions, the hardness of carbides, nitrides and borides is in the range 20–35 GPa while that of semiconductors is less than 20 GPa. Metals are soft.

Lightweight materials, which include aluminium, titanium, nickel, magnesium alloys, polymer, metal and ceramic matrix composites, are the subject of many research programmes. They have potential applications in most industries. For example, there are about half billion motor vehicles worldwide, without counting the other modes of mass transit. The reduction of the weight of transportation vehicles leads to a significant reduction of fuel consumption, greenhouse gas emissions and air pollution. However, the demand of light materials goes beyond these needs. It is growing in many other sectors, in particular in space and defense industries. Nevertheless, lightweight materials are more expensive than iron and steel. The main objective of this research is the decrease of the ratio weight.cost/properties.

With a Vickers hardness equal to about 33 GPa, the β-rhombohedral polymorph of boron is the second hardest elemental crystal [1]. With a mass density equal to 2.3, it is lighter than aluminium (2.7). It has other remarkable properties [2]. It is a p-type covalent semiconductor with an energy band gap of about 1.56 eV, which is higher than that of silicon (1.12) and germanium (0.66). It can be converted to a n-type by doping with atoms like V, Cr, Fe and Ni. It has a very low volatility, a high chemical inertness and melting point (>2,450°C). In what follows, the term boron will always refer to this polymorph. It is probably not possible to harden diamond but it is possible to do so for boron by doping, i.e., by incorporating foreign atoms in its structure. These impurities impede the mobility of dislocations and consequently impart extra hardness to the material. The solid solution hardening theories proposed independently by Friedel, Labusch, Fleischer, Mott-Nabarro, based on different types of dislocation-impurity interaction, are reviewed in the book of Haasen [3]. This hardening depends on the dopant concentration, the relative difference in size, modulus and chemical valency between the foreign and the host atoms. Our goal is to predict the most appropriate dopants for boron. We consider only the solid solutions of boron which have been already synthesized by different groups.

It has been found recently that osmium, which is the heaviest elemental crystal, is less compressible than diamond [4]. Low compressibility materials

are often superhard. It is expected that binary compounds of osmium with light elements, like boron, could be superhard [5]. We recently confirmed the composition and the structure of three borides: $OsB_{1.1}$, Os_2B_3 and OsB_2 [6, 7].

In the present work, we give an extensive study of OsB_2 which includes hardness measurements and ab-initio calculation of its physical properties. Electronic, elastic, plastic and mechanical properties of OsB_2 are investigated in order to get a deeper understanding of bonding, structural stability and hardness. The two other borides are soft and will not be studied here. Our computational investigation is carried out within the density functional theory [8]. We used WIEN2k package [9]. This code uses the full-potential linearized augmented-plane-wave (FP-LAPW). The 5s, 6p and 4f states of osmium were treated as semi-core states and the 1s state of carbon and boron as core states. A value of 0.2 μRy of the energy difference between two successive iterations is used as a convergence criterion.

2. Osmium Diboride

2.1. SYNTHESIS, STRUCTURE AND HARDNESS

The synthesis of osmium borides is not an easy task. Powder mixtures of high purity (>99.5%) osmium and boron were pressed into pellets (mass of 2 g) and then arc-melted under purified (99.9999%) argon atmosphere in a water-cooled crucible. To insure a sufficient homogeneity, samples were cut and melted for several times. Figure 1 shows the complete phase diagram of the binary system Os-B [6, 7]. Metallography was used for the determination of phases and their stability regions.

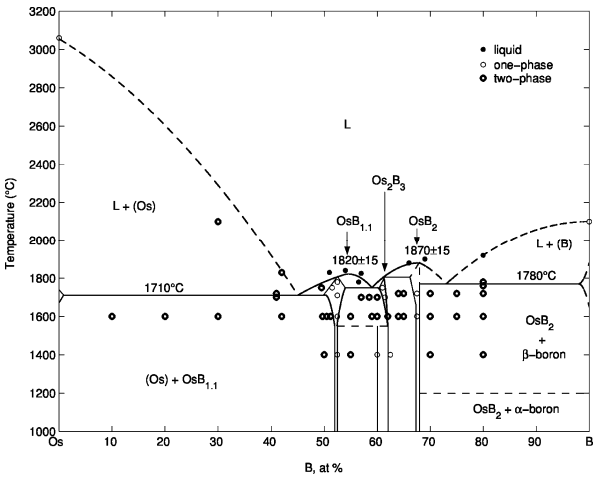

Figure 1. Phase diagram of Os-B system, with $OsB_{1.1}$ (hex.), Os_2B_3 (hex., high and low temperature modification) and OsB_2 phases, respectively.

OsB_2 crystallizes in the RuB_2-type structure with an orthorhombic cell containing two chemical formulae [10]. The unit cell and the structure of the metal and boron layers are shown in Fig. 2. The space group number is 59. The optimized lattice constants ***a***, ***b*** and ***c*** are 4.652, 2.852 and 4.048 Å, respectively. The two osmium atoms occupy the sites (a): (1/4, 1/4, z) and (3/4, 3/4, z) with z = 0.1535 while the four boron atoms occupy the sites (f): (x, 1/4, z), (x + 1/2, 1/4, z), (x, 3/4, z) and (x + 1/2, 3/4, z) with x = 0.058 and z = 0.632. Each boron atom is surrounded by three boron atoms and four metal neighbors while each osmium atom has eight boron atom neighbors. All atoms have a fixed y-coordinate, 1/4 or 3/4, forming dense atomic planes along the ***b***-parameter. Along the ***c***-direction, a description of this structure can be based on atomic layers.

In comparison with the AlB_2 structure, OsB_2 exhibits a deformed two-dimensional network of boron atoms. The latter form corrugated hexagons with four *B–B–B* angles at 106.84° and two at 99.97° instead of six angles at 120°. The boron layer lies between two planar metal layers which are offset.

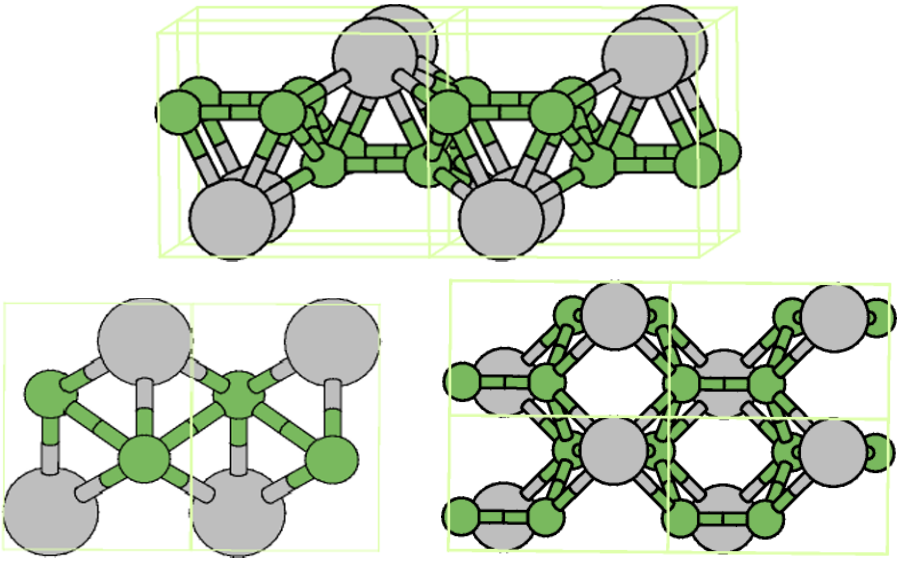

Figure 2. Top: Crystal structure of OsB_2 showing 2 × 2 × 1 unit cells. There are two formula per unit cell. The vertical and the horizontal directions are along ***c***- and ***a***-parameters, respectively. Osmium and boron atoms are represented by large (grey) and small (green) circles, respectively. The corrugated boron layer is between two planar metal layers which are offset. Projection along ***b***-axis can be readily drawn from this perspective. *Bottom-left*: projection of the OsB_2 structure along ***a***-axis. The horizontal direction is along ***b***-parameter. All atoms have a fixed position y = 1/4 or 3/4; forming parallel atomic layers along ***b***-parameter. *Bottom-right*: projection of the OsB_2 structure along ***c***-axis. The vertical and the horizontal directions are along ***b***- and ***a***-parameters, respectively. Boron atoms are at the vertices of corrugated hexagons.

It is well known that transition metal borides exhibit a high hardness [5]. Their Vickers hardness lies in the range of 2,000–3,000 kg/mm^2. We have performed microhardness measurements by means of the PMT-3 tester. We found that the Vickers hardness of OsB_2 is about 3,600 kg/mm^2 for loads in the range of 60–80 g (see Fig. 3). For higher loads, the hardness decreases significantly, e.g., 3,000 kg/mm^2 at 100 g. A hardness greater than 3,000 kg/mm^2 has been quoted in a recent patent [11]. At more higher loads, the hardness depends strongly on crack formation. OsB_2 is then among the hardest transition-metal compounds [5].

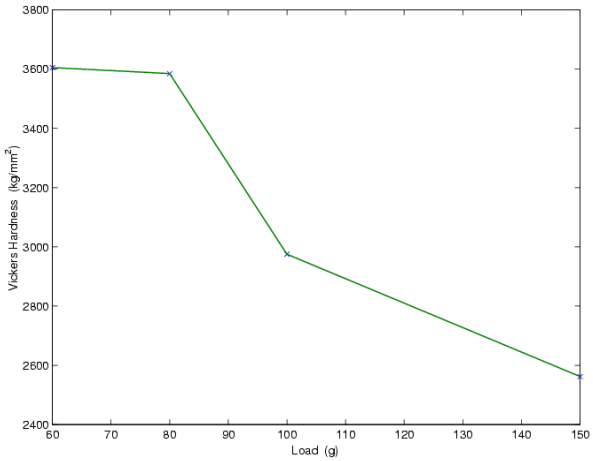

Figure 3. Load dependence of the Vickers hardness of OsB_2.

2.2. ELECTRONIC PROPERTIES

Electronic properties are characterized by energy bands, density of states (DOS) and valence electronic charge density (VECD). The band structure along various directions connecting high-symmetry points of Brillouin zones are shown in Fig. 4. The valence and conduction bands overlap each other. OsB_2 has clearly a metallic character.

The DOS and the integrated DOS of OsB_2 are displayed in Fig. 5. There is a large valence electron concentration, i.e., 28 valence electrons per unit cell. The total DOS is composed of a large *d*-component of Os and small *sp*-components of Os and B. The contribution of the *f*-electrons of Os is negligible. The bonding energy is mainly due to the hybrid state of 5*d* and *sp*-boron orbitals. The Fermi level lies in a DOS minimum. This confers a relatively high stability to the orthorhombic structure of OsB_2.

The charge density profiles in two different planes where the bondings B–B are present, are shown in Fig. 6. On the left hand side of the figure, the VECD is shown in a cross-section of either plane y = 1/4 or 3/4. In these

y-planes, the boron atoms are covalently bonded. The inter-atomic B–B distance, 1.798 Å, is the shortest one. In the atomic plane which links the planes y = 1/4 and 3/4 (see Fig. 2), the inter-atomic B-B distance is 1.874 Å. The boron atoms are less bonded in this incline as shown on the right hand side of Fig. 6. The inter-atomic distances between boron and metal atoms are larger than the B–B inter-atomic distances, i.e., 2.147 and 2.308 Å in y-planes and 2.215 Å in the incline. A significant amount of valence electron charge lies between boron and osmium atoms. The Os-B bonds are also due

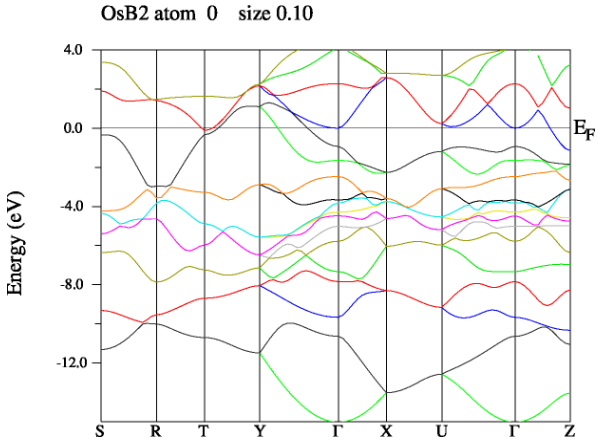

Figure 4. Band structure of OsB_2 along high symmetry directions. The zero of the energy scale corresponds to the Fermi energy E_F.

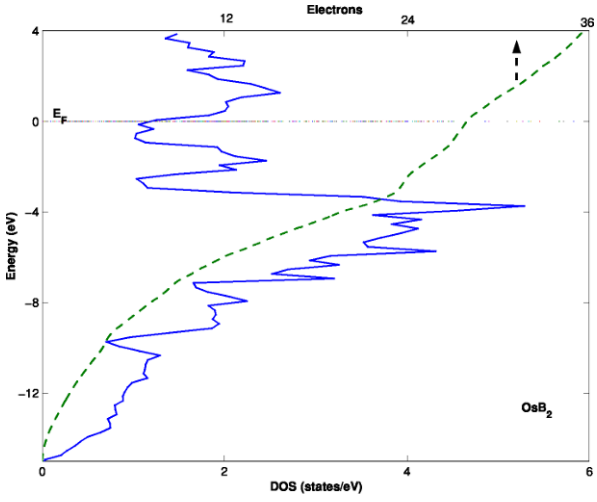

Figure 5. Total density of states of OsB_2 (*solid curve*) and integrated density of states (*dashed curve*).

to the delocalization of metal electrons. In short, the addition of boron leads to the increase of valence electron concentration and to formation of covalent bonds which increase the hardness.

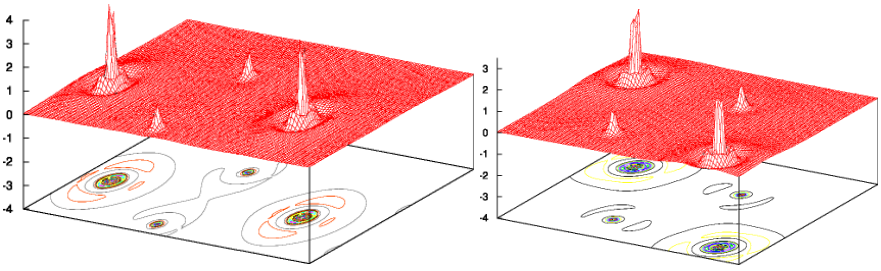

Figure 6. Valence electron charge density (VECD), in atomic units, and contour plots. Large peaks are due to electrons localized at atomic sites. *Left*: VECD in the dense plane y = 1/4 or 3/4 (see Fig. 2). *Right*: VECD in the incline which links the planes y = 1/4 and 3/4. Interatomic distances are given in the text.

2.3. ELASTIC AND PLASTIC PROPERTIES

The hardness is correlated to bulk and shear moduli, which express the material resistance to volume and shape changes, respectively. These coefficients can be expressed by means of elastic constants C_{IJ}. The nine independent elastic constants of OsB_2 can be calculated by imposing small deformations of the unit cell and polynomial fits to the total energy. They are given in Table 1 with that of the two hardest materials, i.e., diamond and cubic boron nitride (c)BN. The value of C_{33}, 875 GPa, is larger than that of c-BN, and almost comparable to that of diamond, 1,079 GPa. This is qualitatively in agreement with the hardness measurements because the elastic constant C_{33} expresses mainly the material resistance to the relative change of the ***c***-parameter. The lower values of C_{11} and C_{22} suggest that the hardness will be reduced by one third along ***a*** and ***b***-axes, i.e., 2,400 kg/mm^2. A strong anisotropy in hardness has also been observed in TiB_2 and is usually taken into account in applications like coating [5]. The bulk modulus B can be deduced from the values of C_{IJ} (see Table 1). We found that B is equal to 342 GPa. Osmium diboride is then a low compressibility material.

For metallic materials, the hardness is mainly associated with the ease to generate and move dislocations by indentation. The shape of the indenter and the orientation of the primary slip systems are of major importance. An orthorhombic crystal possesses only one slip plane, here y-plane, and two slip directions, x and y-axes [14]. These two primary slip systems are

associated with the shear moduli C_{66} and C_{44}. The theoretical value of C_{44} cannot be obtained with accuracy because the orthorhombic lattice of OsB_2 is unstable toward the shear strain. The calculated value of C_{66} is low (see Table 1). This is in agreement with the charge density profiles and hardness measurements. The chemical bonds in the incline which links the y-planes, 1/4 and 3/4, are more sensitive to shear forces than to compressive forces.

TABLE 1. Brugger-type elastic constants and bulk modulus, in unit of GPa, of osmium diboride and that of the two hardest materials, i.e., diamond and cubic boron nitride

Material	C_{11}	C_{22}	C_{33}	C_{12}	C_{13}	C_{23}	C_{44}	C_{55}	C_{66}	B	Ref.
OsB_2 342[a]	611		597	875	204		157	133	-	279	137
(c)BN 400[b]				820				190			480
diamond 442[c]				1076				125			577

[a] This work
[b] Grimsditch et al. [12]
[c] Grimsditch and Ramdas [13]

Osmium diboride is also a superconductor below 2.1 K. Using first-principles calculations, the authors investigated the topology of its Fermi surface [15]. Related physical quantities have also been calculated. The theoretical results were used to predict the frequencies of the Shubnikov-de Haas quantum oscillations. Comparison with the recent measurements of the magneto-resistance oscillations in OsB_2 has been made.

3. β-Rhombohedral Boron

The rhombohedral Bravais lattice of boron with the space group $R\bar{3}m$ and the lattice constants **a** = 10.12 Å and α = 65.28° has been completely described in the literature [16]. The diagonal of the rhombohedral cell coincides with the **c**-axis of the hexagonal cell with lattice constants **a** = 10.95 Å and **c** = 23.73 Å. Before tackling the doping of boron, we give below a short description of its structure which will later facilitate the discussion (see Fig. 7). The framework consists of a spatial arrangement of B_{12} icosahedra which are distorted as a consequence of a Jahn–Teller effect. The idealized structure has 105 atoms which are divided up into 15 non-equivalent atomic sites, noted B(1)–B(15). The icosahedral atoms are each bonded to five neighbors by three-center bonds and the icosahedra are connected to each other by two-center bonds. Because of their unequal

distortion, three types of icosahedra can be distinguished. B(5, 6) atoms form the icosahedra **A** while B(1, 2, 7, 9) atoms form the icosahedra **B**. Icosahedra **C** is composed of B(3, 4, 8, 10, 11, 12, 13, 14) atoms. Three boron icosahedra **C** form a B_{28} cluster by sharing triangular faces (see F ig. 7). Icosahedra of type **A**, **B** and **C** present four, nine and seventeen different intra-icosahedral bond lengths, respectively. The averaged intra- and inter-icosahedral bond lengths are presented in Table 2.

One presentation of the structure of boron places the icosahedra **A** at the vertices of the rhombohedral unit cell, the icosahedra **B** at the edge-centers and a B_{28}–B(15)–B_{28} chain along the cell diagonal. The B(15) atom is located at the center of the cell. In the real structure of boron, the occupancy of the site B(13) is partial. Delocalized B(13) boron atoms end up mainly in the interstitial boron sites B(16), also labeled G in the literature. These structural defects tend to compensate the electron-deficit of boron.

Doped samples can be prepared by arc-melting a mixture of high-purity boron and some impurity or by a solid state diffusion of the impurity into boron. In the past, different atoms have been dissolved in boron. Most of the transition metals and some non-transitions metals (Al, Si, Ge, As, Se) form solid solutions with boron. X-ray direction studies of doped boron revealed eight interstitial sites and two substitutional positions B(1) and B(4). The major interstices are labelled A1, D, E and G (see Table 3). The site A1 is along the diagonal of the rhombohedral cell. It is surrounded by twelve boron neighbours. The six D sites surround the central boron atom B(15). The position E is also located along the cell diagonal, between the A1 site and B_{28} unit. D and E sites can have up to 15 boron neighbours while the G hole has eight boron neighbours. Some tendencies are observed

TABLE 2. Averaged intra- and inter-icosahedral bond lengths in undoped boron

Bond	d (Å)
Intra-icosahedral	
A–A	1.751
B–B	1.840
C–C	1.808
Inter-icosahedral	
B(1)–B(1)	1.880
B(5)–B(7)	1.729
B(2)–B(3)	1.724
B(4)–B(4)	1.678
B(6)–B(8)	1.623
B(9)–B(10)	1.690
B(15)–B(13)	1.686

in the occupancy of the different holes. For example, small atoms (r < 150 pm) tend to occupy A1 holes while large atoms are found more frequently to occupy the E hole. The D hole is occupied in all solutions with the exception of that of Si while the G hole is of suitable size for a boron atom.

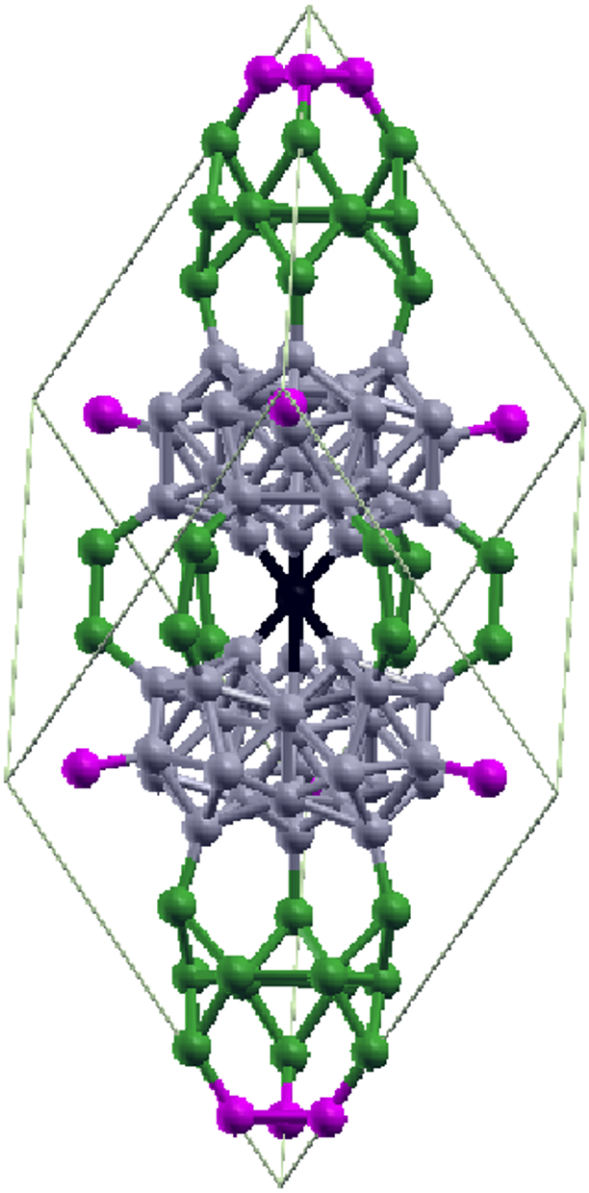

Figure 7. Crystal structure of β-rh boron. Atoms colored gray form a B_{28}–B(15)–B_{28} chain along the diagonal of the rhombohedral cell. The B(15) atom, in black, is at the center of the unit cell. A B_{28} cluster consists of three icosahedra of type **C** sharing triangular faces. Atoms in pink and green are part of the icosahedra of type **A** and **B** respectively.

3.1. SOLID SOLUTION HARDENING

The guest atoms influence the properties of boron. However, only a few works have been devoted to the study of these modifications. Carlsson and Lundstrom [17] investigated the infuence of nine 3d-transition metals (Z = 21–29) on the Vickers hardness of boron. They observed an enhancement of the hardness of boron. The largest hardness, 41.3 GPa, which corresponds to an increase of about 25%, were obtained with Sc and Mn as dopants. The hardening of boron by doping was confirrmed later by different groups [18].

Unfortunately, these authors did not look for the exact compositions of the solid solutions, with the exception of $CrB_{\sim 41}$. Carlsson and Lundstrom also pointed out a correlation between the hardness and the unit cell volume (see Fig. 8). In solid solution hardening theories [3], based on different types of dislocation–impurity interaction, this size effect is usually represented by the linear misfit parameter $\varepsilon = (1 - r_A/r_B)$ where r_A and r_B are the atomic, ionic or Seitz radii of the dopant and host atoms respectively. It has been shown that ε can be related to the relative change of the unit cell volume per at.% solute Ω: $\varepsilon = (\Omega + 1)^{1/3} - 1$ [18].

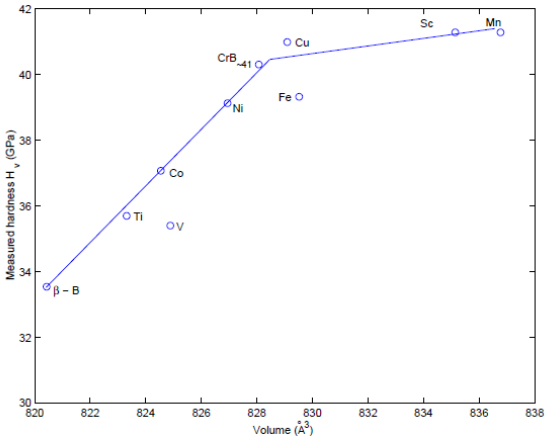

Figure 8. Vickers hardness (50 g load) of doped boron MB_x (M = V, Ti, Co, Ni, Fe, Cr, Cu, Sc and Mn) vs unit cell volume. The atomic fraction x is unknown except for Cr-doped boron ($x \approx 41$). The lines are just guides for the eyes.

In order to calculate the hardness of boron rich solids [20], we considered the model of Gao et al. [21] which defines the hardness of a multibond crystal as the geometrical average of the values of hardness of all bonds:

$$H_v = \left(\prod_{\mu} (H_v^{\mu})^{n^{\mu}}\right)^{1/\sum n^{\mu}} \qquad (1)$$

where

$$H_v\ (\mathrm{GPa}) = 350\,(N_e^{\mu})^{2/3}\, e^{-1.191\ f_i^{\mu}} / (d^{\mu})^{2.5}$$

is the Vickers hardness of the μ-type bond, n^{μ} the number of bonds of type μ in the crystal and d^{μ} the bond length in Å. N_e^{μ} is the number of valence electrons of type μper unit volume and f_i^{μ} the ionicity of the chemical bond. This formula requires only a few parameters for estimating the hardness of a material crystallizing in a simple structure. Nevertheless, the structure of boron is very complex and the counting of the different bonds is tedious. In undoped boron, there are about 322 bonds and 41 inter-atomic distances. The existence of partially ionic three-center bonds and the partial occupancy of some sites add even more difficulties to the use of Eq. (1).

We first calculated the hardness of undoped boron. To this end, we considered the accurate refinement of the structure of boron realized by Callmer [22]. Boron atoms are six-coordinated, except for atoms B(11, 12, 13) which are eight-coordinated and B(14) which is nine-coordinated. For computing Eq. (1), the 41 different bond lengths have been considered. It has been shown that the three-center bonds in the distorted B_{12} icosahedra are not purely covalent [23]. We considered the same values of ionicity of B–B bonds than in the polymorph $\tilde{\alpha}$boron where it is easier to calculate the charge density of each bond by means of a density functional theory based code [23]. The variety of boron is also an arrangement of B_{12} units placed at the vertices of a rhombohedral unit cell with space group $R\bar{3}m$. We found that the hardness of boron is equal to about 32 GPa while the experimental value is 33.5 GPa [1]. The accuracy of calculations is encouraging. Next, we calculated the hardness of doped boron. Each dopant can form several chemical bonds with its boron neighbors. One expects a hardening of boron. Eq. (1) takes into account some effects of doping: the volume expansion, the inter-atomic distances changes, the increase of the chemical bonds number and the electronegativity difference variations. The shear modulus misfit is not considered. First, we only considered the dopants for which measured bond lengths d are available: Ni, Al, V, Fe and Cr. The composition of these boron-rich materials is given in Table 3. In these boron solid solutions, the E hole is empty. The volume of the unit cell increases as the interstitial content increases, without symmetry change. The changes in B–B distances range from 0 to 0.64 Å. Fewer than 12 B–B distances are changed by more than 0.01 Å, with the exception of the Al–B solid solution for which the number of changes is 17. The largest changes, >0.40 A, occur for the B(1)–B(1), B(5)–B(5), B(1)–B(7), B(13)–B(14) and B(13)–B(15) distances. In our calculations, we considered all known valences of each dopant and two different ionicity scales [24, 25].

The obtained values of the hardness were then averaged. For most samples, the chemical valency misfit leads to a hardness shift smaller than 1 GPa. The calculated hardness of doped samples by means of Eq. (1), H_V^1, is given in Table 3. We note that the hardness of boron increases as the dopant concentration c increases.

Due to the lack of X-ray diffraction measurements, we could not apply Eq. (1) to the other known solid solutions. We then followed a different approach. In early articles, the hardening of a doped sample is expressed as follows [3]:

$$H_V(c) = H_V(0) + k\varepsilon^{\alpha} c^{\beta} \qquad (2)$$

where k, α and β are constants and c the dopant concentration. We again omit the shear modulus misfit $\eta = (1/G)(dG/dc)$. To take this effect into account, one should replace ε by :

$$(\eta'^2 + \gamma^2 \varepsilon^2)^{1/2} \quad \text{with} \quad \eta' = \eta/(1 + \tfrac{1}{2}|\eta|)$$

The parameter γ depends on the type of dislocation involved in the interaction. Using the experimental values of c and ε, the hardness values H_V^1 were fitted with Eq. (2). A good fit is obtained with $\alpha \approx 0$ et $\beta \approx 6/5$ and k = 4.71 GPa. The value of α valid the assumption used by Gilman [26] in his theory of solution strengthening of alkali halide crystals. He assumed that ε is equal to the unity and expressed the hardening coefficient k in terms of the electron charge, the static dielectric constant and the lattice constant of the host crystal. Equation (2) was then used to predict the hardness of several solid solutions: CuB_{28}, ScB_{28}, MnB_{23}, MgB_{20} and LiB_{13}. Figure 9 shows that H_V^2 increases with increasing dopant concentration. Table 3 shows that the theoretical values H_V^1 and H_V^2 of CrB_{41} are underestimated by about 10% with respect to the experimental value. This suggests that the predicted hardness values appearing in the lower part of the Table 3 are not particularly overestimated. Clearly, the solid solutions MB_x with $x < 31$ or equivalently a dopant concentration larger than 3.2 at.%, are expected to be very hard, i.e., $H_V > 43$ GPa. The dopants which could harden boron signicantly are the following: Al, Cu, Sc, Mn, Mg and Li. We note that the hardness of LiB_{13} is close to that of (c)BN which is the second hardest material. We hope that these predictions will motivate some experiments. Because of potential applications, the synthesis of one of those hard boron rich solids is patentable.

TABLE 3. Percentage of occupancy of the interstitial sites A1(0, 0, 0.14), D(0.2, 0.4, 0.17), E(0, 0, 0.23) and G[=B16](0.06, 0.11, 0.12) in doped boron. Their approximate hexagonal coordinates are given in parentheses and their symmetry multiplicities in square brackets (see below). The six B(13) sites are partially occupied by boron atoms. H_V^1 and H_V^2 are, respectively, the Vickers hardnesses calculated by means of Eqs. (1) and (2), and H_V^{exp} the data. The hardness is expressed in GPa while the dopant concentration c is in at.%

Material	A1[2]	D[6]	E[2]	G[6]	B(13)[6]	c	H_V^1	H_V^2	H_V^{exp}	Ref.
B_{105}	0.0	0.0	0.0	24.8	73.4	0.00	32	32	33.5	(a)
VB_{165}	31.6	0.0	0.0	14.7	76.3	0.60	32	32		(b)
VB_{65}	64.0	5.3	0.0	0.0	74.6	1.54	33	34		(b)
$NiB_{48.5}$	50.7	18.5	0.0	0.0	72.6	2.06	34	37		(c)
$FeB_{48.5}$	44.7	9.0	0.0	18.0	67.1	2.06	34	38		(d)
CrB_{41}	71.9	18.0	0.0	0.0	71.7	2.48	34	38	40.3	(e)
AlB_{31}	85.7	26.1	0.0	0.0	68.2	3.18	35	43		(f)
CuB_{28}	6.1	43.1	50.5	20.9	61.1	3.58	–	46		(g)
ScB_{28}	0.0	31.4	72.7	0.0	61.3	3.58	–	46		(h)
MnB_{23}	25.6	43.1	66.2	0.0	65.0	4.30	–	50		(g)
MgB_{20}	0.0	49.0	88.0	0.0	59.0	5.05	–	55		(i)
LiB_{13} 0.0	100	100	10.0	64.0	7.73		–	74		(j)

(a) Callmer [22]; (b) Garbauskas [27]; (c) Lundstrom [28]; (d) Callmer [29]; (e) Andersson and Lundstrom [30]; (f) Higashi [31]; (g) Andersson [32]; (h) Callmer [33]; (i) Brutti [34]; (j) Kobayashi [35]

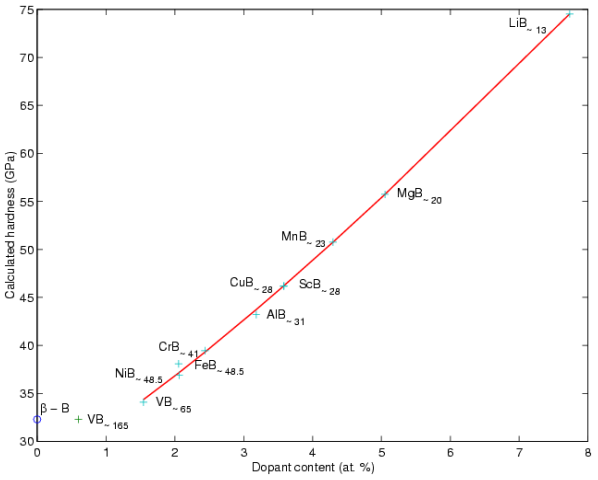

Figure 9. Variation of the hardness of the boron solid solutions with respect to the impurity concentration.

4. Conclusion

We recently synthesized three osmium borides, i.e., $OsB_{1.1}$, Os_2B_3 and OsB_2. We found that OsB_2 is extremely hard. Ab-initio calculations show

that it is also a low compressibility material. With respect to the elemental crystal, the addition of boron atoms decreases the compressibility by 10–20% while the hardness is multiplied by a factor of 5–9. This material can be used as hard coating.

We applied two different approaches to calculate the hardness of several solid solutions of boron. We predict that some of them could have a hardness exceeding 43 GPa. Moreover, these icosahedral boron rich solids are very light, possess high melting points and are semiconductors. They are suitable for applications under extreme conditions: high temperature, high pressure or stress, high-energy neutron or charged particle irradiation, high resistance to chemical attack, etc. They are also important for high-efficiency thermoelectric energy conversion.

References

1. Holcombe CE, Smith DD, Lore JD, Duerksen WK, Carpenter DA (1973) Physical-Chemical Properties Of Beta-Rhombohedral Boron. High Temp Sci 5:349−357
2. Werheit H (1998) Numerical Data and Fundamental Relationships in Science and Technology, edited by Madelung O, Vol Group III 41C. Landolt-Bornstein, Springer, Berlin.
3. Haasen P (1983) Physical Metallurgy, edited by Cahn RW and Haasen P. North-Holland Physics, Amsterdam
4. Cynn H, Klepeis JE, Yoo CS, Young DA (2002) Osmium has the lowest experimentally determined compressibility. Phys Rev Lett 88:135701
5. Holleck H (1986) Material selection for hard coatings. J Vac Sci Technol A 4:2661−2669
6. Stuparević L, Živković D (2004) Phase diagram investigation and thermodynamic study of Os-B system. J Therm Analys Calor 76:975−983
7. Hebbache M, Stuparević L, Živković D (2006) A new superhard material : Osmium diboride OsB_2. Solid State Comm 139:227-231
8. Kohn W, Sham LJ (1965) Self-Consistent equations including exchange and correlation effects. Phys Rev 140 A:1133−1138
9. Blaha P, Schwarz S, Madsen GKH, Kvasnicka D, Luitz J (2001) Computer Code WIEN2k. VUT, Vienna
10. Aronsson B (1963) The crystal structure of RuB_2, OsB_2, and $IrB_{1.35}$ and some general comments on the crystal chemistry of borides in the composition range MeB−MeB_3. Acta Chem Scand 17:2036−2050
11. Kaner RB, Gilman JJ (2002) US Patent UCLA No. 2002-244; Kaner RB, Gilman JJ, Tolbert SH (2005) Designing Superhard Materials. Science 308:1268−1269
12. Grimsditch M, Zouboulis ES, Polian A (1994) Elastic constants of boron nitride. J Appl Phys 76:832−834
13. Grimsditch M, Ramdas AK (1975) Brillouin scattering in diamond. Phys Rev B 11:3139−3148
14. M. Hebbache M (2000) Shear modulus and hardness of crystals: Density-functional calculations. Solid State Commun 113:427−432
15. Hebbache (2009) The Fermi surface of a superconductor : OsB_2. Phys Stat Sol (RRL) 3 :163−165

16. Donohue J (1974) The Structures of The Elements. Krieger Publishing Compagny, Florida
17. Carlsson JO, Lundstrom T (1970) The Solution hardening of β-Rhombohedral boron, J Less Common Met 22:317−320
18. Brodhag, C, Thevenot F, Viala JC (1978) Hardness Study Of β -Rhombohedral Boron. Ann Chim Fr 3:23−26; Thevenot F, Viala JC (1979) Obtention de bore pur sous forme massive ou en couches minces. Caractérisation physique du bore. Les couches minces 195:35−45 (in french); Golikova OA, Amandzhanov N, Kazanin MM, Klimashin GM, Kutasov VV (1990) Electrical activity of impurities in β-Rhombohedral boron. Phys Stat Sol a, 121:579−586
19. King HW (1966) Quantitative size-factors for metallic solid solutions. J Mater Sci 1:79−90; King HW (1971) Quantitative size-factors for interstitial solid solutions. J. Mater Sci 6:1157−1167
20. Hebbache M (2009). The search for superhard materials : doped boron. Euro Phys Lett 87:16001
21. Gao M, He JL, Wu ED, Liu SM, Yu DL, Li DC, Zhang SY, Tian YJ (2003) Hardness of covalent crystals. Phys Rev Lett 91:015502
22. Callmer B (1977) An accurate refinement of the β-rhombohedral boron structure. Acta Crystallogr B33:1951−1954
23. He J, Wu E, Wang H, Liu R, Tian Y (2005) Ionicities of boron-boron bonds in B_{12} icosahedra. Phys Rev Lett 94:015504
24. Levine BF (1973) Bond susceptibilities and ionicities in complex crystal structures. J. Chem. Phys., 59:1463−1486
25. Šimůnek A, Vackář J (2006) Hardness of covalent and ionic crystals**:** first-principle calculations. Phys Rev Lett 96:085501
26. Gilman JJ (1974) Theory of solution strengthening of alkali halide crystals. J Appl Phys 45:508−509
27. Garbauskas MF, Kasper JS, Slack GA (1986). The incorporation of vanadium in β-rhombohedral boron as determined by single-crystal diffractometry. J Solid State Chem 63:424−430
28. Lundstrom T, Tergenius LE (1984) A single-crystal investigation of the solid solution $NiB_{48.5}$ of β-rhombohedral boron type structure. Z. Kristallogr., 167:235−246
29. Callmer B, Lundstrom T (1976) A single-crystal diffractometry investigation of iron in β-rhombohedral boron . J Solid State Chem 17:165−170
30. Andersson S, Lundstrom T (1970) The solubility of chromium in β-rhombohedral boron as determined in CrB_{41} by single-crystal diffractometry. J Solid State Chem 2:603−611
31. Higashi I, Iwasaki H (1989) Single-crystal X-ray diffraction study of AlB_{31} of the β-rhombohedral boron structure. Solid State Chem 82:230−238
32. Andersson S, Callmer B (1974) The solubilities of copper and manganese in β-rhombohedral boron as determined in CuB_{28} and MnB_{23} by single-crystal diffractometry. J Solid State Chem 10:219−230
33. Callmer B (1978) A single-crystal diffractometry investigation of scandium in β-rhombohedral boron. J Solid State Chem 23:391−398
34. Brutti S, Colapietro M, Balducci G, Barba L, Manfrineti P, Palenzona A (2002) Synchrotron powder diffraction Rietveld refinement of MgB_{20} crystal structure . Intermetallics 1:811−817
35. Kobayashi M, Higashi I, Matsuda H, Kimura K (1995) Rietveld analysis of LiB13 with β-rhombohedral boron structure. J Alloys Comp 221:120−124

ELASTIC AND VIBRATION PROPERTIES OF BORON–CARBON ULTRA HARD MATERIALS

J. E. LOWTHER*
DST – NRF Centre of Excellence in Strong Materials and School of Physics, University of the Witwatersrand, Johannesburg, South Africa.

Abstract Various Boron Carbon diamond like phases are examined using ab-initio computational modeling. Trends show that compressibility of B–C diamond like structures remains good but Shear and Young moduli rapidly decrease with increasing B concentration. Calculated vibration spectra are also reported and in light of these some suggestions are made concerning recent reports of the synthesis of these materials.

Keywords: hard materials; diamond; borides; computer modeling

1. Introduction

Boron, carbon and nitrogen form the atomic basis for the hardest materials known to date. Diamond is the hardest known material with cubic boron nitride (c-BN) second – both materials having a simple cubic structure [1, 2]. Recently reports of other hard materials [3–7] with an apparent diamond like structure have appeared and these materials present enormous potential for industrial application. Such materials also have fundamental significance as they contain substantial concentrations of boron thus making very lightweight superhard materials that are lighter than even diamond.

As point defect boron is a well know impurity in diamond that makes the material semiconducting. It gives rise to a defect level lying at 0.37 eV above the valence band edge and is responsible for making the material p-type [8]. Infra red optical spectroscopy has now revealed that the ground state of the bound hole of the boron acceptor is pinned to the valence band [9, 10]. Under high doping concentrations of boron in diamond, various complexes exist and some of these also form shallow acceptor states but with energy levels far different to that of the simple substitutional center

* J.E. Lowther, DST – NRF Centre of Excellence in Strong Materials and School of Physics, University of the Witwatersrand, Johannesburg, South Africa, e-mail: John.Lowther@wits.ac.za

N. Orlovskaya and M. Lugovy (eds.), *Boron Rich Solids: Sensors, Ultra High Temperature Ceramics, Thermoelectrics, Armor*, DOI 10.1007/978-90-481-9818-4_9,

[11] These centers give rise to a complicated electrical conductivity [12, 13] and, if diamond is subject to extreme conditions such as pressure, possibly even to superconductivity [14]. The additional states of boron also give rise to defect energy levels that lie above the valence band and some of these have been observed to give a hopping mechanism for the electrical conductivity [11–13] and thought to be associated with different forms of B-related centers [12]. At high concentrations of boron in diamond a metal insulation transition occurs [13] and then with even higher boron concentrations superconductivity appears [14–16] that is also tentatively associated with Boron pairs [13]. The vibration properties of boron in diamond have revealed that a 500 cm^{-1} band clearly emerges in the Raman spectra that is thought to originate from local vibrations of boron pairs [17].

For even higher concentrations of boron relative to carbon, ultra hard structures emerge of which a B–C compound has now been synthesized [5, 6]. This material had been investigated theoretically [18] where it was found that several of these structures are metastable. The stoichiometry of the synthesized metastable B–C phase has now been suggested to be in the stoichiometry BC_5 with an apparent diamond-like structure [6]. Calculations [18] however had indicated that an exact cubic structure is not probable with heavy B concentrations, and at least in the case of a BC_3 stoichiometry, slight tetragonal or trigonal distortions are expected. More recently a hexagonal structure has been considered as being a possibility for BC_5 [19].

There have been at least two reports of the Raman spectra of synthesized B–C structures. Zinin et al. [20] reported a spectrum of a nominally BC_3 phase that had been synthesized at 50 GPa and temperatures of 2,033 K. They observed a rather broad spectrum consisting of two rather broad bands, the around peaks 496–676 cm^{-1} and the second band extending from 997 to 1,413 cm^{-1}. They concluded that the various peaks relate to the structure of diamond BC_3 and that the low energy peaks are similar to boron-doped diamond. More recently Solozhenko et. al. [6] reported Raman spectra also consisting of two broadened bands centered at just below 600 cm^{-1} and the other just above 1,200 cm^{-1}. They suggested that the lower energy peaks were associated with B–B and B–C bonds and assigned the structure to a BC_5 diamond like phase. In this work there was no report of a vibration structure above 1,200 cm^{-1}. In both reports the origin of the various vibration structures was somewhat tenuous and not really understood.

There have also been extensive studies of graphitic phases of boron containing graphitic phases [20, 21] especially in the stoichiometry BC_3. It is likely that such graphitic materials would play an important role as precursors to a diamond-like B–C phase in a similar way that graphite is the precursor to diamond. There is also need to be precise on the exact

stoichiometry of the diamond like B–C phases and how this will influence the overall physical properties of the material. In this regard a comparison with theory is needed.

In the present work we examine potential models for diamond-like B–C phases and deduce various elastic constants. In addition we also report calculations of the vibration spectra associated with the phases. Comparison is made with similar calculations on Boron pairs in diamond. Suggestions are made concerning recent claims regarding the synthesis of BC_3 and BC_5 superhard phases.

2. Computational

The first-principles calculations have been performed using the VASP (Vienna Ab-Initio Simulation Package) code [22], which performs plane-wave pseudopotential total energy calculations. The total energy and the electronic structure of the materials are calculated using density functional theory (DFT) with the local density approximation (LDA) of Ceperley and Alder [23] used to treat the exchange and correlation functional. The *k*-points are generated according to the Monkhorst-Pack [24] scheme usually on an 8 × 8 × 8 grid with PAW pseudopotentials [25] used throughout. All the calculations carried out are fully relaxed and optimized with respect to volume with an energy criterion of 10^{-5} eV/atom. The equilibrium volume and the Bulk modulus were calculated using the Birch–Murnaghan equation of state [26] and elastic constants using the Energy–displacement method through a least squares fit to a second order polynomial. From these values an effective isotropic Bulk, Shear and Young modulus as well as Poisson ratio can be obtained using the following general expressions:

$$G = \frac{1}{15}(c_{11} + c_{22} + c_{33} + 3(c_{44} + c_{55} + c_{66}) - c_{12} - c_{13} - c_{23})$$

Starting with the optimized structures we also calculated that vibration spectra at the Gamma point of the Brillouin Zone which would be appropriate to Raman spectra. In the present work we do not report on symmetry of the Raman modes but only on the overall vibration spectra as obtained from relative intensities of the vibrations as deduced from the eigenvectors of the dynamical matrix. For example considering three eigenvectors for a phonon of frequency ω directed along the cubic directions x, y, and z for a specific atom as being we can define a probability of localization for that atom at the phonon frequency as:

$$L(\omega) = \alpha_x^2 + \alpha_y^2 + \alpha_z^2$$

Thus we can consider displacements of specific atoms and in this way we are able to associate the localization of the various vibration bands with either B or C in a typical B–C structure.

3. Boron in Diamond

A 64-atom unit cell was used to study properties of boron in diamond with boron being placed as a substitutional atom and then as boron pairs either on adjacent lattice locations or next nearest neighbor positions. In this unit cell a Monkhorst-Pack grid of size 4 × 4 × 4 was used.

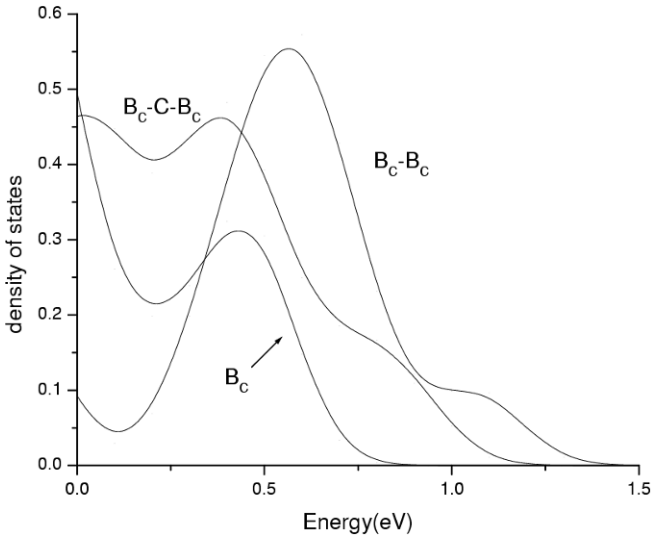

Figure 1. Electronic density of electron states (arb. units/B atom) as measured from the top of the valence band for adjacent substitutional B dimers, next neighbor B pairs and single substitutional B.

The density of states is shown in Fig. 1. In the case of substitutional boron a defect level that follows quite closely – but not exactly – the bulk valence band edge highlights the shallow nature of the B defect and is consistent with the experimental observations discussed earlier that the defect is an acceptor in diamond. In the case of B pairs the electrical energy level structure is different as seen from Fig. 1. When the B dimer is formed from B ions on nearest neighbor locations additional levels arise around the valence band edge. The location of the Fermi level also shows that the defect levels will be partially empty and will thus facilitate a conducting process. As is evident from Fig. 1 the nature of the energy levels depends on the precise location of the two B atoms.

Using the same supercell we evaluated vibration properties of the various boron related structures and using the same 4 × 4 × 4 Monkhorst Pack grid. Without symmetry restrictions, this now lead to a considerably larger number of k-points in the calculation with the energy convergence mentioned earlier. As described above using eigenvectors of the dynamical matrix we can precisely determine atoms amplitudes of the various vibration energies and thus associate the vibration with different atoms. For the various boron atoms in the configurations discussed above this is now shown in Fig. 2.

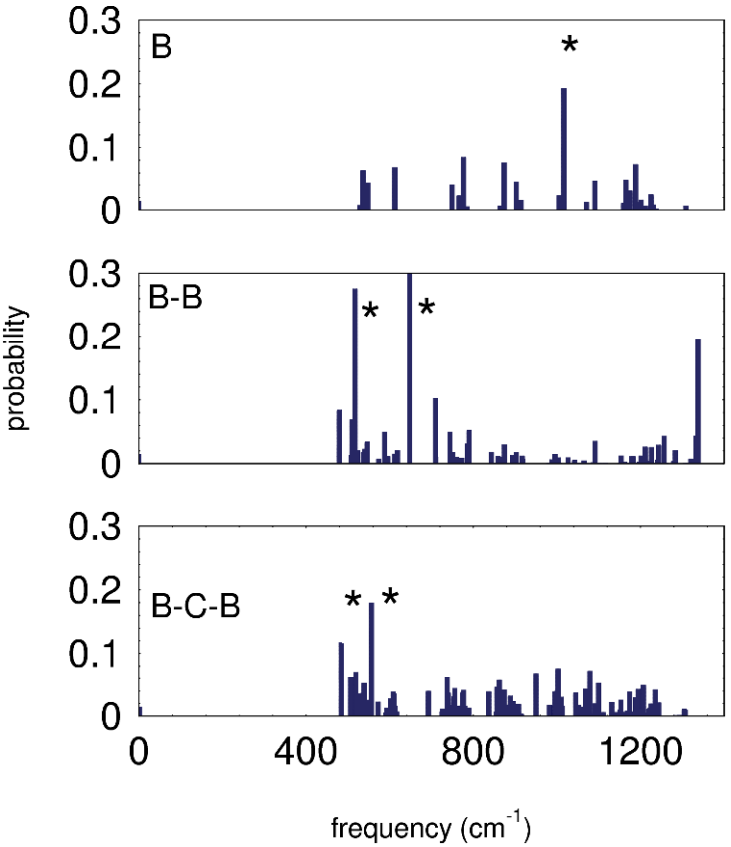

Figure 2. Vibration spectra of various B defects in diamond as represented by a 64-atom unit cell. Vibrations strongly associated with boron atoms are indicated. The proability is obtained from $L(\omega)$ defeined in Section (2).

The calculation has clearly indicated that lower energy vibration modes emerge for boron pairs in the range of about 600 cm^{-1} and that these move to lower energy as the boron atoms are further separated. This feature we suggest, as we shall see, will have implications for boron carbon based new ultra hard materials.

4. Boron–Carbon Diamond-related Structures

Initially to simulate the BC structures we follow the earlier approach [18] of considering an 8-atom unit cell filled with B or C atoms leading to possible structure representing stoichiometries BC, BC_3, BC_7 and diamond as shown in Fig. 3.

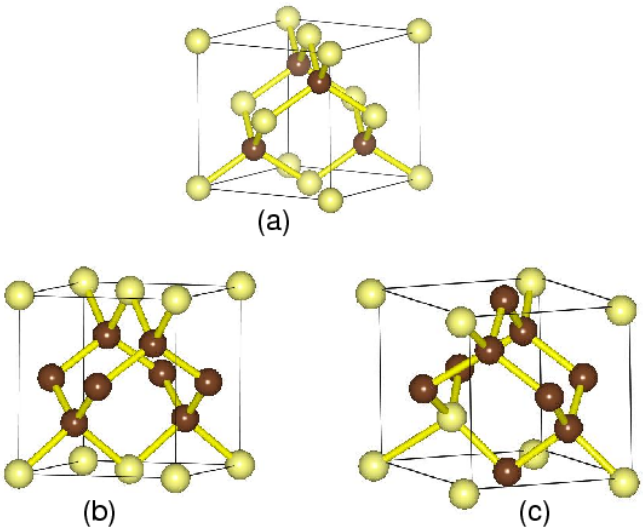

Figure 3. Structure of BC and BC_3 phases. (**a**) Cubic BC, (**b**) tetragonal BC_3 (no B–B bonds), (**c**) trigonal BC_3 (one B–B bond). Dark spheres represent C atoms.

The results of the calculations are given in Table 1 with the various elastic constants in Table 2. There is a clear decrease in all elastic moduli with increasing B concentration. We note that in the case of the BC_3 structure elastic moduli have been calculated in the cubic approximation and also for tetragonal or trigonal symmetry of the distorted 8-atom cell. There are only small differences in the isotropic moduli B, G and E as obtained from expressions above.

TABLE 1 Number of atoms used in unit cell (Z), cellular structure, Birch equation of state and total energy of BC, BC_3, BC_7 and hexagonal BC_3 and BC_5.* crystal structure taken from [19]

	Z	a (*A*)	c (*A*)	B (GPa	B'	E_{tot} (eV/atom)
BC	8	3.745	3.745	301	3.57	−8.346
BC_3 (a)	8	3.509	3.876	379	3.59	−9.265
BC_3(b)	8	3.642	3.611	378	2.94	−9.239
BC_3(c) hexagona	16	5.190	6.782	209	2.27	−9.005
BC_3(d) hexagona	16	5.150 (5.200	4.272	345	3.55	−9.109
BC_5* hexagona	5	2.564	6.326	404	3.6	−9.530
BC_7 diamond	8	3.581	3.581	418	3.62	−9.642
	8					

We have also considered a hexagonal diamond BC_3 phase. This structure is initially derived from the hexagonal diamond structure and in Fig. 4b. A recently suggested structure [19] for hexagonal BC_5 is shown in Fig. 4a. While we find that the hexagonal BC_5 structure is quite stable, this is not so for hexagonal BC_3 at least when all the boron atoms are in a single 111 plane as indicated in the starting structure of Fig. 4b. In fact the relaxed structure is quite graphitic as shown in Fig. 4c where the emergence of two graphitic sheets – one consisting of BC and the other a graphene related sheet is more energetically favorable. Overall the structure still remains hexagonal.

TABLE 2 Elastic constants of diamond like BC_3, BC_5 and BC_7 structures. *crystal structure of BC_5 taken from [19]

	c_{11}	c_{12}	c_{13}	c_{33}	c_{44}	c_{66}	B	G	E	ν
BC	307	299	–	–	38	–	302	24	71	.46
BC_3(a)	749	195	–	–	178	–	380	217	548	.26
	720	206	220	788	464	268	391	344	798	.16
average							385	280	673	.21
BC_3(b)	650	220	–	–	382	–	363	315	733	.16
	628	230	239	380	380	–	367	270	651	.20
average							364	292	692	.18
BC_3(c) (hexagonal)	687	314	0.0	14	0.0	–	223	109	281	.29
BC_3(d) (hexagonal)	844	227	70	694	140	–	346	252	608	.21
BC_5^* (hexagonal)	872	205	113	1,042	371	–	405	372	855	.15
BC_7	789	233	–	–	502	–	418	412	931	.13
Diamond	1,045	99	–	–	584	–	430	539	1,125	.05

We continued to investigate the hexagonal BC_3 structure but now interchanging a boron and carbon atom. The final structure is shown in Fig. 4d – a very near hexagonal structure is still evident. Thus we point out that boron located in the structure of hexagonal BC_3 is quite critical in avoiding a breakdown of the structure to graphite like phase.

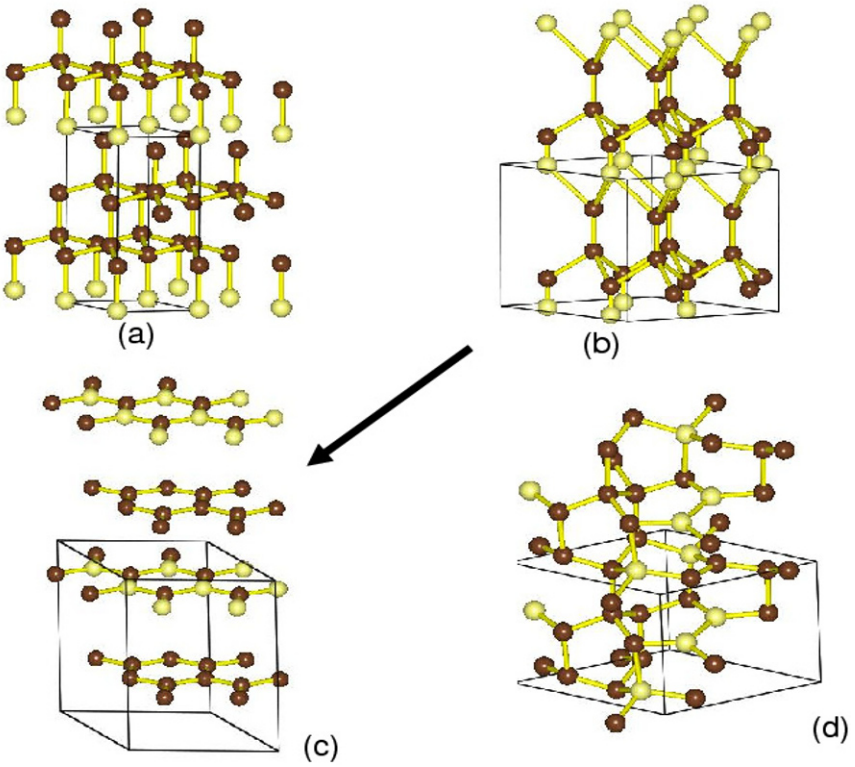

Figure 4. Structure of various B–C phases. (**a**) Final relaxed BC_5 phase [after [19]; (**b**) starting BC_3 phase after hexagonal diamond; (**c**) final relaxed phase starting from phase (**b**) and (**d**) final relaxed phase with a B atoms from the B plane shown in phase (**b**).

Results for all crystal structures are contained in Table 1 – in relation to the graphitic BC_3 structure we note that the phase with B incorporated into the structure (Fig. 4d) is energetically favored over the graphitic structure (Fig. 4c). But even so the nether of the hexagonal BC_3 phases is energetically favored over the diamond like BC_3 phases – i.e. BC_3 (a) or BC_3 (b).

Figure 5 summarizes calculations of the isotropic moduli for the various phases as considered in Table 2. It is noted from Fig. 5 that whereas boron carbon structures generally are incompressible there is a sharp drop in the shear and Young moduli with increasing boron concentration. This implies that the hardness of heavily doped boron carbon diamond like structures will rapidly decline.

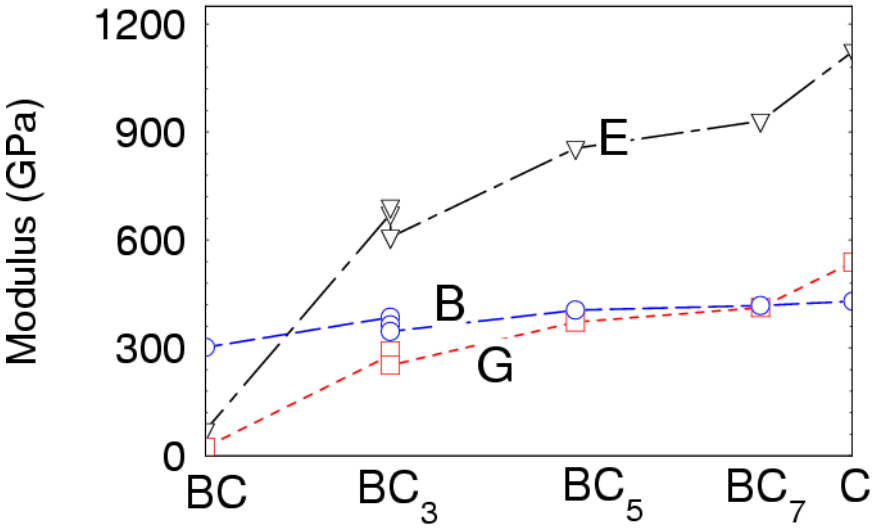

Figure 5. Variation of the elastic moduli of various B–C phases as obtained from the data contained in Table 2. C denotes diamond. As sen from values in Table 2, the Poisson ratio also shows similar trend – decreasing in value with increasing C concentration.

Next we come to the calculations of the vibration structure. Starting from the optimized crystal structures that were given in Table 1 we obtained the vibration frequencies and relative localization of the phonons for either boron or carbon atoms using the method described earlier. For each of the diamond structures of BC, BC_3 and BC_7 the results are now shown in Fig. 6. We note the vibration peaks of the boron atoms. At a stoichiometry of BC_7 there is no vibration structure below about 800 cm^{-1}. This is consistent with our earlier results on the substitutional B defects in diamond – as shown in Fig. 2. However for higher stoichiometries of boron relative to carbon, lower energy vibration structures do appear.

For BC_3 there is a difference in the two possible structures of BC_3 (a) or BC_3 (b) corresponding to the presence of boron pairs. As seen from the figure, boron vibrations lie higher when there are no boron pairs (BC_3 (a)) as opposed to when there is boron pairs (BC_3 (b)). Indeed the presence of boron pairs in the structure does see the emergence of a boron related band at about 600 cm^{-1}. For the very highly metastable structure BC the boron related band has moved to far lower energy around 400 cm^{-1}.

Now we consider hexagonal structures that were shown in Fig. 4. We recall there were two stable hexagonal forms of BC_3 – but in the case of the structure with no boron bonds (BC_3(c)) there was the emergence of two graphitic sheets. It is not unexpected the vibrations of this structure are rather higher in as they are associated with a carbon graphite structure but because the unit cell is different from graphite they occur at slightly lower

energies than for (say) graphene. We find a high energy mode to be present around 1,400 cm^{-1} and there are vibrations associated with the related B–C graphite structure around 800 cm^{-1}. In fact this trend is consistent with results reported earlier for such isolated graphite structures[27]. However the situation when a single boron atom is incorporated into the hexagonal (rather than all being in a layer) leads to a rather complicated system associated with varying carbon bonds. This vibration structure is in no way as intense as the graphitic structure as seen for BC_3 (d). Here there is a rather large unresolved vibration structure emerging – other locations of B in the hexagonal BC_3 structure therefore cannot be excluded.

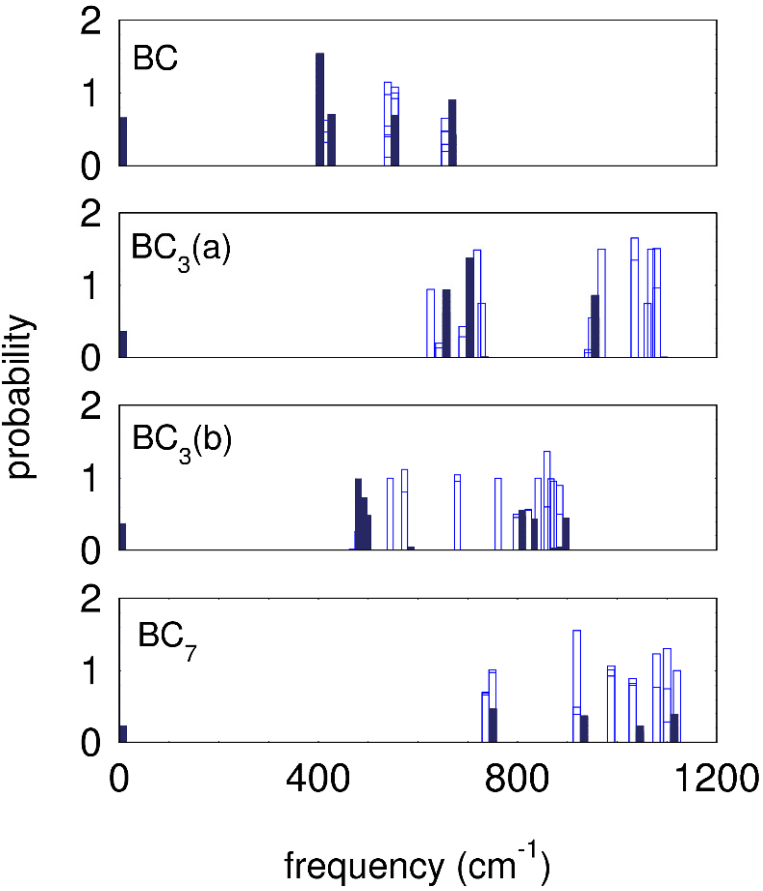

Figure 6. Vibration spectra of B–C phases shown in Fig. (3). *Dark bars* show boron-related vibrations, *open bars* carbon related vibrations. The essential difference between BC_3 (**a**) and BC_3 (**b**) is presence of a boron–boron bond.

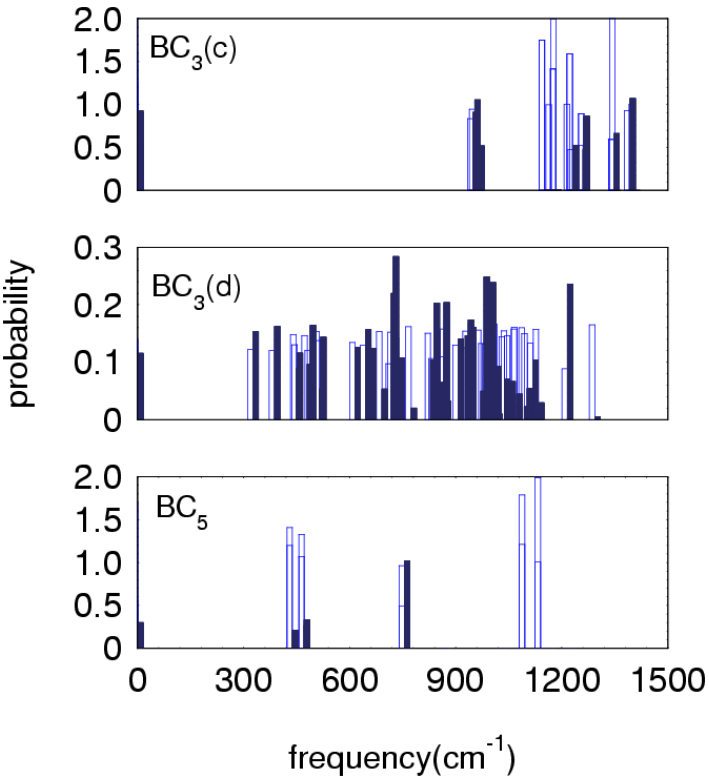

Figure 7. Vibration spectra of hexagonal B–C phases shown in Figure (5). Dark bars show boron-related vibrations, open bars carbon related vibrations. The essential difference between BC_3 (**c**) (a graphitic structure) and BC_3(**d**) is presence of a boron–carbon bond that stabilizes the hexagonal structure.

Thus we suggest that the BC_3 material that has reportedly been synthesized by Zinin et. al. [20] where a rather broad vibration spectrum consisting of two rather broad bands, first between 496 and 676 cm^{-1} and the second extending from 997 to 1,413cm^{-1}. is indeed associated with a phase of BC_3. The higher energy band suggests graphitization is present. The origin of the lower energy peak that these authors observe is far more uncertain but is consistent with either the diamond like BC_3(b) system – the vibration spectrum shown in Fig. 6 or the hexagonal BC_3(d) system the spectrum shown in Fig. 7. Clearly more work is encouraged here.

Finally we considered the vibration structure of BC_5 and this is also shown in Fig. 7. There is a strong boron related peak at about 800 cm^{-1} and a lower energy structure at about 400 cm^{-1} but mainly associated with carbon. A carbon related peak is at about 1,200 cm^{-1}.

We consider implications for the vibration spectrum recently reported by Solozhenko et al. [6] . This consisted of two broadened bands centered at just below 600 cm^{-1} and the other just above 1,200 cm^{-1}. The energy of the higher is consistent with the calculated structure shown in Fig. 7 as is the lower energy band around 400 cm^{-1}. But the peak we calculate to lie around 700 cm^{-1} and associated with boron does not seem to be present in the experimentally reported spectrum [6]. Again some further work is encouraged to elucidate this structure.

5. Conclusion

It is anticipated that many boron–carbon complexes will be metastable relative to diamond at least under ambient conditions. As such these materials will require extreme conditions to be synthesized although it may be possible to stabilize these materials at ambient conditions. In the present work we have considered various possible structures for some boron–carbon structures that have some form of diamond related crystal structure. It was found that diamond-like structures have quite large bulk modulus suggesting such structures would be incompressible new materials. However the calculations also indicate that with very high boron concentrations the other moduli, such as the shear and Young values, decrease rapidly. This would imply that heavy boron concentrations in diamond related structure whilst being incompressible may not exhibit extreme hardness. We also examined the role played by boron in such structures and this is shown in the observed vibration spectra. Comparison is made with point defect boron structures in diamond. We see that the low energy modes – around 600–700 cm^{-1} are primarily associated with boron dimer structures. This is not surprising as boron–carbon bonds are far weaker than carbon–carbon bonds and thus vibrations will be at lower energy. The influence of boron bonds continues to be evident in the various boron–carbon potentials ultra hard structures with strong bands again emerging at the 600 cm^{-1} region of the vibration spectra. This region of the vibration spectra is an important indicator of the potential structure and as boron bonds will essentially weaken the structure of the overall of the hardness of the material.

We have seen that our results have consistencies with recently reported Raman spectra [6, 20] and the suggestions of BC_3 or BC_5 stoichiometries as reported in both works. In the case of the BC_3 spectra however we suggest that there is some graphitization present but the presence of an ultra hard phase cannot be ruled out. At the same time the observed BC_5 spectra does appear consistent with our calculations albeit boron associated structure around 700 cm^{-1} should be further examined.

Acknowledgements

This work has been supported by the National Research Foundation (South Africa).

References

1. A. Badzian and T. Badzian, "Recent developments in hard materials," *International Journal of Refractory Metals and Hard Materials,* **15** 3 (1997).
2. J. Haines, J. M. Leger and G. Bocquillon, "Synthesis and design of superhard materials," *Ann. Rev. Mater. Res.,* **31** 1 (2001).
3. H. W. Hubble, I. Kudryashov, V. L. Solozhenko, P. V. Zinin, S. K. Sharma and L. C. Ming, "Raman studies of cubic BC2N, a new superhard phase," *Journal Of Raman Spectroscopy,* **35** 822 (2004).
4. V. L. Solozhenko, D. Andrault, G. Fiquet, M. Mezouar and D. C. Rubie, "Synthesis of superhard cubic BC2N," *Appl. Phys. Lett.,* **78** 1385 (2001).
5. V. L. Solozhenko, N. A. Dubrovinskaia and L. S. Dubrovinsky, "Synthesis of bulk superhard semiconducting B–C material," *Applied Physics Letters,* **85** 1508 (2004).
6. V. L. Solozhenko, O. O. Kurakevych, D. Andrault, Y. Le Godec and M. Mezouar, "Ultimate Metastable Solubility of Boron in Diamond: Synthesis of Superhard Diamondlike BC5," *Physical Review Letters,* **102 015506** (2009).
7. S. N. Tkachev, V. L. Solozhenko, P. V. Zinin, M. H. Manghnani and L. C. Ming, "Elastic moduli of the superhard cubic BC_2N phase by Brillouin scattering," *Phys Rev B,* **68** 052104 (2003).
8. J. F. Custers, "Boron in Diamond" *Nature,* **176** 173 (1955).
9. A. T. Collins and E. C. Lightowlers, "The boron defect in Diamond," *Physical Review,* **171** 843 (1968).
10. P. A. Crowther, P. J. Dean and W. F. Sherman, "Photoconductivity of Boron in Diamond," *Physical Review,* **154** 772 (1967).
11. R. F. Mamin and T. Inushima, "Conductivity in Boron-Doped Diamond," *Phys. Rev. B,* **63** 033201 (2001).
12. W. B. Wilson, "Several Boron Types of Conductivity in Diamond," *Physical Review,* **127** 1549–57 (1962).
13. M. J. R. Hoch, J. E. Lowther and T. Tshepe, "Boron in diamond at high concentrations," *Proceedings of the 25th International Conference on the Physics of Semiconductors, Pts I and Ii,* **87** 154–55 (2001).
14. E. A. Ekimov, V. A. Sidorov, E. D. Bauer, N. N. Mel'nik, N. J. Curro, J. D. Thompson and S. M. Stishov, "Superconductivity in Diamond," *Nature,* **428** 542 (2004).
15. T. Yokoya, T. Nakamura, T. Matsushita, T. Muro, Y. Takano, M. Nagao, T. Takenouchi, H. Kawarada and T. Oguchi, "Origin of the metallic properties of heavily boron-doped superconducting diamond," *Nature,* **438** 647 (2005).
16. N. Dubrovinskaia, G. Eska, G. A. Sheshin and H. Braun, "Superconductivity in polycrystalline boron-doped diamond synthesized at 20 GPa and 2700 K," *Journal of Applied Physics,* **99** 033903 (2006).

17. M.Bernar, C. Bar and A. Deneuville, "About the origin of the low wave number structures of the Raman spectra of heavily boron doped diamond films," *Diamond & Related Materials,* **13** 896 (2004).
18. J. E. Lowther, "Potential super-hard phases and the stability of diamond-like boron–carbon structures," *J. Phys.-Condes. Matter,* **17** 3221 (2005).
19. M. Calandra and F. Mauri, "High-Tc superconductivity in superhard diamondlike BC5," *Phys Rev Lett,* **101**[1] 016401 (2008).
20. P. V. Zinin, L. C. Ming, I. Kudryashov, N. Konishi and S. K. Sharma, "Raman spectroscopy of the BC_{ϵ} phase obtained under high pressure and high temperature," *Journal of Raman Spectroscopy,* **38** 1362 (2007).
21. Vladimir L. Solozhenko, Oleksandr O. Kurakevych, Elena G. Solozhenko, Jiuhua Chen and J. B. Parise, "Equation of state of graphite-like BC," *Solid State Communications* **137** 268 (2006).
22. G. Kresse and J. Hafner, "Ab initio molecular dynamics for liquid metals" *Phys. Rev. B,* **47** 558 (1993).
23. D. M. Ceperley and B. J. Alder, "Ground State of the Electron Gas by a Stochastic Method" *Phys. Rev. Lett.,* **45** 566 (1980).
24. H. J. Monkhorst and J. D. Pack, "Special points for Brillouin-zone integrations" *Phys. Rev. B,* **13** 5188 (1976).
25. G. Kresse and D. P. Joubert, "From Ultrasoft Pseudopotentials to the Projector Augmented Wave Method," *Phys. Rev. B,* **59** 1758 (1999).
26. F. Birch, "Finite elastic strain of cubic crystals," *Phys. Rev.,* **71** 809 (1947).
27. J. E. Lowther, P. V. Zinin and L. C. Ming, "Vibrational energies of graphene and hexagonal structured planar B–C complexes," *Physical Review B,* **79** 033401 (2009).

PROCESSING AND PROPERTIES OF ULTRA-REFRACTORY COMPOSITES BASED ON Zr- AND Hf-BORIDES: STATE OF THE ART AND PERSPECTIVES

A. BELLOSI*, S. GUICCIARDI, V. MEDRI,
F. MONTEVERDE, D. SCITI, L. SILVESTRONI
CNR-ISTEC, Institute of Science and Technology, 48018 Faenza, Italy

Abstract High performance Ultra-High-Temperature Composites, based on zirconium and hafnium borides, are characterized by relevant and unique thermo-physical and thermo-mechanical properties, suitable for applications in aerospace hot structures and in many industrial sectors where extreme conditions are present.

In spite of the difficult sinterability of Zr- and Hf-diborides, recent results highlight that these ceramics can be produced with full density, fine microstructure and controlled mechanical and thermal properties, through different procedures: pressureless sintering and hot pressing with proper sintering aids, reactive synthesis/sintering procedures starting from precursors, field assisted technologies like spark plasma sintering (SPS).

A proper selection of reinforcing phase (SiC, B_4C, $TaSi_2$, $MoSi_2$, etc) leads to improvements in mechanical properties and oxidation resistance of ZrB_2 and HfB_2 ceramic composites.

Strength as high as ~800 MPa at room temperature and at 1,500°C in air can be obtained for HfB_2-based composites, after an accurate tailoring of compositions and processing parameters. SPS proved to be a very rapid fabrication process leading to refined microstructure and improved properties of ultra-refractory diborides-based composites.

Keywords: zirconium diboride, hafnium diboride, composites, sintering, mechanical properties, microstructure

* A. Bellos, CNR-ISTEC, Institute of Science and Technology, 48018 Faenza, Italy, e-mail: alida.bellosi@istec.cnr.it

N. Orlovskaya and M. Lugovy (eds.), *Boron Rich Solids: Sensors, Ultra High Temperature Ceramics, Thermoelectrics, Armor*, DOI 10.1007/978-90-481-9818-4_10,

1. Introduction

ZrB_2 and HfB_2-based ceramics belong to the class of ceramics defined as Ultra-High Temperature Ceramics (UHTCs). Besides the top refractoriness, these compounds present a unique combination of properties such as high electrical and thermal conductivity, chemical inertness against molten metals or non basic slags [1, 2]. The principal fields of applications are those associated with atmospheric re-entry, hypersonic flights, propulsion [1–7], that need materials and structural components capable of operating at temperatures in excess of 1,600°C.

The open literature in the field of processing and materials science of UHTCs is nearly scarce up to the eighties of the past century [8–13]. In recent years different routes were attempted to improve fabrication procedures and performances of the Zr- and Hf-based borides and carbides:

(i) The incorporation of sintering aids [14–28] associated to a conventional densification technique like hot pressing (HP) or gas-pressure sintering
(ii) Reactive processing that relies on chemical conversion of most or all of the precursors to new phases through displacement reactions [28–34], solution-based methods [35–37] or other solid-state reactions [38–41]
(iii) Innovative densification methods like spark plasma sintering (SPS), successfully used to densify several non oxide ceramics [42–49], and UHTC compounds [50–58];
(iv) A careful "materials design" to increase strength, toughness, oxidation resistance, thermal shock resistance through the addition of reinforcing phases [2–4, 17, 19, 59–62], including short fibers or whiskers [63–70].

The durability in oxidizing environment and the thermal and mechanical properties under severe conditions have been widely studied [71–94]. Moreover, the behaviour in a simulated re-entry environment is a key issue for all the space applications [1–3, 95–97].

In this work, recent results achieved in the development of monolithic and composites based on HfB_2 and ZrB_2 are presented and discussed, with reference to the effects of sintering technologies, of the type of sintering aids, of the role of secondary phases on the main materials properties.

Table 1 lists the starting compositions, processing procedures micro-structural and mechanical features of the monolithic and composite ceramics object of this paper.

2. Role of the Sintering Aids on Microstructure

Due to the high melting point and high vapour pressure of the constituents, undoped Zr- and Hf-borides and carbides can be densified to final relative densities in the range 70–90%, at temperatures above 2,000°C. The very

TABLE 1. Comparison of relative densities (rd) and mechanical properties of some UHTCs. HP: hot pressing; PLS: pressureless sintering; SPS: spark plasma sintering; RHP: reactive hot pressing; HV1.0: Vickers microhardness, 9.81 N; E: Young's modulus (resonance frequency method); σ: 4-pt flexural strength (specimens 25 × 2.5 × 2 mm^3) at room temperature (RT) and high temperature (HT)

Starting composition (wt%)	Sint. tech.	rd (%)	E GPa	HV1.0 GPa	σ RT (MPa)	σ HT (MPa)
ZrB_2 [17]	HP	~85	346	8.7	351 ± 31	312 ± 14 (1,200°C) 220 ± 7 (1,400°C)
ZrB_2 + $2MoSi_2$ [14]	HP	100	500	18.1	750 ± 160	240 ± 25 (1,500°C)
ZrB_2 +4Ni [15]	HP	~98	496	14.4	371 ± 24	15 ± 1 (1,200°C)
ZrB_2 + 2.5AlN [18]	HP	~92	407	9.5	600 ± 35	300 ± 25 (1,400°C) 200 ± 20 (1,500°C)
ZrB_2 + 2.5Si_3N_4 [17]	HP	~99	419	13.4	595 ± 90	240 ± 20 (1,200°C)
HfB_2 + 2.5Si_3N_4	HP	~99			478 ± 45	227 ± 11 (1,400°C)
ZrB_2 + 12SiC + 2Si_3N_4 [17]	HP	~98	421	14.2	725 ± 98	280 ± 20 (1,200°C)
ZrB_2 + 5$MoSi_2$	PLS	~96	516	15.2	569 ± 54	533 ± 87 (1,200°C) 487±46 (1,500°C)
ZrB_2 + 20$MoSi_2$ [22]	PLS	100	489	13.9	530 ± 70	655 ± 45 (1,200°C) 500 ± 49 (1500°C)
ZrB_2 – 15$MoSi_2$ [57]	SPS	100	479	16.2	643 ± 97	357 ± 48 (1,500°C)
ZrB_2 – 15$MoSi_2$	HP	~99	452	14.9	704 ± 98	333 ± 31 (1,500°C)
ZrB_2 – 15$TaSi_2$	HP	~99	444	17.8	840 ± 33	598 ± 25 (1,200°C) 374 ± 5 (1,500°C)
ZrB_2 + 33ZrC + 6SiC[51]	SPS	~99	474	19.8	780 ± 80	594 ± 33 (1,200°C) 418 ± 57 (1,500°C)
HfB_2+ 6.5SiC + 2Si_3N_4 [85]	HP	~99	421	20.4	560 ± 98	150 ± 25 (1,500°C)
HfB_2+ 6.5SiC + 4HfN 19]	HP	~98	506	22.3	650 ± 50	465 ± 45 (1,500°C)
HfB_2 + 32ZrB_2 + 8SiC + 5.5HfN [19]	HP	~99	497	22,0	765 ± 20	250 ± 45 (1500°C)
HfB_2 + 11SiC [53]	SPS	~99	512	26.0	590 ± 50	600 ± 15 (1500°C)
HfB_2 + 1$MoSi_2$ [55]	SPS	~94	562	21.1	663 ± 65	570 (1,500°C)
HfB_2 + 3$MoSi_2$ [55]	SPS	~96	584	22.0	750 ± 34	650 (1,500°C)
HfB_2 + 9$MoSi_2$ [55]	SPS	~99	583	21.9	652 ± 40	820 (1,500°C)
HfB_2 + 7.5SiC+8HfC[21]	RHP	~99	520	24.0	770 ± 35	315 ± 15 (1,500°C)
HfB_2 + 12.2$MoSi_2$ [43]	PLS	~98	482	18.0	388 ± 65	548 ± 30 (1,200°C) 577 ± 50 (1,500°C)
HfB_2 + 15$MoSi_2$ [60]	HP	~99	530	20.6	742 ± 151	664 ± 28 (1,200°C) 548 ± 20(1,500°C)
HfB_2 + 15$TaSi_2$[60]	HP	~99	528	21.9	698 ± 58	704 ± 24 (1,200°C) 597 ± 46 (1,500°C)

high sintering temperatures lead to excessive grain growth [10, 11]. The addition of metal sintering aids (Ni, Fe) results in grain boundary phases that deteriorate the high temperature mechanical and physical properties [14, 15]. Ceramic additives like Si_3N_4 [16], AlN [18], HfN [19], disilicides of Mo and Ta [22, 43, 57, 60] improve densification, microstructures and properties of ZrB_2 and HfB_2.

As examples of these statements, the microstructures of two materials produced by SPS are compared in Fig. 1. Monolithic HfB_2 sintered at 2,200°C shows an extensive porosity (Fig. 1a). Instead, HfB_2 with 1 vol% $MoSi_2$ as sintering aid and sintered at 1,750°C highlights high final density and grain size refinement (Fig. 1b). In the composite, the majority of the HfB_2/HfB_2 boundaries appears flat and depleted of secondary phases that are mainly concentrated at the triple points. The darker areas on the polished surfaces in Fig. 1b correspond to SiC. In addition to HfB_2 and SiC, Hf-O secondary phases were detected.

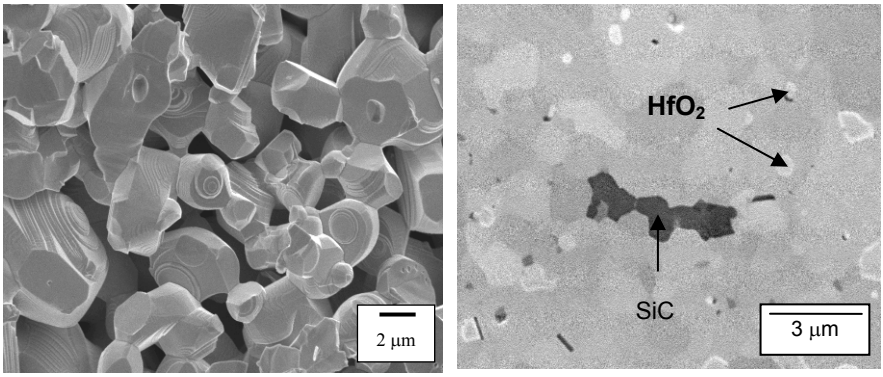

Figure 1. (**a**) Fracture surface of undoped HfB_2 (SPS, 2,200°C). (**b**) Polished surface of HfB_2 with the addition of 1 vol% $MoSi_2$ (SPS, 1,750°C).

Silicon nitride in an amount of 2.5 wt% allows to achieve full dense ZrB_2 ceramics through hot pressing at 1,700°C [17]. The use of AlN as sintering aid greatly limits the formation of secondary grain boundary phases, and good strength values are measured up to 1,500°C [18], Table 1.

The addition of disilicides ($MoSi_2$, $HfSi_2$, $TaSi_2$) acts either as sintering aid, or as strengthening phases.

The addition of molybdenum disilicide in amounts of 5–10 vol% favors the fabrication of dense materials based on ZrB_2 and HfB_2 even through pressureless sintering [43, 53, 57, 60, 70, 77].

3. Effects of Secondary Phases on Densification, Microstructure, Mechanical Properties and Oxidation Resistance

As the reliability of UHTCs is limited by poor toughness, stress corrosion cracking and high temperature oxidation, many applications of these materials require the addition of second reinforcing phases. Successful efforts were made to improve mechanical properties and oxidation resistance of Zr- or Hf- diborides based materials, through appropriate additives [1, 2, 4, 17, 41-43, 46-48]. In particular, it was found that Si-supplier compounds, such as SiC and metal silicides, are suitable to increase the oxidation resistance. Among the disilicides, $MoSi_2$ proved to be very effective. SiC is the most diffused additive for the improvement of oxidation resistance and grain refinement. Furthermore, both SiC and $MoSi_2$ offer the advantage to act as sintering aids [3, 4, 17, 39-44, 45, 49, 54–57]. Figure 2a and b show the microstructure of ZrB_2-12 wt% SiC [17] and HfB_2-6.5 wt% SiC [85] produced by hot pressing at 1,870°C and 1,850°C, respectively, with an applied pressure of 30 MPa. The textures of the two SiC-containing composites appear rather similar, with the grain size of the diboride matrix notably refined in comparison to the monolithic ceramics. The SiC particles are mainly distributed in clusters and are often in contact with secondary phases formed during sintering (BN, MeO_2 and B-N-O-Si-Me glassy systems, where Me= Zr, Hf). Data in Table 1 point out that the proper combination of additives and matrix leads to enhanced high temperature strength.

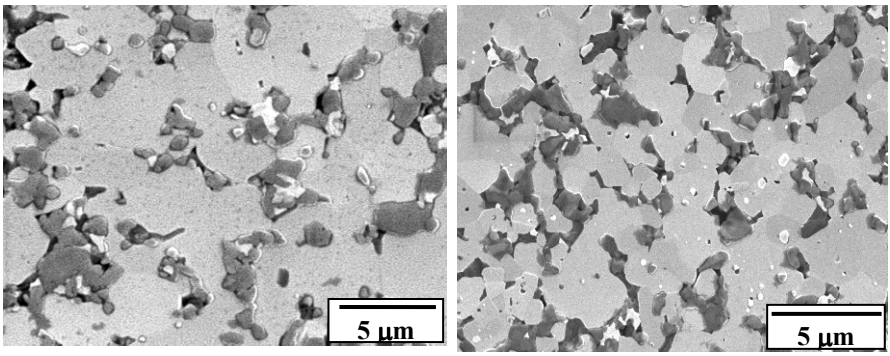

Figure 2. (**a**) Polished surface of a hot pressed ZrB_2-12 wt%SiC composite. (**b**) Polished surface of a hot pressed HfB_2 + 6.5 wt%SiC composite.

The use of HfN as sintering aid for HfB_2-SiC composites [19] is suitable to originate highly refractory grain boundary phases, resulting in flexure strength of about 465 MPa at 1,500°C. On the contrary the addition of Si_3N_4 as sintering aid leads to strength of about 150 MPa at 1,500°C. At the same

time, composites based on HfB_2 and HfB_2+ZrB_2, with the same amount of SiC (second phase) and HfN (sintering aid), evidence a great difference in strength measured in air at 1,500°C: 465 MPa for the former and 250 MPa for the latter.

UHTCs in the systems ZrB_2- and HfB_2- (5–20 vol%) $MoSi_2$ have been densified to near full density by pressureless sintering and hot pressing [22, 43, 53, 60]. Besides, relevant high temperature mechanical strength was measured on composites based on HfB_2 and densified by spark plasma sintering, in the presence of $MoSi_2$ as secondary phase [55, 57]. The results confirm that $MoSi_2$ acts as second reinforcing phase and as effective sintering aid for the densification of borides. Composites with relative densities higher than 98% can be produced by pressureless sintering at 1,850–1,950°C, and by hot pressing at 1,800–1,900°C in the case of ZrB_2- and HfB_2-matrix composites, respectively. The role of $MoSi_2$ can be summarized as follows: it limits the excessive grain growth of borides; it accommodates in the voids left by matrix grains thanks to its plasticity; it promotes oxygen removal from boride particles surface. During sintering, $MoSi_2$ reacts with surface oxides (B_2O_3) of ZrB_2 or HfB_2, forming SiO_2 and Mo-B/Mo-Si-B liquid species that help grain rearrangement and mass transfer. The final microstructure shows the formation of solid solutions around the matrix grains and discrete intergranular pockets [98]. After sintering no residual silica is observed in pressureless sintered composites, due to the reducing sintering atmosphere (Ar flux, graphite crucible and heating elements) and the longer sintering times [22, 43]. Pressure-assisted techniques allow the sintering temperatures to be reduced at 1,750–1,800°C (Table 1), but on the other side, pressureless sintering is also advisable for these materials, since it favors the development of a uniform and fine microstructure without residual glassy phases (Fig. 3) and allows the production of near-net shaped components.

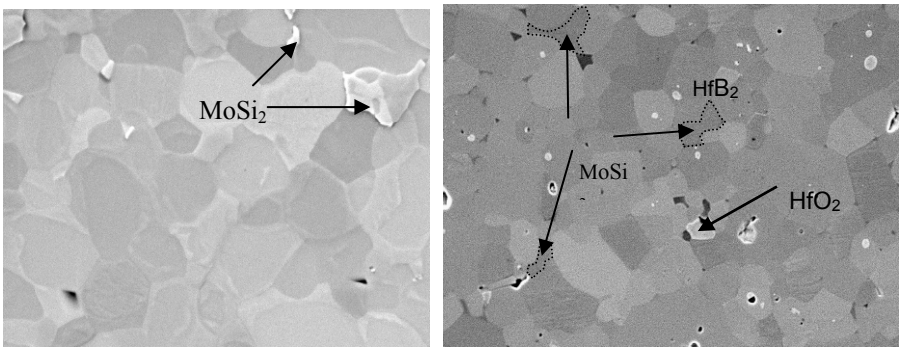

Figure 3. (**a**) Microstructure of pressureless sintered composites: ZrB_2 + 5% $MoSi_2$. (**b**) Microstructure of pressureless sintered composites:HfB_2 + 5% $MoSi_2$.

For the pressureless sintered ZrB_2-20$MoSi_2$ material, the room-temperature flexural strength in air of about 500 MPa was retained up to 1,500°C. This property rises to about 600 MPa in the case of HfB_2 matrix.

As this class of advanced ceramics is designed to be exposed frequently to very hot and hostile environments, the high-temperature stability, especially the resistance to oxidation, is a key property. The upper limit of the service temperature is strongly related not only to the characteristics of the matrix, but also to second and/or grain boundary phases, which depend on the sintering aids used. The addition of SiC and/or of $MoSi_2$ to diboride-matrix composites promotes the formation of an external borosilicate glassy layer, which gives much more oxidation protection than B_2O_3. According to Opeka et al. [2], good oxidation performances at hypersonic use temperatures up to 2,000°C and above are exhibited by materials that form a multi-component oxide scale, composed of a refractory oxide skeleton and an amorphous oxide component. This multicomponent oxide can be achieved by compositional modifications with transition metal additives (i.e. Cr- and Ta-compounds) that promote immiscibility in the glassy component of the outermost surface scale.

4. Densification by Spark Plasma Sintering of UHTC's

In the spark plasma sintering (SPS) process, a pulsed electric direct current is applied in combination with an external mechanical pressure in a graphite die. For electrically conductive materials, heating up is mainly due to the Joule effect. The effectiveness of such a technology in the densification of refractory borides is highlighted by the data on total processing time, which is at least 10 times lower than for conventional hot pressing, and is enough to obtain a final relative density higher than 99%. The micrograph of the composite ZrB_2 + 9% $MoSi_2$ (Fig. 4a), treated by SPS at 1,700°C, displays fine and uniform grain size (less than 2 μm) and traces of SiC and ZrO_2. The picture in Fig. 4b shows that the microstructure of a HfB_2-SiC composite heated for 2 min at 2,100°C is very uniform, and the mean grain size of HfB_2 grains is about 2 μm. As pointed out from the values shown in Table 1, this composite did not undergo strength degradation at 1,500°C in air [53]. A plausible explanation is the absence of thermally unstable grain boundary phases that often form from the sintering aids, or from uncontrolled reactions.

A ternary ZrB_2-30ZrC-10SiC composite was fully densified by spark plasma sintering at a temperature of 2,100°C and 2 min dwell time [52, 53]. For the densification through hot pressing, the same composition needs the addition of a sintering aid. Introducing 2 wt% Si_3N_4, full density is achieved at T = 1,870°C. The entire processing time applied to obtain full density

through SPS was about 23 min (cooling excluded), significantly shorter than that applied for hot-pressing, i.e. 140 min.

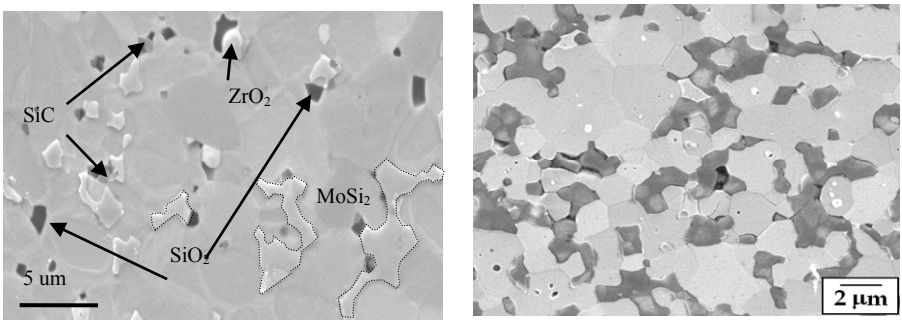

Figure 4. (**a**) Polished surface of the ZrB_2 – 9 vol% $MoSi_2$ densified by SPS. (**b**) Polished surface of the HfB_2+12wt% SiC densified by SPS.

5. The Production of UHTC's through Reactive Processing

The term "reactive processing" includes a variety of displacement reactions to synthesize materials, as well as several methods such as soft solutions or sol-gel processing [29–40]. Regarding solid-state synthesis, reactive heat treatments like hot pressing, self-propagating high-temperature synthesis, or mechano-chemical synthesis perform well to get rather dense final products, once the starting compositions and processing parameters are optimised. To make clear the potential of these techniques, the current example concerns a reactive hot pressed HfB_2-SiC composite fabricated from a stoichimetric Hf/Si/B_4C powder mixture [21], according to the following reaction:

$$2Hf + Si + B_4C = 2HfB_2 + SiC \quad (1)$$

The process consists of two stages. The former is a heat treatment up to 1,450°C and 60 min holding time under Ar atmosphere, to induce and complete reaction 1 among the solid precursors. The latter implies the hot pressing at 1,900°C for 10 min hold time. The final composition of the fully dense composite is HfB_2 + 22 vol% SiC + 6 vol%HfC as secondary by-product of the base reaction. The reactive process develops fine microstructures (Fig. 5) with HfB_2 grains in the range 0.5–4 µm and SiC particles (darker particles of about 2 µm in Fig. 5) located at intergranular sites. The mechanical properties are of great interest (Table 1), particularly the room temperature flexure strength is higher than the values measured on similar composites produced with other techniques. The strength decrease at 1,500°C in air is due to the adverse effect of the oxidation of HfC formed.

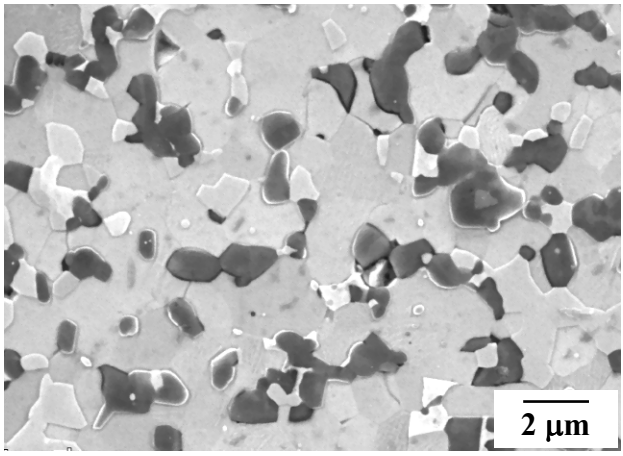

Figure 5. Microstructure of a HfB_2-SiC-HfC composite sintered by reactive hot-pressing.

6. Conclusions

Dense monolithic and composite ceramics based on ultra-refractory compounds like HfB_2 and ZrB_2 can be obtained with addition of SiC, $MoSi_2$, or ZrC as secondary phases and fabricated through different procedures:

- Pressureless sintering, provided that $MoSi_2$ is added, at least in amount of 5 vol%;
- Hot pressing using sintering aids, specifically Si_3N_4, AlN, HfN, $MoSi_2$, SiC, $TaSi_2$
- Spark plasma sintering, with and without additives
- Reactive hot-pressing from solid precursors

The composition of the starting powder mixtures and the fabrication route influence microstructure, physical and mechanical properties. A proper selection of sintering aids and the incorporation of second reinforcing phases allow to obtain near fully dense compacts and high strength values. The best values of room temperature strength approach 900 MPa (for hot pressed ZrB_2 + $TaSi_2$), the strength at 1,500°C in air is about 500 MPa for ZrB_2–$MoSi_2$ composites, while it reaches about 800 MPa for SPS HfB_2–$MoSi_2$-composites.

Improvements in the oxidation resistance can be made with addition of Si-containing species or cations which induce immiscibility in the external glassy layer.

References

1. Upadhya K, Yang J-M., and Hoffmann W. P., Materials for ultrahigh temperature applications, *Am. Ceram. Soc. Bull.*, **58**, 51–56, 1997.
2. Opeka M. M., Talmy I. G., and Zaykoski J. A., Oxidation-based materials selection for 2000°C + hypersonic aerosurfaces: theoretical considerations and historical experience, *J. Mater. Sci*., **39**, 5887–5904, 2004.
3. Levine S. R., Opila E. J, Halbig M. C., Kiser J. D., Singh M., and Salem J. A., Evaluation of ultra-high temperature ceramics for aeropropulsion use, *J. Europ. Ceram. Soc*., **22**, 2757–2767, 2002.
4. Opeka M. M., Talmy I. G., Wuchina E. J., Zaykoski J. A., and Causey S. J., Mechanical, thermal, and oxidation properties of refractory hafnium and zirconium compounds, *J.Europ. Ceram. Soc.*, **19**, 2405–2414, 1999.
5. Sayr A., Carbon fiber reinforced hafnium carbide, *J. Mater. Sci.*, **39**, 5995–6003, 2004.
6. Van Wie D. M., The hypersonic environment: required operation conditions and design challenges, *J. Mater. Sci.*, **39**, 5915–5924, 2004.
7. Øvrebø D. N., and Riley F. L., Densification of zirconium diboride", in S*ixth ECerS Conference & Exhibition of the European Ceramic Society, Extended Abstracts Volume 2, British Ceramic Proceedings No. **60*** IOM Communications Ltd, p.19–21, 1999.
8. Mroz C., Annual mineral review: zirconium diboride, *Am. Ceram. Soc. Bull*., **74**, 165–66. 1995.
9. Pastor H., Metallic borides, preparation of solid bodies-sintering methods and properties, in *Boron and Refractory Borides*. Ed. V. I. Matkovich, Springer Verlag, N. York, p.457–493, 1977.
10. Low I. M.,and McPherson R., Fabrication of new zirconium boride ceramics, *J. Mat. Sci*. *Lett*., **8**, 1281–1285, 1989.
11. Hayami R., Iwasa M., and Kinoshita M., Effects of applied pressure on hot pressing of ZrB_2, *Yogyo-Kyokai-Shi*, **88**, 352–358, 1987.
12. Woo S-K., Han I-S., Kang H-S., Yang J-H., and Kim C-H., Sintering of zirconium diboride through Fe-based liquid phases, *J. Korean Ceram. Soc.*, **33**, 259–262, 1996.
13. Sorrell C. C., Stubican V. S., and Bradt R. C., Mechanical properties of ZrC/ZrB_2 and ZrC/TiB_2 directionally solidified eutectics, *J. Am. Ceram. Soc*., **69**, 317–321, 1986.
14. Monteverde F., The addition of SiC particles into a $MoSi_2$-doped ZrB_2 matrix: effects on densification, microstructure and thermo-physical properties, Mat. Chem Phys*.,* **113**, 626–633, 2009.
15. Monteverde F., Bellosi A., and Guicciardi S., Processing and properties of zirconium diboride-based composites, *J. Europ. Ceram. Soc.*, **22**, 279–288, 2002.
16. Monteverde F., and Bellosi A., Effect of the addition of silicon nitride on sintering behaviour and microstructure of zirconium diboride, *Scripta Materialia*, **46**, 223–228, 2002.
17. Monteverde F., Bellosi A., and Guicciardi S., Advances in microstructure and mechanical properties of zirconium diboride based ceramics, *Mat. Sci. Eng*., **A346**, 310–319, 2003.
18. Monteverde F., and Bellosi A., Beneficial effects of AlN as sintering aid on microstructure and mechanical properties of hot pressed ZrB_2, *Adv. Eng. Mater*., **5,** 508–512, 2003.
19. Monteverde F., and Bellosi A., Efficacy of HfN as sintering aid in the manufacturing of ultra-high temperature metal diborides-matrix ceramics, *J. Mat. Res*.,**19**, 3576–3585, 2004.
20. Chamberlain A. L., Fahrenholtz W. G. and. Hilmas G. E, Pressureless sintering of zirconium diboride, *J. Am. Ceram. Soc.*, **89**, 450–456, 2006.

21. Monteverde F., Progress in the fabrication of ultra-high temperature ceramics: "in-situ" synthesis, microstructure and properties of a reactive hot-pressed HfB_2-SiC, *Composites Science and Technology* **65** [11–12], 1869–1879, 2005.
22. Sciti D., Guicciardi S., Bellosi A., Properties of a pressureless sintered ZrB_2-$MoSi_2$ ceramic composite, J. Amer. Ceram. Soc. **89**, 2320–2322, 2006.
23. Guo S-Q., Densification of ZrB_2-based composites and their mechanical and physical properties: a review. J. Europ. Ceram Soc. **29**, 995–1011, 2009.
24. Li G., Zhang X., Han J., Effect of AlN as sintering aid on hot pressed ZrB_2-SiC ceramic composite. J. Alloy and Comp. (2008).
25. Zou J., Zhang G-J., Kan Y-M., Wang P-L., Pressureless densification of ZrB_2-SiC composites with vanadium carbide. Scripta Mater. **59**, 309–312, 2008.
26. Guo W-M., Zhang G-J., Kan Y-M., Wang P-L., Effect of Yb_2O_3 addition on hot pressed ZrB_2-SiC ceramics, Adv. Eng. Mater. **10**, 559–762, 2008.
27. Meng S., Liu G., An J., Sun S., Effects of different additives on microstructure and crack resistance for an ultra-high temperature ceramic, Int. J. Refr. Met.Hard Mater. **27**, 813–816, 2009.
28. Zhang S. C., Hilmas G. E., Fahrenholtz W. G., Pressureless sintering of ZrB_2-SiC ceramics, J. Amer. Ceram. Soc. **91**, 26–32, 2008.
29. Zhang G-J., Deng Z-Y., Yang J-F., and Ohji T., Reactive hot pressing of ZrB_2-SiC composites, *J. Am. Ceram. Soc.*, **83**, 2330–2332, 2000.
30. Goldstein A., Geffen Y., and Goldenberg A., Boron carbide-zirconium boride in-situ composites by the reactive pressureless sintering of boron carbide-zirconia mixtures", *J. Am. Ceram. Soc.*, **84**, 642–644 (2001)
31. Blum Y. D., and Kleebe H.-J,. Chemical reactivities of hafnium and its derived boride, carbide and nitride compounds at relatively mild temperature, *J. Mat. Sci.*, **39**, 6023–6042, 2004.
32. Wu W-W., Zhang G-.J., Kann Y-M., Wang P-L., Reactive hot pressing of ZrB_2-SiC-ZrC composites at 1600°C. J. Am. Ceram. Soc. **91**, 2501–2508.
33. Wu W-W., V, Kan Y-M., Wang P-L., ZrB_2-$MoSi_2$ composites toughened by elongated ZrB_2 grains via reactive hot pressing. Scripta Mater. **61**, 316–319, 2009.
34. Guo W-M., Zhang G-J., Reaction Process and Characterization of ZrB_2 powder prepared by boro/carbothermal reduction of ZrO_2 in vacuum. J. Am. Ceram. Soc. **92**, (2009) 264–267.
35. Forsthoefel K. and Sneddon L.G., Precursor routes to group 4 metal borides, and metal boride/carbide and metal boride/nitride composites, *J. Mat. Sci.*, **39**, 6043–6049, 2004.
36. Sacks M. D., Wang C. A., Yang Z. and Jain A., Carbothermal reduction synthesis of nanocrystalline zirconium carbide and hafnium carbide powders using solution-derived precursors, *J. Mater. Sci.*, **39**, 6057–6066, 2004.
37. Schwab S. T., Stewart C. A., Ducdeck K. W,. Kozmina S. M, Katz J. D., Bartram B., Wuchina E. J., Kroenke W. J., and G. Courtin, Polymeric precursors to refractory metal borides", *J. Mater. Sci.*, **39**, 6051–6055, 2004.
38. Yen K., Xray diffraction study of mechanochemical synthesis and formation mechanisms of zirconium carbide and zirconium silicides, *J. Alloys & Compounds.*, **286**, 266–269, 1998.
39. Bhanumurthy K., and Schmid-Fetzer R., Interface reactions between SiC/Zr and development of zirconium base composites by in-situ solid state reactions", *Scripta Materialia.*, **45**, 547–553, 200.
40. Brochu M., Gauntt B., Zimmerly T., Ayala A., Loehman R., Fabrication of UHTCs by conversion of dynamically consolidated Zr+B and Hf+B powder mixtures., J. Am. Ceram Soc. 91, 2815–2822, 2008.
41. Spring A., G. W-M., Zhang G-J., Wang P-L., Krstic V. D., Fabrication and characterization of ZrB2-based ceramics using synthesized ZrB_2-LaB_6 powder" J. Am. Ceram. Soc. **91**, 2763–2765, 2008.

42. Nygren M., and Shen Z., Novel assemblies via spark plasma sintering, *Silicates Indust. Special Issue,* **69** (7-8), 211–218, 2004.
43. Sciti D., Silvestroni L., Bellosi A., Fabrication and properties of HfB_2–$MoSi_2$ Composites produced by hot pressing, pressureless sintering and spark plasma sintering., J. Mater. Res. **21**, 1460–1466, 2006.
44. Tokita M., Development of large size ceramic/metal bulk FGM fabricated by spark plasma sintering", p.83-89, in Materials Science Forum, Vol. 308-311, *Proceedings of the 5th Intern. Symposium on Functionally Graded Materials*. Edited by.. Kaysser W. A. Trans Tech Publications Ltd., Aerdermannsdorf, Switzerland, 1999.
45. Khor K. A,. Cheng K. H, Yu L. G., and Boey F., Thermal conductivity and dielectric constant of spark plasma sintered aluminium nitride, *Mat. Sci Eng.* A**, 347**, 300–305, 2003.
46. Feng P., Xiong W., Yu L., Zheng Y., and Xia Y., Phase evolution and microstructure characteristics of ultrafine Ti(C,N)-based cermet by spark plasma sintering, *Intern. J. Refr. Met. & Hard Mat*., **22**, 133–138, 2004.
47. Shen Z., Johnsson M., and Nygren M., TiN/Al_2O_3 composites and graded laminates thereof consolidated by spark plasma sintering, *J. Europ. Ceram Soc.*, **23**, 1061–1068, 2003.
48. Fox, K. M., Hellmann R. J., Izui H., Amateau M. F., Fu W., and Coen P.H, Properties and performance of spark plasma laminated WC-Co cutting tools, *J. Ceram. Proc. Res*., **5**, 18–24, 2004.
49. Perera D. S., Tokita M., and Moricca S., Comparative study of fabrication of Si_3N_4/SiC composites by spark plasma sintering and hot isostatic pressing, *J. Europ. Ceram. Soc.*, **18**, 401–404, 1998.
50. Shim S. H., Niihara K., Auh K. H., and. Shim B, Crystallographic orientation of ZrB_2-ZrC composites manufactured by the spark plasma sintering method, *J. of Microscopy*, **205**, 238–244, 2002.
51. Kim K.H.,and Shim K.B., The effect of lanthanum on the fabrication of ZrB_2–ZrC composites by spark plasma sintering, *Mater. Charact.*, **50**, 31–37, 2003.
52. Medri V., Monteverde F., Balbo A., and Bellosi A., Comparison of ZrB_2-ZrC-SiC composites fabricated by spark plasma sintering and hot pressing", *Adv. Eng. Mater.*, **7**, 159–163, 2005.
53. Bellosi A., Monteverde F., and Sciti D., Fast densification of ultra-high temperature ceramics by spark plasma sintering", *Int. J. Applied Ceram. Technol.*, **3**, 32–40, 2006.
54. Licheri R., Orrù R., Musa C., Locci M. A., Cao G., Consolidation via spark plasma sintering of HfB_2-SiC and HfB_2-HfC-SiC composite powders by self propagating hugh temperature synthesis., J. Alloys and Comp. **478**, 572–578, 2009.
55. Sciti D., Guicciardi S., Nygren M., Densification and mechanical behaviour of HfC and HfB_2 fabricated by Spark Plasma Sintering , J. Amer. Ceram. Soc. **91**, 1433–1440, 2008.
56. Sciti D., Silvestroni L., Nygren M., Spark plasma sintering of Zr- and Hf-borides with decreasing amounts of $MoSi_2$ as sintering aid. J. Europ. Ceram Soc. **28**, 1287–1296, 2008.
57. Balbo A., Sciti D., Spark plasma sintering and hot pressing of ZrB_2-$MoSi_2$ ultra-high temperature ceramics, Mater. Sci. Eng., A**., 475,** 108–112, 2008.
58. Zhao Y., C, Jiang W., Chen L-D., Effect of holding time and pressure on properties of ZrB_2-SiC composite fabricated by the spark plasma sintering reactive synthesis method. Int. J. Refr. Met&Hard Mater., **27**, 177–180, 2009.
59. Guo S-Q., Kagawa Y., Nishimura T., Mechanical Behaviour of two step hot pressed ZrB_2-based composites with $ZrSi_2$. J. Europ. Ceram. Soc. **29**, 787–794, 2009.
60. Sciti D., Silvestroni L., Celotti G., Melandri C., Guicciardi S., Sintering and mechanical properties of ZrB_2-$TaSi_2$ and HfB_2-$TaSi_2$ ceramic composites, J. Am. Ceram. Sic. **91**, 3285–3291, 2008.

61. Monteverde F., and Bellosi A., The resistance to oxidation of an HfB_2-SiC composite, *J. Europ. Ceram. Soc.*, **25**, 1025–1031, 2005.
62. Guo S., Kagawa Y., Nishimura T., Tanaka H., Elastic properties of spark plasma sintered ZrB_2-ZrC-SiC composites. Ceram. Int. **34**, 1811–1817, 2008.
63. Yang F., Zhang X., Han J. Du S., Characterization of hot pressed short carbon fiber reinforced ZrB_2-SiC ultra-high temperature ceramic composites, J. Alloys and Comp. 2008.
64. Du S., Xu L., Zhang X., Hu P., Han W. Effect of sintering temperature and holding time on the microstructure and mechanical properties of ZrB_2-SiCw composites., Mat. Chem and Phys. 116, 76–80, 2009.
65. Zhang X., Xu L., Han W., Weng L., Han L., Du S., Microstructure and properties of silicon carbide whiskers reinforced zirconium diboride ultra-high temperature ceramics. Solid St. Sci. **11**, 156–161, 2009.
66. Yang F., Zhang X., Han J., Du S., Processing and mechanical properties of short carbon fibers toughened zirconium diboride-based ceramics. Mater. And Design **29**, 1817–1820, 2008.
67. Zhu T., Xu L., Zhang X., Han W., Hu P., Weng L., Densification, microstructure and mechanical properties of ZrB_2-SiCw ceramic composites, J. Europ. Ceram. Soc. **29**, 2893–2901, 2009.
68. Yang F., Zhang X., Han J., Du S., Characterization of hot pressed short carbon fiber reinforced ZrB2-SiC ultra-high temperature ceramic composites. J. Alloys and Comp. **472**, 395–399, 2009.
69. Zhang P., Hu P., Zhang X., Han J., Meng S., Processing and characterization of ZrB_2-SiCw ultra-high temperature ceramics. J. Alloys and Comp. **472**, 358–362, 2009.
70. Zhang X., Wang Z., Sun X., Han W., Hong C., Thermal shock behaviour of ZrB_2-20vol%SiC-15vol%graphite flake by hot pressing, Int. J. Modern Phys. B., **23**, 1160–1165 (2009).
71. Weng L., Zhang X., Han W., Han J. , Fabrication and evaluation on thermal stability of hafnium diboride matrix composites at severe oxidation conditions" J. Refr. Metals Hard mat. **27**, 711–717, 2009.
72. Zhang X., Weng L., Han J., Meng S., Han W, Preparation and Thermal Ablation behaviour of HfB_2-SiC-based Ultra-High-Temperature Ceramics under severe heat conditions, Int. J. Appl. Ceram. Technol. **6**, 134–144, 2009.
73. Mitra R., Upender S., Mallik M., Chakraborty S., Ray K. K., Mechanical, Thermal and oxidation behaviour of zirconium diboride based ultra-high temperature ceramic composites, Key Emg. Materials, 395, 55–68, 2009.
74. Zhang H., Yan Y., Huang Z., Liu X., Jang D., Properties of ZrB_2-SiC ceramics by pressureless sintering, J. Am. Ceram. Soc. **92**, 1599–1602, 2009-10-26.
75. Li W., Zhang X., Hong C., Han W., Han W., Han J., Preparation, microstructure and properties of ZrB_2-ZrO_2 ceramics, J. Europ. Ceram. Soc. **29**, 779–786, 2009.
76. Zimmermann J. W., Hilmas G. E., Fahrenholtz W. G., Thermal shock resistance of ZrB_2 and ZrB_2-30%SiC, Mater. Chem and Phys. **112**, 140–145, 2008.
77. D. Sciti, M. Brach and A. Bellosi, "Oxidation behaviour of a pressureless sintered ZrB_2-$MoSi_2$ ceramic composite", *J. Mater. Res*., **20**, 922–930, 2005.
78. Sciti D., Brach M., and Bellosi A., Long term oxidation behaviour and mechanical strength degradation of a pressureless sintered ZrB_2-$MoSi_2$ composite, *Scripta Materialia*, **53**, 1297–1302, 2005.
79. Carney C., Oxidation resistance of hafnium diboride-silicon carbide from 1400 to 2000°C, J. Mater. Sci **44**, 5673–5681, 2009.
80. Zou J., Zhang G-J., Kan Y-M., Formation of tough interlocking microstructure in ZrB_2-SiC – based ultrahigh-temperature ceramics by pressureless sintering, J. Mater. Res. **24**, 2428–2434, 2009.

81. Talmy I., Zaykoski J. A., Opeka M. M., High temperature chemistry and oxidation of ZrB_2 Ceramics containing SiC, Si_3N_4, Ta_5Si_3 and $TaSi_2$. J. Am. Ceram. Soc. **91**, 2250–2257, 2008.
82. Zhang S. C., Hilmas G. E., Fahrenholtz W. G. Improved oxidation resistance of zirconium diboride by tungsten carbide additions, J. Am. Ceram. Soc. 2008.
83. Ni D-W., Zhang G-J., Kan Y-M., Sakka Y., Textured HfB_2-based ultrahigh temperature ceramics with anisotropic oxidation behaviour, Scripta Mater. **60**, 913–916, 2009.
84. Ni D-W., Zhang G-J., Kan Y-M., Sakka Y., Highly Textured HfB_2 based ultrahigh temperature ceramics with strong magnetic field alignment, Scripta Mater. **60**, 615–618, 2009.
85. Monteverde F. and Bellosi A., Microstructure and properties of HfB_2-SiC composite for ultra-high temperature applications", *Adv. Eng. Mater*., **6**, 331–336, 2004
86. Monteverde F., Beneficial effects of an ultra-fine α-SiC incorporation on the sinterability and mechanical properties of ZrB_2-SiC, *Appl.Physics A,* **82***,* 329–337, 2006.
87. Opila E., Levine S., and Lorincz J., Oxidation of ZrB_2- and HfB_2-based ultra-high temperature ceramics: effects of Ta additions, *J. Mat. Sci.*, **39**, 5969–5977, 2004.
88. Tripp W.C., Davis H.H., and Graham H.C., Effects of an SiC Addition on the Oxidation of ZrB_2, *Ceram Bull.*, **52**(8), 612–616, 1973.
89. Monteverde F., and Bellosi A., Oxidation of ZrB_2-based ceramics in dry air, *J. Electr. Soc*., **150**, B552–B559, 2003.
90. Chamberlain A.L., Fahrenholtz W.G., Hilmas G.E., and Ellerby D.T., High strength zirconium diboride-based ceramics, *J. Am. Ceram. Soc.*, **87**, 1170–1172, 2004.
91. Bargeron C. B, Benson R. C., Newman R. W., Jette A. N., and Phillips T. E., Oxidation mechanisms of hafnium carbide and hafnium diboride in the temperature range 1400 to 2100°C, *John Hopkins APL Technical Digest*, **14**[1], 29–35, 1993.
92. Marschall J., Chamberlain A., Crunkleton D., and Rogers B., Catalytic atom recombination on ZrB_2-SiC and HfB_2-SiC ultra-high-temperature ceramic composites, *J. Spacecraft and Rockets*, **41**, 576–581, 2004.
93. Nguyen Q. N, Opila E. J, and. Robinson R. C, Oxidation of ultra-high temperature ceramics in water vapour, *J. Electroch. Soc.*, **151**, B558–B562, 2004.
94. Monteverde F., and Bellosi A., Development and characterization of metal diboride based composites toughened with ultrafine SiC particles", *Solid State Sci.*, **7**, 622–630, 2005.
95. Gasch M., Ellerby D., Irby E., Beckman S., Gusman M. and Johnson S., Processing, properties and arc-jet oxidation of hafnium diboride/silicon carbide ultra-high temperature ceramics, *J. Mat. Sci.*, **39**, 5925–5937, 2004.
96. Savino R., De Stefano Fumo M., Silvestroni L., Sciti D. Arc Jet testing on HfB_2 and HfC-based ultra-high temperature ceramic materials. J. Europ. Ceram. Soc. **28**, 1899–1907, 2008.
97. Monteverde F., Savino R. Stability of ultra-high temperature ZrB_2-SiC ceramics under simulated reentry conditions. J. Europ. Ceram Soc. **27**, 4797–4805, 2007.
98. Silvestroni L., Kleebe H.J., Lauterbach S., Müller M., Sciti D., Transmission electron microscopy on Zr- and Hf-borides with $MoSi_2$ addition: densification mechanisms, accepted to J. of Mater. Research, **25**, N. 5, 828–834, 2010.

BEHAVIOR OF BORON DOPED GRAPHITES AND BORON CARBIDE UNDER ION BEAM AND PLASMA IRRADIATION

L. B. BEGRAMBEKOV[1,*], O. I. BUZHINSKY[2], A. ZAKHAROV[1]
[1]*National Research Nuclear University MEPhI, Moscow, Russia*
[2]*Troitsk Institute for Innovations and Fusion Research, Troitsk, 142190, R.F*

Abstract The paper shortly describes the methods of boron carbide coating deposition and presents the experimental results characterizing the properties of boron carbide coatings and of boron doped graphites important to their application as the plasma facing materials of fusion devices and other plasma apparatus dealing with dense and high temperature plasma. Conclusion is made that thick renewable boron carbide coating can successfully be used as the protecting coating of plasma facing elements of ITER.

Keywords: boron carbide, boron doped graphites, ion, plasma, irradiation

1. Introduction. Graphites and Carbon-Based Materials in Fusion Devices

Graphites of different types, carbon materials and coatings have been widely used during several last decades as plasma facing materials in fusion devices. Application of graphites and carbon films as the plasma facing elements of first walls, limiters and divertors ensured an essential decrease in plasma impurities, and allowed the main plasma parameters in tokamaks to be essentially improved [1].

However, as the plasma parameters (density, temperature, and discharge duration) improved the drawbacks of pure carbon materials appeared, which was a serious obstacle for further advancement of the tokamak performance. The chemical sputtering and radiation enhanced sublimation in the high-temperature region caused an accelerated erosion of graphite surface and a

* L.B. Begrambekov, National Research Nuclear University MEPhI, Moscow, Russia, e-mail: lbb@plasma.mephi.ru

N. Orlovskaya and M. Lugovy (eds.), *Boron Rich Solids: Sensors, Ultra High Temperature Ceramics, Thermoelectrics, Armor*, DOI 10.1007/978-90-481-9818-4_11,

carbon influx into the plasma of tokamak. Graphites, redeposited carbon layers and graphite dust retained a significant amount of hydrogen, causing a high level of hydrogen recycling. The oxygen concentration in the plasma remained very high, which is unacceptable. Cracking and peeling of graphite tile surfaces and emission of microscopic particles into the plasma occurred as a result of low thermal conductivity and brittleness of pure bulk graphites.

Further essential improvement of the plasma performance was because boronization, that is, in-situ plasma chemical vapor deposition of a thin amorphous boron–carbon film [2, 3]. Due to boronization, the chemical sputtering and high temperature erosion were suppressed; the concentration of carbon, metal and oxygen impurities in the plasma decreased.

Unfortunately, further increase in the plasma density and discharge duration reduced the aforementioned effect. The boron–carbon layer deposited in many-hours glow discharge does not usually exceed approximately 100 nm [4], and is sputtered away after several tens of discharges.

Boron carbide and boron doped graphites are devoid of these disadvantages. That is why the efforts were spent for working out the technologies of boron carbide coating deposition and fabrication of different types of boron doped graphites.

The properties of newly prepared materials were tested in different laboratories. The attention was focused on capacity of hydrogen retention, parameters of their erosion under particle irradiation at high temperatures, ability to withstand the particle fluxes with high energy density, erosion and modification due to interaction with oxygen gas and oxygen contaminated plasma.

The paper shortly describes the methods of boron carbide coating deposition and presents the experimental results characterized the properties of boron carbide coatings and of boron doped graphites important to their application as the plasma facing materials of fusion devices and other plasma apparatuses dealing with dense and high temperature plasma.

2. Crystalline Boron Carbide Coating

2.1. PRODUCTION METHODS [5]

Boron carbide (B_4C) is produced as a coating on different types of graphites and metals. Various methods of B_4C production are developed [5]. Among them are gas conversion technique, plasma spray technique, reaction sintering, chemical vapor deposition by means of chloride and fluoride techniques, plasma chemical deposition.

2.1.1. *Gas Conversion Technique*

The coating is produced by a reaction of gaseous B_2O_3 with carbon of substrate $2\ B_2O_3 + 7C \rightarrow B_4C + 6CO$ at high temperatures (≈2,000°C). Boron carbide layer is formed directly inside the substrate by means of penetration the gas into its open pores. The thickness of the layer can amount to 1,700 μm and can be nonuniform. The structure is two phase: B_4C and graphite. Exfoliation of such a layer is not occurred under high heat flux irradiation. The coating may content many micro pores because of removal of carbon atoms during conversion reaction.

2.1.2. *Plasma Spray Technique*

B_4C powder (with particles of some micrometer to some tens micrometers in size) is placed into a plasma gun with the Laval nozzle. The partly melted partly overheated particles impinge a substrate, flatten and form a coating. The method produces single phase (B_4C) coating.

The mixture of substrate material and B_4C is used to produce an intermediate layer. It allows avoiding of stresses at the surface and detachment of coating as a result of strong difference in thermal expansion coefficients between the coating and substrate. The porosity depends on the chamber pressure and can be lowered down to 8%.

The method enables the renewal of the coating in situ.

2.1.3. *Reaction Sintering*

Coating is produced by brush-on technique with the use of powdered boride and carbide refractory compounds (e.g. B_4C) and an organic binder. The reaction is conducted under high temperatures (≈2,400°C) and is a combination both of substrate carbon (and a binder carbon) reacting with refractory compounds and of sintering of the boride and/or carbide particles. The coating consists of two layers: a surface layer and a graded penetration zone in the outer portion of a substrate. The surface layer microstructure is multiphase and range from reaction-sintered structures of sintered B_4C particles in an eutectic formed matrix to that of hypereutectic carbon particles in a B_4C–C eutectic matrix. Because of high surface energy, the coating generally develops a nonuniform thickness and topography.

2.1.4. *Chemical Vapor Deposition*

Chemical vapor deposition technique with use of BCl_3 (chloride technique) of BF_3 (fluoride technique) were used.

Fluoride technique is presented below, since it provides the coating with better parameters. The technique is realized through the method of transport

reactions. A mixture consisting of grains of crystalline boron pellets of amorphous boron or boron nitride wastes is placed into the hottest region of two chamber reactor where the temperature ranges from 1,800 to 1,900°C. Gaseous boron fluoride filters through the mixture producing the lower fluorides by the reactions:

$2BF_3 + B_4C \rightarrow 6BF + C$, $8BF_3 + B_4C \rightarrow 12BF_2 + C$,

$BF_3 + 2B \rightarrow 3BF$, $2BF_3 + 2B \rightarrow 6BF$,

$2BF_3 + 4BN \rightarrow 6BF + 2N_2$, $2BF_3 + BN \rightarrow 3BF_2 + 1/2N_2$.

The coating deposition process consists of two stages. The first one involves reactions producing high activity boron on the substrate surface:

$3BF_2 \rightarrow B + 2BF_3$, $3BF \rightarrow 2B + BF_3$.

The second is an interaction of this boron with carbon of the substrate to form a boron carbide $4B + C \rightarrow B_4C$.

The temperature of the substrate is ≈150°C lower than that of reaction chamber. In this system the partial pressure of boron vapor in a gas phase is lower than the equilibrium boron vapor partial pressure at a solid boron surface but higher than that at a solid boron carbide surface, so that the crystalline boron carbide is the only solid phase possible at temperature sufficient for the reaction of boron vapor with carbon.

The fine grain crystalline coating consisting of B_4C–$B_{13}C_2$ phase of rombohedral boron carbide is deposited.

The deposition rate is 100–150 μm/h. Coating thickness is in the range 100–150 μm.

Due to diffusive character of coating formation and its nonstoichiometric phases, adhesion to substrate is very high.

2.1.5. *Plasma Chemical Deposition*

The methods described above could not be used for coating deposition on plasma facing elements of fusion devices because the procedures need long-term interruption of device operation. The principal advantage of plasma chemical deposition technique is formation of boron carbide coating directly in regular discharges of plasma devices. In [6] deposition was made in plasma with electron temperature ≥30–40 eV. The plasma is fed with vapor of a substance having boron and carbon as the components. The authors of [6] have used carborane ($C_4B_{10}H_{12}$) as the initial substance. It is non-toxic, non-hazardous, non-explosive and relatively cheap compound. The carborane molecules were dissociated in plasma. Boron and carbon atoms were deposited on the substrate forming boron carbide coating. The ratio of B/C in the deposition was found to be 3.0–3.6. Film growth rate

was extremely high – up to 30 nm/s. The coating had a good adhesion to the substrate and high strength.

The authors of [7] got the conclusion that such a high growth rate and close to stoichiometric composition are the result of high degree of carborane ionization and dissociation in the plasma with sufficiently high density and electron temperature and thus, the plasmas of modern fusion devices are perfectly suited to deposition of thick crystalline boron carbide coating.

2.2. PROPERTIES OF CRYSTALLINE BORON CARBIDE AS A PLASMA FACING COMPONENT OF PLASMA DEVICES

2.2.1. *Erosion Under Hydrogen Ion Irradiation*

Temperature dependence of B_4C erosion yield is presented in (Fig. 1) [8]. Chemical sputtering of B_4C is suppressed strongly. Bellow the temperature $T \approx 1{,}100$ K surface erosion occurs mainly through mechanism of cascade (physical) sputtering. Above this temperature boron diffusion from the bulk to the surface is activated, and preferential sputtering of boron atoms occurs through mechanism of ion stimulated desorption. At the same time, in the temperature range $1{,}100 \leq T \leq 1{,}500$°C oxidation of ion irradiated surface and boron oxycarbide formation take place. Nevertheless, the process of radiation-enhanced sublimation is not activated up to 1,600 K. Thus, the erosion rate of B_4C only slightly changes over a wide temperature range and

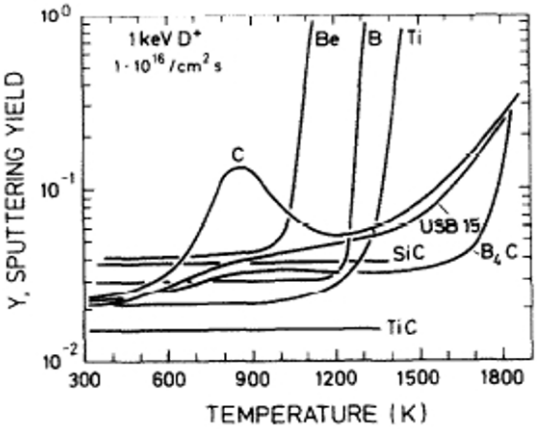

Figure 1. Temperature dependence of B_4C erosion yield due to 1 keV D+ sputtering in comparison with various materials used in plasma devices [8].

appears to be much less than the erosion rate of dense graphites under similar irradiation conditions. Only above T ≈ 1,800 K ion induced decomposition of B_4C and mechanism of radiation enhanced sublimation course acceleration of B_4C erosion.

The sputtering yield of boron carbide in the oxygen contaminated plasma was shown to be much smaller than that of pure graphite in the range of moderate temperatures. The difference decreased, but became significant even at the temperature 1,300°C (see Table 1).

TABLE 1. The temperature of boron carbide coating on MPG-8 and RGT graphites subjected to electron beam irradiation in dependence on heat flux [11]

Heat flux (MW/m^2)	Duration of single irradiation cycle (s)	Number of cycles	T_{max} (^0C)	
			MPG-8	RGT
2.0	5	20	<300	<300
2.3	5	20		
5.0	2.5	10	430	<300
5.8	2.5	10		
5.0	10	10	940	790
5.8	10	10		
10.0	2	2	>1400	
11.0	5	5		**880**
13.0	5	5		**940**

2.2.2. *Hydrogen Retention in B_4C Under Ion Irradiation*

Hydrogen retention in B_4C under high-dose implantation is low in comparison with dense graphites and carbon fiber composite (CFC). The difference increases with irradiation doses because of the saturation of hydrogen retention in B_4C at a dose of approximately 10^{23} at/m^2 (Fig. 2) [9]. Saturation of retention showed that the rate of hydrogen diffusion and trapping in the bulk regions of graphite became equal to the rate of hydrogen removal from the sputtered away surface layers. Reaching saturation of boron carbide at the smaller doses than that of graphite allows concluding that hydrogen diffusion rate in boron carbide is lower than in graphites.

Retention of oxygen in the boron carbide under irradiation in oxygen contaminated plasma was also smaller than in graphite. This effect was explained by formation of the surface B_2O_3 layer acting as the barrier for oxygen diffusion into the bulk [10].

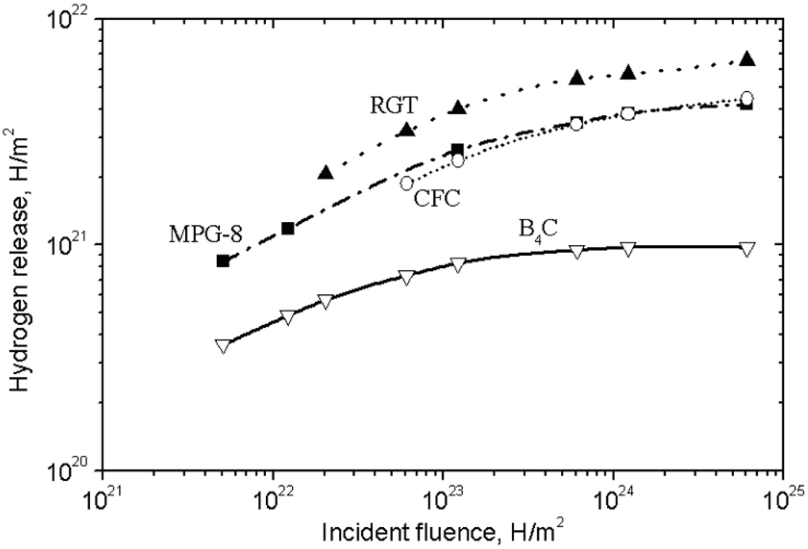

Figure 2. Temperature dependence of hydrogen retention for different materials (H^+, E_i=10 keV, j=5.6×10^{19} m^{-2}) [9].

2.2.3. *Behavior of B_4C Coating Under High Heat Loads*

The boron carbide has a relatively low thermal conductivity; however, it withstands high heat loads without remarkable damages when used as a protecting coating deposited on the graphite with a high thermal conductivity [11]. Table 1 presents the results of irradiation of a boron carbide coating of thickness 100 μm deposited on fine grain isotropic graphite MPG-8 (thermal conductivity ≈ 45 W/mK at 1,100 K) and thermorecrystallized RGT type graphite (C+TiC 15% mass.) (thermal conductivity ≈200 W/mK at 1,100 K) carried out on the electron beam facility at Sandia Laboratory [11]. It can be seen that the temperature of the boron carbide deposited on high thermal conductive RGT graphite remained in the range of low erosion rate (see Fig. 1) even when the heat load was 11.0–13.0 MW/m^2 in contrast to that of MPG-8 graphite. The coating on RGT graphite showed an excellent durability. No cracks, flacks or peels were found on the irradiated surface.

2.2.4. *Composition and Properties of α–H:B–C Layers Redeposited in Plasma Devices Due to B_4C Film Erosion*

Erosion of B_4C films in hydrogen plasma leads to redeposition of components in the shadowing areas and onto the surfaces not subjected to intensive plasma irradiation. The experiments showed that as a result of such a redeposition the α–H:B–C layers are formed. B/C ratio in the layers

appears to be in the range 0.22–0.45. The layers are thermally unstable, and could be easily sputtered away by irradiation of plasma ions. Hence, one can avoid an accumulation of products of B_4C destruction in plasma devices.

2.2.5. *Boron Carbide Layer as a Protective Coating of Plasma Facing Elements of Plasma Devices*

Consideration of the properties of boron carbide coating shows that it can be successfully used as the long-term renewable protective coating of plasma facing components of fusion devices and other plasma apparatuses dealing with dense and high temperature plasma.

"Thick" boron carbide coating with the parameters close to the parameters of stoichiometric B_4C could be deposited (renewed) directly during regular tokamak discharges. The coating ensures a small erosion rate in wide temperature range, low impurity influx into the plasma, small hydrogen recycling. When deposited on the graphites, CFC or metals with high thermal conductivity, it withstands high heat loads without remarkable damages. Erosion of B_4C films in hydrogen plasma leads to redeposition of its components in form of α–H:B–C layers, which are thermally unstable and can be easily sputtered away by irradiation of plasma ions. Hence, one can avoid an accumulation of products of B_4C destruction in plasma devices.

3. Boron Doped Graphites and Carbon Fiber Composites

Outstanding properties of boron carbide coating as a plasma facing material impels number of scientific and technology teams all over the world to create the bulk material with the similar properties. First of all one can speak about low sputtering rate, low hydrogen and oxygen recycling. Different methods of boron introducing into graphites were used. Graphites of different types doped with boron up to concentration of some tens percents were developed and tested as the plasma facing materials.

3.1. STRUCTURE OF BORON DOPED GRAPHITES

The graphite matrix can dissolved not more than 1–1.5% of boron atoms (Fig. 3a). Remaining fraction of boron atoms introduced in graphite is accumulated in boron carbide precipitates with overall dimensions usually ranged between 0.1 and 5 μm (Fig. 3b). The main fraction of boron carbide precipitates is concentrated along the grain boundaries (Fig. 3c).

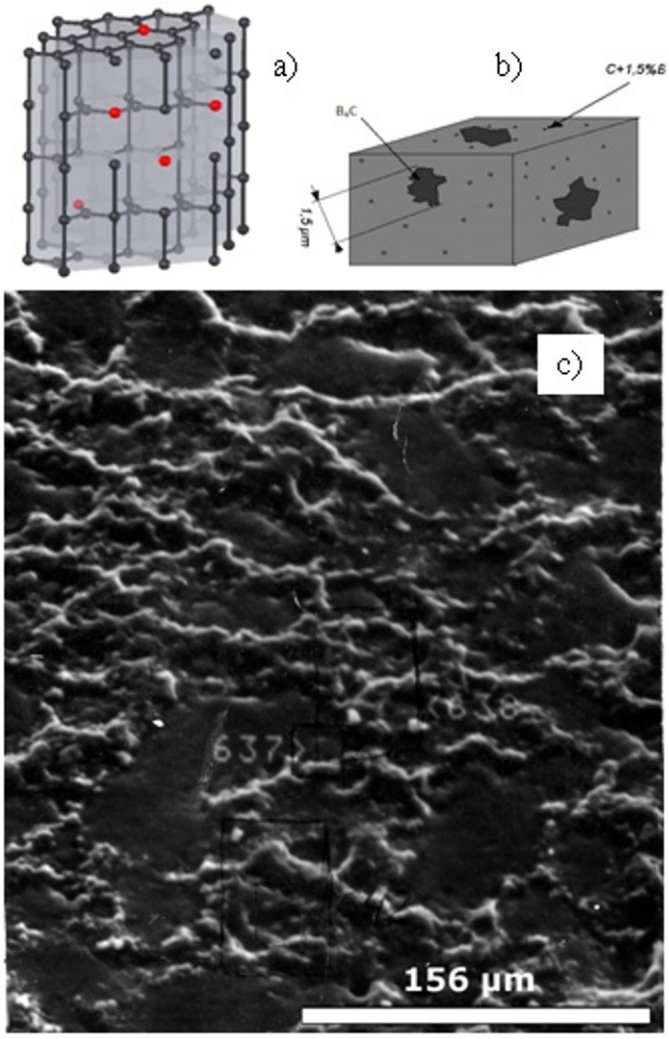

Figure 3. Boron doped graphites. (**a**) graphite lattice with dissolved boron, (**b**) boron carbide precipitate in graphite matrix, (**c**) concentration of boron carbide precipitates at the grain boundaries of boron doped graphite RUM-40 (C+B40%at.) (Russia).

3.2. EROSION AND MODIFICATION OF BORON DOPED GRAPHITES UNDER PLASMA IRRADIATION

In terms of structure modifications and surface erosion the boron doped graphites could be divided in two groups. There is graphites with low boron doping – LBG (boron concentration ≤10% at.) and with high boron doping – HBG (boron concentration ≥10% at.). The boron dopants do not influence remarkably the sputtering rate (at least, when boron concentration is not higher than 40% at.) at the low and moderate temperatures, i.e., up to the

temperatures of hundreds of centigrades, when boron diffusion becomes active (Fig. 4). In such conditions a sputtering of B_4C precipitates on the irradiated surface does not compensate by diffusion from the bulk, and sputtering of graphite matrix does not influenced by presence of boron dopant.

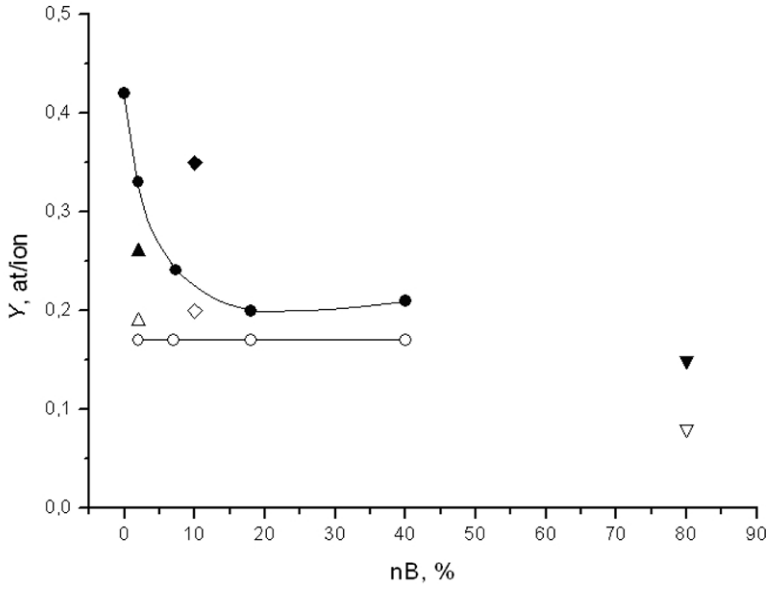

Figure 4. Sputtering yield of boron carbide and boron doped graphites in dependence of boron concentration (He^+, 850 eV) (○ – RUM, 500°C, ● – RUM, 1,300°C Δ – RGB, 500°C,▲ – RGB, 1,300°C, ◊ – GB-110, 500°C, ♦ – GB-110 (C + B10%at) (Japan), 1,300°C, ▽ – B_4C, 500°C, ▼ - B_4C, 1,300°C).

As a result, the sputtering yield of graphites of both groups and of non doped graphites appeared to be closely allied.

Diffusion of dissolved boron to the surface activates in the temperature range 800–900°C. Boron diffusion from boron carbide precipitates starts at significantly higher temperatures (≥1,200°C). Boron atoms reaching surface form boron carbide- and boron oxycarbide precipitates. Concentration of these newly formed precipitates on the surface grows along with temperature growth. They form round projections with dimensions from 0.1 to 1 μm. The number of the projections with higher dimensions was larger at graphites with larger concentration of boron.

On the HBG numerous projections cover main part of the surface (Fig. 5) and prevent an elevation of erosion rate through mechanism of radiation enhanced sublimation under high temperature irradiation. Thus, erosion rate of HBG stays almost unchanged up to 1,300–1,400°C.

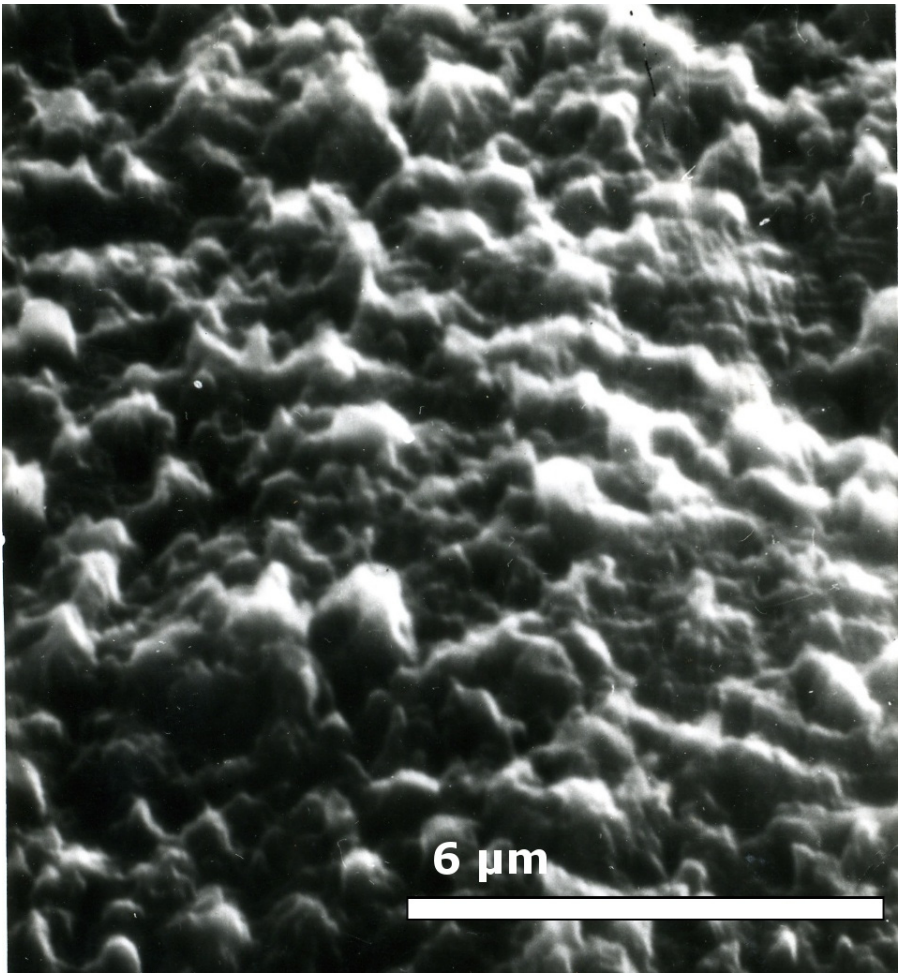

Figure 5. New boron contained precipitates on the surface of RUM type graphite (C + B40% at.) (He^+, 800 eV, T = 1,300°C).

Above these temperatures the probability of boron atom removal from the surface is superior to the probability of new B–C bond formation. As a result, boron contained protecting layer is not formed, and surface erosion starts to grow in agreement with peculiarities of erosion of pure graphite.

Boron concentration in LBG is not enough for formation of intensive diffusion flow of boron atoms to the surface during high temperature ion irradiation. Thus, the surface protecting layer is not appeared, and above temperature 800–900°C erosion rate starts to grow similarly to that of pure graphite.

Diffusion of dissolved boron in the range of high temperatures leads to specific modification of the structure of boron doped graphites. Graphite

grains exfoliate as it is seen on the surface of LBG graphite of RGB type (C + B_3% at.) (Fig. 6). One can believe that similar stratification takes place in HBG, but is hidden by projections described above.

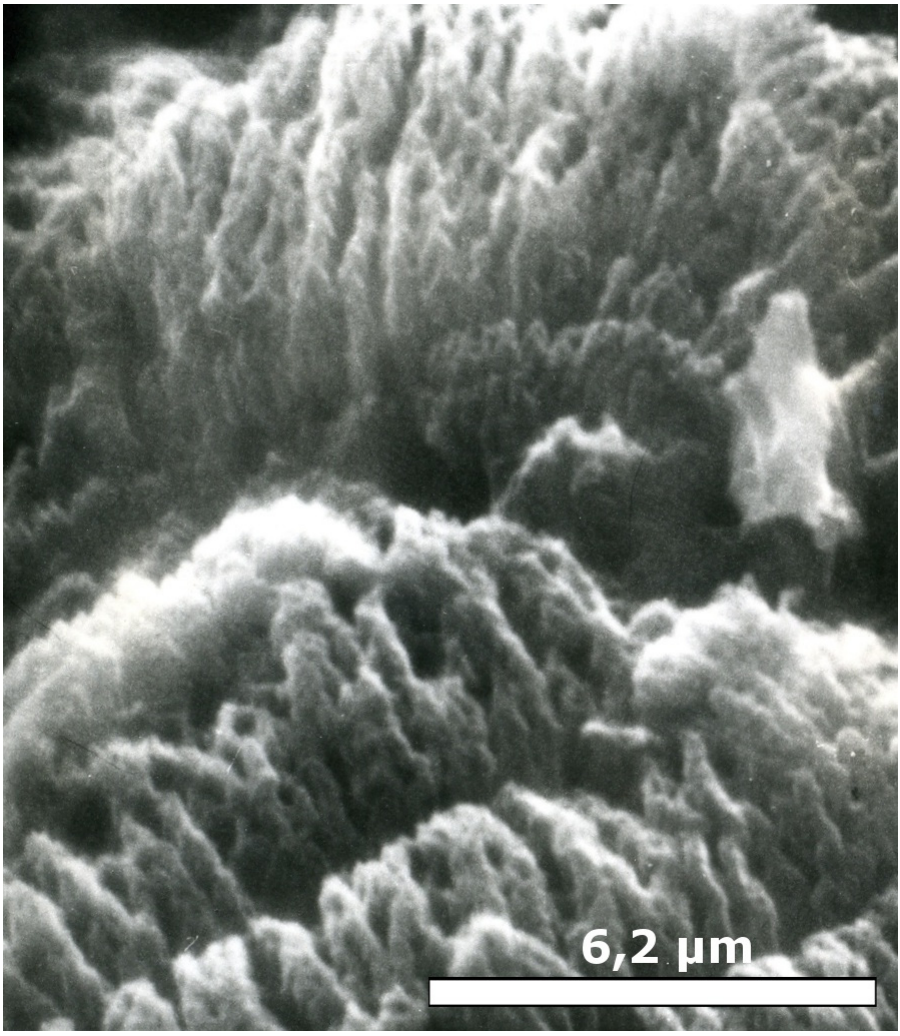

Figure 6. The exfoliation of RGB type graphite. (He^+, 800 eV, T = 1,300°C).

Stratification of graphite matrix under ion irradiation was also registered in RGT type graphite, when boron with concentration 1% at. was dissolved in graphite matrix (Fig. 7).

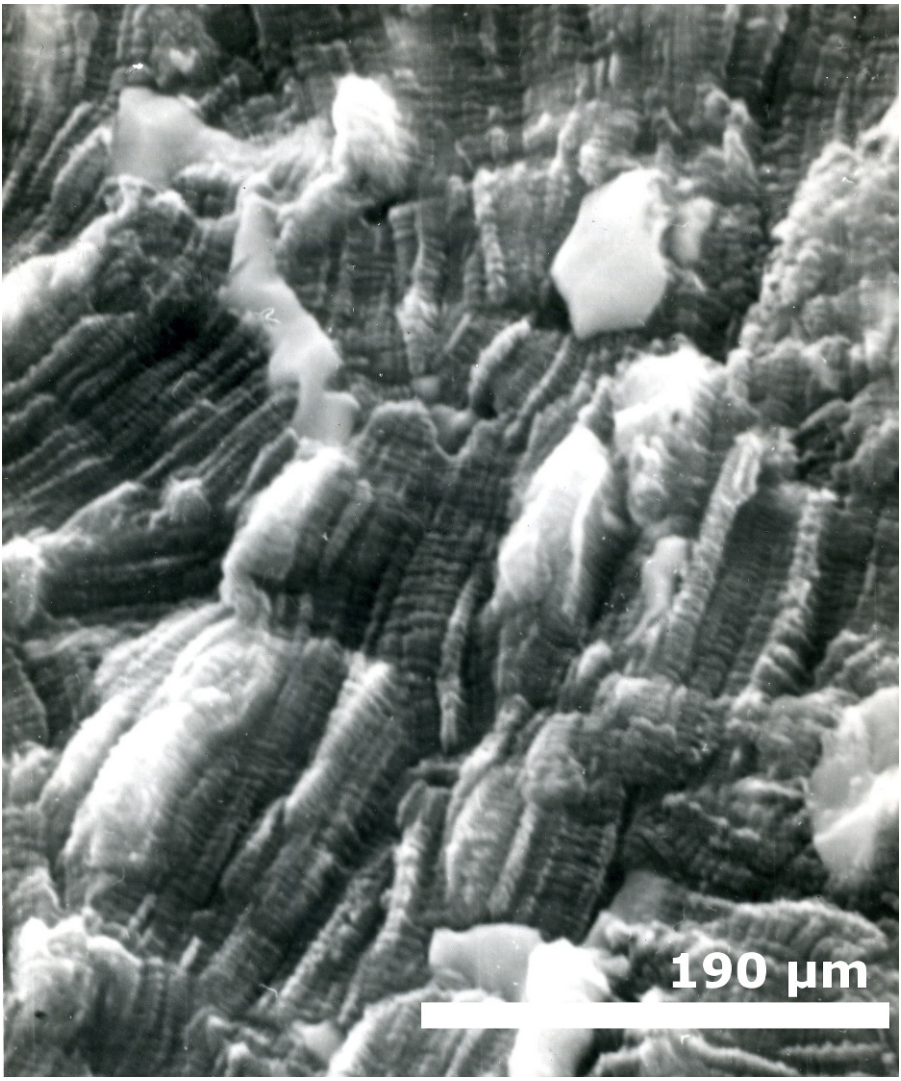

Figure 7. Stratification of RGT type graphite doped with 1%B. (He^+, 800 eV, T=1,300°C). The precipitates of TiC are seen on the surface.

3.3. EROSION AND MODIFICATION OF BORON DOPED CFC UNDER PLASMA IRRADIATION

Doping of CFC is made usually with grains of boron carbide or boron nitride (BN) having average dimensions about 1–5 µm. The dopant is incorporated in the space between carbon fibers.

Irradiation by He-ions (E_i= 800 eV, T = 500°C) of one dimensional CFC of VMN-4 type (PAN fibers) doped with BN (C + BN 30% mass.) showed

that sputtering yield of CFC was equal to 0.28 at/ion. Sputtering yield of carbon fibers was higher (0.31 at/ion) than that of BN particles (0.21 at/ion). At T = 1,300°C the overall sputtering yield increased up to 0.53 at/ion.

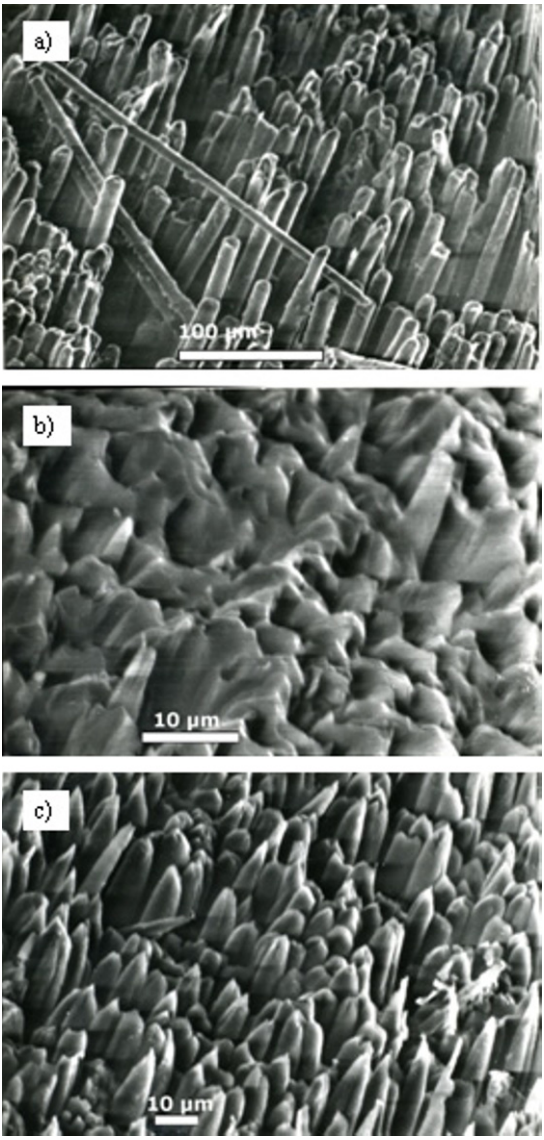

Figure 8. Influence of boron dopant on carbon fiber composite modification under ion irradiation (He^+, 850 eV, T = 500 and 1,300°C) [12]. (**a**) Unirradiated surface of VMN-4, (**b**) irradiated surface of VMN-4, (**c**) irradiated surface of VMN-4 + BN.

Figure 8 shows influence of ion irradiation on surface structure of boron doped CFC in comparison with the pure one. It is seen that ion irradiation lead to destruction of carbon fibers of CFC and to formation of uniform continuous layer on irradiated surface. Formation of the uniform layer was shown to be the result of the diffusion and recrystallization processes initiated by ion induced surface stresses [12]. The structure of BN doped CFC does not change significantly either under "low" temperature irradiation or under high temperature one. It shows that boron prevents elevation of the magnitude of ion induced surface stresses and did not allow of development of the mentioned above processes on irradiated surface.

3.4. EROSION OF BORON DOPED GRAPHITES UNDER IRRADIATION IN OXYGEN CONTAMINATED PLASMA

Table 2 presents the sputtering yields of boron doped graphites irradiated with the ions of He-plasma and of plasma burned in the working gas with composition He + 0.8%O_2. The sputtering yield of dense fine grain graphite of MPG-8 type (Russia) and boron carbide are shown for comparison. It is seen that addition of oxygen increases the sputtering yield of doped graphite to a smaller degree than that of pure graphite, and B_4C demonstrates the smallest increase of sputtering yield, when temperature of irradiated samples equals 500°C. At the temperature1,300°C boron influence on sputtering yield in oxygen contaminated plasma is not so effective. The magnitudes of sputtering yield of pure graphite and boron doped ones appear to be closer to each other.

TABLE 2. The sputtering yields of graphites and boron carbide irradiated in He- and He + 0.8%O_2 plasma at the temperatures 500 and 1300 °C (Impinging ion energy 800 eV)

Material	Y, at/ion (He plasma 500°C)	Y, at/ion (He + 0.8%O_2 plasma 500°C)	Y_{He+O2}/Y_{He} (500°C)	Y, at/ion (He plasma 1,300°C)	Y, at/ion (He + 0.8%O_2 plasma 1,300°C)	Y_{He+O2}/Y_{He} (1,300°C)
MPG-8	0.15	0.7	4.7	0.25	1.30	5.2
B_4C	0.08	0.10	1.25	0.15	0.48	3.2
RGB	0.21	0.44	2.40	0.25	1.25	4.6
GB-110	0.18	0.44	2.40	0.35	0.8	3.4

Secondary-Ion Mass-Spectrometry investigation showed that ion irradiation at the temperature 500°C does not lead to increase to oxygen concentration in boron doped graphites, when oxygen concentration in the working gas grows from 10^{-4}% up to 0.8%, and relatively oxygen particle flux on irradiated surface increases. In this condition an oxidation of boron carbide

precipitates formed on the surface (see Fig. 5) leads to creation of B_2O_3 layer acting as the barrier for oxygen diffusion into the bulk [10].

At the temperature 1,300°C the similar increase of oxygen concentration in the working gas was accompanied by increase of oxygen trapping in ≈100 times reporting about weakening of protective properties of the layer. Activation of oxygen diffusion and partial decomposition of B_2O_3 layer at high temperature could be the reason of this fact.

3.5. NFLUENCE OF DISSOLVED BORON ON MODIFICATION OF TITANIUM DOPED GRAPHITE UNDER IRRADIATION IN OXYGEN CONTAMINATED PLASMA

Ion irradiation of RGT type graphite in He + 0.8%O_2 stimulates formation of pores and recrystallisation processes in the surface layer (Fig. 9a) [13]. The average dimensions of the pores were about 10 μm after irradiation with fluence 2.2×10^{24} ion/m^2. The microscopic particles consisted – as shown by SIMS – of titanium, oxygen and carbon rose above the surface. They were spread out on the RGT surface. The amount of titanium contained in these particles corresponded roughly to the amount of titanium in the RGT layer 30 μm deep. At the same time the depth of sputtered layer of RGT was estimated to be 10 μm.

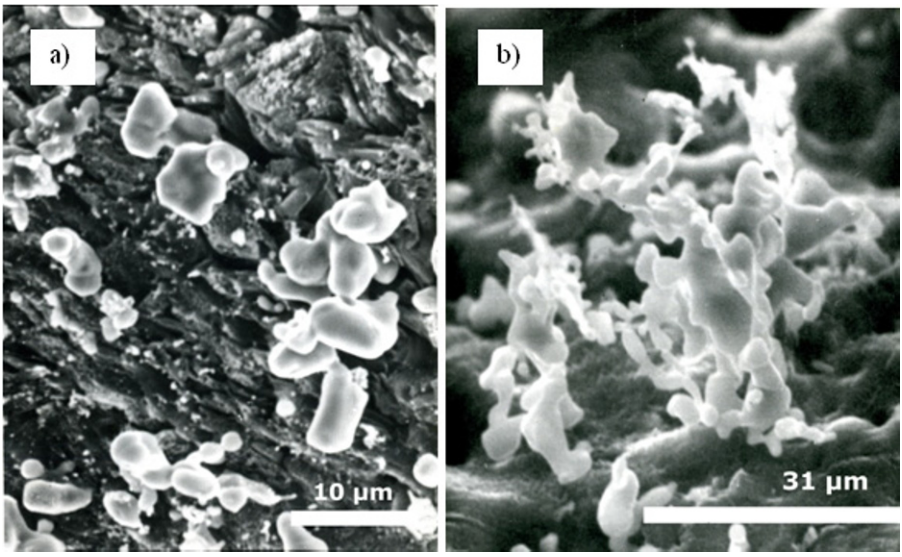

Figure 9. Modification of RGT type graphite under irradiation in oxygen contaminated plasma. (He^+, 800 eV, T = 300°C) [13]. (**a**) RGT; (**b**) RGT + 1% at B.

Addition of 1% B in graphite matrix of RGT activates abruptly titanium segregation on to the surface under the same irradiation conditions. Dendrites

like features of above-mentioned composition were formed on the surface (Fig. 9b). Their total volume was three times larger than on RGT.

It is important to note that titanium output occurred from a depth exceeding the depth of ion implantation by approximately two-three orders of magnitude. This phenomenon cannot be explained by ordinary diffusion alone. It must be assumed that the output of titanium was the result of the specific chain of processes initiated by ion bombardment. Among them are oxygen trapping, formation of C–O bonds inside graphite grains, along grain boundaries and pore surfaces, partial oxidation of TiC precipitates, transfer of Ti-atoms over the surfaces of pores towards outer surface of graphite and finally formation of the oxycarbide features on the surface (Fig. 10).

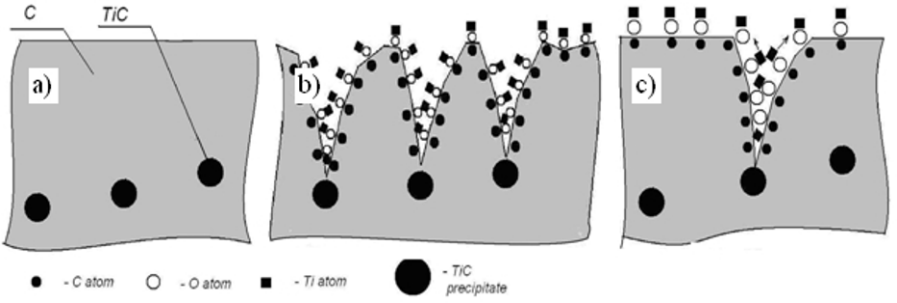

Figure 10. The scheme of titanium segregation onto the surface of titanium doped graphite under irradiation by ions of oxygen contaminated helium plasma. (**a**) titanium doped graphite, (**b**) pore formation, oxidation of pore surfaces, diffusion of Ti atoms along the oxidized pore surfaces towards outer surface, (**c**) formation of the oxycarbide features on the surface.

In the presence of boron, transformation of the modified graphite becomes easier. When boron is dissolved in the graphite grain, the π-bonds are disrupted (Fig. 3) and connections between the basal faces weaken. Thus, the retention of oxygen, and later the transportation of oxygen and titanium through graphite seem to facilitate.

3.6. THERMO-CHEMICAL INTERACTION OF BORON DOPED GRAPHITES AND BORON CARBIDE WITH OXYGEN GAS

Boron presence did not influence on the erosion rate of boron doped graphites and boron carbide annealed at the temperature 1,700°C in residual gas of vacuum device with low concentration of oxygen ($P_{\Sigma} = 6 \times 10^{-3}$ Pa, $P_{O2} = 1.3 \times 10^{-6}$ Pa). Erosion rate of boron doped graphites RGB, RUM-3 (C+3%B), RUM-40 (C+40%B) and B_4C was rather low (≈0.01-0.02 at/mol.O_2). It stayed constant at least over some tens hours and did not differ practically from erosion rate of fine grain graphite of MPG-8 type.

Scanning electron microscope investigation showed that their surfaces did not undergo remarkably modification.

When oxygen pressure grew up to $P_{O2} = 1.1 \times 10^{-2}$ Pa, erosion yield of the all investigated materials were increasing steadily during some hours and then reached constant level, which appeared to be ten or even more times higher (Table 3). It is seen that generally erosion yield increases with elevation of boron concentration.

TABLE 3. The erosion rate of materials during heating at 1700 °C in oxygen atmosphere ($P_{O2}=1.1 \times 10^{-2}$Pa)

Material	Erosion yield (at/mol.O_2)
MPG-8	0.10
RGB	0.10
RUM-3	0.18
RUM-40	0.29
B_4C	0.41

Surface relief of MPG-8 changed rather weakly after annealing in oxygen atmosphere. Contrary to that surface of B_4C was modified significantly. It reminds the distinctive lace already after 2–3-h annealing (Fig. 11a). The effective surface area was drastically increased and it evidently provided grows of erosion yield of the surface.

On the surface of RUM-40 two regions with sharply distinct relief could be observed (Fig. 11b). The near flat regions were similar to the surface of MPG. They seemed to belong to graphite grains and changed very weakly

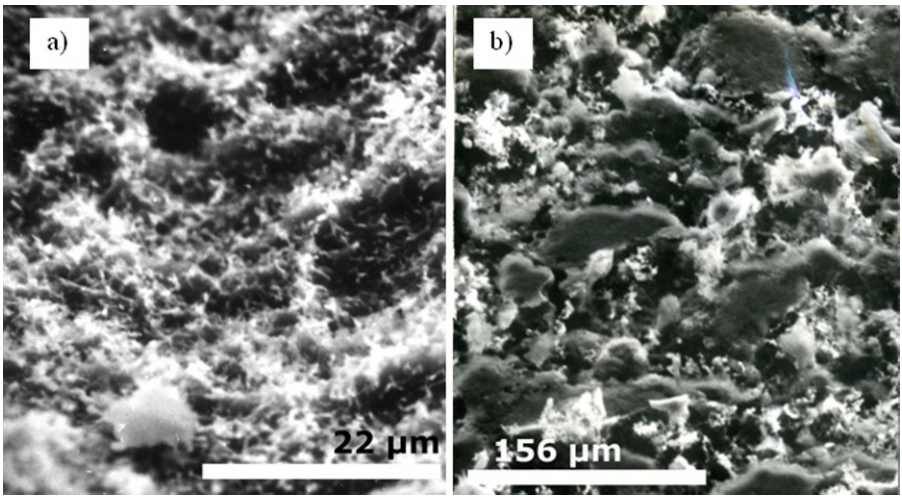

Figure 11. Erosion of boron carbide (**a**) and boron doped graphite of RUM-40 type (**b**) during heating at 1,700°C in oxygen atmosphere ($P_{O2} = 1.1 \times 10^{-2}$Pa).

during annealing. The areas surrounded them had lace-like relief similar to that of B_4C. The flat areas raised above lacy ones. It shows that the last ones were eroded quickly. Their erosion determined higher erosion yield of the surface in a whole in comparison with MPG type graphite.

4. Conclusions

The paper shortly describes the methods of boron carbide coating deposition and presents the experimental results characterized the properties of boron carbide coatings and of boron doped graphites important to their application as the plasma facing materials of fusion devices and other plasma apparatuses dealing with dense and high temperature plasma.

The presented results show that chemical sputtering, ion-induced desorption and radiation-enhanced sublimation of boron carbide are strongly suppressed. Erosion rate stays without remarkable changes up to 1,300–1,400°C. Hydrogen retention in boron carbide is 3-4 times lower than in graphites. Boron carbide can ensure a small erosion rate, low impurity influx into the plasma, small hydrogen recycling and the integrity of surface layers under high heat loads when deposited on tungsten or on graphite with high thermal conductivity. Conclusion is made that boron carbide coatings can meet the requirements for the plasma-facing materials of fusion devices. Development of plasma chemical method of boron carbide deposition opens the way for application of boron carbide coatings as in situ renewable protecting coating for plasma facing materials of fusion devices.

Graphites doped with boron up to considerably high concentration (≥10–20%) perfectly withstand plasma ion irradiation in the moderate temperature range (some hundreds centigrade). The layer of boron carbide precipitates is formed on irradiated surface providing rather low erosion yield.

At the temperature 1,300°C, boron sublimation is activated; influence of the protecting boron carbide film weakens. Graphite matrix undergoes stratification and erosion yield starts to grow.

Sputtering yield of boron doped graphite irradiated by ions of oxygen contaminated plasma is also much lower than sputtering rate of pure graphite. The significant difference between sputtering yields of boron doped graphites and the pure one was observed even at the temperature 1,300°C.

At higher temperatures (1,700°C) boron carbon precipitate actively interact with oxygen from residual gas forming volatile species relieving from the surface. As a result erosion rate of boron doped graphites appears to be higher than that of pure graphites.

References

1. DIII-D research operations annual report (General Atomic, San-Diego, 1997).
2. Winter, J., Esser, H. G., Könen, L. et. al.: Boronization in textor. J. Nucl. Mater., 162-164, 713 (1989).
3. Barsuk, V.A., Buzhinskij, O.I., Vershkov V.A., et al.: Test of the boron-containing coating of the graphite limiter in the T-10 tokamak. J. Nucl. Mater., 191–194, 1417 (1992).
4. Jackson, G.L., Winter, J., Burrell, K.H., et al.: Boronization in DIII-D. J. Nucl. Mater. 196–198, 236 (1992).
5. Buzhinskij, O.I., Semenets, Yr.M.: Thick boron carbide coatings for protection of tokamak first wall and divertor. Fusion Engineering and design, 45(4), 343 (1999).
6. Buzhinskij, O.I., Otroschenko, V.G., Whyte, D.G., et al.: Plasma deposition of boron films with high growth rate and efficiency using carborane. J. Nucl. Mater., 313–316, 214 (2003).
7. Begambekov, L.B., Buzhinsky, O.I.: Features and advantages of boron carbide as a protective coating of the tokamak first wall. Plasma Devices and operations, 15(3), 1 (2007).
8. Roth, J.: Sputtering of limiter and divertor materials. J. Nucl. Mater. 176-177, 132–141 (1990).
9. Begrambekov, L., Buzinskij, O., Gordeev, et al.: TDS investigation of hydrogen isotope retention in graphites and carbon based materials. Physica Scripta, 108, 72 (2004).
10. Hirooka, Y., Conn, R., Causey, R. et.al.: Bulk-boronized graphites for plasma-facing components in ITER. J.Nucl.Mater. 176–177, 473-480 (1990).
11. Magnetic fusion energy program. Annual report SNL. 1989, p.18.
12. Begrambekov, L.B., Buzhinsky, O.I., Legotin, A.L. et al.: Structure and relief modification of titanium and boron doped graphite under light ion irradiation. In “Hydrogen Recycling at Plasma Facing Materials”, Kluwer Academic Publishers, Netherland. 2000. p. 313–318.
13. Begrambekov, L.B., Vergasov, S.V., Zakharov, A.M. et al.: Erosion of graphite and graphite compounds under oxygen gas and light ion irradiation Nucl. Instrum. Meth. B. 90, 491–495 (1994).

VIBRATIONAL SPECTROSCOPY OF ADSORBATES ON THE (111) AND (100) SURFACES OF LANTHANUM HEXABORIDE

THOMAS YORISAKI[1–3], AASHANI TILLEKARATNE[1], YUKIHIRO MORIYA[2,3], CHUHEI OSHIMA[2,3], SHIGEKI OTANI[4], AND MICHAEL TRENARY[1,*]

[1]*Department of Chemistry, University of Illinois at Chicago, 845 W. Taylor St., Chicago, IL 60607, USA*

[2]*Department of Nano Science and Engineering, Waseda University, 3-4-1 Okubo, Shinjuku-ku, Tokyo 169-8555, Japan*

[3]*Kagami Memorial Laboratory for Materials Science and Technology, Waseda University, 2-8-26, Nishiwaseda, Shinjuku-ku, Tokyo 169-0051, Japan*

[4]*National Institute for Materials Science, 1-1 Namiki, Tsukuba-shi, Ibaraki 305-0044, Japan*

Abstract Reflection absorption infrared spectroscopy has been used to study the adsorption of carbon monoxide, oxygen, and decaborane on the (100) and (111) surfaces of lanthanum hexaboride. Exposure of the surface at temperatures of 95 K and above to O_2 produces atomic oxygen on the surface and yields vibrational peaks in good agreement with those observed previously with the technique of high resolution electron energy loss spectroscopy (HREELS). As in the previous HREELS studies, the peaks observed in response to oxygen adsorption are assigned to vibrations of the B_6 octahedra that gain intensity due to a decrease in electronic screening of surface dipoles. In the case of CO, molecular adsorption occurs at 95 K and gives rise to a variety of C–O stretch peaks, depending on adsorption site. Decaborane adsorbs molecularly at 95 K and gives rise to intense peaks in the B–H stretch region that evolve with annealing temperature into a single peak at 2571 cm^{-1} due to an unidentified surface intermediate possessing BH bonds.

Keywords: lanthanum hexaboride, surface vibrational spectroscopy, reflection absorption infrared spectroscopy, carbon monoxide, decaborane

* Michael Trenary, Department of Chemistry, University of Illinois at Chicago, 845 W. Taylor St., Chicago, IL 60607, USA, e-mail: mtrenary@uic.edu

N. Orlovskaya and M. Lugovy (eds.), *Boron Rich Solids: Sensors, Ultra High Temperature Ceramics, Thermoelectrics, Armor*, DOI 10.1007/978-90-481-9818-4_12,

1. Introduction

Lanthanum hexaboride has many bulk properties that are similar to those of typical transition metals. One of the most important properties of transition metals is their ability to catalyze numerous chemical transformations. In the case of heterogeneous catalysis, the key chemical reactions take place on the transition metal surface and so the surface structure and surface chemical properties are of most importance for the use of transition metals as catalysts. One common way to probe the chemical properties of a surface is through the vibrational frequencies of adsorbed atoms and molecules. In this study, we report on the surface vibrational characteristics of three adsorbates: atomic oxygen, the diatomic molecule carbon monoxide, and the polyatomic molecule decaborane. Despite many past studies of the structure of rare earth hexaboride surfaces, the chemical properties of these surfaces have received little attention. Here we use reflection absorption infrared spectroscopy (RAIRS) to study each of these adsorbates as a way to probe different aspects of the surface chemical properties of lanthanum hexaboride.

Lanthanum hexaboride has been the subject of numerous surface science studies with most of the work concerned with the properties of the clean surface [1–14] and its interaction with oxygen [7, 15–24]. These studies are in agreement that the LaB_6(100) surface is terminated in an unreconstructed square lattice of La atoms with the bulk lattice constant of 4.15 Å. In a combined X-ray photoelectron spectroscopy (XPS), inelastic ion scattering spectroscopy (ISS), and low energy electron diffraction (LEED) study [25], it was found that whereas the topmost atomic layer of the (100) surface consists of La atoms, on the (111) surface boron atoms lie above the La-atom plane. Since the (111) surface, like the (100) surface, shows no reconstruction, it follows that the triangular faces of the B_6 octahedra, which are parallel to the (111) plane, constitute the topmost atomic layer on the LaB_6(111) surface. These proposed structures of the (100) and (111) surfaces of LaB_6 were also supported through comparison of surface phonon dispersion curves measured with high resolution electron energy loss spectroscopy (HREELS) with curves calculated with simple force constant models [26]. In forming the surface, the interoctahedral bonds are broken and on the (100) surface this leads to a single boron dangling bond oriented along the surface normal through the middle of a square of four lanthanum atoms, whereas on the (111) surface there are three dangling bonds 55° from the normal along three azimuths 120° apart. The different structures of the (100) and (111) surfaces present different types of adsorption sites for reactive chemistry and information on the nature of these sites can be probed through vibrational spectroscopic studies of adsorbed species.

2. Experimental

The RAIRS experiments were conducted at the University of Illinois at Chicago in a stainless steel ultrahigh vacuum chamber with a base pressure of ~5×10^{-11} torr. The system has been described in detail elsewhere [27]. In brief, it is equipped with (LEED), (XPS), and a Fourier transform infrared spectrometer (FTIR) for RAIRS. The XPS system consists of a VG CLAM2 hemispherical analyzer and a dual anode X-ray source. Mg Kα radiation was used and the spectrometer was previously calibrated with the Pt $4f_{7/2}$ peak at a binding energy of 71.2 eV. The RAIR spectra were obtained at a resolution of 4 cm^{-1} using 1,024 scans for both background and sample spectra. The HREELS experiments were conducted at Waseda University with a spectrometer (Delta0.5 SPECS) that consists of a double stage monochrometer and a rotatable single stage analyzer. The spectrometer was set to the specular reflection geometry, at an incident angle of 60°, and incident energy of 4.0 eV. In cases where the sample was annealed to higher temperatures, it was cooled back to the starting temperature before sample spectra were obtained.

The LaB_6 single crystals were grown and cut at the National Institute for Materials Science in Tsukuba, Japan and were polished to a mirror finish before use. The samples were in the form of disks approximately 1 cm in diameter and 2 mm thick. They were mounted by folding Ta foil or wires over the top and bottom edges of the crystals. The Ta pieces were spot welded to Ta wires which in turn were spot welded to W support wires that were in good contact with a liquid nitrogen cooled reservoir. This allowed the sample to be cooled to a temperature of 90 K. The sample could be heated to 1,850 K by electron bombardment from a Ta filament mounted behind the sample. The sample temperature was measured with a type-C thermocouple spot welded to the upper Ta foil piece. A type K thermocouple attached to the copper block was used to calibrate the type-C thermocouple for temperatures below room temperature. The samples were cleaned by heating to 1,200–1,850 K, which yielded surfaces free of all contaminants including oxygen as determined by XPS and which yielded sharp (1 × 1) LEED patterns for the (100) and (111) surfaces with low backgrounds indicative of well-ordered and unreconstructed surfaces, whereas the (110) surface displayed a (2 × 1) pattern as reported in previous work. Exposures to CO, O_2, and decaborane are given in units of Langmuir, where 1 L = 1×10^{-6} torr-s, and were performed by backfilling the chamber with the pressure measurements based on uncorrected ion gauge readings. The decaborane was purchased from Alpha Aesar with a quoted purity of 99% and was subjected to a freeze-pump-thaw cycle for further purification.

3. Results and Discussion

3.1. OXYGEN ON LaB_6(111) AND LaB_6(100)

Figure 1 shows a comparison of RAIR spectra for oxygen on the (100) and (111) surfaces and an HREEL spectrum for oxygen on the (110) surface of LaB_6. The HREEL spectrum shown is similar to those published previously for oxygen on the (100) surfaces of LaB_6 and PrB_6 [28] and of O on the (100), (111), and (110) surfaces of LaB_6 [29, 30]. Unlike the (100) and (111) surfaces, the clean LaB_6(110) surface undergoes a reconstruction to a (2 × 1) periodicity as detected with LEED [25]. The exact atomic structure of the reconstructed (110) surface has not been established. The principal differences between surface vibrational spectra measured with RAIRS and HREELS are in spectral range and resolution; RAIRS has a higher resolution but a higher low wavenumber limit than HREELS.

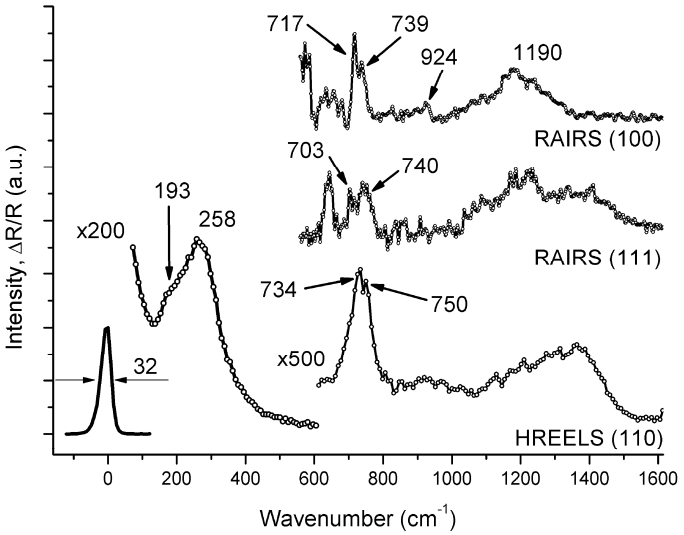

Figure 1. Comparison of an HREEL spectrum of oxygen on a LaB_6(110) surface with RAIR spectra of oxygen on the LaB_6(100) and LaB_6(111) surfaces. In each case, the surface was exposed at room temperature to just enough O_2 to achieve saturation coverage. The RAIR spectra have been inverted so that the peaks are positive to facilitate the comparison.

The RAIR spectra in Fig. 1 were obtained at a resolution of 4 cm^{-1} with a low wavenumber cutoff of 600 cm^{-1}, whereas the HREEL spectrum was obtained with a resolution greater than 32 cm^{-1} (the full width half maximum of the elastic peak) with a low wavenumber limit of approximately 50 cm^{-1}. The most intense peaks in the HREEL spectrum, the one at 258 cm^{-1} with

an unresolved shoulder at 193 cm^{-1}, are associated with O bound to La sites, whereas the other weaker peaks that extend from 600 to 1500 cm^{-1} are associated with vibrations of the B_6 octahedra. In the case of the (100) surface [28], a good match was obtained between the observed peaks and the amplitudes and symmetries of the surface vibrations obtained in a lattice dynamics calculation. With HREELS, several mechanisms lead to the observed loss features, including interaction of the electric field of the scattering electrons with the oscillating dipoles at the surface, whereas the dipole mechanism is the only one contributing to the RAIR spectrum. The good match between the RAIRS and HREELS results in Fig. 1 indicates that the latter are dominated by the dipole scattering mechanism. The higher resolution obtained with RAIRS does not lead to resolvable features in the range of 1100–1500 cm^{-1}, suggesting that features in this region are intrinsically broad. The RAIR spectra do allow separate peaks to be resolved at 703 and 740 cm^{-1} for the (111) surface and at 717 and 739 cm^{-1} for the (100) surface, which were not resolved in the earlier HREELS studies. The spectrum in Fig. 1 shows that HREELS also can resolve separate peaks in this region at 734 and 750 cm^{-1}. As this separation is less than the nominal resolution of the HREELS spectrometer, it may not be real. A more detailed discussion of the RAIRS results and their relationship to the HREELS results for oxygen on LaB_6 surfaces is presented elsewhere [31].

3.2. CARBON MONOXIDE ON LaB_6(111) AND LaB_6(100)

There are well established correlations between the value of the C–O stretch frequency of carbon monoxide adsorbed on surfaces and the nature of the adsorption site; the extensive literature on this topic has been reviewed by Sheppard and coworkers [32–34]. Thus CO stretch values of 2200–2130 cm^{-1} are assigned to adsorption on positive metal ions whereas lower values are assumed to correspond to adsorption on metals in the zero-oxidation state. Values of 2130–2000 cm^{-1} correspond to CO adsorbed at on-top sites; 2000–1880 cm^{-1} corresponds to CO bridge bonded to two metal atoms; 1880–1650 cm^{-1} corresponds to CO bonded to three or more metal atoms. Cases of more unusual bonding modes including those where the CO molecules bond in a side-on fashion, where CO stretch frequencies as low as 1251 cm^{-1}, have been reviewed by de la Cruz and Sheppard [33]. Whether or not the correlations established for CO on transition metal surfaces will apply to a metal boride surface is not clear. Nevertheless, the fact that LaB_6(111) is a boron-terminated surface whereas the (100) surface is La terminated should, at the very least, present distinctly different types of

adsorption sites for carbon monoxide and hence a distinctly different set of C–O stretch frequencies.

Fig. 2 shows a comparison of the RAIR spectra of CO adsorbed on the (111) and (100) surfaces of LaB_6 following CO exposures of 3 and 5 L, respectively, at a surface temperature of 90 K. As expected, the two surfaces give distinctly different results. On LaB_6(111), an unusually low C-O stretch frequency of 1508 cm^{-1} is observed along with three weaker peaks at 1957, 2044, and 2096 cm^{-1}. In contrast, on the (100) surface, a single broad peak at 2100 cm^{-1} is observed. In addition, the height of the 2100 cm^{-1} peak on the (100) surface is about a factor of five greater than the height of the 1508 cm^{-1} peak seen on the (111) surface. Not shown are additional results in which a slight annealing of the surface to only 120 K results in a loss of the 1508 cm^{-1} peak, suggesting that it is associated with a metastable adsorption state.

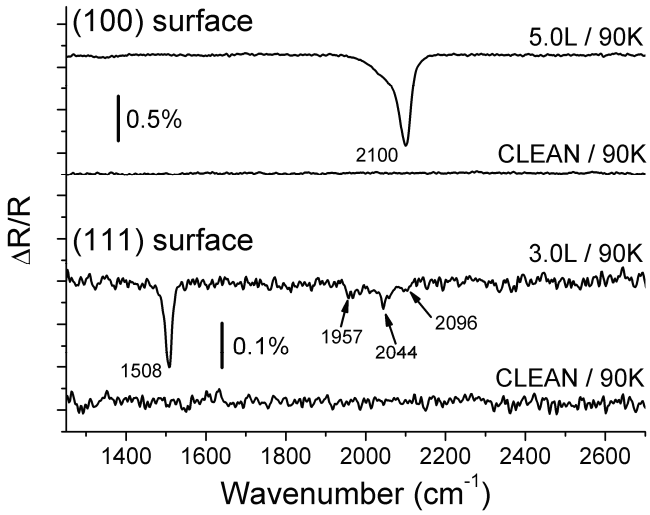

Figure 2. Comparison of CO adsorbed on the (100) and (111) surfaces of LaB_6 following exposures at a surface temperature of 90 K to 5.0 and 3.0 L of CO, respectively. A different intensity scale is used for the two spectra as the 2100 cm^{-1} peak on the (100) surface is approximately five times as intense as the 1508 cm^{-1} peak on the (111) surface.

The unusually low frequency of the 1508 cm^{-1} peak seen on the (111) surface suggests that it might be associated with defect sites. To test this hypothesis, experiments were performed in which the surface was subjected to argon ion sputtering without a high temperature anneal and then exposed to CO. The results are shown in Fig. 3. The spectrum at the bottom was obtained before sputtering and after a 3.0 L CO exposure with the LaB_6

crystal at 90 K. The spectrum shows that after sputtering the sample, exposure to 3.0 L of CO does not lead to any observable peaks. It required repeated annealing of the crystal to high temperatures (1500–1600 K) before the ability of the surface to adsorb CO in a way that led to the 1508 cm^{-1} peak was restored. More specifically, annealing the sample only 30 times was insufficient, whereas a sample that had been annealed 50 times restored the surface to its original condition. It is likely that fewer anneals but at a higher temperature would have produced the same result, but there were practical limits on how high the sample could be heated. The results in Fig. 3 establish that the 1508 cm^{-1} peak is characteristic of the ideal surface rather than of adsorption on defect sites. More detailed interpretations of the adsorption sites for CO on the (100) and (111) surfaces of LaB_6 are presented elsewhere [35].

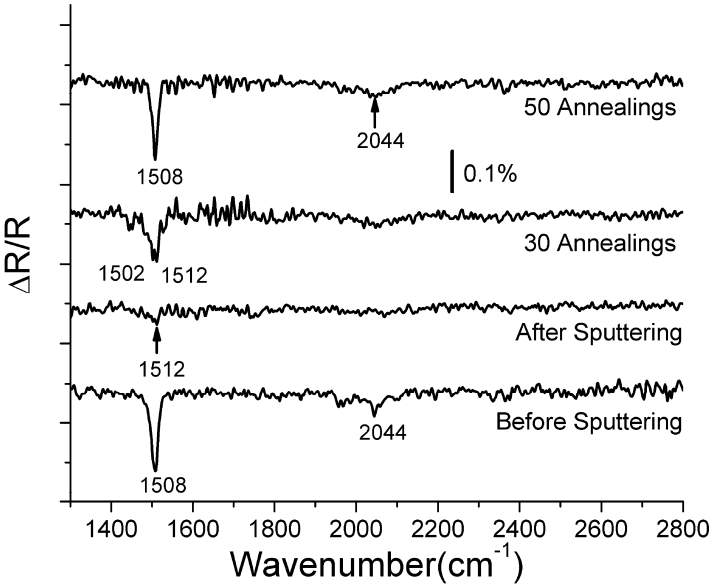

Figure 3. RAIR spectra showing the effect of argon ion sputtering on the ability of the LaB_6(111) surface to adsorb CO. After sputtering but before annealing, a CO peak is just barely visible, whereas after annealing the crystal 50 times to temperatures in the range of 1500–1600 K the surface is restored to its initial condition.

3.3. CARBON MONOXIDE ON OXYGEN COVERED LaB_6(100)

The results presented in Figs. 1–3 show that the surfaces of LaB_6 can adsorb both CO and O separately. It remains to be determined whether adsorbed oxygen can block the adsorption of CO, and conversely, whether adsorbed CO can block the dissociative adsorption of O_2. Figure 4 shows the results

of first exposing the $LaB_6(100)$ surface to O_2 at low temperature, annealing the sample to 1170 K, then exposing to CO with the sample at 95 K. The spectrum obtained after O_2 exposure with the sample at low temperature is essentially the same as obtained following exposure to the sample at room temperature, which indicates that dissociative adsorption occurs just as readily at low temperature. The purpose of annealing to 1170 K was to desorb some of the oxygen in order to make sites available for CO adsorption. Other results, presented elsewhere [31], showed that without the 1170 K anneal, no CO would adsorb. Even with the anneal, the results in Fig. 4 show that a relatively low coverage of CO is obtained as indicated by the weak peak at 2092 cm^{-1}, which is essentially the same position as obtained for CO adsorption on the clean $LaB_6(100)$ surface. This shows that while adsorbed O atoms have the effect of blocking CO adsorption sites, when the O atoms are removed from those sites, the CO that does adsorb is not strongly perturbed by the presence of coadsorbed oxygen. In experiments in which CO is first adsorbed on the surface at low temperature and then exposed to O_2, it is found that no peaks associated with O are observed. This shows that adsorbed CO can block the dissociative adsorption of O_2 on the $LaB_6(100)$ surface.

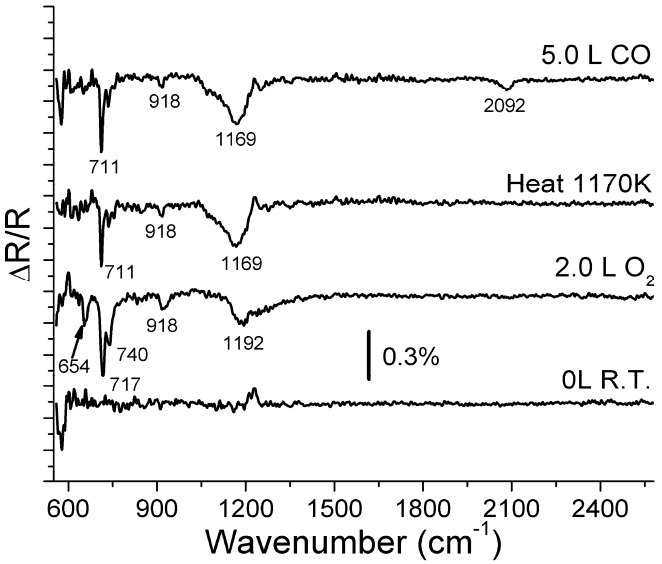

Figure 4. RAIR spectra showing the ability of adsorbed oxygen on the $LaB_6(100)$ surface to block the adsorption of CO. After a 2.0 L exposure of O_2 at 95 K, essentially the same features as observed in Fig. 1 are obtained indicating that O_2 dissociates at 95 K to yield adsorbed O atoms. Heating to 1170 K desorbs some oxygen and leads to a more ordered oxygen overlayer. A subsequent 5.0 L CO exposure leads to only a small peak at 2092 cm^{-1}, indicating that the oxygen remaining on the surface blocks the adsorption of CO without strongly perturbing the CO that does adsorb.

3.4. DECABORANE ($B_{10}H_{14}$) ON THE LaB_6(111) SURFACE

There are several motivations for studying the adsorption and decomposition of decaborane on a LaB_6 surface. First, in interpreting the results of CO adsorption it is desirable to alter the surface B to La ratio by deposition of extra boron on the surface and the thermal decomposition of a borane precursor is a convenient way to accomplish this. Second, decaborane is one of the most stable of the numerous neutral boron hydrides and it is relatively easy to work with. It is a stable, white, crystalline solid with a melting point of 372 K and a boiling point of 486 K. Because it has a vapor pressure of about 100 mTorr at room temperature, it can be dosed onto surfaces under UHV conditions using standard gas-handling methods. Third, in order to establish that RAIRS has the sensitivity to detect B–H bonds at a LaB_6 surface should they form from the reaction of the clean surface with H_2, it is desirable to record RAIRS results for a low coverage of a molecule containing B–H bonds. Finally, a detailed study using various techniques, including RAIRS, of decaborane adsorption and thermal decomposition on the Pt(111) surface was recently published [36] and a comparison of the reactive surface chemistry of the same molecule on an LaB_6 surface and on the surface of a catalytically active metal such as platinum may provide information on the potential catalytic activity of a metal boride. Figure 5 shows RAIR spectra following a 5.0 L exposure of $B_{10}H_{14}$ to LaB_6(111) at 90 K followed by annealing to the indicated temperatures. For the initially adsorbed molecule, a strong B–H stretch band is observed with partially resolved components at 2570, 2596, and 2611 cm^{-1}. Upon annealing to only 115 K, the B–H stretch peak becomes sharper but asymmetric and is centered at 2578 cm^{-1}. Annealing to 300 K produces a weak but more symmetric peak centered at 2571 cm^{-1}, whereas following a 400 K anneal a peak a 2571 cm^{-1} is just barely visible. The general trends are somewhat similar to what was observed on the Pt(111) surface although many of the details are different. On Pt(111), a 10 L exposure of $B_{10}H_{14}$ at 85 K gave a main B–H stretch peak at 2594 cm^{-1} with an unresolved shoulder at 2607 cm^{-1} but with a 200 K anneal the peaks sharpened and at least five separate B–H stretches at 2540, 2571, 2594 and 2615 cm^{-1} were clearly resolved. Annealing the Pt(111) surface to 300 K yields a much weaker B–H stretch peak with a main component at 2555 cm^{-1} and a weaker component at 2596 cm^{-1}. After annealing to 450 K, no peaks are visible in the B–H stretch region, indicating that the molecule has decomposed on Pt(111) by this temperature.

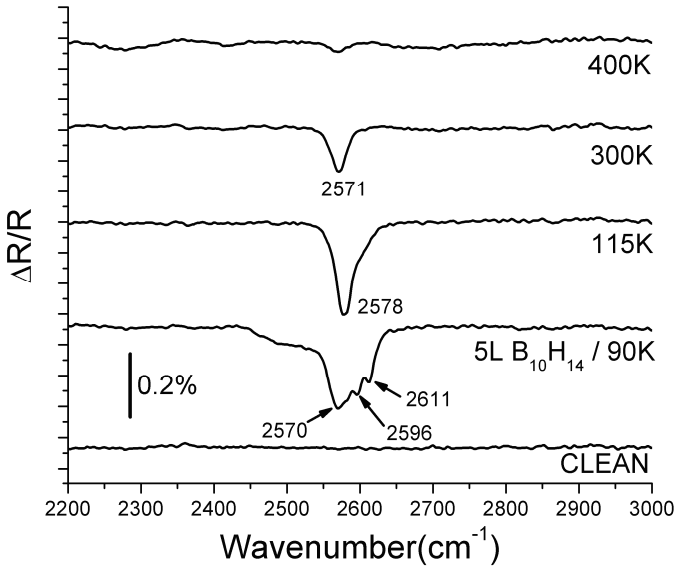

Figure 5. RAIR spectra following a 5 L exposure of decaborane ($B_{10}H_{14}$) to the LaB_6(111) surface at 90 K and after annealing to the indicated temperatures.

The RAIR spectra of $B_{10}H_{14}$ on the (111) surfaces of LaB_6 and Pt are similar in that the complex set of peaks seen after adsorption at low temperature, which match those of the parent molecule and therefore indicate that the molecule initially adsorbs without dissociation, evolve to a single peak after annealing to 300 K. In the case of Pt(111), the single peak at 2555 cm^{-1} was assigned to an unidentified surface intermediate containing B–H bonds. The single peak at 2571 cm^{-1} seen on the LaB_6 surface is likewise attributed to a surface intermediate. The intermediate is likely the same one formed on Pt(111), with the small frequency difference on the two surfaces due to either different coverages or to slightly different interactions with the substrates. Other experiments show that the boron deposited through decaborane decomposition does not suppress CO adsorption as higher wavenumber C–O stretch peaks in the range of 1950–2100 cm^{-1} are still observed, although the 1508 cm^{-1} peak is not observed. Finally, the RAIRS results demonstrate that high signal-to-noise ratios are observable for surface B–H bonds on LaB_6(111), indicating that if B–H bonds were formed from the dissociative adsorption of H_2 they would be observable. In other experiments in which H_2 was exposed to both the (100) and (111) surfaces of LaB_6, no B–H stretch peaks were observed in either case with RAIRS, strongly suggesting but not proving, that H_2 does not dissociatively adsorb on those surfaces.

4. Conclusions

The results presented here demonstrate that the technique of RAIRS can be used to investigate molecular adsorption and decomposition on the surfaces of the boron-rich solid lanthanum hexaboride. In the case of O_2, the results support earlier surface vibrational spectroscopy studies with HREELS in that O_2 dissociates to produce adsorbed O atoms. The O occupies La sites leading to intense low frequency HREELS peaks that are below the low wavenumber cutoff of RAIRS. In addition, the O atoms decrease the surface electron density leading to the observation with both HREELS and RAIRS of vibrational peaks associated with surface B_6 units, which are screened by the free electrons for the clean surface. Molecular adsorption of CO occurs on both $LaB_6(100)$ and $LaB_6(111)$ at a variety of different adsorption sites giving rise to a wide range of C–O stretch frequencies, including an unusually low wavenumber peak at 1508 cm^{-1} on the (111) surface. At higher temperatures, it was found that CO dissociates on the (100) surface. Molecular adsorption of decaborane at low temperatures was also observed followed by step-wise dissociation as the temperature is raised to form an intermediate with a B–H stretch of 2571 cm^{-1} before complete dissociation at temperatures of 400 K and above. The fact that stable molecular adsorption of CO and decaborane occurs on these surfaces followed by dissociation reveals that the surface chemistry of boron-rich borides is similar to that of catalytically active transition metals. This implies that the borides may be useful as catalysts.

Acknowledgements

This work was supported by the U.S. DOE, Basic Energy Sciences grant DE-FG02-05ER15726 and by the National Science Foundation under grant CHE-0714562. The authors also thank the donors of the Petroleum Research Fund administered by the American Chemical Society for partial support of this work.

References

1. Yamauchi, H.; Takagi, K.; Yuito, I.; Kawabe, U., "Work function of LaB_6", *Appl. Phys. Lett.* **1976,** 29, 638–640.
2. Aono, M.; Tanaka, T.; Bannai, E.; Oshima, C.; Kawai, S., "Surface states of $LaB_6(001)$ as revealed by angular-resolved ultraviolet photoelectron spectroscopy", *Phys. Rev. B* **1977,** 16, 3489.

3. Aono, M.; Oshima, C.; Tanaka, T.; Bannai, E.; Kawai, S., "Structure of the LaB_6(001) surface studied by angle-resolved XPS and LEED", *J. Appl. Phys.* **1978,** 49, 2761–2764.
4. Aono, M.; Nishitani, R.; Oshima, C.; Tanaka, T.; Bannai, E.; Kawai, S., "LaB_6 and SmB_6 (001) surfaces studied by angle-resolved XPS, LEED and ISS", *Surf. Sci.* **1979,** 86, 631–637.
5. Swanson, L. W.; McNeely, D. R., "Work functions of the (001) face of the hexaborides of barium, lanthanum, cerium and samarium", *Surf. Sci.* **1979,** 83, 11–28.
6. Futamoto, M.; Kawabe, U., "Field-ion microscopy of rare-earth hexaborides", *Surf. Sci.* **1980,** 93, L117–L123.
7. Nishitani, R.; Aono, M.; Tanaka, T.; Kawai, S.; Iwasaki, H.; Oshima, C.; Nakamura, S., "Surface states on the LaB6(100), (110) and (111) clean surfaces studied by angle-resolved UPS", *Surf. Sci.* **1980,** 95, 341–358.
8. Nakazawa, M.; Futamoto, M.; Usami, K.; Kawabe, U., "Surface compositions of hexaborides at high temperatures", *J. Appl. Phys.* **1981,** 52, 6917–6920.
9. Davis, P. R.; Chambers, S. A.; Swanson, L. W., "The adsorption of cesium on lanthanum hexaboride surfaces", *Proc. Intersoc. Energy Convers. Eng. Conf.* **1980,** 15th, 2327–30.
10. Watson, R. E.; Perlman, M. L., "Dipole effects and the work functions of the single crystal LaB_6", *Surf. Sci.* **1982,** 122, 371–382.
11. Futamoto, M.; Nakazawa, M.; Kawabe, U., "High temperature surface composition of hexaboride thermionic electron emitters", *Vacuum* **1983,** 33, 727–732.
12. Gesley, M.; Swanson, L. W., "A determination of the low work function planes of lanthanum hexaboride", *Surf. Sci.* **1984,** 146, 583–99.
13. Davis, P. R.; Gesley, M. A.; Schwind, G. A.; Swanson, L. W.; Hutta, J. J., "Comparison of thermionic cathode parameters of low index single crystal faces of LaB_6, CeB_6 and PrB_6", *Appl. Surf. Sci.* **1989,** 37, 381–394.
14. Ozcomert, J. S.; Trenary, M., "Atomically resolved surface structure of LaB_6(100)", *Surf. Sci.* **1992**, L227–232.
15. Oshima, C.; Kawai, S., "Auger electron spectroscopy study of oxidation on lanthanum hexaboride", *Appl. Phys. Lett.* **1973,** 23, 215–216.
16. Swanson, L. W.; Dickinson, T., "Single-crystal work-function and evaporation measurements of lanthanum hexaboride", *Appl. Phys. Lett.* **1976,** 28, 578–80.
17. Berrada, A.; Mercurio, J. P.; Etourneau, J.; Alexandre, F.; Theeten, J. B.; Tran Minh, D., "Thermionic emission properties of LaB_6 and CeB_6 in connection with their surface states, examination by XPS, Auger spectroscopy and the Kelvin method", *Surf. Sci.* **1978,** 72, 177–188.
18. Goldstein, B.; Szostak, D. J., "Characterization of clean and oxidized (100)LaB_6", *Surf. Sci.* **1978,** 74, 461–478.
19. Davis, P. R.; Chambers, S. A., "A study of oxygen interaction with a LaB6(100) single crystal surface", *Applications of Surface Science* **1981,** 8, 197–205.
20. Klauser, S. J.; Bas, E. B., "The interaction of oxygen with LaB_6 single crystal surfaces at elevated temperatures", *Applications of Surface Science* **1979,** 3, 356–363.
21. Chambers, S. A.; Davis, P. R.; Swanson, L. W., "Cesium and oxygen coadsorption on LaB_6 single crystal surfaces : II. Thermal desorption of cesium from LaB6 (100)", *Surf. Sci.* **1982,** 118, 93–102.
22. Nishitani, R.; Oshima, C.; Aono, M.; Tanaka, T.; Kawai, S.; Iwasaki, H.; Nakamura, S., "Oxygen adsorption on the LaB_6(100), (110) and (111) surfaces", *Surf. Sci.* **1982,** 115, 48–60.
23. Chambers, S. A.; Swanson, L. W., "Angle-resolved Auger electron emission from lanthanum hexaboride (LaB_6)(001) with and without chemisorbed oxygen", *Surf. Sci.* **1983,** 131, 385–402.

24. Davis, P. R.; Schwind, G. A.; Swanson, L. W., "The effect of oxygen pressure on volatility and morphology of LaB_6 single crystal cathodes", *J. Vac. Sci. Technol. B* **1986,** 4, 112–115.
25. Nishitani, R.; Aono, M.; Tanaka, T.; Oshima, C.; Kawai, S.; Iwasaki, H.; Nakamura, S., "Surface structures and work functions of the LaB_6 (100), (110) and (111) clean surfaces", *Surf. Sci.* **1980,** 93, 535–549.
26. Rokuta, E.; Yamamoto, N.; Hasegawa, Y.; Nagao, T.; Trenary, M.; Oshima, C.; Otani, S., "Surface phonon dispersion curves of the LaB_6(111) surface", *Surf. Sci.* **1996,** 358, 712–716.
27. Kang, D. H.; Trenary, M., "Surface chemistry of ethylenediamine ($NH_2CH_2CH_2NH_2$) on Pt(1 1 1)", *Surf. Sci.* **2000,** 470, L13–L19.
28. Yamamoto, N.; Rokuta, E.; Hasegawa, Y.; Nagao, T.; Trenary, M.; Oshima, C.; Otani, S., "Oxygen adsorption sites on the PrB_6(100) and LaB_6(100) surfaces", *Surf. Sci.* **1996,** 348, 133–142.
29. Yamamoto, N.; Rokuta, E.; Hasegawa, Y.; Nagao, T.; Trenary, M.; Oshima, C.; Otani, S., "Oxygen Adsorption on LaB_6(100) and (111) Surfaces", *Surf. Sci.* **1996,** 357/358, 708–711.
30. Rokuta, E.; Yamamoto, N.; Hasegawa, Y.; Nagao, T.; Trenary, M.; Oshima, C.; Otani, S., "Vibrational spectra of oxygen on LaB_6(100), (110), and (111) surfaces: A comparative study using high resolution electron energy loss spectroscopy", *J. Vac. Sci. Technol. A* **1996,** 14, 1674–1678.
31. Yorisaki, T.; Tillekaratne, A.; Moriya, Y.; Oshima, C.; Otani, S.; Trenary, M., "Vibrational spectroscopy of oxygen on the (100) and (111) surfaces of lanthanum hexaboride", *Surf. Sci.* **2010**, 604, 1202–1207.
32. Sheppard, N.; De La Cruz, C., "The reliability of vibrational spectroscopy as a means of identification of the structures of chemisorbed species on metal surfaces: the cases of CO, NO and C_2 hydrocarbon surface species", *Catal. Today* **2001,** 70, 3–13.
33. de la Cruz, C.; Sheppard, N., "A review of νCO bond-stretching wavenumbers for CO ligands in metal coordination compounds or clusters with emphasis on the less common types of metal/CO bonding patterns, and of the relationship between νCO and the internuclear distance, r(CO)", *J. Mol. Struct.* **1990,** 224, 141–161.
34. Nguyen, T. T.; Sheppard, N., The vibrational spectra of carbon monoxide chemisorbed on the surfaces of metal catalysts - A suggested scheme of interpretation. In *Advances in Infrared and Raman Spectroscopy*, Clark, R. J. H.; Hester, R. E., Eds. Heyden & Son Ltd.: London, 1978; Vol. 5.
35. Yorisaki, T.; Tillekaratne, A.; Ge, Q.; Oshima, C.; Otani, S.; Trenary, M., "Probing the properties of the (1 1 1) and (1 0 0) surfaces of LaB_6 through infrared spectroscopy of adsorbed CO", *Surf. Sci.* **2009,** 603, 3011–3020.
36. Tillekaratne, A.; Trenary, M., "Adsorption and Dehydrogenation of Decaborane on the Pt(111) Surface", *J. Phys. Chem. C* **2009,** 113, 13847–13854.

ZIRCONIUM DODECABORIDE, A NOVEL SUPERCONDUCTING MATERIAL WITH ENHANCED SURFACE CHARACTERISTICS

MIKHAIL BELOGOLOVSKII[1]*, ISRAEL FELNER[2], VLADIMIR SHATERNIK[3]
[1]*Donetsk Institute for Physics and Engineering, 83114 Donetsk, Ukraine*
[2]*The Racah Institute of Physics, The Hebrew University of Jerusalem, 91904 Jerusalem, Israel*
[3]*Institute for Metal Physics, 03680 Kyiv, Ukraine*

Abstract The paper gives a short overview of electronic characteristics of ZrB_{12} single crystals in normal and superconducting states. First-principles calculations of the electronic structure and charge density redistribution reveal that zirconium dodecaboride belongs to the class of 'covalent metals' with itinerant electronic states at the Fermi energy composed by weakly hybridized 2*p* orbitals of B atoms and 4*d* levels of Zr atoms and strong covalent bonding between nearest intra- and inter-cluster boron atoms. Our recent magnetic and tunneling measurements have revealed an enhancement of superconducting properties at the surface of ZrB_{12} comparing with its bulk. Relevant data of some other groups support our conclusion that this material as a first known superconductor with a native near-surface enhanced order parameter.

Keywords: Zirconium dodecaboride, electronic properties, first-principles calculations, superconductivity, surface characteristics

1. Introduction

Discovery of a rather simple diboride compound MgB_2 with a critical temperature T_c up to 39 K triggered intensive studies of a specific class of superconducting materials, belonging to 'covalent metals' [1]. A common feature of such compounds (diamond doped by boron [2], silicon [3], silicon carbide [4, 5], alkali-doped fullerenes [6] and so on with the superconducting

* Mikhail Belogolovskii, Donetsk Institute for Physics and Engineering, 83114 Donetsk, Ukraine, e-mail: bel@fti.dn.ua

N. Orlovskaya and M. Lugovy (eds.), *Boron Rich Solids: Sensors, Ultra High Temperature Ceramics, Thermoelectrics, Armor*, DOI 10.1007/978-90-481-9818-4_13,

critical temperature T_c up to 10, 0.35, 1.4, and 20 K, correspondingly) is the presence of least one relatively light element and strongly directional covalent bonds in the metallic state.

In spite of small T_c values comparing with high-temperature superconducting cuprates, the idea to design new materials which combine transition metals possessing a high valence electron density and high bulk modules, with small, covalent bond-forming *sp* atoms like boron, carbon, nitrogen, or oxygen attracts more and more attention in the last years [7]. The main reason is the possibility to realize high-frequency phonon modes in the crystal lattices from atoms of light elements and simultaneously a large electron–phonon coupling potential due to the covalent bonds of the atoms, the two factors leading due to the conventional theory of superconductivity to the enhancement of T_c. It should be noticed that they do not necessarily warrant a large T_c magnitude because the positive impact of the latter factor may be compensated by appearance of a lattice instability and/or a low density of states at the Fermi level $N(E_F)$ which is observed for the 'covalent metals' in the most cases. However, predictions of huge T_c values up to 150 K for some boron and carbon compounds like BC_x and Li_xBC, as well as bright potential applications in superconducting nano-electromechanical devices and resonators [7] stimulate new activities in this field.

Besides a pure fundamental interest, the most familiar representatives of covalent compounds are known as superhard and ultra-incompressible materials with great practical significance. Under doping, they are usually transformed into degenerate semiconductors with the Fermi level located in a valence band (or in a conduction band) for *p*- or *n*-type doping. *Ab initio* calculations of some novel compounds including transition-metal and light elements provide useful hints about a combination of attractive mechanical and electrical properties but progress in this direction is often limited by difficulties in material preparation [7]. Because of it, recent experimental efforts are partly refocused on those conducting materials (including superconductors) which are not extremely hard bur are thermally and chemically resistant. In particular, it concerns intermetallic compounds with high boron content characterized by high abrasion and chemical resistances [8]. Among them, superconducting zirconium dodecaboride has recently become a subject of intensive studies since large high-quality single crystals of metallic ZrB_{12} were grown by Paderno et al. [9]. Below we give a short overview of experimental and theoretical results obtained by us and some other groups which definitely show that this compound, first, belongs to the category of 'covalent metals' and, second, is the first known superconducting material with enhanced superconducting order parameter at its surface.

It should be noticed that among superconducting MB_6 hexaborides and MB_{12} dodecaborides (*M* is a rare-earth or actinide metal) there are only two

compounds with highest superconducting critical temperatures T_c: yttrium hexaborideYB$_6$ with T_c between 6 and 7 K and ZrB$_{12}$ with $T_c \cong 6$ K. In both cases the basic structural element is a stable boron cluster which forms together with an M atom a simple CsCl lattice in MB$_6$ compounds (M atoms occupy Cs sites, while B$_6$ octahedral clusters are in Cl sites) and NaCl lattice in dodecaborides (M occupies Na sites and B$_{12}$ cubooctahedral clusters are located at Cl sites). In the paper we shall show that, in spite of their similarity (also relating the T_c value), only ZrB$_{12}$ demonstrates a near-surface enhancement of superconducting characteristics whereas YB$_6$ demonstrates conventional surface characteristics. Analyzing the difference between the compounds we suggest possible explanation of the phenomenon.

2. Electronic Properties of Zirconium Dodecaboride from First-Principles Calculations

A unit cell of zrconium dodecaboride contains 52 atoms with positions which can be found in the recent study of its crystal structure [10]. We start our discussion of its electronic properties with first-principles self-consistent simulations of the spatial valence electron density distribution based on a simple and effective theory proposed by Reznik in [11]. The method is based on the concepts of local density approximations and generalizes the well-known Thomas–Fermi statistical approach by taking into account small arbitrary additions to a smoothly varying potential in a crystal. The electronic density is represented as a series of corrections to the Thomas–Fermi equation which may be partially summarized. Analyzing results of his simulations for some comparatively simple compounds, Reznik [11] showed a good agreement with more refined theoretical calculations performed earlier by other authors and proved that his method is an effective tool to study chemical bonding effects, especially, in compounds with a large number of atoms in a unit cell. The initial characteristics required to obtain the valence electron distribution are ionic pseudo-potentials well known from the literature and a particular form of an exchange-correlation potential suggested in [12].

Charge density $\rho(\mathbf{r})$ maps for two (001) planes in zirconium dodecaboride are shown in Figs. 1 and 2. The first map corresponds to the (001) plane including five zirconium and eight boron atoms whereas in the second case the plane (parallel and shifted along the z-axis) incorporates only boron atoms. The profiles reveal that the B–B covalent bond between nearest intra- and intercluster boron atoms holds a considerable amount of charge, while at the center of the boron cluster and in the vicinity of zirconium atoms, the charge drops to quite a low value. Effective charges of Zr and B were calculated within corresponding Wigner–Seitz cells. Different character

of chemical bonding in boron and zirconium subsystems and between them supports the idea about existence of two absolutely different contributions to the phonon spectrum: a quasi-Debye background from the boron atoms and an independent Einstein-like contribution associated with vibrations of Zr atoms [13]. At the same time, an assumption concerning the nature of a low-energy phonon mode forming a superconducting state in ZrB_{12} (attributed in [13] to vibrations of Zr ions) disagrees with our data indicating that the main electron transport occurs within the boron subsystem.

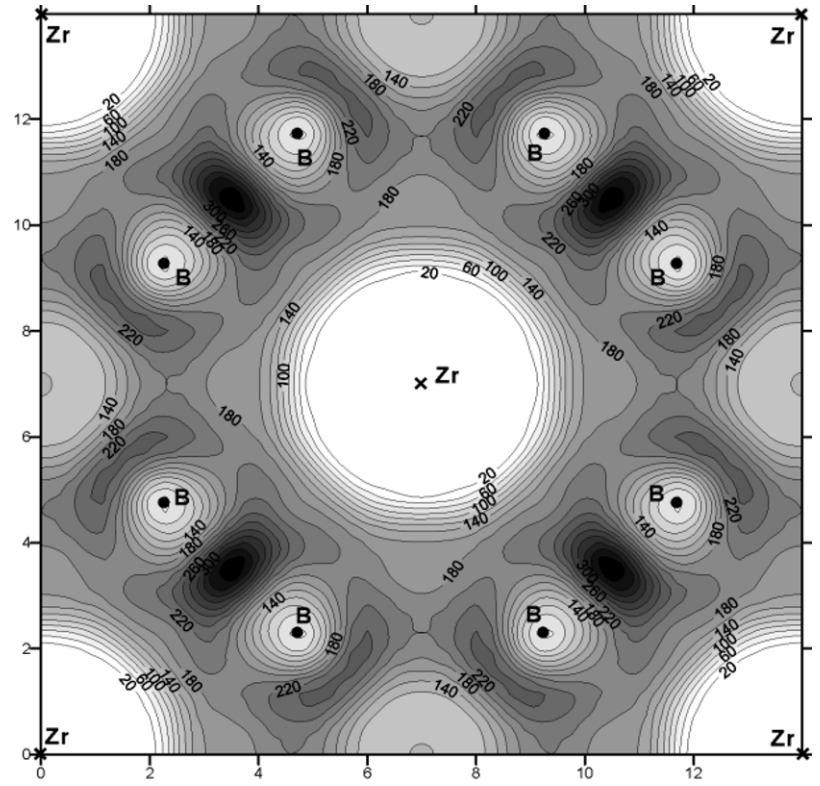

Figure 1. Electronic density map of the (001) plane through five Zr and eight B atoms. Here and below, the distances are given in atomic units and the charge density values are given in *e*/cell.

Let us now discuss the energy band structure and electronic density of states of zirconium dodecaboride. We have calculated them by means of the full-potential linearized-augmented-plane-wave method implemented in the

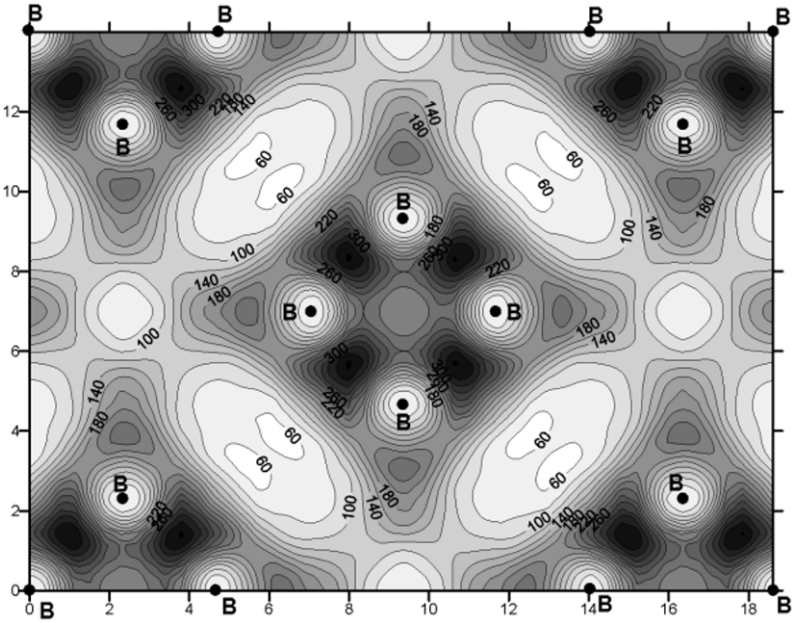

Figure 2. Electronic density map of a plane through 16 B atoms which is parallel to the (001) plane.

WIEN2k code [14] with exchange and correlation effects treated in the framework of the density-functional theory using the local spin density approximations [15]. Before it, similar calculations for ZrB_{12} were performed using the self-consistent full-potential linearized muffin-tin orbital method [16] with atomic-like basic functions and the potential assumed to be spherically symmetric within an atomic sphere surrounding each atom in the crystal. On the contrary, in the WIEN2k code the basic functions are plane waves which are more appropriate for metallic compounds. Hence, a direct comparison of the data followed from two different approaches can provide important and reliable information about the material's electronic structure. It concerns also comparison of charge density distributions obtained within a generalized Thomas–Fermi approach (Figs. 1 and 2) and from the WIEN2k code [14].

Figure 3 demonstrates the electronic band structure of zirconium dodecaboride which is very similar to simulations of Ref. 16. From Fig. 3 it is clear that in ZrB_{12} the Fermi energy E_F enters a conduction band and that in its nearest vicinity the electronic subsystem resembles that of the free-electron model. The latter statement can explain why bulk superconducting characteristics of ZrB_{12} resemble those of textbook BCS superconductors [17].

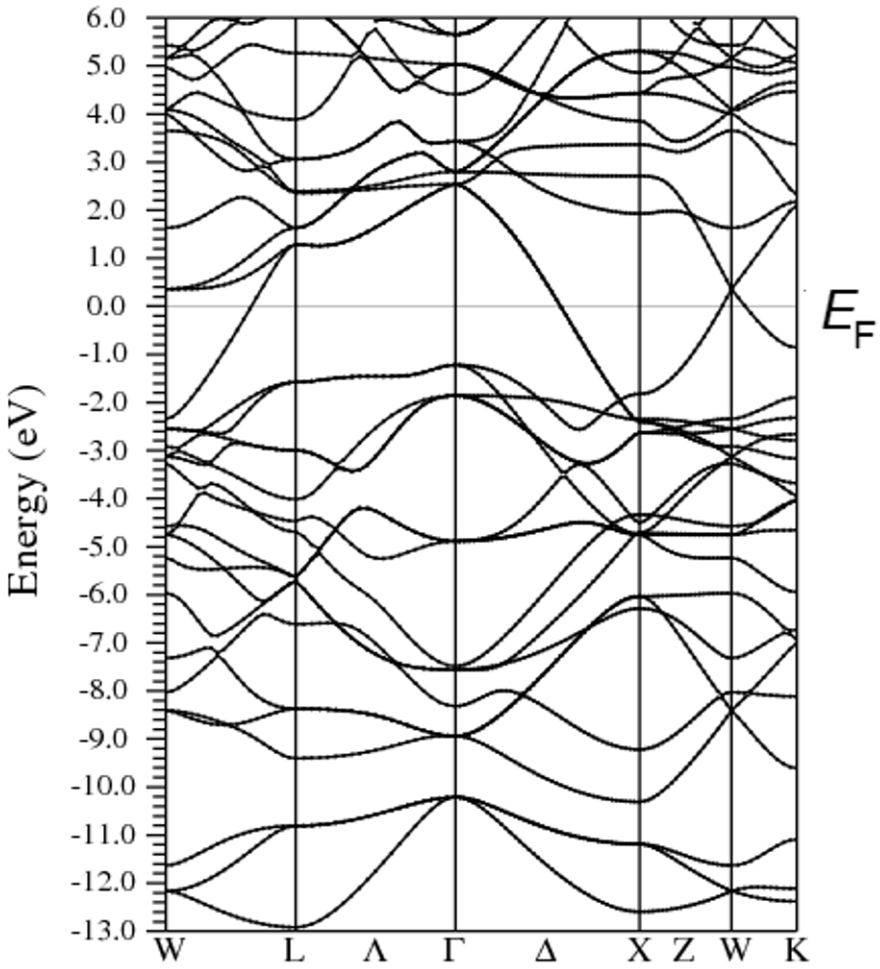

Figure 3. Electronic band structure of ZrB_{12}.

Figure 4 shows the total density of states (DOS) in zirconium dodecaboride. Again, there are no qualitative differences with the data of [16]. For example, the total DOS at the Fermi level calculated within the approximation using atomic-like wave functions [16] is nearly 1.7 states/eV·unit cell, in consistence with our value of 1.4 states/eV·unit cell. As follows from partial densities of states (not shown here) the electronic states at E_F are mainly composed by 2*p* orbitals of boron atoms and 4*d* levels of zirconium atoms which are weakly hybridized. This conclusion agrees with our statement (Figs. 1 and 2) relating a strong covalent character of the B–B bonding in contrast to that between Zr and B atoms.

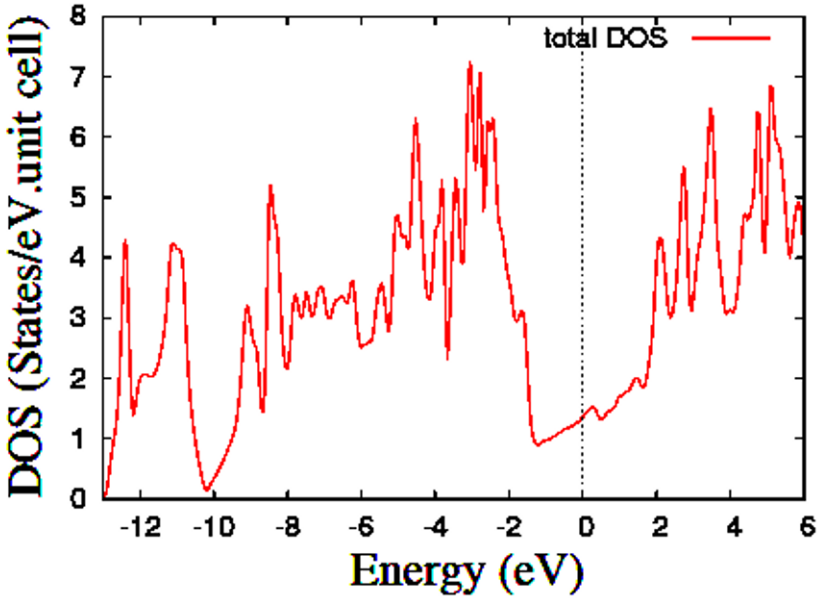

Figure 4. Total density of electronic states in ZrB_{12}.

3. Bulk Versus Surface Superconducting Characteristics of Zirconium Dodecaboride

It is well known that the near-surface change of an order parameter Δ in a superconducting state can be characterized with a surface extrapolation length b. The equation which defines b is a boundary condition for Δ. For a simple geometry we deal with it takes a form

$$\left.\frac{d\Delta}{dx}\right|_{x=0} = \frac{1}{b}\Delta\Big|_{x=0}$$

For a vacuum/superconductor interface $b = \infty$, another extreme limit $b \to 0$ arises when one considers an interface between a ferromagnet and a superconductor. A fairly common case is $b > 0$, which corresponds to a normal-metal/superconductor bilayer and means that the order parameter is suppressed at the superconducting surface. In the first paper where the case of $b < 0$ was raised and studied experimentally Fink and Joiner [18] pointed out that the effect can take place, for instance, when a surface of a superconductor is treated mechanically (in their case, by cold working). After such treatment the authors revealed an increase of the surface critical field H_{c3} and interpreted the observation within the Ginzburg–Landau theory assuming negative b values. A more detailed and quantitative study, involving $b < 0$, was performed later in the context of twinning plane superconductivity

by Khlyustikov and Buzdin [19]. Recently, superconductivity in single-crystal Sn samples with controllable surface-enhanced order parameter was achieved by two ways – mechanical polishing and ion irradiation [20]. It should be noticed that in all papers mentioned above the presence of surface-enhanced superconducting characteristics was confirmed only with indirect experimental methods. In a table below we present a set of experimental data for the ZrB_{12} compound (including our results obtained with surface-sensitive tunneling and bulk SQUID-magnetometry techniques) indicating the natural existence of a negative extrapolation length b in this material.

TABLE 1. Bulk and surface characteristics of superconducting ZrB_{12} and YB_6 single crystals

Parameter	Bulk (B) or surface (S) characteristic	ZrB_{12}	YB_6	BCS theory
Specific heat jump at T_c [a]	B	1.66 [22]	2.02 [23]	1.43
$1 + \lambda_{e\text{-}ph}$ (from γ_n) [b]	B	1.18–1.19 [22]	1.86–2.14 [23]	≥ 1.00
$D(t)$, temperature dependence of H_c [c]	B	close to 0 [17]	As for strong-coupling superconductors [23]	Close to 0 [21]
$2\Delta_0/k_BT_c$ (from Toxen's equation [24]) [d]	B	3.4	4.0	3.52
$2\Delta_0/k_BT_c$ (tunneling spectroscopy data)	S	4.75 [17]	3.59 [25]; 3.96 [26]; 4.02 [27]	3.52
$\lambda_{e\text{-}ph}$ (reconstructed from tunneling data)	S	–	0.9 [27]	≥ 0
$2\Delta_0/k_BT_c$ (point- contact spectroscopy data)	S	4.8 [28]	–	3.52
$2\Delta_0/k_BT_c$ (magnetic penetration depth data)	S	4.77 [29]	–	3.52

[a] $\Delta C/\gamma_n T_c$, γ_n, coefficient of the linear term of the normal-state specific heat at $T \to 0$

[b] $\lambda_{e\text{-}ph}$, electron-phonon coupling constant determined from γ_n

[c] the deviation function $D(t) = h - (1 - t^2)$ is a good indicator of the electron–phonon interaction strength [21], H_c, thermodynamic critical field, $h = H_c(T)/H_c(0)$, $t = T/T_c$

[d] $2\Delta_0/k_BT_c$, normalized superconducting gap, is the best indicator of the electron–phonon coupling strength [21], an empirical Toxen's formula $\frac{2\Delta_0}{T_c} = -\frac{2T_c}{H_c(0)}\left(\frac{dH_c}{dT}\right)_{T=T_c}$ [24], magnetization data are taken from [17] for ZrB_{12} and [25] for YB_6.

Table 1 summarizes known data for bulk and surface parameters of superconducting ZrB_{12} and YB_6 single crystals obtained by different

groups. The main distinction between the two characteristics of ZrB_{12} samples consists in the fact that their bulk properties are always in good accordance with the weak-coupling BCS theory whereas enhanced surface parameters may be understood only within a strong-coupling boson-exchange mechanism [21]. On the contrary, YB_6 in its bulk and at the surface is a medium-coupling superconductor.

If so, the two arising questions are: (1) why the two compounds have so different bulk-versus-surface characteristics and (2) what the nature of the enhancement effect is. Here we should notice that suppression of the electron–phonon interaction in the near-surface layers is a typical feature of complex superconducting compounds. The reliable indicator of the electron-phonon interaction strength $\lambda_{e\text{-}ph}$ is the ratio of the energy gap and the critical temperature $2\Delta_0/k_BT_c$ measured with surface-sensitive techniques. In the conventional theory of superconductivity T_c exponentially depends on $\lambda_{e\text{-}ph}$, thus, even its small changes result in dramatic modifications of T_c, whereas the ratio $2\Delta_0/k_BT_c$ remains almost unchanged (as shown, for example, in recent experiments with MoGe thin films [30]). But in our case we have observed a strong enhancement of the surface value of $2\Delta_0/k_BT_c$ without any noticeable deviation of the critical temperature T_c. Up to our knowledge, it is the first observation of such a phenomenon.

To explain the finding qualitatively, we turn to the so-called percolative theory of superconductivity by Phillips [31] suggested originally for strongly disordered ceramic high-temperature superconductors. It assumes that cuprates are electronic glasses with dopants frozen into configurations which minimize their free energy. According to this theory, the origin of the high-T_c phenomenon is strongly attractive electron–phonon pairing interactions at the interlayer dopants. The self-organized percolative filamentary theory [31], based on topological reasoning, is also well suited for marginally stable (anomalously soft) materials. From the first sight, it has no relation to zirconium dodecaboride, a superhard and chemically stable material with a high-symmetrical lattice. It is clear that any significant amount of disorder cannot appear inside the ZrB_{12} crystal but it may occur at its surface treated as a two-dimensional defect [32]. But why does the effect take place in ZrB_{12} and not in YB_6? Comparing the phase diagrams of the two boron-rich systems [33, 34], we find that yttrium hexaboride is thermodynamically stable in a wide range of temperatures (from very high to room ones) [33]. On the contrary, the ZrB_{12} compound is stable only within a narrow temperature interval above 2,000 K [34]. Although it is easy to stabilize the compound to room temperature [9, 34], the marginal stability of the lattice subsystem can result in the formation of a filamentary network at the ZrB_{12} surface. Due to the disorder, the electron–phonon coupling strength will be enhanced and the near-surface value of the $2\Delta_0/k_BT_c$ ratio would increase

although its value in the bulk should remain unchanged. Thus, the topological network considerations [31, 32] can qualitatively explain the unusual features observed in superconducting ZrB_{12}.

4. Conclusions

1. Using first-principles calculations based on a generalized Thomas–Fermi statistical approach [11] and a full-potential linearized-augmented-plane-wave method [14], we have studied the valence electronic density distribution, the band structure, and the density of electronic states in zirconium dodecaboride. Analyzing our data and comparing them with results of other computational methods, we show that ZrB_{12} belongs to partially covalent compounds of transition metals with light elements where the presence of a three-dimensional directional covalent-banding boron network is responsible for advanced mechanical properties. It is found that electronic states at the Fermi energy mainly composed by weakly hybridized 2*p* orbitals of boron atoms and 4*d* levels of zirconium atoms resemble those following from the free-electron model.
2. We have argued that zirconium dodecaboride is a first known superconductor with a native near-surface enhanced order parameter. The phenomenon is interpreted within a self-organized percolative theory proposed by Phillips [31, 32] in order to explain unusual properties of strongly disordered superconducting cuprates but, at the same time, well suited also for surfaces of marginally stable compounds.
3. Superconducting zirconium dodecaboride with its unique surface-related properties can be used as a very effective coating in superconducting microresonators which have attracted substantial interest for low-temperature detector applications (due to the possibility of large-scale microwave frequency multiplexing) and quantum computing experiments. Further studies of the compound in normal and superconducting states are needed to elucidate the phenomenon of the surface-enhanced superconducting order parameter as well as to reveal its effect on the improvement of material surface characteristics, in particular, for high-frequency applications.

Acknowledgments

The work was partly supported by the Ministry of Education and Science of Ukraine and the Israeli Ministry of Science and Technology within a joint Israeli-Ukrainian project. It is our pleasure to thank all coauthors of the papers [17, 25, 29] for fruitful collaboration and stimulating discussions.

References

1. Nagamatsu J, Nakagawa N, Muranaka T et al (2001) Superconductivity at 39 K in magnesium diboride. Nature 410:63–64.
2. Ekimov EA, Sidorov VA, Bauer ED et al (2004) Superconductivity in diamond. Nature 428:542–545.
3. Bustarett E, Marcenat C, Achatz P et al (2006) Superconductivity in doped cubic silicon. Nature 444:465–468.
4. Ren Z-A, Kato J, Murunaka T et al (2007) Superconductivity in boron-doped SiC. J Phys Soc Jpn 76:103710–103715.
5. Kriener M, Maeno Y, Oguchi T et al (2008) Specific heat and electronic states of superconducting boron-doped silicon carbide. Phys Rev B 78:024517.
6. Varma CM, Zaanen J, Raghavachari K (1991) Superconductivity in the fullerenes. Science 254:989–992.
7. Blase X, Bustarret E, Chapelier C et al (2009) Superconducting Group IV Semiconductors. Nature Mater 8:375–382.
8. Serebryakova TI, Neronov PD (2003) High-temperature borides. Cambridge Sci Publ, Cambridge .
9. Paderno YuB, Layshchenko AB, Filippov VB, Duhnenko AV (2002) Zirconium dodecaboride single crystal growth. In: Skorokhod V (ed) Science for materials in the frontier of centuries: advantages and challenges. IPM NASU, Kiev.
10. Leithe-Jasper A, Sato A, Tanaka T (2002) Z Kristallogr - New Cryst Struct 217:319─320.
11. Reznik IM (1996) Modified statistical method and electron charge distribution in HTS materials. Low Temp Phys 22:403–405.
12. Kolmanovich VJu, Reznik IM (1984) Decompositions of electron density and the shell problem in Hohenberg-Kohn functional theory. Solid State Commun 50:117–120.
13. Lortz R, Wang Y, Abe S et al (2005) Specific heat, magnetic susceptibility, resistivity and thermal expansion of the superconductor ZrB_{12} . Phys Rev B 72:024547.
14. Blaha P, Schwarz K, Madsen GKH et al (2001) WIEN2K, An augmented plane wave + local orbitals program for calculating crystal properties. Techn Univ, Wien.
15. Perdew JP, Wang Y (1992) Accurate and simple analytic representation of the electron-gas correlation energy. Phys Rev B 45:13244–13249.
16. Shein IR, Ivanovskii AL (2003) Band structure of superconducting dodecaborides YB_{12} and ZrB_{12}. Phys Solid State 45:1429–1434.
17. Tsindlekht MI, Leviev GI, Asulin I et al (2004) Tunneling and magnetic characteristics of superconducting ZrB_{12} single crystals. Phys Rev B 69:212508.
18. Fink HJ, Joiner WCH (1969) Surface nucleation and boundary conditions in superconductors. Phys Rev Lett 23:120–123.
19. Khlyustikov IN, Buzdin AI (1987) Twinning-plane superconductivity. Adv Phys 36:271–330.
20. Kozhevnikov VF, Van Bael MJ, Sahoo PK et al (2007) Observation of wetting-like phase transitions in a surface-enhanced type-I superconductor. New J Phys 9:75.
21. Carbotte JP (1990) Properties of boson-exchange superconductors. Rev Mod Phys 62:1027–1157.
22. Wang Y, Lortz R**,** Paderno Yu et al (2005) Specific heat and magnetization of a ZrB_{12} single crystal: characterization of a type-II/1 superconductor. Phys Rev B 72:024548.
23. Lortz R, Wang Y, Tutsch U et al (2006) Superconductivity mediated by a soft phonon mode: specific heat, resistivity, thermal expansion, and magnetization of YB_6 Phys Rev B 73:024512.
24. Toxen AM (1965) New relationship between the critical field and energy gap of a superconductor. Phys Rev Lett 15: 462–463.

25. Tsindlekht MI, Genkin VM, Leviev GI et al (2008) Linear and nonlinear low-frequency electrodynamics of surface superconducting states in an yttrium hexaboride single crystal. Phys Rev B 78:024522.
26. Kunii S, Kasuya T, Kadowaki K et al (1984) Electron tunneling into superconducting YB_6. Solid State Commun 52:659–661.
27. Schneider R, Geerk J, Rietschel H (1997) Electron tunnelling into a superconducting cluster compound: YB_6. Europhys Lett 4:845–849.
28. Daghero D, Gonnelli RS, Ummarino GA et al (2004) Andreev-reflection spectroscopy in ZrB_{12} single crystals. Supercond Sci Technol 17:S250–S254.
29. Khasanov R, Di Castro D, Belogolovskii M et al (2005) Anomalous electron-phonon coupling probed on the surface of superconductor ZrB_{12}. Phys Rev B 72:224509.
30. Tashiro H, Graybeal JM, Tanner DB et al (2008) Unusual thickness dependence of the superconducting transition of α-MoGe thin films. Phys Rev B 78:14509.
31. Phillips JC (2010) Percolative theories of strongly disordered ceramic high-temperature superconductors. Proc Nat Acad Sci USA 107: 1307–1310.
32. Phillips JC (2009) High temperature cuprate-like superconductivity. Chem Phys Lett 473:274–278.
33. Otani S, Korsukova MM, Mitsuhashi T, Kieda N (2000) Floating zone growth and high-temperature hardness of YB_4 and YB_6 single crystals. J Cryst Growth 217:378–382.
34. Chen HM, Zheng F, Liu HS et al (2009) Thermodynamic assessment of B–Zr and Si–Zr binary systems. J Alloys Compd 468:209–216.

BORON UNDER PRESSURE: PHASE DIAGRAM AND NOVEL HIGH-PRESSURE PHASE

ARTEM R. OGANOV[1,2,*]
[1] *Department of Geosciences, Department of Physics and Astronomy, and New York Center for Computational Sciences, Stony Brook University, Stony Brook, New York 11794-2100, USA*
[2] *Geology Department, Moscow State University, 119992 Moscow, Russia*

Abstract Boron has a unique chemistry, responsible for remarkable complexities even in the pure element. I review some of the history of the discovery of this element, and recent surprises found in boron under pressure. I discuss the recent discovery of a new high-pressure phase, γ-B_{28}, consisting of icosahedral B_{12} clusters and B_2 pairs in a NaCl-type arrangement: $(B_2)^{\delta+}(B_{12})^{\delta-}$, and displaying a significant charge transfer $\delta \sim 0.48$. Boron is the only light element, for which the phase diagram has become clear only in the last couple of years, and this phase diagram is discussed here among other recent findings.

Keywords: boron allotropes, ab initio simulations, crystal structure prediction, phase diagram

1. Introduction

Boron can be called a frustrated element: situated between metals and insulators in the Periodic Table, it has only three valence electrons (favoring metallicity), but strongly localized[1] so that insulating states emerge at low pressures. Pressure, temperature and impurities easily shift this balance: for instance, while pure forms of boron are all semiconducting, doped boron is often metallic.

* Department of Geosciences, Department of Physics and Astronomy, and New York Center for Computational Sciences, Stony Brook, University, Stony Brook, New York 11794-2100, USA. Geology Department, Moscow State University, 119992 Moscow, Russia, e-mail: aoganov@notes.cc.sunysb.edu

[1] One parameter quantifying localization of valence electrons is their orbital radius; the outermost valence orbital radius for the boron atom is 0.78 Å, only slightly larger than that of carbon (0.62 Å), and much smaller than that of metals aluminum (1.31 Å) or gallium (1.25 Å).

N. Orlovskaya and M. Lugovy (eds.), *Boron Rich Solids: Sensors, Ultra High Temperature Ceramics, Thermoelectrics, Armor*, DOI 10.1007/978-90-481-9818-4_14,

At low pressures (<89 GPa) boron adopts structures based on icosahedral B_{12} clusters with metallic-like 3-centre bonds within the icosahedra and covalent 2-centre and 3-centre bonds between the icosahedra. Such bonding satisfies the octet rule and produces a delicate insulating state.

Among the reported phases of boron, probably only three correspond to the pure element [1, 2]: rhombohedral α-B_{12} and β-B_{106} phases (with 12 and 106 atoms in the unit cell, respectively) and tetragonal T-192 (with 190-192 atoms/cell).

The high-pressure behaviour of boron is intriguing. On the one hand, pressure favours metallic states and might stabilise metallic-like icosahedral clusters [3]. On the other hand, packing efficiency of icosahedral structures is very low (34% for α-B_{12}, calculated assuming atomic radius equal to half the shortest B–B bond), necessitating the destruction of the icosahedra and formation of denser phases under pressure – e.g., the metallic α-Ga-type phase [4, 5]. Metastable room-temperature compression of β-B_{106} showed amorphization [3] at 100 GPa and the onset of superconductivity [6] at 160 GPa. The nature of the superconducting phase remained unclear, as did the phase diagram of boron, both at high and low pressures.

Before considering in greater detail the high-pressure behaviour of boron and the newly discovered γ-B_{28} phase (subject of Section 3), we delve into the very instructive history of this element in the next section. Our review is based on our previous publications [7–9] and is intentionally non-technical (all the technical details interested readers can find in the original publications cited here).

2. A Bit of History

Boron is arguably the most complex element in the Periodic Table. The history of its studies is full of disputes, with mistakes made even by great scientists. At times this history may even read like a detective story.

A boron-containing mineral borax (probably from Persian “buraq”, meaning “white”), $Na_2[B_4O_5(OH)_4]\cdot 8H_2O$, was known since ancient times. In 1702, starting from borax, W. Homberg obtained a snow-white powder that he called “sedative salt”, now known as metaboric acid, HBO_2. The next stage, marked by the “double discovery” of this element, was at the time of scientific rivalry between great English (Humphry Davy) and French (Louis Joseph Gay-Lussac and Louis Jacques Thenard) chemists. On 21 June 1808, Gay-Lussac and Thenard announced the discovery of the new element, which they called “bore” (the element is still called this name in

French). They obtained boron by reduction of boric acid with potassium[2] [10]. Shortly afterwards, Humphry Davy submitted to the Royal Society of London an article on the discovery of a new element (which he called boracium)[3] [11]. Faithful to his style, which has led to the discovery of a whole pleiad of elements, Davy prepared boron by electrolysis. Curiously, both discoveries did not produce a pure element. It is now clear that both groups synthesized compounds containing not more than 50% of boron [12].

Henri Moissan, who proved that Gay-Lussac, Thenard and Davy did not deal with pure boron; in 1895 he prepared the element by reduction of B_2O_3 with magnesium in a thermite-type reaction [12]. However, even Moissan's material was far being a pure element. It is often quoted that 99%-pure boron was synthesized by E. Weintraub [13] in 1909–1911, but there are reasons for doubt, as pure boron polymorphs are documented only after 1957.

After the element itself got more or less established, a saga of the discovery of boron polymorphs gradually began. And that saga was equally complex and full of misdiscoveries. Already in 1857 Friedrich Wöhler and Henri Sainte-Claire Deville [14, 15], heating up boron oxide and aluminium, obtained three forms of boron. On the basis of hardness and luster, they drew an analogy with carbon polymorphs and called these forms diamond-like, graphite-like and charcoal-like (amorphous). Amorphous form had the same properties as the material synthesized by Gay-Lussac and Thenard (which, as we now know, was not pure boron), while the "diamond-like" and "graphite-like" forms were later proven to be compounds containing not more than 70% of boron [12]. Thus, many, if not most, of the great scientists who studied boron, fell victims of this element's extreme sensitivity to even small amounts of impurities. This sensitivity is evidenced by the existence of such very boron-rich compounds (with unique icosahedral structures) as $YB_{65.9}$, GeB_{90}, B_6O, NaB_{15}, $B_{12}P_2$, $B_{13}P_2$, $B_{13}C_2$, $MgAlB_{14}$, AlC_4B_{40}, $B_{50}C_2$, $B_{50}N_2$, $PuB_{100(?)}$ (e.g., [1]). In particular, the structure of YB_{66} is an icon of structural complexity – it contains 1584 atoms in the unit cell [16].

At least 16 crystalline polymorphs have been described [1], but crystal structures were determined only for four modifications and most of the reported phases are likely to be boron-rich borides rather than pure elemental boron [1–3]. Until 2007, it was the only light element, for which the ground

[2] The story of how Gay-Lussac and Thénard obtained potassium is also quite instructive. Davy's discovery of this element by electrolysis caused a great excitement among chemists. Emperor Napoleon I, who awarded a prestigious prize to English chemist Humphry Davy, wished to foster similar kind of research (discovery of new elements by electrolysis) and presented Davy's competitors, Gay-Lussac and Thénard, with a very large electric battery. Disappointingly, the battery turned out to be not nearly as powerful as was expected. Gay-Lussac and Thénard, however, managed to prepare potassium (used for preparing boron) by heating up potash and iron.

[3] The material obtained by Davy appears to have been metallic, whereas pure boron phases are all semiconducting.

state was not known even at ambient conditions. And none of the polymorphs reported before 1957 actually correspond to pure boron. Most of the discoveries related to pure boron discoveries were done in two "waves" – 1957–1965 and 2001–2009.

The first wave was led by researchers from Cornell University and General Electric (GE) Corporation. The so-called I-tetragonal phase (or T-50, because it contains 50 atoms in the unit cell), produced in 1943 jointly at Cornell and GE [17], was the first one for which the structure was solved – in 1951 [18, 19]. However, this "well-established" phase was proven to be a compound [2, 20, 21] of composition $B_{50}C_2$ or $B_{50}N_2$.

The first pure boron phase discovered was β-B_{106} [22], the structure of which turned out to be extremely complex and was solved only several years later [23]. This discovery was shortly followed by the discoveries of α-B_{12} phase at GE in 1958 [24] and T-192 phase at Polytechnic Institute of Brooklyn in 1960 [25] (the structure of the latter was so complex that it was solved only in 1979 [26]). All these structures contain B_{12} icosahedra and are shown in Fig. 1.

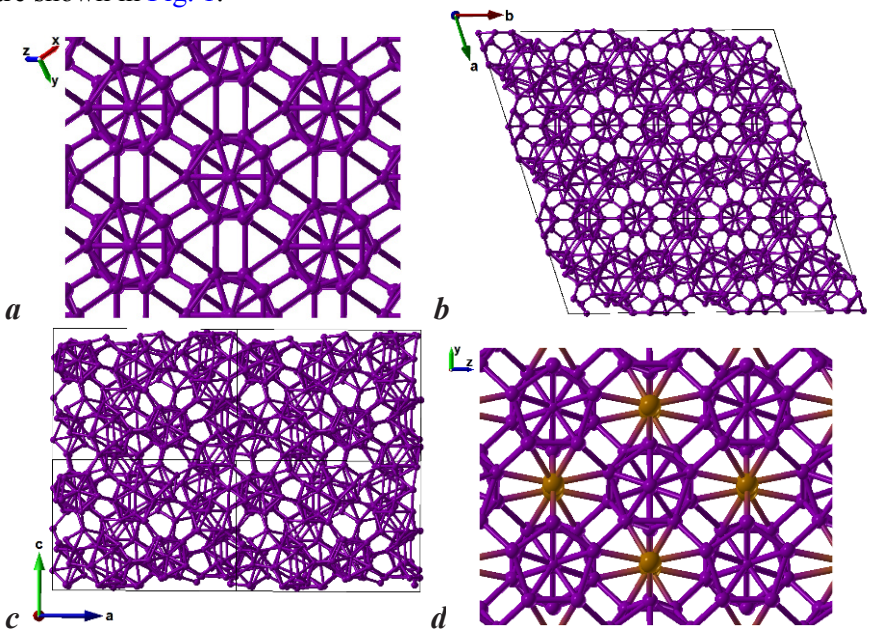

Figure 1. Crystal structures of boron polymorphs. (**a**) α-B_{12}, (**b**) β-B_{106}, (**c**) T-192, (**d**) γ-B_{28}. Panels (**a**) and (**d**) are from [1], (**b**) and (**c**) are from [7].

Because of the sensitivity of boron to impurities different samples of the same polymorph show important differences in structural and thermodynamic properties – as a result, the relative stability of boron phases is still experimentally unresolved even at ambient conditions [27]. It was, for

instance, a matter of a debate (until 2007) whether α-B_{12} or disordered β-B_{106} is stable at ambient conditions. Amberger and Ploog [2] even suggested that only two known phases correspond to pure boron, namely, α-B_{12} and T-192, and possibly β-B_{106}. They obtained boron by CVD using mixture of BBr_3 and H_2 at temperatures 1,200–1,600 K, with deposition on Ta wires in absence of any foreign atoms. This way they observed amorphous boron, α-B_{12} and T-192 phases, and occasionally β-B_{106}.

As we mentioned, much of the progress was done at GE – at that time, GE amassed a unique group of researchers with the aim of enabling industrial-scale synthesis of diamond. Furthermore, GE researchers synthesized cubic BN, an advanced substitute for diamond in cutting and abrasive tools. Both synthetic diamond and cubic BN (commercialized under name "borazon") turned into multimillion-dollar industries. GE was interested in boron, because of its extreme hardness and because of its highly tunable electrical conductivity. At least since the works of Sainte-Claire Deville and Wöhler in 1850s, boron was known to be the second hardest element after carbon (viz. diamond), and Weintraub [13] even entertained ideas that under certain fabrication protocol boron could become harder than black diamond (variety of diamond called "carbonado")[4].

Robert Wentorf of GE, one of the pioneers of high-pressure synthesis of materials and the main author of the synthesis of cubic BN, in 1965 explored the behavior of boron under pressure. At pressures above 10 GPa and temperatures 1,800–2,300 K, he found that both β-B_{106} and amorphous boron transformed into another, hitherto unknown, phase [28]. Wentorf reported a qualitative diffraction pattern of the new material and described the changes of the density and electrical conductivity across the phase transition. Neither the chemical composition, nor structure or even lattice parameters were determined, however. For that time, it was a state-of-the-art work, but nevertheless it was not accepted by the community and Wentorf's diffraction data were deleted from Powder Diffraction Files Database. However, now it can be stated that with good likelihood Wentorf had synthesized phase now known as γ-B_{28} [7] (probably in mixture with other phases).

The second wave of boron studies was probably catalyzed by the 2001 unexpected discovery of superconductivity in MgB_2 [29]. It is clear (e.g., [30]) that superconductivity comes from the boron sublattice of this structure, and that fuelled further research on pure boron. In 2001, compressing β-B_{106}

[4] For example Weintraub wrote that "(pieces of boron) are very hard and scratch with ease the known hard substances except diamond", "in further continuation of the work additional toughness may be imparted to boron and the product become a cheap substitute for black diamond" and "Will it be possible to approach the properties of diamond or perhaps by combining boron and carbon even exceed diamond in its hardness? I can only say that we are working on this problem." [13]

at room temperature, Eremets et al. [6] indeed observed metallization at 160 GPa, and the metallic state displayed superconductivity (with the value of T_c reaching 11.2 K at 250 GPa). The structure of this metallic phase was not determined, but subsequent experiments [3] suggested that room-temperature compression of β-B_{106} results in pressure-induced amorphization at 100 GPa. This implies that there is a kinetically hindered phase transition to some unknown crystalline phase below 100 GPa. Using laser heating to overcome kinetic barriers, Ma et al. [31] found that β-B_{106} transforms into the T-192 phase above 10 GPa at 2,280 K. This proved that the T-192 phase is not only a pure boron phase, but also has a stability field at high pressures and temperatures. Its stability field was further constrained in [7].

At the same time, the stable phase at ambient conditions remained unknown. The debate whether α-B_{12} or β-B_{106} is stable at ambient conditions was finally resolved in 2007–2009 by ab initio calculations of three different groups [32–34], which used different approaches, but all concluded in favor of β-B_{106} and against common intuition that favored the much simpler α-B_{12} structure.

Another major result came from J. Chen and V.L. Solozhenko, who independently found a new phase of pure boron at pressures above 10–12 GPa and temperatures above 1,500 K. Further evolution of ideas and events completed the "second wave of boron research", resolved many old problems and by itself could deserve a detective novel. This discovery is discussed in the following section.

3. Structure and Properties of a New Phase of Boron, γ-B_{28}

a. *Establishing the structure*. Although Chen managed to determine the unit cell parameters of the new phase (orthorhombic cell with a = 5.0544 Å, *b* = 5.6199 Å, *c* = 6.9873 Å), neither he nor Solozhenko succeeded in solving its structure – in spite of intense research and repeated experiments during several years. In 2006, Chen posed this problem to me, with the idea that the method for predicting crystal structures [35] that I was developing at the time could be used for solving this problem. The structure (Fig. 1d) was solved within 1 day[5].

USPEX [35] is an ab initio evolutionary algorithm, which searches for the structure with the lowest theoretical thermodynamic potential and requires no experimental information. However, the use of experimental cell parameters as constraints simplifies search and we took advantage of it.

[5] But it took much longer to publish these results. The paper was submitted to *Nature* on 27 January 2007 and it took 2 years to publish it in *Nature* (the paper came out on 28 January 2009). During this period, I learned about Solozhenko's independent work and our parallel teams merged.

From densities of other boron phases, we estimated the number of atoms in the cell to be between 24 and 32. Since this number has to be even to produce an insulating state, we considered cases of 24, 26, 28, 30 and 32 atoms/cell.

Figure 2 illustrates this search process by the sequence of lowest-energy structures in each generation for the 24-atom system. The first (random) generation did not contain any icosahedral structures. Increasingly large fragments of the icosahedra appear during calculation, until at the 11th generation the lowest-energy structure is found. Figure 3 shows the lowest-energy structures for each number of atoms in the unit cell. The 28-atom *Pnnm* structure (Fig. 1d) has the lowest energy per atom, correct orthorhombic

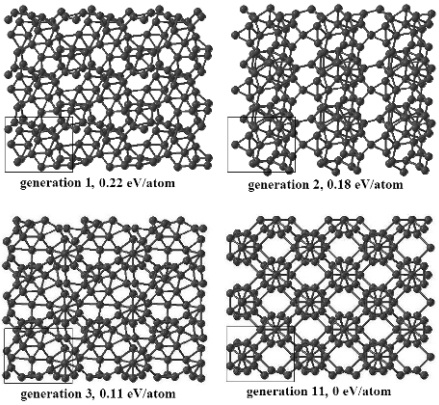

Figure 2. Example of an evolutionary simulation (24-atom system at fixed cell parameters). Best structure at each generation is shown (with total energies relative to the final energy) [7].

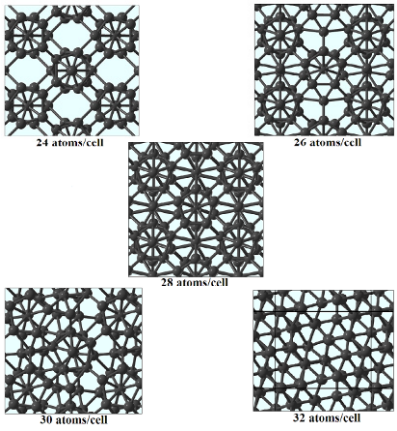

Figure 3. Best structures with 24, 26, 28, 30, 32 atoms/cell [7].

symmetry, and relaxed cell parameters and diffraction pattern in good agreement with experiment (Fig. 4). To make the test challenging and unbiased, it was done "blindly", i.e. theoretical and experimental data were not exchanged until final comparison.

Table 1 gives predicted (at the DFT-GGA level of theory) structural parameters of γ-B_{28} and two other stable boron phases with relatively simple structures (theoretical data on all structures are available from the author). Excellent agreement with available experimental data can be seen.

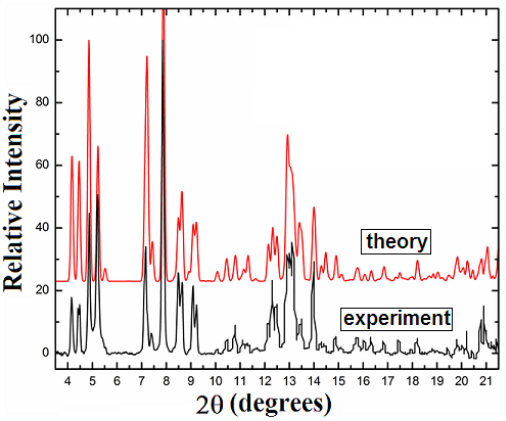

Figure 4. Comparison of theoretical and experimental X-ray powder diffraction profiles of γ-B_{28}. X-ray wavelength λ = 0.31851 Å [7].

TABLE 1. Structures of stable boron phases (optimized at 1 atm), with Bader charges (Q) and volumes (V). Experimental data are in parentheses (Refs.7, 36). Atomic volumes are given in atomic units (a.u. = 1 bohr^3). From [7]

Wyckoff position	x	y	z	Q_{PAW}	$Q_{LCAO-QZ}$	Q_{IAM}	$V_{LCAO-QZ}$, a.u.	V_{IAM}, a.u.
γ-B_{28}. Space group *Pnnm*.								
a = 5.043 (5.054) Å, *b* = 5.612 (5.620) Å, *c* = 6.921 (6.987) Å								
B1 (4g)	0.1702	0.5206	0	+0.2418	+0.1704	+0.0250	47.65	49.94
B2 (8h)	0.1606	0.2810	0.3743	−0.1680	–0.1430	−0.0153	48.46	46.25
B3 (8h)	0.3472	0.0924	0.2093	+0.0029	+0.0218	+0.0035	47.17	46.90
B4 (4g)	0.3520	0.2711	0	+0.0636	+0.0301	−0.0003	44.93	46.40
B5 (4g)	0.1644	0.0080	0	+0.0255	+0.0419	−0.0011	46.38	47.60
α-B_{12}. Space group $R\bar{3}m$. *a* = *b* = *c* = 5.051 (5.064) Å, *α* = *β* = *γ* = 58.04 (58.10)°.								
B1 (18h)	0.0103 (0.0102)	0.0103 (0.0102)	0.6540 (0.6536)	+0.0565	+0.0416	–0.0030	47.64	49.05
B2 (18h)	0.2211 (0.2212)	0.2211 (0.2212)	0.6305 (0.6306)	−0.0565	−0.0416	+0.0030	50.43	49.01
α-Ga structure. Space group *Cmca*. *a* = 2.939 Å, *b* = 5.330 Å, *c* = 3.260 Å.								
B1 (8f)	0	0.1558	0.0899	0	0	0	43.08	43.08

Figure 5 shows results of *ab initio* calculations of relative stability of different phases of boron. As expected, the impurity-stabilized T-50 phase is energetically poor, while α-B_{12}, β-B_{106}, T-192 and γ-B_{28} phases are energetically nearly degenerate at low pressures.

According to these calculations, γ-B_{28} is energetically more favorable than any known or hypothetical phase of boron at pressures between 19 and 89 GPa. At these conditions, it is also dynamically stable, i.e does not have any imaginary phonon frequencies (Fig. 6).

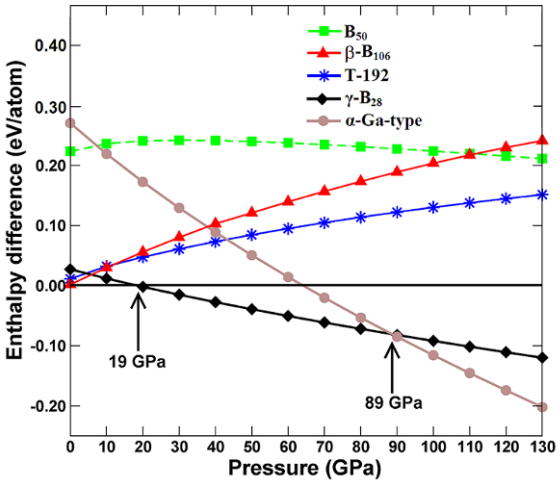

Figure 5. Stability of boron phases at 0 K. Enthalpies are shown relative to α-B_{12}. Phase transformations occur at 19 GPa (α-B_{12} to γ-B_{28}) and 89 GPa (γ-B_{28} to α-Ga-type). From [7].

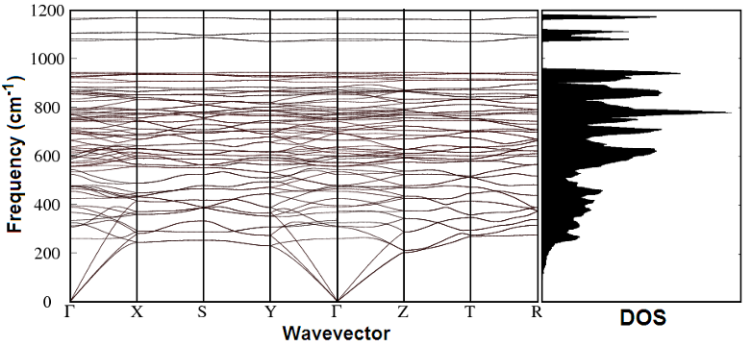

Figure 6. Theoretical phonon dispersion curves and phonon density of states of γ-B_{28} at 1 atm. From [7].

b. *Chemical bonding and physical properties of the new phase*. The γ-B_{28} structure is quite unique: centres of the B_{12} icosahedra (formed by sites B_2–B_5 – Table 1) form a slightly distorted cubic close packing (as in α-B_{12}), in which all octahedral voids are occupied by B_2 pairs (formed by site B1). It can be represented as a NaCl-type structure, the roles of "anion" and "cation" being played by the B_{12} icosahedra and B_2 pairs, respectively. γ-B_{28} is structurally similar to α-B_{12}, but denser due to the presence of additional B_2 pairs. The average intraicosahedral bond length is 1.80 Å and the B–B bond length within the B_2 pairs is 1.73 Å.

γ-B_{28} is the densest, and the hardest, of all known boron phases (all of which are superhard). The best estimates of the hardness of β-B_{106} and α-B_{12} are 45 GPa [37] and 42 GPa [38], respectively, whereas for γ-B_{28} the measured Vickers hardness of this phase is 50 GPa [8], which puts it among half a dozen hardest materials known to date. The high density of this phase is due to the close packing of the B_{12} icosahedra (like in α-B_{12}, the second densest known phase), where the "empty" space is filled by the B_2 pairs.

Detailed investigations showed that the two clusters have very different electronic properties and there is charge transfer (of ~0.5 e) from B_2 to B_{12} (Fig. 7) [7], and this is correlated with the strong IR absorption and large dynamical charges on atoms.

γ-B_{28} is structurally related to several well-known compounds – for instance, B_6P or $B_{13}C_2$, where the two sublattices are occupied by different chemical species (instead of interstitial B_2 pairs there are P atoms or C–B–C groups, respectively). This fact again highlights the chemical difference between the two constituent clusters. One can call γ-B_{28} a "boron boride" $(B_2)^{\delta+}(B_{12})^{\delta-}$ with partial charge transfer δ.

While broken-symmetry structures, with two sublattices of the same element in different chemical roles, are known for some metals (e.g. Rb and Ba under pressure [39]), γ-B_{28} is different: it is non-metallic, its two sublattices are occupied not by single atoms but by clusters (B_{12} and B_2). The exact values of the atomic charges are definition-dependent, but qualitatively consistent: $\delta \sim +0.2$ from differences in the numbers of electrons within atom-centred spheres (sphere radii 0.7–1.0 Å); Born dynamical charges attain much higher values (spherically averaged $\delta = +2.2$). Our preferred estimates of CT are based on Bader theory [40], which partitions the total electron density (ED) distribution into "atomic" regions separated by zero-flux (i.e. minimum-density) surfaces, and give $\delta = +0.48$ (Table 1). Bader partitioning is physically unbiased and ensures maximum additivity and transferability of atomic properties [40].

These relatively large Bader charges originate from the interaction between the B_2 and B_{12} clusters: the Independent Atom Model (IAM, where the total ED is a sum of atomic densities) has negligible charges, an order of

magnitude lower than when the atoms are allowed to interact. Removing the B_2 pairs from the structure, we again obtain negligible charges (within ±0.03) even in the interacting system. The bond asymmetry parameter for this partially "ionic" bond reaches 20%. Because of CT, atomic volumes overall shrink (relative to the IAM) for positively charged and expand for negatively charged atoms (Table 1).

Figure 7 shows the total and local electronic densities of states; it can be seen that there are large differences in local DOSs of the B_2 and B_{12} clusters in the bottom of the valence band (B_{12}-dominated), top of the valence band and bottom of the conduction band (B_2-dominated). While this is consistent with significant charge transfer $B_2 \rightarrow B_{12}$, there is also a strong covalency in the system seen from strong hybridization in the middle of the valence band.

Additional insight is provided by energy-decomposed electron density distribution (Fig. 8). Again, it is clear (even clearer than on Fig. 7) that lowest-energy valence electrons are concentrated around the B_{12} icosahedra, while HOMO and LUMO levels are B_2-dominated.

Ionicity affects many properties of γ-B_{28}: high-frequency (ε_∞) and static (ε_0) dielectric constants are very different (11.4 and 13.2, respectively), implying the LO-TO splitting as in ionic crystals, and strong infrared (IR) absorption. Being extremely sensitive to crystal structure and to the approximations of theory, the IR spectrum provides a very stringent test. The computed and measured (in the range 100–1,200 cm^{-1}) IR spectra show good agreement [7].

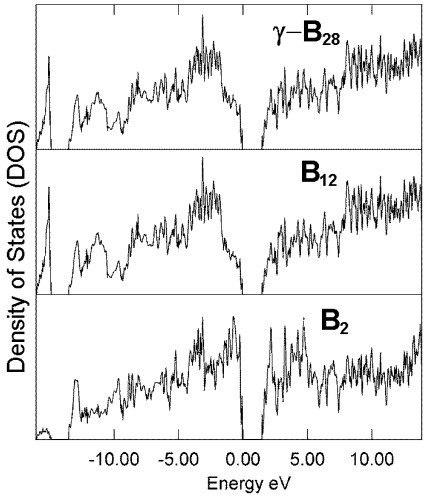

Figure 7. Total electronic density of states of γ-boron and its projections (per atom) onto B_{12} icosahedra and B_2 pairs.

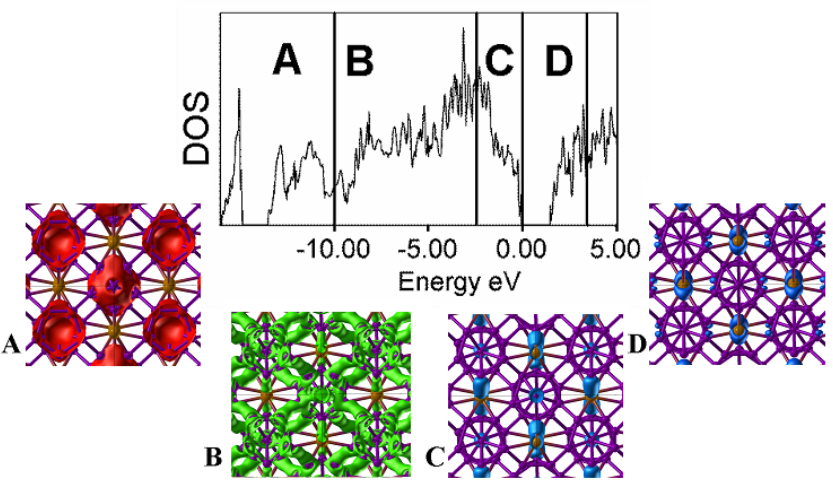

Figure 8. Electronic structure of γ-B_{28}. The total density of states is shown, together with the electron density corresponding to four different energy regions denoted by letters A, B, C, D. Note that lowest-energy electrons are preferentially localized around the B_{12} icosahedra, whereas highest-energy electrons (including the bottom of the conduction band – "holes") are concentrated near the B_2 pairs. The fact that lowest-energy electrons belong to the B_{12} clusters, and highest-energy – to B_2 units, is consistent with the direction of charge transfer: $B_2 \rightarrow B_{12}$. From [9].

The LO-TO splitting is different for all modes and reciprocal-space directions, and the simplest parameter characterising it is $\zeta = \prod_{i=1}^{n} (\frac{\omega_i^{LO}}{\omega_i^{TO}})^2 = \frac{\varepsilon_0}{\varepsilon_\infty}$. ζ=1 for non-ionic crystals (the computed value is 1.01 for α-B_{12}) and $\zeta > 1$ whenever there is CT (1.16 for γ-B_{28} and 1.18 for GaAs). Individual mode splittings tend to be smaller for more complex structures, and the largest splitting in γ-B_{28} (337–375 cm^{-1}) occurs for the most intense IR-active mode, a nearly rigid-body anti-phase motion of the B_2 and B_{12} units. Despite structural relationship with α-B_{12} (Fig. 1), the electronic structure of partially ionic γ-B_{28} is quite different: it shows little pressure dependence of the band gap and even at 200 GPa remains an insulator with a relatively wide gap (1.25 eV – and one has to bear in mind that DFT band gaps are usually ~40% underestimated), whereas for the covalent α-B_{12} the calculated band gap rapidly decreases on compression and closes at ~160 GPa (Fig. 9). The key for this different behaviour is CT.

The example of γ-B_{28} shows that significant ionicity can occur in elemental solids – though similar suggestions (e.g. hydrogen with H^+H^- molecules [41]) existed before. The key is the ability of boron to form clusters with very different electronic properties. The cationic B_2^{4+} group is

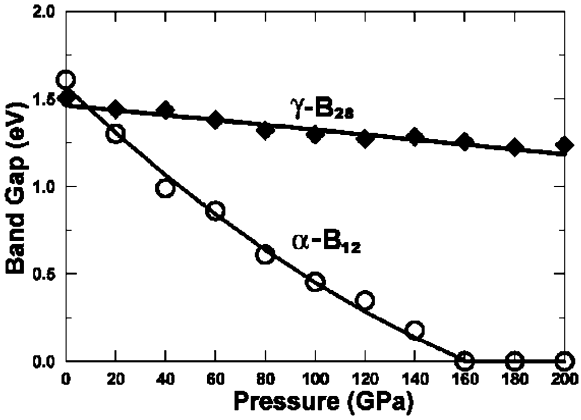

Figure 9. Pressure dependence of the band gap of α-B_{12} and γ-B_{28}. From [7].

well known and its typical B–B distance [42] (1.70-1.75 Å in B_2F_4 and B_2Cl_4) is the same as in γ-B_{28} (1.73 Å). The B_{12} cluster is more stable as the B_{12}^{2-} anion (as in the very stable icosahedral $(B_{12}H_{12})^{2-}$ cluster [42]), because in the neutral state it has an unoccupied bonding orbital (e.g., [43]). This orbital creates an acceptor band above the valence band edge in boron-rich solids. Electrons from dopant metal atoms or from other boron clusters may partially occupy this band, as detected by optical spectroscopy [44]. The B_2 pairs thus behave as electron donors, similar to the metal dopants in boron-rich borides.

Significant charge transfer can be found in other elemental solids, and observations of dielectric dispersion [45], equivalent to LO-TO splitting, suggest it for β-B_{106}. The nature of the effect is possibly similar to γ-B_{28}. Detailed microscopic understanding of charge transfer in β-B_{106} would require detailed knowledge of its structure, and reliable structural models of β-B_{106} finally begin to emerge from computational studies [32–34].

One should realize that ionicity can appear in elements only as a result of many-body interactions, which are strongest under pressure or when atomic orbitals are diffuse (but not diffuse enough to form metallic states) – i.e. at the border between metallic and insulating states. Amphoteric elements close to the Zintl line (B-Si-As-Te-At) are particularly favorable. Solids made of nanoclusters with very different electronic structures can be significantly ionic; and short-lived ionic species may exist in elemental fluids.

c. *Phase diagram of boron*. The discovery of γ-B_{28} provided the missing piece of the puzzle of phase diagram of boron [7]. The stability field of this phase is larger than the fields of all other known boron polymorphs combined (Fig. 11). The diagram shown in Fig. 11 describes all known data in a consistent manner. The upper pressure limit of stability of γ-B_{28} remains to be tested. Theoretical predictions of an α-Ga-type metallic phase above 74

GPa [4, 5] were confirmed [7] using crystal structure prediction tools [35], except that the predicted pressure of this phase transition was shifted to a higher value, 89 GPa, by the presence of a new phase, γ-B_{28} [7]. α-Ga-type boron has been predicted to be a superconductor [46]. It has been found in our fully unconstrained variable-cell evolutionary simulations at 100 and 300 GPa. This structure does not contain B_{12} icosahedra and heralds a new type of boron chemistry under pressure (Fig. 10).

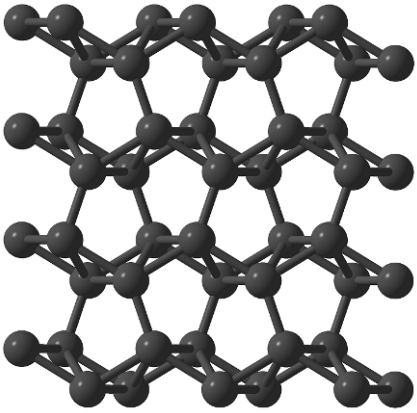

Figure 10. α-Ga-type structure found in evolutionary simulations at 100 and 300 GPa.

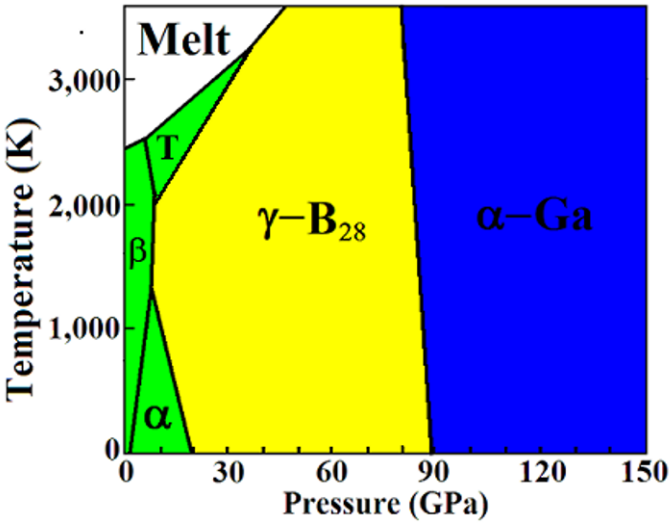

Figure 11. Phase diagram of boron. Reproduced from [7]. This schematic diagram is based on theoretical and experimental results from [7] and previous experimental [31, 47] and theoretical [32, 33] studies. The phase boundary between γ-B_{28} and α-Ga-type phases is based on the static transition pressure (89 GPa) and a Clapeyron slope of −2.71 MPa/K calculated using density-functional perturbation theory and the GGA level of theory (−2.52 MPa/K using the LDA). The calculated Clapeyron slope for the α-γ transition is −4.7 $MPaK^{-1}$.

d. *Subsequent works*. The equation of state of γ-B_{28} was experimentally determined by Le Godec et al. [48] and is in excellent agreement with theoretical calculations of [7]. Very recently, Zarechnaya et al. [49, 50] experimentally confirmed the structure [7] and superhardness [8] of γ-B_{28}, and also presented some calculations. Their main achievement was the synthesis of micron-sized single crystals and single-crystal confirmation of the structure, but unfortunately conditions of synthesis were suboptimal (e.g., the capsules reacted with boron sample), and their papers contained many errors [52]. For instance, their estimated density differences between boron allotropes were wrong by an order of magnitude (they claimed that γ-B_{28} is 1% denser than all other forms of boron, while it is actually 8.3% denser than β-B_{106}), which is possibly a result of incorrectly performed ab initio calculations in their papers. Their equation of state, measured to 30 GPa [49], shows large discrepancies with theory [7, 51] and earlier more careful experiment [48], see Fig. 12. Jiang et al. [51] computed the equation of state, the elastic constants (from which they obtained the bulk modulus of 224 GPa and shear modulus of 236 GPa, whereas the experimental bulk modulus is 238 GPa [48]), and remarkably high ideal tensile strengths (65, 51, and 52 GPa along the three crystallographic axes - similar to the measured hardness of 50 GPa [8]). They found that during deformation of the structure, the first bonds to break are those between the most charged atomic positions [51]. Other calculations showed that the electronic spectra of the different atomic sites in γ-B_{28} are indeed very different [53], confirming

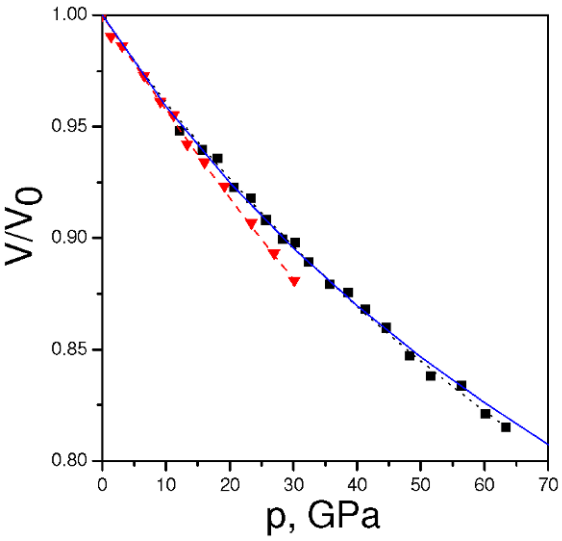

Figure 12. Equation of state of γ-B_{28}: red triangles – experiment [49] (dashed line – Vinet fit), black squares – more careful experiment [48] (dotted line – Vinet fit), solid line – ab initio results [7]. Figure courtesy V.L. Solozhenko and O.O. Kurakevych, from [52].

the charge-transfer model of [7]. Furthermore, charge transfer seems to be required in this structure, which violates the "covalent" Wade-Jemmis electron counting rules [53]. A summary of work on this phase is given in Table 2.

TABLE 2. Summary of work on γ-B_{28} phase

Reference	Main findings	Submission date
Wentorf [28]	Synthesis, density measurement, qualitative X-ray diffraction, electrical conductivity change across β-γ transition. No chemical analysis and no structure determination.	04.10.1964
Oganov et al. [7]	Synthesis and proof of chemical purity, structure determination, demonstration of partial ionicity, phase diagram.	27.01.2007
Solozhenko et al. [8]	Hardness measurement.	03.10.2008
Zarechnaya et al. [50,52]	Confirmation of synthesis and structure. Identified γ-B_{28} with Wentorf's phase.	03.11.2008
Le Godec et al. [48]	Accurate measurement of the equation of state at 300 K.	08.01.2009
Zarechnaya et al. [49,52]	Re-confirmation of structure using single crystals. Measurements of the band gap and electrical conductivity. Inaccurate measurements of the equation of state and hardness at 300 K. Incorrect interpretations of chemical bonding and density differences in boron allotropes.	16.01.2009
Jiang et al. [51]	Simulation of structure deformation.	12.03.2009
Rulis et al. [52]	Simulation of electronic spectra, supporting charge transfer picture.	06.04.2009

4. Conclusions, and What Happens at Still Higher Pressures?

Boron is still an element of surprise, and many aspects of its behavior remain enigmatic. What happens beyond the stability field of γ-B_{28}? We know that at room temperature β-B_{106} amorphizes at ~100 GPa [3], but all this really means is that before 100 GPa β-B_{106} becomes less stable than some other crystalline form, the transition to which is kinetically hindered at 298 K. In the absence of thermodynamically equilibrated experiments, there are several theoretical results, based on educated guesses [4, 5] of high-pressure structures, and on evolutionary crystal structure prediction

[35] – all consistently pointing to the α-Ga-type phase, which has also been predicted [46] to be superconducting. Its structure does not contain any B_{12} icosahedra and heralds an entirely new chemistry for boron. However, due to the strongly localized nature of boron's valence electrons, this phase is only a poor metal, strongly deviating from free-electron behavior. This is reflected in its peculiar structure, which contains B–B pairs. In a sense, γ-B_{28}, discovered in [7] and containing both the B_{12} icosahedra and B_2 pairs, is a step between low-pressure icosahedral structures and the very high-pressure α-Ga structure, which contains only B_2 pairs and is entirely devoid of the icosahedra. Considering all these structural changes, one may conclude that boron chemistry becomes simpler with pressure – thus, high-pressure studies may actually lead to better understanding of low-pressure phenomena, affecting the entire field of boron chemistry. A very exciting field indeed.

Acknowledgments

This chapter is a theoretician's overview of our recent results [7–9] (to which we refer the reader for more details, in particular, about the computational methodology and experimental data) and the related works, and I express deepest gratitude to my collaborators. To Jiuhua Chen for attracting me to the study of boron and, to Vladimir L. Solozhenko for his deep insight and warm friendship, to Carlo Gatti for sharing his exceptional chemical intuition and friendship.

References

1. Douglas, B.E., Ho, S.-M., *Structure and Chemistry of Crystalline Solids* (Springer, N.Y., 2006).
2. Amberger, E., Ploog, K. (1971). Bildung der Gitter des Reinen Bors. *J. Less-Common Metals* **23**, 21–31.
3. Sanz D.N., Loubeyre P., Mezouar M. (2002). Equation of state and pressure induced amorphization of beta-boron from X-ray measurements up to 100 GPa. *Phys. Rev. Lett.* **89**, 245501.
4. Segall D.E., Arias T.A. (2003). Ab initio approach for high-pressure systems with application to high-pressure phases of boron: Perturbative momentum-space potentials. *Phys. Rev.* **B67**, 064105.
5. Haussermann U., Simak S.I., Ahuja R., Johansson B. (2003). Metal-nonmetal transition in the boron group elements. *Phys. Rev. Lett.*, **90**, 065701.
6. Eremets M.I., Struzhkin V.W., Mao H.K., Hemley R.J. (2001). Superconductivity in boron. *Science* **293**, 272–274.
7. Oganov A.R., Chen J., Gatti C., Ma Y.-M., Yu T., Liu Z., Glass C.W., Ma Y.-Z., Kurakevych O.O., Solozhenko V.L. (2009). Ionic high-pressure form of elemental boron. *Nature* **457**, 863–867.

8. Solozhenko V.L., Kurakevych O.O., Oganov A.R. (2008). On the hardness of a new boron phase, orthorhombic γ-B_{28}. *J. Superhard Mater.* **30**, 428–429.
9. Oganov A.R., Solozhenko V.L. (2009). Boron: a hunt for superhard polymorphs. *J. Superhard Materials* **31**, 285–291.
10. Gay-Lussac J.L., Thenard L.J. (1808). Sur la décomposition et la recomposition de l'acide boracique. *Ann. Chim. Phys.* **68**, 169–174.
11. Davy H. (1808). Electro-Chemical Researches, on the Decomposition of the Earths; With Observations on the Metals Obtained from the Alkaline Earths, and on the Amalgam Procured from Ammonia (Read June 30, 1808) *Phil. Trans. R. Soc. Lond.* **98**, 333–370.
12. Moissan H. (1895). Etude du Bore Amorphe. Ann. Chim. Phys. **6**, 296–320.
13. Weintraub E. (1911). On the properties and preparation of the element boron. *J. Ind. Eng. Chem.*, **3**(5), 299–301.
14. Sainte-Claire Deville H., Wöhler F. (1857). Ueber das Bor. *Ann. Physik* **100,** 635–646.
15. Wöhler F., Sainte-Claire Deville H. (1858). Du Bore. *Ann. Chim. Phys.* **52**(3), 63–92.
16. Richards S.M., Kasper J.S. (1969). The crystal structure of YB_{66}. *Acta Cryst.* **B25**, 237–251.
17. Laubengayer A.W., Hurd D.T., Newkirk A.E., Hoard J.L. (1943). Boron. I. Preparation and properties of pure crystalline boron. *J. Am. Chem. Soc*., **65**, 1924–1931.
18. Hoard J.L., Geller S., Hughes R.E. (1951). On the structure of elementary boron. *J. Am. Chem. Soc.*, **73**, 1892–1893.
19. Hoard J.L., Hughes R.E., Sands D.E. (1958). The structure of tetragonal boron. *J. Am. Chem. Soc.*, **80**, 4507–4515.
20. Will G., Ploog K. (1974). Crystal structure of I-tetragonal boron. *Nature* **251**, 406–408.
21. Ploog K., Amberger E. (1971). Kohlenstoff-Induzierte Gitter beim Bor: I-Tetragonales $(B_{12})_4B_2C$ und $(B_{12})_4B_2C_2$. *J. Less-Comm. Metals* **23**, 33–42.
22. Sands D.E., Hoard J.L. (1957). Rhombohedral elemental boron. *J. Am. Chem. Soc.*, **79**, 5582–5583.
23. Hughes R.E., Kennard C.H.L., Sullenger D.B., Weakliem H.A., Sands D.E., Hoard J.L. (1963). The structure of β-rhombohedral boron. *J. Am. Chem. Soc*., **85**, 361–362.
24. McCarty L.V., Kasper J.S., Horn F.H., Decker B.F., Newkirk A.F. (1958). A new crystalline modification of boron. *J. Am. Chem. Soc.*, **80**, 2592.
25. Talley C.P. (1960). A new polymorph of boron. *Acta Cryst.*, **13**, 271–272.
26. Vlasse M., Naslain R., Kasper J.S., Ploog K. (1979). Crystal structure of tetragonal boron related to α-AlB_{12}. *J. Sol. State Chem.*, **28**, 289–301.
27. Chase M.W., Jr. (1998). *NIST-JANAF Thermochemical Tables.* Fourth Edition. J. Phys. Chem. Ref. Data Monograph No. 9. American Chemical Society, American Institute of Physics, National Institute of Standards and Technology. 1951 p.
28. Wentorf, R. H., Jr. (1965). Boron: another form. *Science* **147,** 49–50.
29. Nagamatsu J., Nakagawa N., Muranaka T., Zenitani Y. & Akimitsu J. (2001) Superconductivity at 39 K in magnesium diboride. *Nature* **410**, 63–64.
30. Ma Y., Wang Y., Oganov A.R. (2009). Absence of superconductivity in the novel high-pressure polymorph of MgB_2. *Phys. Rev.* **B79**, 054101.
31. Ma Y.Z., Prewitt C.T., Zou G.T., Mao H.K., Hemley R.J. (2003). High-pressure high-temperature x-ray diffraction of beta-boron to 30 GPa. *Phys. Rev.* **B67**, 174116.
32. van Setten M.J., Uijttewaal M.A., de Wijs G.A., de Groot R.A. (2007). Thermodynamic stability of boron: The role of defects and zero point motion. *J. Am. Chem. Soc.* **129**, 2458–2465.
33. Widom M., Mikhalkovic M. (2008). Symmetry-broken crystal structure of elemental boron at low temperature. Phys. Rev. B77, 064113.

34. Ogitsu T., Gygi F., Reed J., Motome Y., Schwegler E., Galli G. (2009). Imperfect crystal and unusual semiconductor: Boron, a frustrated element. *J. Am. Chem. Soc*. 131, 1903–1909.
35. Oganov A.R., Glass C.W. (2006). Crystal structure prediction using *ab initio* evolutionary techniques: principles and applications. *J. Chem. Phys.* **124**, 244704.
36. Will G., Kiefer B. (2001). Electron deformation density in alpha-boron. *Z. Anorg. Allg. Chem.* **627**, 2100–2104.
37. Gabunia D., Tsagareishvili O., Darsavelidze G., Lezhava G., Antadze M., and Gabunia L. (2004). Preparation, structure and some properties of boron crystals with different content of ^{10}B and ^{11}B isotopes. *J. Solid State Chem*. **177,** 600–604.
38. Amberger E., Stumpf W. (1981). *Gmelin Handbook of Inorganic Chemistry*., Springer-Verlag: Berlin. 1960, pp. 112–238.
39. McMahon M.I., Nelmes R.J. (2006). High-pressure structures and phase transformations in elemental metals. *Chem. Soc. Rev.* **35**, 943–963.
40. Bader R.F.W. (1990). *Atoms in Molecules. A Quantum Theory* (Oxford University Press, Oxford), 438 pp.
41. Edwards B., Ashcroft N.W. (1997). Spontaneous polarization in dense hydrogen. *Nature* **388**, 652–655.
42. Wells A.F. (1986). *Structural Inorganic Chemistry* (Clarendon Press, Oxford).
43. Hayami W. (1999). Theoretical study of the stability of AB_{12} (A = H-Ne) icosahedral clusters. *Phys. Rev.* **B60**, 1523–1526.
44. Werheit H., Luax M., Kuhlmann U. (1993). Interband and gap state related transitions in β-rhombohedral boron. *Phys. Status Solidi B* **176**, 415–432.
45. Tsagareishvili O.A., Chkhartishvili L.S., Gabunia D.L. (2009). Apparent low-frequency charge capacitance of semiconducting boron. *Semiconductors* **43**, 14–20.
46. Ma Y.M., Tse J.S., Klug D.D., Ahuja R. (2004). Electron-phonon coupling of α-Ga boron. *Phys. Rev.* **B70**, 214107.
47. Brazhkin V.V., Taniguchi T., Akaishi M., Popova S.V. (2004). Fabrication of β-boron by chemical-reaction and melt-quenching methods at high pressures. *J. Mater. Res.* **19**, 1643–1648.
48. Le Godec Y., Kurakevych O.O., Munsch P., Garbarino G., Solozhenko V.L. (2009). Equation of state of orthorhombic boron, γ-B_{28}. *Solid State Comm.*, **149**, 1356–1358.
49. Zarechnaya E.Y., Dubrovinsky L., Dubrovinskaia N., Filinchuk Y., Chernyshov D., Dmitriev V., Miyajima N., El Goresy A., Braun H.F., Vansmaalen S., Kantor I., Kantor A., Prakapenka V., Hanfland M., Mikhailushkin A.S., Abrikosov I.A., Simak S.I. (2009). Superhard semiconducting optically transparent high pressure phase of boron. *Phys. Rev. Lett.* **102**, 185501.
50. Zarechnaya E.Y., Dubrovinsky L., Dubrovinskaia N., Miyajima N., Filinchuk Y.,Chernyshov D., Dmitriev V. (2008). Synthesis of an orthorhombic high pressure boron phase. *Sci. Tech. Adv. Mat.* **9**, 044209.
51. Jiang C., Lin Z., Zhang J., Zhao Y. (2009). First-principles prediction of mechanical properties of gamma-boron. *Appl. Phys. Lett*., **94**, 191906.
52. Oganov A.R., Solozhenko V.L., Kurakevzch O.O., Gatti C., Ma Y.M., Chen J., Liu Z., Hemley R.J. (2009). Comment on 'Superhard Semiconducting Optically Transparent High Pressure Phase of Boron'. http://arxiv.org/abs/0908.2126.
53. Rulis P., Wang L., Ching W.Y. (2009). Prediction of γ-B_{28} ELNES with comparison to α-B_{12}. *Phys. Stat. Sol. (RRL)* **3**, 133–135.

BEHAVIOR OF THE CRYSTALLINE BORONCARBIDE COATING UNDER TOKAMAK CONDITIONS

O. I. BUZHINSKIJ*, V.G. OTROSHCHENKO
SRC RF TRINITI, Troitsk, Moscow reg., Russia, 142190

Abstract In the work are presented the results of research of the boroncarbide coatings as shielding elements of graphite limiters in tokamaks T-10, T–11M (RF), divertor tiles of tokamak DIII-D (USA), RF-antenna of tokamak T–11M. The possibility of production the crystalline boroncarbide coating in plasma shots is shown at plasma linear device PISCES-B and tokamak T–11M [11, 12]. As a result of carried out investigations it is opened the possibility of boroncarbide coating application in fusion devices of next generaion ITER and DEMO.

Keywords: tokamak, boroncarbide, coating, plasma, impurety

1. Introduction

The use of materials with low Z for protection of tokamak first wall and vessel elements is a conventional method to decrease heavy impurity influx into tokamak plasma. Presently, one of the most important tendencies is the use of boron-containing materials and films. As a result, chemical and high temperature sputtering were significantly reduced, carbon and oxygen impurities were suppressed, and plasma performance was improved. It seems reasonable to use thick (20–100 μm) boron–carbon coatings on substrates with high thermal conductivity. There are a number of coating fabrication methods [1]: the chemical vapor deposition (CVD) with the use of BCl_3 (chloride technique), BF_3 (fluoride technique), the gas conversion, the plasma spray and the reaction – sintering or the conversion via liquid phase. The coatings produced by BF_3 method have higher heat load durability as compared to other methods. Their B/C ration is higher, and their thermo-mechanical properties (under appropriate choice of substrate) are better. The thermodynamical calculation shows that a layer of a solid boron with a crystalline structure dependent on a substrate temperature is deposited. The

* O. I. Buzhinski, SRC RF TRINITI, Troitsk, Moscow reg., Russia, 142190, e-mail: buzh@triniti.ru

N. Orlovskaya and M. Lugovy (eds.), *Boron Rich Solids: Sensors, Ultra High Temperature Ceramics, Thermoelectrics, Armor*, DOI 10.1007/978-90-481-9818-4_15,

optimum temperature for coating deposition on graphite materials is about 1,850º C for the fluoride technique (Fig. 1). The deposition rate is from 100 to 150 μm/h, coating thickness is in range of 100–500 μm, and structure is a mixture of the B_4C and $B_{13}C_2$ phases. In the work are presented the results of research of boron carbide coating under tokamak conditions.

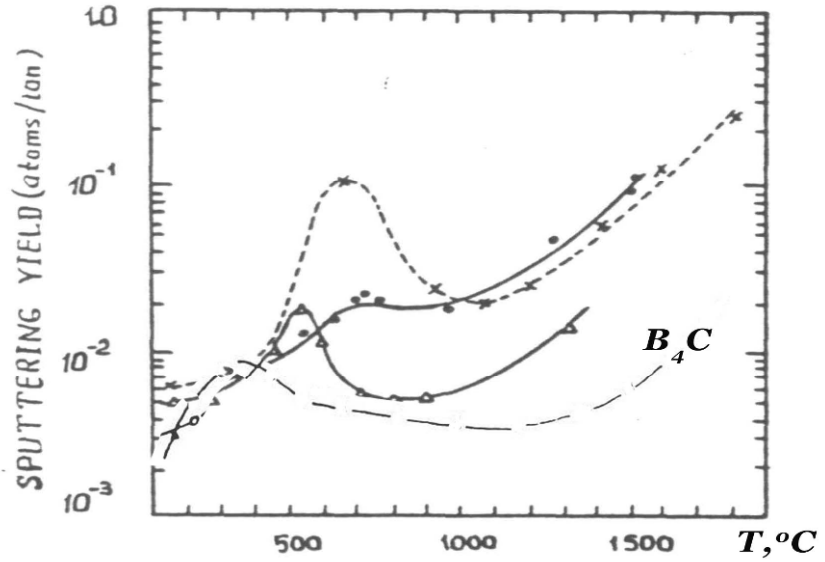

Figure 1. Temperature dependence of the sputtering coefficients for graphites and B_4C. x – pyrolitic graphite, 3 keV H_3^+ [2]; ● – C-SiC general atomic, 6 keV H_3^+; Δ – C/B USB-15, 10 keV H^+; - B_4C – 10 keV H^+.

2. Experimental Techniques

The coating on the MPG–8 and RGT graphites was investigated under electron beam irradiation at SNL [3]. The coating on the MPG–8 graphite had no noticeable damages up to 10 MW/m^2 when erosion occurred. Profilometry showed local damages with maximum crater depth 180 μm and the thickness of the remained layer 200 μm. The depth of the other small defects was about 30 μm. The coating on the RGT graphite was preserved up to the maximum applied power density of 13 MW/m^2 due to the high thermal conductivity of the graphite (~600–800 W/mK). The X-ray analysis revealed no changes in phase content, not even in the bottom of the largest crater.

The fluoride CVD coatings have been investigated in tokamaks: as a limiter in T–10, T-11M and divertor in DIII–D [7–10]. In the T–10 tokamak the discharges were both ohmic and electron cyclotron resonance (ECR) heating and some hundreds of them were with disruptions [8, 9]. Mass losses

of the samples with B_4C coatings were 1.5–2 times lower than those of the USB-15 graphite (Fig. 2). The typical initial thickness of the B_4C layer was 80–100 μm and post exposure thickness was 10–30 μm. Melting of the surface layer followed by recrystallization and the formation of a crystallite grid was observed on the surface of the coated MPG-8, especially on the electron side of the limiter. It means that the surface temperature was very high (>2,000°C). Significant melting of the B_4C coating on pyrolytic graphite was not observed though the heat and particle fluxes on this coating were substantially higher. It can be explained by the high thermal conductivity of the pyrolytic graphite (about 300 W/mK) as compared to that of MPG-8 (70–80 W/mK). The coatings on all substrates had no macrocracks typical of the exposed graphite. Both initial coatings and exposed ones had good adherence to the graphite substrates. X-ray diffraction analysis and Auger spectroscopy showed that the phase and chemical composition of the coatings were preserved: the exposed and initial ones were mixtures of B_4C and amorphous carbon. Some carbon enrichment in the surface layers was observed which can be explained by thermal desorption of boron at high temperatures.

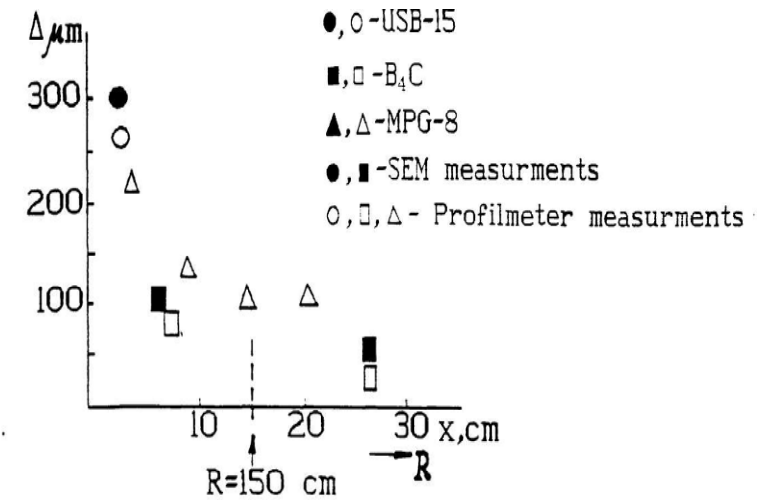

Figure 2. The thickness of eroded layers of limiter coated with various materials.

The T-l 1M tokamak RF-antenna is an oscillatory circuit with a low wave resistance (Fig. 3) The flat vacuum capacitor of the circuit is placed directly in the horizontal port of the tokamak. All structural elements of the antenna are mounted on the port cover and are closed by a Faraday screen – a metal sheathing partially covered with a titanium nitride film. Plasma facing shield has radial cuts. The plasma facing screen surface is reveted by the MPG-8 graphite plates. The graphite plates 1 (Fig. 3b) were deposited with

B_4C boron carbide coating of 40 μm thickness by the method of chemical vapor deposition. It is determined that the obtained coating has a sufficient density, is homogeneous in structure (phase B_4C-$B_{13}C_2$). The lateral copper walls of the RF-antenna are protected by 2 mm pyrolytic boron nitride plates 1 (Fig. 3a). As a result of the RF-antenna modernization and application of the new manner of boronization, the discharge characteristics in the ohmic stage were considerably improved (Ip=100kA), better plasma thermo-insulation was improved, and the efficiency of the ion-cyclotron plasma heating also increased 3 times (η = 3.5 $eVkW^{-1}cm^{-3} \times 10^{-13}$ at P_{RF} = 200 kW). Steady discharges with higher parameters (T_e = 400 eV, $n_e = 3.5 \times 10^{13}$ cm^{-3}) were produced. Process of producing discharges with higher plasma density has become essentially simpler. The total power of energy losses has decreased more than twice, in spite of an increase of the ICR plasma heating efficiency. During ICR-heating, a growth of energy life time τ_E was observed. Comparison with ohmic modes of similar density dynamics allows us to make a conclusion that the energy life time increase is connected to plasma density growth during RF-pulse, and ICR-heating does not result in worse energy confinement retention.

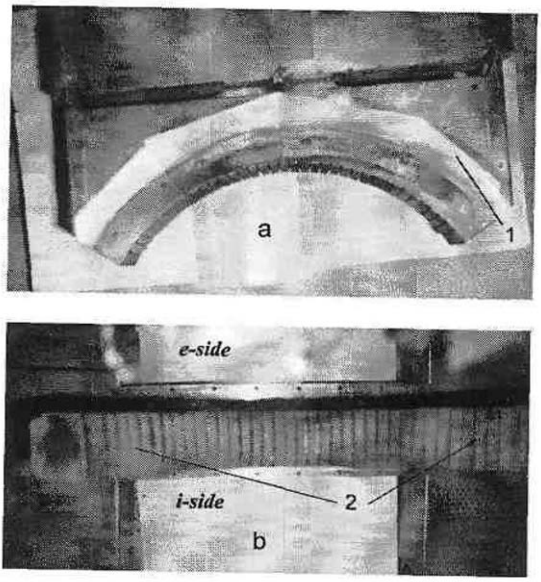

Figure 3. General view of the modernized RF-antenna: (**a**) top view (1 – boron nitride protective plates); (**b**) plasma-facing antenna elements (2 – B_4C coated graphite plates).

In such modes the antenna has worked more than 4 years. After termination of the working campaign, the modernized RF-antenna was drawn out of the tokamak and all its protective element surfaces were investigated with the help of standard surface diagnostics (scanning electron microscopy,

Auger electron spectroscopy, X-ray and neutron diagnostics, profilometer etc.). Absolute values of the hydrogen isotopes concentration in protective elements were obtained by the neutron-induced recoil detection method.

Visual research of the RF-antenna protective elements surface has found out more appreciable roughness of the plasma-facing protective graphite elements surface in comparison with the initial one, and boron nitride elements were smooth. The roughnesses were 1–2 μm, on average. All protective elements were covered with an iridescent film, which spectrum varied from violet to red with various shades. In Fig. 4, surface images of the plasma-facing protective graphite elements, taken from various antenna areas (from the left and right ends and from the middle of the antenna), are presented. Analysis of the protective graphite elements surface has shown that shields surface has undergone a significant erosion, and even separate areas of splitted and ejected surface are observed.

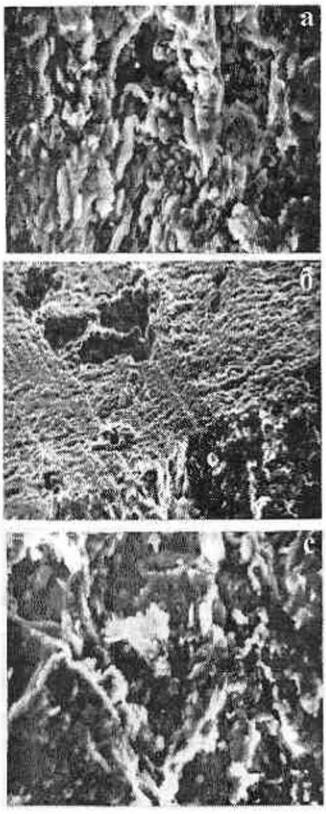

Figure 4. B_4C coating surface: (**a**) ion side of the area from the antenna middle part x700 SEM; (**b**) crystallites on melted surface of the antenna middle part x 180 SEM; (**c**) ion side of the area on the antenna border, x700 SEM.

The B_4C coating on the protective elements has everywhere kept its chemical and phase structure. Some swelling of the crystal lattice is observed near to point defects, where plasma flux heat loads are so great that the coating looks like a melted and boiled surface (Fig. 4a). The surface local defects are the same in character for all elements: craters and holes stipulated by effect of plasma fluxes, arcs and thermal shocks (Fig. 4b). The B_4C ejected layer thickness reaches 35 μm on the electron side and 30 μm on the ion side of the graphite elements. In addition, the remained layer thickness is 5 μm on the e-side and 10 μm on i-side. More intensive erosion on the limiter electron side in comparison with that on the ion-side has also been found earlier on the T-10 tokamak [9, 10]. However, unlike the nonirradiated sample, no explicit B_4C layer. It is possible to assume that boron-carbide coating modification and its partial interaction with the substrate graphite occur under the action of plasma fluxes. This assumption is confirmed by some variation of the axial lengths d for B_4C coating of graphite elements before and after irradiation. Divertor tiles from the B_4C-coated ATJ graphite were exposed to the DIII-D plasma during 16 operation weeks of the 1993 year's campaign [4]. The thickness of the coatings varied from 85 to 180 μm. Typically, the plasma current was 0.5–2.5 MA, pulse duration was about 5 s and the power of neutral beam heating varied from 2 to 16 MW. The crystalline structure, phase and chemical composition of the coatings did not change. There were observed some minor defects such as craters and holes, created by the plasma fluxes, arcs and thermal shocks. The thickness of the eroded layer varied from 40 to 70 μm. In the largest defect, the thickness of the remaining coating was 50 μm. It should be noted that the tile surfaces were overcoated with a redeposited layer consisting mainly of carbon.

The DIII-D experiments were carried out in accordance with the DIMES (divertor materials evaluation system) program, Fig. 5 [4, 6]. The coatings were exposed to the divertor strike point plasma flux. The coating on the MPG-8 graphite was exposed to 11 discharges with low enough heat fluxes of about 0.4 MW/m^2 [3]. The essential erosion was not observed and the surface topography after the exposure did not changed almost. The coating on the RGT graphite was exposed to 14 discharges [5]. The accumulated exposure time was about 11 s of ELMing H-mode plasma with some additional energy deposition from a locked mode disruption that terminate one of the discharges. The average heat flux at the sample radius measured by an infrared camera was 2–3 MW/m^2. However because of not good alignment of the sample the peak flux was estimated to be about 10–12 MW/m^2, somewhat above those loads expected for ITER. A damaged area appeared in the region of the highest heat flux. The thickness of the remaining B_4C layer was about 130 μm and by comparison with neighboring

undamaged layer about 45 μm was eroded. The composition everywhere is consistent with B_4C, even in the damaged area. The concentration of oxygen is seen to be almost doubled in the damaged region (4.5×10^{17} O/cm^2) compared to the undamaged surface (2×10^{17} O/cm^2). The increase in O concentration could be initiated by boron sputtering and activation of boron atoms in the near surface region by the incident heat and particle flux, resulting in higher B reactivity with O followed by formation of oxides.

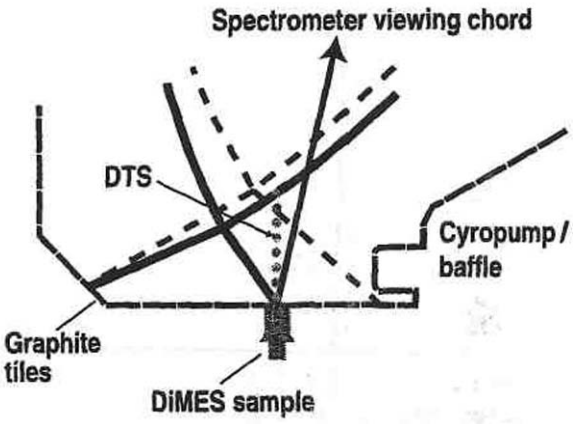

Figure 5. Exposure geometry for DIMES experiments.

The retention of deuterium was measured using NRA along lines both parallel and perpendicular to the magnet field (Fig. 6). The measured areal concentration is about (2–3) $\times 10^{17}$ /cm^2 in the undamaged area, similar to previous measured retention for graphite in DIII-D under similar plasma conditions. However, in the damaged zone, the retention is much higher, about 12×10^{17} D/cm^2. This increase may be due to the increase in particle flux and the thickness of deposited layer as well due to the unexpected tilting of the surface. The development of the coating surface and the increase of the density of radiation defects as well as radiation stimulated diffusion of D in B_4C may also contribute. The relatively high electron temperature, 80 eV, of the plasma would imply a D^+ incident kinetic energy of about 300 eV, with the tail of the distribution extending higher. Any changes in crystalline structure, phase and chemical composition were not observed.

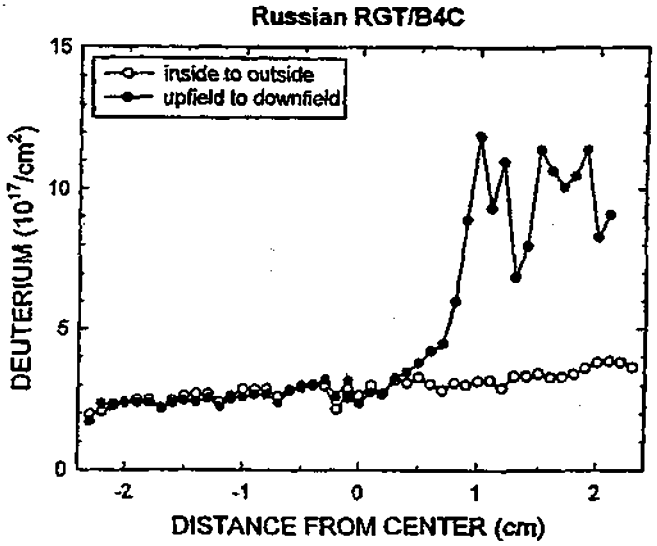

Figure 6. Deuterium retention, NRA data.

3. Conclusion

Plasma contamination with impurities and protection of plasma facing components (PFC) against high heat fluxes are one of the most important issues in present-day tokamaks. To solve these problems several methods can be applied. One of them is protection of PFC using boron-carbide coatings. Contrary to pure carbon materials, B_4C has much lower chemical and high-temperature sputtering and possesses such important features as oxygen gettering and lower hydrogen recycling. In contrast to thin boronization films the thick coatings are capable to resist high heat fluxes such as in tokamak divertors.

References

1. O.I. Buzhinskij and Yu.M. Semenets, Thick boron carbide coatings for protection of tokamak first wall and divertor, Fusion Engineering and Design, **45**, 343–360 (1999).
2. O.I. Buzhinskij, M.I. Guseva, G.V. Gordeeva, et al., Protection of graphite shields in front of the first wall with boron-containing films in tokamaks, J. Nucl. Mater., **175**, 262–265 (1990).
3. O.I. Buzhinskij, I.V. Opimach, V.A. Barsuk et al., Performance of boron containing materials under disruption simulation and tokamak divertor plasma testing, J. Nucl. Mater., **220–222**, 922–925 (1995).
4. O.I. Buzhinskij, V.A. Barsuk, I.V. Opimach et al., The performance of thick B_4C coatings on graphite divertor tiles in the DIII-D tokamak, J. Nucl. Mater. **233–237**, 787–790 (1996).

5. O.I. Buzhinskij, I.V. Opimach, V.A. Barsuk., The study of CVD thick B_4C and SiC coatings on graphite of different types in DIII-D divertor, 19th ISFT, Book of Abstracts, Lisoboa, 1996, p.87.
6. D.G. Whyte, R. Bastasz, J.N. Brooks et al., Divertor erosion in DIII-D, J. Nucl. Mater. **266–269,** 67–73 (1999).
7. O.I. Buzhinskij, V.A. Barsuk, I.A. Kovan and V.G. Otroshchenko, Research of a condition of shields of the RF-antenna tokamak T-11M after four years of work, Plasma Devices and Operation, Vol. 11, No 4, 243–249 (2003).
8. V.A. Barsuk, O.I. Buzhinskij, V.A. Vershkov et al., Test of the boron-containing coating of the graphite limiter in the T-10 tokamak, J. Nucl. Mater., **191–194**, 1417–1422 (1992).
9. V.A. Barsuk, O.I. Buzhinskij, V.A. Vershkov et al., Test of the boron-containing coating of the graphite limiter in the T-10 tokamak, J. Nucl. Mater., **196–198**, 543–548 (1992).
10. O.I. Buzhinskij and Yu.M. Semenets, Review of *in-situ* boronization in contemporary tokamaks, Fusion Techn., **32**, 1–13 (1997).
11. O.I. Buzhinskij, V.G. Otroshchenko, D.G. Whyte et al., Plasma deposition of boron films with high growth rate and efficiency using carborane, J. Nucl. Mater. **313–316**, 214–218 (2003).
12. O.I. Buzhinskij, V.G. Otroshchenko, V.A. Barsuk, Renewable boron carbide coating in plasma shots of tokamak T-11M, J. Nucl. Mater., **390–391**, 996–999 (2009).

ELECTRON STRUCTURE, TRANSPORT, AND SUPERCONDUCTING PROPERTIES OF ZrB_{12}, ZrB_2, YB_6 AND MgB_2

Vitaly A. GASPAROV*
Institute of Solid State Physics RAS, Chernogolovka, 142432, Russian Federation

Abstract We report the review of the measurements of the temperature dependence of the resistivity, ρ(T), magnetic penetration depth, λ(T), the lower, $H_{c1}(T)$, and upper, $H_{c2}(T)$, critical magnetic fields, for single crystals of dodecaboride ZrB_{12}, diboride ZrB_2, hexaboride YB_6 and thin films of diboride MgB_2. Although ZrB_{12} behaves like a simple metal in the normal state, the resistive Debye temperature is three times smaller relative to that calculated from the specific heat data. We observe predominantly quadratic temperature behavior of resistivity in these borides at low temperatures indicating the possible importance of the electron-electron interaction. Superfluid density of ZrB_{12} displays unconventional two step temperature dependence with pronounced shoulder at T/T_c equal to 0.65. Contrary to conventional theories we found a linear dependence of $H_{c2}(T)$ for ZrB_{12} and YB_6 from T_c down to 0.35 K. We suggest that both λ(T) and $H_{c2}(T)$ dependencies in ZrB_{12} can be explained by two band BCS model with different superconducting gap and T_c. In order to shed light on the band structure of ZrB_{12}, the de Haas–van Alphen effect was studied by magnetic torque measurements in magnetic fields up to 28 T at temperatures down to 0.35 K. The dHvA oscillations orbits from different sheets of the Fermi surface were detected. Comparison of the angular dependence of the dHvA frequencies with the theoretical band-structure calculations implies overall agreement with theoretical Fermi surface model.

PACS Codes: **74.70.Ad, 74.60.Ec, 72.15.Gd**

Keywords: ZrB_2, MgB_2, ZrB_{12}, YB_6, borides, superconductivity, resistivity, magnetic penetration depth, lower and upper critical magnetic field, Fermi surface

1. Introduction

Recent discovery of superconductivity in magnesium diboride [1] has initiated a substantial interest to potential "high temperature" superconducting

* V.A. Gasparov, Institute of Solid State Physics RAS, Chernogolovka, 142432, Russian Federation, e-mail: vgasparo@issp.ac.ru

N. Orlovskaya and M. Lugovy (eds.), *Boron Rich Solids: Sensors, Ultra High Temperature Ceramics, Thermoelectrics, Armor*, DOI 10.1007/978-90-481-9818-4_16,

transition in other borides [2]. Actually, only nonstoichiometric boride compounds ($MoB_{2.5}$, $NbB_{2.5}$, Mo_2B, W_2B) has been known as superconductors [3]. We succeeded in preparation of superconducting polycrystalline ZrB_2 compounds with T_c as high as 5.5 K [2]. However lately, we could not confirm this observation on ZrB_2 single crystals [4]. Apparently, the reason for this discrepancy is non stoichiometry of former polycrystalline ZrB_2 samples. Indeed, superconductivity was recently observed in a number of nonstoichiometric borides (Nb_xB_2, $BeB_{2.75}$) [5–8] with T_c up to 9.2 K. It was established from band structure calculations that metal lattice vacancies affect the electronic properties and energy states of of Nb, Zr, and Y layered diborides [9]. It was suggested that the superconducting transition for ZrB_2 [2] and Nb_xB_2 [5–7] can be associated with their nonstoichiometry in the metal sub lattice.

Absence of superconducting transition in stoichiometric borides is clearly not in line with the old idea about superconductivity in metallic hydrogen [10] applied by Kortus et al. [11] to explain superconductivity in MgB_2. Potential clue to this contradiction my lay in the crystal structure of these boron compounds, in particular in their cluster structure. Although it is widely accepted that the layered structure is crucial for high-T_c superconductivity, one can argue that clusters of light atoms are important for high T_c as well. In particular, there are a number of rather high-T_c superconductors among 3D cluster compounds. Those are alkali metal doped C_{60} compounds (fullerides) Me_3C_{60} (*Me* = K, Na, Rb, Cs) with highest T_c up to 33 K for $RbCs_2C_{60}$ [12, 13]. It is also known that boron atoms form clusters. These are octahedral B_6 clusters in MeB_6, icosahedral B_{12} clusters in β-rhombohedral boron, and cubo-octahedral B_{12} clusters in MeB_{12}.

The quest for superconductivity in these cluster compounds has a long history. Several superconducting cubic hexaborides – MeB_6 and dodecaborides – MeB_{12} have been discovered by Matthias et al. back in late 1960s [14] (Me = Sc, Y, Zr, La, Lu, Th). Many other cluster borides (Me = Ce, Pr, Nd, Eu, Gd, Tb, Dy, Ho, Er, Tm) were found to be ferromagnetic or antiferromagnetic [14, 15]. It was suggested [3] that the superconductivity in YB_6 and ZrB_{12} is exactly due to the effect of a cluster of light boron atoms. At the same time, a much smaller isotope effect on T_c for boron in comparison with Zr isotopic substitution suggests that the boron in ZrB_{12} serves as inert background for the Zr-driven superconductivity [16, 17]. Clearly systematic study of YB_6 and ZrB_{12} is needed to address the question of superconductivity in these compounds.

In our recent study of the electron resistivity, ρ(T), magnetic penetration depth, λ(T), and critical magnetic fields of polycrystalline [2, 18, 19] and single crystalline ZrB_{12} and YB_6 [20–22], we demonstrated that these

compounds behaves like a normal metal with the usual Bloch–Grüneisen temperature dependence of $\rho(T)$ but with rather low resistive Debye temperature (T_R = 280 K for ZrB_{12}). The latter is almost three times smaller than Debye temperature obtained from the specific heat, C(T), data [23]. Furthermore, contrary to conventional theories, we found a linear temperature dependence of $H_{c2}(T)$. Recently the band structure calculations of ZrB_{12} [24, 25] by self-consistent full-potential LMTO method have been also reported. Recently, we reported a first detailed study of the de Haas–van Alphen (dHvA) effect in ZrB_{12} single crystals by comparison with predictions of the band-structure calculations [26]. Four branches of dHvA frequencies were clearly resolved in our data and have been assigned to Neck sections of open hole sheet and closed electron "cubic box" of the Fermi surface of ZrB_{12}. The effective masses corresponding to the Neck sections have been measured and compared with our band structure calculations. The comparison shows that the electron–phonon enhancement is very large for the Neck section.

Our data contradict the data of the contact spectroscopy (CS) of Daghero et al. [27] and tunneling and magnetic data of Tsindlekht et al. [28] of single crystals of ZrB_{12} at temperatures close to T_c. It was concluded that ZrB_{12} is a strong coupling s-wave superconductor, with $2\Delta(0)/k_BT_c = 4.7$, while Lortz et al. [23] and Wang et al. [29], observed that ZrB_{12} is a single gap marginal BCS superconductor which undergoes unconventional transition from type-I near T_c to type II superconductor below 4.6 K with $2\Delta(0)/k_BT_c = 3.7$, the value that is lower than that obtained from CS [27] and STM data [28]. Large difference in H_{c2} characteristics reported in the above-mentioned papers was discussed in terms of surface superconductivity [30]. Most of the features of MgB_2 discovered so far can be explained by two band superconductivity model [31, 32]. We have shown that application of this model for ZrB_{12}, may explain observed controversy of published data [21, 22]. Knowledge of the electron transport and superconducting properties in this cluster compound is critical for understanding these conflicting results.

Here, we offer a quantitative analysis of the temperature dependencies of $\rho(T)$, $\lambda(T)$, lower $H_{c1}(T)$, and upper $H_{c2}(T)$, critical magnetic fields in single crystals of ZrB_2, ZrB_{12}, YB_6 and thin MgB_2 films. We consider unusual superconducting properties of ZrB_{12} and argue that the controversy of published results can be reconciled by two-band superconductivity. The structure of this paper is as follows. In Section 2 we report on the samples details and experimental techniques. Section 3 describes the electron transport in these compounds and Section 4 describes the temperature dependence of $\lambda(T)$ in ZrB_{12} samples and MgB_2 thin films. The data on $H_{c1}(T)$ and $H_{c2}(T)$ are presented in Section 5 and the Fermi surface investigations in Section 6. Section 7 contains our conclusions.

2. Experimental Setup

Under ambient conditions, dodecaboride ZrB_{12} crystallizes in the *fcc* structure of the UB_{12} type (space group *Fm3m*, a = 0.74075 nm [21], see Fig. 1). In this structure, the Zr atoms are located at interstitial openings among the close-packed B_{12} clusters. In contrast, ZrB_2 shows a phase consisting of two-dimensional graphite-like monolayers of boron atoms with a honeycomb lattice structure and the lattice parameters a = 0.30815 nm and c = 3.5191 nm (space group *P6/mmm*), intercalated with Zr monolayers [2]. In the cubic structure of YB_6, the Y atom is at the center of a lattice surrounded of B_6 clusters with icosahedral symmetry.

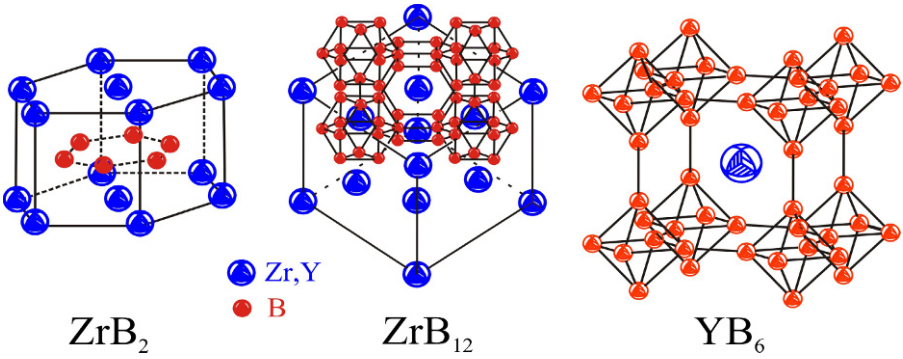

Figure 1. Lattice structure of diboride ZrB_2, dodecaboride ZrB_{12} and hexaboride YB_6. For clarity B_{12} clusters are shown only on the upper face of the ZrB_{12} lattice.

Figure 2. Etching pattern of a ZrB_{12} single crystal cross section in (100) plane from the same parts of ingot as in [23, 27, 29]. The needle like long grains are ZrB_2 phase, while the small black lines correspond to etching pits from small angle boundaries.

The ZrB_{12} single crystals were obtained from a mixture of certain amount of ZrB_2 and an excess of boron (50–95%). The resulting materials were subjected to a crucible-free RF-heated zone-induction melting process in an argon atmosphere [4, 20]. The obtained single crystal ingots had a typical diameter of about 5–6 mm and a length of 40 mm. The XRD measurements confirmed that both ingots are good quality single crystals. However, we discovered that most parts of the ZrB_{12} ingot contained needle like phase of non-superconducting ZrB_2 (see Fig. 2). Therefore, special care has been taken to cut the samples from ZrB_2 phase free parts. The YB_6 single crystals were grown by aid of the RF-heated floating zone method at a pressure of 0.5 MPa of ambient argon, by Tsukuba group [33]. The crystal had a typical diameter of about 1 cm in diameter.

For this study, two highly crystalline, superconducting films of MgB_2 were grown on an *r*-plane sapphire substrate in a two-step process [34]. Deposition of boron precursor films via electron-beam evaporation was followed by ex-situ post annealing at 890°C in the presence of bulk MgB_2 and Mg vapor. We investigated films of 500 and 700 nm thick with corresponding T_{c0}'s of 38 K and 39.2 K, respectively. The details of the preparation technique are described elsewhere [34].

We used spark erosion method to cut the single crystal ingots into rectangular <100> oriented bars of about $0.5 \times 0.5 \times 8$ mm^3. The samples were lapped with diamond paste and etched in hot nitrogen acid, to remove any damage induced by lapping deteriorated surface layers. Magnetic measurements of $\rho(T,H)$ and $\lambda(T,H)$ were carried out using a superconducting coil in applied fields of up to 6 T down to 1.3 K. Additional *dc* and *ac* $\rho(H)$ measurements were performed in the National High Magnetic Field Laboratory in Tallahassee, Florida (NHMFL) at the temperatures down to 0.35 K.

We used radio frequency LC technique [35] to measure $\lambda(T)$ of ZrB_{12} samples. This technique employs a rectangular solenoid coil into which the sample is placed. The coil is a part of the LC circuit driven by a marginal oscillator operating at 2–10 MHz, or by the impedance meter (VM-508 TESLA, 2–50 MHz). The connection between parameters of the circuit and $\lambda(T)$ is described by following Eq. [21]:

$$\lambda(T) - \lambda(0) = \delta \cdot \frac{f^{-2}(T) - f^{-2}(0)}{f^{-2}(T_c) - f^{-2}(0)} \tag{1}$$

Here $\delta = 0.5(c^2\rho/2\pi\omega)^{1/2}$ is the imaginary part of a skin depth above T_c [21], which was determined from the $\rho(T)$ measurements above T_c, $f(T)$ is the resonance frequency of the circuit at arbitrary T, $f(T_c)$ and $f(0)$ are the resonance frequency of the circuit at the superconducting transition and at zero temperature, respectively.

The λ(T) dependence in thin MgB_2 films was investigated employing a single coil self inductance technique. This technique, originally proposed in [36] and improved in [37], takes advantage of the well known two-coil geometry. It was successfully used for the observation of the Berezinskii–Kosterlitz–Thouless vortex–antivortex unbinding transition in ultrathin $YBa_2Cu_3O_{7-x}$ films [38]. In this radio frequency technique one measures the temperature dependence of the complex impedance of the LC circuit formed with a one-layer pancake coil located in the proximity (~0.1 mm) of the film. During the experiment the coil was kept at 2.5 K, whereas the sample temperature has been varied from 2.5 up to 100 K.

The complex self inductance *M* of the coil on the film can be obtained through:

$$\mathrm{Re}\,M(T) = L_0 \cdot \left(\frac{f_0^{\,2}}{f^2(T)} - 1\right) \tag{2}$$

$$\mathrm{Im}\,M(T) = \frac{1}{2\pi \cdot f(T) C^2}\left[\frac{1}{Z(T)} - \frac{1}{Z_0(T)}\frac{f^2(T)}{f_0^{\,2}}\right] \tag{3}$$

Here L, Z(T), f(T), L_0, Z_0 and f_0 are the inductance, the real part of impedance and the resonant frequency of the circuit with and without the sample, respectively. In the London regime, where the high frequency losses are negligible, one can introduce ΔReM(T) – the difference between temperature dependant real part of *M* of the coil with the sample, ReM(T), and that of the coil at T_0, ReM_o. This difference is a function of the London penetration depth λ(T):

$$\Delta\,\mathrm{Re}\,M(T) = \pi\mu_0 \int_0^{\infty} \frac{M(q)}{1 + 2q\lambda \cdot \coth\left(\frac{d}{\lambda}\right)}\,dq \tag{4}$$

where M(q) plays the role of self inductance at a given wave number q in the film plane and depends on the sample-coil distance, d is the sample thickness [21, 37]. Thanks to Eq. 4, we can obtain the λ(T) of superconducting film by measuring the variation ΔReM(T) of coil impedance and convert them into λ(T).

3. Electron Transport

Figure 3 shows the temperature dependence of ρ(T) of ZrB_{12} and YB_6 single crystal samples. To emphasize the variation of ρ(T) in a superconductive state, we plot these data in the inset. The transition temperature (T_{c0} = 6.0 K for ZrB_{12} and 7.8 K for YB_6) is consistent with the previously reported values

and is larger than that of ZrB_2 polycrystalline samples (5.5 K) [2]. The ZrB_{12} samples demonstrate a remarkably narrow transition with $\Delta T = 0.04$ K, while this width is much larger for YB_6.

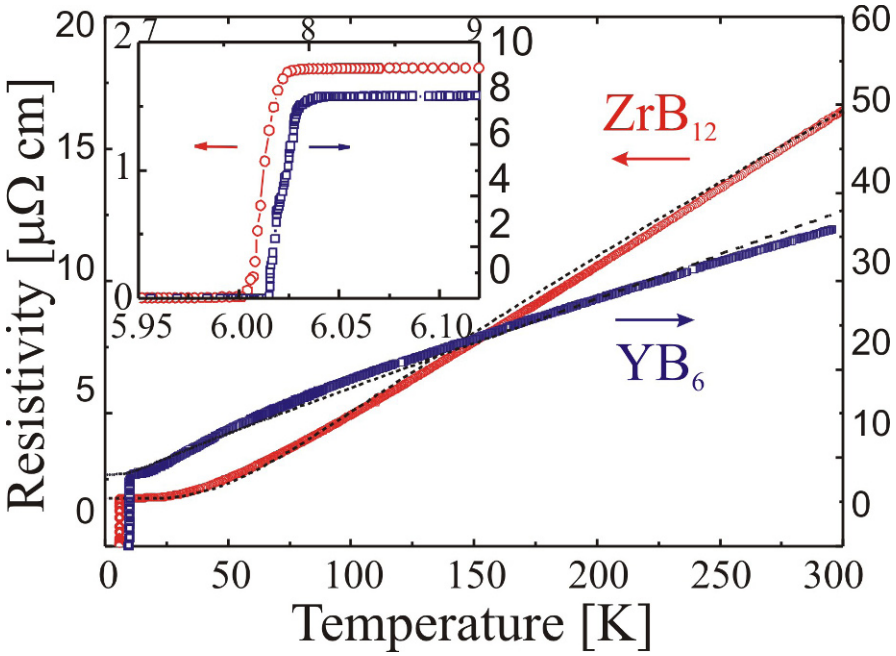

Figure 3. Temperature dependence of ρ(T) for ZrB_{12} (*circles*) and YB_6 (*squares*) single crystal samples. The dashed lines represent BG fits to the experimental data by Eq. 5. The inset shows the ρ(T) data near the transition.

We did not found any hints of the superconducting transition in ZrB_2 single crystals down to 1.3 K [21], even though superconductivity was observed before at 5.5 K in polycrystalline samples [2]. Based on the electron structure calculation it was suggested that the presence of Zr defects in $Zr_{0.75}B_2$ leads to the appearance of a very intense peak in the density of states and subsequent superconductivity [9]. Apparently, observation of superconductivity in polycrystalline samples of ZrB_2 was due to non stoichiometry of our samples which is in line with recent observations of superconductivity in non stoichiometric $Nb_{1-x}B_2$ compounds [5–7] as well as in other nonstoichiometric borides [3, 8].

As we can see from Fig. 3, the ρ(T) of ZrB_{12} is linear above 90 K with rather low residual resistivity ratio $\rho_{300K}/\rho_{6K} \approx 10$, while this one is only 7.2 for YB_6. One can predict a nearly isotropic ρ(T) dependence for *fcc* ZrB_{12}, which can be described by Bloch–Grüneisen (BG) equation of the electron–phonon (*e-p*) scattering rate [39]:

$$\rho(t) - \rho(0) = 4\rho_1 \cdot t^5 \int_0^{1/t} \frac{x^5 e^x dx}{(e^x - 1)^2} = 4\rho_1 \cdot t^5 J_5(1/t) \quad (5)$$

Here, ρ(0) is the residual resistivity, ρ_1=dρ(T)/dt is the slope of ρ(T) at high T > T_R, t = T/T_R, T_R is the resistive Debye temperature and $J_5(1/t)$ is the Debye integral.

It is clear from Fig. 3 that the BG model nicely describes the ρ(T) dependence of both borides, indicating the importance of *e-p* interaction. It is remarkable that this description works well at low temperatures with constant T_R = 300 K for ZrB_{12}. Clearly, ZrB_2 (T_R = 700 K), ZrB_{12} (T_R = 300 K) and YB_6 (T_R = 62 K) have very different ρ(T) dependence due to different T_R. At the same time, the phonon Debye temperature, T_D, for ZrB_{12} calculated from C(T) is three times higher. Furthermore T_D increases from 800 to 1,200 K as temperature rises from T_c up to room temperature. We believe that this inconsistency of T_R and T_D can be explained by limitation of T_R by a cut-off phonon wave vector q = $k_BT/\hbar s$. The latter is limited by the Fermi surface (FS) diameter $2k_F$ rather than the highest phonon frequency in the phonon spectrum [21, 40]. Besides some problems may arise in [23] due to use of ZrB_2 phase rich samples as in Fig. 2.

Actually, ρ(T) of ZrB_{12} and YB_6 samples deviates from the BG model at low temperatures. We have been reported for ZrB_{12}, ZrB_2 and MgB_2 that such deviation are consistent with a sum of electron–electron (*e–e*), aT^2, and *e–p*, bT^5 contributions to the low-*T* ρ(T) data. The coefficient b = 497.6 ρ_1/T_R^5 in this plot, gives another measure of T_R from low-*T* ρ(T) data. Therefore, the data extracted from this two-term fit are self consistent with the full Eq. 5 fit.

Borides have rather high T_D that depresses the *e–p* scattering, as a result *e–e* scattering term may be much more pronounced. Indeed, we find very similar values of a coefficient for ZrB_{12} and ZrB_2 samples in the basal plane (a = 22 pΩcmK^{-2} and 15 pΩcmK^{-2}, respectively) [21], while for YB_6 a is 100 times more: 2.5 nΩcm. Actually, the T^2 term could be due to electron-impurity, electron-dislocation scattering, etc. induced deviation from Mattiessen rule. It is difficult to separate the contributions of these effects, thus it is presently not clear where exactly this T^2 term comes from [21].

As we mentioned in the introduction there is a contradiction between our description of the ρ(T) and that of Refs.27,28. Daghero et al. suggested BG fit with T^3 dependence rather than T^5 on the similar single crystals at low T < 170 K [27]. We have shown that there is no way to fit ρ(T) by a modified BG T^3 equation in whole temperature range [21]. Lortz et al. [23] report temperature dependence of ρ(T) obtained on the samples cut from ones provided by our group. They fitted ρ(T) with the generalized BG formula, using a decomposition into Einstein modes of $\alpha^2(k\omega)F(\omega)$, rather then

BG model. However, the fit to ρ(T) data was obtained using six fitting parameters for $\alpha^2_k F_k$ and ρ(0) for ZrB_{12} which is not better than a simple Debye fit (Eq. 5) with just two free parameters: T_R and ρ(0). Finally, we note that only phonons with a phonon wave vector $q = k_B T/\hbar s < 2k_F$ can participate in ρ(T) [40].

4. Magnetic Penetration Depth

In the BCS theory the London penetration depth is identical with λ(T) for specular and diffuse surface scattering and for negligible non local effects. For a BCS-type superconductor with the conventional *s*-wave pairing form, the λ(T) has an exponentially vanishing temperature dependence below $T_c/2$ (where ΔT) is almost constant) [41]:

$$\lambda(T) = \lambda(0) \cdot [1 + \sqrt{\frac{\pi\Delta(0)}{2k_B T}} \cdot \exp(-\frac{\Delta(0)}{k_B T})] \tag{6}$$

for clean limit: $l > \xi$.and

$$\lambda(T) = \lambda(0) \cdot \sqrt{\frac{1}{\tanh(\frac{\Delta(0)}{2k_B T})}} \tag{7}$$

for dirty limit: $l < \xi$. Here Δ(0) is the energy gap and λ(0) is the penetration depth at zero temperature. Close to T_c λ(T) dependence has a BCS form [21]:

$$\lambda(T) = \frac{\lambda(0)}{\sqrt{2 \cdot (1 - \frac{T}{T_c})}} \tag{8}$$

Important problems for λ(T) measurements are: (i) determination of basic superconducting parameter λ(0) and (ii) temperature dependence law, to see whether *s*-wave or *d*-wave pairing form exist. Both these problems can be addressed from low-*T* λ(T) dependence according to Eqs. 6 and 7.

The unconventional *d*-wave pairing symmetry causes the energy gap to be suppressed along nodal directions on the Fermi surface. This type of pairing should manifest itself through the linear temperature dependence of $\lambda(T) - \lambda(0) \propto T$ at low-*T*. Such a linear *T* dependence of λ(T) has been used as an indicator of *d*-wave pairing in cuprates [42–44]. At the same time the microwave λ(T) data in fully oxygenated YBCO films show a picture which is consistent with the two-band *s*-wave superconductivity [45]. We believe that the question about linear dependence of λ(T) is still open [21] because

it strictly violates the third law of thermodynamics [46]. Thus we use BCS Eqs. 6 and 7 in order to fit our data (see Fig. 4).

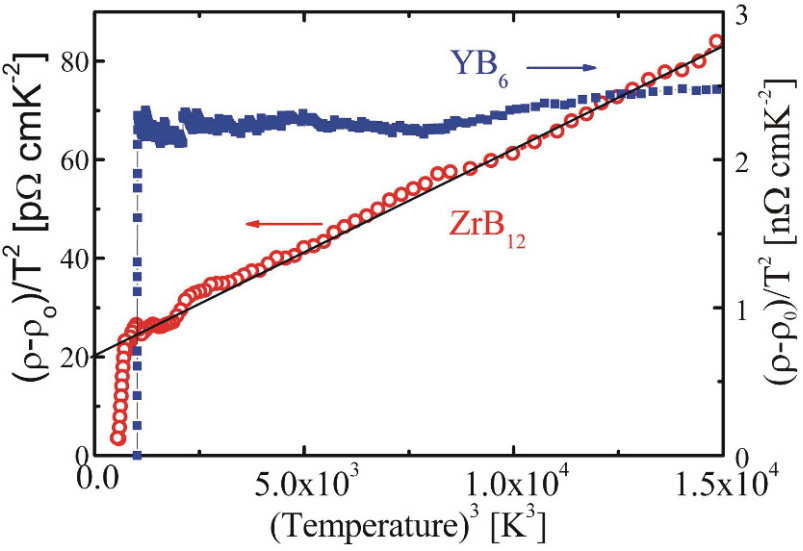

Figure 4. Temperature dependence of $\rho(T) - \rho(0)/T^2$ for ZrB_{12} (*circles*) and YB_6 (*squares*) single crystal samples.

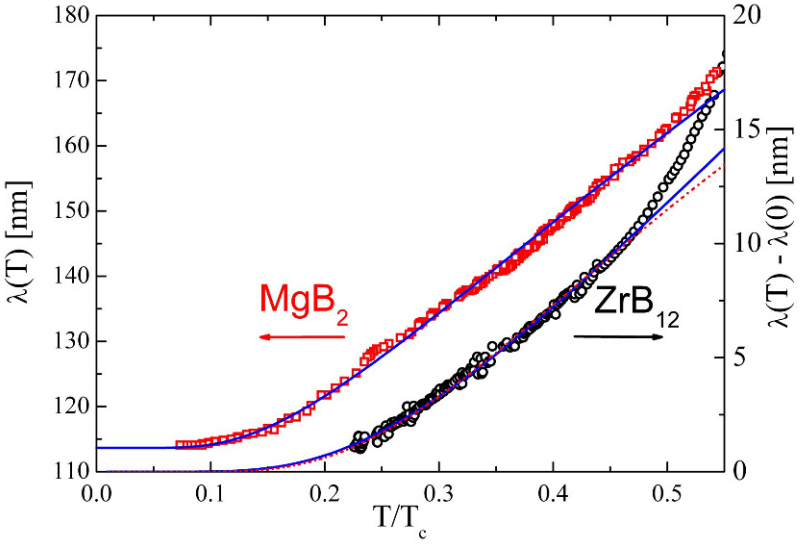

Figure 5. Temperature variations of $\lambda(T)$ for ZrB_{12} and MgB_2 samples.

Figure 5 shows how $\lambda(T) - \lambda(0)$ changes with reduced temperature, T/T_c, at low-T for both MgB_2 (red squares) and ZrB_{12} (black circles). We would like to stress that $\lambda(T) - \lambda(0)$ data are robust relative to the change of the oscillator frequency. Our ZrB_{12} data do not extend to as low reduced temperatures as our data for MgB_2. This could lead to somewhat larger uncertainty in the estimates for the zero temperature $\lambda(0)$ and $\Delta(0)$ from low-T data for ZrB_{12}. The value of $\lambda(0) = 143$ nm and $T_c = 5.992$ K used in this data analysis is obtained by getting best linear fit of the $\lambda(T) - \lambda(0)$ versus $1/\sqrt{2(1-T/T_c)}$ plot, according to Eq. 8 [21].

We employ Drude formula, ($\rho(0) = 3/N_0 l v_F e^2$) where we use measured $\rho(0) = 1.8$ μΩcm, the electron density of states determined from C(T) data, $N_0 = 1.83 \times 10^{22}$ st/eV cm^3 [23], and the electron Fermi velocity of $v_F = 1.9 \times 10^8$ cm/s, determined from dHvA data [26], to obtain $l = 33$ nm. This value is smaller than a coherence length ($\xi(0) = 45$ nm, see below) indicating that our samples are in dirty limit.

One can easily notice from Fig. 6 an unconventional behavior of ZrB_{12} superfluid density with pronounced shoulder at T/T_c equal to 0.65. This feature can be explained by a model of two independent BCS superconducting bands with different plasma frequencies, gaps and T_c's [21, 32]. We label these two bands as Belly and Box sheets according to electron structure of ZrB_{12} (see below) [26]. Assuming parallel currents through alternating subsystems, the conductivity is a sum of partial bands conductivities. The imaginary part of the conductivity is proportional to $1/\lambda^2$. For a dirty limit [47] we can write in:

$$\frac{1}{\lambda^2(T)} = \frac{\Delta_p(T)\cdot\tanh(\frac{\Delta_p}{2k_BT})}{\lambda^2{}_p(0)\Delta_p(0)} + \frac{\Delta_d(T)\cdot\tanh(\frac{\Delta_d}{2k_BT})}{\lambda^2{}_d(0)\Delta_d(0)} = \frac{1}{\lambda_p{}^2(T)} + \frac{1}{\lambda_d{}^2(T)}. \qquad (9)$$

Here Δ_i is the superconducting energy gap and $\lambda_i(0)$ is residual penetration depth in Belly or Box sheets of the FS. Using this two gap $\lambda(T)$ BCS – like dependence we fit the experimental data with six fitting parameters: $T^p{}_c = 6.0$ K, $T^d{}_c = 4.35$ K, $\Delta^p(0) = 0.73$ meV, $\Delta_d(0) = 1.21$ meV, $\lambda_p(0) = 170$ nm and $\lambda_d(0) = 260$ nm, for Belly or Box sheets, respectively. Clearly low temperature dependence of $\lambda^2(0)/\lambda^2(T)$ is dominated by the Belly band with the smallest T_c, whereas the high temperature behavior results from the Box band with the larger T_c. The reduced energy gap for Belly band, $2\Delta_p(0)/k_BT_c^p = 2.81$, is rather small relative to the BCS value 3.52, while Box band value, $2\Delta_d(0)/k_BT_c^d = 6.44$, is twice as big. Thus, we suggest that ZrB_{12} may have two superconducting bands with different T_c and order parameters. Also, the $\Delta(0)$ of ZrB_{12} may not be constant over the FS. Here we just fit a data assuming a two gap distinct values.

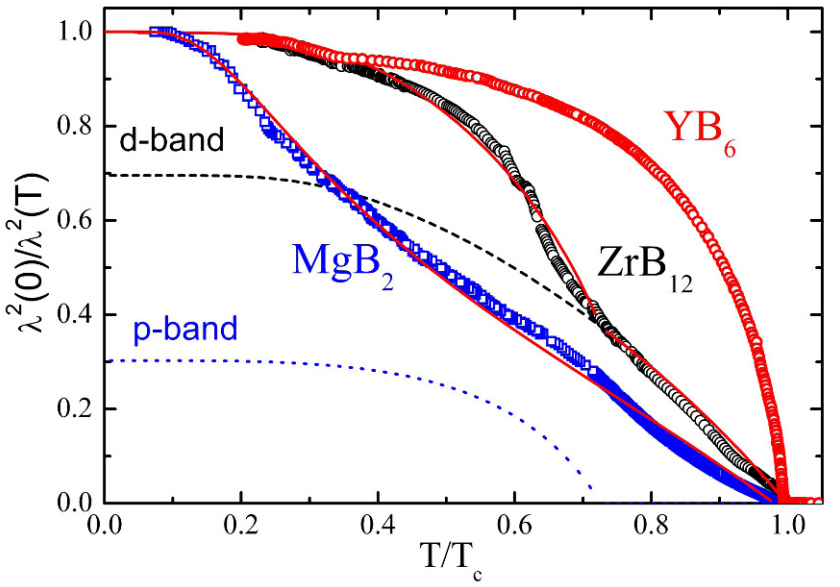

Figure 6. Superfluid density, $[\lambda(0)/\lambda(T)]^2$, of the ZrB_{12} ($\lambda(0)$ = 143 nm) and YB_6 ($\lambda(0)$ = 300 nm) single crystal samples and MgB_2 thin film (*squares*). The predicted behavior of $[\lambda(0)/\lambda(T)]^2$ for ZrB_{12} within the two band model as described in the text is shown by the *solid*, *dashed* (*p*-band) and *dotted* (*d*-band) lines.

It is not clear from band structure calculations whether the wave functions of carriers on these sheets are due to predominantly *p*- or *d*-states. However it follows, that the dominant contribution to the density of states $N(E_F)$ is made by the Zr_{4d} and B_{2p} states, with $N_d = 7.3 \times 10^{21}$ st./eVcm^3 and $N_p = 8.7 \times 10^{21}$ st./eV cm^3, respectively [24]. The B_{2p} bonding states are responsible for the formation of B_{12} intra-cluster covalent bonds. In turn, Zr_{4d} bands are due to Zr sub-lattice. A much smaller boron isotope effect on T_c in comparison with Zr isotopic substitution [16, 17] may be an indication of the existence of two separate subsystems with different gaps and T_c values. We use this two band approach to obtain *p*-band diffusivity (D = lv/3) of $D_p = 57$ cm^2/sec and *d*-band diffusivity of $D_d = 10$ cm^2/s. Note that there is almost a six times difference between *p*-and *d*-band diffusivity.

The important goal of this study is comparison of ZrB_{12}, YB_6 with MgB_2 data. In Fig. 5 we show the temperature variation of $\lambda(T)$ at $T < T_c/2$ and in Fig. 6 a superfluid density, $\lambda^2(0)/\lambda^2(T)$, versus reduced temperature T/T_c for the best MgB_2 film as determined from the one-coil technique and inversion procedure from Eq. 4 with $\lambda(0)$ = 114 nm. The solid line represent BCS single gap calculations by aid of single term of Eq. 9 and using finite energy gap $\Delta(0)$ = 1.93 meV as fit parameter. Simple conventional *s*-wave dirty case fit by Eq. 7, agrees remarkably well with the low-T data at $T < T_c/2$.

The reduced energy gap $2\Delta(0)/k_BT_c$ is evaluated to be 1.14. It is actually within the range of values for 3D π-bands obtained by CS on MgB_2 single crystals (Δ_π = 2.9 meV) [48], and it agrees with Δ(0) data obtained from similar radio-frequency experiments on single crystals (1.42 meV [49]) and with the theoretical prediction of the two-band model [31]. Rather small $2\Delta(0)/k_BT_c$ observed correspond to the small energy gap in the two-gap model for 3D π-band. Notice, that we studied here the penetration depth in the *ab* plane due to the samples being c-axis oriented thin films. This feature predicts that our $\lambda_{ab}(T)$ is determined by the small energy gap for π-band. Both Δ(0) and λ(0) are consistent with microwave measurements on similar c-axis oriented thin films (3.2 meV and 107 nm, respectively) [50].

5. Upper and Lower Critical Magnetic Field

We now turn to the electronic transport data acquired in magnetic field. We measured the dependence of ρ vs *H* in the temperature range between 0.35 and 6 K in two different magnets at NHMFL, Tallahassee, FL as well in our superconducting coil. Figure 7 displays the resistive magnetic field transitions at various temperatures with the fields oriented along the sample bar.

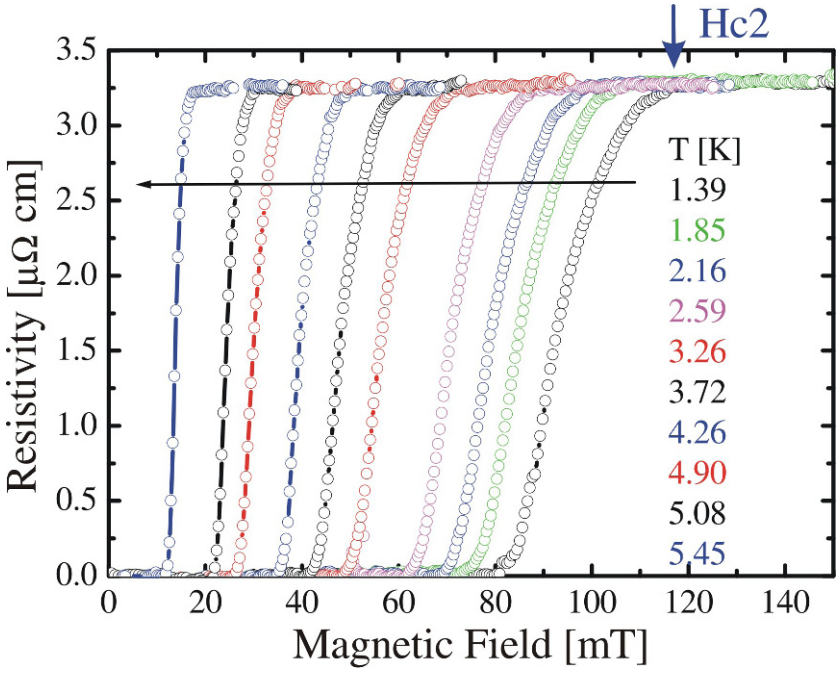

Figure 7. Resistivity of ZrB_{12} in the vicinity of the superconducting transition as a function of *H* at different *T*: 5.45, 5.08, 4.9, 4.26, 3.72, 3.26, 2.59, 2.16, 1.85, 1.39 K from the left to the right.

Two features are clearly seen: (i) as temperature decreases the resistive transition continuously moves to higher fields without any saturation, (ii) longitudinal magnetoresistivity in the normal state is very small. Despite a clear broadening at the higher fields, the onset of the resistive transition remains well defined even at rather low temperatures. We defined H_{c2} as the field where $d\rho/dH$ just starts to deviate from zero (see Fig. 7).

Actually, the resistance can be affected by the defects and surface superconductivity. To get even better fill for H_{c2} we used our $\lambda(H)$ data [21]. Changes in the magnetic field dependence of $\lambda(H)$ are directly proportional to the RF susceptibility of the sample and reflect the surface properties of it in the length of λ, while the resistivity reflects the bulk properties. We determined $H_{c1}(T)$ from $\lambda(H)$ behavior at very small fields [21]. The $\lambda(H)$-$\lambda(0)$ curves display clear linear dependence at low fields caused by the Meissner effect. We determined the value of H_{c1} from crossing point of two linear dependences below and above the break point on $\lambda(T)$ [21].

Figure 8 presents the $H_{c2}(T)$ dependence obtained from those defined at the onsets of the finite $\rho(H)$ and $\lambda(H)$ for ZrB_{12} and YB_6. Remarkable feature of this plot is an identical linear increase of H_{c2} with decreasing temperature for both compounds. As we can see, the H_{c2} data obtained at three different magnets agree remarkably well and are aligned along corresponding straight lines indicating linear $H_{c2}(T)$ dependence down to 0.35 K for ZrB_{12}.

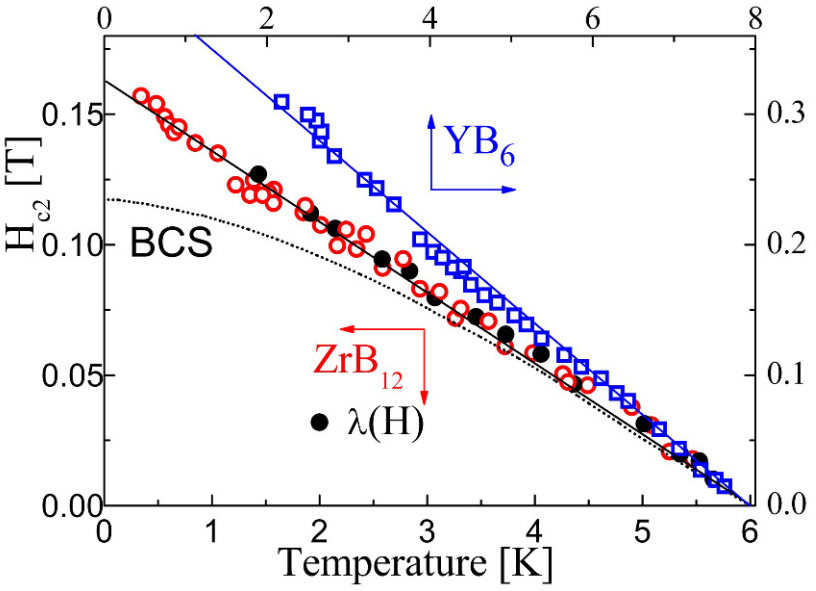

Figure 8. Temperature variations of $H_{c2}(T)$ of ZrB_{12} and YB_6. Dotted line is the BCS $H_{c2}(T)$ data determined from the onset data and HW formula [52].

To see whether one gap BCS model may work for ZrB_{12}, we extrapolate $H_{c2}(T)$ to zero temperature by use of the derivative of $dH_{c2}(T)/dT$ close to T_c and the assumption that the zero temperature $H_{c2}(0) = 0.69T_c dH_{c2}/dT|_{Tc}$ [42]. The resulting $H_{c2}(0)$ = 114 mT is substantially lower than the low temperature onset data below 3 K (see Fig.8). Linear extrapolation of $H_{c2}(T)$ to T = 0 gives $H_{c2}(0)$ = 162 mT for ZrB_{12} and 431 mT for YB_6. We used these values to obtain the coherence length $\xi(0)$, by employing the relations $H_{c2}(0) = \phi_0/2\pi\xi^2(0)$. The latter yields $\xi(0)$ = 45 nm, for ZrB_{12} which is substantially larger than a few angstroms coherence length of high-T_c superconductors.

In contrast to [23, 28, 29] our estimations agree well with the Ginzburg–Landau parameter $\kappa = \lambda/\xi$. Using our values of λ_p and λ_d data we obtain κ_p = 3.8 and κ_d = 5.8. Both values of κ_d are larger then $1/\sqrt{2}$ that implies that ZrB_{12} is type II superconductor at all T. Using the GL expression for $H_{c1}(T) = \phi_0 \ln\kappa /4\pi\lambda^2$ we obtain: $H_{c2}/H_{c1} = 2\kappa^2/\ln\kappa$. From the value $H_{c2}(0)$ obtained above and the H_{c1} data, we find κ = 6.3 and $\lambda(0)$ = 280 nm for ZrB_{12} which is in good agreement with the value $\lambda_p(0)$ = 260 nm obtained from two gap BCS fit for *d*-band. One could argue that the $H_{c1}(T)$ obtained from our magnetic field measurements of $\lambda(T)$ may reflect the flux entry field because of the Bean-Livingston surface barrier, rather then trough H_{c1}. However the entry field $H_{BL} = H_{c1}\kappa/\ln\kappa$ [51] is three times larger than H_{c1} even when one uses κ = 6.3, so if we assume κ = 23 given by a ratio of H_{c2}/H_{c1} we obtain zero temperature $\lambda(0)$ = 1030 nm, which is unreasonably large compared to one obtained from a BCS fit. In contrast to the conventional BCS theory [52], $H_{c2}(T)$ dependence is linear over an extended temperature range with no evidence of saturation down to 0.35 K. Similar linear $H_{c2}(T)$ dependence have been observed in MgB_2 [53, 54] and $BaNbO_x$ [55] compounds. One can describe this behavior of upper critical filed using two-gap approach. According to Gurevich [47], the zero-temperature value of the $H_{c2}(0)$ is significantly enhanced in the two gap dirty limit superconductor model:

$$H_{c2}(0) = \frac{\phi_0 k_B T_c}{1.12\hbar\sqrt{D_1 D_2}} \exp(\frac{g}{2}) \qquad (10)$$

as compared to the one-gap dirty limit approximation $H_{c2}(0) = \phi_0 k_B T_c/1.12\hbar D$. Here g is rather complicated function of the matrix of the BCS superconducting coupling constants.

In the limit of $D_2 << D_1$ we can simply approximate $g \approx |\ln(D_2/D_1)|$. Large ratio of D_2/D_1 leads to the enhancement of $H_{c2}(0)$ and results in the upward curvature of the $H_{c2}(T)$ close to T = 0 [47]. According to our $\lambda(T)$ data (see above), we found very different diffusivities for *p*- and *d*-bands:

$D_p/D_d \approx 3$. Thus we can speculate that the limiting value of $H_{c2}(0)$ is dominated by *d*-band with lower diffusivity $D_d = 17$ cm^2/sec, while the derivative dH_{c2}/dT close to T_c is due to larger diffusivity band ($D_p = 56$ cm^2/s). Indeed, simple estimation of $D_p = 4\phi_0 k_B/\pi^2 \hbar dH_{c2}/dT = 39$ cm^2/s from derivative $dH_{c2}/dT = 0.027$ T/K close to T_c, gives almost the same diffusivity relative to one estimated from $\lambda(T)$ for p-band. Thus, we believe that two gap theoretical model of Gurevich, qualitatively explains the unconventional linear $H_{c2}(T)$ dependence, which supports our conclusion about two gap nature of superconductivity in ZrB_{12}.

The $H_{c2}(T)$ dependence of ZrB_{12} single crystals from the same Kiev group has been measured by three different groups mentioned above. Our $H_{c2}(T)$ data are very similar to those obtained by Daghero et al. [27]. The disagreement is in the interpretation. The authors of [27] concluded that ZrB_{12} is a conventional one gap s-wave superconductor with $\Delta(0) = 1.22$ meV. Thus a strong coupling scenario with reduced energy gap of $2\Delta(0)/k_BT_c = 4.8$ was proposed. One should note however, that the gap signature in CS data has been observed in a temperature range close to T_c (4.2–6 K), although the second gap signature feature should have been seen only below $T_c^d = 4.35$ K, and could have been simply missed by the authors of [27] because of the limited temperature range of their measurements. There is nearly two times difference between H_{c2} obtained from our data and that obtained from tunneling and magnetic characterization data of Tsindlekht et al. [28] and specific heat and resistivity data of Lortz et al. [23] and Wang et al. [29]. Tsindlekht et al. concluded that ZrB_{12} is a type-II superconductor with the Ginzburg–Landau parameter κ slightly above the marginal value of $1/\sqrt{2}$. At the same time Wang et al. [29] observed a crossover between type I and type II behavior of $\kappa(T)$ at 4.7 K. Notice, that this is exactly the same temperature where we observed a break in slope of $\lambda(T)$ dependence. In all those approximations, the validity of the one gap BCS picture is implicitly assumed. Large contradiction between the $\rho(H)$ and $C(H)$ data was attributed to surface superconductivity. One can mention however another possibly reason for this contradiction. In particular, data of [23, 29] have been measured on the samples cut by diamond saw without chemical etching of surface damaged layer. This procedure may create a strong concentration gradient of boron in a surface layer and a substantial manifestation of the surface barriers for the flux lines resulting in this contradiction.

We believe that this inconsistency of our data and the data of [23, 28, 29] can be: (i) due to the two gap nature of superconductivity in ZrB_{12}, (ii) due to large uncertainty in determining of the zero temperature gap from very narrow temperature range of the measurements and (iii) last but not least due to potentially large non homogeneity of the ZrB_{12} samples that have been used by other authors (see Fig. 2). Although observed two gap behavior

of $\lambda^2(0)/\lambda^2(T)$ in ZrB_{12} is similar to that in high-T_c superconductors, observation of two different T_c in these bands is unconventional. This also relates to the linear $H_{c2}(T)$ dependence in ZrB_{12} and YB_6 in the wide temperature range up to T_c. Striking two gap BCS behavior observed calls certainly for a new study of low-T energy gap and $H_c(T)$ of ZrB_{12} and YB_6 for understand the nature of superconductivity in these cluster compounds.

6. The Fermi Surface of ZrB_{12}

The dHvA oscillations (Fig. 9) were observed by measuring the torque with a capacitive cantilever technique [26]. The measurements of the magnetic torque were performed on M10 28 Tesla resistive magnet of the Grenoble High Magnetic Field Laboratory. In the measurements, <110> and <111> axis of the sample were parallel to the rotation axis. The measurements were made at different temperatures in the range 0.35–4.2 K with the sample immersed in a pumped ^{3}He or ^{4}He bath. The oscillatory part of torque is given by $\tilde{T} = -(1/F)\tilde{M}_{//}(\partial F/\partial\theta)BV$ [56] where $\tilde{M}_{//}$ - the oscillatory component of the parallel magnetization, F is the dHvA frequency, θ is the orientation of the Fermi surface with respect to the applied filed B and V is the crystal volume. Here each dHvA frequency $F = S_F\hbar c/2\pi e$ is proportional to the extremal cross-section area S_F of the Fermi surface. In a normal metal, $\tilde{M}_{//}$ would be given by the usual Lifshitz-Kosevich formula. According to this formula, the dHvA amplitude A of a fundamental frequency can be written as follows [56, 57]:

$$A \propto B^{1/2}\left|\frac{\partial^2 S_F}{\partial k^2}\right|^{-1/2} \frac{\alpha m_c T/B}{\sinh(\alpha m_c T/B)}\exp(-\alpha m_c T_D/B), \qquad (11)$$

$$\alpha = \frac{2\pi^2 c k_B m_0}{e\hbar} = 14.693(T/K)$$

here $m_c = \hbar^2(\partial S_F/\partial E)/2\pi$ is the cyclotron effective mass and $T_D = \hbar/2\pi k_B\tau$ is the Dingle temperature, inversely proportional to the quasiparticle lifetime τ. We can estimate the residual τ from Drude formula for residual resistivity, to obtain the Fermi surface averaged $\tau = 1.74\ 10^{-14}$ sec.

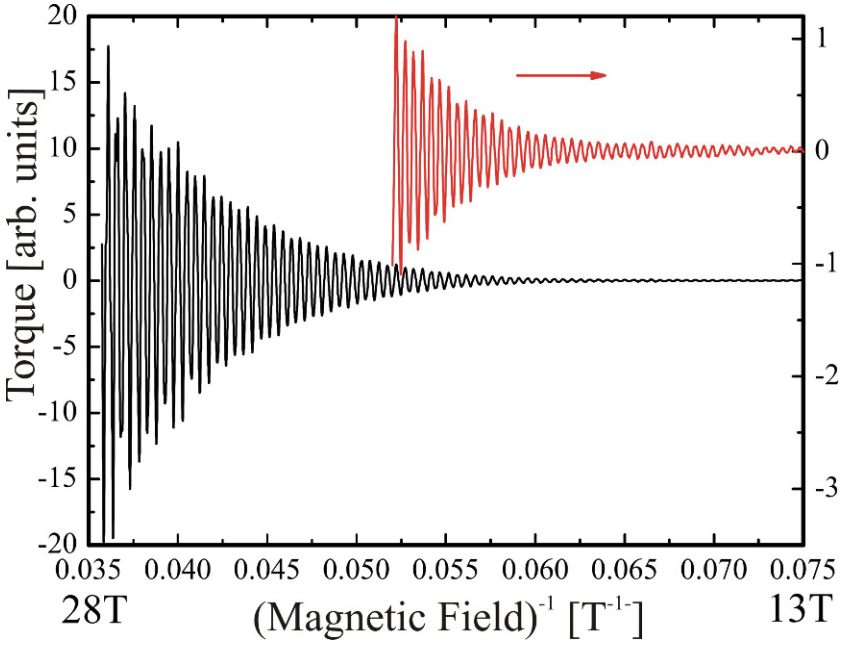

Figure 9. Typical dHvA oscillations signal in ZrB_{12} observed with magnetic field applied along <110> direction.

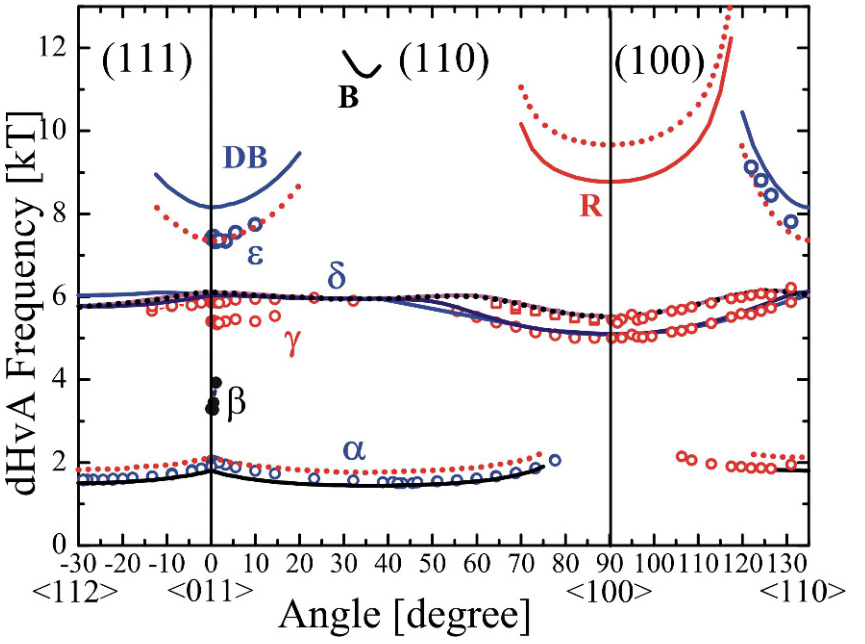

Figure 10. Experimental (*symbols*) and calculated (*solid lines*) dHvA frequencies of ZrB_{12}. DB, B and R denote the Dog's bone, Belly and Rosette orbits, respectively. Dotted lines shows result of calculations for $E_F - 0.16$ eV.

Figure 10 shows the angular dependence of the dHvA frequencies. The circles represent the experimental data. The solid lines shows the results of the band-structure calculation described below. The dHvA oscillations denoted by α, γ, δ and ε are fundamental. The details of the calculation are presented elsewhere [25, 26]. The corresponding extremal orbits from the first Cu-like but hole FS sheet and those from the second electron "box"-like sheet are shown in Fig. 11.

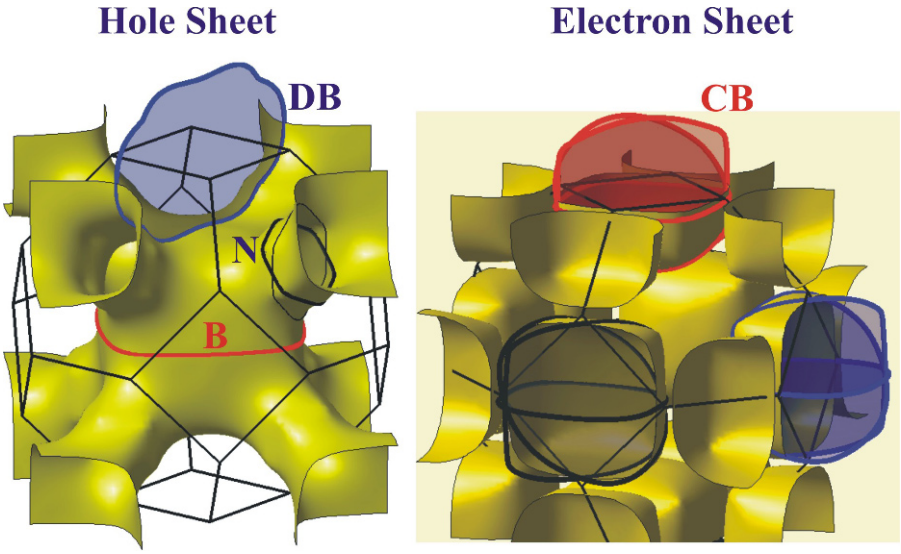

Figure 11. Theoretical model of the Fermi surface of ZrB_{12}: electron and hole sheets considered in the dHvA branch calculation.

The solid lines in Fig.10, shows the excellent agreement between the *ab initio* electronic structure calculations and the measured one. The lowest frequency α branch between 1.5 and 2 kT corresponds to the Necks of the hole sheet. The branches δ in the vicinity of 6 kT are the signature of the nearly cubic boxes of electron sheet. The deviation from cubistic is evidenced by the splitting of the δ branch between the <111> and <100> field directions (Fig.10). Also, the δ peak is split into two satellites δ and γ close to <110> direction. Apparently, this splitting is due to a small warping of the cubic box sheet not seen from calculations.

The highest measured frequency of 7.4 kT in the <110> direction, ε, does not seem to match any of the calculated orbits. The dHvA frequency of ε branch however is about 15% lower than results of calculated branch due to the "Dog's-bone" orbits. One possible explanation for this discrepancy is that the calculated orbit is too large (by approximately 0.8 kT), i.e. that the distance between the Necks is smaller in the real electronic structure than in the calculation. In order to check this problem, we have done a calculation

with E_F shifted by -0.16 eV. However, the resulting shift of the Neck branch moves to another direction, while does not strongly affect the agreement with experimental points.

Another possible explanation for ε branch relies on the observation that two FS sheets are nearly or fully degenerate in several points of the Brillouin zone (BZ), i.e. the box-like FS sheets touch the Belly and the Necks. Also, the fact that the observation the dHvA frequencies of the ε -branch depends on the applied magnetic field, moved us towards the magnetic breakdown scenario. There are different possibilities of reconnecting these magnetic breakdown orbits combining the two bands of the Fermi surface. Apparently, observation of two additional oscillations (due to different magnetic breakdown orbits) above ε peak, support this magnetic breakdown conclusion [26].

The cyclotron effective masses m_c were measured for the Neck orbit from the temperature dependence of the dHvA amplitude of α branch determined from fast Fourier transform (FFT) by performing field sweeps at different temperatures. According to Eq.11, the temperature dependence of the dHvA amplitude can be approximated as: $A/T = \text{const}/\sinh(\alpha m_c T/B)$. From the fitting of A/T vs T dependence, we determined the cyclotron effective mass equal to $0.5m_e$ for B//<111> where dHvA amplitude of α branch is strongest.

The Dingle temperature was obtained from the plot of $\ln[AB^{1/2}\sinh(\alpha m_c T/B)]$ versus $1/B$ according to Eq.11. For the B//<111>, the Dingle temperatures is 12.7 K for the α branch of dHvA oscillations. From the equation of T_D we estimate the electron scattering time $\tau = 9.35\ 10^{-14}$ sec almost five times larger than the one deduced from residual resistivity. Unfortunately, the dHvA oscillations for β, γ, δ and ε sheets of the FS have too small intensities to allow an estimation of the m_c and T_D and comparison with a Neck data. Both cubic box and Neck sheets have similar very wide belt of the extremal orbits due to the form of those sheets. Nevertheless, the dHvA amplitude of α peak is almost ten times larger than the one for δ peak. One source of this difference could be a large difference in the scattering rate, i.e. T_D.

Our experimental values of m_c for Neck orbit can be compared with the calculated band masses. The difference observed is the experimental mass enhancement due to the electron-phonon interaction [40]: $m_{exp}/m_{calc}=\lambda_{ep}+1$. The results show that the value of λ_{ep} on Neck section is unusually large, 1.38. Optics also gave similar large electron-phonon constant (1.0) averaged for whole Fermi surface [25], while from specific heat very small $\lambda_{ep} = 0.2$ was observed [23]. In the Neck region the hybridization of the wave functions and umklapp processes are very important on top of the k dependence of the matrix element of the electron – phonon interaction [40].

Figure10 shows that the values of the extremal areas S_F found from dHvA effect and band structure calculations are in very good agreement. The remaining discrepancy with band structure calculations concerns the absence of big Belly, Dog's bone and Rosette sections of the hole sheet dHvA orbits in the present study and the absence of extremal sections corresponding to β branch in calculated FS. The non-observation of these orbits could be due to the large m_c for Belly sections and relatively short mean-free-path l on the hole sheet relative to electron sections. Thus future experiments with purer samples are essential for observation of Belly sections of the FS in a first BZ which may clarify the anisotropy of λ_{ep} and validity of two-band model.

7. Conclusion

We performed systematic study of the temperature and magnetic field dependencies of the resistivity, magnetic penetration depth, lower, $H_{c1}(T)$, and upper, $H_{c2}(T)$, critical magnetic fields of the single crystals ZrB_{12}, YB_6 and ZrB_2, as well as the magnetic penetration depth in thin films of MgB_2. While the temperature dependence of $\lambda(T)$ in thin c-axis oriented thin film MgB_2 samples and YB_6 single crystals is well described by an isotropic *s* - type order parameter, we find unconventional behavior of ZrB_{12} superfluid density with pronounced shoulder at T/T_c equal to 0.65. The $H_{c2}(T)$ dependences have been deduced from the $\rho(H)$ and $\lambda(H)$ data. Both techniques reveal an unconventional linear temperature dependence of $H_{c2}(T)$ for ZrB_{12} and YB_6, with a considerably low value of $H_{c2}(0)$. We have presented the first experimental study of the Fermi surface of the cluster superconductor ZrB_{12}, using dHvA effect. It is in excellent agreement with band structure calculations of the Fermi surface topology of this compound. The comparison of the experimental and calculated cyclotron mass shows unusually large electron-phonon interaction on Neck sections of the hole sheet of the Fermi surface. Results support observation of magnetic breakdown from Neck and Box sheets in fields above 25 T. We conclude that ZrB_{12} presents an evidence of the unconventional two-gap superconductivity with different T_c in the different bands.

Acknowledgement

We would like to thank V.F. Gantmakher, A. Gurevich, R. Huguenin, D. van der Marel, I.R. Shein, for very useful discussions, V.B. Filipov, A.B. Lyashenko and Yu.B. Paderno for preparation of ZrB_2 and ZrB_{12} single crystals, Hong-Ying Zhai, H.M. Christen, M.P. Paranthaman and D.H.

Lowndes for providing us of high quality MgB_2 films, S. Otani for providing YB_6 single crystals, I. Sheikin, F. Levy, J. Teyssier, G. Santi for cooperation in Fermi surface investigations, A. Suslov for help in low-*T* measurements in NHMFL, L.S. Uspenskaja for help in metallographic analysis. This work was supported by the RAS Program: New Materials and Structures (Grant 4.13) and by the INTAS (Grant No. 2001-0617). A portion of this work was performed at the National High Magnetic Field Laboratory and at the Grenoble High Magnetic Field Laboratory, which is supported by NSF Cooperative Agreement No.DMR-0084173, State of Florida,. and by CNRS (Ref. SM0606), respectively. We acknowledge also a support from Swiss National Science Foundation through grant 200020-109588 and the NCCR MaNEP for support of band structure calculation.

References

1. Nagamatsu, J., Nakagawa, N., Muranaka, T., Zanitani, Y., and Akimitsu, J., Nature **410**, 63 (2001).
2. Gasparov, V.A., Sidorov, N.S., Zver'kova, I.I., Kulakov, M.P., JETP Lett.**73**, 532 (2001).
3. Fisk, Z., AIP Conf. Proc. **231**, 155 (1991).
4. Gasparov, V.A., Kulakov, M.P., Zver'kova, I.I., Sidorov, N.S., Filipov, V.B., Lyashenko, A.B., Paderno, Yu.B., JETP Lett., **80**, 376 (2004).
5. Yamamoto, A., Takao, C., Masui, T., Izumi, M., Tajima, S., Physica C **383**, 197 (2002).
6. Escamilla, R., Lovera, O., Akachi, T., Durán, A., Falconi, R., Morales, F., and Escudero, R., J. Phys.: Condens. Matter **16**, 5979 (2004).
7. Yamada, N., Nakamura, J., Iwaki, T., Kobayashi, D., Kanno, Y., Abstract Book 25th Int. Conf. on Low Temp. Phys., Amsterdam 6-13, 2008, PB-Fr96.
8. Young, D.P., Goodrich, R.G., Adams, P.W., Chan, J.Y., Fronczek, F.R., Drymiotis, F., and Henry, L.L., Phys. Rev. B **65**, 180518(R) (2002).
9. Shein, I.R., Medvedeva, N.I., and Ivanovskii, A.L., Physics of the Solid State **45**, 1617 (2003), [Translated from Fizika Tverdogo Tela **45**, 1541, (2003)].
10. Ashcroft, N., Phys. Rev. Lett. **21**, 1748 (1968).
11. Kortus, J., Mazin, I.I., Belashchenko, K.D., Antropov, V.P., Boyer, L.L., Phys. Rev. Lett. **86**, 4656 (2001).
12. Tanigaki, K., Ebbesen, T.W., Saito, S., Mizuki, J., Tsai, J.S., Kubo, Y., and Kuroshima, S., Nature (London) **352**, 222 (1991).
13. Gunnarsson, O., Reviews of Modern Physics **69**, 575 (1997).
14. Matthias, B.T., Geballe, T.H., Andres, K., Corenzwit, E., Hull, G., Maita, J.P., Science **159**, 530 (1968).
15. Paderno, Y., Shitsevalova, N., Batko, I., Flahbart, K., Misiorek, H., Mucha, J., Jezowski, A., J. Alloys Comp. **219**, 215 (1995).
16. Chu, C.W., and Hill, H.H., Science **159**, 1227 (1968).
17. Fisk, Z., Lawson, A.C., Matthias, B.T., and Corenzwit, E., Phys. Lett. A **37**, 251 (1971).
18. Gasparov, V.A., Sidorov, N.S., Kulakov, M.P., Zver'kova, I.I., Kobyakov, V.P., Zhai, Hong-Ying, Christen, H.M., Paranthaman, M.P., Lowndes, D.H., Book of abstracts of BOROMAG Conf. (Genoa, Italy), p. 52 (2002).

19. Gasparov, V.A., Sidorov, N.S., Zver'kova, I.I., Khassanov, S.S., Kulakov, M.P., JETP **128**, 115 (2005).
20. Gasparov, V.A., Sidorov, N.S., Zver'kova, I.I., Filippov, V.B., Lyashenko, A.B., and Paderno, Yu.B., Book of Abstracts of 6th Biennial International Workshop on Fullerenes and Atomic Clusters (St. Petersburg, 2003), p. 83; Book of Abstracts of 10th International Workshop on Oxide Electronics (Augsburg, 2003), p. 184.
21. Gasparov, V.A., Sidorov, N.S., Zver'kova, I.I., Phys. Rev. B **73**, 094510 (2006).
22. Gasparov, Vitaly, Sheikin, Ilya, and Otani, Shigeki, Physica C **460–462** (2007) 623.
23. Lortz, R., Wang, Y., Abe, S., Meingast, C., Paderno, Yu.B., Filippov, V., and Junod, A., Phys. Rev. B **72**, 024547 (2005).
24. Shein, I.R., and Ivanovskii, A.L., Physics of the Solid State **45**, 1429 (2003); [Translated from Fizika Tverdogo Tela **45**, 1363 (2003)].
25. Teyssier, J., Kuzmenko, A.B., van der Marel, D., F. Marsiglio, Liashchenko, A.B., Shitsevalova, N., and Filippov, V., Phys. Rev. B **75**, 134503 (2007).
26. Gasparov, V.A., Sheikin, I., Levy, F., Teyssier, J., Santi, G., Phys. Rev. Lett. **101**, 097006 (2008).
27. Daghero, D., Gonnelli, R.S., Ummarino, G.A., Calzolari, A., Dellarocca, V., Stepanov, V.A., Filippov, V.B., and Paderno, Y.B., Supercond. Sci. Technol., **17**, S250 (2004).
28. Tsindlekht, M.I., Leviev, G.I., Asulin, I., Sharoni, A., Millo, O., Felner, I., Paderno, Yu.B., Filippov, V.B., Belogolovskii, M.A., Phys. Rev. B **69**, 212508 (2004).
29. Wang, Y., Lortz, R., Paderno, Yu., Filippov, V., Abe, S., Tutsch, U., and Junod, A., Phys. Rev. B **72**, 024548 (2005).
30. Leviev, G.I., Genkin, V.M., Tsindlekht, M.I., Felner, I., Paderno, Yu.B., Filippov, V.B., Phys Rev B **71,** 064506 (2005).
31. Brinkman, A., Golubov, A.A., Rogalla, H., Dolgov, O.V., Kortus, J., Kong, Y., Jepsen, O., and Andersen, O.K., Phys. Rev. B **65**, 180517(R) (2001).
32. Golubov, A.A., Brinkman, A., Dolgov, O.V., Kortus, J., and Jepsen, O., Phys. Rev. B **66**, 054524 (2002).
33. Otani, S., Korsukova, M.M., Mitsuhashi, T., Kieda, N., J. of Crystal Growth, **217,** 378 (2000).
34. Paranthaman, M., Cantoni, C., Zhai, H.Y., Christen, H.M., Aytug, T., Sathyamurthy, S., Specht, E.D., Thompson, J.R., Lowndes, D.H., Kerchner, H.R., and Christen, D.K., Appl. Phys. Lett. **78,** 3669 (2001).
35. Gasparov, V.A., Mkrtchyan, M.R., Obolensky, M.A., Bondarenko, A.V., Physica C **1**, 197 (1994).
36. Gasparov, V.A., and Oganesyan, A.P., Physica C (Amsterdam) **178**, 445 (1991).
37. Gauzzi, A., Cochec, J.Le., Lamura, G., Jönsson, B.J., Gasparov, V.A., Ladan, F.R., Plaçais, B., Probst, P.A., Pavuna, D., Bok, J., Rev. Sci. Instr. **71**, 2147 (2000).
38. Gasparov, V.A., Tsydynzhapov, G., Batov, I.E., and Li, Qi, J. Low Temp. Phys., **139**, 49 (2005).
39. Ziman, J.M., Electrons and Phonons, Theory of Transport Phenomena in Solids (Oxford U.P., Oxford, England, 1960).
40. Gasparov, V.A., and Huguenin, R., Adv. Phys. **42**, 393 (1993).
41. Halbritter, J., Z. Phys. **243**, 201 (1971).
42. Ketterson, J.B. and Song, S.N., S*uperconductivity* (Cambridge University Press, Cambridge, 1999).
43. Hardy, W.N., Bonn, D.A., Morgan, D.C., Liang, R., and Zhang, K., Phys. Rev. Lett. **70**, 3999 (1993).
44. Bonn, D.A., Kamal, S., Zhang, K., Liang, R., Baar, D.J., Klein, E., and Hardy, W.N., Phys. Rev. B **50**, 4051 (1994).
45. Klein, N., Tellmann, N., Schulz, H., Urban, K., Wolf, S.A., Kresin, V.Z., Phys. Rev. B **71**, 3355 (1993).
46. Schopohl, N., and Dolgov, O.V., Phys. Rev. Lett. **80**, 4761 (1998); Ibid **81**, 4025 (1998).

47. Gurevich, A., Phys. Rev. B **67**, 184515 (2003).
48. Gonnelli, R.S., Daghero, D., Ummarino, G.A., Stepanov, V.A., Jun, J., Kazakov, S.M. and Karpinski, J., Phys. Rev. Lett. **89**, 247004 (2002).
49. Manzano, F., Carrington, A., Hussey, N.E., Lee, S., Yamamoto, A., and Tajima, S., Phys. Rev. Lett. **88**, 047002 (2002).
50. Jin, B.B., Klein, N., Kang, W.N., Kim, H.-J., Choi, E.-M., Lee, S.-I., Dahm, T., Maki, K., Phys. Rev. B **66**, 104521 (2002).
51. de Gennes, P.G., Superconductivity of Metals and Alloys (Addison-Wesley, New York, 1989, p. 79).
52. Helfand, E., and Werthamer, N.R., Phys. Rev. Lett. **13**, 686 (1964); Phys. Rev. **147**, 288 (1966).
53. Lyard, L., Samuely, P., Szabo, P., Klein, T., Marcenat, C., Paulius, L., Kim, K.H.P., Jung, C.U., Lee, H.-S., Kang, B., Choi, S., Lee, S.-I., Marcus, J., Blanchard, S., Jansen, A.G.M., Welp, U., Karapetrov, G., and Kwok, W.K., Phys. Rev. B **66**, 180502 (R) (2002).
54. Sologubenko, A.V., Jun, J., Kazakov, S.M., Karpinski, J., and Ott, H.R., Phys. Rev. B **66**, 180505 (R) (2002).
55. Gasparov, V.A., Ermolov, S.N., Strukova, G.K., Sidorov, N.S., Khassanov, S.S., Wang, H.-S., Schneider, M., Glaser, E., and Richter, Wo., Phys. Rev. B **63**, 174512 (2001); Gasparov, V.A., Ermolov, S.N., Khasanov, S.S., Strukova, G.K., Gasparov, L.V., Wang, H.-S., Li, Qi, Schnider, M., Richter, Wo., Glaser, E., Schmidl, F., Seidel, P., Brandt, B.L., Physica B **284-288**, 1119 (2000).
56. Sheikin, I., Gröger, A., Raymond, S., Jaccard, D., Aoki, D., Harima, H., and Flouquet, J., Phys. Rev. B **67**, 094420 (2003).
57. Shoenberg, D., *Magnetic Oscillations in Metals,* (Cambridge University Press, Cambridge, England, 1984).

DENSIFICATION, MICROSTRUCTURE EVOLUTION AND MECHANICAL PROPERTIES OF ULTRAFINE SIC PARTICLE-DISPERSED ZrB_2 MATRIX COMPOSITES

FRÉDÉRIC MONTEVERDE*, STEFANO GUICCIARDI, CESARE MELANDRI, DANIELE DALLE FABBRICHE
National Research Council - Institute of Science and Technology for Ceramics
Via Granarolo 64, 48018 Faenza – Italy

Abstract The densification behavior along with the microstructure evolution and some mechanical properties of four ultrafine SiC particle-dispersed ZrB_2 matrix composites were studied. The SiC–ZrB_2 composites, with a SiC content of 5, 10, 15 and 20 vol%, were densified to near full density by vacuum hot pressing at 1,900°C under a maximum uniaxial pressure of 45 MPa. The presence of SiC greatly improved the sinterability of ZrB_2. Grain growth of the diboride matrix was increasingly inhibited for larger amounts of SiC added. Elastic modulus, Poisson ratio, microhardness, flexural strength and fracture toughness were measured at room temperature. Unexpectedly, no obvious effect of the increasing amount of SiC on flexural strength and fracture toughness was found. The former property ranged from 650 to 715 MPa but was actually affected by the exaggerated size of several tenths of micrometers of sintered SiC clusters which acted as dominant critical defects. Also fracture toughness did not receive a marked contribution from the increase of the SiC content. As for the matrix, the prevailing fracture mode of the composites was intragranular, regardless of the SiC content.

Keywords: ZrB_2, fracture toughness, X-ray diffraction, residual stresses

1. Introduction

Ultra-high temperature ceramics (UHTC's) are pivotal to the current development of structural components for future high performance aircrafts, re-usable spaceplanes or hypersonic vehicles, owing to their reduced specific weight,

* Frédéric Monteverde, National Research Council - Institute of Science and Technology for Ceramics, Via Granarolo 64, 48018 Faenza – Italy, e-mail: frederic.monteverde@istec.cnr.it

N. Orlovskaya and M. Lugovy (eds.), *Boron Rich Solids: Sensors, Ultra High Temperature Ceramics, Thermoelectrics, Armor*, DOI 10.1007/978-90-481-9818-4_17,

extremely high melting temperature, strength retention at high temperature, and superior resistance to oxidation. Among them, transition metal diborides like HfB_2 and ZrB_2 are currently under intensive investigation [1]. These UHTC's are intended to constitute structural components like external heat shields or leading edges which operate in severely reactive environments at temperatures well above 2,300°C where commercially available composites like C/C or C/SiC do not hold performance margins to resist to any further extent [2].

The use of those single-phase UHTC's for structural applications at elevated temperature is limited to some extent by the poor oxidation and ablation resistance, as well as poor damage tolerance. The introduction of second phases like SiC has been successfully adopted in order to enhance the oxidation and ablation resistance, as well as key mechanical properties for structural applications like fracture toughness and flexural strength [1, 3–5]. In this sub-class of materials, the SiC–ZrB_2 system, which has densities below 6 g/cm^3, melting point above 3,500°C coupled with good strength and thermal conductivity, is currently the most studied.

Densification of the single-phase ZrB_2 is difficult, due to strong covalent bonds that demand very high sintering temperatures. Sintering aids such as B and C [6], metal silicides [7] or Si_3N_4 [8] have been used to improve densification and reduce processing temperatures. The addition of SiC to ZrB_2 has been also recognized to enhance sinterability, limit grain growth and therefore improve mechanical properties. Micro-sized SiC particulates were added to ZrB_2 for most of the studies reported, and SiC distributed intergranularly along ZrB_2/ZrB_2 interfaces typically characterizes the microstructure of such a class of UHTC composites. Recent works [1, 9] have shown that the introduction of ultrafine SiC particles should cause an increase of the flexural strength, at least at room temperature, suggesting that nanosized SiC would result in superior strength for SiC–ZrB_2 composites. However, reproducibility of properties like flexural strength or fracture toughness has also been recognized as an important concern, mostly when the starting SiC content of the order of 20 vol% or higher has to be properly dispersed by conventional mechanical means inside the diboride matrices [3].

Up to now, inadequate emphasis was focused on the aspect that the achievement of near full density in SiC–ZrB_2 systems was very often promoted also by the beneficial effects of some sintering aids intentionally added to enhance sinterability of ZrB_2. In that way, the role of SiC as primary strengthening factor of ZrB_2 matrices was not adequately separated as it should from the influence of secondary grain boundary phases present after sintering. Accordingly, in the present study, densification, microstructure evolution and mechanical properties of hot-pressed SiC–ZrB_2 composites, prepared from a

single grade of ZrB_2 powder without any sintering aid, and four different concentrations of an ultrafine SiC powder were examined and compared.

2. Experimental

2.1. MATERIALS AND PROCESSING

Commercial ZrB_2 and SiC powders were used in this study (some characteristics from the producer are reported in Table 1). Prior to hot-pressing, the as-received ZrB_2 was batched with SiC in the following volume ratios into polyethylene bottles for the homogenization.

ZS05: 95% ZrB_2 + 5% SiC
ZS10: 90% ZrB_2 + 10% SiC
ZS15: 85% ZrB_2 + 15% SiC
ZS20: 80% ZrB_2 + 20% SiC

TABLE 1. Some characteristics of the raw powders: granulometric size distribution d_{90}, and specific surface area (s.s.a)

Phase	Producer	grade	d_{90} (μm)	s.s.a. (m^2/g)	Impurity (wt%)
ZrB_2	H.C.Starck GmbH, Germany	B	4–6	–	O 2, Hf 0.2
SiC	H.C.Starck GmbH, Germany	UF25	0.8	23–26	O 2.5

Before batching powders, the SiC powder was ultrasonically dispersed in absolute ethanol using a pulsed ultrasonication under continuous magnetic stirring. The batched powders were ball-mixed in absolute ethanol for 24 h, using SiC balls. The resulting slurries were then dried by rotary evaporator, and sieved (mesh size 150 μm). The so-obtained powder mixtures were hot-pressed in vacuum (50 Pa) using an inductively heated graphite die. For each composition, a cold compacted pellet of about 50 g of powder was put inside the graphite die (32 mm internal diameter) lined with a BN-sprayed graphitized sheet. The average heating rate from 1,000 to 1,900°C was about 20°C/min, 30 MPa of applied pressure. Dwell times during the isothermal stage (45 MPa of applied pressure) were adjusted from 25 min (ZS05) to 15 min (ZS20). The temperature was measured by means of an optical pyrometer focused on the graphite die. The linear shrinkage of the powder compacts was recorded by measuring the displacement of the rams. At the end of the hold time, the external mechanical pressure of 45 MPa was released, and the sample cooled by turning off the power supply. An additional hot-pressing run was performed using the only ball-milled ZrB_2 powder to

compare the densification behavior between the aforementioned compositions and a nominally SiC-free ZrB_2 (ZSO).

2.2. MATERIALS CHARACTERIZATION

2.2.1. *Microstructure*

The bulk densities d_B were determined using the Archimedes' method (water as immersing medium). Prior to measuring d_B, the external surfaces of the hot-pressed pellets were ground in order to remove any of the graphitized sheet. The phase composition was analyzed with an X-ray diffractometer (XRD, Bruker, mod. D8 Advance, Germany). Microstructure and composition were analyzed with a scanning electron microscope (SEM, mod. S360, Leica Cambridge – UK) combined with an energy dispersive X-ray micro-analyzer (EDS, mod. INCA Energy 300, Oxford Instruments – UK) using polished sections prepared with successively finer diamond-based abrasives down to 0.25 μm. Using XRD, residual macro-strain (ε_I) was also determined in the hot-pressed materials by measuring the change in lattice spacings d_{hkl} (2-theta interval 90°–157°, and Bragg–Brentano configuration) according to

$$\varepsilon_{I,hkl} = (d_{X,hkl} - d_{ZS0,hkl})/d_{ZS0,\,hkl} \qquad X = ZS05, ZS10, ZS15, ZS20 \qquad (1)$$

where $d_{ZS0,\,hkl}$ is the lattice spacing of the SiC-free hot-pressed ZrB_2. A mean value $\langle\varepsilon_I\rangle$ was obtained by averaging six different d_{hkl} spacings. In addition, according to the Williamson–Hall approach [10], short-range residual strain ε_{II} in the hot-pressed composites was also determined as the slope of the graph plotting

$$\beta_{hkl}\cos(\theta_{hkl}) = \varepsilon_{II}\sin(\theta_{hkl}) + 0.9\,\lambda/L \qquad (2)$$

where λ, L, β_{hkl} and θ_{hkl} are the CuKα wavelength, crystallite size, peak broadening and angle satisfying the Bragg's law for a specific set of hkl planes, respectively. The values of θ_{hkl} and β_{hkl} were determined applying a whole pattern-fitting routine over the experimental XRD patterns [11]. Instrumental peak broadening was determined using a Si powder standard, and then de-convoluted from the measured peak broadening accordingly. For the peak analysis, the pseudo-Voigt profile shape function was used.

2.2.2. *Mechanical Properties*

The Young's modulus (E) and Poisson's ratio (ν) were measured on rectangular plates using the resonance frequency method. Microhardness

(HV1.0) was evaluated on polished surface by Vickers indentation, using a 9.81 N applied load for 15 s. Flexural strength (σ) was tested in air using an universal testing machine Zwick Z050 (Zwick Roell AG, Ulm, Germany): 4-pt configuration on (25 × 2.5 × 2) mm^3 chamfered bars, 20 mm and 10 mm as outer and inner span respectively, and a crosshead speed of 0.5 mm/min. For each SiC–ZrB_2 composite, at least four bars were tested. Fractographic analyses of the broken bars were performed by SEM-EDS in order to identify position, size and nature of the critical defects which caused failure. Fracture toughness (K_{Ic}) was measured using the Single Edge Notched Beam (SENB) method. The bars were notched using a 0.1 mm-thick diamond blade with a cut depth of 50 μm/pass. The notch depth was set to 1 mm corresponding to a notch/thickness ratio of about 0.4. Before testing, the notch root radius was estimated by optical imaging and resulted to be about 74 μm. Using the same universal testing machine Zwick Z050, the notched bars were fractured in three-point bending on a span of 8 mm and with a crosshead speed of 0.2 mm/min. Thickness, width and notch depth of each specimen were measured after test in correspondence of the fracture surface. At least four specimens were tested for each composition.

3. Results and Discussion

3.1. DENSIFICATION AND MICROSTRUCTURE EVOLUTION

In Fig. 1, the shrinkage rate vs. temperature during the non-isothermal stage gives a clear indication of the strong influence of the SiC content on the densification of the ZrB_2-based systems. No sintering aids were intentionally introduced into the starting powder mixtures, therefore the observed effects on densification of ZrB_2 can be entirely attributed to the increasing SiC content (and its impurities). The earliest measurable shrinkage occurred at different temperature T_{ON}, depending on the starting amount of SiC. The values listed in Table 2 show that the increase of the initial SiC content shifted T_{ON} to lower onset values. In the nominally pure ZrB_2, no measurable shrinkage up to 1,900°C was recorded. The role of the ultrafine SiC particles was to activate the densification of ZrB_2 by means of chemical reactions involving the surface oxides. These reactions very likely facilitated the removal of oxide species, which typically cover the ZrB_2 particle surfaces, by the formation of a liquid phase. Traces of such a liquid phase were found at triple points or inside clusters of sintered SiC grains. The SEM-EDS analysis of the liquid phase residues confirmed a basic chemical composition in the Si-O system, but did not indicate the presence of other elements.

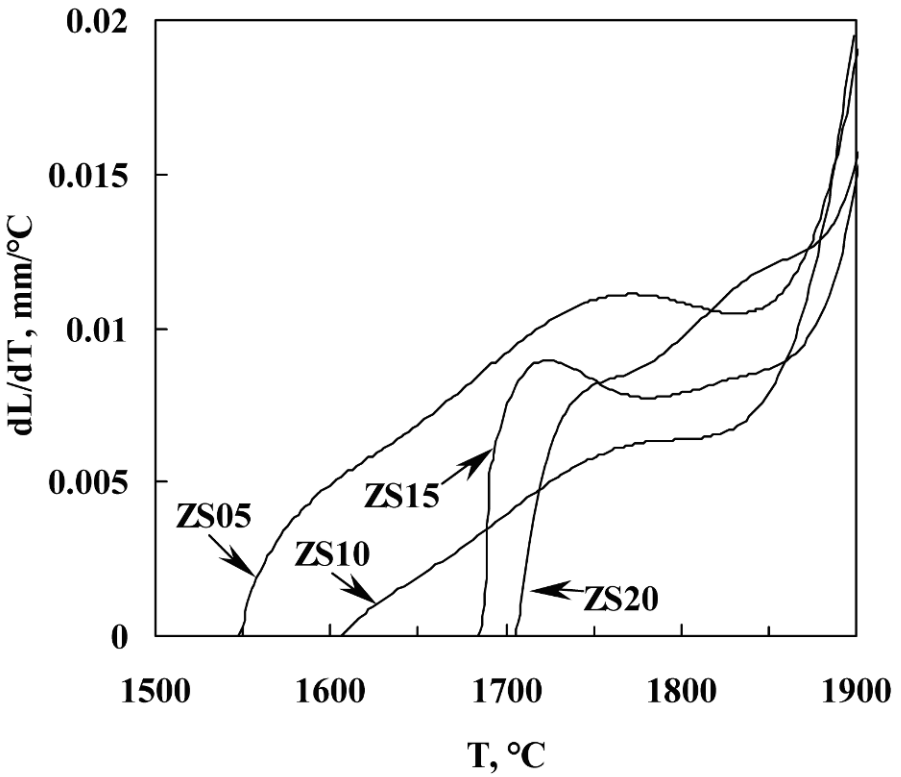

Figure 1. Shrinkage rate (dL/dT) vs. temperature (T) during non-isothermal stage of the hot-press runs, 30 MPa of applied pressure.

TABLE 2. Onset temperature (T_{ON}), dwell time (dw), expected density (d_{EXP}), measured bulk density d_B, and relative density ($Rd = d_B/d_{EXP}$)

Sample	T_{ON}, °C	dw, min	Density		
			d_{EXP} (g/cm^3)	d_B (g/cm^3)	Rd (%)
ZS0	n.r.[a]	25	6.09	4.26	70
ZS05	1550	25	5.95	5.95	100
ZS10	1610	20	5.8	5.76	99.3
ZS15	1680	15	5.65	5.65	100
ZS20	1710	15	5.51	5.45	98.9

[a]n.r.: not registered up to 1,900°C

This last finding does not actually clarify the effective role of the liquid phase during sintering, which will be the object of future analyses. In the case of the SiC-free mixture ZS0, non-densifying vapor-phase and surface transport mechanisms induced primarily an enhanced coarsening of the microstructure and thus reduced the driving force for densification. Typical

microstructural features of the ZrB_2-based composites with ultrafine SiC particles observed under SEM are shown in Fig. 2 (fracture surfaces) and Fig. 3 (polished surfaces). The microstructure basically consists of equiaxed ZrB_2 and round SiC (dark contrast) grains. Grain growth of the diboride matrix was hindered by introducing larger amount of SiC: the grain size varied roughly from about 5 μm (ZS05) down below 3 μm (ZS10/15/20). The XRD analysis of the ZrB_2–SiC composites identified the only starting compounds ZrB_2 and SiC (Fig. 4). However, the observed diffraction peaks of the hexagonal ZrB_2 shifted slightly to higher 2-theta compared to the ZS0 material. In addition, the (expected) decrease in intensity of the ZrB_2 peaks in the composites containing larger amount of SiC (i.e. lower content of ZrB_2) was also accompanied by the broadening of the ZrB_2 peak width. The concomitant shift and (part of) broadening of peaks were attributed to the development of internal residual thermal strains (RTS) at macroscale and microscale (short-range) level, respectively, as a result of the thermal and elastic mismatches between the diboride matrix and the SiC-dispersed particulate upon cooling from the hot-pressing temperature.

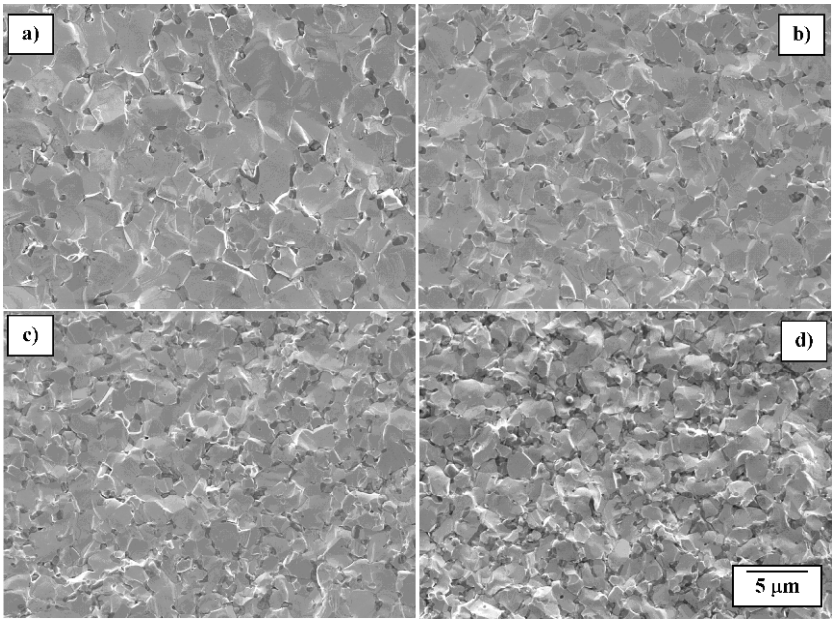

Figure 2. Fracture surfaces of ZS05 (a) ZS10 (b), ZS15 (c) and ZS20 (d): SEM micrographs.

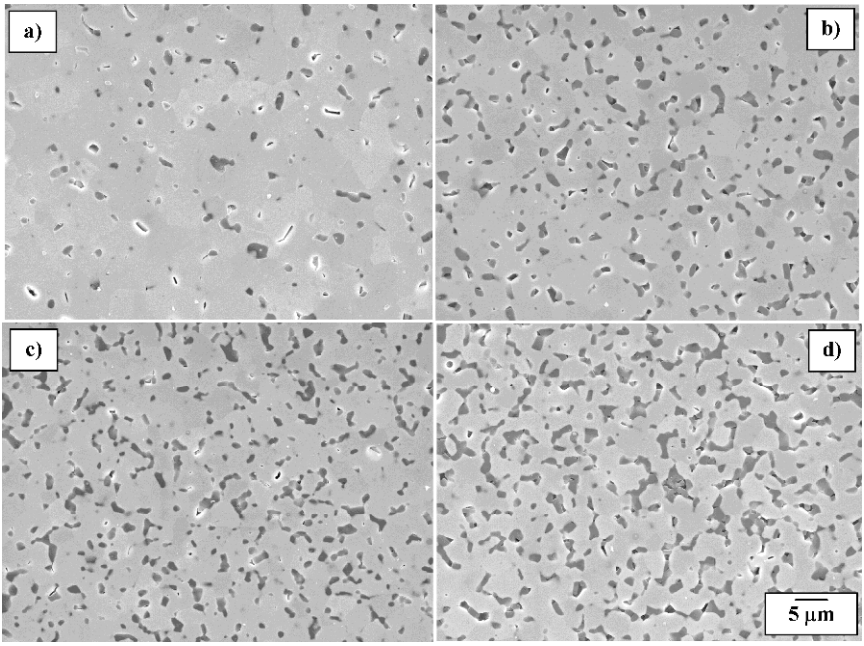

Figure 3. (Plasma-etched) polished surfaces of ZS05 (a) ZS10 (b), ZS15 (c) and ZS20 (d): SEM micrographs.

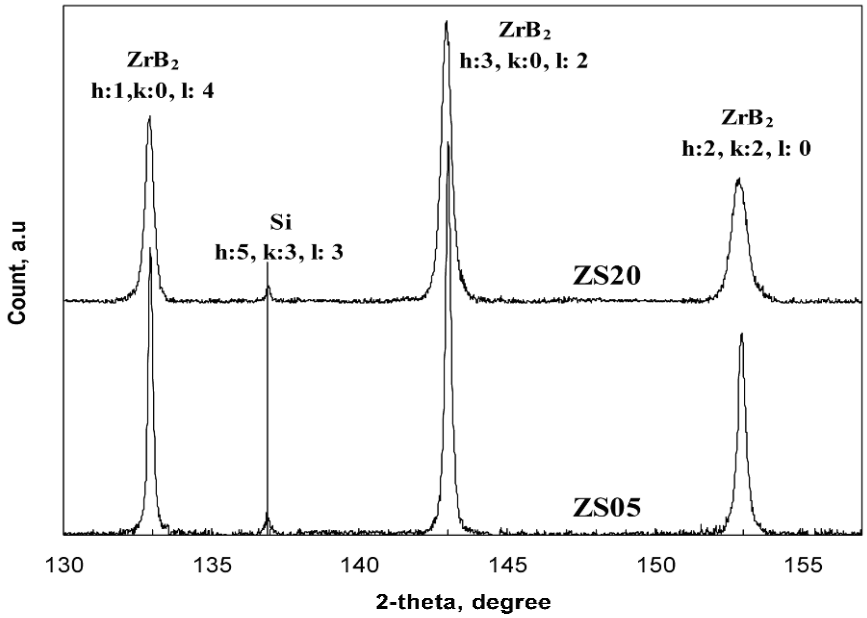

Figure 4. XRD patterns of sample ZS05 and ZS20; Si used as internal standard.

TABLE 3. Average macro-strain $<\varepsilon_I>$ (±1 st.dev) and short-range strain ε_{II} (±1 st.dev)

Sample	$<\varepsilon_I>$ (%)	ε_{II} (%)
ZS05	0.011 ± 0.002	0.018 ± 0.004
ZS10	0.021 ± 0.007	0.024 ± 0.003
ZS15	0.031 ± 0.01	0.032 ± 0.002
ZS20	0.042 ±0.005	0.045 ±0.002

$<\varepsilon_I>$ is an average over six different directions hkl.

In fact, the faster migration speed of the ZrB_2 grain boundaries, compared to that of the ultrafine SiC, caused a partial entrapment of some SiC particles inside the ZrB_2 grains. This led SiC particles to reside not only at grain boundaries but also intragranularly. Such a duplex arrangement of the SiC phase influenced type, magnitude and distribution of the internal RTS. Only the diffraction peaks of ZrB_2 were intense enough to measure position and width, and therefore to estimate sign and magnitude of the RTS, according to the relationships 1 and 2. On one hand, the macro-strain of the present case refers to the situation where the entire composite is subject to a tensional RTS in the diboride phase, and a compressive RTS in the SiC phase. No quantitative conclusions on the RTS for SiC were drawn out, due to the low intensities of the diffraction peaks along the back-reflection 2-theta interval. On the other hand, the short-range strain refers to the situation in which the directions and magnitude of the internal strains vary from one grain to another, or from one part of a grain to another inner sub-structure at microscopic level. The resultant elastic strains give rise to a broadening of the diffraction peaks (and not a shift), from which an estimate of the short-range strain can be made. The increase of the SiC content implies a larger percentage of the carbide entrapped inside the diboride matrix. Such a distribution of SiC favors the occurrence of the RTS at short range. Also the grain size refinement of the diboride matrix (see Fig. 2) contributes to a further broadening of the XRD peaks of ZrB_2 due to smaller crystallite size L (see Eq. 2), but was properly separated by applying the Williamson–Hall approach. XRD analyses of the nominally pure ZrB_2 ruled out the occurrence of any measurable short-range elastic strains. Values of the tensional average macro-strain $<\varepsilon_I>$ and of the short-range strain ε_{II} are reported in Table 3.

3.2. MECHANICAL PROPERTIES

Table 4 summarizes the measured mechanical properties. Increasing the SiC content decreased the Young's modulus, as SiC is a less stiff phase, and slightly increased the microhardness. Even though the grain size of the diboride matrix had an overall refinement for increasing content of SiC, the average strength of the different compositions resulted rather similar.

The fractographic analysis of the broken bars revealed critical defects composed of clustered SiC grains with a typical size of several tenths of micrometers (Fig. 5). This result pointed out that the mixing process was not effective in preventing the tendency of the ultrafine SiC to agglomerate during powder processing. Therefore, the verification of some beneficial effects on strength through a refining of SiC size remained unanswered. Differently from what could be expected from the value of residual strain reported in Table 3, the introduction of ultrafine SiC dispersoids changed the composite fracture toughness in a non-monotonous way. Values ranged from a bottom value of 4 MPa·√m (ZS10) up to a top value of 5.4 MPa·√m (ZS15). No clear microstructural feature was observed in order to justify the K_{Ic} trend. Similarly to the ZS0 matrix (K_{Ic} not measured), in fact, all the SiC–ZrB_2 composites showed a typical intragranular fracture mode. Moreover, from Fig. 2, it can be seen that the fracture surface roughness increased with the increase of SiC content. This could indicate crack deflection as a possible toughening mechanism [12]. However, this toughening mechanism, which is an increasing function of the reinforcement volumetric fraction, was not reflected by the K_{Ic} values as a function of SiC content, Table 3. A deeper investigation of the toughening mechanisms in this type of composites is demanded to a future work.

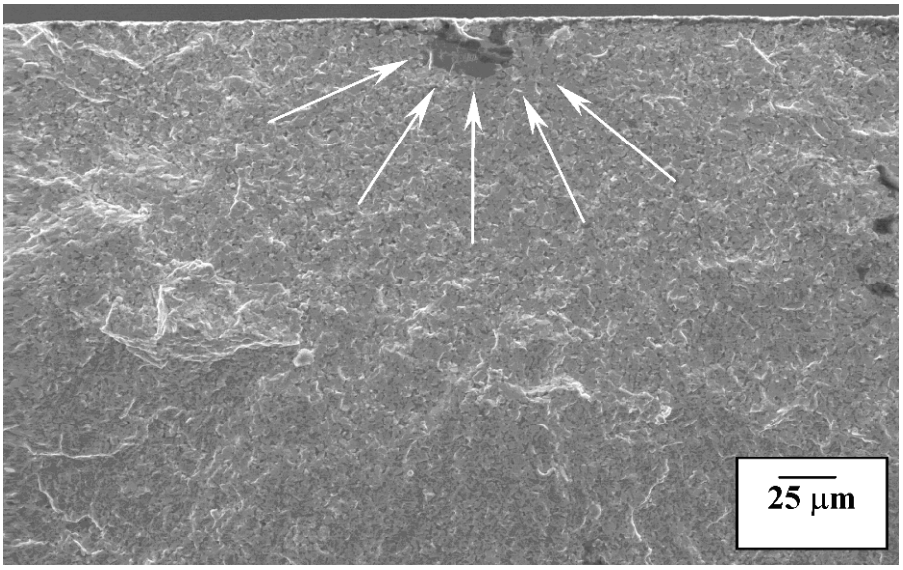

Figure 5. Fracture surface of a broken bar from ZS20 sample (SEM micrograph): the critical defect is indicated.

TABLE 4. Elastic modulus (E), Poisson ratio (ν), microhardness (HV1.0, mean ± 1st.dev), flexural strength (σ, mean ± 1st.dev) and fracture toughness (K_{Ic}, mean ± 1st.dev)

Sample	E (GPa)	ν	HV1.0 (GPa)	σ (MPa)	K_{Ic} (MPa·√m)
ZS05	518	0.103	19.3 ± 0.4	647 ± 57	4.49 ± 0.47
ZS10	514	–	20.1 ± 0.4	637 ± 80	3.93 ± 0.43
ZS15	484	0.117	21.7 ± 0.8	715 ±104	5.42 ± 0.56
ZS20	477	0.115	21.5 ± 0.6	716 ± 50	4.83 ± 0.66

4. Conclusion

The effects on densification, microstructural evolution and some mechanical properties were studied in a series of four ultrafine SiC particle-dispersed ZrB_2 matrix composites, with a SiC content of 5, 10, 15 and 20 vol%. All the compositions, densified by vacuum hot pressing at 1,900°C, reached near full density. SiC added to ZrB_2 greatly improved its sinterability. Grain growth of the diboride matrix also occurred, but was increasingly inhibited for larger amounts of SiC added. Elastic modulus, microhardness, Poisson ratio, flexural strength and fracture toughness were measured at room temperature. Increasing the SiC content decreased the Young's modulus and slightly increased the microhardness. On the other hand, no clear effect of the SiC content was observed on the flexural strength and fracture toughness. In all composites, the fracture mode was transgranular with an increase of fracture surface roughness with the SiC volumetric fraction. The flexural strength (varying from 650 to 715 MPa) was definitively dominated by the size of SiC clusters abnormally grown up to several tenths of micrometers during hot-pressing. For the systems at hand, the measurements of K_{Ic} seem to indicate that the increasing amount of ultrafine SiC contributed to vary K_{Ic} in an unpredictable fashion. For the investigated range of SiC content, the K_{Ic} variation was about 38% with the highest value measured in the composite with a SiC content of 15 vol%. A major achievement in the strengthening of the microstructure could be definitely expected when an homogeneous distribution of the ultrafine SiC dispersoids will be obtained.

References

1. Guo S-Q (2009) Densification of ZrB_2-based composites and their mechanical and physical properties: a review. J. Europ. Ceram. Soc 29: 995–1011.
2. Tang S, Deng J, Wang S et al (2007) Ablation behaviors of ultra high temperature ceramic composites. Mat. Sci. & Engineering A 465: 1–7.

3. Guo S-Q, Yang J-M, Tanaka H et al (2008) Effect of thermal exposure on strength of ZrB_2-based composites with nano-sized SiC particles. Comp. Sci & Tech. 68: 3033–3040.
4. Zhu S, Fahrenholtz W.G., Hilmas G.E (2007) Influence of silicon carbide particle size on the microstructure and mechanical properties of zirconium diboride-silicon carbide ceramics. J. Europ. Ceram. Soc. 27: 2077–2083.
5. Guo W-M, Zhang G-J, Wang P-L (2009) Microstructural evolution and grain growth kinetics in ZrB_2-SiC composites during heat treatment, J. Amer. Ceram. Soc. 92[11]: 2780–2783.
6. Zhu S,. Fahrenholtz W.C, Hilmas G.E et al (2007). Pressureless sintering of zirconium diboride using boron carbide and carbon additions. J. Amer. Ceram. Soc. 90(11): 3660–3663.
7. Talmy I.G., Zaykoski J.A., Opeka M.M et al (2006) Properties of ceramics in the system ZrB_2-Ta_5Si_3. J. Mater.Res. 21(10): 2593–2599.
8. Monteverde F., Bellosi A (2002) Effect of the addition of silicon nitride on sintering behaviour and microstructure of zirconium diboride. Scrip.Mater. 46: 223–228
9. Liu Q, Han W, Hu P (2009) Microstructure and mechanical properties of ZrB_2-SiC nanocomposite ceramic, Scr. Mater. 61: 690–692.
10. Williamson G.K, Hall W.H (1953) X-ray line broadening from filed aluminium and wolfram. Acta Metall. 1: 22–31.
11. JADE 5.03.37 (MDI – Livermore – CA).
12. Faber K.T, Evans G (1983) Crack deflection processes-I. Theory. Acta Metal. 31: 565–576.

MECHANOCHEMICALLY DRIVEN SYNTHESES OF BORIDE NANOMATERIALS

RICHARD G. BLAIR*
Department of Chemistry
University of Central Florida

Abstract Solid state metathesis reactions have proven to be a viable route to the production of unfunctionalized nanomaterials. However, current implementations of this approach are limited to self-propagating reactions. We have been investigating mechanically driven metathesis reactions. The use of high-energy ball mills allows control of crystallite sizes without the use of a capping group. Reinforcement materials with crystallite sizes on the order of 5–30 nm can be produced in such a manner. Borides are of particular interest due to their strength, high melting point, and electrical conductivity. The ultimate goal of this work is to prepare oxide and capping group-free nanoparticles suitable for incorporation in thermoelectric, polymer, and ceramic composites. Ultimately this work will facilitate the production of improved thermoelectric materials that will provide robust, deployable, power generation modules to supplement or replace fuel cell, Stirling, and battery-derived power sources. It will also result in scalable, bulk syntheses of tough, refractory, conductive nanomaterials for polymer composites with improved electrical properties, ceramic composites with enhanced fracture toughness, and composites with enhanced neutron reflectance and/or absorbance.

Keywords: borides, mechanochemistry, ball mill, solid-state syntheses, ZrB_2, nanoparticles, electroceramics, thermoelectrics

1. Introduction

Nano-sized conductors could potentially improve a variety of materials through use as components of composites. Conductive nano-materials produced from metals such as gold, silver, palladium, or platinum are easily prepared through a variety of solution and gas-phase routes.[16] However, the controlled synthesis of nanoconductors from borides, carbides, nitrides, and silicides has been largely unexplored. These materials have superior

* Richard G. Blair, Department of Chemistry, University of Central Florida, e-mail: rblair@mail.ucf.edu

N. Orlovskaya and M. Lugovy (eds.), *Boron Rich Solids: Sensors, Ultra High Temperature Ceramics, Thermoelectrics, Armor*, DOI 10.1007/978-90-481-9818-4_18,

thermal and mechanical properties and incorporation into composite matrices offers a route to materials with enhanced thermal, structural, and electrical properties. Most synthetic approaches currently employed utilize capping groups to reduce particle surface energies. Although this effectively eliminates agglomeration and Ostwald ripening, large capping groups hinder electrical communication between the nanoparticle and any matrix. Unfunctionalized or weakly functionalized, nano-sized materials are needed for applications that depend upon the electrical properties of the reinforcing agent. Our approach uses mechanochemical synthesis to achieve size control in the synthesis of refractory borides without the need for bulky capping groups.

Conductive nanomaterials offer a route to improve the efficiencies of existing thermoelectric compounds. Thermoelectric power generation offers the potential for producing small, lightweight, rugged power modules. These modules could be employed for waste heat recovery in a variety of combat and non-combat situations. For example, thermoelectric modules could be used improve the efficiency of vehicles by removing the load on the engine produced by existing power generating technologies (such as the alternator). [22] In another application, small, efficient units could be used a field-deployable power generation from locally available fuels such as trash.

In order to realize these applications, the efficiency of thermoelectric power generation must be increased. State-of-the-art thermoelectric power generation is 16% efficient.[4] Improvement of thermoelectric power generation has been approached through the application of new materials and through nanostructuring [21]. New thermoelectric materials offer the promise of large increases in the Figure of Merit, however there is no *a priori* method for predicting the performance of novel compounds. Nanostructuring offers a way to improve the Figure of Merit of existing materials, but complex and difficult to reproduce processing steps are often needed.

The incorporation of reinforcement particles into a thermoelectric matrix will produce materials with significantly improved mechanical and thermoelectric properties. These materials can be prepared by incorporating nanoparticles of refractory conductors into a thermoelectric matrix. Transition metal borides, carbides, nitrides, and silicides are potential candidates for use as inclusions (Fig. 1). Borides are particularly suited to mechanochemical synthetic methods since both precursor materials can be solids and they possess the highest conductivities. Based on success in the synthesis of $ZrSi_2$ we have focused on the Group IV transition metal boride ZrB_2. Bi_2Te_3-based thermoelectric materials have been explored as the thermoelectric matrix. Bi_2Te_3 compounds form the basis for thermoelectric modules that operate near room temperature. These materials have been well characterized and the effect of conductive nanoinclusions can be accurately assessed.

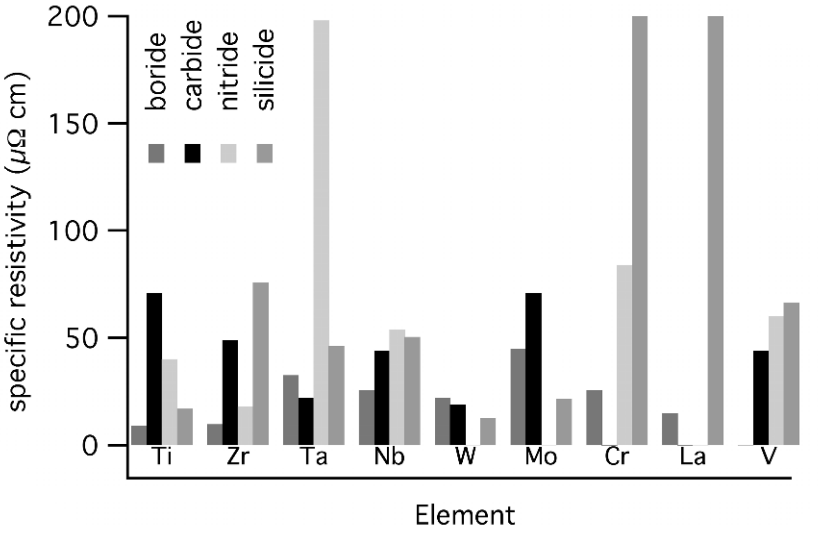

Figure 1. Specific resistivities for selected transition metal borides, carbides, nitrides, and silicides. Initial successes with $ZrSi_2$ led to the focus on ZrB_2 which is much more conductive. A typical matrix material like $Bi_{0.4}Sb_{1.6}Te_3$ has a specific resistivity of 1260 μΩ cm.

The Figure of Merit is a dimensionless value that is used to rank the performance of a thermoelectric material. (Eq. 1). A good thermoelectric material has a high Seebeck coefficient (α), high electrical conductivity (σ), and low thermal conductivity (κ). By incorporating nano-sized conductive materials into a thermoelectric matrix it will be possible to simultaneously reduce the composite's thermal conductivity while raising its electrical conductivity. The result will be a material with an enhance Figure of Merit.

$$Z = \frac{\alpha^2 \sigma}{\kappa} \tag{1}$$

It is important to note that these particles will be more conductive (electrically and thermally) than the thermoelectric matrix. As long as the volume percent of conductive inclusion is kept below the percolation threshold (25 vol%) the properties of the bulk composite with be closer to that of the matrix material. There has been work in introducing non-conductive inclusions [15, 17, 30] as well as conductive inclusions.[8, 26, 29]

The choice of reinforcement material is critical to success. Beauchamp et al. [3] observed that the addition of tungsten to PbTe resulted in a reduced Seebeck coefficient. This may be due to a reaction between PbTe and the W fibers. This suggests that it important to choose a material that will not react with the thermoelectric matrix. Borides, which are refractory,

conductive, strong, and relatively inert offer an attractive choice for reinforcement materials. Additionally, high concentrations of borides at the thermoelectric/interconnect interface can be used to limit the diffusion of reactive elements into the interconnect material increasing their effective life.

2. Synthesis and Characterization of Non-reactive, Conducting Nanoparticles

In order to increase phonon scattering, it is desirable to use nano-sized conductors in a thermoelectric matrix.[12, 18, 28] In order to take advantage of the phenomena a scalable synthetic approach to unfunctionalized or weakly functionalized nanomaterials is required.

Refractory borides have been prepared through self-propagating high temperature synthesis (SHS), borothermal reduction, [2] magnesothermic reduction [23], carbothermal reduction [32], co-reduction [9], and self-propagating metathesis reactions (SSM).[13] Table 1 summarizes the various routes to preparing ZrB_2.

However, these reactions are difficult to scale and do not allow control of product size. Additionally, the use of oxide precursors adds the possibility of oxide contamination; which will adversely affect the electrical properties of the material. Zirconium oxides are difficult to remove from the final product.

By using milling technology, a scalable approach to the synthesis of nanocrystalline materials as well as nanoparticles can be realized. Several terms have been used to describe this approach. Among these are mechanical activation (MA), mechanical alloying (also MA), mechanochemical syntheses, and high-energy ball milling (HEBM). The most accurate description of this phenomenon is mechanochemical synthesis. Mechanical activation assumes that milling inputs energy into a system continuously until the activation energy of a reaction is achieved. This incorrectly assumes that energy is being "stored" in the materials as they are ground. A more realistic explanation is that the attrition of the reactants results in a more efficient energy transfer to supply a reaction's activation energy. The use of the term mechanical alloying implies that solid solutions are being synthesized and completely neglects the chemical thermodynamics of the reaction. Although alloys can be produced by milling, a wide variety of compounds are also accessible. A proper understanding of these reactions cannot be achieved without understanding the heat released due to reaction exotherms. There is large body of work examining mechanochemical syntheses[1, 7, 24, 33] Mechanochemical methods have been successfully employed in the synthesis of borides.[19, 25].

TABLE 1. Routes to ZrB_2

Reaction	Type	Comments
$Zr + 2B \rightarrow ZrB_2$	Self-propagating high-temperature synthesis (SHS)	Requires pure metals and high initiation temperatures. Difficult to scale and control.
$3ZrO_2 + 10B \rightarrow 3ZrB_2 + 2B_2O_3$	Borothermal reduction	Requires temperatures >1,600°C, 40% of the boron used is wasted
$3ZrO_2 + 10B \rightarrow 3ZrB_2 + 2B_2O_3$ *grind* then *heat*	Mechanically activated borothermal reduction	Requires temperatures less than traditional borothermal reduction 1,100°C. ZrO_2 is very hard and significant mill wear can be problematic.
$ZrO_2 + B_2O_3 + 5Mg \rightarrow ZrB_2 + 5MgO$	Mechanochemically driven magnesothermal reduction	No external heating required. ZrO_2 is very hard and significant mill wear can be problematic.
$ZrO_2 + B_2O_3 + 5C \rightarrow ZrB_2 + 5CO$	Carbothermal reduction	ZrO_2 is produced by precipitation from an organometallic complex. Carbon is introduced in the form of hydrocarbons. Requires temperatures >1,300°C.
$ZrCl_4 + 2BBr_3 + 10Na \rightarrow ZrB_2 + 4NaCl + 6NaBr$	Co-reduction	Carried out at 400°C in an autoclave. BBr_3 is very corrosive.
$ZrCl_4 + MgB_2 + Mg \rightarrow ZrB_2 + 2MgCl_2$	Solid-state metathesis reaction (SSM)	Requires temperatures >650°C

We have approached the mechanochemical synthesis of refractory borides through milling in a SPEX mixer mill. Although not a scalable solution, its vigorous motion allows rapid assessment of reaction parameters. The dynamic nature of the processing ensures that the reaction goes to completion. An added benefit is that it is possible to scale mechanochemical reactions through modification of mill design.[11] Table 2 summarizes potential mechanochemical routes to ZrB_2 and borides in general.

As can be seen in Table 2 that it is possible to synthesize the boride from the elements. However, this approach requires high purity metals. For

example, TiB_2 can be synthesized in this manner [20]. The boride can be synthesized in as little as one hour. The reaction is not continuous and most probably proceeds though an SHS route. Although continued milling results in size reduction down to crystallites on the order of 9.5 nm, WC contamination through media wear becomes a problem.

TABLE 2. Mechanochemical routes to ZrB_2. Reactions performed in the Blair lab are **bolded**

Reaction	Comments
$Zr + 2B \rightarrow ZrB_2$	Produces ZrB_2 after prolonged milling. Significant media wear occurs unless WC, alumina, or zirconia is used. Media contamination is a significant problem.
$ZrCl_4 + MgB_2 + Mg \rightarrow ZrB_2 + 2MgCl_2$	**No reaction occurred - MgB_2 is stable to mechanical treatment.**
$ZrCl_4 + 2B + 2Mg \rightarrow ZrB_2 + 2MgCl_2$	**Amorphous, pyrophoric product after 2 hours of milling.**
$ZrCl_4 + 2B + 4Li \rightarrow ZrB_2 + 4LiCl$	**Amorphous, pyrophoric product after 2 hours of milling. Partial synthesis after 15 minutes of milling, 62% Zr + 38% ZrB_2. Small crystallites produced (9 nm).**

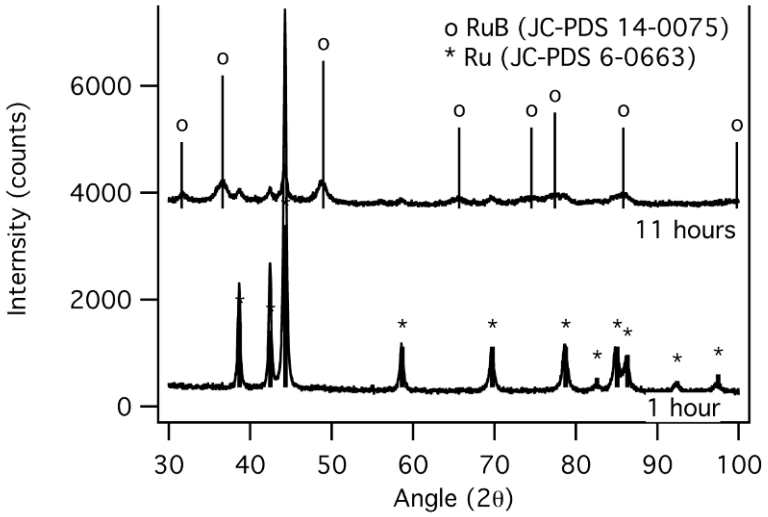

Figure 2. Prolonged milling of Ru + 2B in a WC vial results in the formation of RuB with a portion of the Ru still unreacted.

Less reactive metals are more difficult to convert to borides by this method. For example the compound RuB_2 has attracted interest as an ultrahard material.[31] Syntheses involving arc melting require excess boron in order to produce X-ray pure RuB_2. A mechanochemical route would allow stoichiometric reactions to be performed. However, the wear resistance of ruthenium slows down attrition process and limits reactivity. After prolonged milling (11 h) Ru is still present along with RuB (Fig. 2).

A attractive route to the synthesis of borides is through solid state metathesis (SSM) [13]. Reactions using metal halides and MgB_2 offer the potential for producing a wide range of diborides.

$$MX_n + MgB_2 + (n/2 - 1)Mg \rightarrow MB_2 + (n/2)MgX_2 \quad (2)$$

The starting materials are much softer than the pure metals and result in less media wear. The production of metal salts as by-products also serves to cushion the milling media and reduce wear. These reactions offer the potential for size control through dilution. By adding inert salt to the reaction, Ostwald ripening will be limited. Unfortunately, traditional methods of performing SSM reactions do not work if the reactions are diluted. Propagation depends on the heat generated by the reaction. To much dilution lowers the amount of heat available and results in incomplete reactions [6]. This limitation can be eliminated by using a mill to continuously add energy to the system. Reactions are forced to completion by the vigorous mechanical action in the milling container. We have had success in the size-controlled synthesis of $ZrSi_2$ (Eq. 2)

In this method, a mill such as a SPEX mixer mill is utilized to supply the activation energy for the reaction. By using soft precursors ($ZrCl_4$ and CaSi), it is possible to use hardened steel vials for the synthesis instead of more exotic materials like WC.

$$ZrCl_4 + 2CaSi \rightarrow ZrSi_2 + 2CaCl_2 \quad (3)$$

The analogous reaction to produce ZrB_2 requires the addition of additional reductant metal since no reactive monoborides exist (Eq. 3).

$$ZrCl_4 + MgB_2 + Mg \rightarrow ZrB_2 + 2MgCl_2 \quad (4)$$

The by-products are removed by washing with a suitable solvent. Lithium salts are soluble in a variety of ethers, amides, and alcohols. Size control is achieved by diluting the reaction with NaCl or other non-reactive salt. It is important to note that diluted reactions do not self-propagate. It is the continuous input of energy from milling that forces the reaction to completion. This type of synthesis can be used to effectively produce bulk quantities of unfunctionalized nanomaterials.

It was discovered that MgB_2 is not a reactive boron source under mechanochemical reaction conditions. It is stable even after extended milling. Since MgB_2 has been formed though mechanical processing,[27] a possible approach to boride synthesis would be through the transient formation of reactive borides. Equations 4 and 5 illustrate these reactions. During milling of these reactions there are two possible routes: reduction of $ZrCl_4$ to Zr metal followed by an SHS reaction with B, or reaction of B with the reductant followed by an SSM reaction with $ZrCl_4$.

$$ZrCl_4 + 2B + 2Mg \rightarrow ZrB_2 + 2MgCl_2 \quad (5)$$

$$ZrCl_4 + 2B + 4Li \rightarrow ZrB_2 + 4LiCl \quad (6)$$

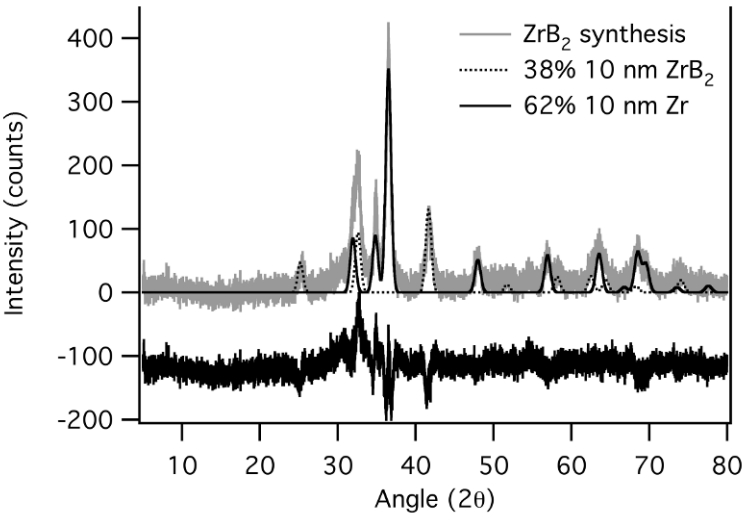

Figure 3. Mechanochemical synthesis of ZrB_2 from the reaction $ZrCl_4 + 2B + 4Li \rightarrow ZrB_2 + 4LiCl$. A total reaction mass of 1.5 grams was milled with 3 0.5" balls for 30 minutes in a SPEX mixer mill. Sizes of 10 nm were derived using the Scherrer equation. Although nanomaterials were produced, incomplete conversion to the boride was observed.

We found that reactions performed for longer than 30 min resulted in amorphous, pyrophoric products. Using lithium as a reductant and milling for 15–45 min resulted in the formation of ZrB_2 with crystallite sizes on the order of 9 nm (Fig. 3 and Table 3). The fact that Zr metal is observed in this product suggests that the reaction proceeds by the reduction of $ZrCl_4$ to the Zr followed by reaction with B to form the diboride. Essentially, the reactant is reduced followed by SHS. Grinding serves to reduce particle size and increase reactant interactions. The heat is supplied by the reaction exotherms that occur during the course of the reaction. If there is not enough chemical energy available then the reaction will not go to completion. We

have found that ZrB_2 prepared in this manner forms stable colloidal suspensions. Pure ZrB_2 powders can be isolated by removal of any soluble by-products through dialysis followed by drying *in vacuo*. A uniform mixture of these materials with a thermoelectric powder can be prepared by using a mixer-mill.

TABLE 3. Summary of mechanochemical reduction reactions leading to ZrB_2. The reaction was $ZrCl_4 + 2B + 4Li \rightarrow ZrB_2 + 4LiCl$. $ZrCl_4$ concentration was controlled by either changing the reactant mass or through dilution with NaCl

$[ZrCl_4]$ (mol/L)	Reactant mass (g)	Size (nm)	$\%ZrB_2$ (%)	Comments
0.0826898	1.5	10.0	38	Milled 30 min
0.162816	2.92	13.9	63	Milled 45 min
0.14619	2.92	8.3	51	Milled 45 min, 10% dilution with NaCl

In choosing the reductant it is important to consider the reaction enthalpy that would result and bulk modulus of the metal. Possible reductants are the alkali metals, alkaline earth metals, aluminum, and zinc. The reaction enthalpies for reductions utilizing these metals range from −172.3 kJ for zinc to −1114.1 kJ for cesium. The choice of lithium (−976.5 kJ) and magnesium (−624.7 kJ/mol) as reductants provide reaction pathways energetic enough to produce ZrB_2. Metals with low bulk modulus will undergo plastic deformation and reduce the amount of kinetic energy available to the reaction. For this reason sodium, potassium, rubidium, and cesium are not ideal choices as mechanochemical reductants. Lithium (bulk modulus = 11 GPa) and magnesium (bulk modulus = 45 GPa) represent the extreme ranges of bulk moduli in the possible reductants.

3. Improving the Properties of Thermoelectric Materials

3.1. THERMAL CONDUCTIVITY

Borides have a high electrical conductivity, but also possess a higher thermal conductivity (5.5 $Wm^{-1}K^{-1}$ for ZrB_2 versus 0.796 $Wm^{-1}K^{-1}$ for $Bi_{0.4}Sb_{1.6}Te_3$). In fact, the thermal conductivity of ZrB_2 is higher than most commonly used thermoelectric materials. This will result in a composite with a higher thermal conductivity than that of the pure thermoelectric material. This effect can be minimized by utilizing nanoscale inclusions (Fig. 4).

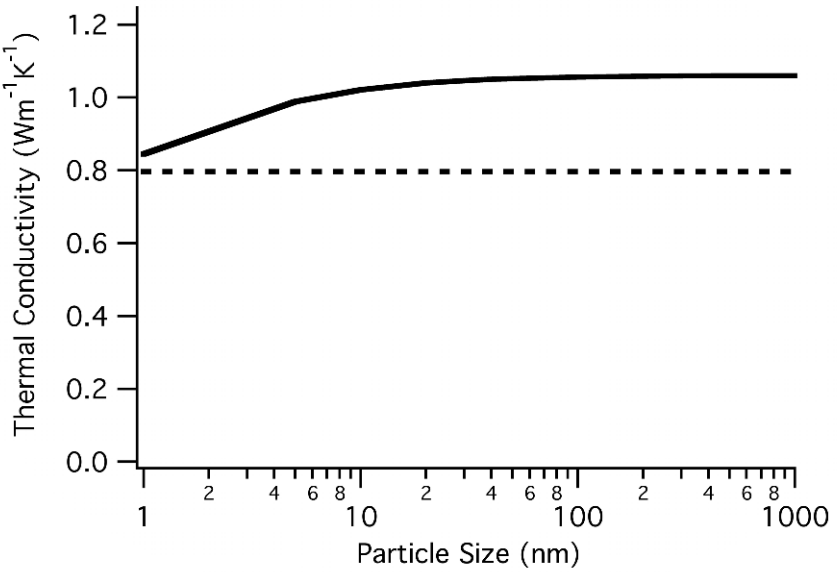

Figure 4. The effect of particle size on the thermal conductivity of a thermoelectric composite. Here p-type $Bi_{0.4}Sb_{1.6}Te_3$ with 15 vol% ZrB_2 inclusions was modeled.[14] The enhancement in electrical conductivity (Figure 5) overcomes the overall increase in thermal conductivity.

The use of nanoinclusions increases the number of grain boundaries present in the composite. These have been predicted to reduce thermal conductivity in thermoelectric materials through phonon scattering [10]. We have found that the thermal conductivity of p-type $Bi_{0.4}Sb_{1.6}Te_3$ is slightly reduced when prepared mechanochemically and that the addition of 15 vol% reinforcement material does not detrimentally affect the thermal conductivity of the composite.

3.2. ENHANCED ELECTRICAL CONDUCTIVITY

The electrical conductivity of thermoelectric composites with conductive inclusions can be modeled by treating the composite as a three dimensional resistor network [5].

Using this model, the conductivity enhancement outweighs any increase in thermal conductivity. Sample calculations (Fig. 5) show that the electrical conductivity of a p-type $Bi_{0.4}Sb_{1.6}Te_3$ matrix reinforced with ZrB_2 would result in a 14-fold increase in the composite's conductivity (793 S/cm for the matrix and 11,528 S/cm for a 25 vol% composite with ZrB_2).

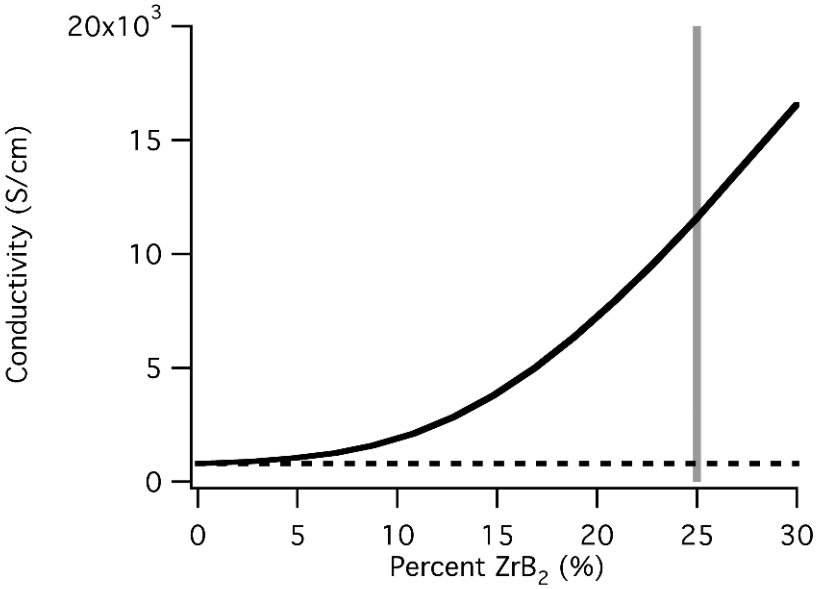

Figure 5. Expected improvement in the conductivity for p-type $Bi_{0.4}Sb_{1.6}Te_3$ composites reinforced with 10 nm conductive inclusions or ZrB_2. The gray line indicates the percolation threshold. ZrB_2 concentrations higher than this value can result in a continuous path of ZrB_2 in the sample and reduced thermoelectric properties.

4. Conclusions

Mechanochemical syntheses of borides is a scalable route to bulk quantities of conductive nanomaterials. Materials produced in this manner will possess electrical properties superior to those produced by traditional methods for synthesizing nanomaterials. Thermoelectric composites incorporating conductive borides will have enhanced efficiencies. This enhancement is due to increased electrical conductivities and decreased thermal conductivities predicted for these composites. The approach outlined here can also be used to produce nanocrystalline materials for toughening of ceramics; highly conductive, easily dispersible materials for polymer composites; and neutron absorbing (HfB_2) compounds for potential shielding applications

References

1. Barraud, E., S. Begin-Colin, G. Le Caer, O. Barres, and F. Villieras, *Mechanically activated solid-state synthesis of hafnium carbide and hafnium nitride nanoparticles.* J. Alloys Compd., 2008. **456**(1-2): p. 224–233.

2. Barton, L. and D. Nicholls, *The hydrogenation of boron monoxide to diborane and the reactions of boron and boron carbide with titanium and zirconium dioxides.* Journal of Inorganic and Nuclear Chemistry, 1966. **28**(6-7): p. 1367–1372.
3. Beauchamp, E.K. and J.E. Morenz, *Fiber-strengthened, lead telluride thermoelectric material*, Application: US Patent 68-761057 3546026, 1970
4. Bell, L., *Thermoelectric and Waste Heat Recovery*, in *International Physics Forum*. 2007.
5. Bigalke, J., *Investigation of the Conductivity of Random Networks.* Physica A, 1999. **272**: p. 281–293.
6. Blair, R.G., E.G. Gillan, N.K.B. Nguyen, D. Daurio, and R.B. Kaner, *Rapid solid-state synthesis of titanium aluminides.* Chemistry of Materials, 2003. **15**(17): p. 3286–3293.
7. Boldyrev, V.V. and K. Tkacova, *Mechanochemistry of solids: past, present, and prospects.* J. Mater. Synth. Process., 2000. **8**(3/4): p. 121–132.
8. Cai, K.F., E. Mueller, C. Drasar, and C. Stiewe, *The effect of titanium diboride addition on the thermoelectric properties of beta -FeSi2 semiconductors.* Solid State Commun., 2004. **131**(5): p. 325–329.
9. Chen, L., Y. Gu, L. Shi, J. Ma, Z. Yang, and Y. Qian, *Low-Temperature Synthesis of Nanocrystalline ZrB_2 via Co-reduction of $ZrCl_4$ and BBr_3.* Bulletin of the Chemical Society of Japan, 2004. **77**(7): p. 1423–1424.
10. Dresselhaus, M.S., Y.M. Lin, S.B. Cronin, M.R. Black, O. Rabin, and G. Dresselhaus, *Investigation of low-dimensional thermoelectrics.* Therm. Conduct., 2005. **26**: p. 3–15.
11. Dushkin, A.V., *Potential of Mechanochemical Technology in Organic Synthesis and Synthesis of New Materials.* Chem. Sust. Dev., 2004. **12**: p. 251–273.
12. Faleev, S.V. and F. Léonard, *Theory of enhancement of thermoelectric properties of materials with nanoinclusions.* Phys. Rev. B, 2008. **77**: p. 214304.
13. Gillan, E.G. and R.B. Kaner, *Synthesis of refractory ceramics via rapid metathesis reactions between solid-state precursors.* Chemistry of Materials, 1996. **8**(2): p. 333–343.
14. Hasselman, D.P.H. and K.Y. Donaldson, *Effect of Reinforcement Particle Size on the Thermal Conductivity of a Particulate-Silicon Carbide-Reinforced Aluminum Matrix Composite.* J. Am. Ceram. Soc., 1992. **75**(11): p. 3137–3140.
15. Huang, X.Y., Z. Xu, and L.D. Chen, *The thermoelectric performance of ZrNiSn/ZrO2 composites.* Solid State Comm., 2004. **130**: p. 181–185.
16. Katz, E., A.N. Shipway, and I. Willner, *Chemically functionalized metal nanoparticles: Synthesis, properties and applications.* Nanoscale Mater., 2003: p. 5–78.
17. Liu, H.N., M. Sakamoto, and T. Satoh, *Structures of the $Al_2O_3/FeSi_2$ thermoelectric composite fabricated by infiltration process.* J. Mater. Sci. Lett., 2003. **22**(13): p. 941–943.
18. Mingo, N., D. Hauser, N.P. Kobayashi, M. Plissonnier, and A. Shakouri, "*Nanoparticle-in-Alloy*" *Approach to Efficient Thermoelectrics: Silicides in SiGe.* Nano Lett., 2009. **9**(2): p. 711–715.
19. Radev, D.D. and D. Klissurski, *Mechanochemical synthesis and SHS of diborides of titanium and zirconium.* J. Mater. Synth. Process., 2001. **9**(3): p. 131–136.
20. Radev, D.D. and D. Klisurski, *Properties of TiB_2 powders obtained in a mechano-chemical way.* Journal of Alloys and Compounds, 1994. **206**(1): p. 39–41.
21. Sales, B.C., *Critical overview of recent approaches to improved thermoelectric materials.* Int. J. Appl. Ceram. Technol., 2007. **4**(4): p. 291–296.
22. Saqr, K.M., M.K. Mansour, and M.N. Musa, *Thermal design of automobile exhaust-based thermoelectric generators: objectives and challenges.* J. Thermoelectr., 2008(1): p. 59–66.
23. Setoudeh, N. and N.J. Welham, *Formation of zirconium diboride (ZrB_2) by room temperature mechanochemical reaction between ZrO_2, B_2O_3 and Mg.* Journal of Alloys and Compounds, 2006. **420**(1-2): p. 225–228.

24. Takacs, L., *Solid state reactions induced by ball milling.* Hyperfine Interact., 1997. **111**(1-4, Industrial Applications of the Moessbauer Effect, Pt. 1): p. 245–250.
25. Tsuchida, T. and T. Kakuta, *Synthesis of NbC and NbB_2 by MA-SHS in air process.* Journal of Alloys and Compounds, 2005. **398**(1-2): p. 67–73.
26. Uehara, M., R. Shiraishi, A. Nogami, N. Enomoto, and J. Hojo, *SiC-B_4C composites for synergistic enhancement of thermoelectric property.* Journal of the European Ceramic Society, 2003. **24**(2): p. 409–412.
27. Varin, R.A. and C. Chiu, *Synthesis of nanocrystalline magnesium diboride (MgB_2) metallic superconductor by mechano-chemical reaction and post-annealing.* Journal of Alloys and Compounds, 2006. **407**(1-2): p. 268–273.
28. Wang, S. and N. Mingo, *Improved thermoelectric properties of $Mg_2Si_xGe_ySn_{1-x-y}$ nanoparticle-in-alloy materials.* Appl. Phys. Lett., 2009. **94**(20): p. 203109/1-203109/3.
29. Wang, X., *Preparation of SiC-B_4C composite film and its mechanical and thermoelectric properties.* Fuhe Cailiao Xuebao, 2004. **21**(3): p. 49–53.
30. Wang, Z.-s., D.-h. Wang, J.-z. Zhang, and X. Shi, *Preparation and properties of $CoSb_3$/BN composite material.* Dianyuan Jishu, 2003. **27**(4): p. 387–389.
31. Weinberger, M.B., J.B. Levine, H.Y. Chung, R.W. Cumberland, H.I. Rasool, J.M. Yang, R.B. Kaner, and S.H. Tolbert, *Incompressibility and Hardness of Solid Solution Transition Metal Diborides: $Os_{1-x}Ru_xB_2$.* Chemistry of Materials, 2009. **21**(9): p. 1915–1921.
32. Xie, Y.L., T.H. Sanders, and R.F. Speyer, *Solution-based synthesis of submicrometer ZrB_2 and ZrB_2-TaB_2.* Journal of the American Ceramic Society, 2008. **91**(5): p. 1469–1474.
33. Yang, H. and P.G. McCormick, *Mechanochemical reactions during mechanical milling.* Trans. Mater. Res. Soc. Jpn., 1994. **14A**(Ceramics, Powders, Corrosion and Advanced Processing): p. 617–20.

VIBRATIONAL PROPERTIES OF $Zr(Hf)B_2$–SiC UHTC COMPOSITES BY MICRO-RAMAN SPECTROSCOPY

M. DONOHUE, C. CARPENTER, N. ORLOVSKAYA*
Department of Mechanical, Materials, and Aerospace Engineering
University of Central Florida, Orlando, USA

1. Introduction

Development and characterization of novel materials that are lightweight, possess high mechanical properties, can withstand high temperatures, and provide superior thermal properties are crucial to meet the future demands of Air Force, Army, Navy, Missile Defense Agency (MDA), and other military and space agencies. Materials for such applications (hypersonic air-breathing vehicles, including Single-To-Orbit vehicles and Two-Stage-To-Orbit aerospace planes, fully reusable space transport vehicles, hypersonic cruise missiles) experience severe aero-thermal loads with nose-cone and nozzle temperatures in excess of 2,000°F and 4,000°F, respectively. High G acceleration is also a problem. Even the most advanced materials, such as Ti, Inconel X, carbon-carbon, and silicon carbide based composites cannot withstand the excessive heat generated, especially during re-entry, and they cannot meet the guidelines for future high performance aircrafts, kinetic energy interceptors and reusable space planes. Thus, the demand for low-cost, light weight high temperature materials for thermal protection systems (TPS) is expected to be on the significant rise in the near future.

The objective of the "High Temperature and Aerospace Materials" research program at AFOSR is to provide a fundamental knowledge to enable … the discovery and characterization of high temperature materials….". Applications of these materials include air-breathing and rocket propulsion systems, airframe and spacecraft structures and hypersonic vehicle systems. Specifically, the research on high temperature materials that exibit superior structural and/or functional performance at temperatures above 1,000°C is sought. In particular, it is stated that one of the thrust areas of the program is developing and using characterization methods for probing the microstructural evolution at high temperatures as well as study

* Department of Mechanical, Materials, and Aerospace Engineering, University of Central Florida, Orlando, USA, e-mail: norlovsk@mail.ucf.edu

N. Orlovskaya and M. Lugovy (eds.), *Boron Rich Solids: Sensors, Ultra High Temperature Ceramics, Thermoelectrics, Armor*, DOI 10.1007/978-90-481-9818-4_19,

the mechanics of materials at elevated temperatures [1, 2]. Accordingly, the current proposal addresses this particular need by exploring the possibility of probing vibrational and mechanical properties of the ultra high temperature ceramic composites used as a component of the thermal protection system of the air vehicles. One of the critical issues of high-speed flight vehicles is the significant overheating, encountered at the sharp leading edges. Hypersonic vehicles require sharp leading edges, and recent estimates suggested that such edges should have a radius of curvature on the order of 3 mm [3]. As a result of such sharp geometry, temperatures in excess of 2,600^{o}C are generated, at the tip of a leading edge, and the resulting stagnation temperature exceeds the realistic upper use temperature of most materials. It was observed that even the most advanced materials such as Ti, Inconel X, carbon–carbon, and silicon carbide-based composites cannot withstand the excessive heat generated, especially during reentry, resulting in blunting of the sharp leading edges.

Thus, sharp leading edges and nose cones require thermal protection system (TPS) to prevent spacecraft from high aerodynamic heating loads, during reentry into atmosphere. The schematic presentation of the hypersonic vehicle [5] along with the local geometry and flow conditions near leading edge [6] are shown in Fig. 1. The sharp leading edges experience extreme aerodynamic heating loads resulting in a temperature gradient as high as 1,000^{o}C within 2 mm beneath the surface. Only a few materials can withstand such high heating loads. It has been identified that the ultra high temperature ceramics (UHTCs), such as refractory metal diborides (ZrB_2 and HfB_2) based ceramics, with high melting temperatures and large thermal conductivities are ideally suited for the protection of sharp edges and yet capable of maintaining their sleek shapes without significant deformation or melting. Based on their unique combination of properties, $Zr(Hf)B_2$ ceramics are prime candidates for use in the extreme environments associated with hypersonic flight, atmospheric re-entry, and rocket propulsion.

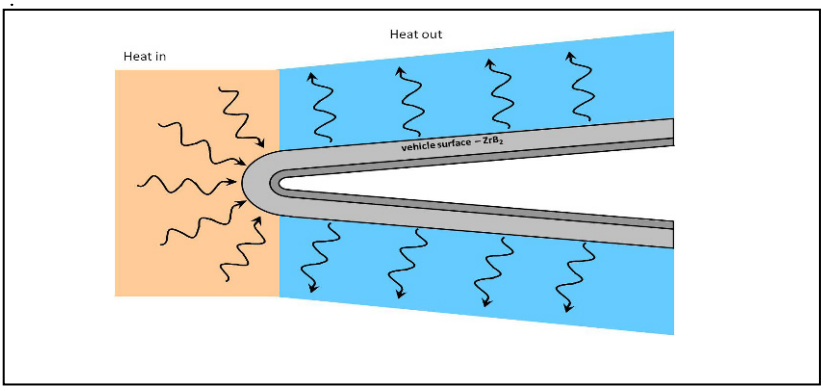

Figure 1. A schematic presentation of leading edge configuration [4].

2. Zr(Hf)B_2–SiC UHTC Materials

Ultra-high temperature ceramics (UHTCs) such as ZrB_2 and HfB_2 diborides and their composites are identified as the next generation materials for high temperature aerospace applications [7–12]. The high melting point of ZrB_2 and HfB_2 coupled with their high hardness, low density, and ability to form refractory oxide layers make them potential candidates for operation in the ultra high temperature range of 2,000–3,000°C. Both ZrB_2 and HfB_2 are reported to have excellent resistance to thermal shock and oxidation [13–16], they both have high melting temperatures (T_m = 3,245°C for ZrB_2 [17] and 3,380°C for HfB_2 [17]) that very few materials exhibit. Also they exhibit high elastic modulus (E = 489 GPa for ZrB_2 [18] and 480 GPa for HfB_2 [19]), high hardness (H_v = 23 GPa for ZrB_2 [18, 20] and 28 GPa for HfB_2 [21–24]) along with very high thermal conductivity (k = 60 W/mK for ZrB_2 [18] and 104 W/mK for HfB_2 [21]). As is typical for ceramics, the fracture toughness of ZrB_2 and HfB_2 is not very high, which is a major drawback for their most promising aerospace applications [11]. Their reported linear coefficients of thermal expansion are 5.9×10^{-6} for ZrB_2 [21] and 6.3×10^{-6} for HfB_2 [21]. The ceramics also have excellent chemical resistance to HCl and HF and are stable in metal melts (Al, Cu, Mg, Zn, Cd, Fe, Pb), cryolite, and non-basic slags [25–29]. Physical and mechanical properties of ZrB_2 and HfB_2 are reported in [30–35]. Additions of SiC are used to enhance oxidation resistance of ZrB_2–SiC particulate composites, which have shown exceptional stability, even at temperatures above 2,600°C in the presence of environmentally aggressive high velocity dissociated air. Thus, this particular set of composites, Zr(Hf)B_2–SiC, have emerged as the most promising ceramic composites for UHT industrial, military and aerospace applications.

While there is no better alternative to Zr(Hf)B_2–SiC ceramic composites for use in ultra high temperature applications, the brittleness of the composites is a significant drawback in the applications where a sufficiently high mechanical performance and reliability are required. One feasible way the composite's low toughness could be increased is to design the proper distribution of thermal residual stresses, which originate due to mismatch of coefficients of thermal expansion (CTE) and Young's moduli between Zr(Hf)B_2 and SiC phases. Thus, a better control of the mechanical behavior and reliability of Zr(Hf)B_2–SiC ceramics can be obtained through a thorough design, measurements of residual stresses and their redistribution during loading.

For successful design of a composite, with respect to the residual stress distribution, understanding the evolution of residual stresses in the material is a prime requirement. However, such understanding does not necessarily ensure superior mechanical performance because the designed residual

stress state and the magnitude of stress can alter considerably as a result of the applied stress and temperature during service. To control the mechanical behavior and reliability of components made out of $Zr(Hf)B_2$–SiC composites, redistribution of residual stresses also needs to be measured and understood. Therefore, understanding the evolution of residual stresses, their redistribution as a function of stress and temperature as well as measurement of the residual stresses are critical issues in the design and operation of $Zr(Hf)B_2$–SiC composites. Techniques that can be used with a high precision to map microstress distributions (i.e., to measure the absolute magnitude of micro-stress at different points within the material) would represent an important advancement in the evaluation of the mechanical properties that are relevant to real world applications.

3. Residual Stresses in $Zr(Hf)B_2$–SiC Composites

Thermal or mechanical processing of materials often results in inelastic strains which generate residual stresses. Such processing- or mechanical deformation-induced residual stresses can be categorized as macrostresses and microstresses. Macroscopic surface residual stresses often result either during cooling of large size components due to poor thermal conductivity, especially in ceramics (resulting from differential thermal contraction between bulk of the material and surface) or when different macroscopic regions of a component deform non-uniformly but are constrained to fit together (such as the surface and interior). In contrast, residual microstresses can occur at the microstructural level (intergranular or interfacial microstresses) or at the level of the crystal structure (intragranular microstresses) [36]. Such stresses are, by necessity, balanced by opposing stresses in other locations within the material.

The processing-induced intergranular microstresses develop during the cooling of multiphase composite whenever materials with different coefficients of thermal expansion (CTE) and elastic moduli are bonded together [37–39] where as the intragranular residual microstresses result in anisotropic single phase polycrystalline material due to thermal contraction differences between the crystallites [40–42]. Mechanical deformation-induced microstresses develop due to elastic-plastic deformation within the material or due to strain incompatibility within the grains. Development of such microstresses is critically dependent upon the elastic and plastic anisotropy intrinsic to the material because variations in the degree of elasto-plastic anisotropy strongly influence the magnitude of microstress [43]. The inter-/intra-granular micro-stresses are of critical importance in failure mechanisms of the ceramics, such as ratio of the trans- and inter-granular fracture, crack branching or bridging [44], microcracking [45, 46], stress-induced phase transformation

[47, 48], subcritical crack growth [49], fatigue [50], etc. These microstresses govern crack-propagation induced energy dissipation [51, 52] and affect the ceramic toughness and strength.

The appearance of the residual microstresses in the as-processed Zr(Hf)B_2–SiC composite is explained by the mismatch in Young's moduli (E) and CTE (α) between ZrB_2 (E = 489 GPa, $\alpha = 5.9 \times 10^{-6}\,K^{-1}$) [11] or HfB_2 (E = 480–510 GPa, $\alpha = 6.3 \times 10^{-6}\,K^{-1}$) [53–55] and 3C-SiC (E = 694 GPa, $\alpha = 3.5 \times 10^{-6}\,K^{-1}$) [56, 57], as well as the difference between room temperature (25°C) and sintering temperature (typically at ~2,100°C) of the composite. The equiaxed and almost spherical SiC grains can be assumed as elastic spheres of uniform size distributed in an infinite elastic continuum of ZrB_2 matrix [58]. This results in axially symmetric stress distribution around SiC grains. It has been shown that the ceramic grain will be under a uniform/hydrostatic pressure P which can be expressed as [58]

$$P = \frac{(\alpha_m - \alpha_p)\Delta T}{\left[\dfrac{0.5(1+\nu_m)+(1-2\nu_m)V_p}{E_m(1-V_p)} + \dfrac{1-2\nu_p}{E_p}\right]} \tag{1}$$

where ν is Poisson's ratio, ΔT is temperature change, V_p is volume fraction of grains, and subscripts m and p stand for matrix and grain. On the other hand, radial (σ_{rad}) and tangential (σ_{tan}) stresses within the ZrB_2 matrix and at a distance r from the center of grain are expressed, respectively, as [58]

$$\sigma_{rad} = \frac{P}{1-V_p}\left[\frac{a^3}{r^3} - V_p\right] \text{ and } \sigma_{\tan} = -\frac{P}{1-V_p}\left[\frac{a^3}{2r^3} + V_p\right] \tag{2}$$

Thus, from the above equations it can be seen that when $\alpha_m > \alpha_p$, as is the case for ZrB_2–SiC composites, cooling of the composite from the sintering temperature will induce a uniform compressive stress within the SiC grains. The radial and tangential stresses within ZrB_2 will be compressive and tensile, respectively, and both the stresses will be at maximum at the ZrB_2–SiC interface.

When modeling multiphase particle-reinforced composites, residual microstresses in the matrix and inclusions (different phases) can be a-priori estimated based on simplified composite theory [59–63]. However, experimental determination of these microstresses as a function of microstructural parameters would allow not only the stress state of a particular composite to be better assessed but also design of the composites with specific properties to suit desired/target applications.

4. Measurement of Residual Stresses by Micro-Raman

Measurement of the residual stresses and their redistribution during loading is a critical issue in the development of composites. Techniques that could be used with a high precision to map stress distributions (i.e., to measure the absolute magnitude of the stress at different points within the material) would represent an important advance in the evaluation of composite performance. In recent years the stress analysis of ceramics using so-called piezo-spectroscopic techniques, such as Raman spectroscopy, has been developed. It is based on the fact that in crystalline materials, the atomic vibrational frequencies depend on the interatomic force constants [64]. In strain-free crystalline materials, interatomic force constants as well as the vibrational frequencies correspond to the equilibrium atomic spacing. Residual stress resulting from either thermal processing or mechanical deformation causes a definitive residual strain which in turn changes the equilibrium atomic spacing within a material and thus the interatomic force constants. Depending upon the nature of the residual stress, bond lengths and force constants either increase or decrease compared to the equilibrium values. As a result Raman scattering wavenumbers from solids are perturbed by elastic strain, and this fact can be used as a tool for the non-destructive analysis of stress and strain. Therefore, the analysis is based on the measurements of a peak shift of Raman bands when the material is subjected to a stress field. Although, there is no unique general relationship between the Raman spectrum parameters (the wavenumber shift) and the stress, very often a higher Raman wavenumber means that compressive stresses are present on the surface, while a shift to a lower wavenumber is due to tensile stress present at the surface. One way to firmly establish the definite relation between wavenumber shift and the sign of the residual stress is to perform the calibration procedure, which directly correlates Raman peak shift in a material with the known applied stress. Then, using the calibration curve, unknown residual stresses can be determined from the changes in Raman peak positions for that particular material. The technique is very attractive because of its potential for high spatial resolution. The diameter of the focused laser beam can be as small as 20–50 nm (using a near-field microscope), and the penetration depth can vary from tens of nanometers to several millimeters, depending on material and laser excitation wavelength. Thus, sampling a potentially large volume of the strained structure or analysis with a pin-point accuracy is possible. The technique was successfully applied to carbon [65, 66], Si [67, 68], Si_3N_4 [69, 70], SiC [71], Al_2O_3[72], $LaCoO_3$ [73], $LaGaO_3$ [74], ZrO_2 [75–77], GaN [78] and other ceramic materials. *To the best of our knowledge no spectroscopic studies of the ZrB_2–SiC ceramics have ever been reported in the past,* except of our preliminary work [79, 80].

However, considerable fundamental insights can be gained by conducting in-situ high temperature Raman spectroscopy studies to fully characterize the vibrational response and stress distribution in Zr(Hf)B_2–SiC composites. Measurements and proper engineering of residual microstresses can contribute to an important correlation between microstructural parameters (grain size and distribution, grain morphology, particulate phase content in a composite) and the macroscopic mechanical behavior.

5. Vibrational Response of ZrB_2 and SiC Phases in ZrB_2–SiC Composite

It is well know that all SiC polytypes give Raman scattering from a transverse optic (TO) phonon at approximately 790 cm^{-1} and a longitudinal optic phonon (LO) at 973 cm^{-1} (Fig. 2a) [81-83]. Both TO and LO bands are stress sensitive [65], therefore, both of the bands are highly suitable for stress measurements. Vibrational properties of Zr(Hf)B_2 ceramics are not available in the open literature. The analysis of residual stresses in ternary AlN-SiC-ZrB_2 and AlN-SiC-$MoSi_2$ electrocoductive composites by micro-Raman was reported in [84], where stress analysis was performed using the piezo-spectroscopic coefficients of the AlN and SiC phases. ZrB_2 constituent of the composite has not been studied and the authors stated that to the best of their knowledge, there were no studies of ZrB_2 vibrational properties performed as of 2006. In our preliminary studies, it was indicated that ZrB_2 exhibits a very weak Raman activity (Fig. 2b) and its two Raman active bands could be used to study the vibrational temperature and stress dependent properties of ZrB_2 [80]. The fact was simply overlooked in the previous studies because of the difficulties in obtaining the Raman spectrum of ZrB_2.

The crystal structure and Brillouin zone of transition metals diborides were described in earlier publications [85–88]. However, the analysis of the ZrB_2 phonon dispersion has just appeared in the paper in press [89]. The paper reported on two infrared active modes (E_{1u} at 60.61 meV and A_{2u} at 63.49 meV) as well as two Raman active modes (B_{1g} at 67.76 meV and E_{2g} at 98.45 meV) of calculated Γ point frequencies of ZrB_2 compound. It was also reported that the calculated phonon dispersion curves do not contain soft modes at any direction thus pointing out at the stability of the *P6/mmm* ZrB_2 phase. The crystal structure of Zr(Hf)B_2 is primitive hexagonal [90–93] with the unit cell of ZrB_2 containing three atoms [94], which gives rise to a total of nine phonon branches, consisting of three acoustic modes and six optical modes. The boron atoms lie on the corners with three nearest neighbor boron atoms in each plane. The Zr(Hf) atoms lie directly in the centers of each boron hexagon, but midway between adjacent boron layers.

Each Zr(Hf) atom has 12 nearest neighbor B atoms, six nearest neighbor in plane Zr(Hf) atoms. The Zr(Hf) atom is positioned at (000), one B atom is at $(\frac{1}{3}\frac{1}{6}\frac{1}{2})$ and another B atom is at $(\frac{2}{3}\frac{1}{3}\frac{1}{2})$. The Zr(Hf) layers alternate with the B layers, however it is not considered as a layered compound because of the very strong interaction between interlayers. While the main contribution to acoustic phonons results from the transition metal sublattice, the high frequency phonons stem from the boron ions, which is expected since the boron atom is lighter than the transition metal atoms, which leads to comparatively weaker electron-phonon interactions. The covalent character of the B-B bonding is also important for the high frequency of phonons involving boron atoms.

Yet, there is no experimental data published to confirm results of the theoretical calculations of the vibrational properties of ZrB_2 or HfB_2 ceramics. Our preliminary results indicate that ZrB_2 are indeed weakly Raman active with two Raman active bands (Fig. 2c), however, more in-depth research is required to determine their stress/strain/temperature sensitivity.

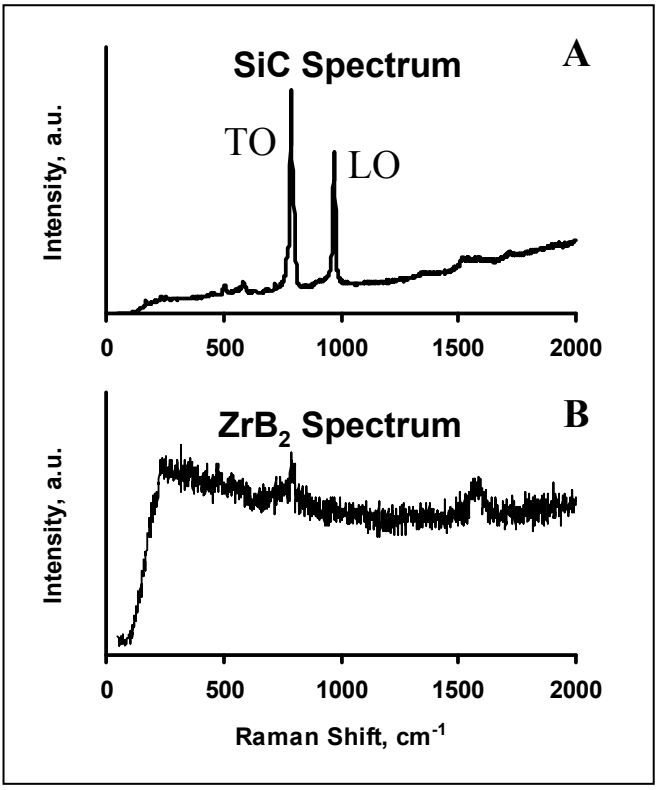

Figure 2. Raman spectra of SiC (**a**) and ZrB_2 (**b**) ceramics.

6. Two Dimensional Maps and Peak Positions of TO and LO SiC bands in ZrB_2–SiC Composites

Raman spectra were collected using 2D mapping from the surfaces of three ZrB_2–SiC composites with 10, 20, and 30wt% SiC content. The optical micrographs of the ZrB_2 with 10, 20, and 30wt% SiC added phase are shown in Fig. 3a–c along with the maps of the peak intensities of the SiC TO mode (Fig. 3d–f). The location of the SiC grains could be easily detected on the 2D Raman maps, since it is represented by the high intensity of the TO band and is shown as a yellow/red spots of the map. The locations presented by the black color are ZrB_2 matrix. Based on the collected maps, the SiC peak positions have been analyzed as a function of the SiC content (Fig. 4). As one can see from Fig. 4, the definitive relationships exist between the amount of the SiC phase in ZrB_2–SiC composite and the position of the TO and LO bands of SiC. The position of the bands is directly related to the strain/stress in SiC grains and therefore could be used as an indicator of the existing thermal residual stresses if the piezo-spectroscopic calibration coefficient for each of the Raman active peaks was known. It is also important to relate the values of residual stresses to the mechanical properties of the ZrB_2–SiC composites, such as strength, fracture toughness, Young's modulus, etc.

7. Conclusions

It was shown that the ZrB_2 phase is weakly Raman active and exhibits two Raman bands which are very difficult to separate from the background. There is an established dependence between the content of the SiC in ZrB_2–SiC ceramic composite and peak positions of TO and LO Raman bands of SiC phase. Therefore, it is possible, by way of the proper calibration, to establish the piezospectroscopic coefficients and perform the calculation of the surface residual microstress distribution in ZrB_2–SiC UHTC ceramic composites. Further research will include the exploration of the properties of the Raman bands of ZrB_2 – what is their nature, stress and temperature sensitivity, etc. The ZrB_2–SiC system must be studied by at least two lasers in order to establish if there are peaks that are caused by the electronic phase transitions in the impurities.

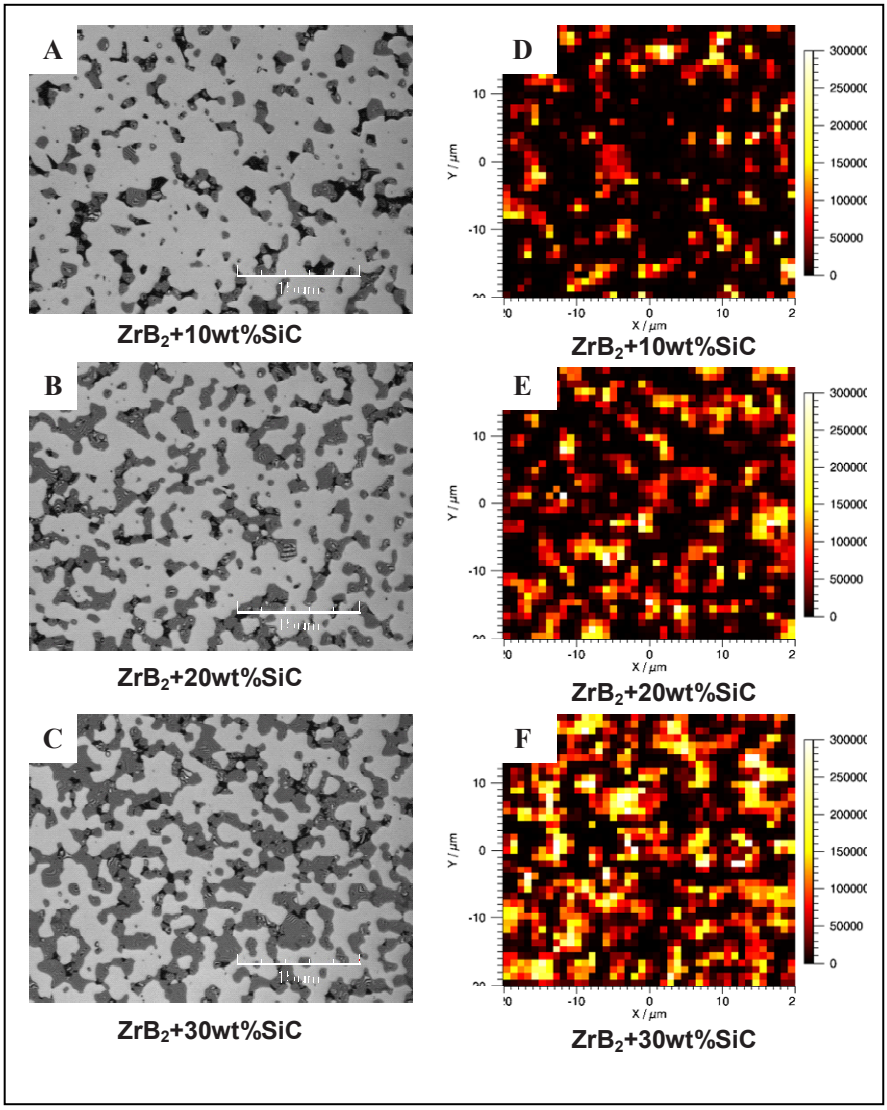

Figure 3. Optical micrographs (**a**–**c**) along with 2D Raman maps of the peak intensity of LO SiC band (**d**–**f**) of ZrB_2–SiC ceramic composite.

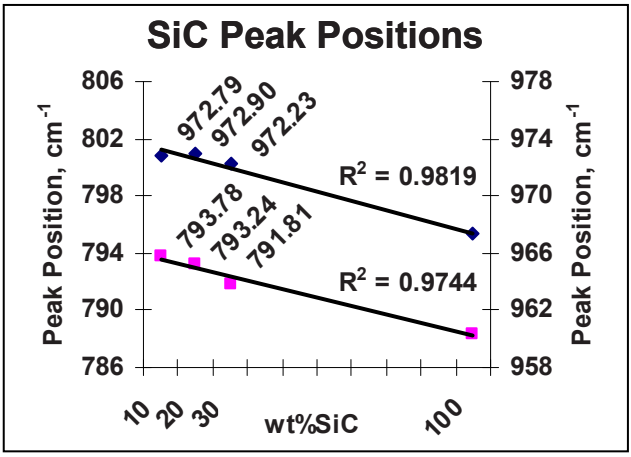

Figure 4. Peak positions of LO and TO SiC optic phonon modes measured in ZrB_2–SiC ceramic composite as a function of SiC amount. For comparison, the positions of LO and TO peaks in pure ceramics is provided.

Acknowledgment

This work was supported by NSF project 0748364 "CAREER: Hard and tough boron rich ceramic laminates designed to contain thermal residual stresses".

References

1. http://www.wpafb.af.mil/library/factsheets/factsheet.asp?id=9222.
2. Boyd, I.D., Padilla, J.F., Simulation of sharp leading edge aerothermodynamics, 12th AIAA International Space Planes and Hypersonic System and Technologies, American Institute of Aeronautics and Astronautics, 15–19 December 2003, Norfolk, Virginia, 2003–7062.
3. Brown, A.S., Hypersonic designs with a SHARP edge, *Aerospace America*, 9, 20–21, 1997.
4. Steeves, C.A., He, M., Valdevit, L., Evans, A.G., Metallic structural heat pipes as sharp leading edges from MACH 7 vehicles, IMECE2007-42397, Proceedings of IMECE 2007, ASME International Mechanical Engineering Congress and Exposition, November 11–15, 2007, Seattle, USA.
5. Erbland, P. J., Duffield, C., Homan, D., Gillard, W., Technology development roadmap for the space operations vehicle, AIAA2001-4604, Space 2001 Conference and Exposition, Albuquerque, NM, 2001.
6. Steeves, C.A., Valdevit, L., He, M., Evans, A., Structural heat pipes as sharp leading edges for Mach 7 vehicles, Proceedings of IMECE2007-42397, ASME International Mechanical Engineering Congress and Exposition, November 11–15, 2007, Seattle, USA.

7. Loehman, R., Corral, E., Dumm, H.P., Kotula, P., Tandon, R., Ultra-high temperature ceramics for hypersonic vehicle applications, Sandia Report, Sandia National Laboratories (SAND 2006-2925).
8. NSF-AFOSR Joint Workshop on "Future ultra-high temperature materials," Draft Workshop Report, National Science Foundation, April 12, 2004.
9. Fahrenholtz, W.G., Hilmas, G.E., Talmy, I.G., Zaykoski, J.A., Refractory diborides of zirconium and hafnium, *J. Am. Ceram. Soc*., 90, 5, 1347–1364, 2007.
10. Opeka, M.M., Talmy, I.G., Zaykoski, J.A., Oxidation-based materials selection for 2000 degrees C plus hypersonic aerosurfaces: Theoretical considerations and historical experience, *J. Mater. Sci.,* 39, 19, 5887–5904, 2004.
11. Van Wie DM, Drewry DG JR, King DE and Hudson CM, The hypersonic environment: Required operating conditions and design challenges, *J. Mater. Sci.*, 39, 19, 5915–5924, 2004.
12. Jackson TA, Eklund DR and Fink AJ, High speed propulsion: Performance advantage of advanced materials, *J. Mater. Sci.*, 39, 19, 5905–5913, 2004.
13. Cutler, R.A., In Ceramics and Glasses, Engineered Materials Handbook, Ed. Schneider, S.J., ASM International, Materials Park, OH, 787, 1991.
14. Opila, E., Levine, S., Lorincz, Oxidation of ZrB_2- and HfB_2-based ultra-high temperature ceramics: Effect of Ta additions, *J. Mat. Sci*., 39, 5969–5977, 2004.
15. Rezaie, A., Fahrenholtz, W., Hilmas, G.E., Evolution of structure during the oxidation of zirconium diboride-silicon carbide in air up to 1500^{o}C, *J. Europ. Ceram. Soc*., 27, 2495–2501, 2007.
16. Kalish, D., Clougherty, E.V., Kreder, K., Strength, fracture mode, and thermal stress resistance of HfB_2 and ZrB_2, *J. Am. Ceram. Soc*., 52, 1, 3036, 1969.
17. McHalle, A.E., (Ed.), Data Vollected from Phase Diagrams for Ceramics, Vol.X, American Ceramic Society, Westerville, OH, 1994.
18. Cutler, R.A., Engineering Properties of Borides, pp.787–803 in Ceramics and Glasses: Engineering Materilas Handbook, Vol. 4, Ed. Schneider, S.J., ASM International, Materials Park, OH, 1991.
19. Wuchina, E., Opeka, M., Causey, S., Buesking, K., Spain, J., Cull, A., Routbort, J., Guitirrez-Mora, F., Designing for ultra high temperature applications: The mechanical and thermal properties of HfB_2, HfC_x, and α-Hf(N), *J. Mater. Sci*., 39, 19, 5939–5949, 2004.
20. Malendez-Martinez, J.J., Dominguez-Rodriguez, A., Manteverde, F., Melandri, C., de Portu, G., Characterization and high temperature mechanical properties of zirconium boride-based materials, *J. Europ. Ceram. Soc*., 22, 2543–2549, 2002.
21. Chamberlain, A.L., Fahrenholtz, W., Hilmas, G., Ellerby, D.T., High strength ZrB_2-based ceramics, *J. Am. Ceram. Soc*., 87, 6, 1170-1172, 2004.
22. Koester, R.D., Moak, D.P., Hot hardness of selected borides, oxides, and carbides to 1900^{o}C, *J. Am. Ceram. Soc.*, 50, 6, 290–296, 1967.
23. Sanders, W.A., Probst, H.B., Hardness of five borides at 1625^{o}C, *J. Am. Ceram. Soc*., 49, 4, 231–232, 1966.
24. Bsenko, L., Lundstrom, T., The high temperature hardness of ZrB_2 and HfB_2, *J. Less Common Metals*, 34, 2, 273–278, 1974.
25. Mortz, C., Zirconium Diboride, *Am. Ceram. Soc. Bull*., 73, 6, 141–142, 1994; Cutler, R.A., Engineering Properties of Borides, 787, in Engineered Materials Handbook, Ceramics and Glasses, 4, ASM Handbook, Ed. By S.J. Schneider, The Materials Information Society, USA, 1991.
26. Powell, C.F., in Borides in High Temperature Materials and Technology, Ed. By I.E. Campbell, E.M. Sherwood, John Wiley & Sons Inc., New York, 1967.

27. Schwarzkopf, P., Kieffer, R., Refractory Hard Metals: Borides, Carbides, Nitrides, and Silicides, Macmillan, New York, 1953; Sigl, L.S., Schwatz, K.A., in D. Emin (Ed.), Boron Rich Solids, AIP Conference Proceedings, 231, American Institute of Physics, New York, 468–472, 1991.
28. Opeka, M.M., Talmy, I.G., Zaykoski, J.A., Oxidation-based materials selection for 2000°C hypersonic aerosurfaces: Theoretical considerations and historical experience, *J. Mater. Sci*., 39, 5887–5904, 2004.
29. Setoudeh, N., Welham, N.J., Formation of zirconium diboride (ZrB_2) by room temperature mechanochemical reaction between ZrO_2, B_2O_3 and Mg, *J. Alloys and Comp*., 420, 225–228, 2006.
30. Opeka, M., Talmy, I., Wuchina, E., Zaykoski, J., Causey, S., Mechanical, thermal, and oxidation properties of refractory hafnium and zirconium compounds, *J. Europ. Ceram. Soc*., 19, 2405–2414, 1999.
31. Keihn, F.G., Keplin, E.J., High temperature thermal expansion of certain group IV and group V diborides, *J. Am. Ceram. Soc*., 50, 2, 81–84, 1967.
32. Mahmud, S.T., Islam, A.K.M.A., Islam, F.N., VB_2 and ZrB_2: a density functional study, *J. Phys.: Condens. Matter*, 16, 2335–2344, 2004.
33. Fahrenholtz, W.G., The ZrB_2 volatility diagram, *J. Am. Ceram. Soc*., 88, 12, 3509–3512, 2005.
34. Monteverde, F., Bellosi, A., Guicciardi, S., Processing and properties of zirconium diboride based composites, *J. Europ. Ceram. Soc*., 22, 3, 279–288, 2002.
35. Milman, V., Winkler, B., Probert, M.I., Stiffness and thermal expansion of ZrB_2: and ab initio study, *J. Phys.: Condens. Matter*, 17, 2233–2241, 2005.
36. Dye, D., Stone, H.J., Reed, R.C., Intergranular and interphase microstresses, *Current Opinion in Solid State and Materials Science*, 5, 31–37, 2001.
37. Davidge, R.W., Green, T.J., The strength of two-phase ceramic/glass materials, *J. Mater. Sci.*, 3, 629–634, 1968.
38. Selsing, J., Internal stresses in ceramics, *J. Am. Ceram. Soc.*, 44, 419–426, 1961.
39. Kingery, W.D., Note on thermal expansion and microstresses in two-phase compositions, *J. Am. Ceram. Soc.*, 40, 10, 351–352, 1957.
40. Grigoriev, O.N., Krell, A., Trefilov, V.I., Determination of thermal residual stresses in single phase ceramic materials, *Zavodskaya Laboratoriya*, (in Russian) 7, 36–39, 1990.
41. Krell, A., Grigoriev, O.N., Residual stresses and microporosity in oxide ceramics, *Sprechsaal*, 123, 10, 1012–1015, 1990.
42. Krell, A., Teresiak, A., Schlaefer, D., Grain size dependent residual microsresses in submicron Al_2O_3 and ZrO_2, *J. Europ. Ceram. Soc*., 16, 803–811, 1996.
43. Clausen, B., Lorentzen, T., Leffers, T., Self-consistent modeling of the plastic deformation of FCC polycrystals and its implications for diffraction measurements of internal stresses, *Acta Mater.*, 46, 9, 3087–3098, 1998.
44. Wu, C.Cm., Freiman, S.W., Rice, R.W., Mecholsky, J.J., Microstructural aspects of crack propagation in ceramics, *J. Mater. Sci.*, 13, 12, 2659–2670, 1978.
45. Green, D.J., Microcraking mechanisms in ceramics, In Fracture Mechanics of Ceramics, Vol. 5, Eds. Bradt, R.C., Evans, A.G., Hasselman, D.P.H., Lange, F.F., Plenum Press, New York, 1983, pp. 457–478.
46. Evans, A.G., Microfracture from thermal expansion anisotropy – I. Single phase systems, *Acta Metall*., 26, 12, 1845–1853, 1978.
47. Heuer, A.H., Ruehle, M., On the nucleation of the martensitic transformation in zirconia (ZrO_2), *Acta Metall*., 33, 12, 2101–2112, 1985.
48. Schmauder, S., Schubert, H., Significance of internal stresses for the martensitic transformation in yttria-stabilized tetragonal zirconia polycrystals during degradation, *J. Am. Ceram. Soc.*, 69, 7, 534–540, 1986.

49. Becher, P.F., Feber, M.K., Grain size dependence of the slow crack growth behavior in noncubic ceramics, *Acta Metall.*, 33, 7, 1217–1221, 1985.
50. Almer, J.D., Cohen, J.B., Moran, B., The effects of residual macrostresses and microstresses on fatigue crack initiation, *Materials Science and Engineering*, A284, 268–279, 2000.
51. Pompe, W., Kreher, W., Theoretical approach to energy-dissopative mechanisms in zirconia and other ceramics, In Advances in Ceramics, Vol. 12, (Zirconia II), Eds. N. Claussen, M. Ruehle, A.H. Heuer, The American Ceramic Society, Columbus, Ohio, 1983, pp.283–292.
52. Fu, Y., Evans, A.G., Microcrack zone formation in single phase polycrystals, *Acta Metall*., 30, 8, 1619–1625, 1982.
53. Vajeeston, P., Ravindran, P., Ravi, C., Asokamani, R., Electronic structure, bonding, and ground state properties of AlB2-type transition metal diborides, *Phys.Rev.B*, 63, 4, 04115-1-11, 2001.
54. Opeka, M.M., Talmy, I., Wuchina, E.J., Zaykoski, J.A., Causey, S.J., Mechanical, thermal, and oxidation properties of hafnium and zirconium compounds, *J. Eur. Ceram. Soc*., 19, 13–14, 2405–2414, 1999.
55. Wiley, D.E., Manning, W.R., Hunter, O., Elastic properties of polycrystalline TiB_2, ZrB_2, and HfB_2 from room temperature to 1300K, *J. Less-Common Metals*, 18, 149–157, 1969.
56. Talwar, D.N., Sherbondy, J.C., Thermal expansion coefficient of 3C-SiC, *Appl Phys Lett*, 67, 22, 3301–3303, 1995.
57. Su, C.M., Wuttiga, M., Fekade, A., Spencer, M., Elastic and anelastic properties of chemical-vapor-deposited epitaxial 3C-SiC, *J. Appl Phys*, 77, 11, 5611–5615, 1995.
58. Chawla KK, Ceramic Matrix Composites, Kluwer Academic Publishers, Massachusetts, 2003.
59. Eshellby, J.D., The determination of the elastic field of an ellipsoidal inclusion, and related problems, *Proc. Roy. Soc.*, A241, 376–396, 1957.
60. Taya, M., Hayashi, S., Kobayashi, A.S., Yoon, H.S., Toughening of a particulate-reinforced ceramic-matrix composite by thermal residual stress, *J. Am. Ceram. Soc.*, 73, 5, 1382–1391, 1990.
61. Kreher, W., Janssen, On microstructural residual stresses in particle reinforced ceramics, *J. Eur. Ceram. Soc.*, 10, 167, 1992.
62. Hsueh, C.-H., Becher, P.F., Residual thermal stresses in ceramic composites, *Mater. Sci. Eng. A*, 212, 1, 22, 1996.
63. Awaji, H., Choi, S.-M., Yagi, E., Mechanisms of toughening and strengthening in ceramic-based nanocomposites, *Mech. Mater.*, 34, 7, 411, 2002.
64. Chen J, De Wolf I. IEEE Trans Components Packaging Technol, 2004:1.
65. Gouadec, G., Colomban, P., Bansal, N., Raman study of Hi-Nicalon-fiber reinforced Celsian composites: II. Residual stress in fibers, *J. Am. Ceram. Soc*., 84, 5, 1136–1142, 2001.
66. Mu, M., Osswald, S., Gogotsi, Y., Winey, K.I., An in situ Raman spectroscopy study of stress transfer between carbon nanotubes and polymer, *Nanotechnology*, 20, 335703, 2009.
67. Lucazeau. G., Abello, L., Micro-Raman analysis of residual stresses and phase transformations in crystalline silicon under microindentation, *J. Mat. Res.*, 12, 9, 2262–2273, 1997.
68. Gogotsi, Y., Baek, C., Kirscht, F., Processing-induced phase transformations and residual stress in silicon, *Semicond. Sci. Technol.* 14. 10, 928–935, 1999.
69. Orlovskaya, N., Kuebler, J., Subbotin, V., Lugovy, Design of Si_3N_4 based ceramic laminates by residual stresses, *J. Mat. Sci*., 40, 5443–5450, 2005.

70. Pezzotti, G., In situ study of fracture mechanisms in advanced ceramics using fluorescence and Raman microprobe spectroscopy, *J. Raman Spectrosc*., 30, 867–875, 1999.
71. DiGregorio, J.F., Furtak, T.E., Analysis of residual stress in 6H-SIC particles within AL_2O_3/SIC composites through Raman spectroscopy *J. Am. Ceram. Soc*., 75, 1854–1857, 1992.
72. Pezzotti, G., Sergo, V., Sbaizero, Muraki, N., Meriani, S., Nishida, T., Strengthening contribution arising from residual stresses in Al_2O_3/ZrO_2 composites: a piezo-spectroscopy investigation, *J. Eur. Ceram. Soc.*, 19, 247–253, 1999.
73. Orlovskaya, N., Steinmetz, D., Yarmolenko, S., Pai, D., Sankar, J., Goodenough, J., Detection of temperature and stress induced modifications of $LaCoO_3$ by micro-Raman spectroscopy, *Phys. Rev. B*, 72, 014122-1-7, 2005.
74. Orlovskaya, N., Lugovy, M., Carpenter, C., Pathak, S., Steinmetz, D., Lara-Curcio, E., Klemenz,C., Radovic, M., On thermal and vibrational properties of $LaGaO_3$ single crystals, *Acta Materialia,* 57, 2984–2992, 2009.
75. Lukich, S., Carpenter, C., Orlovskaya, N., Temperature and stress induced changes of the vibrational response of cubic and rhombohedral 10 mol%Sc_2O_3-1 mol%CeO_2-ZrO_2 ceramics, *J. Power Sources*, 195, 8, 2301–2309, 2010.
76. Limarga, A.M., Clarke, D.R., Piezo-spectroscopic coefficients of tetragonal-prime yttria-stabilized zirconia, *J. Am. Ceram. Soc*., 90, 4, 1272–1275, 2007.
77. Li, M., Feng, Z., Xiong, G., Ying, P., Xin, Q., Li, C., Phase transformation in the surface region of zirconia detected by UV Raman spectroscopy, *J. Phys. Chem. B*, 105, 8107–8111, 2001.
78. Puech, P., Demangeot, F., Frandon, J., Pinquier, C., Kuball, M., Domnich, V., Gogotsi, GaN nanoindentation: A micro-Raman spectroscopy study of local strain fields, *J. Appl. Physics*, 96, 5, 2853–2856, 2004.
79. Ghosh, D., Subhash, G., Orlovskaya, N., Scratch-induced residual stress measurements within SiC particles in a ZrB_2 – SiC composite using micro-Raman spectroscopy, *Acta Mater*., 56, 5345–5354, 2008.
80. Donohue, M., Carpenter, C., Orlovskaya, N., Stress effect on vibrational properties of ZrB_2–SiC ceramic composites, unpublished results.
81. Mukaida, H., Okumura, H., Lee, J.H., Diamon, H., Sakuma, E., Misawa, S., Endo, K., Yoshida, S., *J. Appl. Phys*., 62, 254, 1987.
82. Rohmfeld, S., Hundhausen, M., Ley, L., Raman scattering in polycrystalline 3C-SiC: Influence of stacking faults, *Phys. Rev. B*, 58, 15, 9558–9862, 1998.
83. Feng, Z.C., Choyke, W.J., Powell, J.A., Raman determination of layer stresses and strains for heterostructures and its application to the cubic SiC/Si system, *J. Appl. Phys.,* 64, 12, 6827–6835, 1988.
84. Sciti, D., Guicciardi, S., Celotti, G., Tochino, S., Pezzotti, G., Analysis of residual stresses in ternary electroconductive composites, *Appl. Phys. A*, 82, 317–324, 2006.
85. Cadeville, M.C., Meyer, A.J.P., Hebd, C.R., *Seances Acad. Sci*., 255, 3391, 1962.
86. Liu, S.H., Kopp, L., England, W.B., Myron, H.W., Energy-bands, electronic properties and magnetic ordering of CrB_2, *Phys. Rev. B*, 11, 9, 3463–3468, 1975.
87. Ihara, H., Hirabayashi, M., Nakagawa, H., Band structure and X-ray photoelectron spectrum of ZrB_2, *Phys. Rev. B*, 16, 2, 726–730, 1977.
88. Perkins, P.G., Sweeney, A.V.J., Investigation of electronic band structures of NaB_6, KB_6, TiB_2, and CrB, *J. Less-Common Met*., 47, 165–173, 1976.
89. Deligoz, E., Colakoglu, K., Ciftci, Y.O., Phonon dispersion and thermodynamical properties in ZrB_2, NbB_2, and MoB_2, *Solid State Communications*, in press, 2010.
90. Samsonov, G.V., Serebryakova, T.I., Neronov, V.A., Borides, Atomizdat, Moscow, 1975.

91. Shein, I.R., Ivanovski, A.L., The band structure of hexagonal diborides ZrB_2, VB_2, and TaB_2 in comparison with superconducting MgB_2, *Phys. Solid State* (translation of Fizika Tverdogo Tela (Sankt-Peterburg)), 44, 10, 1833–1839, 2002.
92. Spear, K.E., Chemical bonding in AlB_2-type borides, *J.Less-Common Metals*, 47, 195–201, 1976.
93. Grimvall, G., Guillermet, A.F., Phase stability properties of transition metal diborides, pp. 423–430 in Boron-Rich Solids, AIP Conference Proceedings, Vol. 231, Eds. Emin, D., Aselage, T.L., Switendick, A.C., Morosin, B., Beckel, C.L., American Institute of Physics, New York, 1990.
94. Epelbaum, V.A., Gurevich, M.A., On Zr-B phase diagram: Formation of ZrB_2 phase, *Zh. Fiz. Khim*., 32, 2274, 1958 (Russian).

SYNTHESIS AND SINTERING STRATEGIES OF BORON RICH SOLIDS

LINA SARTINSKA*
Institute for Problems of Materials Science, Kyiv, Ukraine

Abstract In this contribution the recent results on a catalyst-free transformation of fine-grained graphite-like h-BN powders and h-BN – lamp black composite are presented. The transformation to nanotubes, fullerenes, whiskers and crystals was performed in an optical furnace under a light-induced heating effect in a flow of dried and purified nitrogen. It was demonstrated that obtained whiskers are multiwalled nanotubes which are covered with polycrystalline shell. Structure, morphology and phase composition of the new structures were studied by transmission electron microscopy (TEM), scanning electron microscopy (SEM), optical microscopy and X-ray Diffraction (XRD) study. The new structures deposition results in a formation of a coating on the titanium electrodes for detection of a dissolved oxygen. Boron nitride coating didn't improve properties of the titanium electrodes. However, coatings produced after h-BN – lamp black composite transformation were stable and catalytically active in the oxygen electro-reduction process in physiologic NaCl solution. A x-ray Diffraction study has shown a prevalence of carbon amorphous phases in composition of these coatings.

Keywords: light-induced heating, boron nitride and lamp black transformation, catalytic activity

1. Introduction

There is fundamental altering of the electrical properties of materials when the quantum effects come into play, because the behavior of individual atoms becomes significant on the nanostructure level. Just after the discovery of carbon nanotubes, boron nitride nanotubes (BNNTs) were prepared by Chopra et al. [1] in 1995. In contrast to carbon nanotubes, BNNTs have semiconducting properties, with a large band gap, which is independent of the diameter and chirality of the nanotube.

* Lina Sartinska, Institute for Problems of Materials Science, Kyiv, Ukraine, e-mail: sart@ipms.kiev.ua

N. Orlovskaya and M. Lugovy (eds.), *Boron Rich Solids: Sensors, Ultra High Temperature Ceramics, Thermoelectrics, Armor*, DOI 10.1007/978-90-481-9818-4_20,

High-temperature methods for the preparation of nanostructures all involve sublimation or melting and evaporation in a reduced atmosphere or rare (inert) gases, brought to temperatures above 3,200^{o}C and condensing the resulting vapor under a high temperature gradient. What is different about the various processes is the method used for sublimating. As an optical furnace can be used instead of a solar furnace, it was researched that the formation of nanostructures of boron nitride and carbon in nitrogen flow in an optical furnace.

A report [2] declared that electrical characteristics of the BN film are strongly influenced by humidity, suggesting application to a sensor. The absorption and reactivity of O_2 on perfect and defective boron nitride nanotubes were investigated employing the density-functional theory. Obtained results indicate that O_2 prefers to physically adsorb on perfect BNNT. The point defects on the wall of BN nanotubes reduce the oxidation resistance of the tubes. The electronic properties analysis indicates that chemisorbed O_2 can reduce the energy-gap of BN tubes [3].

Recently, boron carbon nitride (BCN) has attracted much attention due to its potential for having highly desirable mechanical, thermal, electrical, and optical properties. The BCN compounds with the layered structures should have properties intermediate between those of graphite and hexagonal boron nitride (h-BN). For example, polyhedral and tubular graphitic nanoparticles made of carbon layers and boron nitride (BN) layers have been synthesized [4].

Electronic and structural properties of CO and NO molecules adsorbed on boron nitride nanotubes (BNNTs) and carbon doped BNNTs have been investigated using first principles calculations [5]. The results indicated that for non defective nanotubes, small binding energies are obtained. When a carbon substitution impurity is present in the BNNT the binding energies are substantially increased and a chemical adsorption is observed. The calculated band structures show that the defect electronic levels inside the band gap are sensitive to the presence of the adsorbed molecules. This increasing of the functionalization capacity of the tubes due to carbon doping is an important mechanism to open up new possibilities for nanodevices applications.

It is known that there is an urgent necessity to develop devices sensing the presence of the oxygen in bioactive substances. Existing sensitive elements don't satisfy the requirements for use in medicine because of their grave shortcomings, particularly, a selectivity of devices. Thus, due to high sensitivity and selectivity of the oxygen, the electrochemical technique of an electro reduction process for the analysis of a concentration of oxygen in bioactive substances is the most promising. The selectivity of this technique emphasizes mainly the fact that a potential range of the oxygen

electro reduction process, that exclude an effect of other processes to compare with potentiometric technique.

Thus, producing the coating with proper structure and phase composition on the surface of titanium substrates in the result of transformations of fine-grained graphite-like h-BN powders and h-BN lamp black composite in nitrogen flow in an optical furnace for research of their electro-catalytic activity in the oxygen electro reduction process is a very important task.

2. Experimental

The platelet-like fine-grained powders of boron nitride (Chempur, CH070802) and lamp black have been used as an initial (Fig. 1). The origin powders are h-BN textured on 002 with impurity of B_2O_3. The diameter of platelets of boron nitride is ~0, 6 – 1, 0 μm and thickness – ~0, 1 μm. Detail description of initial powders and experimental presented in [6–10].

A quartz chamber was used for the process of sublimation, melting and evaporation of powders (Fig. 2). Heating the surface of initial powders was done in a furnace of high intensity optical energy in the flow of nitrogen. Light sources can produce over 2 kW of the energy concentrated in the focal zone. A diameter of the spot is 10 mm.

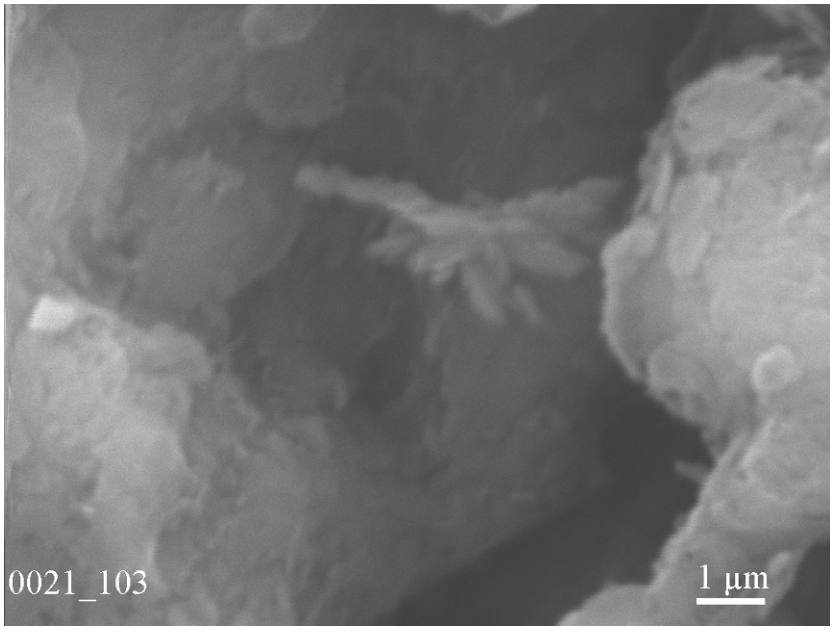

Figure 1. Electron micrograph of the initial powders of h-BN. A diameter of platelets 0, 6 – 1, 0 μm and a thickness – 0, 1 μm.

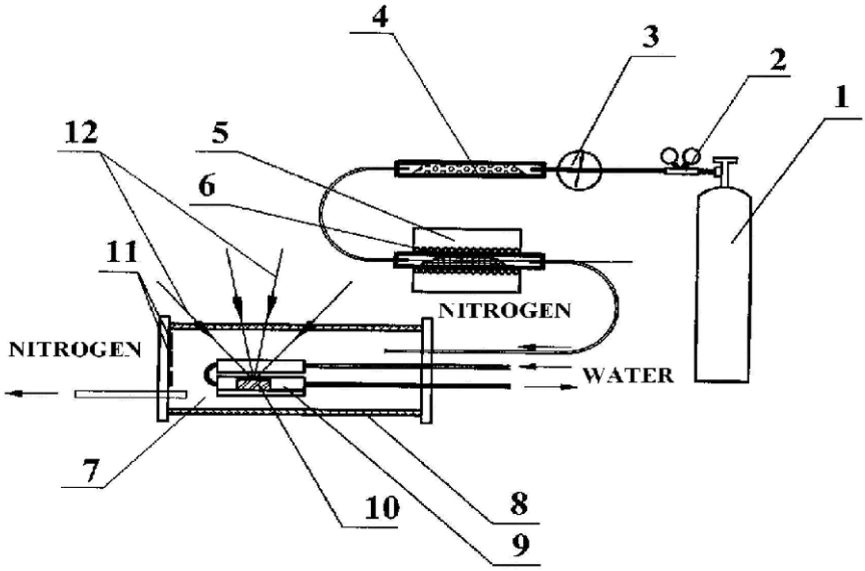

Figure 2. The experimental arrangement, where: 1 – a pressure tank filled by gaseous nitrogen; 2 – a pressure regulator; 3 – a pressure gauge; 4 – a glass tube filled by KOH; 5 – a furnace; 6 – copper chips; 7 – a working chamber; 8 – a quartz cylinder; 9 – copper screens cooled by water; 10 – an origin sample of h-BN; 11– flanges cooled by water and place for substrates; 12 – concentrated light flux.

The optical furnace involves three ellipsoidal reflectors and three xenon tubes which are centered in the focus of every ellipsoidal reflector. Direct measurements of the temperature were not provided. Sublimation, melting, and evaporation of h-BN was carried out at the average densities of energy of the light flux in a focal zone of set-up $E \sim 0,7 \cdot 10^4$ kW/m^2 which corresponds to ~1,400 K as an emission spectrum of the xenon tubes is closely matched by that of the black-body radiation [11]. The time of the experiment was 60 min.

Produced compacted samples of initial h-BN powders and h-BN – 25 wt% lamp black composite were tablets (diameter 20 mm and thickness 10 mm). The last were placed on a copper water-cooling screen of the quartz chamber (Fig. 2).

The chamber was flowed by purified and dried nitrogen. Cooper chips heated up to 500°C purified the nitrogen from oxygen and other pollutions. Platelets of KOH made drying of the nitrogen from the water.

Titanium foil was used as a substrate. In natural conditions the foil is oxidized to TiO_2 and is sensing to oxygen in the electro reduction process, however, its sensing ability is not enough to be sensing elements of the device. So, titanium foil was purified from TiO_2 in an etching solution

based on a mix of HF and HNO_3 and placed in a face of chamber (Fig. 2) to precipitate coatings.

All new structures on the surfaces of compacted samples and on the surface of titanium substrate were examined by scanning electron (SEM), transmission electron (TEM) and optical microscopes. X-ray Diffraction (XRD) study (diffractometer "DRON-3.0", radiation of K_{α} – Cu) has supplemented information about coatings.

The coated titanium foil was used as an electrode for sensing elements of the device to analyse an oxygen content in the electro reduction process, which can occur with participation of two or four electrons [12].

3. Results and Discussion

3.1. A SURFACE TRANSFORMATION OF H-BN AND H-BN – LAMP BLACK COMPOSITE AFTER PROCESSING IN AN OPTICAL FURNACE

Surface observation of the compacted samples of h-BN and h-BN – lamp black composite after processing in an optical furnace has demonstrated the formation of the new different structures (Figs. 3 and 4) because during heating in the central part of the light beam occurs sublimation, melting, evaporation and decomposition of the boron nitride and carbon. As a result, whiskers were formed at the edge of the crater on the surface of the compacted samples of the initial h-BN powders (Fig. 3). Such structures were not found in any of the other parts of the chamber. It means that a proper temperature gradient occurs in the compacting powder enabling vapor transporting from the lower part of the powder to the surface and the growth of filament structures only on the surface of compacted samples like in [13] under continues laser heating. The vapors of boron and nitrogen will re-condense and re-vaporize as they are rising and will favour the appearance of bushy whiskers around the crater edge during light heating if they keep the proper temperature gradient in the samples changeless. TEM investigations of their structure have demonstrated that whiskers consist of thin threads which are multiwalled nanotubes with a diameter about 80 nm covered by a shell or a case (Fig. 5). Apart from whiskers, there were tiny droplets around the crater which are a result of the splashing of melted boron nitride inside the crater (Fig. 3).

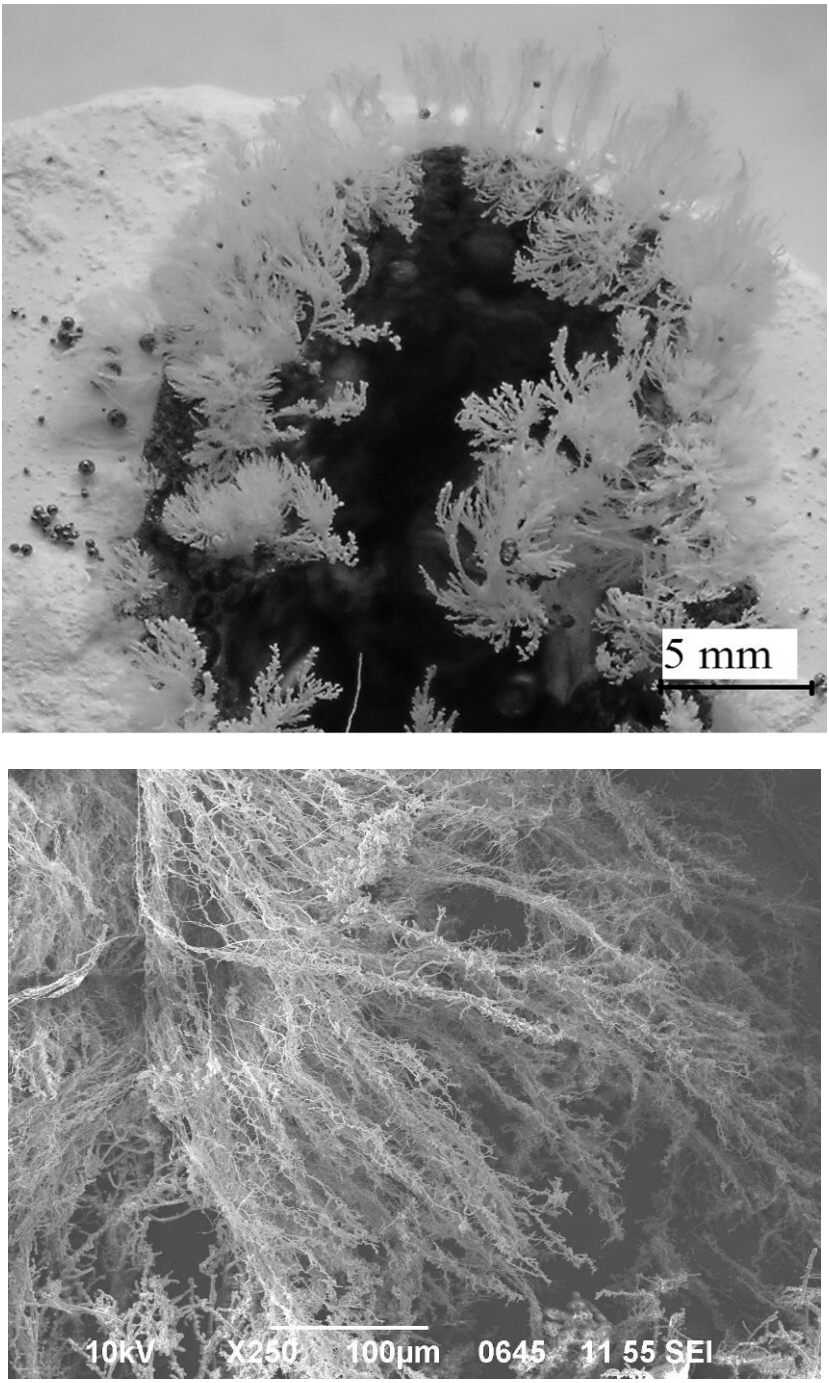

Figure 3. Transformations after processing in optical furnace on the surface of the compacted samples of the h-BN powders (a) and structure of the obtained whiskers (b).

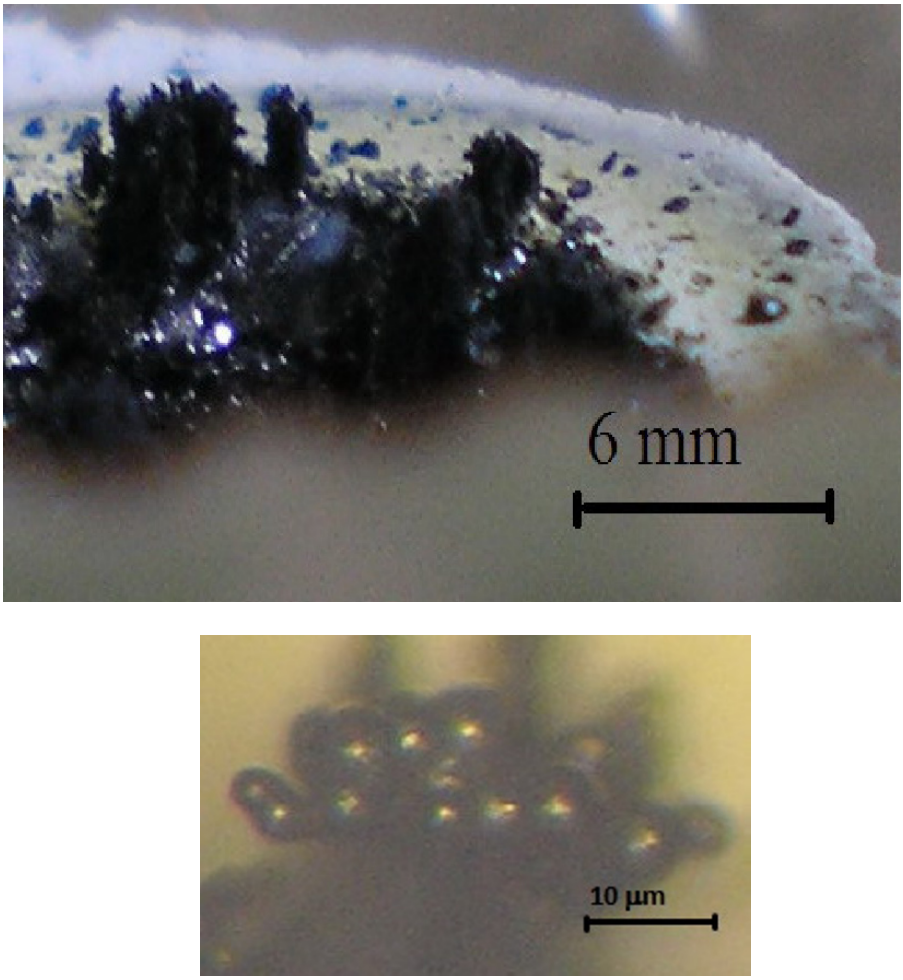

Figure 4. Transformations after processing in optical furnace. on the surface of the compacted samples of the h-BN - lamp black composite (a) and structure of the obtained material (b).

Structures produced on the surface of h-BN – lamp black composite are completely different (Fig. 4a). First of all, there is a rim around the crater with a width of about 4 mm, because for h-BN and lamp black, different heating is needed to initiate vaporization and melting. The morphology of the surface formed in the centre of the heated compacted sample of h-BN – lamp black composite indicates that the surface tension coefficient of melted h-BN – lamp black composite is lower than the surface tension coefficient of melted h-BN. Accordingly, the easy growth and bursting of the bubbles and also the modest pressure of the ambient atmosphere at the surface results in the formation of the coarse rock-like structure of the melted composite in the crater and its nonround fragments around (Fig. 4a). It was

demonstrated at a higher magnification that coarse structures consist of fullerene-like structures (Fig. 4b).

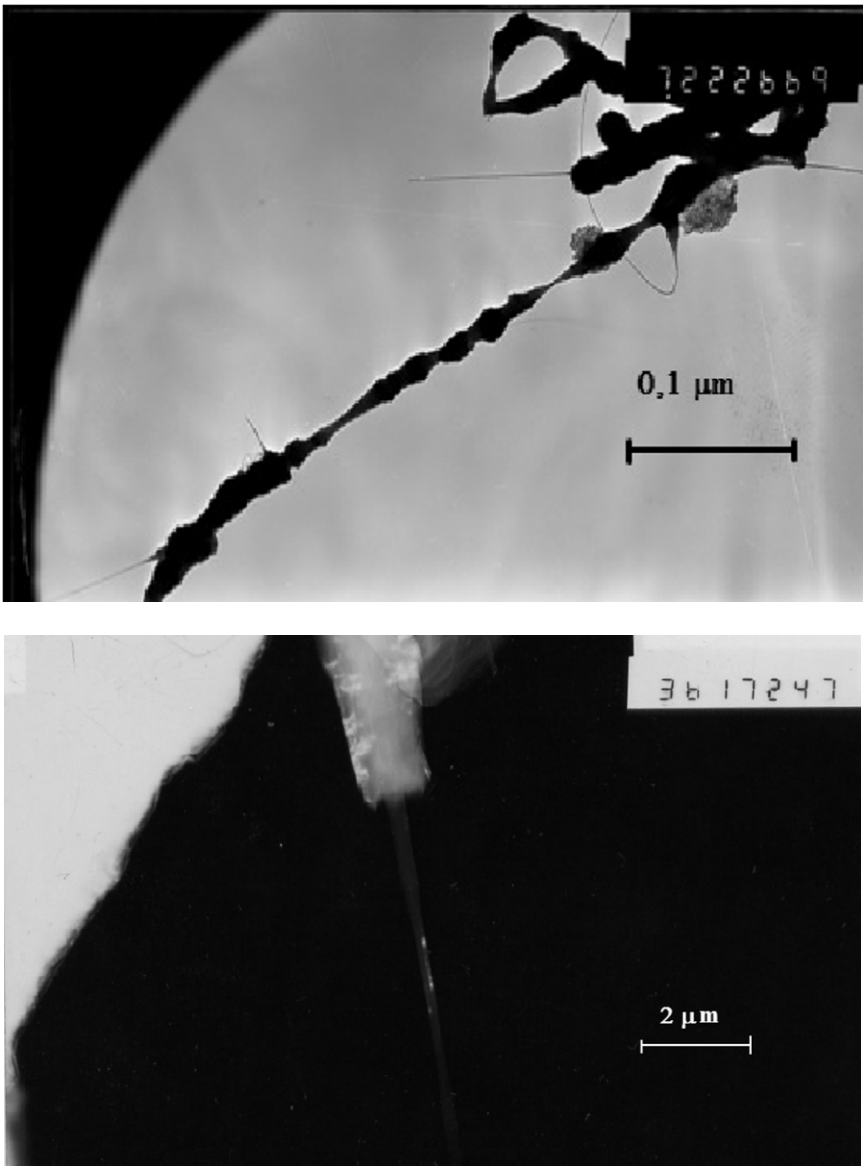

Figure 5. TEM study of the whiskers formed at the edge of the crater after processing in an optical furnace of h-BN: (a) whiskers consist of the thin threads; (b) step fracture across the fiber of whiskers.

3.2. STRUCTURES PRECIPITATED ONTO A SURFACE OF TITANIUM SUBSTRATE

Melting, sublimation and evaporation in the optical furnace results in transformations of h-BN and h-BN – 25 wt% lamp black composite argets and precipitation on a surface of a titanium substrate with nonuniform, thin

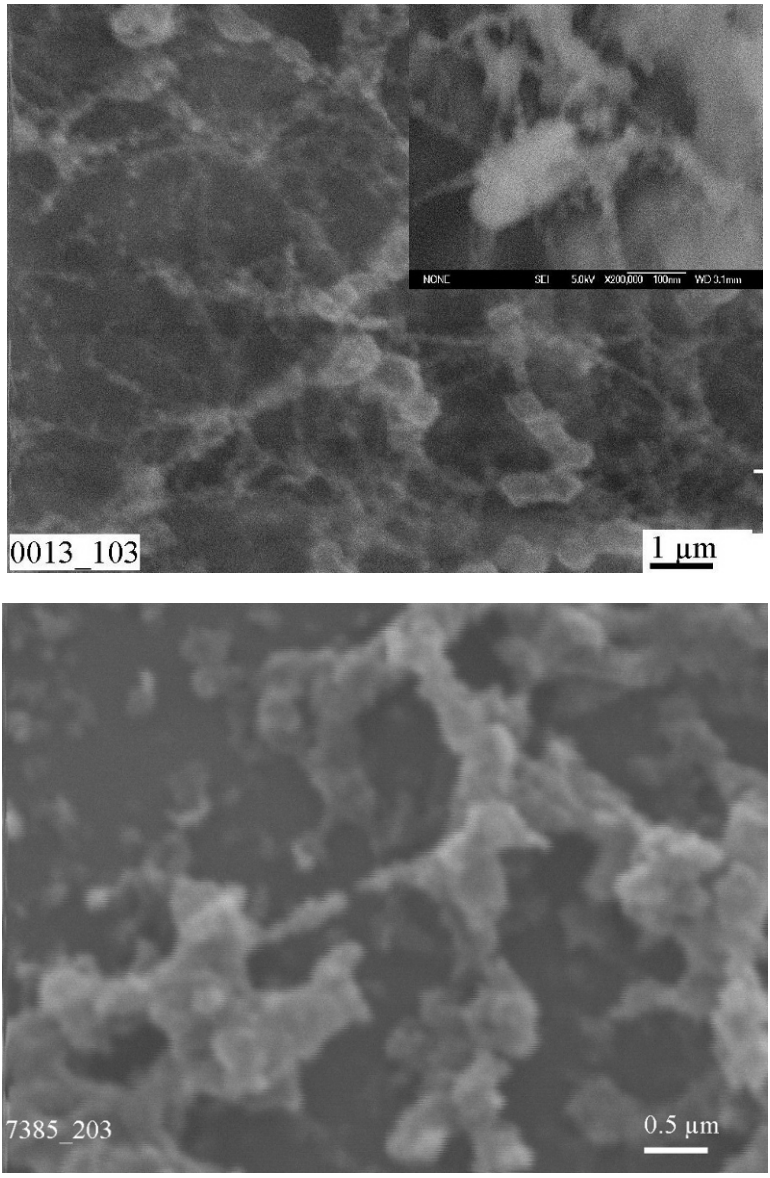

Figure 6. Micrographs of structures precipitated on the titanium substrate after processing the surface of the compacted samples in an optical furnace: (a) h-BN; (b) h-BN – lamp black composite.

coatings (Fig. 6). The formation of separate thread-like structures along with coarse equiaxed particles on titanium substrates has demonstrated SEM observations after transformation h-BN (Fig. 6a). Presumably, thread-like structures, being very volatile, were trapped by nitrogen flow from a sample surface and then precipitated on a substrate without an additive shell, which is formed inevitably around them on the surface of h-BN compacted initial sample [14]. The particles on the surface can appear due to their capture by nitrogen flow from the heated sites of a sample during sublimation and vaporizing.

The separate threat-like structures had a diameter of about 80 nm (Fig. 6a). The equiaxed particles with a mean size of about 200 nm (Fig. 6) form obtained coatings in conditions of high temperature gradients.

Carefully TEM investigations of the precipitated coating after processing in an optical furnace h-BN – lamp black composite have also shown threat-like structures (Fig. 7), together with the equiaxed particles of different sizes, (Fig. 6) which were formed in the conditions of high temperature gradients.

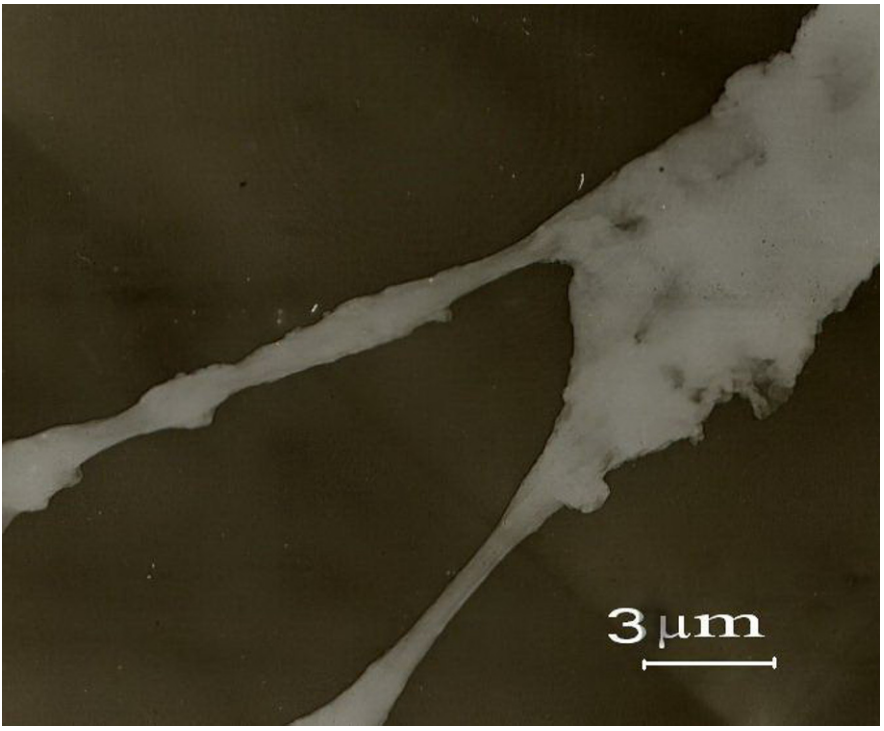

Figure 7. TEM study of the structures precipitated on the surface of titanium substrate after processing in an optical furnace h-BN – lamp black composite.

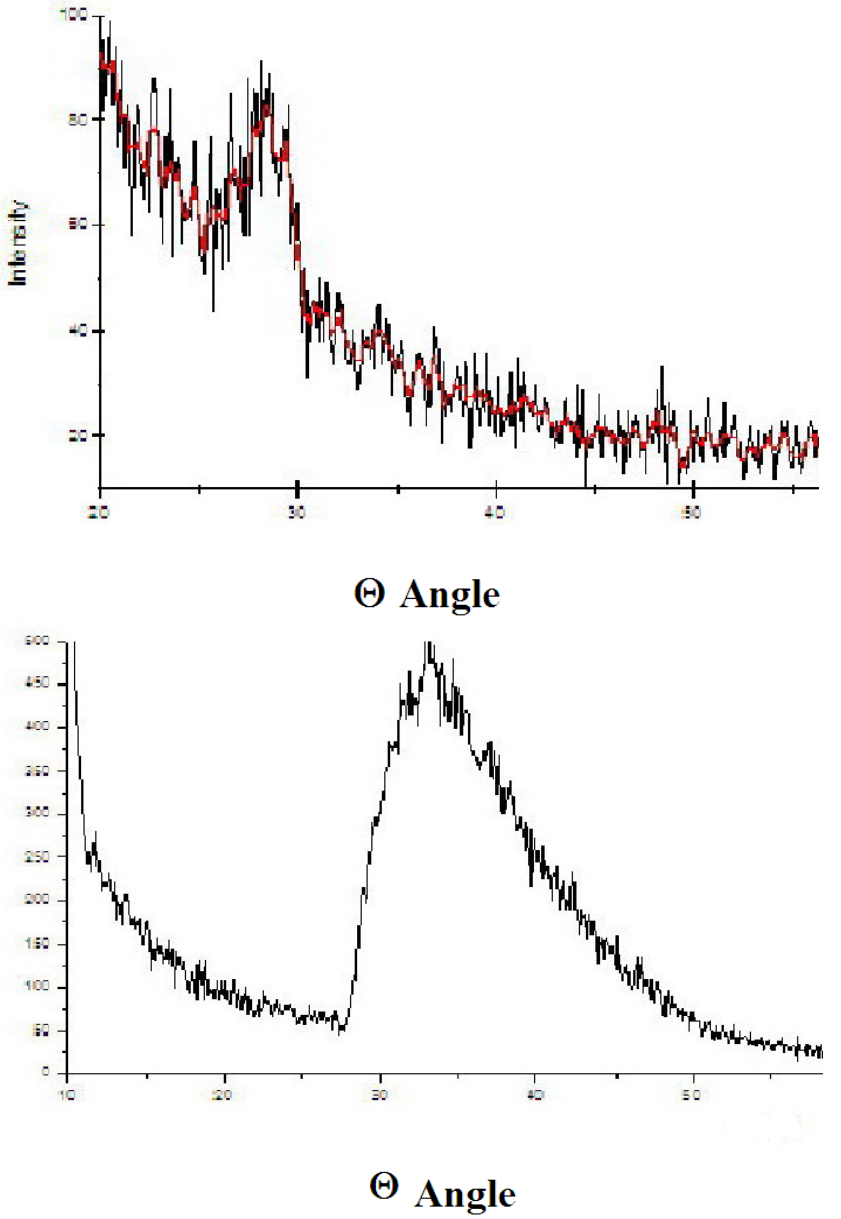

Figure 8. The results of X-ray Diffraction study of structures precipitated on titanium substrate after processing the surface of the compacted samples in an optical furnace: (a) h-BN; (b) h-BN – lamp black composite.

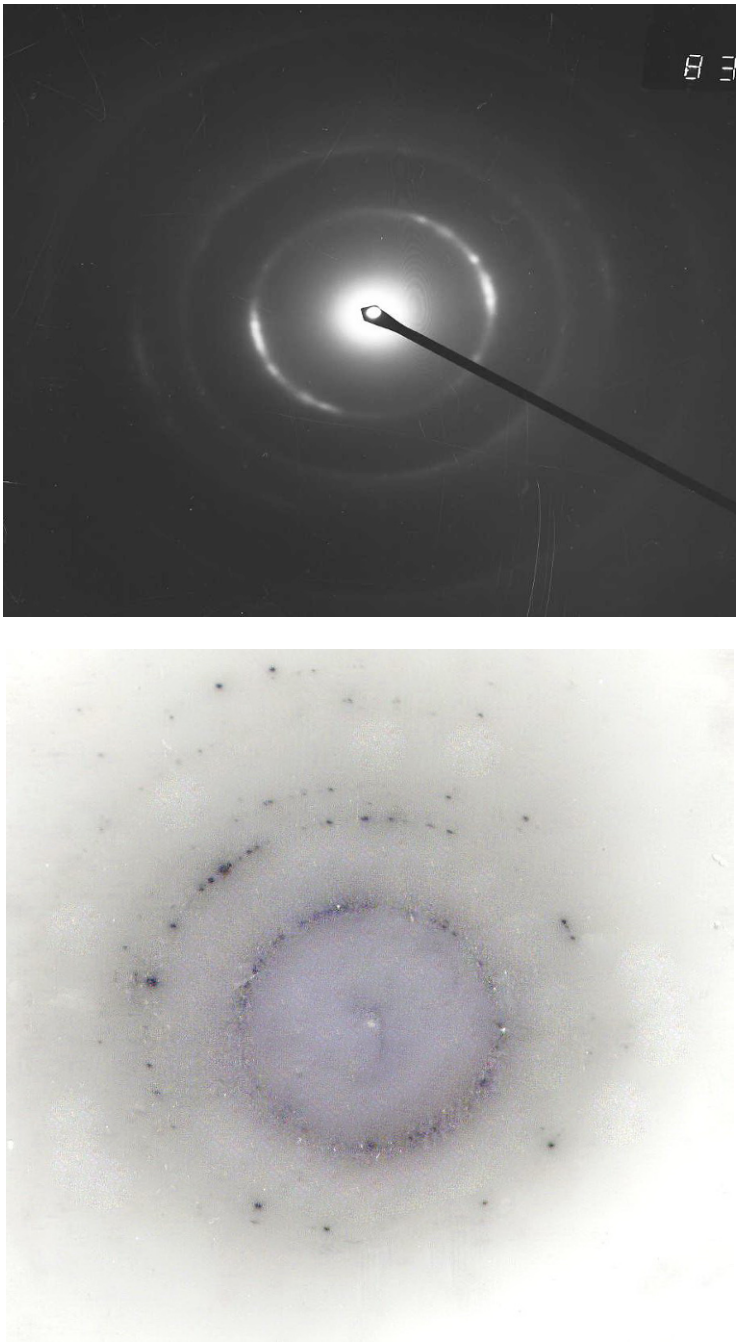

Figure 9. An electron diffraction patterns of structures precipitated on titanium substrate after processing of the surface of the compacted samples in an optical furnace h-BN (a) and h-BN – lamp black composite (b). Where: a – mixture of h-BN and boron-enriched tetragonal phase $B_{51,2}N$; (b) hexagonal $(BN)_{0,26}C_{0,74}$.

Structures of the coatings produced after transformations of h-BN in the hard condition of high temperature gradients are characterized by the XRD with a poor spectrum (Fig. 8a), which may be ascribed to nano grain size and poor crystallinity. Matching the data of the XRD study (Fig. 8a) with the results of electron-diffraction pattern analysis (Fig. 9a), it can take that phase composition of the precipitated material consists of amorphous phase, h-BN, boron-rich tetragonal $B_{51,2}N$ and $B_{25}N$ and also pure boron. The last are the tetragonal and rhombohedric phases of boron, which were formed through modest nitrogen pressure in the chamber and a high rate of transformations. However, it was not possible to get an electron-diffraction pattern of thread-like formations, because of the size of the electron beam and its power did not allow an investigation of a separate thread.

The XRD study also demonstrated complicated phase composition of the obtained coatings after transformations of h-BN – 25 wt% lamp black composite (Fig. 8b). Perhaps, like in [4] in conditions of high temperature gradients, precipitated particles are made of carbon and boron nitride layers. Based on XRD data it is safe to say that surface is covered by different graphite structures with a prevalence of carbon amorphous phases, although boron carbide and boron carbon nitride phases may also compose this precipitation. This phase composition can be explained by the lower temperature of the melting of the lamp black.

The results of the electron-diffraction pattern analysis of the separate particles precipitated on the surface of the titanium substrate after processing in an optical furnace h-BN – lamp black composite has shown that they are enriched boron, and have a hexagonal $(BN)_{0,26}C_{0,74}$ structure (Fig. 9b).

The research on electrocatalytic activity in the oxygen electroreduction process of the electrodes, with coatings precipitated after processing in an optical furnace compacted samples of h-BN in the physiological solution of NaCl, has not shown any improvement their properties. However, the electrodes with coatings precipitated after processing in an optical furnace compacted samples of h-BN – lamp black composite changed their sensitivity to better. It was shown, that on I–E curves the one polarographic wave of the O_2 reduction at potentials $E = -0.5 \div -1.4$ V (vs Ag/AgCl electrode) is observed (Fig. 10). Hydrogen appears at potential $E = -1{,}4$ V. The half-wave potential of oxygen electroreduction in the physiologic NaCl solution on these electrodes was $-0.45 \div -20.46$ V (vs Ag/AgCl electrode), dynamic interval of potentials of oxygen reduction $\Delta Å = -0.4$ V. The highest sensitivity of electrodes studied to dissolved oxygen was achieved at cathode potentials of −0.5 to −0.9 V (vs Ag/AgCl electrode) and was $(5–7)\cdot 10^{-6}$ g * l^{-1}, which is close to the sensitivity of Pt-electrode. Also, it has been found that the produced electrodes are characterized by high stability and reproducibility

of values in long-time potential cycling, which did not change after the third cycle.

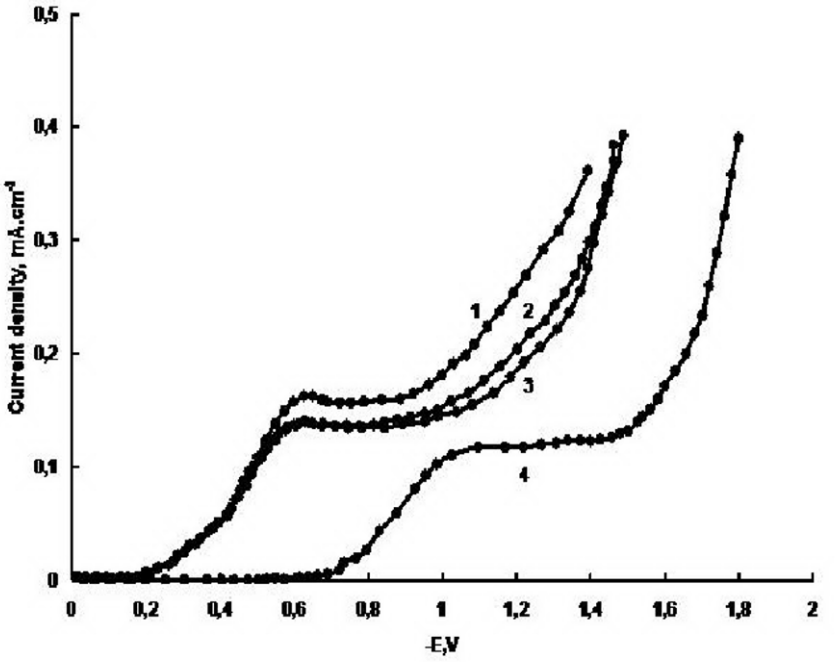

Figure 10. The polarized curves of the oxygen reduction on: 1–3 – B-N-C composite coated electrodes vs number of cycle (1–2nd cycle, 2,3 – 3rd and 4th cycles); 4 – on the titanium substrate with TiO_2 layer received by oxidation in natural conditions. A scanning speed of potential is 10 $mV.c^{-1}$.

4. Conclusion

Processing of fine-grained graphite-like and h-BN – lamp black composite in an optical furnace, in a flow of dried and purified nitrogen, results in nano-crystals, whiskers, nanotubes, and fullerenes formations. The obtained whiskers are multiwalled nanotubes which are covered with a polycrystalline shell.

The coatings produced after the h-BN powders transformation consist of a mixture of h-BN, a boron-enriched tetragonal phase of BN (B51,2N), pure boron, an amorphous phase, and are not catalytically active.

The processing of h-BN – lamp black composite conduces to the formation of the coatings and consists of amorphous carbon and hexagonal (BN) 0,26C0,74. These coatings are stable and catalytically active in oxygen electro-reduction processes in physiologic NaCl solution and can be used as the

sensitive elements in a device for the determination of the dissolved oxygen concentration in bioactive substances and other liquids.

Acknowledgements

I acknowledge the support of Frolov A.A. for the processing in an optical furnace; Timofeeva I.I. for XRD study; Danilenko M.I., Tinkov V.A. and Koval' A.Yu. for TEM and SEM investigations; Kolbasov G.Ya. and Vorobets V.S. for the research of electrocatalytic activity in the oxygen electroreduction process.

References

1. Nasreen G. Chopra, R. J. Luyken, K. Cherrey, Vincent H. Crespi, Marvin L. Cohen, Steven G. Louie, and A. Zettl. Boron Nitride Nanotubes. *Science* 18 August 1995: Vol. 269. no. 5226, pp. 966–967.
2. A. Soltani, P. Thévenin, H. Bakhtiar and A. Bath. Humidity effects on the electrical properties of hexagonal boron nitride thin films. Thin Solid Films Vol. 471, Issues 1–2, 3 January 2005, pp. 277–286.
3. Yong Chen, Chun-Li Hu, Jun-Qian Li, Gui-Xiao Jia, Yong-Fan Zhang. Theoretical study of O_2 adsorption and reactivity on single-walled boron nitride nanotubes. Chemical Physics Letters 449 (2007) 149–154.K.
4. K. Suenaga, C. Colliex, N. Demoncy, A. Loiseau, H. Pascard, F. Willaime. Synthesis of Nanoparticles and Nanotubes with Well-Separated Layers of Boron Nitride and Carbon. *Science* 24 October 1997: Vol. 278. no. 5338, pp. 653 – 655.
5. R.J. Baierle, T.M. Schmidt, A. Fazzio. Adsorption of CO and NO molecules on carbon doped boron nitride nanotubes. Solid State Communications 142 (2007) 49–53.
6. L.L.Sartinska, S. Barcikowski, N. Wardenga, B.M. Rud', I.I. Timofeeva, Laser Induced Modification of Surface Structures. Appl. Surface Science, Vol. 253, Issue 9, 2007, pp. 4295–4299.
7. L.L.Sartinska, L.L.Fedorenko, A.A.Frolov, I.I.Timofeeva, B.M.Rud', Nanostructure boron nitride fabrication. Int. conf. "Modern Materials Science: Achievements & Problems", Proceedings, 26–30 Sept. 2005. Kyiv, Ukraine, 729 – 730pp. (in Russian).
8. L.L.Sartinska, L.L.Fedorenko, A.A.Frolov, I.I.Timofeeva, B.M.Rud', Obtaining of nanostructure boron nitride. Digest: "Modern Problems of Physical Materials Science", Kyiv, IPMS NASU, Ukraine, 2005. 177–182pp. (in Russian).
9. A.A.Frolov, E.P.Andrievskaya, L.L.Sartinska, Peculiarity of physico-chemical interaction of concentrated solar radiation of the optical furnace and its application for solution of the materials science practical tasks. Int. conf. "Modern Materials Science: Achievements & Problems", Proceedings, 26–30 Sept. 2005. Kyiv, Ukraine, 174–175pp. (in Russian).
10. A.A.Frolov, L.L.Sartinska, A.Yu.Koval', Set-up for obtaining of nanostructure boron nitride by evaporation of concentrated solar radiation and condensation on the cooling surface. Science & Development of Techno Biosphere of Arctic:: Experience and Challenge Time. Proc. Int. Conf. 29 Nov.-1 Dec. 2005. Apatity, Russia, pp.128–130. (in Russian).

11. Laszlo, T. S., Image Furnace Techniques, Interscience, New York (1965).
12. Fetter K. Elektrochemische Kinetik. Berlin, Gottingen, Heidelberg: Springer-Verlag, 1961.
13. T. Laude, PhD thesis, Boron Nitride Nanotubes Grown by Non-Ablative Laser Heating: Synthesis, Characterization and Growth Processes. Two editions: University of Tsukuba and Ecole Centrale Paris (March 2001). (Ask: t.laude @ teijin.co.jp for a copy.)
14. L.L.Sartinska, A.A.Frolov, A.Yu..Koval', N.A.Danilenko, I.I.Timofeeva, B.M.Rud', Transformation of Fine-grained Graphite Boron Nitride Induced by Concentrated Light Energy. Materials Chemistry and Physics 109 (2008) 20–25.

FIELD-ASSISTED DENSIFICATION OF SUPERHARD B_6O MATERIALS WITH Y_2O_3/Al_2O_3 ADDITION

M. HERRMANN[1,*], J. RAETHEL[1], K. SEMPF[1], M. THIELE, A. BALES[1], I. SIGALAS[2]

[1] *Fraunhofer Institute of Ceramic Technologies and Systems, Dresden, Germany*

[2] *University of the Witwatersrand, Johannesburg, South Africa*

Abstract B_6O is a possible candidate of superhard materials with a hardness of 45 GPa measured on single crystals. Up to now, densification of these materials was only possible at high pressure. However, recently it was found that different oxides can be utilized as effective sintering additives. In this work the effect of addition of Y_2O_3/Al_2O_3 on the densification behaviour as a function of applied pressure, its microstructure evolution, and resulting mechanical properties were investigated. A strong dependence of the densification with increasing pressure was found. The material revealed characteristic triple junctions filled with amorphous residue composed of B_2O_3, Al_2O_3 and Y_2O_3, while no amorphous grain-boundary films were observed along internal interfaces. Mechanical testing revealed on average hardness of 33 GPa, a fracture toughness of 4 $MPam^{1/2}$, and a strength value of 500 MPa.

Keywords: Boron suboxide, sintering behavior, microstructure, mechanical properties

1. Introduction

B_6O-based materials are known as the hardest materials after diamond and cubic boron nitride, with a hardness of 45 GPa measured on single crystals [1–3]. However, in contrast to the promising properties, B_6O materials have not yet been used, because full densification requires high pressures (1–5 GPa) [4]. The materials densified at high pressures have good hardness but a very low fracture toughness of 1–2 $MPam^{0.5}$.

* M. Herrmann, Fraunhofer Institute of Ceramic Technologies and Systems, Dresden, Germany, e-mail: Mathias.Herrmann@ikts.fraunhofer.de.

N. Orlovskaya and M. Lugovy (eds.), *Boron Rich Solids: Sensors, Ultra High Temperature Ceramics, Thermoelectrics, Armor*, DOI 10.1007/978-90-481-9818-4_21,

Efforts have been made to enhance the fracture toughness of B_6O by forming B_6O composites with other hard materials such as diamond, boron carbide and cBN. These efforts result in high hardness values but still low fracture toughness values (<1.8 $MPam^{0.5}$) [5–7].

B_6O materials were prepared by hot pressing mixtures of B and B_2O_3 at temperatures up to 2,000°C [8, 9]. These materials had high microhardness, but no other mechanical properties were determined. Hot pressing of B_6O powders in a wide temperature range described by C. Brodhag et al. resulted only in porous materials [10].

Recently, it was reported that B_6O-materials with oxide additions can be hot pressed or densified by FAST/SPS up to densities of more than 98%. The resulting materials showed improved fracture toughness with a slight reduction in hardness, as compared to pure B_6O materials [11-15]. Microstructural investigation revealed that the material densify predominantly via liquid phase assisted sintering. The development of SPS (Spark Plasma Sintering,) or FAST (Field Assisted Sintering Technology, FCT Systeme GmbH, Germany) offers the possibility of fast densification of materials. Typical sintering cycles are counted in minutes and not in hours as for standard hot pressing. This offers new possibilities for effective densification of B_6O with minimal decompositions. In this paper, the densification behaviour of Y_2O_3/Al_2O_3-doped B_6O was evaluated and the resulting microstructure and mechanical properties were investigated.

2. Experimental

The starting B_6O-powder was produced in laboratory scale as described elsewhere [14]. The chemical composition of the B_6O powder was determined by ICP-OES. The following cation impurities were determined: Fe = 0.081 wt%, Cr = 0.077 wt%, Al = 0.047 wt%, Mg = 0.12 wt%. The mean grain size of the starting powder was 0.5 μm. The powders used beside B_6O were Al_2O_3 (AKP50, Sumitomo Chemicals, Japan) and Y_2O_3 (Grade C, HC STARCK, Germany). The powder mixing was carried out in a attrition mill with ethanol as solvent and alumina milling balls (1–2 mm, 99.6% pure Al_2O_3). After milling, the suspension was dried using a rotavap.

Consolidation was carried out using a FAST HP D25 furnace (FCT Systeme GmbH, Germany) using graphite dies and graphite foils. The graphite foils were coated with a BN suspension to prevent a chemical reaction between the sample and the graphite die/foil. Densification was carried out in Ar and the temperature measurement was performed with an axially

positioned pyrometer obtaining temperature data close to sample center. A heating rate of 50 K/min was chosen. Densification was monitored by recording the piston travel, which was converted into a relative density change, normalizing the end position of the piston at the end of the isothermal dwell time with final density. The piston travel contains a small contribution from the thermal expansion of the system employed. Before characterization all sample surfaces were sand blasted and grounded to remove h-BN and some formed B_4C material adhering to the sample. Cross sections of the materials were polished and analysed with a Field-Emission Scanning Electron Microscope (FESEM, Leo 982) with an EDS system attached to it. The phase composition was determined by X-ray diffraction (XRD, GE Inspection Technologies, Germany, $Cu_{K\alpha}$).

For microhardness testing, a MHT-10 apparatus with Vickers indenter from Anton Paar (Germany) was used. The indentation was held at the highest load for 10 s. Five indentations were made for every material and every load. The high temperature hardness (HV_5) was determined in equipment developed in cooperation with Hegewald & Peschke (Germany) which can measure the hardness up to 1,500°C in vacuum.

From grounded samples with 60 mm diameter and 5 mm height, bending bars of dimensions 3.5 × 4 × 50 mm were cut and fracture toughness (SEVNB method, notch radius = 20–30 μm) and strength was determined by the 4-point technique (40/20 mm span of the supports).

3. Results and Discussion

3.1. DENSIFICATION

Densification with the FAST system was carried out at different pressures (up to 115 MPa) and at various temperatures in Ar atmosphere. Since a non-conductive h-BN lining or coating was used, the densification process can be considered as a fast hot pressing run rather than a typical SPS process, since the latter is characterized by a current that runs through the powder sample during sintering.

The densification curves of pure B_6O materials in comparison to B_6O with oxide additives are given in Fig. 1. The curves show the improved densification behaviour even with the low additive content.

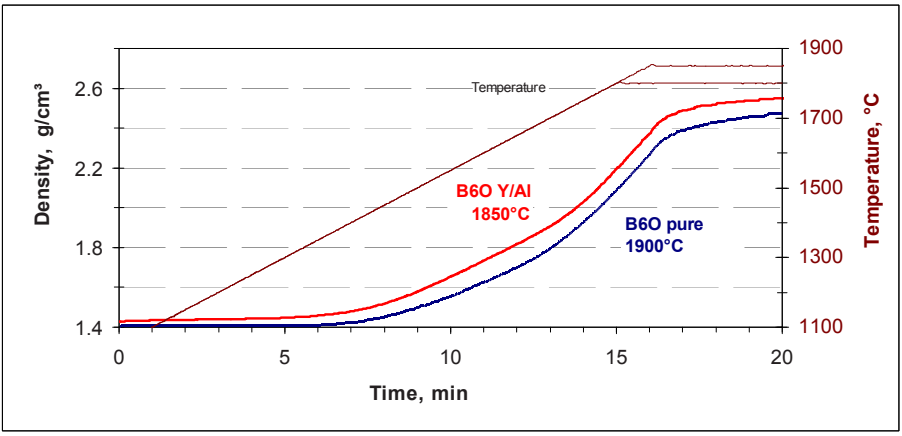

Figure 1. Densification behavior of pure B_6O- and a B_6O-material with Y_2O_3/Al_2O_3 additives (3.07 vol%) at a pressure of 50 MPa.

Densification of the B_6O samples with oxide additives starts at around 1,250–1,350°C, depending on the applied pressure. This onset temperature of densification is lower than observed for undoped B_6O-materials. Moreover, the reduction of the densification temperature by nearly 100 K due to the addition of oxide additives (Fig. 2) strongly improves the reproducibility of the densification process due to less interaction with the dies and decomposition of B_6O. The microstructural features observed indicating that these materials are densified by a liquid assisted process.

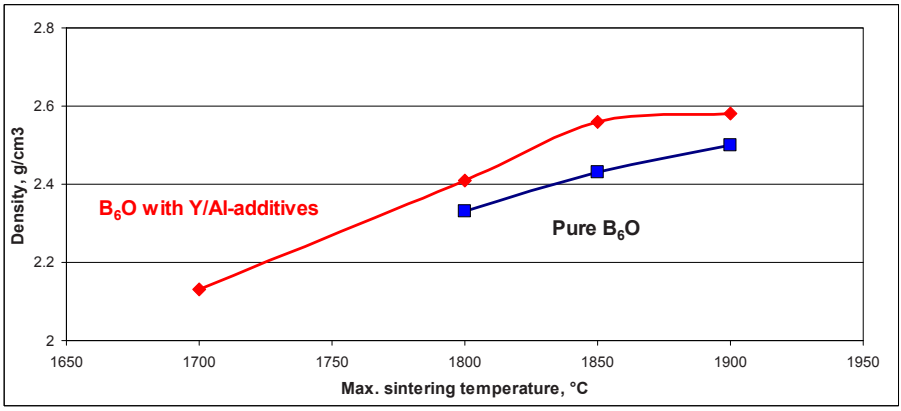

Figure 2. Density of pure B_6O- and a B_6O-material with Y_2O_3/Al_2O_3 additives (3.07 vol%) densified at different temperatures for 5 min and a pressure of 50 MPa.

The densification curves given in Fig. 3 show a strong pressure dependence of the densification. Using a pressure as high as 115 MPa, full densities could be achieved at a temperature as low as 1,700°C. This also explains why during conventional hot pressing (loads of 20–30 MPa) a higher temperature and longer dwell times are required, which in turn are assumed to be the reason why earlier attempts to produce dense B_6O materials showed limited success. The low densification rate during hot pressing also results in less homogeneous materials and degradation of mechanical properties.

3.2. MICROSTRUCTURE

A typical SEM micrograph of the material is shown in Fig. 4. The SEM images revealed a rather homogeneous distribution of the secondary phase, finely dispersed between the B_6O matrix grains. The XRD investigations showed that the grain boundary phase is amorphous. A more detailed analysis of the microstructure evolution by transmission electron microscopy (TEM) analysis confirmed the amorphous state of the grain boundaries [12, 15]. The used Y_2O_3 and Al_2O_3 sintering additives reacted with B_2O_3, commonly present on the surface of the starting powder particles, forming a liquid during densification.

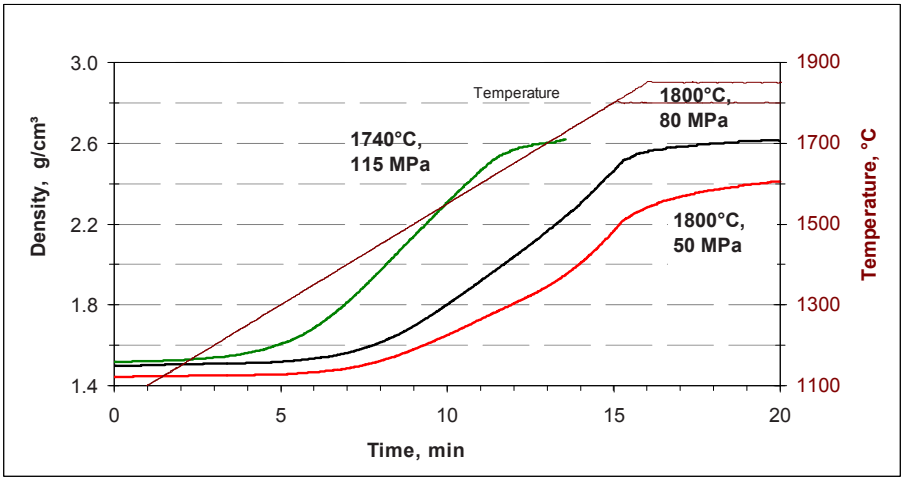

Figure 3. Densification behavior of a B_6O-material with Y_2O_3/Al_2O_3 additives (3.07 vol%) as a function of the applied pressure.

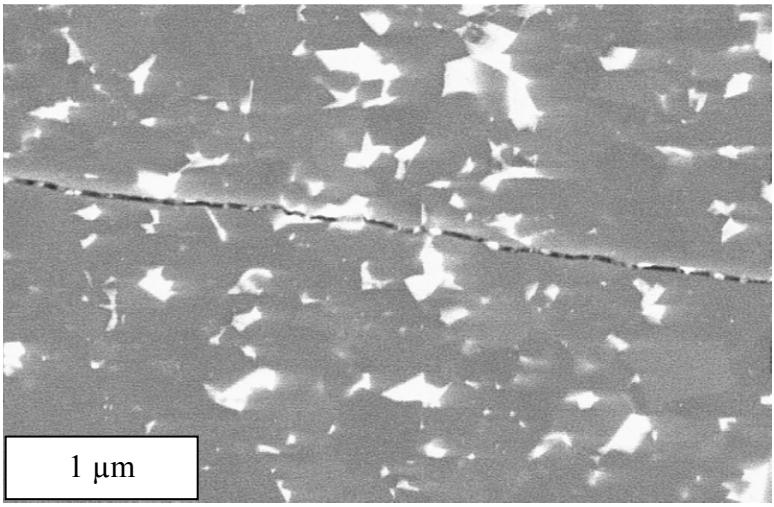

Figure 4. Typical FESEM micrograph of the B_6O-material with sintering additives with the crack introduced by a Vickers indentation (the white areas are the grain boundary phases).

During cooling from sintering temperature, the liquid transforms into the amorphous grain boundary phase. High-resolution TEM of the B_6O grain boundaries did not confirm the assumption of wetted interfaces [15]. Therefore, this material is characterized by triple pockets filled with an amorphous phase, while the interfaces are non-wetted.

3.3. MECHANICAL PROPERTIES

The hardness and fracture toughness values as a function of the additive content are given in Fig. 5. Small additions of oxide additives increase the fracture toughness by 50–100% in comparison to the pure B_6O material. The crack path analysis of the cracks produced by indentations does not show a strong crack deflection (Fig. 4). A possible toughening mechanism could be connected with the glass filled triple pockets, which are homogeneously distributed throughout the sample. These inclusions with low elastic constants may act as crack arresting sites. Additionally, due to different thermal expansion coefficients, internal stress can be generated altering the crack path.

Four point bending strength values of 515 ± 35 MPa were observed for the B_6O-materials with sintering additives. The main fracture origins were located at the surface indicating the problems of the defect free finishing of the materials.

The hardness values ($HV_{0.4}$) of the materials are in the range of 32–35 GPa and only slightly reduces with increasing additive content.

The HV_5 values of 2,001 ± 35 and 1,907 ± 20 were observed at 800 and 1,000°C respectively. This is higher than values observed for commercial cBN cutting tools.

From the analysis of borate glasses [16] it is known that glasses similar to the compositions of the triple junctions soften at 700–800°C. Therefore, a strong reduction of hardness in this area would be expected. This strong reduction is not observed due to the non wetted grain boundaries.

Although the overall hardness of the B_6O materials studied did not reach the potential of B_6O single crystals, these polycrystals are considered attractive candidates for industrial application, in particular, due to the synergetic effect of high hardness and increased toughness.

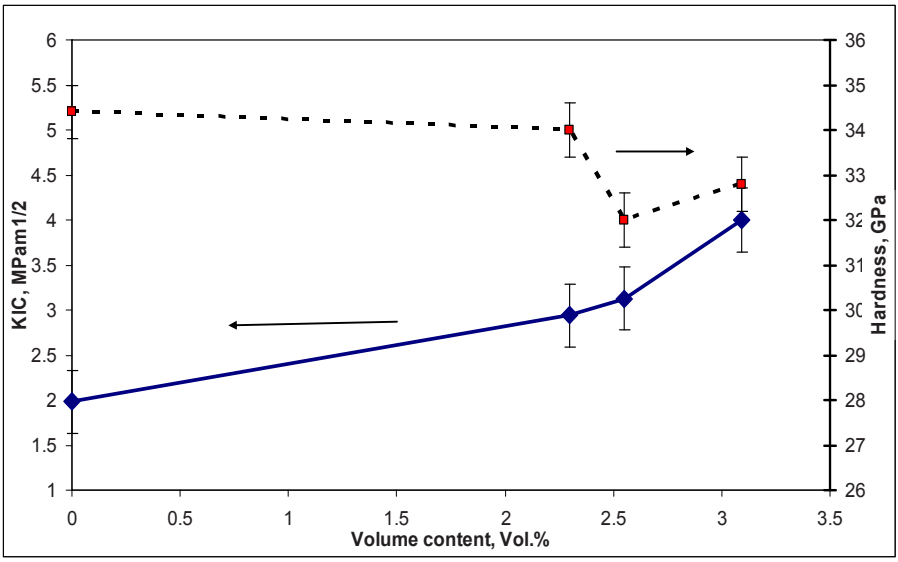

Figure 5. Fracture toughness and microhardness ($HV_{0.4}$) as function of total additive content in FAST/SPS sintered B_6O composites.

4. Conclusions

B_6O materials doped with yttria and alumina were densified via field assisted sintering technique (FAST). Microstructure characterization via SEM/TEM revealed the presence of triple pockets which contain a Y-Al-borate glass. These glass pockets with low bulk modulus could be the reason for the improved fracture toughness recorded, since these areas of residual glass can act as crack arresting sites. The existence of non-wetted grain boundaries result in a less pronounced reduction of the hardness resulting in hardness values (HV_5) of 2,000 at 1,000°C.

The research showed, that densification of B_6O polycrystals with the addition of Y_2O_3 and Al_2O_3 sintering aids is a very promising approach to fabricate dense, homogeneous and reproducible compounds with high hardness (~33 GPa) and improved fracture toughness (~4 $MPam^{0.5}$).

Acknowledgements

The authors acknowledge E6 for financial support of the research.

References

1. D. He, Y. Zhao, L. Daemen, J. Qian, T.D. Shen, and T.W. Zerda, “Boron suboxide: As Hard as Cubic Boron Nitride”, *Appl. Phys. Lett*., 81 [4] 643–645 (2002).
2. P. F. MCMillan “Pressing on: The legacy of Percy W. Bridgman”, Nature Materials, 4, 715–718, (2005).
3. D. Nieto-Sanz, P. Loubeyre, W. Crichton, and M. Mezouar, “X-Ray Study of the Synthesis of Boron Oxides at High Pressure: Phase Diagram and Equation of State”, Phys. Rev. B, 70 [21] 214108 6pp. (2004).
4. H. Hubert, L. A. J. Garvie, B. Devouard, P. R. Buseck, W.T. Petuskey, and P.F. McMillan, “High-Pressure, High-Temperature Synthesis and Characterization of Boron Suboxide (B_6O)”, *Chem. Mater*. 10 1530–1537 (1998).
5. R. Sasai, H. Fukatsu, T. Kojima, and H. Itoh, J. Mater. Sci.; 36; (2001); pp.5339–5343
6. H. Itoh, I. Maekawa, and H. Iwahara; J. Mater. Sci.; 35; (2000); pp.693–698.
7. H. Itoh, R. Yamamoto, and H. Iwahara; J. Am. Ceram. Soc.; 83(3); (2000); pp.501–506
8. C. Ellison-Hayashi, M. Zandi, M. Murray, F.J. Csillag, S. Kuo, “Boron suboxide material and method for its preparation”, 5,135,895, 1992. US Patent.
9. B. F. Goosey, S.C.Anderson, “Method of fabricating boron suboxide articles”, 3,816,586, 1974, US Patent .
10. C. Brodhag, C. F. Thévenot, “Hot pressing of boron suboxide $B_{12}O_2$”, J. Less Comm. Met., Vol. 110, 1986, pp. 1–6.
11. A. Andrews, M. Herrmann, T.C. Shabalala, and I. Sigalas, “Liquid Phase Assisted Hot Pressing of Boron Suboxide Materials”, J. Europ. Ceram. Soc. 28, 1613–1621 (2008).
12. H.-J. Kleebe, S. Lauterbach, T.C. Shabalala, M. Herrmann and I. J. Sigalas, “B_6O: A Correlation Between Mechanical Properties and Microstructure Evolution Upon Al_2O_3 Addition During Hot-Pressing”, J. Amer. Ceram. Soc., 91 [2] 569–575 (2008).
13. M. Herrmann, J. Raethel, A. Bales, K. Sempf, I.J. Sigalas, M. Hoehn, “Liquid phase assisted densification of superhard B_6O-materials” Journal of the European Ceramic Society 29 (2009) 2611–2617.
14. T.C. Shabalala, D.S. Mclachlan, I.J. Sigalas, M. Herrmann, “Hard and Tough Boron Suboxide based Composites”, Advances in Science and Technology”, 45 (2006), 1745–1750.
15. M. Herrmann, H.-J. Kleebe, J. Raethel, K. Sempf,. S. Lauterbach, M.Mueller, I. Sigalas, Field-Assisted Densification of Superhard B6O Materials withY2O3/Al2O3 Addition; J. Am. Ceram. Soc., 92 (2009) 2368–2372.
16. A.L. Applewhite D.E. Day Proc.XVth Intern.Congr.on Glass, Leningrad, 1989, Vol. 2b, 337.

INDEX